Max Planck Graduate Center
mit der Johannes Gutenberg-Universität Mainz

Towards Multi-Ferroic Nanocomposites from Ferroelectric Polymer and Magnetic Nanoparticles

Kumulative Dissertation

zur Erlangung des akademischen Grades eines
„Doctor rerum naturalium“ (Dr. rer. nat.) der Fachbereiche:

08 - Physik, Mathematik und Informatik
09 - Chemie, Pharmazie, Geographie und Geowissenschaften
10 - Biologie
Universitätsmedizin

vorgelegt von

Hamed Sharifi Dehsari

Mainz, February 2019

Acknowledgment

None of the work presented in this thesis would have been possible without the generous support of my supervisor, all my friends, family and colleagues. First of all, I would like to express my deepest gratitude to my supervisor Dr. Kamal Asadi for his guidance, motivation, endless patience and his immense support. When I joined his group, I didn't have any experience regarding the synthesis of inorganic nanoparticles and ferroelectric polymers, but he fully trusted me and gave me the freedom to explore and find my own way throughout this process. I really appreciate that. My sincere thanks to Prof. Dr. Wolfgang Tremel (Johannes Gutenberg University Mainz) for his support, guidance and appraising my work. I am grateful for the fruitful discussions that we had. It was also very delighting for me to see great scientists, such as Prof. Dr. Paul WM Blom and Prof. Dago M de Leeuw. Working with them at Max Planck Institute for Polymer Research (MPIP) is the source of most valued experiences of my scientific life. I am profoundly grateful to them for their everlasting support, guidance and sharing their immense wisdom.

My appreciation also goes to my colleagues and friends at AK-Blom and Humboldt research group at MPIP. You have each provided me with endless joyful moments and encouragement both inside and outside of the laboratory. Special thanks go to the current and former members of Humboldt research group especially Saleem Anwar, Manasvi Kumr and Morteza Hassanpour for their kind help and scientific cooperation. Additionally, I would like to thank my master students, Bora Ersöz, Anielen Halda Ribeiro, Chengcheng Yan and Amr Saad for their assistances in part of this work. Many thanks to my wonderful friends Alexander Kunz, Leona Lingstedt, Kai Philips, Ann-Kathrin Schönbein, Thomas Lenz and Irina Rörich, each of you made a unique contribution to this endeavor. Special thanks to Mohammad Sajedi, Paschalis

Gkoupidenis and Manfered Wagner for joining me always in playing table soccer and real football. The time we spent together playing was one of the highlights of my time at MPIP.

I truly appreciate Dr. Jasper J Michels for the fruitful discussions and considerable help in simulating the results in Chapter 6. I thank Prof. Dr. Gerhard Jakob (Johanes Gutenberg University of Mainz) for the collaboration and kind discussions regarding magnetic data. I thank Maziar Heidari (MPIP), Dr. Richard Anthony Harris (University of University of the Free State, South Africa) and Dr. Davide Donadio (University of California Davis, United State) for their collaboration in simulation part presented in Chapter 3.

Many special thanks to Petra Pausch who was always warm-hearted and helpful with all kind of issues. In addition, I want to express my appreciations to all the technicians in the AK-Blom group at MPIP for their considerable technical support. Especial thanks go to Verona Maus, Michelle Beuchel, Christian Bauer and Frank Keller. Thanks to Christoph Sieber, Gunnar Glasser and Katrin Kirchhoff who taught me how to manage TEM and SEM and spent time in kind discussions on a wide variety of topics. I also would like to thank my committee members, Prof. Dr. Paul WM Blom, Prof. Dr. R. Zentel, Prof. Dr. G. Jakob for their valuable time.

Finally, I would like to thank my dearest family. In particular, thank you to my father, mother and sister. Thank you for enduring difficulties of long distances through my PhD and providing me with unwavering support even from thousands of miles away. Last, but certainly not least, my heartfelt gratitude is extended to my beautiful wife for her love, patience, sacrifice, support and encouragement in all of these years. Her continued support provided light in even the darkest of nights and gave this journey meaning. You're the best. My achievements are your achievements and they could not be possible without all your sacrifices and support throughout the years. I strive to make you all proud.

Abstract

Ferromagnetism and ferroelectricity are seemingly two orthogonal physical properties that may not coexist in a single compound. The discovery of coupling between polarization and magnetization has brought a promise for novel multi-functional materials. Realization of multiferroic materials that exhibit a magneto-electric coupling, *i.e.* the ability to influence the electric polarization by a magnetic field and vice versa, has led to worldwide research interest.

Nanocomposites of organics namely ferroelectric polymers (copolymer of vinylidene fluoride and trifluoroethylene, abbreviated as P(VDF-TrFE)) with inorganic metal ferrite magnetic nanoparticles (MNPs) is an interesting approach to realize a multiferroic material. However, several challenges have limited advancement of multiferroic polymer nanocomposites; I) Thin film processing of the P(VDF-TrFE) polymers leads to the rough and pours structure which results in low functional device yield and high leakage current. II) Synthesize of monodisperse MNPs with optimum size and decent magnetic properties. III) Uniform dispersion of the nanoparticles by preventing agglomeration and phase separation of the MNPs within the P(VDF-TrFE) matrix. Therefore, in realizing the multiferroic polymer nanocomposite thin films, many come into play, which requires systematic addressing.

This thesis provides a detailed study on the synthesis of the constituents of the nanocomposite, *i.e.* MNPs, and addresses the aforementioned challenges regarding thin-film processing, achieving uniform MNP dispersion, and demonstrates coexistence of both ferroelectric and ferromagnetic properties at room-temperature. This work begins with the synthesis of truly monodisperse superparamagnetic (Fe_3O_4) and ferromagnetic ($Co_xFe_{3-x}O_4$) nanoparticles using thermal decomposition technique, and explores the effect of different reaction parameters on physical and chemical properties of MNPs to obtain the optimum synthesis condition and magnetic properties. Then the surface of the MNPs (both superparamagnetic and ferromagnetic) is modified as such to allow for grafting polymer chains from the surface of the nanoparticle by Surface Initiated Atom Transfer Radical Polymerization (SI-ATRP). The polymer shell is chosen so that agglomeration of the modified-MNPs inside polymer matrix is circumvented. The resulting MNPs-P(VDF-TrFE) nanocomposite thin films shows both remanent/saturation polarization and magnetization and electric/magnetic coercive fields at room-temperature.

Table of Contents

List of Figures

List of Tables

Chapter 1

Introduction and Outline

1.1 Motivation

Ferromagnetism, the spontaneous bistable ordering of the spin of electrons in magnetic field, typically occurs in certain metals, whereas ferroelectricity, the spontaneous bistable ordering of electrical dipoles in an electric field, occurs in certain dielectrics. The polarization (magnetization) can be switched by application of an electric (magnetic) field, as schematically shown in **Figure 1.1**.

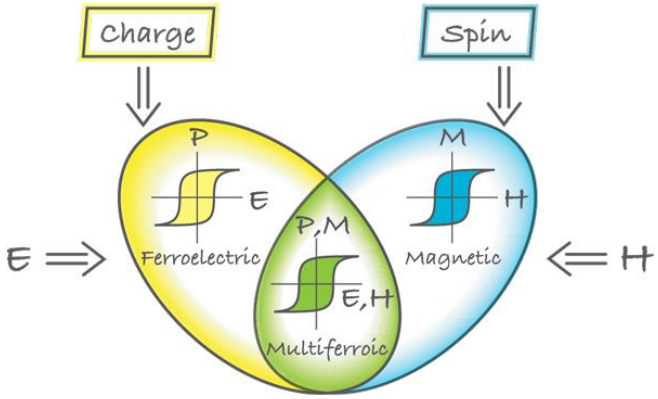

Figure 1.1 Ferroelectric, ferromagnetic and multiferroic materials. The hysteresis loops of the polarization (*P*) and the magnetization (*M*) in a ferroelectric and a ferromagnetic material, as a function of electric and magnetic field, respectively, are represented in yellow and blue. In a multiferroic material, the existing coupling allows to control a magnetic polarization by applying an external electric field, or vice versa. The image has been adapted from reference [1].

Based on the classical Maxwell equations the scientific community was convinced that ferroelectricity and ferromagnetism are two mutually exclusive properties that cannot coexist in a single material. Nonetheless, there can be a weak interaction between ferroelectricity and ferromagnetism. The coupling that allows to control a magnetic polarization by applying an external electric field, or vice versa, the so-called magneto-electric (ME) effect, was noted in the 1960's.[2] Experimental verification turned out to be a challenge, and the field remained static until early 2000.

Multi-ferroics are scarce materials because the mechanisms for ferroelectricity and ferromagnetism have different origins. Ferroelectricity results from relative shifts of positive and negative ions, that induce spontaneous electrical polarization, whereas in ferromagnets ordering of electrons' spin in incomplete shells induces magnetization.[3] It is highly unlikely that these mechanisms are simultaneously operative in a single compound. The field took off again in 2003[4-5] with the discovery of ferroelectric polarization in epitaxially grown thin films of the ferromagnetic $BiFeO_3$[6] and with the discovery of magneto-electric coupling in $TbMnO_3$[7] and $TbMn_2O_5$.[8] The coupling however usually existed at low temperatures which was not useful for practical applications.[9-10] The search for a room-temperature multiferroic is on-going.

Utilizing composite materials of two magnetic and ferroelectric phases is a promising way to obtain high magneto electric (ME) effect at room temperature. ME composites can be categorized into two main groups: ceramic- and polymer-based.[11] Although ceramic-based ME composites reveal ME coefficients three orders of magnitude higher than the ones present in polymer-based ME materials,[12-13] piezoelectric ceramics are dense, fragile and might be limited by reactions at the interface regions, causing higher dielectric losses.[14-15] In contrast, such flaws are absent in highly flexible and non-brittle polymer-based ME nanocomposites and they have facile, cheap, low-temperature, and scalable production methods compatible with industrial requirements.[14-15] Three main types of magnetoelectric polymer-based composites can be found in the literatures: nanocomposites, polymer as a binder, and laminated composites.[14] Despite the lower ME effect in polymer nanocomposites (ferroelectric polymer and magnetic nanoparticles), its flexibility, simple fabrication, easy shaping, possibilities of miniaturization, large uniform

area production, and the absence of degradation at the interface are obvious advantages of ME polymer nanocomposites.[9, 14, 16]

Composites of organics namely ferroelectric polymers with magnetic nanoparticles (MNPs) can be an interesting system for the study of multi-ferocity. The most commonly used ferroelectric is poly(vinylidenefluoride) (PVDF) or its random copolymer with trifluoroethylene (P(VDF-TrFE)), **Figure 1.2**. They are applied in piezo sensors and actuators and are presently being investigated as active components in ferroelectric memory for data storage.[17-19] Metal ferrite MNPs or spinel ferrite (MFe_2O_4 where M is a divalent transition metal, M= Fe, Co, Ni, Zn) is one of the most promising candidates to be applied as a magnetic part in multiferroic nanocomposites due to its ease of synthesis, its low cost and the good magnetic properties.[9, 14] In addition, the magnetic properties of the nanoparticles can be tuned by changing the size, shape or stoichiometry.

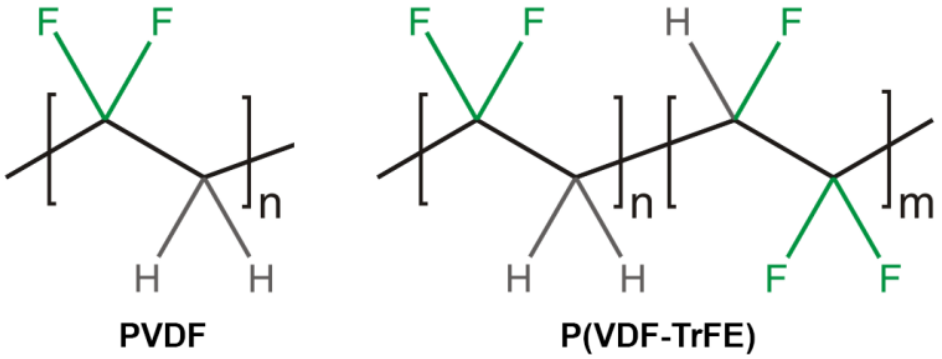

Figure 1.2 Chemical structures of the homopolymer PVDF and the random copolymer P(VDF-TrFE).

The number of papers on organic multiferroic composites however is very limited.[10, 14, 20-24] A possible reason for this hesitation could be the presumption that strain is required for the coupling of the two separated ferroelectric and ferromagnetic phases. In organic composites and thin-films strain is absent; therefore, this field has so far been overlooked. However, there are indications for non-zero coupling.[14] Moreover, the limited previous attempts have not been successful for some reasons. Firstly, solution processing of PVDF polymers at room temperature results in a polymer phase which is paraelectric, not ferroelectric.[25] Beside that, thin film processing of the PVDF polymers leads to the rough and pours structure which results in low functional device yield and high leakage current. Secondly, it is challenging to synthesize

monodisperse magnetic nanoparticles (MNPs) with optimum size, low poly dispersity index (PDI<10%) and decent magnetic properties. Thirdly, the surface of nanoparticles has to be functionalized to allow solution processing of smooth thin film. Agglomeration and eventually phase separation of the MNPs within the P(VDF-TrFE) matrix is the long standing issue. It has been well recognized that the aggregation and inhomogeneity of nanoparticles are the main reasons resulting in deterioration of electrical properties in polymer nanocomposites thin films. In addition, in composite systems the magnetoelectric effect arises from a mechanical coupling between a magnetostrictive and a piezoelectric phase. In order to enhance this coupling the interfacial area between the two phases should be maximized. This can be accomplished with homogenously distributed nanoparticles inside ferroelectric matrix, which have a large surface to volume ratio. Therefore, it is necessary to prevent phase separation and aggregation of MNPs inside the polymer matrix. Surface modification of nanoparticles is an efficient way to avoid aggregation inside polymer matrix and improve compatibility. However, until now surfactants have been used that are not compatible with PVDF polymers.

1.2 Objectives and outline of this work

In developing multi-phase material systems, many variables like nanocomposite processing technique, synthesis and optimization of the constituent phases as well as their implementation into polymer matrix come into play. Only by addressing each step systematically, a new material with novel properties can be developed. The main objective of this research work is to develop a new type of ME polymer-based nanocomposites thin films with ferroelectric polymer and ferromagnetic/superparamagnetic nanoparticles as fillers. Many phases from initial step of synthesis to application are systematically studied and then combined, culminating in these nanocomposite materials.

This work begins with the synthesis of truly monodisperse superparamagnetic (Fe_3O_4) and ferromagnetic ($Co_xFe_{3-x}O_4$) nanoparticles with different size and composition by thermal decomposition technique. Thermal decomposition is a heat-up synthesis technique in which a precursor decomposes in a high boiling point solvent in the presence of surfactants and reducing agent. We systematically investigate the effect of different reaction parameters on physical and chemical properties of MNPs to obtain the optimum condition. Then the surface of the

nanoparticles (both superparamagnetic and ferromagnetic) is modified as such to allow for grafting polymer chains from the surface of the nanoparticle by Surface Initiated Atom Transfer Radical Polymerization (SI-ATRP). In the next step, we outline how the MNPs aggregation inside polymer matrix can be circumvented by grafting polymers of methyl methacrylate (MMA) from the surface of both superparamagnetic and ferromagnetic nanoparticles. We chose PMMA, since it is miscible with VDF polymers (as a ferroelectric phase in the nanocomposite) and thermodynamically stable at all compositions due to the dipole/dipole interaction between the $>CF_2$ groups of P(VDF-TrFE) and the >C=O groups of PMMA and to the hydrogen bonding between the double bonded oxygen of the carbonyl group and the acidic hydrogen of the $–CH_2$-CF_2- group.[25] Then, by modifying thin film processing condition, we obtain smooth and pin-hole free thin films of homogeneously dispersed MNPs inside PVDF or P(VDF-TrFE), as schematically shown in **Figure 1.3**. Finally, the ferroic properties of the hybrid films of MNPs/P(VDF-TrFE) in different loadings are characterized in capacitors. The hysteresis loops are measured and the remanent/saturation polarization, remanent/saturation magnetization and electric/magnetic coercive fields are determined as a function of nanoparticle content.

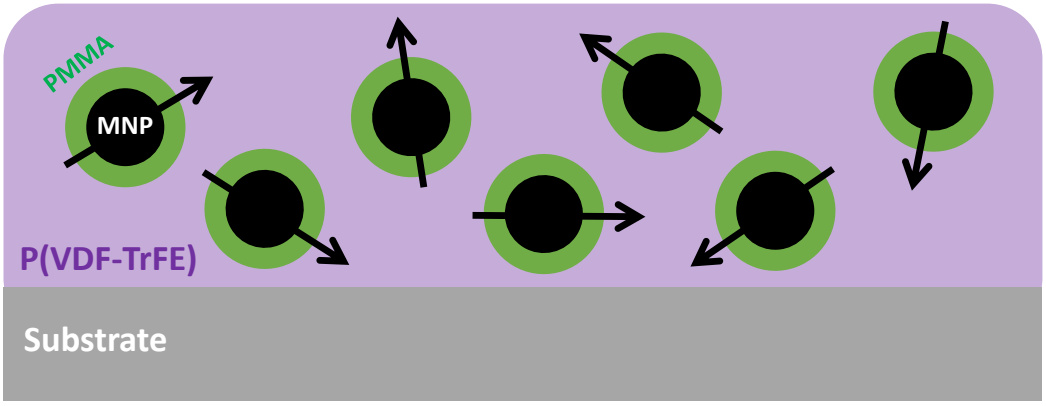

Figure 1.3 MMA-grafted MNPs homogeneously dispersed in a PVDF or P(VDF-TrFE) thin film (not to scale).

This thesis outlines how ultra-smooth P(VDF-TrFE) thin-films can be prepared, how the nanoparticle aggregation problem can be circumvented using chains of MMA as a polymer shell for the MNPs, and how thin films of homogeneously dispersed MNPs in PVDF or P(VDF-TrFE) can be obtained. This dissertation is mainly focused on the development of the required materials for the proposed multiferroic polymer nanocomposite. Hence, majority of the work is centered

about synthesis and modification of the MNPs and proper characterizations of the nanocomposites thin films. This dissertation is organized as follows:

Chapter 2: *Background*

In this chapter the theoretical background regarding multiferroic, ferroelectric, ferromagnetic, synthesis of nanoparticles and surface polymerization are given.

Chapter 3: *Synthesis and Characterization of Iron Oxide Nanoparticles*

In this chapter, we present theoretical and experimental studies on the synthesis of iron oxide nanoparticles using thermal decomposition route. We systematically investigate different synthesis parameters to achieve nanoparticles with well-controlled size and with low polydispersity index (PDI), below 10%. In addition, we have fully characterized the chemical, physical and magnetic properties of the nanoparticles. This chapter contains three different sections, which cover all the aforementioned topics.

In the first section, we present a combined experimental and theoretical study on the influence of the reaction heating rate on crystal growth, size, and monodispersity of iron-oxide nanoparticles. Using numerical calculations based on the classical theory of nucleation and growth, we identify the relative time scales associate with the heating rate and precursor to monomer (growth species) conversion rate as a decisive factor influencing the final size and PDI of the nanoparticles. The results of this section have been published in *Chemistry of Materials* (*DOI: 10.1021/acs.chemmater.7b02872*).

In the second section, we address the effect of precursor concentration on the final size of iron oxide nanoparticles and their magnetic properties. We control the concentration of precursor by carefully varying the amount of solvent, precursor and surfactants. We note that, there are conflicting reports showing both trends of increase and decrease in size of MNPs with increasing precursor concentration. We show that the conflicting observations in the literatures can be explained by the ratio of surfactant to precursor. The results of this section have been published in *CrystEngComm* (*DOI: 10.1039/C7CE01406F*).

In the third section, we present series of experiments in which we experimentally determine a “golden” surfactants molar ratio of 3/1 (oleic acid/oleylamine) at which all synthesis

with different reactants concentration produce truly monodisperse nanoparticles of the same size with remarkably low PDI, less than 8%, without any post synthesis purification steps. With molecular dynamic simulation we show that the binding energy of surfactant to the nanoparticle is maximum at the particular surfactant ratio of 3/1, leading to a better-controlled reaction. The results of this chapter have been published in *Langmuir* (*DOI:10.1021/acs.langmuir.8b01337*).

Chapter 4: *Composition and Size Dependent Properties of $Co_xFe_{3-x}O_4$ Nanoparticles*

In this chapter, we present detailed synthesis of cobalt ferrite nanoparticles with different cobalt stoichiometry and size by changing different reaction parameters. Following an optimization algorithm, we systematically vary all the reaction parameters to determine the lowest nanoparticle size at which the cobalt ferrite nanoparticles exhibited room-temperature ferromagnetic properties. We first show precise fine-tuning of the cobalt stoichiometry and perform a detailed survey of the magnetic properties to determine the optimum range for the cobalt stoichiometry. Next, we thoroughly investigate the influence of variation in different synthesis parameters on the size, polydispersity, and the cobalt stoichiometry, followed by another full survey of the magnetic properties. Moreover, we investigate the origin of the commonly observed bi-magnetic behavior of cobalt-ferrite NPs. The results of this chapter have been published in *Journal of Physical Chemistry C(DOI: 10.1021/acs.jpcc.8b09276).*

Chapter 5: *Surface Modification of the Nanoparticles with PMMA Shell*

In this chapter, first we study the ligand exchange of the surfactant (oleate) with surface initiator of the polymerization in different reaction conditions. Then we grow a poly methyl methacrylate (PMMA) polymer shell from the surface of both iron oxide and cobalt ferrite nanoparticles via SI-ATRP route. We suggest a new method of SI-ATRP in which the polymerization is performed in the bath sonication in order to keep MNPs separated during reaction. We show that, this process provides perfectly dispersed MNPs grafted with well-defined and dense PMMA shell of variable thicknesses. Then, we investigate the effect of different polymerization reaction conditions on molecular weight and poly dispersity index. Moreover, we show that, PMMA improvs the colloidal stability of MNPs by reducing the inter-particle magnetic interactions. Owing to the excellent dispersibility and colloidal stability of the MNP-PMMA, these hybrid nanoparticles can form thin films of the superparamgnetic and

ferri/ferromagnetic successfully by different solution processing methods with a high degree of structural order and wide controllability of the inter-particle distances. Then we comprehensively investigate the effect of polymer shell thickness on the magnetic properties of MNPs. We show that, by changing the thickness of polymer shell, the inter-particle magnetic interaction changes, which affects magnetic properties of MNPs. The results of this chapter are ready for submission to *Advanced Functional Materials*.

Chapter 6: *Thin Film Processing of PVDF Polymers*

In this chapter, we provide detail theoretical and experimental studies on the thin film processing of PVDF polymers. We obtain ultra-smooth and pinhole free thin film and hence improve functional device yield. We highlight the crucial role of solvent and its miscibility with water as an overlooked parameter in obtaining smooth thin film of PVDF and P(VDF-TrFE). The results of this section have been published in *Journal of Material Chemistry C* (DOI: 10.1039/C7TC01495C).

Chapter 7: *Nanocomposite of Ferroelectric Polymers and Magnetic Nanoparticle*

In this chapter we comprehensively characterize nanocomposite thin films based on unmodified and modified MNPs (both superparamagnetic and ferromagnetic) inside P(VDF-TrFE) matrix. This chapter contains two different sections which cover the aforementioned topics.

In the first section, we systematically vary the amount of unmodified MNPs (both iron oxide and cobalt ferrite) in different loadings inside the P(VDF-TrFE) polymers matrix. Then we investigate the microstructure, crystal structure, ferroelectric, polarization switching, dielectric and magnetic properties of the nanocomposite thin films. We show that the non-grafted nanoparticles start to aggregate especially in high loadings leading to huge leakage and extremely low functional device yield. The results of this section have been published in *ACS Applied Nano Materials* (DOI: 10.1021/acsanm.8b01443).

In the second section, we study the same properties of nanocomposites thin films based on the modified MNPs and P(VDF-TrFE). We show that MMA coated nanoparticles and P(VDF-TrFE) are interacting system and miscible. Therefore, the aggregation inside polymer

matrix is effectively prevented leading to remarkably low leakage current and increased functional device yield.

Chapter 8: *Conclusion and Outlook*

This chapter summarizes all results and main conclusions of this dissertation, provides prospective future work, remaining challenges, and forecasts potential future applications.

1.3 References

1. Khomskii, D., Trend: Classifying multiferroics: Mechanisms and effects. *Physics* **2009,** *2*, 20.
2. Ramesh, R.; Spaldin, N. A., Multiferroics: progress and prospects in thin films. In *Nanoscience And Technology: A Collection of Reviews from Nature Journals*, World Scientific: 2010; pp 20-28.
3. Spaldin, N. A.; Fiebig, M., The renaissance of magnetoelectric multiferroics. *Science* **2005,** *309*, 391-392.
4. Cheong, S.-W.; Mostovoy, M., Multiferroics: a magnetic twist for ferroelectricity. *Nat. Mat.* **2007,** *6*, 13.
5. Fiebig, M., Revival of the magnetoelectric effect. *J. Phys. D: Appl. Phys.* **2005,** *38*, R123.
6. Wang, J.; Neaton, J.; Zheng, H.; Nagarajan, V.; Ogale, S.; Liu, B.; Viehland, D.; Vaithyanathan, V.; Schlom, D.; Waghmare, U., Epitaxial BiFeO3 multiferroic thin film heterostructures. *Science* **2003,** *299*, 1719-1722.
7. Kimura, T.; Goto, T.; Shintani, H.; Ishizaka, K.; Arima, T.-h.; Tokura, Y., Magnetic control of ferroelectric polarization. *Nature* **2003,** *426*, 55.
8. Hur, N.; Park, S.; Sharma, P.; Ahn, J.; Guha, S.; Cheong, S., Electric polarization reversal and memory in a multiferroic material induced by magnetic fields. *Nature* **2004,** *429*, 392.
9. Martins, P.; Kolen'ko, Y. V.; Rivas, J.; Lanceros-Mendez, S., Tailored magnetic and magnetoelectric responses of polymer-based composites. *ACS Appl. Mater. Interfaces* **2015,** *7*, 15017-15022.
10. Martins, P.; Costa, C. M.; Lanceros-Mendez, S., Nucleation of electroactive β-phase poly (vinilidene fluoride) with CoFe2O4 and NiFe2O4 nanofillers: a new method for the preparation of multiferroic nanocomposites. *Appl. Phys. A* **2011,** *103*, 233-237.
11. Silva, M.; Martins, P.; Lasheras, A.; Gutiérrez, J.; Barandiarán, J.; Lanceros-Mendez, S., Size effects on the magnetoelectric response on PVDF/Vitrovac 4040 laminate composites. *J. Magn. Magn. Mater.* **2015,** *377*, 29-33.
12. Kulawik, J.; Szwagierczak, D.; Guzdek, P., Magnetic, magnetoelectric and dielectric behavior of CoFe2O4–Pb (Fe1/2Nb1/2) O3 particulate and layered composites. *J. Magn. Magn. Mater.* **2012,** *324*, 3052-3057.
13. Guzdek, P., The magnetostrictive and magnetoelectric characterization of Ni0. 3Zn0. 62Cu0. 08Fe2O4–Pb (FeNb) 0.5 O3 laminated composite. *J. Magn. Magn. Mater.* **2014,** *349*, 219-223.
14. Martins, P.; Lanceros-Méndez, S., Polymer-based magnetoelectric materials. *Adv. Funct. Mater.* **2013,** *23*, 3371-3385.

15. Kulkarni, A.; Meurisch, K.; Teliban, I.; Jahns, R.; Strunskus, T.; Piorra, A.; Knöchel, R.; Faupel, F., Giant magnetoelectric effect at low frequencies in polymer-based thin film composites. *Appl. Phys. Lett.* **2014,** *104*, 022904.
16. Silva, M.; Reis, S.; Lehmann, C.; Martins, P.; Lanceros-Mendez, S.; Lasheras, A.; Gutiérrez, J.; Barandiarán, J., Optimization of the magnetoelectric response of poly (vinylidene fluoride)/epoxy/vitrovac laminates. *ACS Appl. Mater. Interfaces* **2013,** *5*, 10912-10919.
17. van Breemen, A. J.; van der Steen, J.-L.; van Heck, G.; Wang, R.; Khikhlovskyi, V.; Kemerink, M.; Gelinck, G. H., Crossbar arrays of nonvolatile, rewritable polymer ferroelectric diode memories on plastic substrates. *Applied Physics Express* **2014,** *7*, 031602.
18. Naber, R. C.; Asadi, K.; Blom, P. W.; de Leeuw, D. M.; de Boer, B., Organic nonvolatile memory devices based on ferroelectricity. *Adv. Mater.* **2010,** *22*, 933-945.
19. Asadi, K.; De Leeuw, D. M.; De Boer, B.; Blom, P. W., Organic non-volatile memories from ferroelectric phase-separated blends. *Nat. Mat.* **2008,** *7*, 547.
20. Prabhakaran, T.; Hemalatha, J. In *Highly flexible poly (vinyldine fluoride)/bismuth iron oxide multiferroic polymer nanocomposites*, *AIP Conference Proceedings*, AIP: 2012; pp 1309-1310.
21. Martins, P.; Costa, C.; Benelmekki, M.; Botelho, G.; Lanceros-Méndez, S., Interface characterization and thermal degradation of ferrite/poly (vinylidene fluoride) multiferroic nanocomposites. *J. Mater. Sci.* **2013,** *48*, 2681-2689.
22. Jin, J.; Lu, S. G.; Chanthad, C.; Zhang, Q.; Haque, M.; Wang, Q., Multiferroic polymer composites with greatly enhanced magnetoelectric effect under a low magnetic bias. *Adv. Mater.* **2011,** *23*, 3853-3858.
23. Pardo, E.; Train, C.; Liu, H.; Chamoreau, L. M.; Dkhil, B.; Boubekeur, K.; Lloret, F.; Nakatani, K.; Tokoro, H.; Ohkoshi, S. i., Multiferroics by Rational Design: Implementing Ferroelectricity in Molecule-Based Magnets. *Angew. Chem. Int. Ed.* **2012,** *51*, 8356-8360.
24. Ma, J.; Hu, J.; Li, Z.; Nan, C. W., Recent progress in multiferroic magnetoelectric composites: from bulk to thin films. *Adv. Mater.* **2011,** *23*, 1062-1087.
25. Li, M.; Stingelin, N.; Michels, J. J.; Spijkman, M.-J.; Asadi, K.; Feldman, K.; Blom, P. W.; de Leeuw, D. M., Ferroelectric phase diagram of PVDF: PMMA. *Macromolecules* **2012,** *45*, 7477-7485.

Chapter 2

Background

2.1 Multiferroic materials and magnetoelectric coupling

Ferroics are an important type of materials with distinctive properties. Ferroelectricity, ferromagnetism, and ferroelasticity are the three main 'ferroic' order parameters in a material. The brief definition of each ferroics are given in the following:

Ferroelectricity: characteristic of certain materials that have a spontaneous electric polarization (*P*) that can be reversed by the application of an external electric field (*E*).

Ferromagnetism: characteristic of certain materials that have a spontaneous net magnetic moment *M* in the absence of an external magnetic field *H*.

Ferroelasticity: characteristic of certain materials that have a spontaneous strain ε upon application of an external stress σ or phase change when stress is applied.

Materials in which more than one order parameters coexist simultaneously are called multiferroics. **Figure 2.1** shows the relation between the different ferroic order parameters magnetization *M*, polarization *P* and strain ε that response to magnetic field *H*, electric field *E* and stress σ, respectively.[1] In multiferroic materials, all three order parameters may be influenced by all three fields. Thus, in addition to the direct effects of the fields on their respective order

parameter (depicted by the blue, yellow and red arrows in **Figure 2.1**), the following six effects may be observed:

- $H \rightarrow P$ magnetoelectric effect
- $E \rightarrow M$ converse magnetoelectric effect
- $H \rightarrow \varepsilon$ magnetostrictive effect
- $\sigma \rightarrow M$ magnetoelastic effect
- $E \rightarrow \varepsilon$ inverse piezoelectric effect
- $\sigma \rightarrow P$ piezoelectric effect.

Materials showing the existence of both coupling between ferroelectricity and ferromagnetism, *i.e.*, magnetoelectric (ME) materials, are of high interest.[2-3] These characteristics provide the extra degrees of freedom in the materials which allows a control on the magnetic properties by applying an external electric field and vice-versa, providing a possibility to develop new devices based on these materials. Therefore, in the case of ME multiferroic an electric field not only induces polarization but also changes the spin direction, or magnetic field can control magnetization as well as the polarization. This has brought a promise for novel multi-functional data storage devices that can be written electrically and read magnetically, or vice versa.[4] In the following discussion, different types of ME multiferroic materials will be discussed in detail.

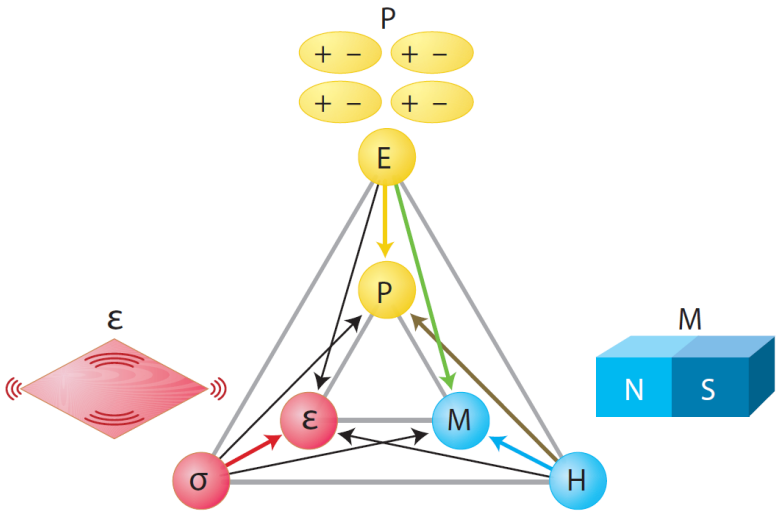

Figure 2.1 In ferroic ordered materials, the electric filed *E*, magnetic field *H*, and stress σ lead to spontaneous electric polarization *P*, magnetization *M*, and strain ε, respectively. In multiferroics, additional interactions are possible due to the presence of at least two ferroic orders. In magnetoelectric multiferroics, *H* may control *P* or *E* may control *M* directly (indicated with green arrows) or indirectly (indicated with black arrows). The image has been adapted from reference [1].

2.2 Types of ME multiferroics

ME multiferroics can be divided into two groups: (a) single-phase multiferroic compounds and (b) multiferroic composite systems.[2, 5-8]

2.2.1 Single-phase multiferroic materials

In general, the ME effect in the single-phase materials stems from the long-range interaction between the magnetic moments and electric dipoles in ordered magnetic and ferroelectric sub-lattices.[3] ME coefficient is an important parameter in the evaluation of multiferroic materials. Generally, the ME voltage coefficient (α_{ME}) is defined as the change in voltage across the sample with the change in applied magnetic field, which can describe the ME response of composite materials as:

$$\alpha_{ME} = \frac{dE}{dH} \qquad (2.1)$$

and it has a unit of $V.cm^{-1}.Oe^{-1}$. The ME coefficient for single-phase ME multiferroic material is very small (≈ 1mV/cm.Oe) and usually exists at low a temperature which is not useful for practical applications (for example in R_2CuO_4, R: Rare earth element, it occurs at 6 K).[3, 9-10] Therefore, practical applications of single phase multiferroics is limited.[11]

2.2.2 Composite multiferroic materials

Due to the remarkable advances in the micro- and nanotechnologies, the research in the field of ME has been directed towards composite ME materials.[5, 12] On the other hand, the ME effect in composites occur extrinsically by combining ferroelectric and ferromagnetic phases.[5, 13] The ME effect in composite materials is the result of the magnetostrictive effect and the piezoelectric effect as given below:

$$Direct\ ME = \frac{magnetic}{mechanical} \times \frac{mechanical}{electric} \qquad (2.2)$$

$$Converse\ ME = \frac{electric}{mechanical} \times \frac{mechanical}{magnetic} \qquad (2.3)$$

The ME nanocomposites can be designed and fabricated by combining different phases at atomic levels. Moreover, different nanostructure types with different connectivity schemes can

be fabricated. Recently research interests were shifted towards ME composite thins films.[6-7] For two phases ME nanocomposites, particulate films type 0-3 where one material is dispersed inside a matrix of the other, layered films type 2-2 where the two phases are layered in bilayer, tri-layer or multilayer, and vertical heterostructures type 1-3 known as nano pillars with one phase as nano pillars embedded in a matrix of the second phase are the most common connectivity schemes. Schematic illustration of these connectivity schemes are shown in **Figure 2.2**.[6, 14-15] In all kinds of ME composites, coupling always takes place at the interface between the ferroelectric and the ferromagnetic material. Hence, coupling strongly depends on the characteristics of the interface between the two phases. Given these considerations, the major area of focus should be on maximizing the interaction between the two constituent phases and hence focus on maximizing the interfacial area between the phases via geometry engineering.

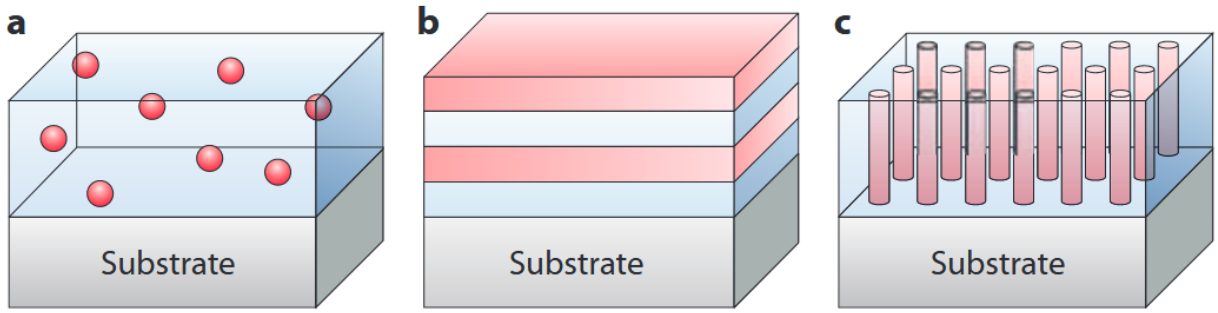

Figure 2.2 Schematic illustration of common connectivity schemes (a) 0-3 particulate, (b) 2-2 laminate and (c) 1-3 nanopillers type composite. The image has been adapted from reference [14].

In general, ME composites can be divided into two main classes: ceramic and polymer based ME materials.[16] Ceramic-based ME composites shows ME coefficients which is almost three orders of magnitudes higher than the ones exist in polymer-based ME composites.[17-18] However, piezoelectric ceramics are expensive, dense, brittle and might be limited by reactions at the interface regions, causing higher dielectric losses.[5, 19] Flexibility plays an important role in device fabrication, which improves the creativity in design. In comparison with the ceramic ME composites, polymer-based ME materials can be easily fabricated by conventional room-temperature processing into a variety of forms, such as thin films or molded shapes, and can exhibit improved mechanical properties.[5, 20] Therefore, polymer-based ME materials are better candidate for flexible and versatile wearable electronic applications. Depending on the interface between the ferromagnetic and the polymer matrix, three main types of ME polymer composites

can be found in the literature: 1) nanocomposite; 2) laminate composites; and 3) polymer as a binder composite as shown in **Figure 2.3**.[5, 21] The first type received the least attention among researchers.[5, 20, 22]

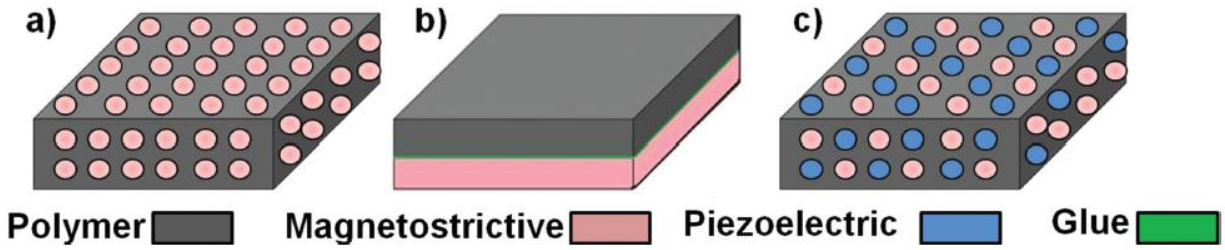

Figure 2.3 Types of polymer-based ME composites: a) nanocomposites, b) laminated composites, and c) polymer as a binder composites. The image has been adapted from reference [5].

In **Table 2.1** we have provided a summary of recent works which have been done regarding polymer based multi-ferroic composites.[5, 15] Composites of organics namely ferroelectric polymers with magnetic nanoparticles (MNPs) is an interesting system for the study of multi-ferroic properties. The highest ME response reported for polymer nanocomposites (42 mV/cm·Oe)[23] is almost four orders of magnitude lower than the ME response (383 V/cm·Oe) reported for polymer laminates.[21] Despite that, its flexibility, simple fabrication, easy shaping, possibilities of miniaturization, large uniform area production, and the absence of degradation at the interface are obvious advantages of ME polymer nanocomposites.[5, 9, 24]

Several challenges have limited research advancement for the case of polymer nanocomposites. First, it is challenging to synthesize truly monodisperse magnetic nanoparticles (MNPs) with optimum size and magnetic properties. Then the agglomeration of MNPs inside the ferroelectric polymer matrix is hard to avoid due to the high surface energy of inorganic nanoparticles. Particularly in the case of high nanoparticle loading and the presence of magnetically induced aggregation of MNPs. It has been well recognized that the aggregation and inhomogeneity of nanoparticles are the main reasons resulting in deterioration of electrical properties in polymer nanocomposites.[25-26] The agglomeration will not only increase loss (leakage) but also give rise to low breakdown strength, particularly when thin films of ME nanocomposites are used. Moreover, it might also reduce the functional device yield. Moreover, in composite systems the magnetoelectric effect arises from a mechanical coupling between a magnetostrictive and a piezoelectric phase. In order to enhance this coupling the interfacial area

between the two phases should be maximized. This can be accomplished with homogenously distributed nanoparticles inside ferroelectric matrix, which have a large surface to volume ratio.

The most commonly used ferroelectric polymer is poly(vinylidenefluoride) (PVDF) or its random copolymer with trifluoroethylene (P(VDF-TrFE)). They are applied in piezo sensors and actuators and are presently being investigated as active components in ferroelectric memory for data storage.[27-29] Metal ferrite MNPs or spinel ferrite (MFe_2O_4 where M is a divalent transition metal, M= Fe, Co, Ni, Zn) is one of the most promising candidates to be applied as a magnetic part in multiferroic nanocomposites due to its ease of synthesis, its low cost and the good magnetic properties.[5, 9] In the following a brief review of the ferroelectric and ferromagnetic properties, introduction about PVDF and P(VDF-TrFE), metal ferrite nanoparticles, their synthesis and surface functionalization are provided.

Table 2.1 Literature review regarding the comparison of the ME coefficient of the developed polymer-based multi-ferroic composits.

Type	Constitution	α_{ME} (mv/cmOe)	Reference
Nanocomposite	P(VDF-TrFE)/$CoFe_2O_4$(NPs)	40	30
	P(VDF-TrFE)/$CoFe_2O_4$(NPs)	41.3	31
	P(VDF-TrFE)/$No_{0.5}Zn_{0.5}Fe_2O_4$(NPs)	1.35	32
	Polyurethane/Fe_3O_4(NPs)	11.4	33
	Polyurethane/Ni (NPs)	6	33
	PVDF/$CoFe_2O_4$ (NPs)	11.2	34
	P(VDF-TrFE)/$CoFe_2O_4$ (NPs)	0.04	23
	Dimines 2CN&OCN/$CoFe_2O_4$(NPs)	0.8	35
	P(VDF-TrFE)/$CoFe_2O_4$ (NPs)	6.5	36
	P(VDF-TrFE)/Fe_3O_4 (NPs)	0.8	36
	P(VDF-TrFE)/$Zn_{0.2}Mn_{0.8}Fe_2O_4$	0.16	36

	Polyurethane/Fe_3C (NWs)	2400	37
	P(VDF-TrFE)/Ni(NWs)	2370	38
	P(VDF-TrFE)/FeO(OH) (nanosheet)	0.4	36
	P(VDF-TrFE)/$SmFeO_3$	45	39
	PVDF/$(Bi_{0.5}Ba_{0.25}Sr_{0.25})(Fe_{0.5}Ti_{0.5})O_3$	18.4	40
	PVDF/$MnFe_2O_4$	6.4	41
	PVDF/$BiFeO_3$-$CoFe_2O_4$	22.18	42
	PVDF/$BaTiO_3$	22.2	43
	PVDF/CNT/$CoFe_2O_4$	16.7	44
	P(VDF-TrFE)/ Terfenol-D	38	45
Polymer as a binder composite	PVDF/Terfenol-D/PZT	42	46
	PEO/Terfenol-D/PZT	1.3	47
	Li^+-PEO/Terfenol-D/PZT	3.2	47
	PMMA/Terfenol-D/PZT	4.8	47
Laminate	PVDF/Terfenol-D/PZT	3000	48
	PVDF/Terfenol-D/PZT	6000	49
	Epoxy/Terfenol-D/PZT	1100	50
	PE/PVDF/Fe_3O_4	753	51
	VER/Terfenol-D/PZT	2700	52
	PVDF/Metglas unimorph	238000	53
	PVDF/Metglas three layers	310000	53

	PVDF/Metglas	21460	54
	PVDF/Metglas	400	55
	PVDF-HPFP/Metglas	120000	56
	Cross-linked P(VDF-TrFE)/Metglas	383000	57
	PVDF/$Ni_{0.5}Mn_{0.5}Ga_{21}$	1240	58
	Gd crystals/P(VDF-TrFE)/Silver conductive epoxy	500	59

2.3 Ferroelectricity

Ferroelectricity was discovered in 1921 by Valasek in the Rochelle salt, sodium potassium tartrate.[60] There are several books[61] and excellent reviews[28, 62-65] dealing with ferroelectricity in different materials and their applications. Here, we present a brief but essential introduction to ferroelectricity in materials. In the following, we discuss the different responses that different types of insulating materials can show in response to an electrical field, starting with dielectric materials and ending with ferroelectric materials.

Dielectrics: dielectric materials exhibit low conductivities. If dielectric materials with dielectric constant, ε_r, fill the volume between two metal electrodes of a capacitor, the capacitance can be written in a simplified way as:

$$C = \frac{\varepsilon_0 \varepsilon_r A}{l} \qquad (2.4)$$

Where A is the area of the plates, l is the distance between the electrodes (or equally the thickness of the dielectric layer) and ε_0 is the permittivity of the vacuum. By the application of an external electric field, the dielectric polarizes. Depending on the frequency of the electrical excitations, there are three different mechanisms: electronic, ionic and orientational polarization.[66] The electronic polarization is due to the influence of the electric field on the electronic cloud. The ionic polarization originates from the displacement of electrical charges while an electrical field is applying. The orientational polarization is due to the rotation of the polar molecules in the direction of the electric field.

The dielectric displacement (D_i) in the capacitor with a dielectric layer, is defined as the total surface charge density induced by application of an electric field (E, V/m) and is the sum of induced spontaneous polarizations (P_i, the dipole moment p per unit volume, C/m^2) inside the material and in a vacuum ($\varepsilon_0 E_i$):

$$D_i = P_i + \varepsilon_0 E_i = \chi \varepsilon_0 E_i + \varepsilon_0 E_i = \varepsilon_0 (1 + \chi) E_i = \varepsilon_0 \varepsilon_r E_i \qquad (2.5)$$

where χ is dielectric susceptibility. Dielectrics are categorized into subclasses of materials based on how the polarization varies with the applied external electric field and how is the polarity of the crystal structure.

Piezoelectrics: If the dielectric is crystalline and the unit cell is not centrosymmetric, a relatively large mechanical strain is induced that is proportional to the applied field E. Therefore, under electrical stress, piezoelectric crystals deform, and a macroscopic dipole appears (inverse piezoelectric effect). The polarization disappears after field removal. Piezoelectrics generate voltage under mechanical stress (direct piezoelectric effect).[65]

Pyroelectrics: Pyroelectrics are a subclass of piezoelectrics, wherein the crystal possesses a unique polar axis, and the material is polarized even in the absence of an external electric field.[67] Spontaneous polarization in pyroelectrics varies with temperature. At temperatures that are high enough, the crystal goes through a phase transition, and spontaneous polarization disappears. Therefore, pyroelectrics show a sharp peak in their pyroelectric current at the phase-transition temperature.[65]

Ferroelectrics: Ferroelectrics are a subclass of pyroelectrics, for which the crystalline polarization can be reversed by an external electric field. Therefore, ferroelectrics possess a permanent electric dipole in their crystalline unit cell, the direction of which can be switched with the external electric field E to produce hysteretic behavior in their polarization response versus E, as shall be discussed below.[65] **Figure 2.4** presents the relationship between the ferroelectric, pyroelectric and piezoelectric materials.

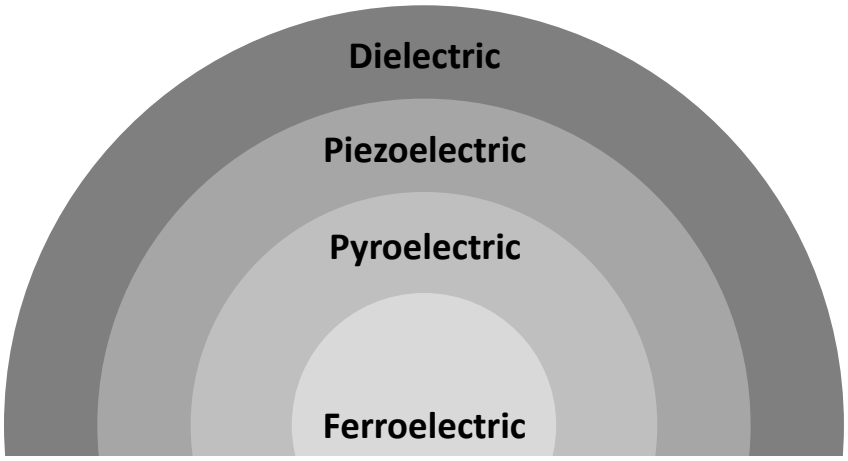

Figure 2.4 Schematic representation of ferroelectric, pyroelectric and piezoelectric materials.

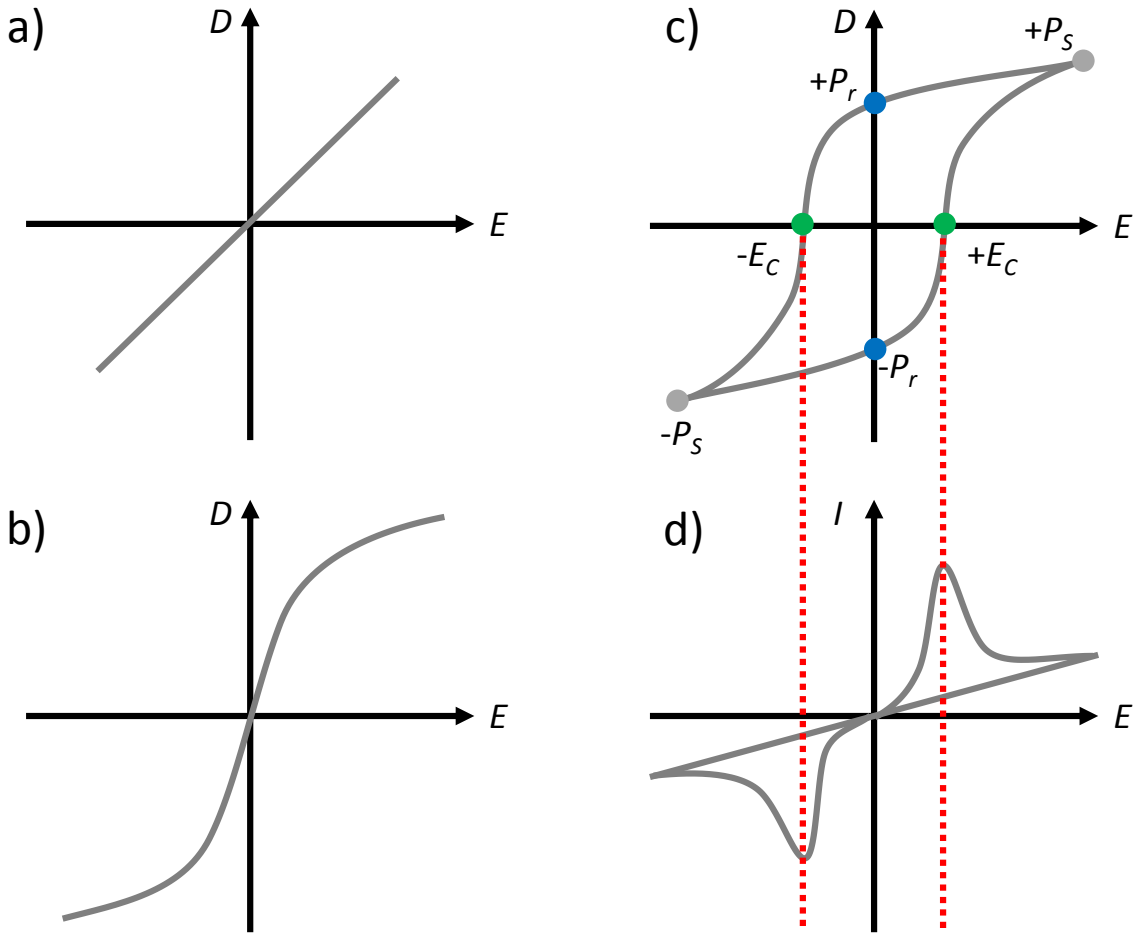

Figure 2.5 Schematic representations of the displacement (or polarization) of (a) an ideal linear dielectric, (b) an ideal nonlinear dielectric, (c) an ideal true ferroelectric with the inner loops at low and intermediate fields, (d) shunt measurements of ideal ferroelectrics, wherein the switching peaks are clearly visible and the maxima coincide with the coercive fields.

Ferroelectric materials show a non-linear hysteretic dielectric polarization as a function of applied electric field (as depicted in **Figure 2.5 c**). This is different from normal dielectrics, which show a spontaneous polarization which disappears after the removal of the field, **Figure 2.5 a** and **b**. The direction of the spontaneous polarization can be switched by applying a reverse external electric field. The amount of electric field which is required to bring down the polarization to zero in ferroelectric materials is denoted as the coercive field, E_C. The coercive field determines how easy or hard it is for the ferroelectric material to switch the dipoles directions. Ferroelectric materials maintain a spontaneous remanent electric dipole moments polarization P_r even under the absence of an external electrical field. Another important characteristic of ferroelectric materials is the saturation polarization P_S. All these previous are shown and labeled on the schematic polarization in **Figure 2.5 c**. Moreover, for ferroelectric materials, instead of measuring charges (Q), the displacement current ($i = \frac{dQ}{dt}$) shows two distinct peaks at the same value of E_C in their current response owing to polarization switching, as schematically shown in **Figure 2.5 d**.[65]

Ferroelectricity is temperature dependent phenomena. Spontaneous polarization exists below a temperature defined as Curie temperature T_C. Above T_C, ferroelectric materials undergo a phase transition to paraelectric phase. The variation of P_r as a function of temperature in ferroelectric materials is schematically shown in **Figure 2.6 a**. Moreover, upon heating, the dielectric permittivity of the ferroelectric phase presents an irregular variation; that increases abruptly around the Curie temperature to decrease again at temperatures above the transition point. The decrease of the dielectric permittivity above the Curie temperature is conventionally described by the Curie-Weiss' law:

$$\frac{\varepsilon_r}{\varepsilon_0} = \frac{C}{T - T_C} \qquad (2.6)$$

where C is a material-specific Curie constant, T is absolute temperature, measured in kelvin, and T_C is the Curie temperature, measured in kelvin. **Figure 2.6 b** schematically depicts the temperature dependence of the dielectric constant around the Curie temperature.

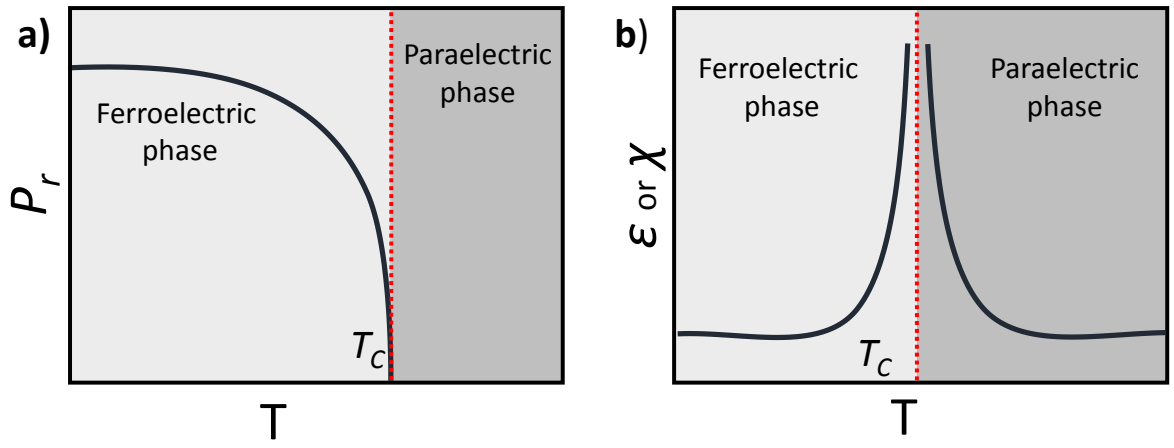

Figure 2.6 (a) polarization and (b) dielectric constant or susceptibility of ferroelectric materials as a function of temperature close to the Curie temperature.

In ferroelectrics, the spontaneous polarization is not aligned throughout the entire polycrystalline. A polycrystalline ferroelectric material contains small regions called domains. Inside each domain, the electrical dipoles are parallel to each other and point to the same direction but their orientation changes from one domain to another. Domains are separated by small regions called domain walls. Domain structures form spontaneously in bulk ferroelectrics below the Curie temperature due to the tendency of the system to minimize its energy. Ferroelectric domains are randomly oriented before applying an external electrical field (as schematically depicted in **Figure 2.7 a**). Whereas, upon applying the electrical field above E_C, the domains orientation will be all in parallel to the direction of the field (**Figure 2.7 b**).

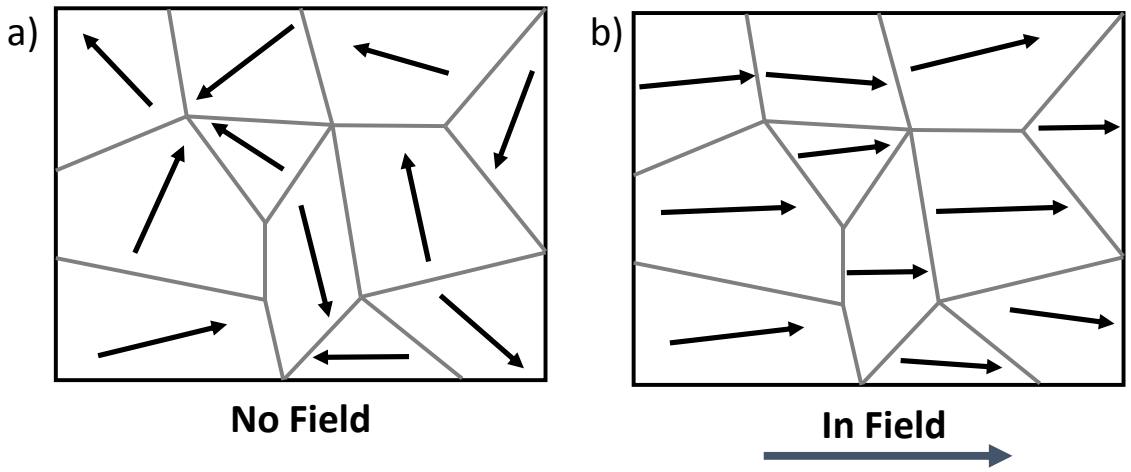

Figure 2.7 Alignment of dipole domains with and without applying electric field.

The dynamics of polarization switching can mathematically be described by the Kolmogorov-Avrami-Ishibashi (KAI) model,[68-70] where polarization reversal starts with the statistical formation of a huge quantity of nucleation sites followed by homogeneous domain growth.[69] The variation in polarization as a function of time, $\Delta P(t)$, is expressed as:[71-73]

$$\frac{1}{2P_r}\Delta P(t) = 1 - \exp(-\sum_i \frac{S_i}{S_0}) \qquad (2.7)$$

where S_0 is the area of the sample and S_i reflects the area of growing sporadic domains. The change of polarization is normalized to $2P_r$. This normalized value equals 1 for complete polarization reversal. The basic assumption of the KAI model is that a domain can expand unrestrictedly after successful nucleation. Therefore:

$$S \sim (v.t)^n \qquad (2.8)$$

where v is a constant domain-wall velocity, t is the time, and n is the Avrami index, which depends on the dimensionality of the domains. The normalized variation of polarization upon switching can then be written as a compressed exponential function:

$$\frac{1}{2P_r}\Delta P(t) = 1 - \exp\left(-\left(\frac{t}{t_0}\right)^n\right) \qquad (2.9)$$

According to the empirical Merz law,[74] the switching time, t_0, is related to the activation field, E_{act}, and can be written as:

$$t_0 = t_\infty \, exp\left(\frac{E_{act}}{E}\right) \qquad (2.10)$$

where t_∞ is the switching time at infinite applied field. The activation field inversely relates with the temperature: $E_{act} \sim 1/T$. Hence, it is straightforward to conclude that polarization reversal in ferroelectric thin films is faster for large electric fields and for higher temperatures. The latter implies a decrease of the activation field.

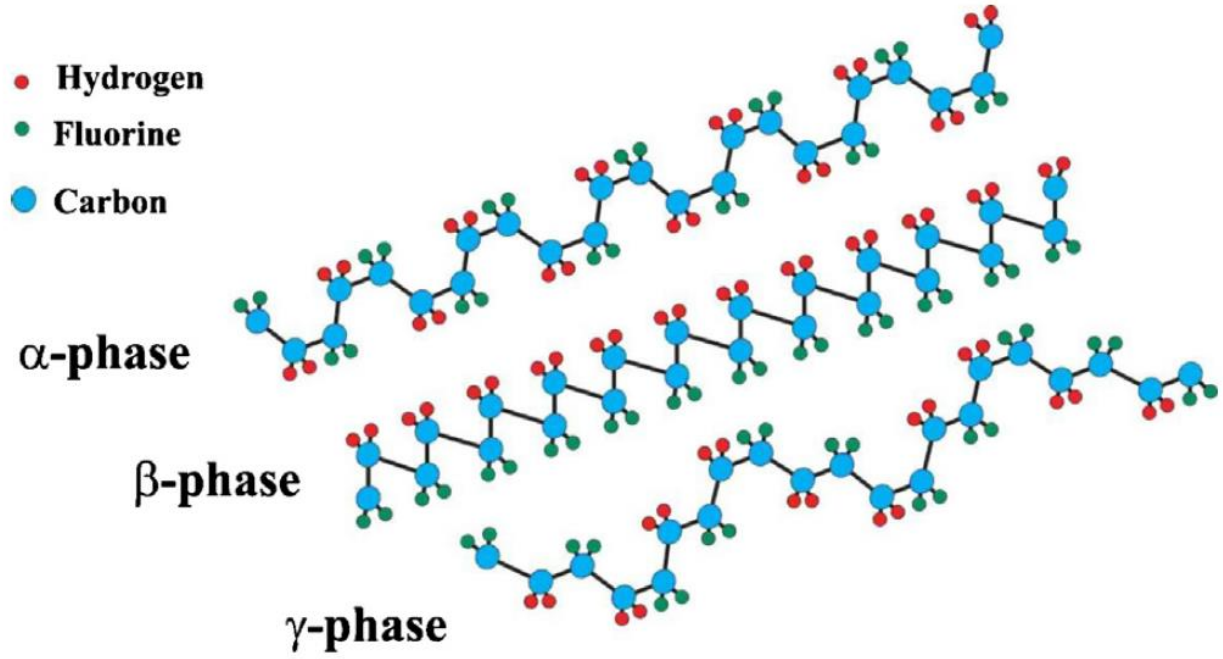

Figure 2.8 Schematic representation of the chain conformation for the α, β and γ phases of PVDF. The image has been adapted from reference [75].

The most widely studied ferroelectric materials are ferroelectric polycrystalline ceramics belonging to the octahedral cubic perovskite structure in the form of ABO_3. Barium Titanate ($BaTiO_3$) was the first perovskite to be discovered back in the mid-1940s with an unusual high dielectric constant; and a decade later, Lead Zirconate Titanate (PZT) was reported. In practical applications, PZT and $BaTiO_3$ have already dominated many fields of smart technologies.[76-77] Ferroelectricity is not limited to inorganic materials. Different organic materials and polymers have shown ferroelectric properties. Among them for instance poly(vinylidene fluoride) (PVDF), nylon, cyanopolymers, polythioureas, and polyureas are well-known.[78] Although their ferroelectric parameters (such as P_r) are poorer with respect to inorganic materials, ferroelectric polymers received considerable attention in the last decades especially due to their processing simplicity, good mechanical properties, flexibility and typically low-temperature fabrication requirements.[79-81] PVDF and its copolymers are the most commonly studied ferroelectric polymers and most widely used. This semi-crystalline polymer shows five distinct crystalline phases related to different chain conformations designed as all-trans (TTT) for the β-phase,

TGTG′ (trans-gauche–trans-gauche) for the α and δ phases and T_3GT_3G' for γ and ε phases.[75, 82] **Figure 2.8** shows the most investigated PVDF phases α, β, and γ-phases.

Many of the interesting properties of PVDF are due to the presence of strong electrical dipole moment of the PVDF monomer unit (5–8 × 10^{-30} C m). The strong dipole moment originates from the electronegativity of fluorine atoms as compared to those of hydrogen and carbon atoms.[75, 83-84] The highest net dipole moment per unit cell and hence most electroactive is the β phase (8 × 10^{-30} C m)[85] due to the optimal alignment of the strong electronegative fluorine atoms with respect to hydrogen and carbon atoms, forming a net dipole moment perpendicular to the polymer chain.[75] The thermodynamically stable phase at ambient conditions is the α phase. The α phase is non-polar because of antiparallel packing of the dipoles within the unit cell and centro-symmetric symmetry of the unit cell.[83, 86-87] Thick paraelectric α-PVDF films can be converted to ferroelectric β-PVDF films by biaxial stretching.[75, 88-89] Another way of inducing β-phase formation is to blend PVDF with a second polymer, like poly(methyl methacrylate) (PMMA).[90-92] The conformation of the polymer chains in γ-PVDF is in between that of the α and β-phases. The γ-phase is ferroelectric but experimentally hardly accessible. Formation typically requires extreme temperature control and high pressure.[93] The δ-phase is a polar version of the α-phase. It can be formed by electro-forming from an originally α-phase bulk sample in a high electric field of about 250 MV/m.[94]

Copolymerization of PVDF with TrFE units introduces sterichindrance and renders formation of the ferroelectric β phase and the all-trans conformation regardless of processing methods. In addition, P(VDF-TrFE) copolymer shows lower Curie temperature below the melting point in comparison with PVDF.[75, 95-96] It has been shown that when the amount of VDF in copolymer is more than 50 Mol %, the copolymer starts to show ferroelectric properties (as depicted in **Figure 2.9**).[97] By increasing the amount of VDF inside copolymer chains, the Curie temperature increase until it reaches to the melting temperature for percentages above 80%.

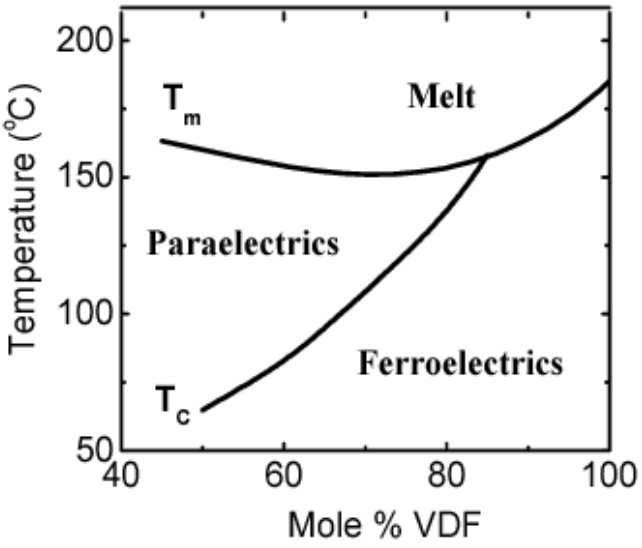

Figure 2.9 Phase diagram of P(VDF-TrFE). The image has been adapted from reference [98].

A schematic of polymer ferroelectric capacitor is shown in **Figure 2.10 a**. For P(VDF-TrFE) a typical value for E_c is 50-70 MV/m and for P_r is 5-8 μC/cm^2 (as depicted in **Figure 2.10 b**). These values depend on the ratio between VDF and TrFE.[82, 99] Generally the higher the amount of VDF inside copolymer, the higher P_r and E_C.

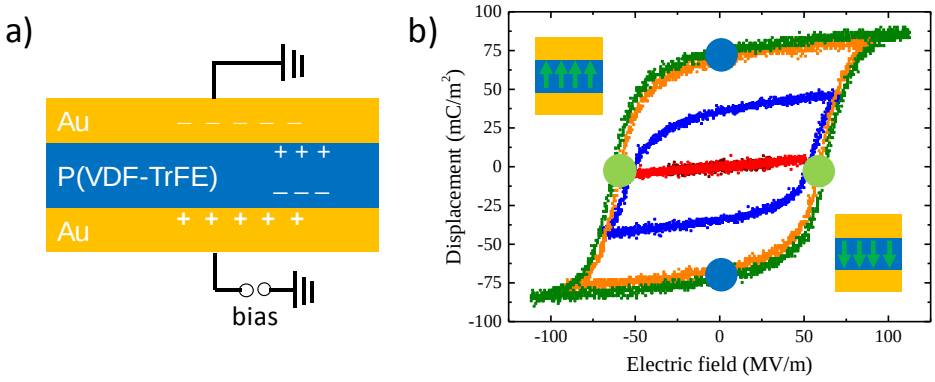

Figure 2.10 (a) Sketch of a thin film capacitor, where P(VDF-TrFE) is stacked between two electrodes. b) The application of an alternating electric field (triangular wave) with sufficient amplitude allows the measurement of a ferroelectric hysteresis loop. The displacement at zero electric field is called remanent polarization, P_r. The field needed to reverse the polarization is called coercive field, E_C; it is extracted at zero displacement in the *D-E* curve.

The mechanism of polarization switching in P(VDF-TrFE) unit cells is based on successive 60° degrees reorientation processes rather than a simple 180° flipping. The reorientation polarization switching of dipoles mechanism was supported with experimental

observations as well as theoretical investigations at the molecular level.[95, 100] **Figure 2.11** shows a schematic illustration of the polarization switching mechanism of P(VDF-TrFE).[15, 95, 100]

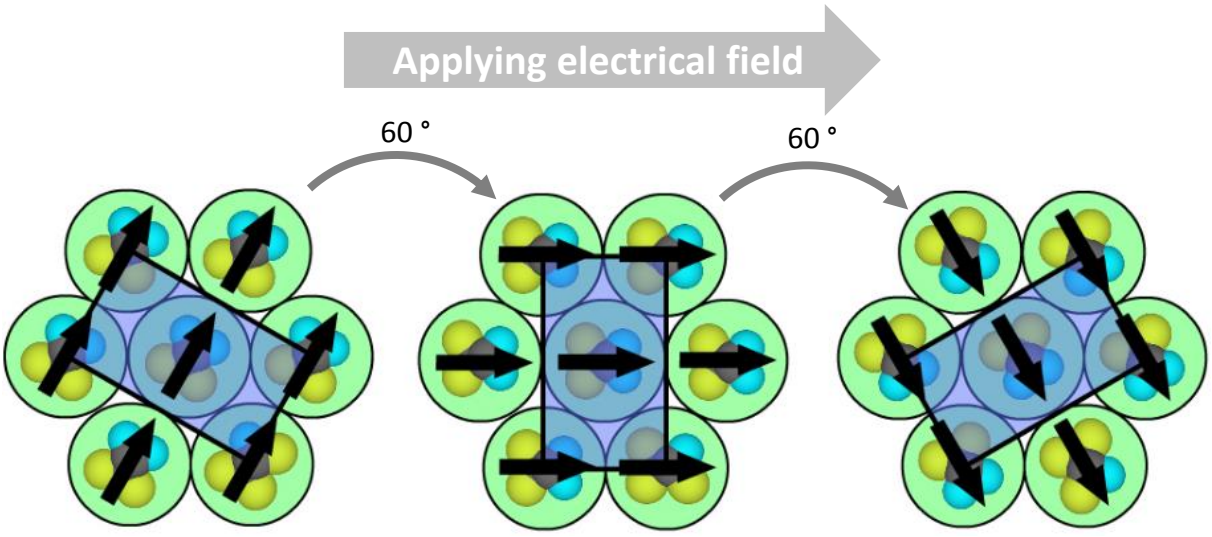

Figure 2.11 Illustration of dipole switching by successive rotation model. The image has been adapted from references [15, 95, 100].

2.4 Ferri/Ferromagnetic

When a magnetic material is exposed to a magnetic field of strength *H*, the magnetic moments response to the field, they align in the direction of the applied magnetic field, and thereby the material is magnetized.[101] The overall induced magnetization, denoted as flux density *B* in Tesla, is given by:

$$\vec{B} = \mu_0(\vec{H} + \vec{M}) \qquad (2.11)$$

with $\mu_0 = 4\pi \times 10^{-7}$ H/m the permeability of vacuum and *M* magnetization is given by:

$$\vec{M} = \frac{\vec{m}}{V} \qquad (2.12)$$

where *m* is the net magnetic moment of volume *V* of the magnetic material.

General speaking, all materials are to some extent magnetic and in a simple classification, their magnetization *M* is linearly proportional to the magnetic field *H* via volumetric magnetic

susceptibility χ , which are often defined by how the magnetic material vary with an applied magnetic field and may be written as:

$$\vec{M} = \chi\vec{H} \qquad (2.13)$$

with χ a dimensionless parameter which is known as magnetic susceptibility.

Substituting **Equation 2.13** into **Equation 2.11**, **Equation 2.11** can be rewritten as:

$$\vec{B} = \mu_0(1+\chi)\vec{H} = \mu_0\mu_r\vec{H} \qquad (2.14)$$

$$\mu = \vec{B}/\vec{H} \qquad (2.15)$$

in which μ_r is the relative permeability of a magnetic material.

The difference between "magnetic" materials and the rest is how they respond to an external magnetic field. The classification considers the orientation of atomic magnetic moments with respect to each other. In the following, the main classes of magnetism are presented (**Figure 2.12**).[102]

Diamagnetism: a material is called a diamagnet if it has no magnetic dipoles in the absence of an external magnetic field and shows a very weak induced dipole in the opposite direction of the applied magnetic field as shown in **Figure 2.12 a**. Therefore, diamagnetic materials show small magnetic responses with the negative magnetic susceptibility (χ<0) and permeability of $\mu \sim 10^{-6}$.[103]

Paramagnetism: **i**n paramagnetic materials, unpaired electrons result in magnetizability upon applying an external magnetic field. The magnetic moments get (partially) aligned parallel to the external magnetic field (as depicted in **Figure 2.12 b**). The thermal energy causes a randomization of the moments of different atoms. Therefore, there is no remanent magnetization after removal of the external magnetic field. Commonly, paramagnetic materials possess $\mu > 1$ and $0 < \chi < 0.01$. The susceptibility of paramagnetic materials is temperature dependent and follows the Curie-Weiss law:

$$\chi_M = \frac{C_M}{T - T_C} \qquad (2.16)$$

where C_M is Curie constant, T is absolute temperature and T_C is Curie temperature. The T_C is a critical temperature above which spin alignment is disordered and the magnetization turns zero. The magnetic response of the paramagnetic materials is relatively weak. The positive magnetic response of paramagnets compared to the negative one of diamagnets is seen in their magnetization versus an applied field *M-H* curves as shown in **Figure 2.12 f**.

Ferromagnetism: ferromagnetic materials are characterized by their spontaneous magnetization regardless of the absence or presence of an external magnetic field. The magnetic moments are aligned parallel in one specific direction depending on the crystal structure as depicted in **Figure 2.12 c**. In ferromagnetic materials, the magnetic moments align in parallel, giving rise to very high susceptibility and remanent magnetization. **Figure 2.12 g** shows a typical *M-H* hysteresis loop of ferromagnetic materials. By applying a sufficiently large DC magnetic field, the magnetic spins become aligned in the field direction and the magnetization reaches a plateau, the so-called saturation magnetization M_S. By decreasing the H value to zero, spins start to relax and do not any longer follow the field and thereby the net magnetization drops to a residual magnetization denoted as remanent magnetization M_r. Eventually, to reach zero magnetization, a magnetic field in the opposite direction has to be applied. The magnitude of the requiring field is called coercivity H_C which depends on both structural features such as size, shape, vacancies, impurities, or grain boundaries and intrinsic properties including crystalline anisotropy, etc. of the investigated material. The coercivity is given by:

$$H_C = \frac{H^+ - H^-}{2} \qquad (2.17)$$

with H^+ and H^- being the positive and negative coercivities.

Ferrimagnetism: the difference between ferrimagnet and ferromagnetic materials is related to the alignment of adjacent dipoles. In ferrimagnet materials, in the absence of a magnetic field, weaker magnetic dipoles lined up antiparallel to their adjacent stronger dipoles. Thereby, it reduces the net magnetization as depicted in **Figure 2.12 d**.

Antiferromagnetism: antiferromagnetic materials consist of two magnetic sublattices in each the atomic magnetic moments are coupled ferromagnetically, but the magnetic moments belonging to two different sub-lattices are oriented antiparallel. Thus, essentially the net

magnetization of an antiferromagnet is zero. The described mechanism can be seen in **Figure 2.12 e**.

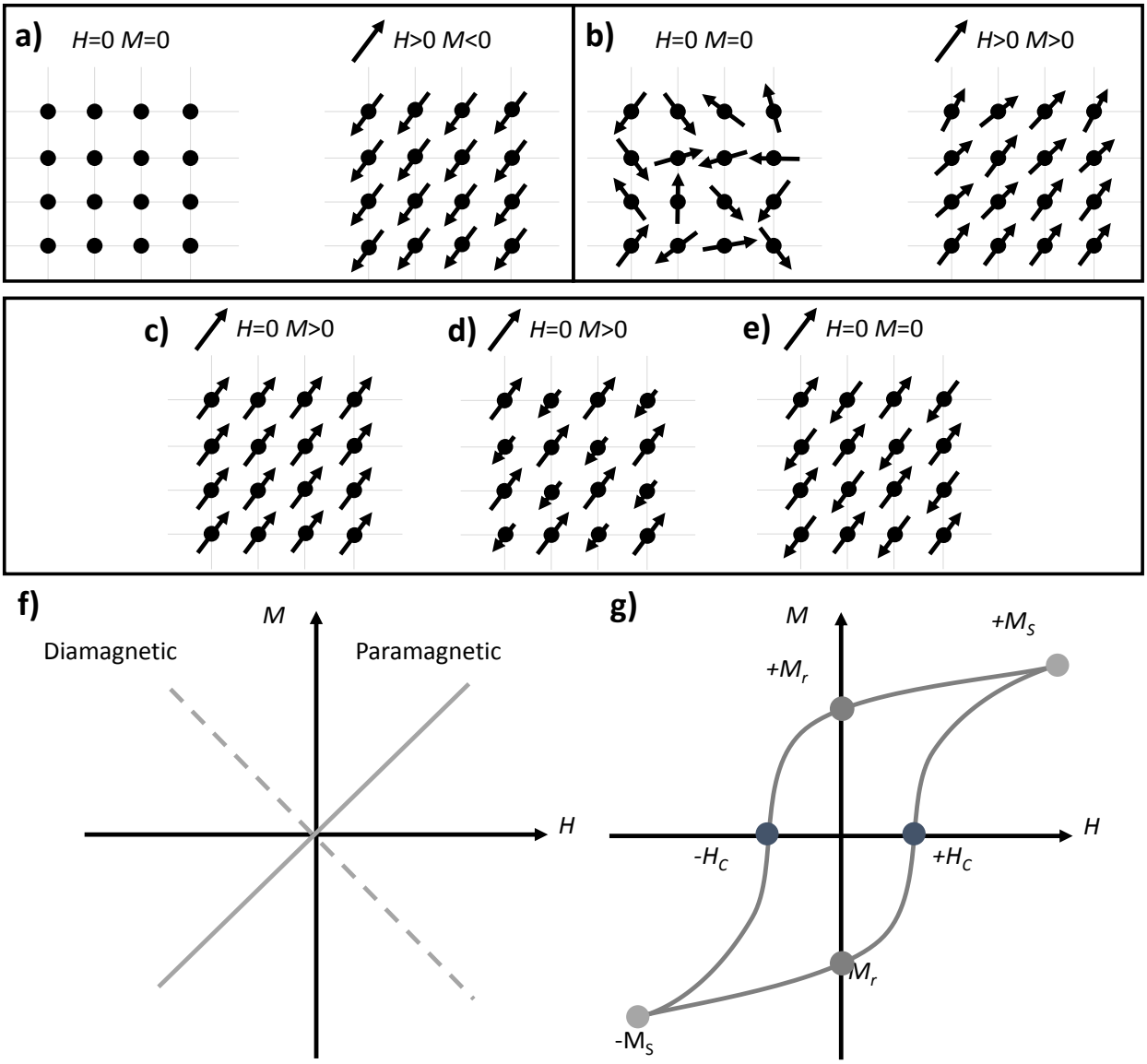

Figure 2.12 Most common types of magnetism, (a) diamagnetic, (b) paramagnetic, (c) ferromagnetic, (d) ferrimagnetic, (e) antiferromagnetic [104]. A typical *M-H* hysteresis loop of a (f) diamagnet, paramagnet and (g) ferromagnet.

Magnetic nanoparticles have received considerable interest not only because of their fundamental scientific interest,[105] but also due to their promising properties.[106-126] When MNPs experience an external magnetic field in equilibrium, the total magnetization points in a direction

in which the minimum anisotropy energy is achieved.[127] The magnetic anisotropy energy, being assumed uniaxial for spherical particle, is given by:

$$E_A = KVSin^2\theta \qquad (2.18)$$

with *V* the magnetic core volume, *K* the effective anisotropy coefficient and θ the angle between the magnetization easy axis (tendency of the magnetization in MNPs in a certain crystallographic direction known as the magnetization easy axis) and magnetic moment. The term *KV* in is recognized as the anisotropy energy barrier.

The magnetization of MNPs is affected by two general types of anisotropy: bulk and surface. The most common sorts of the bulk anisotropy in nanomaterials are magnetocrystalline and shape anisotropy. The magnetocrystalline anisotropy is an intrinsic property of a material independent of its shape. In polycrystalline particles, containing some primary crystallites oriented in different directions, tiny net magnetocrystalline anisotropy is expected due to averaging over all directions. The shape anisotropy, also known as the magnetostatic anisotropy, is the anisotropy of a magnetic material, which depends on its shape. For spheroidal magnetic nanoparticles, the shape will lead to a magnetization process, which is intrinsically uniform in all directions. On the other hand, non-spherical magnetic materials magnetize easier along the long axis than along a short one. The surface to volume ratio for nanomaterials is much higher than in the case of their bulk counterpart. In such cases, the coordination environment of the atoms on the surfaces is significantly lowered compared to the bulk volume of the material.[128-129] This is known as surface anisotropy. The relation between the effective *K*, bulk K_b and surface K_S anisotropies per unit volume for spherical particles can be described using a phenomenological model given by:[103, 130]

$$K = K_b + \frac{6}{d_c}K_S \qquad (2.19)$$

The surface anisotropy plays a crucial role in the magnetization of MNPs especially for smaller MNP due to the higher surface to volume ratio.[127]

In general, for an interacting MNPs, extra energy factor introduces in the expression of the anisotropy energy barrier (E_A):

$$E_A = KVSin^2\theta + E_d + E_{ex} \qquad (2.20)$$

where E_d and E_{ex} are energy factors describing the interparticle interactions and exchange interaction energy, respectively.[128, 131-133] For a magnetic system of single-domain particles, the energy corresponding to the dipole–dipole interactions can be expressed as:

$$E_d = -\frac{\mu_0 m_0^2}{4\pi d^3} \qquad (2.21)$$

According to the above equation, increasing the distance between MNPs (d) results in the reduction of the strength of the dipolar interaction. Thereby, decrease of the anisotropy energy barrier (E_A).[128]

Similar to ferroelectric materials, the spatial regions in bulk magnetic materials in which the spins are aligned parallel to each other are known as magnetic domains. MNPs can be categorized into two general groups: single and multi-domain particles. The domain walls form due to the energy competition between magnetostatic energy, depending on the size of nanoparticles, and the domain wall energy depending on the inter-domain areas. This means that a new domain wall forms when the cost of the magnetostatic energy is larger than the domain wall formation. Therefore, the bigger the particle size, the higher the chance to form further domain walls. On the other hand, when the particle size drops below a certain limit, the energy of the formation of a new domain wall will be higher than the magnetostatic energy of a single domain-particle and thus being single-domain is energetically more favorable.

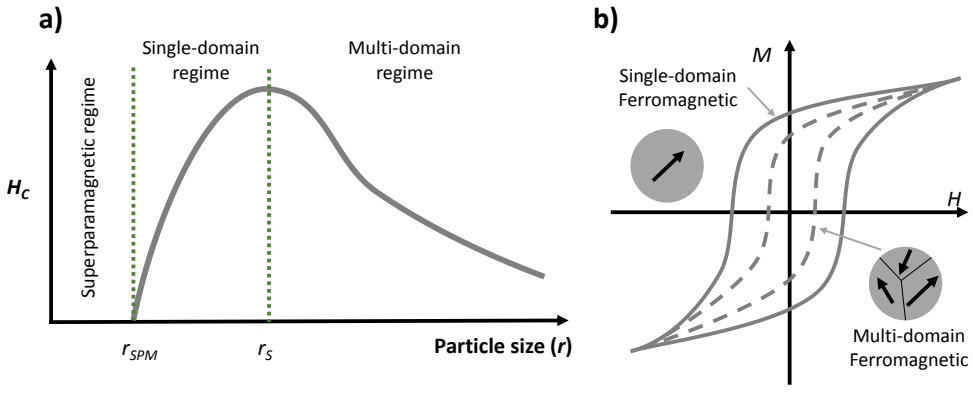

Figure 2.13 (a) Size dependent coercivity in single and multi-domain and superparamagnetic particles and (b) *M-H* hysteresis loops of single and multi-domain ferromagnetic materials.

The dependence of the coercivity H_C on the particle size is depicted in **Figure 2.13 a**. When the particle size is below so-called superparamagnetic size (r_{SPM}) there is no H_C. By further increasing the size of particles, H_C starts to appear and increases by increasing particle size and at specific particle size (r_S) it reduces. Different magnetization responses (H_C) originate from the fact that a much higher energy is required to homogeneously rotate the spins in single domains than in multi-domains due to the presence of domain walls (as depicted in **Figure 2.13 b**).[102, 134-135]

The superparamagnetism appears when the anisotropy energy barrier E can be overtaken by thermal fluctuations and consequently, its condition is given by:

$$E = 25k_BT_B \qquad (2.22)$$

where k_B is the Boltzmann constant and T_B is the blocking temperature. Superparamagnetism depends strongly on temperature. Above a certain temperature known as the superparamagnetic blocking temperature T_B and in zero magnetic field, the thermal fluctuation destroys the magnetic ordering and therefore the net magnetization is zero. The superparamagnetic blocking temperature T_B is the temperature at which the maximum magnetization is achieved in the zero field cooled (ZFC) magnetization branch. Typical field cooled (FC) and ZFC magnetizations for superparamagnetic nanoparticle is shown in **Figure 2.14**. It is reported that this temperature for magnetic nanoparticles depends on the applied field, inter-particle interaction (dipole-dipole) and to a much higher extend on the particle size distribution.[136] Therefore ferri/ferromagnetism occurs at T < T_B < T_C and superparamagnetism for T_B < T < T_C.[137]

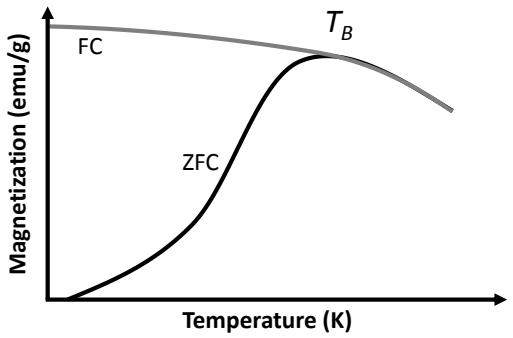

Figure 2.14 FC and ZFC magnetization curves.

Metal ferrite MNPs or spinel ferrites are among the most promising candidates to be applied in industrial scale due to their ease of synthesis, its low cost, its biocompability and the good magnetic properties. The general chemical formula of spinel ferrites is MFe_2O_4 (where M is a divalent transition metal, M= Fe, Co, Ni, Zn) and their crystal structure can be described as a closed-packed arrangement of the voluminous oxygen ions with the cations distributed over the 64 tetrahedral and 32 octahedral sites. When the oxygen ions arrange in a faced centered closed pack structure thereby defining two types of interstitial sites: tetrahedral and octahedral, respectively. There are 32 octahedral sites and 64 tetrahedral sites, respectively, When 1/8 of the tetrahedral sites are occupied with the smaller Fe^{3+} cations and 1/2 of the octahedral interstices are occupied by the M^{2+} ions, the structure of the ferrite is called normal. When the divalent ions swap up with half of the trivalent Fe^{3+} species the structure is called an inverse spinel.[138]

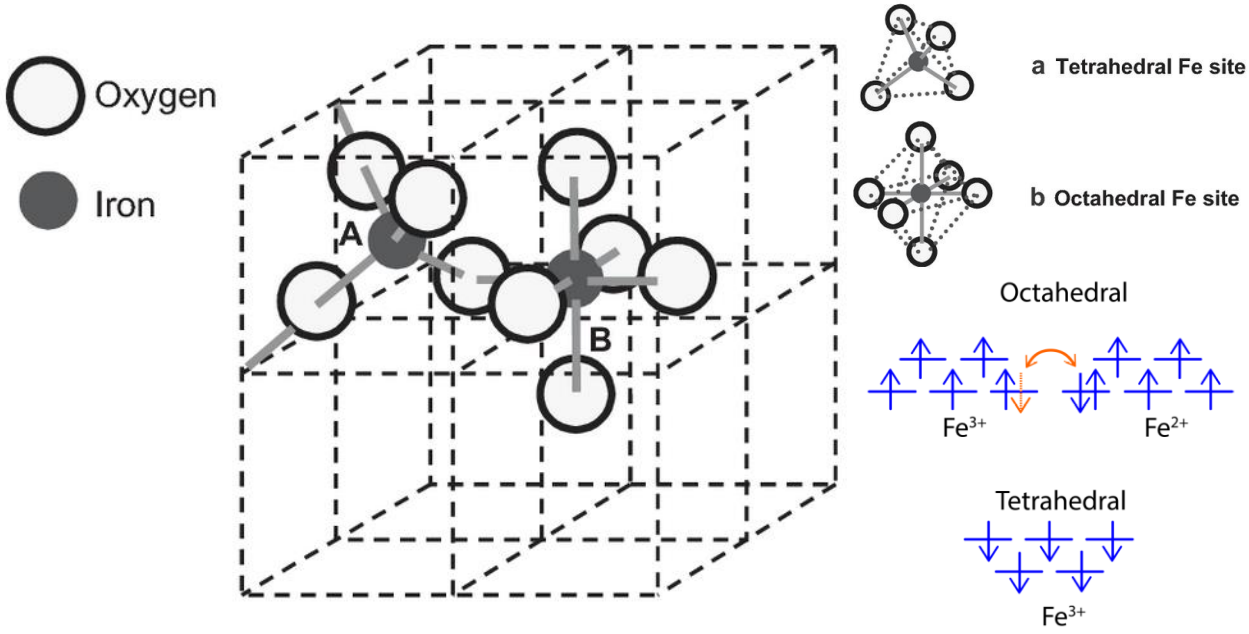

Figure 2.15 Inverse spinel structure of magnetite (Fe_3O_4) and electron states of magnetite. Arrows depict spin of electrons. The image has been adapted from references [139].

The most well-known metal ferrite MNPs is iron oxide. Iron oxide can be found in four different phases in the nature including $Fe_{1-x}O$ (wustite), α-Fe_2O_3 (hematite), γ-Fe_2O_3 (maghemite) and Fe_3O_4 (magnetite). The most common iron oxides are magnetite and maghemite. The physical properties of them are listed in **Table 2.2**.

Magnetite and maghemite have the same crystal structure. The iron and oxygen ions form a face-centered cubic crystal system, and the oxygen ions are in the cubic close-packed arrangement. Magnetite has an inverse spinal structure, and Fe^{3+} ions occupy all the tetrahedral sites and both Fe^{3+} and Fe^{2+} ions occupy all the octahedral sites. Maghemite has a spinel structure. Differing from magnetite, vacancies exist in the octahedral sites in maghemite, and Fe^{3+} ions occupy two-thirds of the sites.[138, 140] The magnetic properties of the ferrites (Fe_3O_4, or Fe_2O_3), the conventional material used in tapes, changes upon nano-sizing.[141-146] The ferrite nanoparticles become superparamagnetic or weak ferro/ferrimagnetic as the particle diameter falls below 25 nm. Increased spin-orbit coupling strength of the divalent ions in octahedral sites enhances magnetocrystalline anisotropy,[126, 147] where for instance an increasing strength can be observed for $Mn^{2+} < Fe^{2+} < Co^{2+}$.[126, 142, 148] Then the incorporation of Co^{2+} in to the ferrite structure ($CoFe_2O_4$) results in an increase in magnetocrystalline energy and hence increase in T_B.[142] This means that magnetic hysteresis and the occurrence of remanence and coercivity can be even observed at room temperature for very small particles in cobalt ferrite. Beside the size of MNPs, in ferrites ($M_xFe_{3-x}O_4$) the composition/stoichiometry also strongly affects the magnetic properties.[110, 142, 146] It strongly depends on the magnetic moment of the M^{2+} cation, e.g. in increasing order for Ni, Co, Fe, Mn, $m = n \cdot \mu_B$ with n= 2, 3, 4 and 5, respectively.

Table 2. 2 Physical properties of iron oxides (magnetite and maghemite) [140].

Properties	Magnetite (Fe_3O_4)	Maghemite (Fe_2O_3)
Density (g/cm^3)	5.18	4.87
Melting point (°C)	1583-1597	-
Hardness	5.5	5
Curie temperature (K)	850	820-986
M_S at 300 K (emu/g)	80-100	60-80
Lattice parameter (nm)	a= 0.8396	a= 0.8346

As we mentioned earlier, compared to bulk ferrite MNPs, surface effects play a more important role. On the one hand, the stoichiometry on the surface differs from the center and thereby the surface can be regarded as amorphous due to non-periodicity of the crystal structure.

Both result in a spin-disordered surface layer ("dead layer") where spin-canting effects occur and magnetic properties deviate. Spin canting means a non-collinear coupling of surface spins, producing magnetically disordered shell. The effect of spin canting is higher at lower temperature due to the collectively frozen state of spins. The saturation magnetization in this layer is lowered due to harder alignment of magnetic moments with respect to each other (higher activation energy due to presence of disorders).[128-129]

2.5 Synthesis of ferrite MNPs

A vast number of chemical and physical routes have been recommended for the synthesis of ferrite MNPs with focus on obtaining different aspect such as monodispersity, reproducibility and high crystallinity, to name a few. The chemical methods usually follow bottom-up approaches. Physical methods are mainly top-down approaches. Around 90% of the publications on the synthesis of ferrite MNPs are based on the chemical routes and around 10% on physical methods. In the following, the most common synthesis techniques will be explained.

Co-precipitation: co-precipitation is considered as the easiest method to prepare MNPs (like Fe_3O_4 or Fe_2O_3). For example, for the synthesis of iron-oxide MNPs, salts of ferrous and ferric iron are dissolved in water and precipitated with alkali.

$$Fe^{2+} + 2\,Fe^{3+} + 8OH^- \rightarrow Fe_3O_4 + 4H_2O$$

The physical and chemical properties of particles strongly depend on the nature of the iron salt (chlorides, sulfates, and nitrates), the ferric to ferrous ions ratio, the reaction temperature, the pH value, the ionic strength of the media, *etc*. Apparently, having a reasonable control over the long listed influential parameters is not a trivial task and thus the reproducibility and robustness of this method are controversial.[137, 149] In the same way, the particles synthesized by this method show a relatively poor crystallinity and imperfect spin ordering on the surface. These phenomena lead to a lower M_S value (30-70 emu/g) compared to the one reported for bulk iron oxide (80-100 emu/g) in literature.[150-151] In addition, the synthesized particles through this method show a large polydispersity distribution, leading to a broad range of magnetic properties (like blocking temperatures) which eventually hinders their usage for some applications. These features limit

the feasibility of using particles, for instance inhomogeneous bioassays where size monodispersity is highly required.[152-153]

Microemulsion: microemulsion is a solution phase synthesis technique, which has been recently used for the preparation of metallic and oxide MNPs with defined size and shape. A microemulsion is a dispersion of two immiscible liquids of an aqueous and oily phase. There are two types of microemulsions; water-in-oil and oil-in-water. The second one, which is the most common one, is known as reverse micelles. In a normal microemulsion synthesis, water microdroplets are formed in a mixture of an oily phase and surfactants. The generated micelles act as micro-reactors, with a certain volume, which can be tuned by varying the ratio between water and surfactant. These microdroplets are surrounded by an interfacial layer of surfactants and contain a certain amount of metal salts acting as a precursor. The metal salt is subjected to a reduction process and eventually, particles are formed inside microdroplets. By adjusting the concentrations of the dispersed phase and surfactant, the size of the droplets can be tuned in the range 1 – 100 nm approximately. The availability of the precursor inside micelles determines the particle growth rate.[154-155] The main advantage of this method is that the reactions can be done economically at ambient conditions within a few hours. However, the adjustment of many parameters renders this method complicated to control. The low yield of this method and the proneness for agglomeration when no additional surfactants are used to speak against the use of the microemulsion method.[156-157]

*Sol-gel: s*ol-gel technique is used as a general scheme for wet chemical synthesis. It consists of the hydrolysis as well as condensation of precursor to a "sol" and the subsequent (poly-) condensation as well as polymerization to a metal oxide network "gel". The rates of hydrolysis and condensation are very important parameters in the method, and it largely influences the properties of particles produced. The lower and more controlled hydrolysis rate can produce smaller particles. The size of the particles is also related to the solvent, concentration, pH, and temperature.[158-159] One of the advantages of this method is the economic synthesis of variously shaped particles with narrow size distribution. The main drawback of sol-gel method is its requirement for an additional annealing step in order to a yield highly crystalline material with high magnetization.[153]

Hydrothermal/solvothermal: A very well investigated synthesis method for ferrite MNP is the hydrothermal method, where aqueous solutions of iron precursors are heated to high temperatures (200°C) in the presence of autogenous pressure (2000 psi). Ferrites are formed either by hydrolysis and oxidation or neutralization of metal hydroxides, where the former is more common. The key parameters in this technique are the selection and concentration of solvent, temperature and reaction time. With this method, size and morphology of particles can be tuned precisely; with a very narrow size distributions are usual. A further plus is a very high crystallinity, yielding excellent magnetic properties. Nevertheless, the use of hydrothermal methods requires special safety measures due to the high pressures in the reaction vessel. Furthermore, reactions can take many hours up to many days.[160-161]

Sonochemical: exposing an aqueous solution of metal salts to the probe sonication produces bubbles, which causes very high local temperature and pressure inside a confined volume upon rapid collapsing. The high power applied to the precursor solution activates nucleation and growth of particles. The introduction of such a high amount of energy can also favor the production of metastable phases. The main advantage of this method is the very fast production of small particles with acceptable size distribution even though the particle size cannot be controlled precisely. The main drawbacks is the low degree of crystallization resulting in weak magnetic properties. In addition, the deficiency in large-scale production makes it an unfavorable method.[153]

Polyol: metal ferrite nanoparticles can be also produced by the reduction of dissolved metal slats (such as iron acetyl acetonate, $Fe(acac)_3$) and direct precipitation in the presence of polyol (such as polyethylene glycol). In this method, the precursor is suspended inside a polyol liquid. Increasing the temperature of solution to the boiling point of polyol makes the precursor soluble in diol. Then it reduces the precursor to form metal nucleuses that finally form metal particles. The particles with the desired size and shape can be produced by controlling the kinetics of the process. The yield and properties of nanoparticles produced by this method depends on the type of polyols, ferrous salts, concentration, and temperature.[162-163]

Thermal decomposition: with this method, a metal organic precursor (like $Fe(acac)_3$) is decomposed in a high boiling point organic solvent (like benzyl ether) at high temperatures in the presence of surfactants (like oleic acid and oleylamine). In some cases reducing agents, such as 1,2-hexadecanediol or oleylamine, are used.[150, 164-166] In order to control size, morphology and particle size distribution, many parameters have to be controlled: concentration[167-169] and nature of the solvent,[145] reaction duration,[170] temperature,[145] ratio of surfactant to the precursor,[168-169] heating rate,[171] ratio between surfactants[172] and etc. By adjusting these parameters, truly monodisperse particles in a broad range of size with a variety of morphologies can be obtained precisely. The crystallization process at high temperatures yields particles with high crystallinity and high magnetic properties. Further advantages of thermal decomposition are the high yield and the scalability of the reaction while using inexpensive standard lab equipments. Besides the control of many parameters, however, usually the reaction should be performed in an inert atmosphere and it requires long reaction times in order to obtain well-defined particles. The yielding synthesized nanoparticles possess a core shell structure, where the highly crystalline core is surrounded by an inner shell of disordered iron oxide (dead layer) and an outer shell consisting of a monolayer of organic surfactant (oleate surfactant). The presence of surfactant makes the MNPs dispersable in the none polar solvent like hexane directly after synthesis.[164] In addition, doping of MNPs with other metals like cobalt is simply possible during synthesis by using the combination of both iron and cobalt precursors with different feed ratios.[142]

By comparing the advantages and drawbacks of all aforementioned methods, thermal decomposition turns out to be the superior method for the synthesis of the desired MNPs.[135, 144, 173] Generally two routes for conducting thermal decomposition experiments exist: hot-injection and heat-up method.[164, 174] For the hot-injection method, a solution which contains the metal-organic precursor is injected into the heated mixture of the remaining reactants with controlled injection rate.[174] Unfortunately, syntheses that employ the well-established hot-injection method cannot be readily scaled, as inherent within this method are a number of insoluble drawbacks as follows. (i) *Reagent mixing time*: it becomes slower and less predictable as the volume of the batch and the consequent injection volume increases. (ii) *Reaction cooling time*: the cooling rate does not scale linearly with reaction volume, hence leading to a scale-dependent cooling time,

which varies the reaction product. (iii) *Practicality*: that typical injection volumes are in the range of 25−50% of the volume of the mother solution. It becomes impractical and less feasible to inject large volumes. (iv) *Reproducibility*: the time taken to inject a reagent often changes from user-to-user and from batch-to-batch. This leads to change in reaction kinetics and hereby hinders reproducibility.[175]

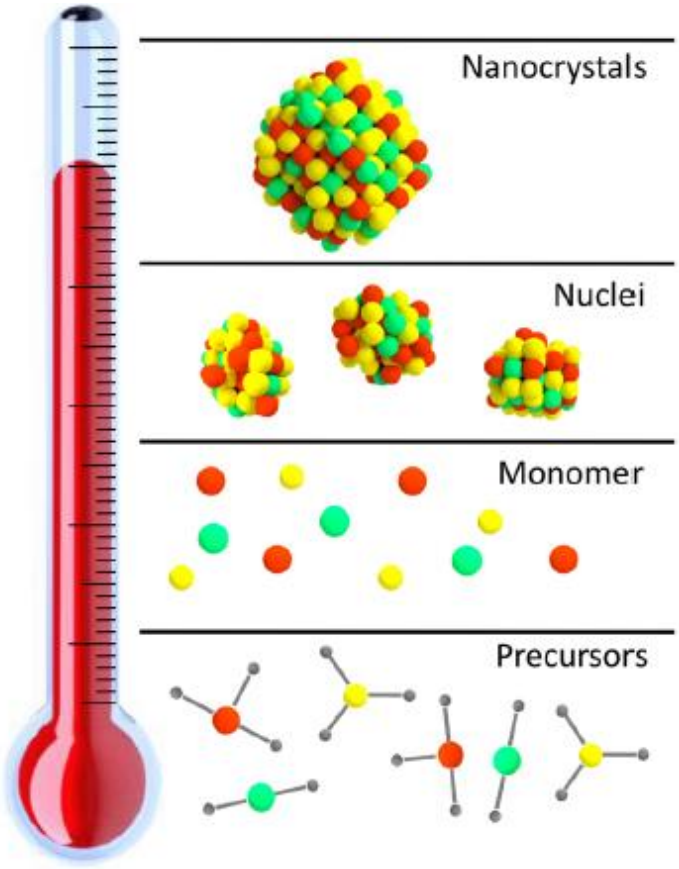

Figure 2.16 Schematic of typical heat-up syntheses method. The image has been adapted from references [175].

The formation of NPs using a heat-up approach avoids all of the aforementioned drawbacks and provides a way to completely control and scale-up syntheses. In contrast, for the hot-injection route, all reactants are already combined before starting the reaction. **Figure 2.16** shows the schematic of the main phases of the NP formation in a typical heat-up synthesis and their relation to the temperature of the reaction vessel. At low temperatures the reaction solution contained precursor and surfactants. Precursor is considered to be the initial source of growth species. By increasing the temperature, these precursors experience an increased thermodynamic

driving force to form monomer. The heating process finally triggers the nucleation of nascent crystallites, with continued heating required to grow these nuclei into mature NPs by growing the rest of monomers.[175] Despite the slightly different experimental procedure of both methods, the principles of nanoparticle formation are the same. Both routes yield particles of similar monodispersity when synthesis parameters are well adjusted.[173]

In the following, the basic theoretical background knowledge, i.e. the classical crystallization theory, for the synthesis of NP will be explained. This includes homogeneous nucleation, growth by kinetically and thermodynamically controlled processes and Ostwald ripening.

2.5.1 Classical theory of nucleation and growth

The theory for the synthesis of monodisperse colloidal suspensions was originally proposed by LaMer & Dinegar in 1950.[176] In their study they showed that, in order to synthesis particles with well-defined size and low poly dispersity, the nucleation and growth processes should occur at two different temperatures. This nucleation and growth concept, later known as LaMer model, has been exploited extensively to design new solution phase syntheses since it was discovered. Based on LaMer model, first, a precursor is decomposed in solution, *e.g.* by thermal activation. This decomposition yields monomers, which are considered as the smallest building units of the final particles. The more precursor gets decomposed, the higher the monomer concentration, *C*, gets, leading to a supersaturation *S* ($S = \frac{[C]}{[C_\infty]}$, where $[C_\infty]$ is equilibrium concentration) of this species (stage I in **Figure 2.17**). When the supersaturation of the monomer is high enough to overcome the energy barrier for nucleation ($C > C_{min}$), burst of nucleation will take place (stage II in **Figure 2.17**). At this point, the solution is supersaturated. As monomer is rapidly consumed during the nucleation event, the concentration of free monomer eventually drops below $[C_{min}]$ and nucleation ceases. For newly formed nuclei, growth occurs by the diffusion of the monomers (stage III in **Figure 2.17**). This step does not last for a long time due to the lack of monomers. In this case, due to the lack of monomer concentration, smaller particles dissolve in order to support the growth of larger particles (Ostwald ripening).

This stage is typically characterized by a broadening of the particle size distribution (stage IV in **Figure 2.17**).

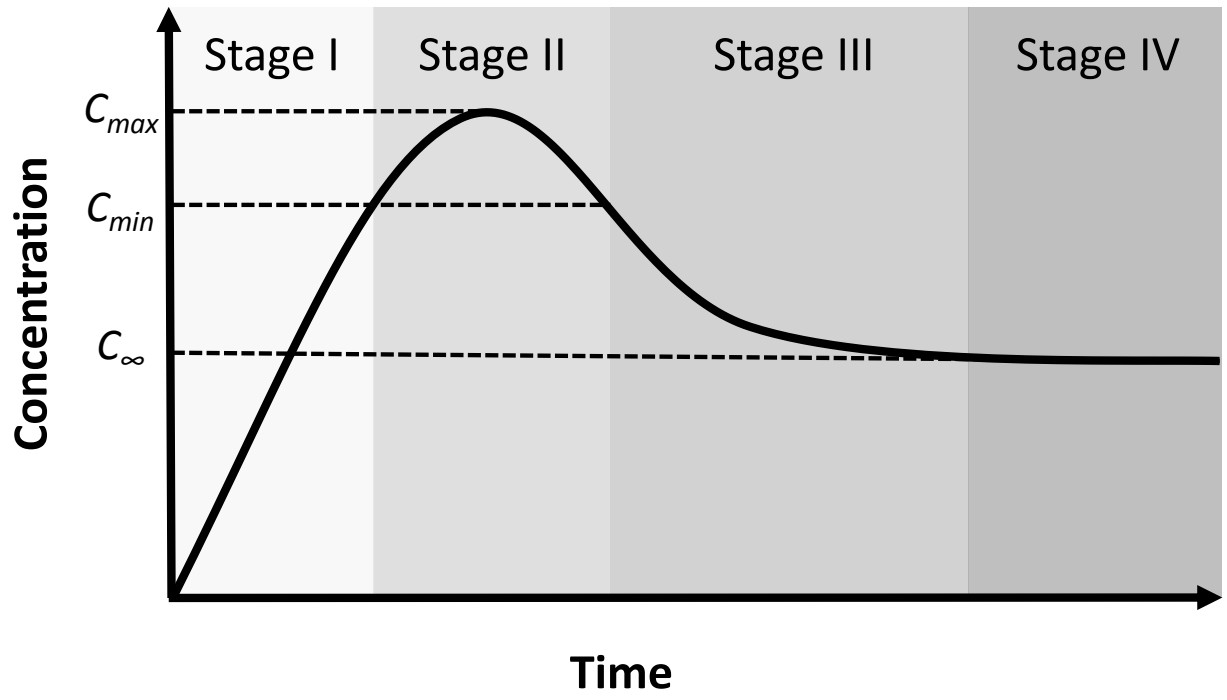

Figure 2.17 Evolution of monomer concentration during heat-up thermal decomposition method. Stages: I: Monomer formation, II: Nucleation, III: Growth, IV: Growth+Ripening.

To gain a deeper understanding of the LaMer model, the theory of nucleation and growth in solution will be reviewed in the following.

Nucleation: nucleation is the process in which nuclei act as templates for crystal growth. Homogeneous nucleation takes place when nuclei form homogeneously inside the phase of reaction. On the other hand, heterogeneous nucleation occurs in the presence of inhomogeneities (such as impurities). In liquid phase, heterogeneous takes place much easier, since a stable nucleating surface is already present and there is no need to form new surface. Homogeneous nucleation is the formation of a new surface surrounding a bulk component. The process of homogeneous nuclei formation can be considered thermodynamically[130, 175, 177-178] by looking at the total free energy of a nanoparticle. In the case of spherical nuclei, the surface contribution (ΔG_S) enhances the free energy of the system according to $\Delta G_S = 4\pi r^2\gamma$, where γ is the surface

energy. Meanwhile, the bulk contribution (ΔG_v) reduces the free energy through $\Delta G_V = -\frac{4\pi r^3 RT}{3V_m}\ln S$, where R, T, V_m and S are the gas constant, temperature, molar volume of a monomer and supersaturation respectively. The total (radius dependent) free energy of the system (ΔG_T) is given by the sum of the surface and bulk terms:

$$\Delta G_T = \Delta G_v + \Delta G_S \qquad (2.23)$$

by replacing the ΔG_S and ΔG_B terms in the equation, the total free energy as a function of the nuclei radius can be given as:

$$\Delta G_T = -\frac{4\pi r^3 RTlnS}{3V_M} + 4\pi r^2\gamma \qquad (2.24)$$

Figure 2.18 depicts a schematic of the surface, bulk, and total free energies for a given standard set of reaction conditions as a function of radius. For very small nuclei, the surface to volume ratio is high. Therefore, the surface term dominates the free energy. However, by increasing the size of nuclei, the bulk free energy term dominates and, as such, ΔG_T rises to a maximum and then declines. Consequently, the critical energy barrier ΔG_N is obtained by inserting $d\Delta G_T/dr=0$ and may be written as:

$$\Delta G_N = \frac{16\pi\gamma^3 V_M^2}{3R^2T^2(lnS)^2} \qquad (2.25)$$

This thermodynamic barrier represents the energy required to form a stable nuclei for a given supersaturation, surface energy, and temperature. The corresponding radius at this maximum is known as the critical radius, r_C, which is given by:

$$r_C = \frac{2\gamma V_M}{RTlnS} \qquad (2.26)$$

Given that a system tries to lower its free energy, existing nuclei with $r > r_C$ will reduce their ΔG_T through growth via accretion of monomer, while nuclei with $r < r_C$ will reduce their ΔG_T by partially or completely dissolving. As such, the critical radius represents the size that divides stable from metastable nuclei.

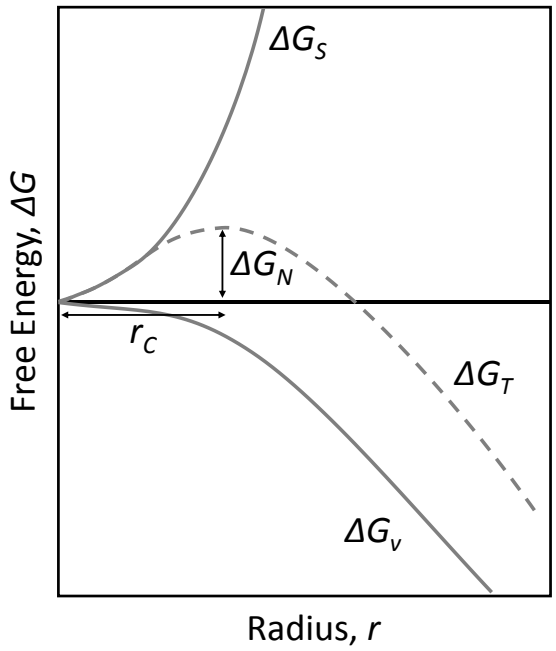

Figure 2.18 Total free energy of nucleation as a function of radius.

It has been shown that, for a system containing monomers of size r_m and corresponding volume of V_m, based on the nucleation kinetics, the nucleation rate is given by:[175]

$$R_{nuc} = 8\pi r_m D N_A S^{pu+1} [C]_\infty^2 exp\left\{\frac{-(4\pi r_c^2 \gamma)}{3k_B T}\right\} \qquad (2.27)$$

where D is the monomer diffusion coefficient, N_A is the Avogadro constant, $S=[C]/[C]_\infty$ is the dimensionless supersaturation which is defined as the bulk concentration of the monomer normalized to the equilibrium concentration of the monomers near an infinitely flat surface. The exponents of the supersaturation are the normalized critical radius to the monomer radius, $p=(r_c/r_m)^3$ and the coagulation parameter u. The surface energy is given by γ which is normalized to the thermal energy k_BT.

Growth: stable nuclei participate in a growth process. The growth of the nuclei is governed by diffusion of the monomer to the surface of the particle and the subsequent incorporation into the crystal structure by surface reactions (see **Figure 2.19**). For isotropic particles, a spherical diffusion layer is assumed by the model, leading to three main stages of the crystal growth.[177]

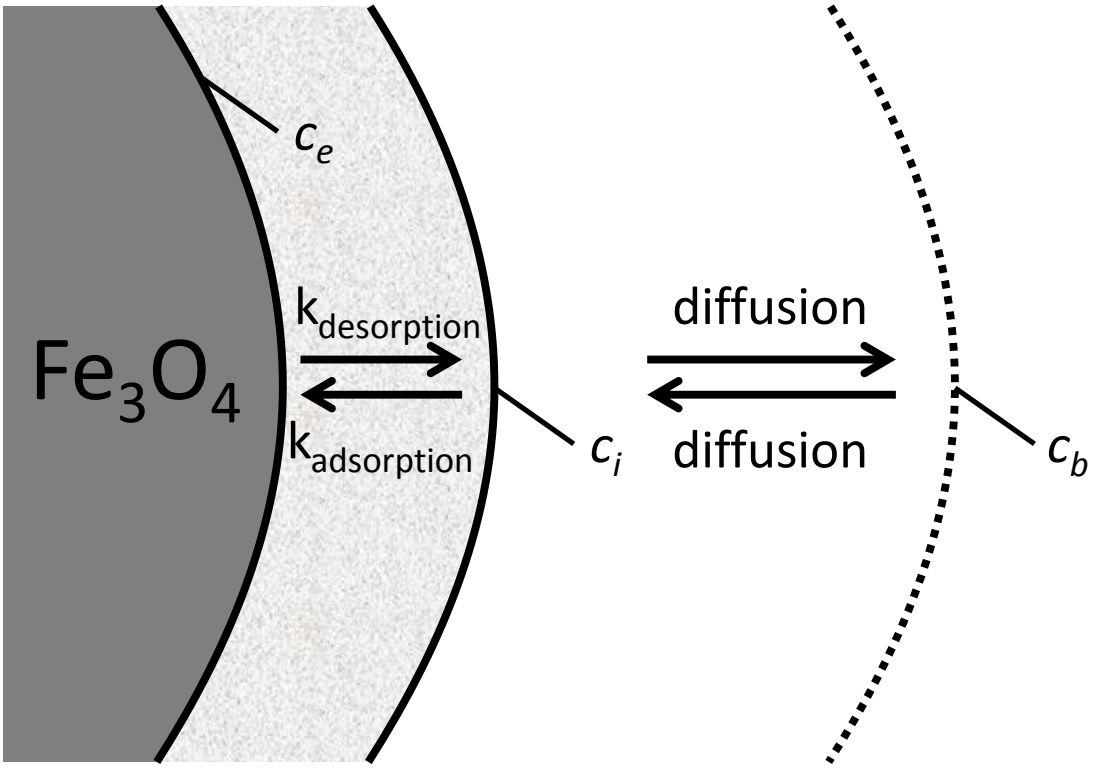

Figure 2.19 Surface and diffusion processes involved in the growth of particles in solution.

For the first stage, Fick's first law of diffusion describes the flux of monomers through a diffusion layer of infinite dimensions ($r \rightarrow \infty$):

$$J_{diff} = 4\pi \mathrm{rD}(c_b - c_i) \qquad (2.28)$$

Where r is particle radius, x is distance from surface, D is diffusion coefficient and c is monomer concentration. In the next stage, monomers diffuse on the crystal surface in stick-slip motion, *i.e.* they get adsorbed (k_i) and desorbed (k_{des}) continuously. These processes govern the flux of monomers in the surface. The ratio of the rate constants for both processes yields the equilibrium solubility. Finally, the incorporation of the monomer into the crystal structure takes place. The deposition rate depends on molar volume and surface area of the crystal.

The classical (crystallization) theory implies two limiting cases for growth. If the concentration of monomer is high in bulk solution (c_b), diffusion D exceeds the monomer deposition rate k_r ($D>>k_r$) and the monomer concentration at the interface c_i and in the bulk are

equal ($c_i \sim c_b$). Thus the growth rate is governed by reactions on the surface, making it a reaction controlled growth process (thermodynamically controlled).[179]

$$J_{react} = 4\pi r^2 k_r (c_b - c_e) \qquad (2.29)$$

$$\frac{dr}{dt} = V_M k_r (c_b - c_e) \qquad (2.30)$$

where r is particle radius, k_r is monomer deposition rate, V_m is molar volume, c_b and c_e are concentration in solution or bulk crystal.

In the other limiting case, the diffusion controlled growth, bulk monomer concentration is very low or surface reactions are very fast ($D << k_r$), thus diffusion determines the growth rate (kinetically controlled):

$$J_{diff} = 4\pi r D (c_b - c_e) \qquad (2.31)$$

$$\frac{dr}{dt} = V_M D \frac{1}{r} (c_b - c_e) \qquad (2.32)$$

Both cases have different influence on the particle size distribution. So far, it still remains unclear whether NP growth is diffusion or reaction limited. An argument for diffusion limited growth is based on the experimental observation of narrowing polydispersity, which due to the form of the growth rate is most easily simulated under diffusion limited growth conditions. However, it has recently been shown that narrowing polydispersity can also occur in the reaction limit region.[175, 180-181]

2.6 Surface Modification of MNPs

The as-synthesized MNPs (like iron oxide) after thermal decomposition are covered with surfactants (oleate) which make them dispersable in different organic solvents (such as hexane or toluene). However, due to the presence of strong magnetic attraction between MNPs, the surfactants are not enough to protect particles against magnetically induced aggregation for long time.[106] In addition, the surfactant, which provides good dispersion in organic solvent, does not necessarily prevent agglomeration in a polymer matrix because surfactant and polymer have to be miscible, too. In order to overcome these issues and to prevent degradation of properties, the

particles have to be modified with a surfactant, which is compatible with the matrix and long enough to avoid agglomeration of MNPs. The most promising approach is to graft polymer shell around the surface of MNPs, which are miscible with the host polymer matrix. In the following, we will introduce different methods for the grafting of polymer chains on the surface of MNPs.

Two general approaches exist for obtaining polymer chains on the surface of NPs: grafting to and grafting from approach.[182-185] Grafting-to is achieved through covalent grafting of a pre-synthesized polymer with anchoring groups on the particle surface (see **Figure 2.20**).[186-188] For the grafting from method, the polymer chains are grown from the surface of the particle by using a surface-initiator which is usually a small molecule covalently bound to the particle surface (see **Figure 2.20**).[182-183] The advantage of the first method is that the desired polymer can be synthesized by well-known methods and apply size-selection processes in order to obtain polymers with controlled molecular weight. However, the drawback of grafting to technique is entropy-driven coiling of the polymer chains at the interface which block the suitable anchoring sites on the NP. This results in a lower grafting density, lower coverage of the NPs and eventually weak stability and dispersion of NPs.[182-183, 189-190] In grafting from strategy, the polymer chains are grown directly from an initiator that is pre-grafted to the surface of MNPs. As a result, the grafting density and the efficiency are higher in comparison to grafting to, especially for higher molecular weight of grafted polymer.

For growing polymer brushes, there are several techniques including anionic polymerization, cationic polymerization, ring-opening polymerization, ring-opening metathesis polymerization, conventional free radical polymerization.[182, 185, 191] However, among the various grafting from approaches, surface initiated living radical polymerization (SI-LRP) is one of the most promising ones, because of its tolerance to impurities and versatility to various monomers and versatility of LRP techniques.[182, 184-185, 192] Examples of SI-LRP techniques are stable nitroxide-mediated polymerization, NMP,[193-194] iodide-mediated polymerization,[195] atom transfer radical polymerization, ATRP,[196-197] reversible addition-fragmentation chain transfer, RAFT, [198] organotellurium-mediated radical polymerization, TERP,[199] and *etc*.[200] The reversible activation reactions in most successful LRPs are classified into three types, which are (a) the dissociation-combination (for NMP and TERP), (b) the atom transfer (for ATRP), and (c) the degenerative

chain transfer (for iodide, RAFT, and TERP) mechanisms. Among these available techniques, atom transfer radical polymerization (ATRP) has been most extensively used to produce polymer brushes from the surface of NPs.[192, 201-215] Compared to other LRP techniques, ATRP is chemically versatile and robust which allows to precisely control the molecular weight and polydispersity of graft polymers.

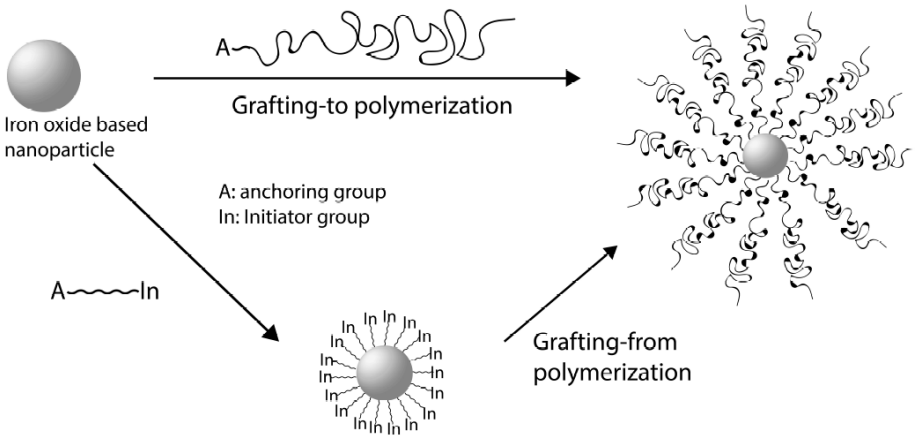

Figure 2.20 Surface polymerization with two different approaches of grafting to and grafting from.

Atom transfer radical polymerization (ATRP) represents a method to obtain controlled/"living" radical polymerizations with well-controlled molecular weight and narrow molecular weight distribution.[216] ATRP is controlled by an equilibrium between propagating radicals ($P_n^{\bullet}$) and dormant species, predominately in the form of initiating organic halides/polymer species (P_n-X).

The normal schematic of the ATRP equilibrium is given in **Figure 2.21**. The active radicals form with a measurable rate constant of activation k_{act}, subsequently propagate with a rate constant k_p and are reversibly deactivated k_{deact}, but, since ATRP is a radical based process, the active species can also terminate with a rate constant k_t. This emphasizes the repetitive nature of the activation and deactivation steps and the need to push the equilibrium to the left hand side. Hence, by pushing the reaction to the left side, lower concentration of radical forms which leads to the reduction of radical-radical termination reactions, and ensure a high mole fraction of dormant chains, as it is shown in **Figure 2.21**.

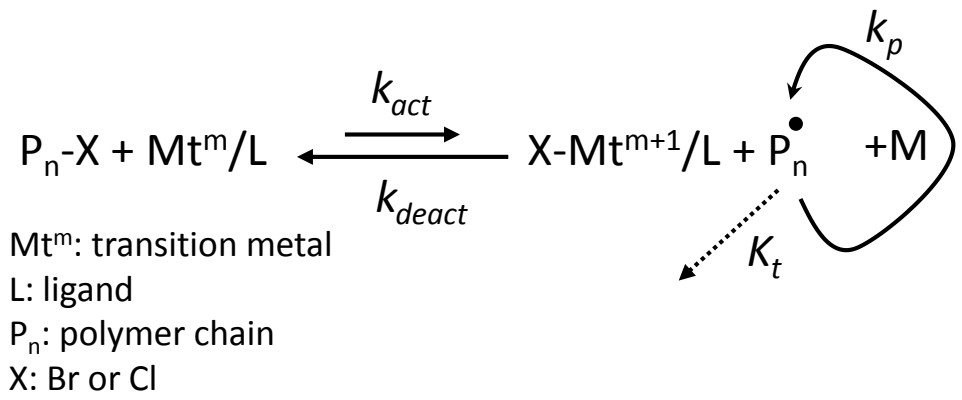

Figure 2. 21 Mechanism of metal complex-mediated ATRP.

The ligand (*L*) form complex with the metal (Mt^m) salt and is responsible for improving its solubility in organic solvents during polymerization. The radical generation process involves the alkyl halide (P-X) undergoing a reversible redox reaction catalyzed by a transition metal compound, where the metal center will undergo an electron transfer and a simultaneous halogen atom abstraction. As a result, a radical species ($R^{\bullet}$) and a complex with a metal in a higher oxidation state (deactivator) ($X\text{-}Mt^{m+}1/L$) will be generated. The formed radical can polymerize by reaction with the monomer (*M*) (k_p) or in majority it will react with the deactivator (k_{deact}), where the propagating radicals will coordinate with the deactivator and form dormant species. The formed dormant species react periodically with the transition metal complexes in their lower oxidation state to form the growing radicals (k_{act}).[216-217] As the reaction progresses, radical termination is diminished as a result of the persistent radical effect (PRE),[218-219] chain length increases, as well as conversion and viscosity.[220] Consequently, the equilibrium is strongly shifted towards the dormant species ($k_{act} << k_{deact}$).

The livingness of this polymerization process can be determined from a linear first-order kinetic plot (**Figure 2.22**), accompanied by a linear increase in polymer molecular weight with conversion, with the value of the number-average degree of polymerization (DP_n) determined by the ratio of reacted monomer to initially introduced initiator (i.e., $DP_n = D[M]/[RX]_0$). It is known that, the semi-logarithmic plot of $Ln([M]_0/Ln[M])$ (where $[M]_0$ and $[M]$ are initial concentration of monomer and concentration of monomer in defined time) as a function of time is very sensitive to any change of the concentration of the active propagating species. A constant

concentration of propagating species is revealed by a straight line. A steady concentration of propagating species in an ATRP is established by balancing the rates of activation and deactivation and not by balancing the rates of initiation and termination as in a conventional radical polymerization (**Figure 2.22**). An upward curvature in the kinetic plot indicates an increase in the concentration of propagating species, which occurs in case of slow initiation (**Figure 2.22**). On the other hand, a downward curvature suggests a decrease in the concentration of propagating species, which may result from termination reactions increasing the concentration of the persistent radical, or some other side reactions such as the catalytic system being poisoned or redox processes on the radical (**Figure 2.22**).[213]

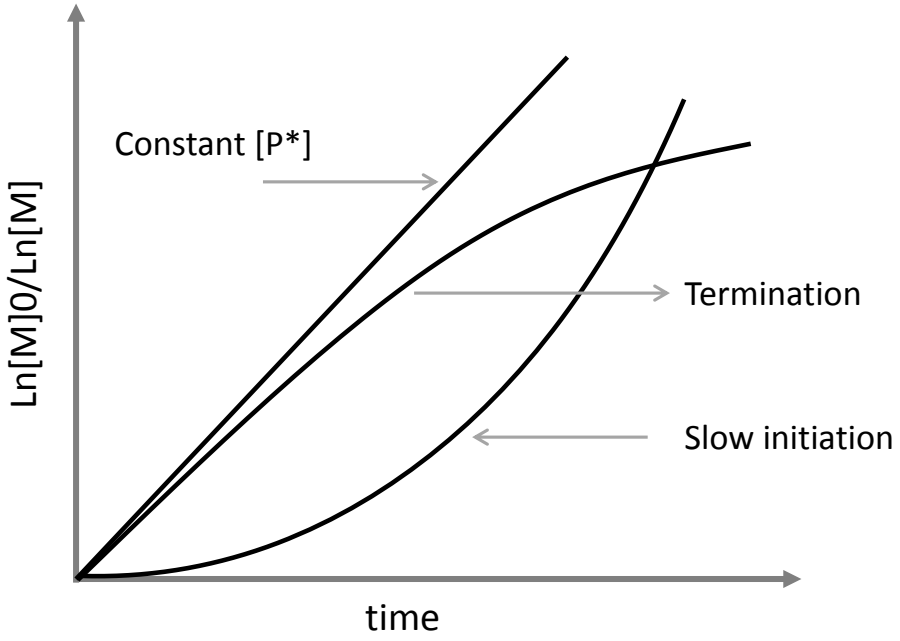

Figure 2.22 The evolution of Ln($[M]_0$/Ln[M]) as a function of time (kinetic of polymerization).[195]

Understanding the process and kinetics of the atom transfer technique is necessary to run a successful ATRP. Therefore, it remains a very important objective to get to know the kinetic of polymerization. In ATRP method, the concentration of the propagating radicals can be calculated by:[221]

$$R^{\cdot} = \frac{K[I][Mt^{m}]}{[Mt^{m+1}]} \qquad (2.33)$$

Where, $K=k_{act}/k_{deact}$, $[I]$ is concentration of initiator, $[Mt^m]$ and $[Mt^{m+1}]$ are concentrations of transition metal species in lower and higher state of oxidation, respectively. The polymerization rate can be calculated by:

$$R_P = \frac{k_p K[I][Mt^m]}{[Mt^{m+1}]} \qquad (2.34)$$

Where $[M]$ is the concentration of the monomer. The polymerization rate expressed by monomer concentration over time is demonstrated in:

$$ln\frac{[M]_0}{[M]} = \frac{k_p K[I][Mt^m]}{[Mt^{m+1}]}t \qquad (2.35)$$

Following the conditions for a living polymerization, where all propagating chains grow at the same rate and for the same length of time, the degree of polymerization can be calculated by:

$$\bar{X} = \frac{[M]_0 - [M]}{[I]_0} = \frac{p[M]_0}{[I]_0} \qquad (2.36)$$

Where $[M]_0$ and $[I]_0$ are initial concentrations of monomer and initiator, respectively and p is the fractional conversion of monomer at any time in the reaction.

The polydispersity index (PDI) is given by:

$$\frac{\overline{X_w}}{\overline{X_n}} = 1 + \left[\frac{k_p[I]_0}{k_{deact}[Mt^{m+1}]}\right]\left[\frac{2}{p} - 1\right] \qquad (2.37)$$

To obtain a narrow polydispersity value some requirements are necessary, such as low initiator concentration, fast initiation of the propagating chains, high values of conversion, high values of k_{deact} and $[D]$ (rapid deactivation), and low value of k_p. By fulfilling these conditions, the resultant molecular weight distribution follows the Poisson distribution and can be calculated by:

$$\frac{\overline{X_w}}{\overline{X_n}} = 1 + \frac{\overline{X_n}}{(\overline{X_n}+1)^2} \qquad (2.38)$$

Which can be approximated to:

$$\frac{\overline{X_w}}{\overline{X_n}} = 1 + \frac{1}{\overline{X_n}} \qquad (2.39)$$

There are several important parameters that affect atom transfer radical polymerizations. Like monomer, initiator, catalyst, ligand, temperature, solvent and *etc*. Typical monomers in ATRP are for examples styrenes, (meth)acrylates, (meth)acrylamides, and acrylonitrile.[222] When the concentration of the propagating radical balances the rate of radical termination, high molecular weight with low dispersity can be obtained by ATRP. The propagating rate is unique for each individual monomer. Hence, it is important that other parameters of the polymerization (initiator, catalyst, ligand, and solvent) are optimized in a way that the concentration of the dormant species to be greater than that of the propagating radical while not being too low to stop or slow down the reaction.[213]

Initiator plays an important role in kinetic of ATRP. The number of growing polymer chains is determined by the concentration of initiator. The rate of initiation should be faster than the rate of propagation in order to obtain polymer chains with low polydispersity in a controlled condition. Then, in an ideal condition, all the chains initiate quickly and propagate at the same rate. Initiators are usually alkyl halides with similar structure to that of the propagating radical.[213, 222] Alkyl halides such as alkyl bromides and alkyl chlorides are the most known initiators. The former is more reactive than the later. [213, 222]

The catalyst plays a vital role in ATRP, since it controls the equilibrium constant between the active and dormant species and therefore the polymerization rate. Too small equilibrium constant may hinders or slows down the rate of polymerization while too high equilibrium constant may leads to a large polydispersity.[213, 222] In most of the researches copper (Cu) has been used as a transition metal[213] but a wide range of other metals can be employed in an ATRP including Ti, Mo, Re, Fe, Ru, Os, Rh, Co, Ni, and Pd.[223-226]

There are also other parameters that affect K_{ATRP} like temperature,[227-228] pressure,[229-230] media/solvent (which increases with polarity: toluene < anisole < MeCN < DMF < DMSO < H_2O)[231] and obviously alkyl halide and catalyst.[232] Reaction temperatures are usually in the range of room temperature to 150 °C and the reaction usually conducts under vacuum or inert gas.[233] On the other hand, there are some techniques, which enable polymerization under air, moisture and oxygen or using lower amount of catalyst.[234-237] Sometimes the higher oxidation state transition metal (deactivator) are added directly to a reaction prior to initiation. Since this may

increase the efficiency of initiation, by reducing the fraction of low molecular weight termination reactions initially required to generate the PRE,[238] or can be formed in situ by reaction with dissolved oxygen.[239] Addition of the persistent radical, (Mt^{m+1} in the case of ATRP) is of really useful especially during performing a grafting from reaction with a multifunctional initiator or grafting from a surface. Often for SI-ATRP sacrificial initiator is added to the reaction medium to provide a means of following the reaction, assist in controlling initiation from the surface and avoid intra-particle polymerization.[192, 203-204]

2.7 Conclusion

In this chapter, the basic theoretical concepts needed as background for this dissertation have been discussed. Note that for the convenience of the reader, certain equations from this chapter will be given again later, when the theory is applied to the experimental results.

2.8 References

1. Spaldin, N. A.; Fiebig, M., The renaissance of magnetoelectric multiferroics. *Science* **2005,** *309*, 391-392.
2. Eerenstein, W.; Mathur, N.; Scott, J. F., Multiferroic and magnetoelectric materials. *Nature* **2006,** *442*, 759.
3. Scott, J. F., Room-temperature multiferroic magnetoelectrics. *NPG Asia Mater.* **2013,** *5*, e72.
4. Scott, J., Data storage: Multiferroic memories. *Nat. Mater.* **2007,** *6*, 256.
5. Martins, P.; Lanceros-Méndez, S., Polymer-based magnetoelectric materials. *Adv. Funct. Mater.* **2013,** *23*, 3371-3385.
6. Ma, J.; Hu, J.; Li, Z.; Nan, C. W., Recent progress in multiferroic magnetoelectric composites: from bulk to thin films. *Adv. Mater.* **2011,** *23*, 1062-1087.
7. Ramesh, R.; Spaldin, N. A., Multiferroics: progress and prospects in thin films. In *Nanoscience And Technology: A Collection of Reviews from Nature Journals*, World Scientific: 2010; pp 20-28.
8. Vopson, M. M., Fundamentals of multiferroic materials and their possible applications. *Crit. Rev. Solid State Mater. Sci.* **2015,** *40*, 223-250.
9. Martins, P.; Kolen'ko, Y. V.; Rivas, J.; Lanceros-Mendez, S., Tailored magnetic and magnetoelectric responses of polymer-based composites. *ACS Appl. Mater. Interfaces* **2015,** *7*, 15017-15022.
10. Martins, P.; Costa, C. M.; Lanceros-Mendez, S., Nucleation of electroactive β-phase poly (vinilidene fluoride) with CoFe2O4 and NiFe2O4 nanofillers: a new method for the preparation of multiferroic nanocomposites. *Appl. Phys. A* **2011,** *103*, 233-237.
11. Nan, C.-W.; Bichurin, M.; Dong, S.; Viehland, D.; Srinivasan, G., Multiferroic magnetoelectric composites: Historical perspective, status, and future directions. *J. Appl. Phys.* **2008,** *103*, 1.
12. Fiebig, M., Revival of the magnetoelectric effect. *J. Phys. D: Appl. Phys.* **2005,** *38*, R123.
13. Van Suchtelen, J., Product properties: a new application of composite materials. *Philips Res. Rep* **1972,** *27*, 28-37.

14. Wang, Y.; Hu, J.; Lin, Y.; Nan, C.-W., Multiferroic magnetoelectric composite nanostructures. *NPG Asia Mater.* **2010,** *2*, 61.
15. Al-Nassar, M. Y. Magnetoelectric Nanocomposites for Flexible Electronics. 2015.
16. Silva, M.; Martins, P.; Lasheras, A.; Gutiérrez, J.; Barandiarán, J.; Lanceros-Mendez, S., Size effects on the magnetoelectric response on PVDF/Vitrovac 4040 laminate composites. *Journal of Magnetism and Magnetic Materials* **2015,** *377*, 29-33.
17. Kulawik, J.; Szwagierczak, D.; Guzdek, P., Magnetic, magnetoelectric and dielectric behavior of CoFe2O4–Pb (Fe1/2Nb1/2) O3 particulate and layered composites. *Journal of magnetism and magnetic materials* **2012,** *324*, 3052-3057.
18. Guzdek, P., The magnetostrictive and magnetoelectric characterization of Ni0. 3Zn0. 62Cu0. 08Fe2O4–Pb (FeNb) 0.5 O3 laminated composite. *Journal of Magnetism and Magnetic Materials* **2014,** *349*, 219-223.
19. Kulkarni, A.; Meurisch, K.; Teliban, I.; Jahns, R.; Strunskus, T.; Piorra, A.; Knöchel, R.; Faupel, F., Giant magnetoelectric effect at low frequencies in polymer-based thin film composites. *Applied Physics Letters* **2014,** *104*, 022904.
20. Scott, J. F., Applications of magnetoelectrics. *J. Mater. Chem.* **2012,** *22*, 4567-4574.
21. Jin, J.; Lu, S. G.; Chanthad, C.; Zhang, Q.; Haque, M.; Wang, Q., Multiferroic polymer composites with greatly enhanced magnetoelectric effect under a low magnetic bias. *Adv. Mater.* **2011,** *23*, 3853-3858.
22. Martins, P.; Costa, C. M.; Botelho, G.; Lanceros-Mendez, S.; Barandiaran, J.; Gutierrez, J., Dielectric and magnetic properties of ferrite/poly (vinylidene fluoride) nanocomposites. *Mater. Chem. Phys.* **2012,** *131*, 698-705.
23. Martins, P.; Gonçalves, R.; Lanceros-Mendez, S.; Lasheras, A.; Gutiérrez, J.; Barandiarán, J., Effect of filler dispersion and dispersion method on the piezoelectric and magnetoelectric response of CoFe2O4/P (VDF-TrFE) nanocomposites. *Appl. Surf. Sci.* **2014,** *313*, 215-219.
24. Silva, M.; Reis, S.; Lehmann, C.; Martins, P.; Lanceros-Mendez, S.; Lasheras, A.; Gutiérrez, J.; Barandiarán, J., Optimization of the magnetoelectric response of poly (vinylidene fluoride)/epoxy/vitrovac laminates. *ACS Appl. Mater. Interfaces* **2013,** *5*, 10912-10919.
25. Xie, L.; Huang, X.; Huang, Y.; Yang, K.; Jiang, P., Core@ double-shell structured BaTiO3–polymer nanocomposites with high dielectric constant and low dielectric loss for energy storage application. *The Journal of Physical Chemistry C* **2013,** *117*, 22525-22537.
26. Zhu, M.; Huang, X.; Yang, K.; Zhai, X.; Zhang, J.; He, J.; Jiang, P., Energy storage in ferroelectric polymer nanocomposites filled with core–shell structured polymer@ BaTiO3 nanoparticles: understanding the role of polymer shells in the interfacial regions. *ACS applied materials & interfaces* **2014,** *6*, 19644-19654.
27. van Breemen, A. J.; van der Steen, J.-L.; van Heck, G.; Wang, R.; Khikhlovskyi, V.; Kemerink, M.; Gelinck, G. H., Crossbar arrays of nonvolatile, rewritable polymer ferroelectric diode memories on plastic substrates. *Applied Physics Express* **2014,** *7*, 031602.
28. Naber, R. C.; Asadi, K.; Blom, P. W.; de Leeuw, D. M.; de Boer, B., Organic nonvolatile memory devices based on ferroelectricity. *Adv. Mater.* **2010,** *22*, 933-945.
29. Asadi, K.; De Leeuw, D. M.; De Boer, B.; Blom, P. W., Organic non-volatile memories from ferroelectric phase-separated blends. *Nat. Mat.* **2008,** *7*, 547.
30. Zhang, J.; Dai, J.; So, L.; Sun, C.; Lo, C.; Or, S.; Chan, H. L., The effect of magnetic nanoparticles on the morphology, ferroelectric, and magnetoelectric behaviors of CFO/P (VDF-TrFE) 0–3 nanocomposites. *J. Appl. Phys.* **2009,** *105*, 054102.
31. Martins, P.; Lasheras, A.; Gutiérrez, J.; Barandiaran, J. M.; Orue, I.; Lanceros-Mendez, S., Optimizing piezoelectric and magnetoelectric responses on CoFe2O4/P (VDF-TrFE) nanocomposites. *J. Phys. D: Appl. Phys.* **2011,** *44*, 495303.
32. Martins, P.; Moya, X.; Phillips, L.; Kar-Narayan, S.; Mathur, N.; Lanceros-Mendez, S., Linear anhysteretic direct magnetoelectric effect in Ni0. 5Zn0. 5Fe2O4/poly (vinylidene fluoride-trifluoroethylene) 0-3 nanocomposites. *J. Phys. D: Appl. Phys.* **2011,** *44*, 482001.
33. Guyomar, D.; Guiffard, B.; Belouadah, R.; Petit, L., Two-phase magnetoelectric nanopowder/polyurethane composites. *J. Appl. Phys.* **2008,** *104*, 074902.
34. Martins, P.; Moya, X.; Caparrós, C.; Fernandez, J.; Mathur, N.; Lanceros-Mendez, S., Large linear anhysteretic magnetoelectric voltage coefficients in CoFe 2 O 4/polyvinylidene fluoride 0–3 nanocomposites. *J. Nanopart. Res.* **2013,** *15*, 1825.

35. Maceiras, A.; Martins, P.; Gonçalves, R.; Botelho, G.; Ramana, E. V.; Mendiratta, S.; San Sebastián, M.; Vilas, J.; Lanceros-Mendez, S.; León, L., High-temperature polymer based magnetoelectric nanocomposites. *Eur. Polym. J.* **2015,** *64*, 224-228.
36. Martins, P.; Larrea, A.; Gonçalves, R.; Botelho, G.; Ramana, E.; Mendiratta, S.; Sebastian, V.; Lanceros-Mendez, S., Novel anisotropic magnetoelectric effect on δ-FeO (OH)/P (VDF-TrFE) multiferroic composites. *ACS Appl. Mater. Interfaces* **2015,** *7*, 11224-11229.
37. Fiorido, T.; Galineau, J.; Salles, V.; Seveyrat, L.; Belhora, F.; Cottinet, P.-J.; Hu, L.; Liu, Y.; Guiffard, B.; Bogner-Van De Moortele, A., Bifunctional organic/inorganic nanocomposites for energy harvesting, actuation and magnetic sensing applications. *Sens. Actuators, A* **2014,** *211*, 105-114.
38. Nguyen, T. H. L.; Laffont, L.; Capsal, J.-F.; Cottinet, P.-J.; Lonjon, A.; Dantras, E.; Lacabanne, C., Magnetoelectric properties of nickel nanowires-P (VDF–TrFE) composites. *Mater. Chem. Phys.* **2015,** *153*, 195-201.
39. Ahlawat, A.; Satapathy, S.; Shirolkar, M. M.; Li, J.; Khan, A. A.; Deshmukh, P.; Wang, H.; Choudhary, R.; Karnal, A., Tunable Magnetoelectric Nonvolatile Memory Devices Based on SmFeO3/P (VDF-TrFE) Nanocomposite Films. *ACS Appl. Nano Mater.* **2018,** *1*, 3196-3203.
40. Behera, C.; Choudhary, R.; Das, P., Development of multiferroic polymer nanocomposite from PVDF and (Bi 0.5 Ba 0.25 Sr 0.25)(Fe 0.5 Ti 0.5) O 3. *J. Mater. Sci.: Mater. Electron.* **2017,** *28*, 2586-2597.
41. Behera, C.; Choudhary, R., Electrical and multiferroic characteristics of PVDF-MnFe2O4 nanocomposites. *J. Alloys Compd.* **2017,** *727*, 851-862.
42. Adhlakha, N.; Yadav, K.; Truccato, M.; Rajak, P.; Battiato, A.; Vittone, E., Multiferroic and magnetoelectric properties of BiFeO3-CoFe2O4-poly (vinylidene-flouride) composite films. *Eur. Polym. J.* **2017,** *91*, 100-110.
43. Mayeen, A.; Kala, M.; Jayalakshmy, M.; Thomas, S.; Rouxel, D.; Philip, J.; Bhowmik, R.; Kalarikkal, N., Dopamine functionalization of BaTiO 3: an effective strategy for the enhancement of electrical, magnetoelectric and thermal properties of BaTiO 3-PVDF-TrFE nanocomposites. *Dalton Trans.* **2018,** *47*, 2039-2051.
44. Jing, W.; Fang, F., A flexible multiferroic composite with high self-biased magnetoelectric coupling. *Compos. Sci. Technol.* **2017,** *153*, 145-150.
45. Brito-Pereira, R.; Ribeiro, C.; Lanceros-Mendez, S.; Martins, P., Magnetoelectric response on Terfenol-D/P (VDF-TrFE) two-phase composites. *Composites Part B* **2017,** *120*, 97-102.
46. Nan, C.-W.; Liu, L.; Cai, N.; Zhai, J.; Ye, Y.; Lin, Y.; Dong, L.; Xiong, C., A three-phase magnetoelectric composite of piezoelectric ceramics, rare-earth iron alloys, and polymer. *Appl. Phys. Lett.* **2002,** *81*, 3831-3833.
47. Chau, K.; Wong, Y.; Shin, F., Magnetoelectric effect of polymer electrolyte composites with Terfenol-D and lead zirconate titanate inclusions. *Appl. Phys. Lett.* **2009,** *94*, 202902.
48. Cai, N.; Nan, C.-W.; Zhai, J.; Lin, Y., Large high-frequency magnetoelectric response in laminated composites of piezoelectric ceramics, rare-earth iron alloys and polymer. *Appl. Phys. Lett.* **2004,** *84*, 3516-3518.
49. Nan, C.-W.; Cai, N.; Shi, Z.; Zhai, J.; Liu, G.; Lin, Y., Large magnetoelectric response in multiferroic polymer-based composites. *Phys. Rev. B* **2005,** *71*, 014102.
50. Wan, H.; Shen, R.-F.; Wu, X.-Z., A theoretical study on symmetrical magnetostrictive/piezoelectric laminated composite. *Acta Phys. Sin.* **2005**.
51. Belouadah, R.; Guyomar, D.; Guiffard, B.; Zhang, J.-W., Phase switching phenomenon in magnetoelectric laminate polymer composites: Experiments and modeling. *Physica B: Condensed Matter* **2011,** *406*, 2821-2826.
52. Nersessian, N.; Or, S. W.; Carman, G. P., Magnetoelectric behavior of Terfenol-D composite and lead zirconate titanate ceramic laminates. *IEEE Trans. Magn.* **2004,** *40*, 2646-2648.
53. Zhai, J.; Dong, S.; Xing, Z.; Li, J.; Viehland, D., Giant magnetoelectric effect in Metglas/polyvinylidene-fluoride laminates. *Appl. Phys. Lett.* **2006,** *89*, 083507.
54. Fang, Z.; Lu, S.; Li, F.; Datta, S.; Zhang, Q.; El Tahchi, M., Enhancing the magnetoelectric response of Metglas/polyvinylidene fluoride laminates by exploiting the flux concentration effect. *Appl. Phys. Lett.* **2009,** *95*, 112903.
55. Dong, X.; Wang, B.; Wang, K.; Wan, J.; Liu, J. M., Ultra-sensitive detection of magnetic field and its direction using bilayer PVDF/Metglas laminate. *Sens. Actuators, A* **2009,** *153*, 64-68.
56. Lu, S.; Jin, J.; Zhou, X.; Fang, Z.; Wang, Q.; Zhang, Q., Large magnetoelectric coupling coefficient in poly (vinylidene fluoride-hexafluoropropylene)/Metglas laminates. *J. Appl. Phys.* **2011,** *110*, 104103.
57. Ullakko, K., Magnetically controlled shape memory alloys: a new class of actuator materials. *J. Mater. Eng. Perform.* **1996,** *5*, 405-409.

58. Zeng, M.; Or, S. W.; Chan, H. L. W., Large magnetoelectric effect from mechanically mediated magnetic field-induced strain effect in Ni–Mn–Ga single crystal and piezoelectric effect in PVDF polymer. *J. Alloys Compd.* **2010,** *490*, L5-L8.
59. Lu, S.; Fang, Z.; Furman, E.; Wang, Y.; Zhang, Q.; Mudryk, Y.; Gschneidner Jr, K.; Pecharsky, V.; Nan, C., Thermally mediated multiferroic composites for the magnetoelectric materials. *Appl. Phys. Lett.* **2010,** *96*, 102902.
60. Valasek, J., Piezo-electric and allied phenomena in Rochelle salt. *Phys. Rev.* **1921,** *17*, 475.
61. Lines, M. E.; Glass, A. M., *Principles and applications of ferroelectrics and related materials*. Oxford university press: 2001.
62. Setter, N.; Damjanovic, D.; Eng, L.; Fox, G.; Gevorgian, S.; Hong, S.; Kingon, A.; Kohlstedt, H.; Park, N.; Stephenson, G., Ferroelectric thin films: Review of materials, properties, and applications. *J. Appl. Phys.* **2006,** *100*, 051606.
63. Scott, J., Applications of modern ferroelectrics. *science* **2007,** *315*, 954-959.
64. Dawber, M.; Rabe, K.; Scott, J., Physics of thin-film ferroelectric oxides. *Reviews of modern physics* **2005,** *77*, 1083.
65. Asadi, K.; van der Veen, M. A., Ferroelectricity in Metal–Organic Frameworks: Characterization and Mechanisms. *Eur. J. Inorg. Chem.* **2016,** *2016*, 4332-4344.
66. Bunget, I.; Popescu, M., *Physics of solid dielectrics*. Elsevier Science Ltd: 1984; Vol. 19.
67. Paufler, P., JF Nye. Physical Properties of Crystals. Clarendon Press—Oxford. First published in paperback with corrections and new material 1985. XVII+ 329 p.£ 15.00. ISBN 0-19-851165-5. *Cryst. Res. Technol.* **1986,** *21*, 1508-1508.
68. Avrami, M., Kinetics of phase change. I General theory. *J. Chem. Phys.* **1939,** *7*, 1103-1112.
69. Hu, W. J.; Juo, D.-M.; You, L.; Wang, J.; Chen, Y.-C.; Chu, Y.-H.; Wu, T., Universal ferroelectric switching dynamics of vinylidene fluoride-trifluoroethylene copolymer films. *Sci. Rep.* **2014,** *4*, 4772.
70. Ishibashi, Y.; Takagi, Y., Note on ferroelectric domain switching. *J. Phys. Soc. Jpn.* **1971,** *31*, 506-510.
71. Zhao, D.; Katsouras, I.; Asadi, K.; Blom, P. W.; de Leeuw, D. M., Switching dynamics in ferroelectric P (VDF-TrFE) thin films. *Phys. Rev. B* **2015,** *92*, 214115.
72. Lenz, T. Device physics and nanostructuring of organic ferroelectric memory diodes. Johannes Gutenberg-Universität Mainz, 2017.
73. Zhao, D.; Katsouras, I.; Li, M.; Asadi, K.; Tsurumi, J.; Glasser, G.; Takeya, J.; Blom, P. W.; De Leeuw, D. M., Polarization fatigue of organic ferroelectric capacitors. *Sci. Rep.* **2014,** *4*, 5075.
74. Merz, W. J., Domain Formation and Domain Wall Motions in Ferroelectric BaTi O 3 Single Crystals. *Phys. Rev.* **1954,** *95*, 690.
75. Martins, P.; Lopes, A.; Lanceros-Mendez, S., Electroactive phases of poly (vinylidene fluoride): determination, processing and applications. *Prog. Polym. Sci.* **2014,** *39*, 683-706.
76. Haertling, G. H., Ferroelectric ceramics: history and technology. *J. Am. Ceram. Soc.* **1999,** *82*, 797-818.
77. Xu, Y., *Ferroelectric materials and their applications*. Elsevier: 2013.
78. Nalwa, H. S., *Ferroelectric polymers: chemistry: physics, and applications*. CRC Press: 1995.
79. Lovinger, A. J., Ferroelectric polymers. *Science* **1983,** *220*, 1115-1121.
80. Park, Y. J.; Bae, I.-s.; Kang, S. J.; Chang, J.; Park, C., Control of thin ferroelectric polymer films for non-volatile memory applications. *IEEE Trans. Dielectr. Electr. Insul.* **2010,** *17*.
81. Furukawa, T., Structure and functional properties of ferroelectric polymers. *Adv. Colloid Interface Sci.* **1997,** *71*, 183-208.
82. Furukawa, T.; Takahashi, Y.; Nakajima, T., Recent advances in ferroelectric polymer thin films for memory applications. *Curr. Appl.Phys.* **2010,** *10*, e62-e67.
83. Salimi, A.; Yousefi, A., Analysis method: FTIR studies of β-phase crystal formation in stretched PVDF films. *Polym. Test.* **2003,** *22*, 699-704.
84. Giannetti, E., Semi-crystalline fluorinated polymers. *Polym. Int.* **2001,** *50*, 10-26.
85. Correia, H. M.; Ramos, M. M., Quantum modelling of poly (vinylidene fluoride). *Computational materials science* **2005,** *33*, 224-229.
86. El Mohajir, B.-E.; Heymans, N., Changes in structural and mechanical behaviour of PVDF with processing and thermomechanical treatments. 1. Change in structure. *Polymer* **2001,** *42*, 5661-5667.

87. Martins, P.; Costa, C. M.; Benelmekki, M.; Botelho, G.; Lanceros-Mendez, S., On the origin of the electroactive poly (vinylidene fluoride) β-phase nucleation by ferrite nanoparticles via surface electrostatic interactions. *CrystEngComm* **2012,** *14*, 2807-2811.
88. Imamura, R.; Silva, A.; Gregorio Jr, R., γ→ β Phase transformation induced in poly (vinylidene fluoride) by stretching. *J. Appl. Polym. Sci.* **2008,** *110*, 3242-3246.
89. Banik, N.; Boyle, F.; Sluckin, T.; Taylor, P.; Tripathy, S.; Hopfinger, A., Theory of structural phase transitions in crystalline poly (vinylidene fluoride). *J. Chem. Phys.* **1980,** *72*, 3191-3196.
90. Leonard, C.; Halary, J.; Monnerie, L., Crystallization of poly (vinylidene fluoride)-poly (methyl methacrylate) blends: analysis of the molecular parameters controlling the nature of poly (vinylidene fluoride) crystalline phase. *Macromolecules* **1988,** *21*, 2988-2994.
91. Li, M.; Stingelin, N.; Michels, J. J.; Spijkman, M.-J.; Asadi, K.; Feldman, K.; Blom, P. W.; de Leeuw, D. M., Ferroelectric phase diagram of PVDF: PMMA. *Macromolecules* **2012,** *45*, 7477-7485.
92. Kang, S. J.; Park, Y. J.; Bae, I.; Kim, K. J.; Kim, H. C.; Bauer, S.; Thomas, E. L.; Park, C., Printable ferroelectric PVDF/PMMA blend films with ultralow roughness for low voltage non-volatile polymer memory. *Adv. Funct. Mater.* **2009,** *19*, 2812-2818.
93. Kang, S. J.; Bae, I.; Choi, J.-H.; Park, Y. J.; Jo, P. S.; Kim, Y.; Kim, K. J.; Myoung, J.-M.; Kim, E.; Park, C., Fabrication of micropatterned ferroelectric gamma poly (vinylidene fluoride) film for non-volatile polymer memory. *J. Mater. Chem.* **2011,** *21*, 3619-3624.
94. Li, M.; Wondergem, H. J.; Spijkman, M.-J.; Asadi, K.; Katsouras, I.; Blom, P. W.; De Leeuw, D. M., Revisiting the δ-phase of poly (vinylidene fluoride) for solution-processed ferroelectric thin films. *Nat. Mater.* **2013,** *12*, 433.
95. Ling, Q.-D.; Liaw, D.-J.; Zhu, C.; Chan, D. S.-H.; Kang, E.-T.; Neoh, K.-G., Polymer electronic memories: Materials, devices and mechanisms. *Prog. Polym. Sci.* **2008,** *33*, 917-978.
96. Lovinger, A. J.; Furukawa, T.; Davis, G.; Broadhurst, M., Curie transitions in copolymers of vinylidene fluoride: Curie transitions in PVF2 copolymers. *Ferroelectrics* **1983,** *50*, 227-236.
97. Lu, S.-G.; Rozic, B.; Kutnjiak, Z.; Zhang, Q., Electrocaloric effect in ferroelectric P (VDF-TrFE) copolymers. *Integr. Ferroelectr.* **2011,** *125*, 176-185.
98. Lu, S.; Rozic, B.; Kutnjiak, Z.; Zhang, Q., Electrocaloric effect in ferroelectric P (VDF-TrFE) copolymers. *Integr. Ferroelectr.* **2011,** *125*, 176-185.
99. Yamada, T.; Kitayama, T., Ferroelectric properties of vinylidene fluoride-trifluoroethylene copolymers. *J. Appl. Phys.* **1981,** *52*, 6859-6863.
100. Furukawa, T.; Nakajima, T.; Takahashi, Y., Factors governing ferroelectric switching characteristics of thin VDF/TrFE copolymer films. *IEEE Trans. Dielectr. Electr. Insul.* **2006,** *13*, 1120-1131.
101. Morrish, A. H., The physical principles of magnetism. *The Physical Principles of Magnetism, by Allan H. Morrish, pp. 696. ISBN 0-7803-6029-X. Wiley-VCH, January 2001.* **2001**, 696.
102. Kolhatkar, A. G.; Jamison, A. C.; Litvinov, D.; Willson, R. C.; Lee, T. R., Tuning the magnetic properties of nanoparticles. *Int. J. Mol. Sci.* **2013,** *14*, 15977-16009.
103. Varadan, V. K.; Chen, L.; Xie, J., *Nanomedicine: design and applications of magnetic nanomaterials, nanosensors and nanosystems*. John Wiley & Sons: 2008.
104. Jeong, U.; Teng, X.; Wang, Y.; Yang, H.; Xia, Y., Superparamagnetic colloids: controlled synthesis and niche applications. *Adv. Mater.* **2007,** *19*, 33-60.
105. Batlle, X.; Labarta, A., Finite-size effects in fine particles: magnetic and transport properties. *Journal of Physics D: Applied Physics* **2002,** *35*, R15.
106. Dai, Q.; Berman, D.; Virwani, K.; Frommer, J.; Jubert, P.-O.; Lam, M.; Topuria, T.; Imaino, W.; Nelson, A., Self-assembled ferrimagnet− polymer composites for magnetic recording media. *Nano Lett.* **2010,** *10*, 3216-3221.
107. Jun, Y.-w.; Choi, J.-s.; Cheon, J., Heterostructured magnetic nanoparticles: their versatility and high performance capabilities. *Chemical Communications* **2007**, 1203-1214.
108. Skumryev, V.; Stoyanov, S.; Zhang, Y.; Hadjipanayis, G.; Givord, D.; Nogues, J., Beating the superparamagnetic limit with exchange bias. *Nature* **2003,** *423*, 850-853.
109. Sun, S., Recent advances in chemical synthesis, self-assembly, and applications of FePt nanoparticles. *Advanced Materials* **2006,** *18*, 393-403.
110. Yu, Y.; Mendoza-Garcia, A.; Ning, B.; Sun, S., Cobalt-substituted magnetite nanoparticles and their assembly into ferrimagnetic nanoparticle arrays. *Adv. Mater.* **2013,** *25*, 3090-3094.

111. Wu, L.; Jubert, P.-O.; Berman, D.; Imaino, W.; Nelson, A.; Zhu, H.; Zhang, S.; Sun, S., Monolayer Assembly of Ferrimagnetic Co x Fe3–x O4 Nanocubes for Magnetic Recording. *Nano letters* **2014,** *14*, 3395-3399.
112. Sahoo, B.; Sahu, S. K.; Nayak, S.; Dhara, D.; Pramanik, P., Fabrication of magnetic mesoporous manganese ferrite nanocomposites as efficient catalyst for degradation of dye pollutants. *Catalysis Science & Technology* **2012,** *2*, 1367-1374.
113. Schätz, A.; Reiser, O.; Stark, W. J., Nanoparticles as Semi-Heterogeneous Catalyst Supports. *Chemistry–A European Journal* **2010,** *16*, 8950-8967.
114. López-López, M.; Durán, J.; Delgado, A.; González-Caballero, F., Stability and magnetic characterization of oleate-covered magnetite ferrofluids in different nonpolar carriers. *Journal of colloid and interface science* **2005,** *291*, 144-151.
115. Viota, J.; González-Caballero, F.; Durán, J.; Delgado, A., Study of the colloidal stability of concentrated bimodal magnetic fluids. *Journal of colloid and interface science* **2007,** *309*, 135-139.
116. De, M.; Ghosh, P. S.; Rotello, V. M., Applications of nanoparticles in biology. *Advanced Materials* **2008,** *20*, 4225-4241.
117. Frey, N. A.; Peng, S.; Cheng, K.; Sun, S., Magnetic nanoparticles: synthesis, functionalization, and applications in bioimaging and magnetic energy storage. *Chemical Society Reviews* **2009,** *38*, 2532-2542.
118. Jiang, S.; Eltoukhy, A. A.; Love, K. T.; Langer, R.; Anderson, D. G., Lipidoid-coated iron oxide nanoparticles for efficient DNA and siRNA delivery. *Nano letters* **2013,** *13*, 1059-1064.
119. Khandhar, A. P.; Ferguson, R. M.; Arami, H.; Krishnan, K. M., Monodisperse magnetite nanoparticle tracers for in vivo magnetic particle imaging. *Biomaterials* **2013,** *34*, 3837-3845.
120. Lartigue, L.; Innocenti, C.; Kalaivani, T.; Awwad, A.; Sanchez Duque, M. d. M.; Guari, Y.; Larionova, J.; Guérin, C.; Montero, J.-L. G.; Barragan-Montero, V., Water-dispersible sugar-coated iron oxide nanoparticles. An evaluation of their relaxometric and magnetic hyperthermia properties. *Journal of the American Chemical Society* **2011,** *133*, 10459-10472.
121. Mornet, S.; Vasseur, S.; Grasset, F.; Veverka, P.; Goglio, G.; Demourgues, A.; Portier, J.; Pollert, E.; Duguet, E., Magnetic nanoparticle design for medical applications. *Progress in Solid State Chemistry* **2006,** *34*, 237-247.
122. Patel, D.; Moon, J. Y.; Chang, Y.; Kim, T. J.; Lee, G. H., Poly (D, L-lactide-co-glycolide) coated superparamagnetic iron oxide nanoparticles: Synthesis, characterization and in vivo study as MRI contrast agent. *Colloids and Surfaces A: Physicochemical and Engineering Aspects* **2008,** *313*, 91-94.
123. Reddy, L. H.; Arias, J. L.; Nicolas, J.; Couvreur, P., Magnetic nanoparticles: design and characterization, toxicity and biocompatibility, pharmaceutical and biomedical applications. *Chemical reviews* **2012,** *112*, 5818-5878.
124. Kim, J.; Piao, Y.; Hyeon, T., Multifunctional nanostructured materials for multimodal imaging, and simultaneous imaging and therapy. *Chemical Society Reviews* **2009,** *38*, 372-390.
125. Zhao, M.; Josephson, L.; Tang, Y.; Weissleder, R., Magnetic sensors for protease assays. *Angewandte Chemie International Edition* **2003,** *42*, 1375-1378.
126. Mohapatra, J.; Mitra, A.; Bahadur, D.; Aslam, M., Surface controlled synthesis of MFe 2 O 4 (M= Mn, Fe, Co, Ni and Zn) nanoparticles and their magnetic characteristics. *CrystEngComm* **2013,** *15*, 524-532.
127. Batlle, X.; Labarta, A. l., Finite-size effects in fine particles: magnetic and transport properties. *J. Phys-London-D Appl. Phys.* **2002,** *35*, R15-R42.
128. Caruntu, D.; Caruntu, G.; O'Connor, C. J., Magnetic properties of variable-sized Fe3O4 nanoparticles synthesized from non-aqueous homogeneous solutions of polyols. *J. Phys. D: Appl. Phys.* **2007,** *40*, 5801.
129. Morales, M. d. P.; Veintemillas-Verdaguer, S.; Montero, M.; Serna, C.; Roig, A.; Casas, L.; Martinez, B.; Sandiumenge, F., Surface and internal spin canting in γ-Fe2O3 nanoparticles. *Chem. Mater.* **1999,** *11*, 3058-3064.
130. Lak, A. Synthesis and Characterization of Magnetic Iron Oxide Nanoparticles. Technischen Universit□at Carolo-Wilhelmina zu Braunschweig, 2013.
131. Aslibeiki, B.; Kameli, P.; Salamati, H., The effect of dipole-dipole interactions on coercivity, anisotropy constant, and blocking temperature of MnFe2O4 nanoparticles. *J. Appl. Phys.* **2016,** *119*, 063901.
132. Frankamp, B. L.; Boal, A. K.; Tuominen, M. T.; Rotello, V. M., Direct control of the magnetic interaction between iron oxide nanoparticles through dendrimer-mediated self-assembly. *J. Am. Chem. Soc.* **2005,** *127*, 9731-9735.
133. Dormann, J.; Fiorani, D.; Tronc, E., On the models for interparticle interactions in nanoparticle assemblies: comparison with experimental results. *J. Magn. Magn. Mater.* **1999,** *202*, 251-267.

134. Krishnan, K. M., Biomedical nanomagnetics: a spin through possibilities in imaging, diagnostics, and therapy. *IEEE Trans. Magn.* **2010,** *46*, 2523-2558.
135. Wu, L.; Mendoza-Garcia, A.; Li, Q.; Sun, S., Organic phase syntheses of magnetic nanoparticles and their applications. *Chem. Rev.* **2016,** *116*, 10473-10512.
136. Kim, D. K.; Mikhaylova, M.; Zhang, Y.; Muhammed, M., Protective coating of superparamagnetic iron oxide nanoparticles. *Chem. Mater.* **2003,** *15*, 1617-1627.
137. Gupta, A. K.; Gupta, M., Synthesis and surface engineering of iron oxide nanoparticles for biomedical applications. *Biomaterials* **2005,** *26*, 3995-4021.
138. Yourdkhani, A., Synthesis and Characterization of Ferroic and Multiferroic Nanostructures by Liquid Phase Deposition. **2012**.
139. Sheng-Nan, S.; Chao, W.; Zan-Zan, Z.; Yang-Long, H.; Venkatraman, S. S.; Zhi-Chuan, X., Magnetic iron oxide nanoparticles: Synthesis and surface coating techniques for biomedical applications. *Chinese Physics B* **2014,** *23*, 037503.
140. Cornell, R. M.; Schwertmann, U., *The iron oxides: structure, properties, reactions, occurrences and uses*. John Wiley & Sons: 2003.
141. Demortiere, A.; Panissod, P.; Pichon, B.; Pourroy, G.; Guillon, D.; Donnio, B.; Begin-Colin, S., Size-dependent properties of magnetic iron oxide nanocrystals. *Nanoscale* **2011,** *3*, 225-232.
142. Sathya, A.; Guardia, P.; Brescia, R.; Silvestri, N.; Pugliese, G.; Nitti, S.; Manna, L.; Pellegrino, T., Co x Fe3–x O4 nanocubes for theranostic applications: effect of cobalt content and particle size. *Chem. Mater.* **2016,** *28*, 1769-1780.
143. López-Ortega, A.; Lottini, E.; Fernandez, C. d. J.; Sangregorio, C., Exploring the magnetic properties of cobalt-ferrite nanoparticles for the development of a rare-earth-free permanent magnet. *Chemistry of Materials* **2015,** *27*, 4048-4056.
144. Zhou, Z.; Zhu, X.; Wu, D.; Chen, Q.; Huang, D.; Sun, C.; Xin, J.; Ni, K.; Gao, J., Anisotropic shaped iron oxide nanostructures: controlled synthesis and proton relaxation shortening effects. *Chem. Mater.* **2015,** *27*, 3505-3515.
145. Baaziz, W.; Pichon, B. P.; Fleutot, S.; Liu, Y.; Lefevre, C.; Greneche, J.-M.; Toumi, M.; Mhiri, T.; Begin-Colin, S., Magnetic iron oxide nanoparticles: reproducible tuning of the size and nanosized-dependent composition, defects, and spin canting. *J. Phys. Chem. C* **2014,** *118*, 3795-3810.
146. Li, D.; Yun, H.; Diroll, B. T.; Doan-Nguyen, V. V.; Kikkawa, J. M.; Murray, C. B., Synthesis and Size-Selective Precipitation of Monodisperse Nonstoichiometric M x Fe3–x O4 (M= Mn, Co) Nanocrystals and Their DC and AC Magnetic Properties. *Chem. Mater.* **2016,** *28*, 480-489.
147. Vestal, C. R.; Zhang, Z. J., Effects of surface coordination chemistry on the magnetic properties of MnFe2O4 spinel ferrite nanoparticles. *J. Am. Chem. Soc.* **2003,** *125*, 9828-9833.
148. Cullity, B. D.; Graham, C. D., *Introduction to magnetic materials*. John Wiley & Sons: 2011.
149. Yang, C.; Wu, J.; Hou, Y., Fe 3 O 4 nanostructures: synthesis, growth mechanism, properties and applications. *Chem. Commun.* **2011,** *47*, 5130-5141.
150. Guardia, P.; Labarta, A.; Batlle, X., Tuning the size, the shape, and the magnetic properties of iron oxide nanoparticles. *J. Phys. Chem. C* **2010,** *115*, 390-396.
151. Roca, A. G.; Marco, J. F.; Morales, M. d. P.; Serna, C. J., Effect of nature and particle size on properties of uniform magnetite and maghemite nanoparticles. *J. Phys. Chem. C* **2007,** *111*, 18577-18584.
152. Lu, A. H.; Salabas, E. e. L.; Schüth, F., Magnetic nanoparticles: synthesis, protection, functionalization, and application. *Angew. Chem. Int. Ed.* **2007,** *46*, 1222-1244.
153. Laurent, S.; Forge, D.; Port, M.; Roch, A.; Robic, C.; Vander Elst, L.; Muller, R. N., Magnetic iron oxide nanoparticles: synthesis, stabilization, vectorization, physicochemical characterizations, and biological applications. *Chem. Rev.* **2008,** *108*, 2064-2110.
154. Paul, B. K.; Moulik, S. P., Uses and applications of microemulsions. *Curr. Sci.* **2001**, 990-1001.
155. Tartaj, P.; del Puerto Morales, M.; Veintemillas-Verdaguer, S.; González-Carreño, T.; Serna, C. J., The preparation of magnetic nanoparticles for applications in biomedicine. *J. Phys. D: Appl. Phys.* **2003,** *36*, R182.
156. Tang, J.; Myers, M.; Bosnick, K. A.; Brus, L. E., Magnetite Fe3O4 nanocrystals: spectroscopic observation of aqueous oxidation kinetics. *J. Phys. Chem. B* **2003,** *107*, 7501-7506.
157. Munshi, N.; De, T. K.; Maitra, A., Size modulation of polymeric nanoparticles under controlled dynamics of microemulsion droplets. *J. Colloid Interface Sci.* **1997,** *190*, 387-391.

158. Lam, U. T.; Mammucari, R.; Suzuki, K.; Foster, N. R., Processing of iron oxide nanoparticles by supercritical fluids. *Ind. Eng. Chem. Res.* **2008,** *47*, 599-614.
159. Tavakoli, A.; Sohrabi, M.; Kargari, A., A review of methods for synthesis of nanostructured metals with emphasis on iron compounds. *Chem. Pap.* **2007,** *61*, 151-170.
160. Mao, B.; Kang, Z.; Wang, E.; Lian, S.; Gao, L.; Tian, C.; Wang, C., Synthesis of magnetite octahedrons from iron powders through a mild hydrothermal method. *Mater. Res. Bull.* **2006,** *41*, 2226-2231.
161. Zhu, H.; Yang, D.; Zhu, L., Hydrothermal growth and characterization of magnetite (Fe3O4) thin films. *Surf. Coat. Technol.* **2007,** *201*, 5870-5874.
162. Joseyphus, R. J.; Kodama, D.; Matsumoto, T.; Sato, Y.; Jeyadevan, B.; Tohji, K., Role of polyol in the synthesis of Fe particles. *J. Magn. Magn. Mater.* **2007,** *310*, 2393-2395.
163. Cai, W.; Wan, J., Facile synthesis of superparamagnetic magnetite nanoparticles in liquid polyols. *J. Colloid Interface Sci.* **2007,** *305*, 366-370.
164. Sun, S.; Zeng, H.; Robinson, D. B.; Raoux, S.; Rice, P. M.; Wang, S. X.; Li, G., Monodisperse mfe2o4 (m= fe, co, mn) nanoparticles. *J. Am. Chem. Soc.* **2004,** *126*, 273-279.
165. Park, J.; An, K.; Hwang, Y.; Park, J.-G.; Noh, H.-J.; Kim, J.-Y.; Park, J.-H.; Hwang, N.-M.; Hyeon, T., Ultra-large-scale syntheses of monodisperse nanocrystals. *Nat. Mater.* **2004,** *3*, 891.
166. Park, J.; Lee, E.; Hwang, N. M.; Kang, M.; Kim, S. C.; Hwang, Y.; Park, J. G.; Noh, H. J.; Kim, J. Y.; Park, J. H., One-nanometer-scale size-controlled synthesis of monodisperse magnetic Iron oxide nanoparticles. *Angew. Chem.* **2005,** *117*, 2932-2937.
167. Zeng, H.; Rice, P. M.; Wang, S. X.; Sun, S., Shape-controlled synthesis and shape-induced texture of MnFe2O4 nanoparticles. *J. Am. Chem. Soc.* **2004,** *126*, 11458-11459.
168. Hufschmid, R.; Arami, H.; Ferguson, R. M.; Gonzales, M.; Teeman, E.; Brush, L. N.; Browning, N. D.; Krishnan, K. M., Synthesis of phase-pure and monodisperse iron oxide nanoparticles by thermal decomposition. *Nanoscale* **2015,** *7*, 11142-11154.
169. Guardia, P.; Pérez, N.; Labarta, A.; Batlle, X., Controlled synthesis of iron oxide nanoparticles over a wide size range. *Langmuir* **2009,** *26*, 5843-5847.
170. Vreeland, E. C.; Watt, J.; Schober, G. B.; Hance, B. G.; Austin, M. J.; Price, A. D.; Fellows, B. D.; Monson, T. C.; Hudak, N. S.; Maldonado-Camargo, L., Enhanced nanoparticle size control by extending LaMer's mechanism. *Chem. Mater.* **2015,** *27*, 6059-6066.
171. Guardia, P.; Perez-Juste, J.; Labarta, A.; Batlle, X.; Liz-Marzán, L. M., Heating rate influence on the synthesis of iron oxide nanoparticles: the case of decanoic acid. *Chem. Commun.* **2010,** *46*, 6108-6110.
172. Harris, R. A.; Shumbula, P. M.; van der Walt, H. t., Analysis of the interaction of surfactants oleic acid and oleylamine with iron oxide nanoparticles through molecular mechanics modeling. *Langmuir* **2015,** *31*, 3934-3943.
173. Park, J.; Joo, J.; Kwon, S. G.; Jang, Y.; Hyeon, T., Synthesis of monodisperse spherical nanocrystals. *Angew. Chem. Int. Ed.* **2007,** *46*, 4630-4660.
174. Ho, C.-H.; Tsai, C.-P.; Chung, C.-C.; Tsai, C.-Y.; Chen, F.-R.; Lin, H.-J.; Lai, C.-H., Shape-controlled growth and shape-dependent cation site occupancy of monodisperse Fe3O4 nanoparticles. *Chem. Mater.* **2011,** *23*, 1753-1760.
175. van Embden, J.; Chesman, A. S.; Jasieniak, J. J., The heat-up synthesis of colloidal nanocrystals. *Chem. Mater.* **2015,** *27*, 2246-2285.
176. LaMer, V. K.; Dinegar, R. H., Theory, production and mechanism of formation of monodispersed hydrosols. *J. Am. Chem. Soc.* **1950,** *72*, 4847-4854.
177. Thanh, N. T.; Maclean, N.; Mahiddine, S., Mechanisms of nucleation and growth of nanoparticles in solution. *Chem. Rev.* **2014,** *114*, 7610-7630.
178. Kwon, S. G.; Hyeon, T., Formation mechanisms of uniform nanocrystals via hot-injection and heat-up methods. *Small* **2011,** *7*, 2685-2702.
179. Waurisch, C. Thermodynamic and kinetic investigations into the syntheses of CdSe and CdTe nanoparticles. Saechsische Landesbibliothek-Staats-und Universitaetsbibliothek Dresden, 2012.
180. van Embden, J.; Sader, J. E.; Davidson, M.; Mulvaney, P., Evolution of colloidal nanocrystals: theory and modeling of their nucleation and growth. *J. Phys. Chem. C* **2009,** *113*, 16342-16355.
181. Rempel, J. Y.; Bawendi, M. G.; Jensen, K. F., Insights into the kinetics of semiconductor nanocrystal nucleation and growth. *J. Am. Chem. Soc.* **2009,** *131*, 4479-4489.

182. Barbey, R.; Lavanant, L.; Paripovic, D.; Schuwer, N.; Sugnaux, C.; Tugulu, S.; Klok, H.-A., Polymer brushes via surface-initiated controlled radical polymerization: synthesis, characterization, properties, and applications. *Chem. Rev.* **2009,** *109*, 5437-5527.
183. Kango, S.; Kalia, S.; Celli, A.; Njuguna, J.; Habibi, Y.; Kumar, R., Surface modification of inorganic nanoparticles for development of organic–inorganic nanocomposites—a review. *Prog. Polym. Sci.* **2013,** *38*, 1232-1261.
184. Hui, C. M.; Pietrasik, J.; Schmitt, M.; Mahoney, C.; Choi, J.; Bockstaller, M. R.; Matyjaszewski, K., Surface-initiated polymerization as an enabling tool for multifunctional (nano-) engineered hybrid materials. *Chem. Mater.* **2013,** *26*, 745-762.
185. Tsujii, Y.; Ohno, K.; Yamamoto, S.; Goto, A.; Fukuda, T., Structure and properties of high-density polymer brushes prepared by surface-initiated living radical polymerization. In *Surface-initiated polymerization I*, Springer: 2006; pp 1-45.
186. Brandani, P.; Stroeve, P., Adsorption and desorption of PEO− PPO− PEO triblock copolymers on a self-assembled hydrophobic surface. *Macromolecules* **2003,** *36*, 9492-9501.
187. Kenausis, G. L.; Vörös, J.; Elbert, D. L.; Huang, N.; Hofer, R.; Ruiz-Taylor, L.; Textor, M.; Hubbell, J. A.; Spencer, N. D., Poly (L-lysine)-g-poly (ethylene glycol) layers on metal oxide surfaces: attachment mechanism and effects of polymer architecture on resistance to protein adsorption. *J. Phys. Chem. B* **2000,** *104*, 3298-3309.
188. Tran, Y.; Auroy, P., Synthesis of poly (styrene sulfonate) brushes. *J. Am. Chem. Soc.* **2001,** *123*, 3644-3654.
189. Rühe, J.; Knoll, W., Functional polymer brushes. *J. Macromol. Sci., Polym. Rev.* **2002,** *42*, 91-138.
190. Mansky, P.; Liu, Y.; Huang, E.; Russell, T.; Hawker, C., Controlling polymer-surface interactions with random copolymer brushes. *Science* **1997,** *275*, 1458-1460.
191. Edmondson, S.; Huck, W. T., Controlled growth and subsequent chemical modification of poly (glycidyl methacrylate) brushes on silicon wafers. *J. Mater. Chem.* **2004,** *14*, 730-734.
192. Ohno, K.; Morinaga, T.; Koh, K.; Tsujii, Y.; Fukuda, T., Synthesis of monodisperse silica particles coated with well-defined, high-density polymer brushes by surface-initiated atom transfer radical polymerization. *Macromolecules* **2005,** *38*, 2137-2142.
193. Georges, M. K.; Veregin, R. P.; Kazmaier, P. M.; Hamer, G. K., Narrow molecular weight resins by a free-radical polymerization process. *Macromolecules* **1993,** *26*, 2987-2988.
194. Benoit, D.; Grimaldi, S.; Robin, S.; Finet, J.-P.; Tordo, P.; Gnanou, Y., Kinetics and mechanism of controlled free-radical polymerization of styrene and n-butyl acrylate in the presence of an acyclic β-phosphonylated nitroxide. *J. Am. Chem. Soc.* **2000,** *122*, 5929-5939.
195. Matyjaszewski, K.; Gaynor, S.; Wang, J.-S., Controlled radical polymerizations: the use of alkyl iodides in degenerative transfer. *Macromolecules* **1995,** *28*, 2093-2095.
196. Kato, M.; Kamigaito, M.; Sawamoto, M.; Higashimura, T., Polymerization of methyl methacrylate with the carbon tetrachloride/dichlorotris-(triphenylphosphine) ruthenium (II)/methylaluminum bis (2, 6-di-tert-butylphenoxide) initiating system: possibility of living radical polymerization. *Macromolecules* **1995,** *28*, 1721-1723.
197. Wang, J.-S.; Matyjaszewski, K., Controlled/" living" radical polymerization. Atom transfer radical polymerization in the presence of transition-metal complexes. *J. Am. Chem. Soc.* **1995,** *117*, 5614-5615.
198. Krstina, J.; Moad, G.; Rizzardo, E.; Winzor, C. L.; Berge, C. T.; Fryd, M., Narrow polydispersity block copolymers by free-radical polymerization in the presence of macromonomers. *Macromolecules* **1995,** *28*, 5381-5385.
199. Yamago, S.; Iida, K.; Yoshida, J.-i., Organotellurium compounds as novel initiators for controlled/living radical polymerizations. Synthesis of functionalized polystyrenes and end-group modifications. *J. Am. Chem. Soc.* **2002,** *124*, 2874-2875.
200. Wayland, B. B.; Poszmik, G.; Mukerjee, S. L.; Fryd, M., Living radical polymerization of acrylates by organocobalt porphyrin complexes. *J. Am. Chem. Soc.* **1994,** *116*, 7943-7944.
201. Babu, K.; Dhamodharan, R., Synthesis of polymer grafted magnetite nanoparticle with the highest grafting density via controlled radical polymerization. *Nanoscale Res. Lett.* **2009,** *4*, 1090.
202. Pyun, J.; Jia, S.; Kowalewski, T.; Patterson, G. D.; Matyjaszewski, K., Synthesis and characterization of organic/inorganic hybrid nanoparticles: kinetics of surface-initiated atom transfer radical polymerization and morphology of hybrid nanoparticle ultrathin films. *Macromolecules* **2003,** *36*, 5094-5104.

203. Ohno, K.; Akashi, T.; Huang, Y.; Tsujii, Y., Surface-initiated living radical polymerization from narrowly size-distributed silica nanoparticles of diameters less than 100 nm. *Macromolecules* **2010,** *43*, 8805-8812.
204. Ohno, K.; Mori, C.; Akashi, T.; Yoshida, S.; Tago, Y.; Tsujii, Y.; Tabata, Y., Fabrication of contrast agents for magnetic resonance imaging from polymer-brush-afforded iron oxide magnetic nanoparticles prepared by surface-initiated living radical polymerization. *Biomacromolecules* **2013,** *14*, 3453-3462.
205. Kang, C.; Crockett, R.; Spencer, N. D., The influence of surface grafting on the growth rate of polymer chains. *Polym. Chem.* **2016,** *7*, 302-309.
206. Sun, Y.; Ding, X.; Zheng, Z.; Cheng, X.; Hu, X.; Peng, Y., Surface initiated ATRP in the synthesis of iron oxide/polystyrene core/shell nanoparticles. *Eur. Polym. J.* **2007,** *43*, 762-772.
207. Galeotti, F.; Bertini, F.; Scavia, G.; Bolognesi, A., A controlled approach to iron oxide nanoparticles functionalization for magnetic polymer brushes. *J. Colloid Interface Sci.* **2011,** *360*, 540-547.
208. Louis Chakkalakal, G.; Alexandre, M.; Abetz, C.; Boschetti-de-Fierro, A.; Abetz, V., Surface-Initiated Controlled Radical Polymerization from Silica Nanoparticles with High Initiator Density. *Macromol. Chem. Phys.* **2012,** *213*, 513-528.
209. Garcia, I.; Zafeiropoulos, N.; Janke, A.; Tercjak, A.; Eceiza, A.; Stamm, M.; Mondragon, I., Functionalization of iron oxide magnetic nanoparticles with poly (methyl methacrylate) brushes via grafting-from atom transfer radical polymerization. *J. Polym. Sci., Part A: Polym. Chem.* **2007,** *45*, 925-932.
210. Choi, J.; Hui, C. M.; Pietrasik, J.; Dong, H.; Matyjaszewski, K.; Bockstaller, M. R., Toughening fragile matter: mechanical properties of particle solids assembled from polymer-grafted hybrid particles synthesized by ATRP. *Soft Matter* **2012,** *8*, 4072-4082.
211. Marutani, E.; Yamamoto, S.; Ninjbadgar, T.; Tsujii, Y.; Fukuda, T.; Takano, M., Surface-initiated atom transfer radical polymerization of methyl methacrylate on magnetite nanoparticles. *Polymer* **2004,** *45*, 2231-2235.
212. Xue, Y.-H.; Zhu, Y.-L.; Quan, W.; Qu, F.-H.; Han, C.; Fan, J.-T.; Liu, H., Polymer-grafted nanoparticles prepared by surface-initiated polymerization: the characterization of polymer chain conformation, grafting density and polydispersity correlated to the grafting surface curvature. *Phys. Chem. Chem. Phys.* **2013,** *15*, 15356-15364.
213. Matyjaszewski, K.; Xia, J., Atom transfer radical polymerization. *Chem. Rev.* **2001,** *101*, 2921-2990.
214. Yan, J.; Pan, X.; Schmitt, M.; Wang, Z.; Bockstaller, M. R.; Matyjaszewski, K., Enhancing initiation efficiency in metal-free surface-initiated atom transfer radical polymerization (SI-ATRP). *ACS Macro Lett.* **2016,** *5*, 661-665.
215. Yan, J.; Kristufek, T.; Schmitt, M.; Wang, Z.; Xie, G.; Dang, A.; Hui, C. M.; Pietrasik, J.; Bockstaller, M. R.; Matyjaszewski, K., Matrix-free particle brush system with bimodal molecular weight distribution prepared by SI-ATRP. *Macromolecules* **2015,** *48*, 8208-8218.
216. Wang, J.-L.; Grimaud, T.; Matyjaszewski, K., Kinetic study of the homogeneous atom transfer radical polymerization of methyl methacrylate. *Macromolecules* **1997,** *30*, 6507-6512.
217. Matyjaszewski, K., Atom transfer radical polymerization (ATRP): current status and future perspectives. *Macromolecules* **2012,** *45*, 4015-4039.
218. Fischer, H., The persistent radical effect: a principle for selective radical reactions and living radical polymerizations. *Chem. Rev.* **2001,** *101*, 3581-3610.
219. Tang, W.; Tsarevsky, N. V.; Matyjaszewski, K., Determination of equilibrium constants for atom transfer radical polymerization. *J. Am. Chem. Soc.* **2006,** *128*, 1598-1604.
220. Vana, P.; Davis, T. P.; Barner-Kowollik, C., Easy access to chain-length-dependent termination rate coefficients using RAFT polymerization. *Macromol. Rapid Commun.* **2002,** *23*, 952-956.
221. Odian, G., *Principles of polymerization*. John Wiley & Sons: 2004.
222. Patten, T. E.; Matyjaszewski, K., Atom transfer radical polymerization and the synthesis of polymeric materials. *Adv. Mater.* **1998,** *10*, 901-915.
223. Le Grognec, E.; Claverie, J.; Poli, R., Radical polymerization of styrene controlled by half-sandwich Mo (III)/Mo (IV) couples: all basic mechanisms are possible. *J. Am. Chem. Soc.* **2001,** *123*, 9513-9524.
224. Matyjaszewski, K.; Wei, M.; Xia, J.; McDermott, N. E., Controlled/"living" radical polymerization of styrene and methyl methacrylate catalyzed by iron complexes. *Macromolecules* **1997,** *30*, 8161-8164.
225. Ishio, M.; Katsube, M.; Ouchi, M.; Sawamoto, M.; Inoue, Y., Active, versatile, and removable iron catalysts with phosphazenium salts for living radical polymerization of methacrylates. *Macromolecules* **2008,** *42*, 188-193.
226. Braunecker, W. A.; Brown, W. C.; Morelli, B. C.; Tang, W.; Poli, R.; Matyjaszewski, K., Origin of activity in Cu-, Ru-, and Os-mediated radical polymerization. *Macromolecules* **2007,** *40*, 8576-8585.

227. Seeliger, F.; Matyjaszewski, K., Temperature effect on activation rate constants in ATRP: new mechanistic insights into the activation process. *Macromolecules* **2009,** *42*, 6050-6055.
228. Seeliger, F.; Matyjaszewski, K., Temperature Effect on Activation Rate Constants in ATRP: New Mechanistic Insights into the Activation Process. *Macromolecules* **2010,** *43*, 5478-5478.
229. Morick, J.; Buback, M.; Matyjaszewski, K., Activation–deactivation equilibrium of atom transfer radical polymerization of styrene up to high pressure. *Macromol. Chem. Phys.* **2011,** *212*, 2423-2428.
230. Mueller, L.; Jakubowski, W.; Matyjaszewski, K.; Pietrasik, J.; Kwiatkowski, P.; Chaladaj, W.; Jurczak, J., Synthesis of high molecular weight polystyrene using AGET ATRP under high pressure. *Eur. Polym. J.* **2011,** *47*, 730-734.
231. Braunecker, W. A.; Tsarevsky, N. V.; Gennaro, A.; Matyjaszewski, K., Thermodynamic components of the atom transfer radical polymerization equilibrium: quantifying solvent effects. *Macromolecules* **2009,** *42*, 6348-6360.
232. Tang, W.; Kwak, Y.; Braunecker, W.; Tsarevsky, N. V.; Coote, M. L.; Matyjaszewski, K., Understanding atom transfer radical polymerization: effect of ligand and initiator structures on the equilibrium constants. *J. Am. Chem. Soc.* **2008,** *130*, 10702-10713.
233. Kwiatkowski, P.; Jurczak, J.; Pietrasik, J.; Jakubowski, W.; Mueller, L.; Matyjaszewski, K., High molecular weight polymethacrylates by AGET ATRP under high pressure. *Macromolecules* **2008,** *41*, 1067-1069.
234. Qiu, J.; Charleux, B.; Matyjaszewski, K., Controlled/living radical polymerization in aqueous media: homogeneous and heterogeneous systems. *Prog. Polym. Sci.* **2001,** *26*, 2083-2134.
235. Matyjaszewski, K.; Beers, K. L.; Metzner, Z.; Woodworth, B., Controlled/living radical polymerization in the undergraduate laboratories. 2. Using atrp in limited amounts of air to prepare block and statistical copolymers of n-butyl acrylate and styrene. *J. Chem. Educ.* **2001,** *78*, 547.
236. Min, K.; Gao, H.; Matyjaszewski, K., Preparation of homopolymers and block copolymers in miniemulsion by ATRP using activators generated by electron transfer (AGET). *J. Am. Chem. Soc.* **2005,** *127*, 3825-3830.
237. Dong, H.; Matyjaszewski, K., ARGET ATRP of 2-(dimethylamino) ethyl methacrylate as an intrinsic reducing agent. *Macromolecules* **2008,** *41*, 6868-6870.
238. Matyjaszewski, K.; Nanda, A. K.; Tang, W., Effect of [CuII] on the rate of activation in ATRP. *Macromolecules* **2005,** *38*, 2015-2018.
239. Mishra, V.; Kumar, R., Living radical polymerization: A review. *J. Sci. Res* **2012,** *56*, 141-176.

Chapter 3

Section1

Combined Experimental and Theoretical Investigation of Heating Rate on Growth of Iron Oxide Nanoparticles[1]

3.1.1 Introduction

As discussed in Chapter 2, the synthesis of monodisperse magnetic MNPs with well-defined sizes is a key factor for different applications, as the size strongly influences the NPs' magnetic properties.[1-8] We have chosen thermal decomposition synthesis route to make size controlled NPs.[9-12] In a typical reaction, an organometallic precursor is decomposed at high temperature in a solvent with a high boiling point. Organic ligands, such as oleic acids and oleylamine, are typical surfactants that serve as stabilizers during the reaction.[10, 13]

3.1.1.1 Motivation

[1] **The results of this chapter are fully or in part published in *Chem. Mater.* with DOI: *10.1021/acs.chemmater.7b02872* and J. Phys. Chem. C. with DOI: *10.1021/acs.jpcc.8b06927* by H. Sharifi et al.**

In a typical thermal decomposition reaction, the precursors - either reagents or the secondary complexes - undergo an increased thermodynamic driving force to form "monomers". Reaction of monomers with each other leads to the formation of nuclei. The nucleation of nascent NPs is triggered by the growth heating process. Upon continued heating during reflux time, the initial nuclei grow into mature NPs. Thermal decomposition endows specific subtleties due to the complex interplay between reaction variables, such as concentrations of precursors,[14] solvent[15], surfactants,[16] as well as solvent boiling point,[10-11, 17] reaction time,[18-19] and precursor to surfactant ratio,[14, 16-17] all of which drastically influence the final size and the respective size distribution of the NPs. In a typical thermal decomposition synthesis, the heating rate is a crucial factor because it affects nucleation through the monomer concentration. Tuning the heating rate is therefore a rational way to modulate the nucleation process and consequently to tune the final size and polydispersity of the NPs.[20-21]

The underlying phenomenology of the particle formation mechanism can be usually understood within the context of classical nucleation and growth theory and within a model proposed by LaMer.[22] The nucleation and growth of NPs is described by a set of coupled time-dependent equations that govern the dynamics of monomer concentration, nucleation rate, and particle size distribution.[20, 23-26] A numerical treatment provides a powerful tool for a better understanding of the nucleation and growth processes of NPs at the molecular level and therefore provides information on how to design an effective synthesis. As a result, a more systematically controlled synthesis can be devised.

3.1.1.2 Aim of this section

This section presents a combined experimental and theoretical study on the size evolution and polydispersity of magnetic iron-oxide NPs while varying only the growth heating rate during synthesis. NPs with controllable sizes from 6 nm to 27 nm were obtained with a narrow size distribution (typically below 10%). Crystallinity and the magnetic properties of the NP were investigated using different analytical techniques. To gain further insight concerning the NPs formation we numerically simulated the nucleation and growth process at different heating rates to understand the time-dependent evolution of the NP size distribution (among other observables).

3.1.2 Experiment

3.1.2.1 Materials

Iron (III) acetylacetonate (97%), oleylamine (OAM, >70%), benzyl ether (BE, technical grade 98%), oleic acid (OAC, technical grade, 90%), hexane, ethanol and acetone were purchased from Sigma Aldrich. Hexadecandiol (99%) was purchased from TCI. All chemicals were used as received.

3.1.2.2 Synthesis method

To synthesize the NPs, 2.0 mmol of iron acetylacetonate, 10 mmol of hexadecandiol, 6 mmol of oleylamine and 6 mmol of oleic acid were mixed in 20 mL of benzyl ether in a three-necked round bottom flask under a gentle flow of N_2. The mixture was magnetically stirred and degassed under vacuum (0.1-0.2 mbar) at 383 K (110 °C) for 60 min. Under N_2 blanketing, the temperature was then raised to 453 K (180 °C), with a heating rate (H.R.) of about 6.5 K/min. The solution was kept at 453 K for two hours to ensure full decomposition of the precursor. Subsequently, the solution was heated to a reflux temperature of almost 567 K (~ 294 °C) at a constant heating rate. Different syntheses were performed in which the heating rates were systematically varied from 6.4 K/min (A_1), 5.4 K/min (A_2), 4.2 K/min (A_3), 3.2 K/min (A_4), 2.2 K/min (A_5), 1.5 K/min (A_6) and 0.8 K/min (A_7), where A_i represents the synthesis batch. The reaction was kept at the reflux temperature for 1 h. **Figure 3.1.1** schematically summarizes the reaction conditions. The resultant black solution was cooled down to room temperature under N_2 blanketing. After precipitation of the product by adding 40 mL of ethanol/acetone, a mild centrifugation (6000 rpm for 8 min) was applied to collect the purified product. The NPs formed a stable dispersion in toluene/hexane after further purification by dispersion in hexane and precipitation by ethanol.

3.1.2.3 Characterizations

The NPs were characterized by transmission electron microscopy (TEM) and high resolution TEM (HRTEM), with an accelerating voltage of 120kV on JEOL JEM1400 and 200kV on FEI Tecnai F20 200kV respectively. The size distributions of NPs were calculated

from the size measurements of more than 2000 NPs using image J software. Samples were prepared using the self-assembly method at the water-air interface.[27]

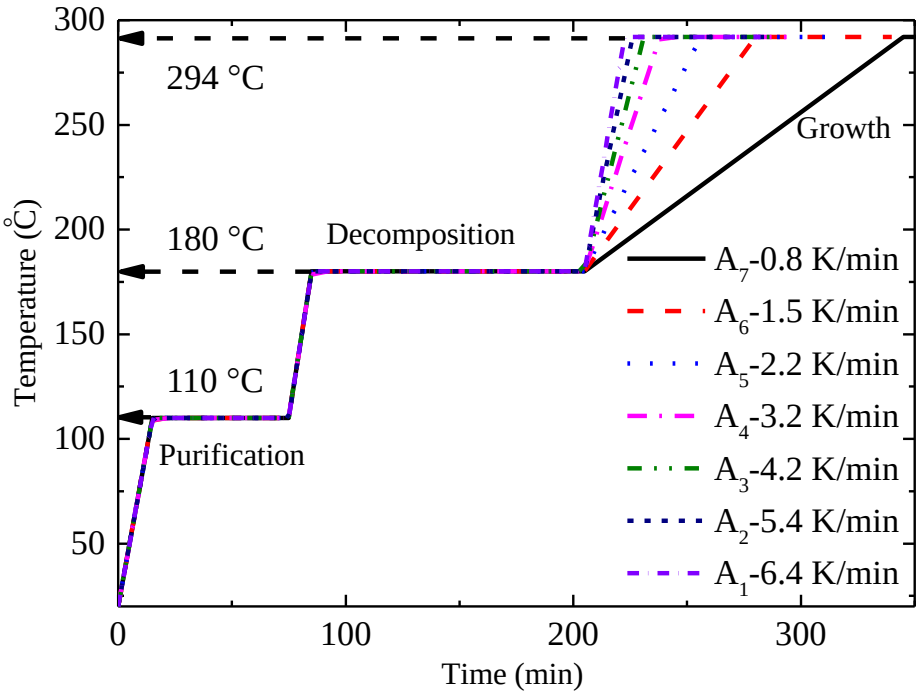

Figure 3.1.1 Heating conditions of samples (A_1-A_7).

The X-ray diffraction (XRD) was performed at room temperature with a monochromatic copper radiation source CuKα (λ=1.5406 Å) in the 15−65° (2θ) range with a scan step of 0.03°. The mean size and lattice parameter of the crystal domains calculated from XRD pattern by using Scherrer and Bragg equations,[28-30] respectively. The crystallite size of NPs for the most intense, (311) plane was determined using Scherrer formula:[29]

$$D = K\lambda/\beta\mathrm{Cos}\theta \qquad (3.1.1)$$

where λ is the wavelength of X-ray (λ=1.5406 Å); β the full width at half maximum (obtained from fitting the 311 peak); Θ is Bragg's diffraction angle (around 35°-obtained from fitting the 311 peak) and K is the shape factor which is normally taken as 0.9-1.0 for ferrites. The interplanar distances d_{hkl} (A˚) (for 311) were calculated using Bragg's law [29-30] and then the lattice constant of the samples was calculated using the relations:

$$n\lambda = 2dSin\theta \qquad (3.1.2)$$

$$a = d_{hkl}\sqrt{h^2 + k^2 + l^2} \qquad (3.1.3)$$

where *a* is lattice constant; (*hkl*) is the indexing plane of atoms which can be obtained from X-ray diffraction data.[31] Infrared spectra were recorded between 4000 and 400 cm^{-1} with a Fourier transform infrared (FTIR) spectrometer. The NPs were gently ground and diluted with KBr and compressed into a pellet. Thermogravimetric measurements were performed on dried powder samples from 20 to 800 °C at 10 °C/min under N_2. Using TGA, one can determine the grafting density of the surfactant on the surface of NPs. The amount of grafting was calculated from the TGA and DTA data, according to the following equations:

$$\text{Number of surfactants (molecules)} \qquad N_s = \frac{m_1 - m_3}{M} \times N_A \qquad (3.1.4)$$

$$\text{Number of NPs} \qquad N_P = \frac{m_3}{\rho \times V} \qquad (3.1.5)$$

$$\text{Graft density (molecules/nm}^2\text{)} \qquad G.D. = \frac{N_s}{N_P \times A} \qquad (3.1.6)$$

where m_1 and m_3 are the amount of mass in the first and third DTA peaks, ρ is the density of NPs (~ 5.18 g/cm^3), *M* is the molecular weight of capped surfactant (282.46 g/mol-here is oleate), *V* is the volume of each individual NP and *A* is the average surface area of single NP. Magnetization measurements of powder samples were performed using a quantum design SQUID magnetometer. Hysteresis loops *M(H)* were measured at room temperature and 2 K. Zero-field-cooling (ZFC) and field-cooling (FC) magnetization curves were performed in the temperature range between 5 K and 300 K to determine blocking temperature, T_B, and magnetic anisotropy constant, *K*. Mössbauer experiments (^{57}Fe) were performed at two different temperatures, above the Verwey transition at 124 K and below at 5 K, in transmission geometry in a closed cycle cryostat (Montana Inst.) with a custom built sample holder. We obtained from Lorentzian Site Analysis of the experimental data (Recoil software)[32] three Fe-sextets which we ascribed to the magnetic hyperfine splitting of iron-sites on tetrahedral and octahedral positions as present in magnetite and maghemite. The spectral intensities associated with the charge ordering of Fe^{2+} in octahedral and tetrahedral coordination was used as an indicator for the fraction of magnetite. Furthermore, paramagnetic Fe-contributions were absent in all Mössbauer spectra of this series. Mössbauer spectra of sample with small size shows superparamagnetic behavior in zero field and could not be resolved down to lowest experimental temperature of 5 K. In order to slow down the magnetic fluctuations of these particles, we applied an external magnetic field of 1 T.

3.1.2.4 Simulation details

Using standard population balance model,[20-21, 23, 26] the population (number) of the particles with radius r and at time t is given by $N(r,t)$. The evolution of the particles with different size is propagated by the governing equation obtained from the mass conservation:

$$\frac{\partial N(r,t)}{\partial t} + \frac{\partial [N(r,t)\Gamma(r,t)]}{\partial t} = R_{nuc} g(r) \qquad (3.1.7)$$

where $\Gamma(r,t)$ is the instantaneous growth rate, R_{nuc} is the nucleation rate and $g(r)$ is the nucleation distribution function.

The surface free of a particle of radius r is $\Delta G_S = 4\pi r^2 \gamma$ where γ is the surface energy. The bulk free energy is given by $\Delta G_V = -\frac{4\pi r^3 RT}{3V_m} \ln S$, where R, T, V_m and S are the gas constant, temperature, molar volume of a monomer and supersaturation respectively. The nucleation process occurs for the particles having a radius comparable to the critical radius, which is obtained by the minimization of total free energy $\Delta G_T = \Delta G_S + \Delta G_V$ with respect to the particle radius r,

$$r_c = 2\gamma V_m / RT \ln S \qquad (3.1.8)$$

For a system containing monomers of size r_m and corresponding volume of V_m, based on the nucleation kinetics, the nucleation rate is given by

$$R_{nuc} = 8\pi r_m D N_A S^{pu+1} [C]_\infty^2 \exp\left\{\frac{-(4\pi r_c^2 \gamma)}{3k_B T}\right\} \qquad (3.1.9)$$

Where D is the monomer diffusion coefficient, N_A is the Avogadro constant, $S = [C]/[C]_\infty$ is the dimensionless supersaturation which is defined as the bulk concentration of the monomer normalized to the equilibrium concentration of the monomers near an infinitely flat surface. The exponents of the supersaturation are the normalized critical radius to the monomer radius, $p = (r_c/r_m)^3$ and the coagulation parameter u. The surface energy is given by γ which is normalized to the thermal energy $k_B T$. The new nuclei are formed by a thermalized Gaussian distribution around the critical radius with fwhm $\approx k_B T$

$$g(r) = \frac{1}{\sigma\sqrt{2\pi}} e^{-\frac{k(r-r_C)^2}{2\sigma^2}} \qquad (3.1.10)$$

Where $k = 1.0\ kJ\ mol^{-1}\ nm^{-1}$ and $\sigma^2 \cong k_B T/2$.

The mechanism of the particle growth is carried out when the bulk monomers diffuse to the interface of the particles. Using the Fick's law, the total diffusive flux of monomers to the surface of spherical particle of radius r is determined by

$$I_{diff} = 4\pi r D([C]_b - [C]_i) \qquad (3.1.11)$$

Where $[C]_b$ and $[C]_i$ are the bulk and interfacial monomer concentrations. At the interfacial region, the diffused monomers adsorb on the particle surface according to the reaction rate k_r which is leading to the particle growth or the monomers which are already adsorbed on the particle surface desorb with the rate of k_{des} into the interface. The reaction flux becomes

$$I_{react} = 4\pi r^2(k_r[C]_i - k_{des}) \qquad (3.1.12)$$

In the steady state, the diffusive and reactive fluxes should be equal $I_{diff} = I_{react}$. This enables us to find the interfacial concentration

$$[C]_i = \frac{D[C]_b + k_{des} r}{k_r r + D} \qquad (3.1.13)$$

By replacing **Equation (3.1.12)** into **Equation (3.1.10)**, the steady state flux becomes

$$I_{SS} = 4\pi r D\left[[C]_b - \left(\frac{D[C]_b + k_{des} r}{k_r r + D}\right)\right] \qquad (3.1.14)$$

For a particle of size r based on the equilibrium solubility, the equilibrium concentration is given by

$$[\mathrm{C}]_\mathrm{e} = \frac{k_{des}}{k_r} \qquad (3.1.15)$$

Moreover, using Gibbs-Thomson equation, the equilibrium concentration is obtained by

$$[\mathrm{C}]_\mathrm{e} = [\mathrm{C}]_\infty \exp\left\{\frac{2\gamma V_m}{rRT}\right\} \qquad (3.1.16)$$

The total steady state flux is related to the particle volume change over time

$$I_{SS} = \frac{d}{dt}\frac{4\pi r^3}{3V_m} = \frac{4\pi r^2}{V_m}\frac{dr}{dt} \qquad (3.1.17)$$

where V_m is the molar volume of a monomer. Combining **Equations (3.1.13)-(3.1.16)**, the instantaneous growth rate of a particle of size r becomes

$$\Gamma(\mathrm{r,t}) = \frac{dr}{dt} = \frac{DV_m S\left(1 - e^{\frac{2\gamma V_m}{rRT}}\right)}{\left(r + \frac{D}{k_r}\right)} \qquad (3.1.18)$$

By rescaling the radius and time in the above relation, it is possible to rewrite the relation in the following dimensionless relation

$$\Gamma = \frac{d\beta}{d\tau} = \frac{\left(S - \exp\left\{\frac{1}{\beta}\right\}\right)}{(\beta + \xi)} \qquad (3.1.19)$$

Where $\beta = r\phi$, $\tau = t\psi$, $\phi = RT/2\gamma V_m$, $\psi = \phi^2 D V_m [C]_\infty$. The dimensionless number ξ, which is known as Damkohler number, determines the ratio of diffusion to reaction rates

$$\xi = \frac{D\phi}{k_r} \qquad (3.1.20)$$

As it is clear from **Equation (3.1.11)**, the growth rate asymptotically tends to zero as the Damkohler number increases. For systems possessing $\xi \gg 1$, the kinetics of the growth is reaction limited. Since in this regime $k_r \ll D$, the reaction rate has slower kinetics in comparison to the diffusion mechanism of the monomers. On the other hand, when $\xi \ll 1$, the kinetics of the growth becomes diffusion limited since in this regime, $k_r \gg D$, accordingly the diffusion mechanism has relatively slower kinetics with respect to reaction of monomers to the particle surface.

The precursor disassociates from its ligands or reacts to form free monomer. The dynamics of the precursor release is determined by

$$\frac{d[P]}{dt} = -\frac{d[C]}{dt} = -A\exp\left\{\frac{-E_A}{RT}\right\}[P] \qquad (3.1.21)$$

Here A is a prefactor, E_A is the activation energy and the temperature of the solution is given by T.

The conservation of monomer mass of the system between time t_i and t_{i+1} is given by

$$S(t_{i+1}) = S(t_i) - Q\int_0^\infty dr\, r^3\{n(r, t_{i+1}) - n(r, t_i)\}, \qquad (3.1.22)$$

$$Q = \frac{4\pi\rho}{3M_w V_{tot}[C]_\infty}$$

Here $n(r, t_i)$ is the number density of the particles with radius of r at timet_i. The Constant Q is determined by the density of the material (ρ), monomeric molecular weight (M_w) and the volume of the solution V_{tot}. A finite but infinitesimal initial bulk concentration of free monomers 0.857 mol/m^3 was assumed.

Coupling **Equation (3.1.13)** and **(3.1.14)**, we can write the following generalized equation for the supersaturation at time $t_{i+1} = t_i + \Delta t$:

$$S(t_{i+1}) = S(t_i) - Q \int_0^\infty dr\, r^3 \{n(r, t_{i+1}) - n(r, t_i)\} \qquad (3.1.23)$$
$$+ \frac{A[P]\Delta t}{[C]_\infty} e^{\frac{-E_A}{RT}}$$

In the heating process, the temperature of the solution is linearly increased from the initial temperature T_0 to the final temperature T_f via heating rate H_R:

$$\frac{dT}{dt} = H_R \text{ for } T \leq T_f \qquad (3.1.24)$$

To numerically solve the coupled equations, **Equation (3.1.7)** is discretized over the bin size of Δr and explicit time-stepping procedures with timestep of Δt are used. The Van Leer limiter function is used to interpolate functions on the grids and to avoid false numerical diffusion. The stability and accuracy of the discretization is ensured by the Courant condition via lowering the value of

$$\frac{|\Gamma|\Delta t}{\Delta r} \leq 1 \qquad (3.1.25)$$

3.1.3 Results and discussion

3.1.3.1 Experimental study of nanoparticle size evolution

Figure 3.1.2 shows the TEM images of NPs. It exhibits that the heating rate has a dramatic effect on the NPs size. The particle shape evolves with size and varies from pseudo-spherical for A_1 and A_2 to faceted polyhedra for A_3-A_6. Due to monodispersity and shape regularity, the NPs have a strong tendency to self-assemble as shown in the TEM images of **Figure 3.1.2** and also large view TEM images of **Figure A3.1.1** in appendix. The average particle diameter, D_{TEM}, and the standard deviations, σ_{TEM}, were derived from size distribution histograms obtained from the TEM images. The size distribution histograms of the NPs are given in **Figure 3.1.3**.

As the heating rate increased from 0.8 K min^{-1} to 6.4 K min^{-1} the size of the NP decreased from 27 nm to 6.3 nm. The polydispersity index for all NP batches was typically

around 10%. We note that the heating rate (first heating rate) used to reach the decomposition temperature of 453 K has no influence on the final NP size. To unambiguously rule out the effect of the first heating rate, synthesis with three different rates of 5 K/min, 6.5 K/min and 8 K/min were performed. The mean NP size did not show variation with different first heating rate as shown in **Figure 3.1.4** and in agreement with previous literature reports.[33]

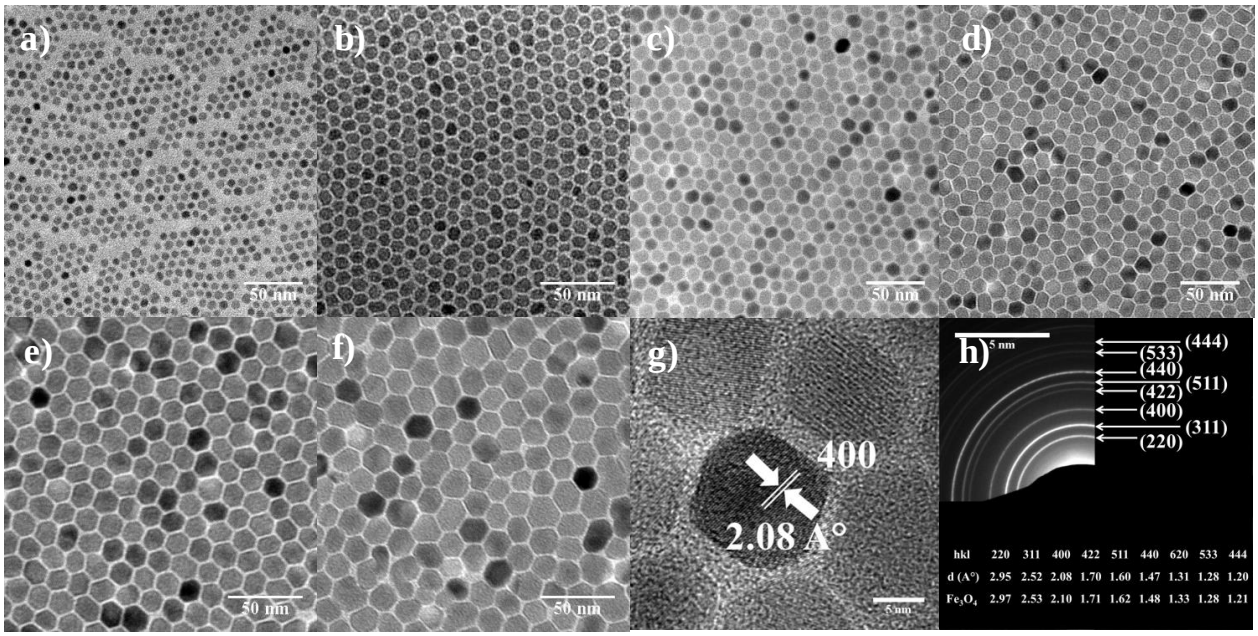

Figure 3.1.2 TEM images of (a) A_1, (b) A_2, (c) A_3, (d) A_4, (e) A_5 and (f) A_6 reactions. (g) HRTEM images of sample A_4 and (h) SAED pattern of the same A_4 sample and measured lattice spacings, d (Å), using the rings and standard atomic spacings for NPs following with their respective hkl indices.

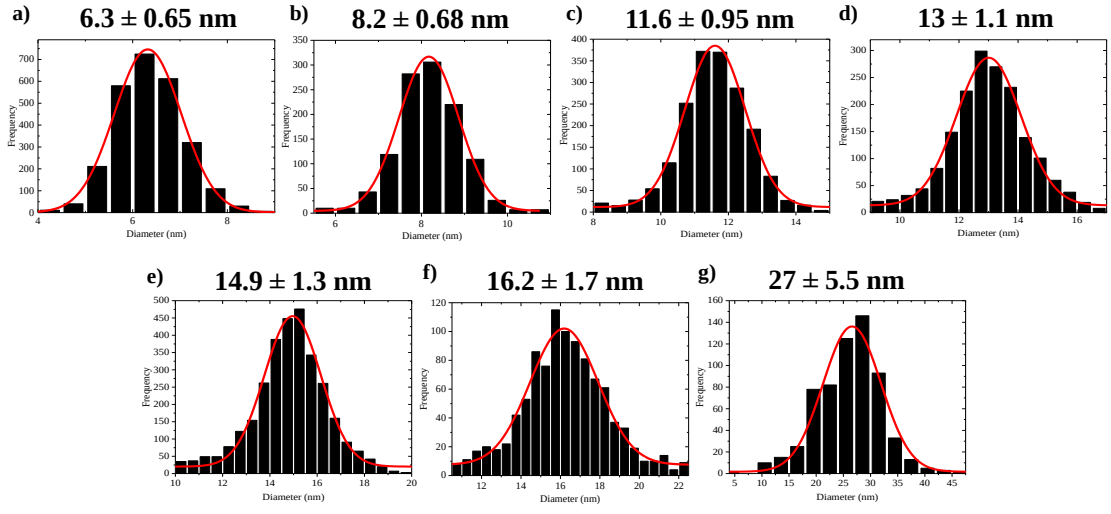

Figure 3.1.3 Particle size distributions obtained by fitting TEM histograms for (a) A_1, (b) A_2, (c) A_3, (d) A_4, (e) A_5, (f) A_6, and (g) A_7.

Further structural information was obtained from high resolution TEM, HRTEM, and selected area electron diffraction, SAED. A representative HRTEM image of a single NP with a diameter of 13.0 nm (A_4) is shown in **Figure 3.1.2 a**. HRTEM images of other samples are given in **Figure A3.1.2** in appendix. The HRTEM images show the presence of high-quality single-crystalline phase in the A_4 (and likewise for other) NPs. The measured inter-planar distances from adjacent lattice fringes are consistent with known values of face centered cubic (fcc) Fe_3O_4 [10, 17, 29] (**Figure 3.1.2 g**). A characteristic SAED pattern is shown in **Figure 3.1.2 h** for sample A_4. The measured d_{hkl} for A_4 NPs are listed in the inset of **Figure 3.1.2 h** and match well with the reported values for bulk magnetite (Fe_3O_4).[10, 17]

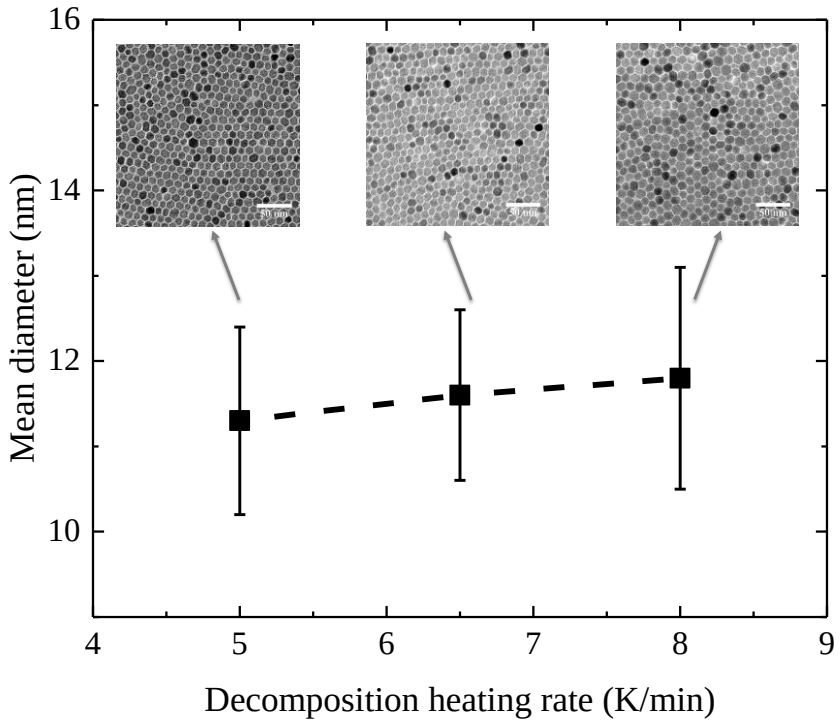

Figure 3.1.4 The mean diameter of NPs as a function of different first heating rates (383 to 453K) with corresponding TEM images. The growth heating rate was fixed at 4.4 K/min.

The crystal size and structure of the NPs were further investigated with XRD. The diffraction patterns and the intensities, as shown in **Figure 3.1.5 a**, could be indexed to an inverse spinel structure. Interplanar distances d_{hkl} (A˚) (311) for all NPs were calculated, as shown in **Figure 3.1.5 b** and compared with that of stoichiometric magnetite Fe_3O_4 (8.396 Å) (0.8396 nm, JCPDS file 19-629) and maghemite γ-Fe_2O_3 (8.346 Å) (0.8346 nm, JCPDS file 39-1346) phases.[17, 34-35]

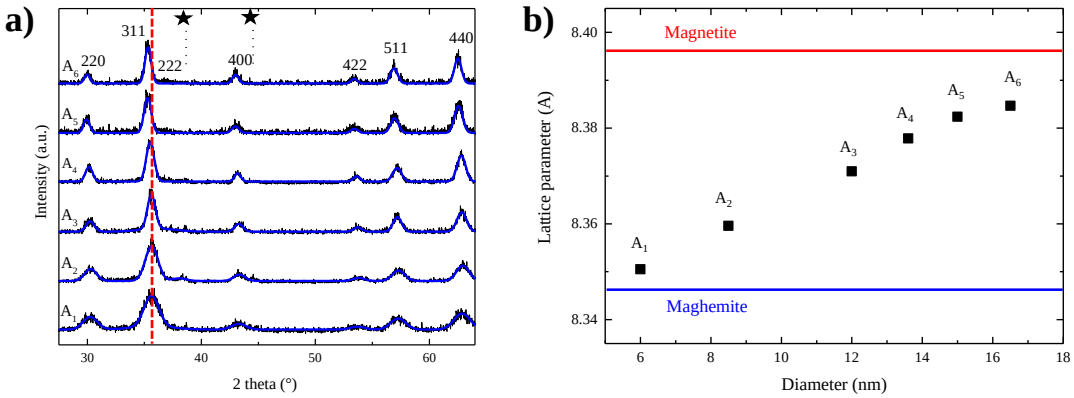

Figure 3.1.5 (a) XRD diffractograms of all nanoparticles (black) and their corresponding modelling (blue). Positions of the Bragg reflections of the sample holder are indicated by stars. Red dashed line is for highlighting the peak position in (311). (b) Lattice parameter as a function of NPs diameter, compared with those of the stoichiometric magnetite (red line) and of maghemite (blue line).

The value of the lattice constant increases with increasing particle size, and changes from maghemite for the smallest particles A_1 to stoichiometric magnetite for the larger particles. The crystalline sizes were also obtained from (311) reflection. A summary of the NPs crystal size evolution with heating rate is given in **Figure 3.1.6**. The particle crystal size for A_1-A_6 is consistent with the statistical analysis of the TEM images, implicitly indicating single crystallinity of the individual particles.

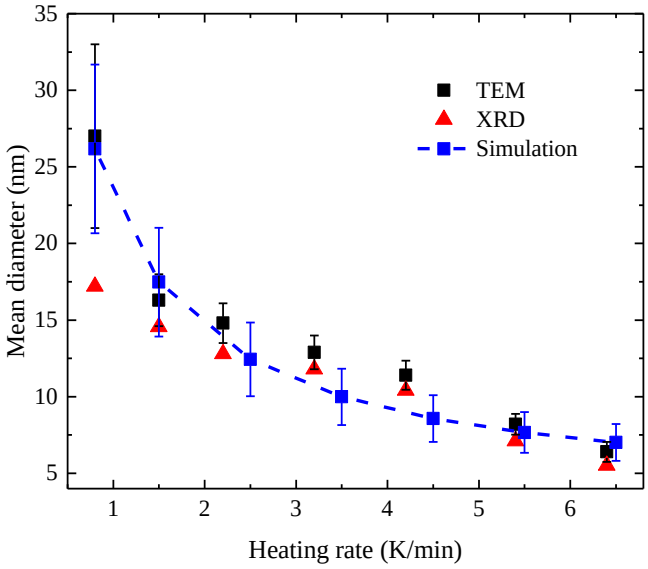

Figure 3.1.6 Mean diameter of NPs as a function of heating rate obtained via TEM and XRD. The simulated NP size is obtained with an activation energy of E_A=70 kJ/mol. The error bars represent size dispersion at FWHM of the particle size histograms.

Effective hindrance of particles aggregation in solvent is a qualitative indication of good surfactant coverage. To survey the surface of the nanoparticles fourier transform infrared, FTIR, spectroscopy was performed. A representative FTIR spectrum is given and discussed in **Figure 3.1.7 a** for A_4 nanoparticles. The bands around 3000 cm^{-1} and 2800 cm^{-1} are assigned to methyl groups on the surface of the particles. The bands between 1300 cm^{-1}-1650 cm^{-1} are due to the asymmetric and symmetric COO^- bands of oleate. Hence the ligand adsorbed on the particle surface is oleate.[36-39]

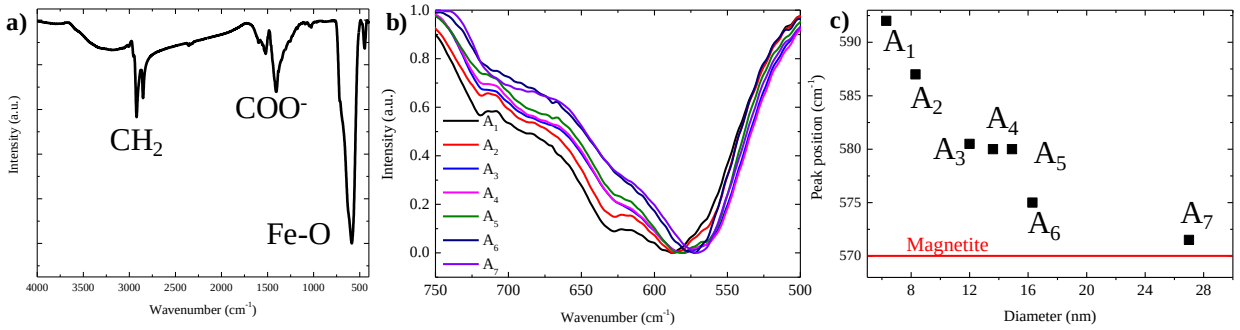

Figure 3.1.7 (a) IR spectrum of sample A_4 between 4000 and 400 cm^{-1}. (b) IR spectra of all samples between 750 and 500 cm^{-1}, (c) position of the most intense IR band for all samples.

The magnetite (Fe_3O_4) shows a single broad peak at 580−590 cm^{-1} and a shoulder at around 700 cm^{-1} due to the oxidation of surface. On the other hand, the maghemite (γ-Fe2O3) phase displays several peaks between 800 and 400 cm^{-1} whose number and resolutions depend on the structural order of vacancies in maghemite.[36, 40] considering a qualitative study of the ratio of magnetite (and maghemite) in synthesized NPs, the position of Fe-O peak has been compared among different sizes. For all samples peak position is intermediate between that characteristic of maghemite (630 cm^{-1}) and magnetite (570 cm^{-1}) which shifted to magnetite via increasing size (**Figure 3.1.7 b** and **c**). Moreover, some other revealing differences are observed between the spectra in **Figure 3.1.7 b**. It is worth noting that a drop in the depth of the peak at around 630 cm^{-1} is observed when the size of the NPs increased indicating the evolution from maghemite to magnetite. So that, the qualitative results of both XRD and FTIR confirm the evolution of the composition from maghemite to magnetite by increasing sizes which is in consistence with literatures.[36] However for quantitative study Mössbauer spectrometry is used in the literature, which measures the composition of NPs by determining the oxidation state of iron species.[36, 41]

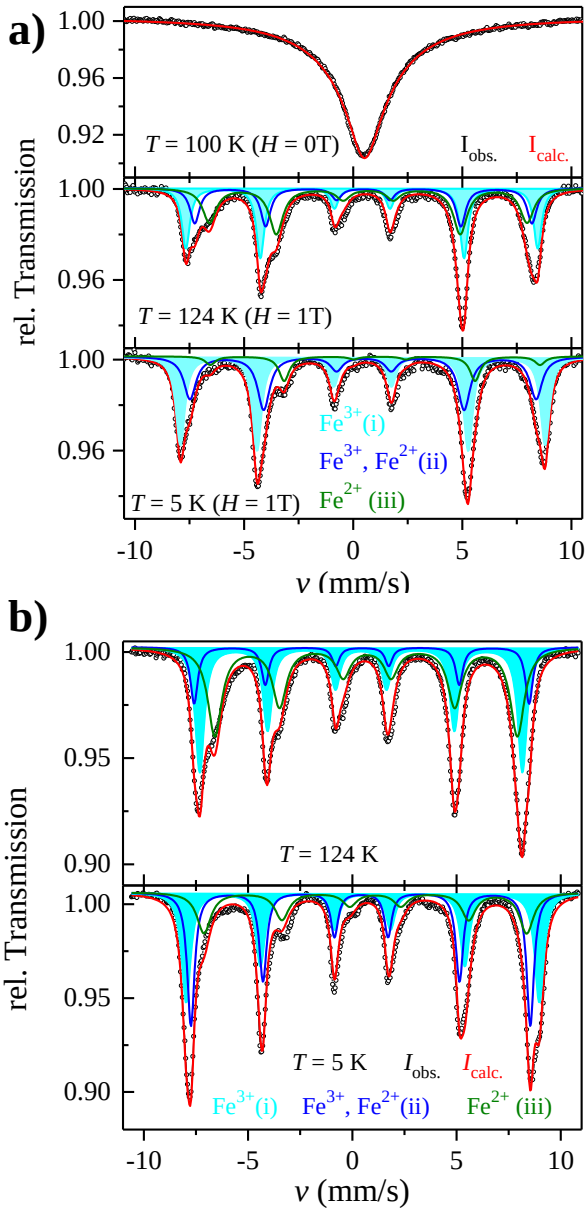

Figure 3.1.8 Mössbauer spectra for sample (a) 8.6 ± 0.8 nm and (b) 12.7 ± 1 nm taken at 124 K and 5K fitted as a superposition of three magnetic sextets.

Mössbauer spectroscopy of ^{57}Fe was performed on two different nanoparticle batches with nominal small and intermediate sizes with diameters that amount to 8.6 ± 0.8 and 12.7 ± 1.0 nm, respectively. We obtained from Lorentzian site analysis of the experimental data (Recoil software)[32] three Fe-sextets which we ascribed to the magnetic hyperfine splitting of iron-sites on tetrahedral and octahedral positions as present in magnetite and maghemite. The spectral

intensities associated with the charge ordering of Fe^{2+} in octahedral and tetrahedral coordination was used as an indicator for the fraction of magnetite. Furthermore, paramagnetic Fe-contributions were absent in all Mössbauer spectra of this series. **Figure 3.1.8** shows the Mössbauer spectra for samples at two different temperatures T = 124 K and 5K above and below Verwey transition, respectively. All the fitting parameters of the Mössbauer data have been included in the **Table 3.1.1**. The fitted three sextets at 5 K are assigned to (i) Fe^{3+} octahedral (chemical shift 0.52(1) mm/s, hyperfine field 527.9(3) kOe), (ii) Fe^{2+} and Fe^{3+} in tetrahedral coordination (chemical shift 0.41(1) mm/s, hyperfine field 506.7(2) kOe), and (iii) Fe^{2+} in octahedral coordination (chemical shift 0.88(2) mm/s, hyperfine field 472(1) kOe). We observe corresponding spectral fractions of 29:49:22 at 5 K and 19:36:45 at 124 K for intermediate size sample and conclude that the changes stem from charge ordering across the Verwey transition of the magnetite fraction. The spectra for the first, second and third sextets, give a magnetite percentage of ~55 % and ~66 % for small and large samples respectively. Mössbauer spectroscopic data show an increase in magnetite phase fraction upon nanoparticle size increase, in agreement with XRD and FTIR results.

Table 3.1.1 Hyperfine Parameters obtained from Lorentzian fits to ^{57}Fe-Mössbauer spectra at selected temperatures. The respective chemical assignment of Fe-species to specific sites are given. The labels (i, ii, iii) refer to the spectra shown in **Figure 3.1.8.**

Sample	Site	H_{hf} (kOe)		CS (mm/s)		Fraction (%)	
		T = 5 K	T = 124 K	T = 5 K	T = 124 K	T = 5 K	T = 124 K
8.6 ± 0.9 nm	Fe^{3+} (i)	519.2 (8)	500.0 (8)	0.44 (1)	0.41 (1)	48.5	37
	Fe^{3+}, Fe^{2+} (ii)	497 (2)	479 (2)	0.47 (1)	0.47 (1)	32	25
	Fe^{2+} (iii)	469 (3)	451 (1)	0.90 (4)	0.90 (4)	18.5	38
12.7 ± 1.2 nm	Fe^{3+} (i)	527.9 (3)	491.1 (3)	0.52 (1)	0.45 (1)	29	19.0
	Fe^{3+}, Fe^{2+} (ii)	506.70 (2)	470.6 (3)	0.41 (1)	0.43 (1)	49.0	36
	Fe^{2+} (iii)	472.4 (1)	438.5 (5)	0.88 (2)	0.65 (1)	22	45

The TGA curves of iron oxide nanoparticles under nitrogen shows a weight loss between 7.2 % and 28.2 % (**Figure 3.1.9 a**) from bigger to smaller particle size (from A_7 to A_1) which can be explained by the larger surface area/volume ratio for smaller nanoparticles. TGA spectra of all samples show three weight loss plateaus.[37, 42] The slight weight-loss below 200 °C is attributed to the evaporation of adsorbed water molecule and solvent remainders in the powder. The second and the third lost between 200–400 °C and 500–750 °C correspond to the decomposition of the monolayer of surfactant molecules adsorbed on the surface of nanoparticles.[37, 42] Moreover,

grafting density of the surfactants on the nanoparticle surface remains fairly constant for all the different sizes (~ 3 molecules/nm^2) as shown in **Figure 3.1.8 b**. This observation confirms the effective attachment of surfactants on the surface regardless of the size of the nanoparticles. Furthermore, using TGA data and subtraction of the mass of the organic ligand, the "mass reaction yield" of the pure inorganic nanoparticle for three different heating rates of 2.2 K/min, 3.2 K/min and 5.4 K/min, amounted to 75.5 %, 80.5 % and 81 % respectively in good agreement with reported literature values.[43]

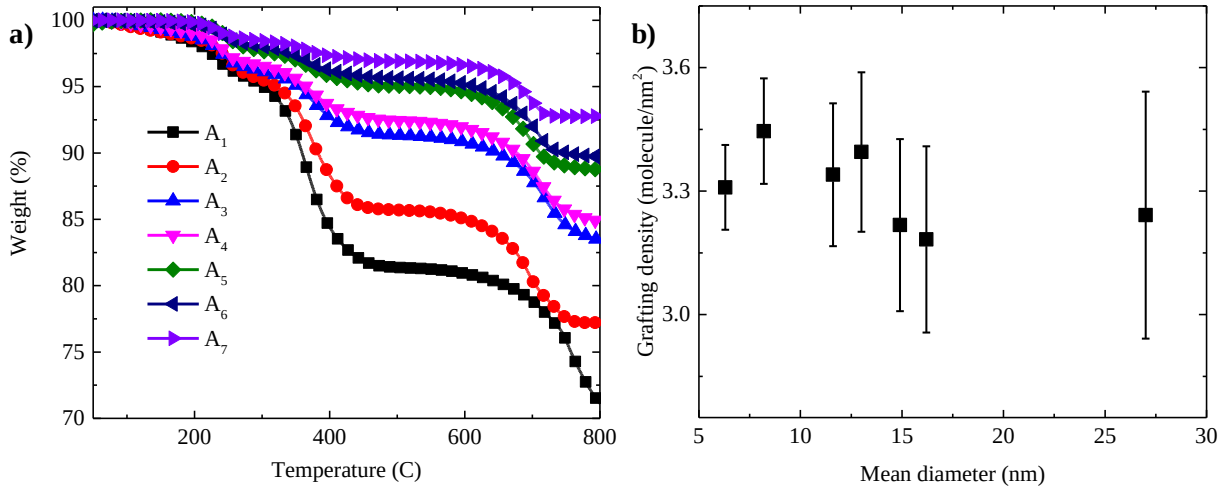

Figure 3.1.9 (a) TGA graph of all samples (30-800 °C) and (b) graft density of the surfactants as a function of size.

3.1.3.2 Modeling of nanoparticle nucleation and growth

To gain insight on NPs' nucleation and growth process at the molecular level, we set up a numerical model based on classical nucleation theory.[20, 23, 25-26] The model relies on a rate equation that accounts for population balance,[20-21, 23, 44-49] which describes the dynamics of the precursor-to-monomer conversion:

$$\frac{d[P]}{dt} = -\frac{d[C]}{dt} = -Ae^{\frac{-E_A}{RT}}[P] \qquad (3.1.26)$$

where $[P]$ and [C] are the concentrations of precursors and monomers, respectively, E_A is the precursor-to-monomer activation energy, R is the gas constant, T is the system temperature and A is a constant prefactor. The model is based on the kinetics of a population of Fe_3O_4 monomers. For the sake of simplicity, the surfactant is ignored. The population of monomers, and therefore supersaturation, defined as $S = [C]/[C]_\infty$, increases up on heating. Formation of the nuclei is

then thermodynamically allowed by the reaction of monomers. For the nuclei larger than a critical radius, r_c, further reaction of the monomers decreases the Gibbs free energy leading to stable nuclei. The rate at which the nuclei are formed, the nucleation rate, is determined by monomer concentration, surface energy, critical radius, and temperature, $R_{nuc} = f([C], \gamma, r_c, T)$. The nucleated NPs grow further to larger sizes as the time lapses. The number of NPs of radius r at time t has a distribution, $N(r,t)$, the time evolution of which reads as:

$$\frac{dN(r,t)}{dt} = \frac{\partial N(r,t)}{\partial t} + \frac{\partial [N(r,t)\Gamma(r,t)]}{\partial r} = R_{nuc} g(r) \qquad (3.1.27)$$

where, $\Gamma(r,t)$ is the instantaneous growth rate. The nucleation rate, R_{nuc}, is the source term which accounts for the possibility of nucleating new NPs at a given time modulated by the size-dependent distribution function, $g(r)$. When nucleation is terminated, $R_{nuc} = 0$. **Equation 3.1.27** still describes the growth of NPs with time, based on $\Gamma(r,t)$. A full description of the model is given section 3.1.2.4. The values of parameters which used in the simulation is given in **Table 3.1.2**.

Table 3.1.2 The values of parameters being used in the simulation.

Parameter	Value
Δt	1e-4 s
Δr	0.5e-10 m
M_i	708e-3 g [Exp.]*
M_w	231.54 $g\ mol^{-1}$ [50]
V_{tot}	0.0252e-3 m^3 [Exp.]
ρ	5.17e6 $g\ m^{-3}$ [50]
D	1e-11 $m^2 s^{-1}$ [20]
C_∞	1e-3 $mol\ m^{-3}$[20]
γ	0.4 $J\ m^{-2}$ [51-52]
u	0.42 [20-21, 24]
ξ	7e4 [20]
A	4e3 s^{-1}

* Experimental values

To investigate the NPs size evolution with heating rate, simulations were performed by mimicking the experimental conditions. The following parameters needed in the model, namely molar mass (M_W), initial mass of the precursors (M_i), and reaction volume (V_{tot}), are known *a priori* from the experimental setups. It was assumed that at t=0, there are no particles *i.e.*,

$N(r, t = 0) = 0$. At *t*=0, the temperature was set at $T_0 = 453$ K (180 °C), and linearly increased up to $T_f = 567$ K (294 °C) with different heating rates. The system is kept at reflux temperature T_f for 3600 s. The amount of the NPs at the end of the simulation ($t = t_f$), was calculated by summing the number of NPs of all sizes *i.e.* $N_{tf} = \sum_r N(r, t_f)$. Unfixed parameters, such as precursor-to-monomer activation energy, E_A, were explored within the physical range reported for nanocrystals growth.[20] An optimal set of parameters was identified, so that the simulated results follow closely the experimental trend for the NP size evolution. **Figure 3.1.6** shows that the numerically calculated mean NPs diameter monotonically decreases as a function of increasing heating rate, in excellent agreement with the experiment.

The effect of the heating rate on the final NPs size can be explained quantitatively. We investigated the relative conversion rates of the precursor-to-monomers process as well as the relative dynamics of the system supersaturation. Selected three different heating rates, namely 1.5 K/min, 3.5 K/min and 6.5 K/that represent slow, intermediate and fast heating rates, respectively. **Figure 3.1.10 a** shows the time evolution of supersaturation. For a slow heating rate of 1.5 K/min, the precursor is slowly converted into monomers and supersaturation increases slowly in time. The change in the total number of NPs in time, *dN/dt*, is directly proportional to nucleation rate, see **Equation 3.1.27**. It has to be emphasized that for all heating rates, the nucleation rate at the beginning of the simulation is negligible which is a key feature of the heat-up reaction. As supersaturation increases, after an elapsed time, *t*= 1600s, nucleation starts. Despite the initiation of nucleation process and monomer consumption, supersaturation does not drop, due to the fact that monomers are being produced progressively faster as the temperature rises (see **Equation 3.1.26**). Once nucleation is triggered, increase in the supersaturation is sustained for a period of time until the system contains enough nuclei to result in a net decrease in the monomer concentration, which is associated with a substantial drop in supersaturation and subsequently quenching of the nucleation rate. Upon termination of the nucleation process, the remaining population of monomers then acts as a reservoir for the continued growth of the nascent nuclei. The remaining monomers are consumed at a rate faster than the precursor conversion rate until the monomers concentration becomes infinitesimally small and/or final simulation time is reached.

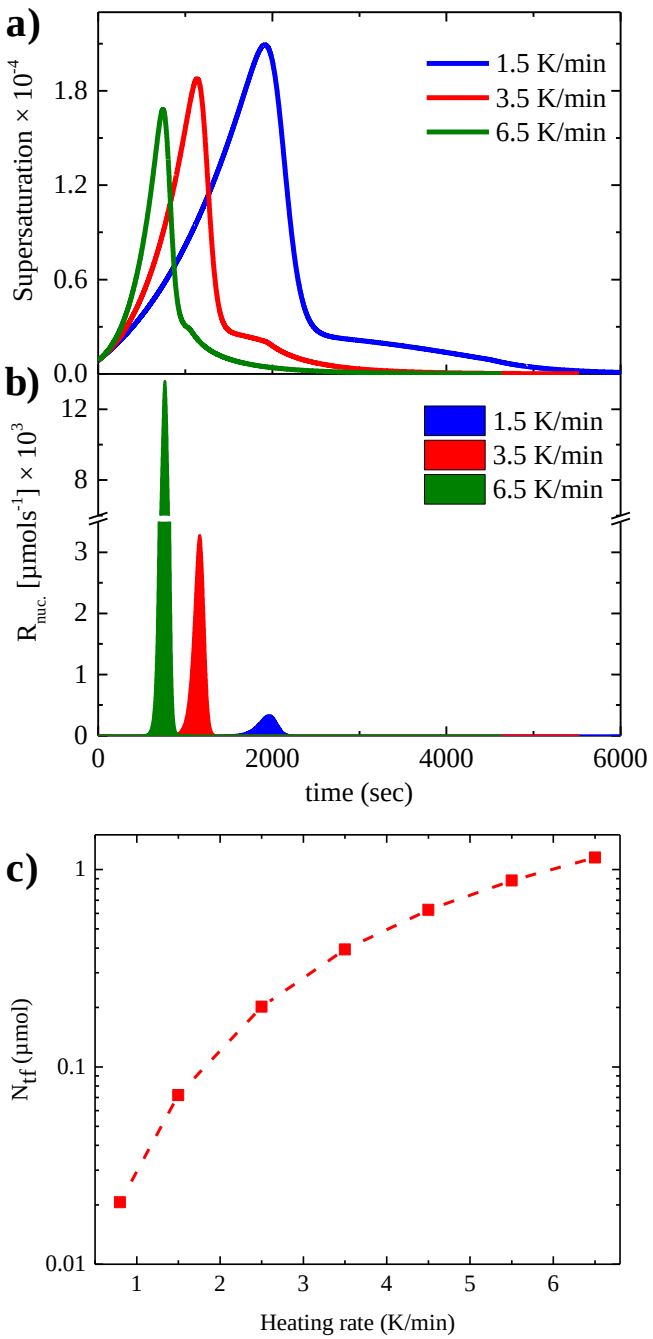

Figure 3.1.10 a) The simulated supersaturation profiles of reactions at different heating rates along the simulation time. b) The corresponding nucleation rate for the same heating rates used in part (a). c) The number of NPs at the end of simulation reflux time, 3600 second.

For higher heating rates the supersaturation shows a faster increase with time. The nucleation therefore occurs in earlier stages with relatively higher rates, as shown on **Figure 3.1.10 a** and **b**. For fast heating rates, the release of monomer is much faster than the growth of

the existing nuclei. The available monomers contribute almost solely to nucleation, resulting in a higher number of nascent nuclei. Upon termination of the nucleation, in contrast to the case of slow heating rate, the majority of the monomers are consumed. The remaining monomers must then be evenly distributed among a much larger number of nuclei, leading to significantly reduced final NP size.[53] The nucleation process is much shorter (**Figure 3.1.10 b**). A narrower nucleation window means that all NPs are formed and subsequently grow "almost" simultaneously. As a result, a higher heating rate would yield NPs with a narrower size distribution and better monodispersity. A good agreement between the calculated and experimentally observed polydispersity is obtained, as shown in **Figure 3.1.6**. We found out that activation energy, E_A = 70 kJ/mol gives the best description of the experimental trend (as shall be discussed later). A natural consequence of higher heating rates is that N_{tf} at the end of simulation time increases as a function of increasing heating rate, as shown in **Figure 3.1.10 c**. The evolution of the total number of NPs in the course of simulation time for three representative different heating rates is shown in **Figure 3.1.11 a**. Moreover, experimentally from the nanoparticle mean diameter as determined from TEM images, an approximate nanoparticle count, *N*, could be determined. The experimentally determined N for three different heating rates is included in **Figure 3.1.11 b**. The *N* showed an increase with the heating rate, in agreement with simulation prediction. We note however that the simulation and experimental determined *N* cannot be directly compared, due to the loss in *N* as result of post synthesis purification steps.

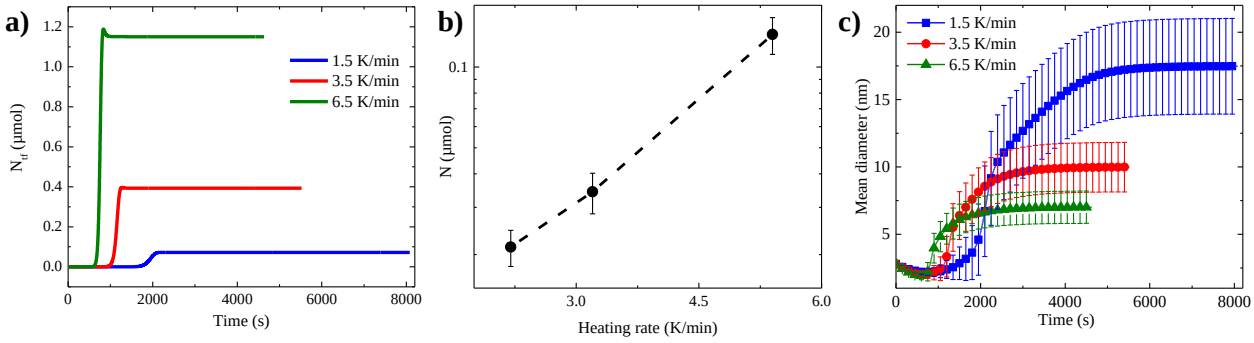

Figure 3.1.11 (a) The number of nanoparticles in the course of simulation time for three heating rates. (b) The number of NPs as a function of heating rate from experimental data. (c) The evolution of mean diameter as well as the standard deviation of the nanoparticles in the course of simulation time for three heating rates.

The evolution of mean diameter is predominantly determined during the heating stage. Shortly after the final temperature has reached, the nanoparticle size and its deviation from the

mean value approaches the final mean value and does not change further with increasing the reflux time, as shown in **Figure 3.1.11 c**. Further syntheses were performed at a fixed heating rate of 3.2 K/min, and different reflux time from ranging from 0 min to 360 min. The size of the resulting nanoparticles was fixed at 13.0 ± 1.2 nm, in accordance with the simulation data, and previous reports. [17, 54]

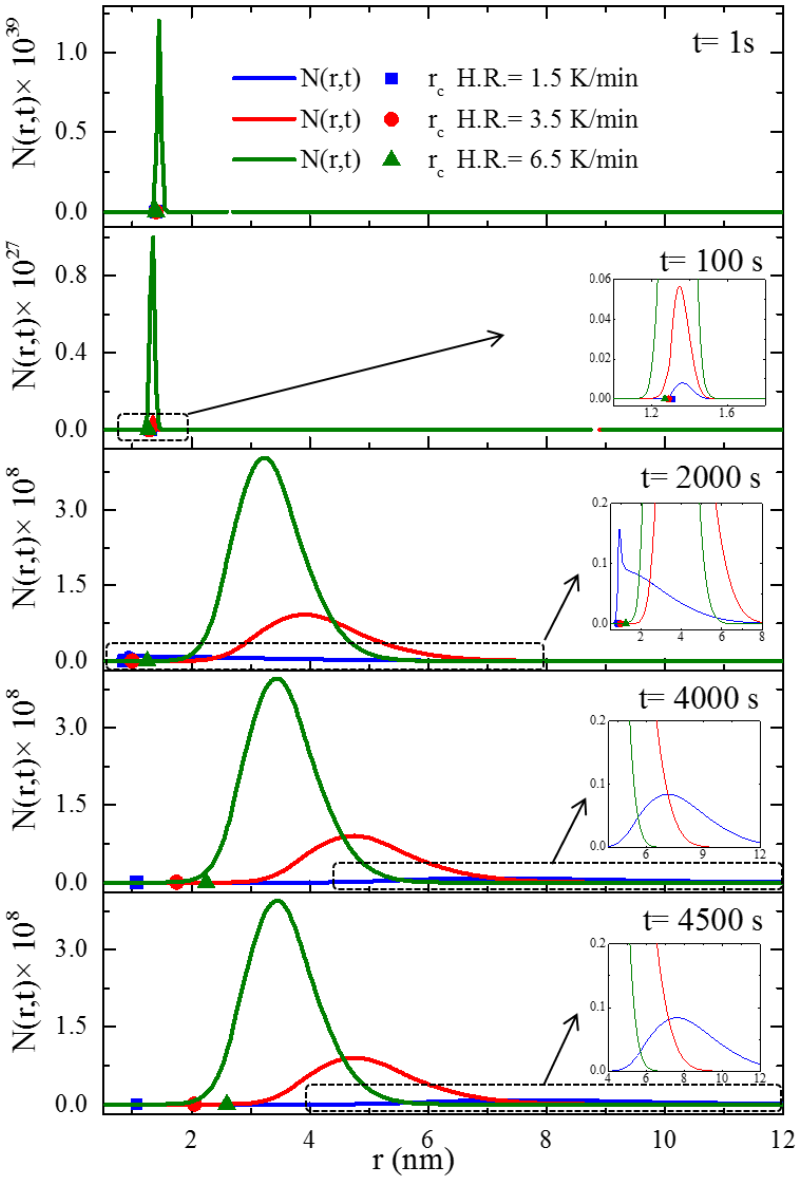

Figure 3.1.12 The simulated size distribution of nanoparticles at different simulation times, (a) t = 1 sec, (b) t = 100 sec, (c) t = 2000 sec, (d) t = 4000 sec and (e) t = 4500 sec. The precursor activation energy is $\boldsymbol{E_A = 70 kJmol^{-1}}$. In each panel the size distributions of the heating rates of 1.5 K/min (blue), 3.5 K/min (red), and 6.5 K/min (green), the critical radii are represented with blue square, red circle and green triangle. The insets show an enlarged view of the marked region of the curves.

The populations of the NPs for representative heating rates at different reaction times are shown in **Figure 3.1.12**. The critical radius, r_c, for each heating rate is marked with a symbol. At the beginning of the simulation, $t = 1s$, the nascent nuclei appear around the critical radius. As the nucleation process continues, $t = 100s$, the nascent nuclei grow to larger NPs and approximately reach the steady-state distribution around $t = 2000s$. For the slowest heating rate critical radius, r_c, does not change substantially with time. Therefore, the nuclei that are formed are stable and can grow further to NPs of larger sizes. For the fastest heating rate however, r_c grows to larger values as the time lapses. Hence early Ostwald ripening [24] takes place and particles that are formed with $r<r_c$ dissolved into monomers favoring the growth of the larger particles.

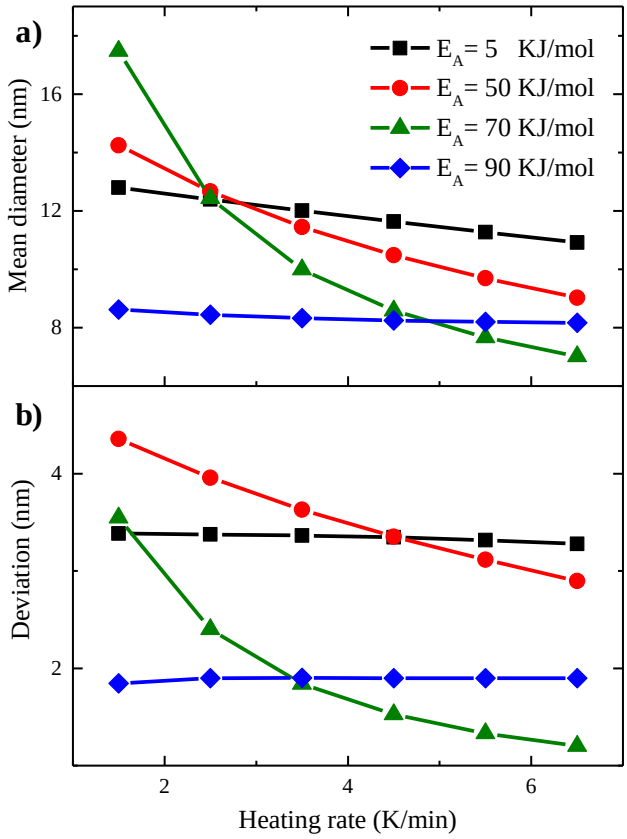

Figure 3.1.13 (a) The simulated nanoparticle size as a function of heating rate for different precursor activation energies ($\boldsymbol{E_A}$). (b) Standard deviation (Polydispersity) of the nano particles as the function of the heating rates. The legend is similar to panel (a).

The activation energy of the precursor-to-monomer conversion, E_A, is an influential parameter as it determines the relative timescales of the temperature rise and the monomer

release rate. The sensitivity of the final NPs' diameter and standard deviation to the heating rates was therefore tested for very high and low activation energies, $E_A = 90kJmol^{-1}$ and $E_A = 5kJmol^{-1}$ respectively (**Figure 3.1.13**). For high precursor activation energy ($E_A = 90kJmol^{-1}$), the timescale of the temperature rise is much shorter compared to that of the monomer release rate, leading to a low concentration of bulk monomers during the temperature rise. Hence, the growth of nuclei into larger NPs is hindered. Since the rate of the temperature rise does not effectively change the monomer release rate (see **Equation 3.1.26**), the dynamics of the system is approximately the same for all heating rates. For the low activation energy ($E_A = 5\ kJmol^{-1}$), the precursors are rapidly converted into the monomers, irrespective of the heating rate, leading to rapid rise in the supersaturation, while the temperature of the system is not significantly changed. Therefore, the same nucleation rate is obtained for all heating rates, and the subsequent temperature rise with different rates does not remarkably change the growth dynamics of the nascent nuclei and the final NP size. The slightly larger NP size obtained for the case of lower activation energy compared to high activation energy is due to much higher supersaturation.

3.1.3.3 Size dependent magnetic properties

The hysteresis loops of the NPs at 300 and 2K are shown in **Figure 3.1.14 a** and **b**, respectively. At 300K the A_1-A_6 NPs are superparamagnetic, whereas at 2K particles show ferrimagnetic behavior.

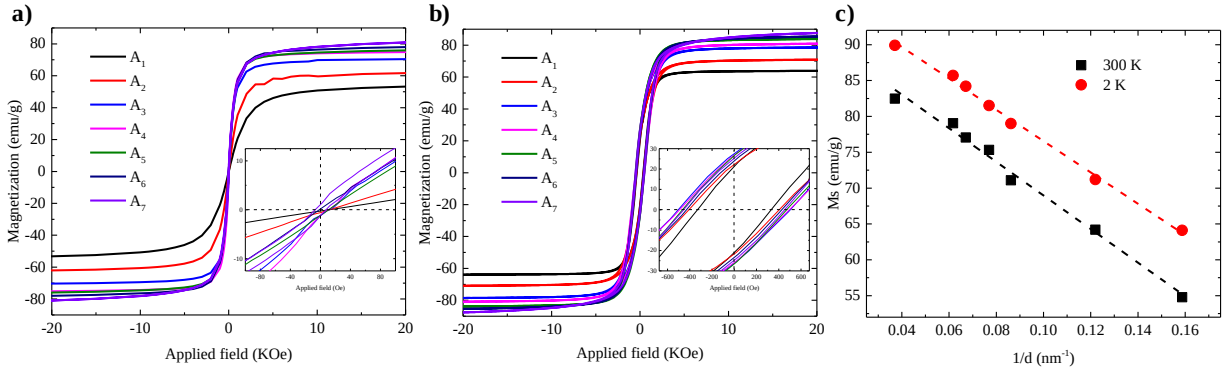

Figure 3.1.14 Hysteresis lopes of all samples at 300 K (a) and (b) 2 K. (c) Saturation magnetization (M_S) versus the average diameter (1/d) of the NPs.

The values of the saturation magnetization (M_S) of samples A_1-A_6 at room temperature and 2K are plotted in **Figure 3.1.14** as a function of inverse diameter. As the size of the NPs increases from 6.3 nm to 16.2 nm, M_s increases at 300 K from 54.8 emu/g to 79 emu/g and at 2K from 64.1 emu/g to 85.7 emu/g. The M_S values are close to the reported values of 84 emu/g for pure bulk magnetite at 300K.[10, 55-57] The reduction in M_S with decreasing size can be explained by the existence of surface spin disorder layer on the surface of the NPs, which is formed due to the lack of some oxygen ions from the spinel lattice, weak coordination of surface atoms and the capping of the NPs with surfactants.[58-60] The thickness of the magnetically disordered shell can be calculated using the following relation:[59]

$$Ms = Ms_{(bulk)}(1 - \frac{6e}{d}) \qquad (3.1.28)$$

where e is thickness of the disordered layer and d is the particle diameter. Using least square fitting, $M_{S(bulk)}$ values of 92.4 emu/g and 98.4 emu/g at 300K and 2K were obtained, respectively. The values of $M_{S\,(bulk)}$ at 2K is remarkably close to the theoretical value of 98 emu/g for Fe_3O_4.[56, 61-62] The thickness of the spin disordered layer was estimated using the values of $M_{S(bulk)}$, and amounted to 0.42 nm and 0.35 nm at 300 K and 2 K, respectively (in agreement with previous reports).[15, 59, 63-64] The measured saturation magnetization was obtained for NPs covered with an organic surfactant. The saturated magnetization can be corrected by using only the mass of the iron oxide NPs obtained by TGA (**Figure 3.1.9 a**). Corrected M_S values for different NPs do not show a strong dependence on the size for NPs larger than 8 nm, as shown in **Figure 3.1.15 a**. Low temperature M_S values approach the theoretical bulk value for pure single crystalline magnetite (98 emu/g)[56, 62] indicating size-independent, bulk-like magnetic properties.[65-66] By increasing the size of the NPs the coercive field (H_C) raises up to the size of 11.6 nm and then by further increasing the size, H_C decreases slightly as shown in **Figure 3.1.15 b**. The behavior can be explained by the shifting of NPs from single domain to multi-domain regime.[7, 17, 67] The flipping of magnetic moments in each domain is controlled by magnetic anisotropy energy, domain wall motion and thermal energy. When a NP is in the regime of a single domain, domain wall motion does not exist and by increasing the size magnetic anisotropy the energy increases. As a result, H_C becomes higher. However, by further increasing the size, the domains will be shifted to the multi-domain regime and due to the existence of domain wall motions the coercively becomes lower.

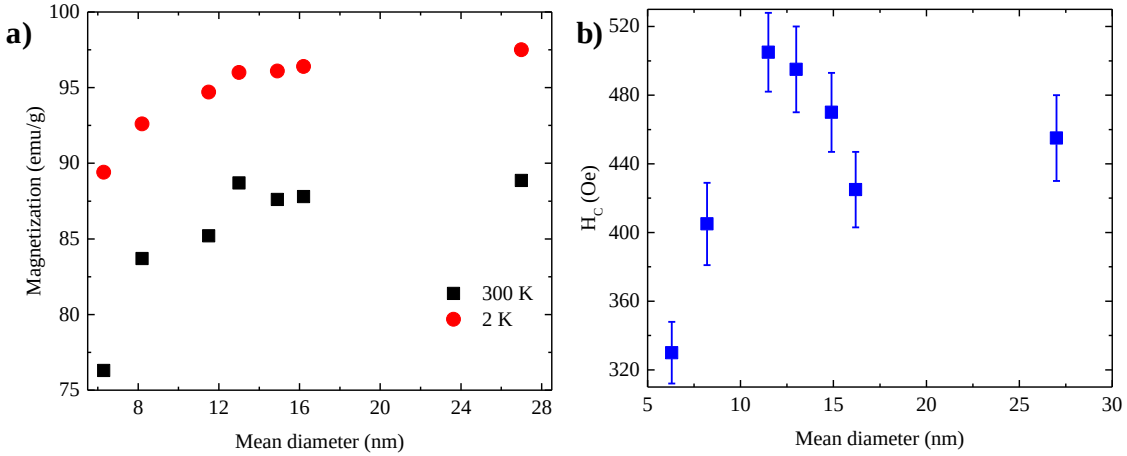

Figure 3.1.15 (a) Saturation magnetization of the sample after removing the mass of surfactant at 300 K and 2 K. (b) the values of H_C as a function of size.

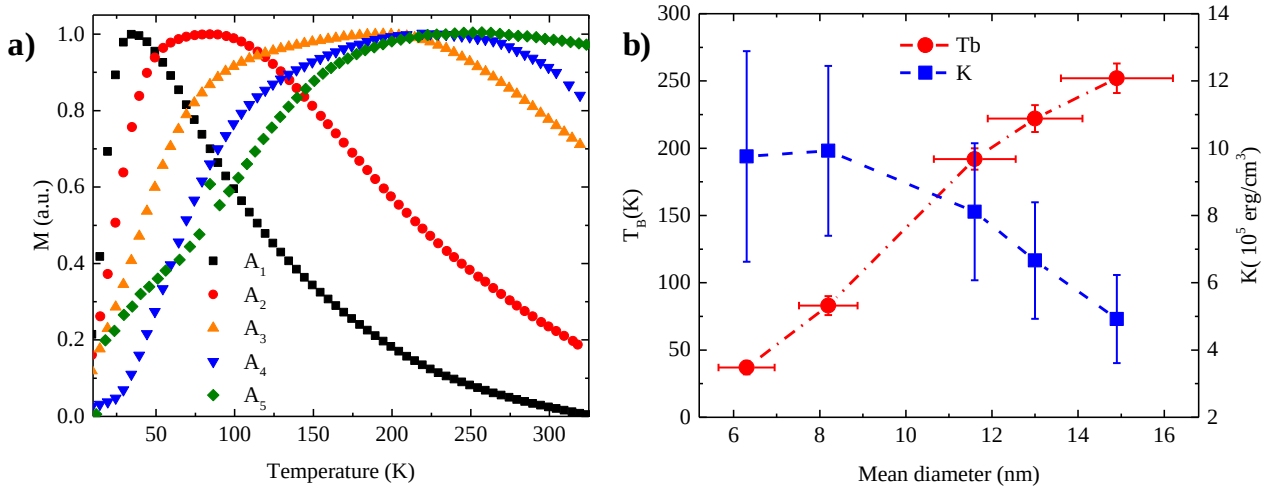

Figure 3.1.16 A representative M_{ZFC}-M_{FC} curves as a function of temperature for samples (a) A_1-A_5. (b) size dependence of T_B and K obtained from ZFC-FC curve

The magnetic anisotropy constant was determined via zero-field-, and field-cooling (ZFC-FC) measurements. Upon increasing the temperature from 5K to 300K, at blocking temperature, T_B, the thermal energy overcomes the magnetic anisotropy energy [55, 67] and the transition from ferro-ferrimagnetic to superparamagnetic takes place. A representative measurement at an applied magnetic field of 100 Oe, for all the samples is given in **Figure 3.1.16 a**. Evolution of T_B as a function of size is shown in **Figure 3.1.16 b**. Upon decreasing size from 14.9 nm to 6.3 nm the value of T_B is shifted to lower temperatures, in agreement with previous reports.[9, 17, 59] The magnetic anisotropy constant, K, was determined using following equation.[9, 59]

$$K = \frac{25 k_B T_B}{V} \qquad (3.1.29)$$

where k_B is Boltzmann's constant and V is the volume of a single NP determined by TEM. The value of K are shown in **Figure 3.1.16 b**, show an increase with decreasing particle size. The disorder of the NP's surface results in broken spin symmetry *i.e.* surface anisotropy.[14, 58, 60] Therefore the NPs with smaller sizes have higher surfaces to volume ratio (higher surface anisotropy) and as a result higher anisotropy constant and lower magnetization.

3.1.4 Conclusion

In this section, we have presented a combined experimental and theoretical study on the size evolution of iron oxide NPs by varying only the growth heating rate during synthesis. Superparamagnetic highly crystalline NPs with controllable size from 6 nm to 27 nm were obtained with a narrow size distribution typically below 10%. NPs showed nearly ideal magnetization values, which evolved with their size. Numerical simulations of nucleation and growth provided a valuable insight into the formation of the Fe_3O_4 NPs at different heating rates. The model reproduced the experimental trends, and showed that the relative time scales associated with the heating and precursors to monomer conversion rates is a decisive factor influencing the NP final size in thermal decomposition synthesis processes. For slow heating rates, large NPs with high polydispersity are predicted and obtained. The NPs were crystallized in inverse spinel structure with a high degree of crystallinity. The particles were superparamagnetic and showed increase in saturation magnetization with increasing size, with a disorder magnetic shell of less than 0.5 nm.

3.1.5 References

1. Park, J.; Lee, E.; Hwang, N. M.; Kang, M.; Kim, S. C.; Hwang, Y.; Park, J. G.; Noh, H. J.; Kim, J. Y.; Park, J. H., One-nanometer-scale size-controlled synthesis of monodisperse magnetic Iron oxide nanoparticles. *Angew. Chem.* **2005,** *117*, 2932-2937.
2. Demortiere, A.; Panissod, P.; Pichon, B.; Pourroy, G.; Guillon, D.; Donnio, B.; Begin-Colin, S., Size-dependent properties of magnetic iron oxide nanocrystals. *Nanoscale* **2011,** *3*, 225-232.
3. Dai, Q.; Berman, D.; Virwani, K.; Frommer, J.; Jubert, P.-O.; Lam, M.; Topuria, T.; Imaino, W.; Nelson, A., Self-assembled ferrimagnet− polymer composites for magnetic recording media. *Nano Lett.* **2010,** *10*, 3216-3221.

4. Yu, Y.; Mendoza-Garcia, A.; Ning, B.; Sun, S., Cobalt-substituted magnetite nanoparticles and their assembly into ferrimagnetic nanoparticle arrays. *Adv. Mater.* **2013,** *25*, 3090-3094.
5. Frey, N. A.; Peng, S.; Cheng, K.; Sun, S., Magnetic nanoparticles: synthesis, functionalization, and applications in bioimaging and magnetic energy storage. *Chem. Soc. Rev.* **2009,** *38*, 2532-2542.
6. Kim, J.; Piao, Y.; Hyeon, T., Multifunctional nanostructured materials for multimodal imaging, and simultaneous imaging and therapy. *Chem. Soc. Rev.* **2009,** *38*, 372-390.
7. Kolhatkar, A. G.; Jamison, A. C.; Litvinov, D.; Willson, R. C.; Lee, T. R., Tuning the magnetic properties of nanoparticles. *International journal of molecular sciences* **2013,** *14*, 15977-16009.
8. Mohapatra, J.; Mitra, A.; Bahadur, D.; Aslam, M., Surface controlled synthesis of MFe 2 O 4 (M= Mn, Fe, Co, Ni and Zn) nanoparticles and their magnetic characteristics. *CrystEngComm* **2013,** *15*, 524-532.
9. Park, J.; An, K.; Hwang, Y.; Park, J.-G.; Noh, H.-J.; Kim, J.-Y.; Park, J.-H.; Hwang, N.-M.; Hyeon, T., Ultra-large-scale syntheses of monodisperse nanocrystals. *Nat. Mater.* **2004,** *3*, 891-895.
10. Sun, S.; Zeng, H.; Robinson, D. B.; Raoux, S.; Rice, P. M.; Wang, S. X.; Li, G., Monodisperse MFe2O4 (M= Fe, Co, Mn) nanoparticles. *J. Am. Chem. Soc.* **2004,** *126*, 273-279.
11. Kovalenko, M. V.; Bodnarchuk, M. I.; Lechner, R. T.; Hesser, G.; Schäffler, F.; Heiss, W., Fatty acid salts as stabilizers in size-and shape-controlled nanocrystal synthesis: the case of inverse spinel iron oxide. *J. Am. Chem. Soc.* **2007,** *129*, 6352-6353.
12. Guardia, P.; Pérez, N.; Labarta, A.; Batlle, X., Controlled synthesis of iron oxide nanoparticles over a wide size range. *Langmuir* **2009,** *26*, 5843-5847.
13. Sun, S.; Zeng, H., Size-controlled synthesis of magnetite nanoparticles. *J. Am. Chem. Soc.* **2002,** *124*, 8204-8205.
14. Huang, J.-H.; Parab, H. J.; Liu, R.-S.; Lai, T.-C.; Hsiao, M.; Chen, C.-H.; Sheu, H.-S.; Chen, J.-M.; Tsai, D.-P.; Hwu, Y.-K., Investigation of the growth mechanism of iron oxide nanoparticles via a seed-mediated method and its cytotoxicity studies. *J. Physc. Chem. C* **2008,** *112*, 15684-15690.
15. Zheng, M.; Wu, X.; Zou, B.; Wang, Y., Magnetic properties of nanosized MnFe 2 O 4 particles. *J. Magn. Magn. Mater.* **1998,** *183*, 152-156.
16. Meledandri, C. J.; Stolarczyk, J. K.; Ghosh, S.; Brougham, D. F., Nonaqueous magnetic nanoparticle suspensions with controlled particle size and nuclear magnetic resonance properties. *Langmuir* **2008,** *24*, 14159-14165.
17. Baaziz, W.; Pichon, B. P.; Fleutot, S.; Liu, Y.; Lefevre, C.; Greneche, J.-M.; Toumi, M.; Mhiri, T.; Begin-Colin, S., Magnetic iron oxide nanoparticles: reproducible tuning of the size and nanosized-dependent composition, defects, and spin canting. *J. Physc. Chem. C* **2014,** *118*, 3795-3810.
18. Bronstein, L. M.; Huang, X.; Retrum, J.; Schmucker, A.; Pink, M.; Stein, B. D.; Dragnea, B., Influence of iron oleate complex structure on iron oxide nanoparticle formation. *Chem. Mater.* **2007,** *19*, 3624-3632.
19. Hyeon, T.; Lee, S. S.; Park, J.; Chung, Y.; Na, H. B., Synthesis of highly crystalline and monodisperse maghemite nanocrystallites without a size-selection process. *J. Am. Chem. Soc.* **2001,** *123*, 12798-12801.
20. van Embden, J.; Chesman, A. S.; Jasieniak, J. J., The heat-up synthesis of colloidal nanocrystals. *Chem. Mater.* **2015,** *27*, 2246-2285.
21. van Embden, J.; Sader, J. E.; Davidson, M.; Mulvaney, P., Evolution of colloidal nanocrystals: theory and modeling of their nucleation and growth. *J. Physc. Chem. C* **2009,** *113*, 16342-16355.
22. LaMer, V. K.; Dinegar, R. H., Theory, production and mechanism of formation of monodispersed hydrosols. *J. Am. Chem. Soc.* **1950,** *72*, 4847-4854.
23. Kwon, S. G.; Piao, Y.; Park, J.; Angappane, S.; Jo, Y.; Hwang, N.-M.; Park, J.-G.; Hyeon, T., Kinetics of monodisperse iron oxide nanocrystal formation by "heating-up" process. *J. Am. Chem. Soc.* **2007,** *129*, 12571-12584.

24. van Embden, J.; Mulvaney, P., Nucleation and growth of CdSe nanocrystals in a binary ligand system. *Langmuir* **2005,** *21*, 10226-10233.
25. Talapin, D. V.; Rogach, A. L.; Haase, M.; Weller, H., Evolution of an ensemble of nanoparticles in a colloidal solution: theoretical study. *J. Phys. Chem. B* **2001,** *105*, 12278-12285.
26. Park, J.; Joo, J.; Kwon, S. G.; Jang, Y.; Hyeon, T., Synthesis of monodisperse spherical nanocrystals. *Angew. Chem. Int. Ed.* **2007,** *46*, 4630-4660.
27. Wu, L.; Jubert, P.-O.; Berman, D.; Imaino, W.; Nelson, A.; Zhu, H.; Zhang, S.; Sun, S., Monolayer Assembly of Ferrimagnetic Co x Fe3–x O4 Nanocubes for Magnetic Recording. *Nano Lett.* **2014,** *14*, 3395-3399.
28. Klug, H. P.; Alexander, L. E., *X-ray diffraction procedures*. Wiley: New York, 1954.
29. Eom, Y.; Abbas, M.; Noh, H.; Kim, C., Morphology-controlled synthesis of highly crystalline Fe 3 O 4 and CoFe 2 O 4 nanoparticles using a facile thermal decomposition method. *RSC Adv.* **2016,** *6*, 15861-15867.
30. Abbas, M.; Torati, S. R.; Kim, C., A novel approach for the synthesis of ultrathin silica-coated iron oxide nanocubes decorated with silver nanodots (Fe 3 O 4/SiO 2/Ag) and their superior catalytic reduction of 4-nitroaniline. *Nanoscale* **2015,** *7*, 12192-12204.
31. Venkatesan, K.; Babu, D. R.; Bai, M. P. K.; Supriya, R.; Vidya, R.; Madeswaran, S.; Anandan, P.; Arivanandhan, M.; Hayakawa, Y., Structural and magnetic properties of cobalt-doped iron oxide nanoparticles prepared by solution combustion method for biomedical applications. *Int. J. Mol. Sci.* **2015,** *10*, 189-198.
32. Lagarec, K.; Rancourt, D., Extended Voigt-based analytic lineshape method for determining N-dimensional correlated hyperfine parameter distributions in Mössbauer spectroscopy. *Nuclear Instruments and Methods in Physics Research Section B: Beam Interactions with Materials and Atoms* **1997,** *129*, 266-280.
33. Miguel-Sancho, N.; Bomati-Miguel, O.; Roca, A. G.; Martinez, G.; Arruebo, M.; Santamaria, J., Synthesis of magnetic nanocrystals by thermal decomposition in glycol media: effect of process variables and mechanistic study. *Ind. Eng. Chem. Res.* **2012,** *51*, 8348-8357.
34. Cornell, R. M.; Schwertmann, U., *The iron oxides: structure, properties, reactions, occurrences and uses*. John Wiley & Sons: New York, 2003.
35. Belaïd, S.; Laurent, S.; Vermeersch, M.; Vander Elst, L.; Perez-Morga, D.; Muller, R. N., A new approach to follow the formation of iron oxide nanoparticles synthesized by thermal decomposition. *Nanotechnology* **2013,** *24*, 055705-055713.
36. Baaziz, W.; Pichon, B. P.; Fleutot, S.; Liu, Y.; Lefevre, C.; Greneche, J.-M.; Toumi, M.; Mhiri, T.; Begin-Colin, S., Magnetic iron oxide nanoparticles: reproducible tuning of the size and nanosized-dependent composition, defects, and spin canting. *The Journal of Physical Chemistry C* **2014,** *118*, 3795-3810.
37. Castellanos-Rubio, I.; Insausti, M.; Garaio, E.; de Muro, I. G.; Plazaola, F.; Rojo, T.; Lezama, L., Fe 3 O 4 nanoparticles prepared by the seeded-growth route for hyperthermia: electron magnetic resonance as a key tool to evaluate size distribution in magnetic nanoparticles. *Nanoscale* **2014,** *6*, 7542-7552.
38. Klokkenburg, M.; Hilhorst, J.; Erne, B., Surface analysis of magnetite nanoparticles in cyclohexane solutions of oleic acid and oleylamine. *Vib. Spectrosc* **2007,** *43*, 243-248.
39. Yang, K.; Peng, H.; Wen, Y.; Li, N., Re-examination of characteristic FTIR spectrum of secondary layer in bilayer oleic acid-coated Fe 3 O 4 nanoparticles. *Appl. Surf. Sci.* **2010,** *256*, 3093-3097.
40. Tartaj, P.; del Puerto Morales, M.; Veintemillas-Verdaguer, S.; González-Carreño, T.; Serna, C. J., The preparation of magnetic nanoparticles for applications in biomedicine. *J. Phys. D: Appl. Phys.* **2003,** *36*, R182-R197.

41. Santoyo Salazar, J.; Perez, L.; de Abril, O.; Truong Phuoc, L.; Ihiawakrim, D.; Vazquez, M.; Greneche, J.-M.; Begin-Colin, S.; Pourroy, G., Magnetic iron oxide nanoparticles in 10− 40 nm range: Composition in terms of magnetite/maghemite ratio and effect on the magnetic properties. *Chem. Mater.* **2011,** *23*, 1379-1386.
42. Moya, C.; Batlle, X.; Labarta, A., The effect of oleic acid on the synthesis of Fe 3− x O 4 nanoparticles over a wide size range. *Phys. Chem. Chem. Phys.* **2015,** *17*, 27373-27379.
43. Pascu, O.; Carenza, E.; Gich, M.; Estradé, S. n.; Peiró, F.; Herranz, G.; Roig, A., Surface reactivity of iron oxide nanoparticles by microwave-assisted synthesis; comparison with the thermal decomposition route. *J. Physc. Chem. C* **2012,** *116*, 15108-15116.
44. Lynch, J.; Zhuang, J.; Wang, T.; LaMontagne, D.; Wu, H.; Cao, Y. C., Gas-bubble effects on the formation of colloidal iron oxide nanocrystals. *J. Am. Chem. Soc.* **2011,** *133*, 12664-12674.
45. Voss, B.; Haase, M., Intrinsic focusing of the particle size distribution in colloids containing nanocrystals of two different crystal phases. *ACS nano* **2013,** *7*, 11242-11254.
46. Perala, S. R. K.; Kumar, S., On the two-step mechanism for synthesis of transition-metal nanoparticles. *Langmuir* **2014,** *30*, 12703-12711.
47. Singh, A.; Puri, S.; Dasgupta, C., Growth kinetics of nanoclusters in solution. *J. Phys. Chem. B* **2012,** *116*, 4519-4523.
48. Rempel, J. Y.; Bawendi, M. G.; Jensen, K. F., Insights into the kinetics of semiconductor nanocrystal nucleation and growth. *J. Am. Chem. Soc.* **2009,** *131*, 4479-4489.
49. Rinaldo, S. G.; Lee, W.; Stumper, J.; Eikerling, M., Nonmonotonic dynamics in Lifshitz-Slyozov-Wagner theory: Ostwald ripening in nanoparticle catalysts. *Phys. Rev. E* **2012,** *86*, 041601.
50. Patnaik, P., *Handbook of inorganic chemicals*. McGraw-Hill New York: 2003; Vol. 529.
51. Baumgartner, J.; Dey, A.; Bomans, P. H.; Le Coadou, C.; Fratzl, P.; Sommerdijk, N. A.; Faivre, D., Nucleation and growth of magnetite from solution. *Nat. Mater.* **2013,** *12*, 310-314.
52. Bergermayer, W.; Schweiger, H.; Wimmer, E., Ab initio thermodynamics of oxide surfaces: O 2 on Fe 2 O 3 (0001). *Phys. Rev. B* **2004,** *69*, 195409-195421.
53. Timonen, J. V.; Seppälä, E. T.; Ikkala, O.; Ras, R. H., From Hot-Injection Synthesis to Heating-Up Synthesis of Cobalt Nanoparticles: Observation of Kinetically Controllable Nucleation. *Angew. Chem. Int. Ed.* **2011,** *50*, 2080-2084.
54. Muscas, G.; Singh, G.; Glomm, W.; Mathieu, R.; Kumar, P. A.; Concas, G.; Agostinelli, E.; Peddis, D., Tuning the size and shape of oxide nanoparticles by controlling oxygen content in the reaction environment: morphological analysis by aspect maps. *Chem. Mater.* **2015,** *27*, 1982-1990.
55. Wu, L.; Mendoza-Garcia, A.; Li, Q.; Sun, S., Organic phase syntheses of magnetic nanoparticles and their applications. *Chem. Rev.* **2016,** *116*.
56. Roca, A. G.; Marco, J. F.; Morales, M. d. P.; Serna, C. J., Effect of nature and particle size on properties of uniform magnetite and maghemite nanoparticles. *J. Physc. Chem. C* **2007,** *111*, 18577-18584.
57. O'grady, K.; Bradbury, A., Particle size analysis in ferrofluids. *J. Magn. Magn. Mater.* **1983,** *39*, 91-94.
58. Morales, M. d. P.; Veintemillas-Verdaguer, S.; Montero, M.; Serna, C.; Roig, A.; Casas, L.; Martinez, B.; Sandiumenge, F., Surface and internal spin canting in γ-Fe2O3 nanoparticles. *Chem. Mater.* **1999,** *11*, 3058-3064.
59. Caruntu, D.; Caruntu, G.; O'Connor, C. J., Magnetic properties of variable-sized Fe3O4 nanoparticles synthesized from non-aqueous homogeneous solutions of polyols. *J. Phys. D: Appl. Phys.* **2007,** *40*, 5801-5809.
60. Kodama, R.; Berkowitz, A.; McNiff Jr, E.; Foner, S., Surface spin disorder in ferrite nanoparticles. *J. Appl. Phys.* **1997,** *81*, 5552-5557.
61. Guardia, P.; Labarta, A.; Batlle, X., Tuning the size, the shape, and the magnetic properties of iron oxide nanoparticles. *J. Physc. Chem. C* **2010,** *115*, 390-396.

62. Roca, A.; Morales, M.; O'Grady, K.; Serna, C., Structural and magnetic properties of uniform magnetite nanoparticles prepared by high temperature decomposition of organic precursors. *Nanotechnology* **2006,** *17*, 2783-2788.
63. Chen, J.; Sorensen, C.; Klabunde, K.; Hadjipanayis, G.; Devlin, E.; Kostikas, A., Size-dependent magnetic properties of MnFe 2 O 4 fine particles synthesized by coprecipitation. *Phys. Rev. B* **1996,** *54*, 9288-9296.
64. Liu, C.; Zhang, Z. J., Size-dependent superparamagnetic properties of Mn spinel ferrite nanoparticles synthesized from reverse micelles. *Chem. Mater.* **2001,** *13*, 2092-2096.
65. Guardia, P.; Perez-Juste, J.; Labarta, A.; Batlle, X.; Liz-Marzán, L. M., Heating rate influence on the synthesis of iron oxide nanoparticles: the case of decanoic acid. *Chem. Commun.* **2010,** *46*, 6108-6110.
66. Perez, N.; Guardia, P.; Roca, A. G.; Morales, M. d. P.; Serna, C. J.; Iglesias, O.; Bartolome, F.; Garcia, L. M.; Batlle, X.; Labarta, A., Surface anisotropy broadening of the energy barrier distribution in magnetic nanoparticles. *Nanotechnology* **2008,** *19*, 475704.
67. Leslie-Pelecky, D. L.; Rieke, R. D., Magnetic properties of nanostructured materials. *Chem. Mater.* **1996,** *8*, 1770-1783.

Chapter 3

Section 2

Effect of Precursor Concentration on Size Evolution of Iron Oxide Nanoparticles[1]

3.2.1 Introduction

Precise control over the size and dispersity of magnetic nanoparticles is crucial for different applications.[1-3] In a thermal decomposition reaction, the nanoparticle size, morphology, dispersity, and crystallinity are controlled, among the other factors, by the precursor,[4-5] solvent,[6-7] surfactant[5, 8] and their respective concentrations.[9-11] Typically, LaMer model[12] is used to explain the nucleation and growth of the nanoparticles.

3.2.1.1 Motivation

[1] **The results of this chapter are fully or in part published in *CrystEngComm* with DOI: *10.1039/C7CE01406F* and J. Phys. Chem. C. with DOI: *10.1021/acs.jpcc.8b06927* by H. Sharifi et al.**

Under identical heating and synthetic conditions for different reactions the nucleation rate depends on supersaturation and thereby the initial precursor concentration. Therefore, tuning the precursor concentration has been used to control the size of the nanoparticles.[5-6] Concentration tuning can be obtained in different ways, *e.g.* changing the amount of solvent or precursor. Concentration tuning by solvent is straightforward because the solvent has only a dilution effect. By changing the precursor concentration, the ratio between surfactant and precursor is also varies. Several studies have shown that an increase of the concentration may lead to both, an increase[4, 6, 13-14] and a decrease[5, 15] of the particle size. A conclusive explanation is still lacking.

3.2.1.2 Aim of this section

This section addresses the effect of concentration on the final size (distribution) and the magnetic properties of the nanoparticles. First, as reference, a nanoparticle batch is prepared and characterize under "standard condition". Size tuning by controlling the precursor concentration is achieved in two ways: by changing (1) the amount of solvent, or (2) the amount of the precursor. We show that the particle size monotonically decreases with increasing amount of solvent whereas for changing the precursor amount two size regimes are observed, first an increase and then a decrease in size as the amount of precursor increases. We show that the ratio of surfactant to precursor plays a crucial role in tuning the size by changing the concentration, and we explain the observed opposite increasing/decreasing trend reported in literature.[4-6, 13-14] Magnetic measurements show that the nanoparticles are superparamagnetic at room temperature and possess magnetizations close to the theoretically predicted values.

3.2.2 Experiment

The same materials as Section 1 of Chapter 3 have used for the synthesis of nanoparticles. The standard sample was prepared under "standard condition", wherein a three-necked round-bottom flask was charged with 2 mmol of iron acetylacetonate, 6 mmol of OAC and 6 mmol of OAM, 10 mmol of 1,2 hexadecandiol, and 20 mL of benzyl ether. The mixture was heated to 110 °C, and stayed at that temperature for 60 min under vacuum. Temperature was

then raised to 180 °C, under N_2 blanket with a heating rate of 6.5 °C/min and kept at that temperature for 120 min to fully decompose the precursor. Subsequently, temperature was raised to ~295 °C with a constant heating rate of 3.3 °C/min and refluxed for 1 hour. Upon cooling of the solution, the nanoparticles were precipitated by addition of ethanol. The nanoparticles were washed three times by a mixture of toluene/ethanol/acetone followed by centrifugation (6000rpm, 10 min), and finally stored under argon in toluene or hexane.

From standard condition, the amount of solvent (series A), the total amount of precursor (series B) and the total amount of surfactant (series C) were varied. Other synthesis and post synthesis parameters/processes were kept unchanged with respect to the standard condition. A summary of the experimental conditions is given in **Table 3.2.1**. The particles were characterized by TEM, HR-TEM, XRD, FTIR, TGA and VSM (Cryogenic Ltd). The conditions of the characterization techniques were given in previous section (Section 1 of Chapter 3).

Table 3.2.1 Summary of experimental conditions. A, B and C are the variable parameters, where A = 28 ml (A_1), 24 ml (A_2), 16 ml (A_3), 12 ml (A_4); B = 0.6 mmol (B_1), 1.2 mmol (B_2), 1.6 mmol (B_3), 3 mmol (B_4), 4.5 mmol (B_5), 6 mmol (B_6); C = 2 mmol (C_1), 4 mmol (C_2), 8 mmol (C_3), 10 mmol (C_4).

Reactants	Standard condition	Series A	Series B	Series C
Benzyl ether (ml)	20	**A_1-A_4**	20	20
$Fe(acac)_3$ (mmol)	2	2	**B_1-B_6**	2
OAC (mmol)	6	6	6	**C_1-C_4**
OAM (mmol)	6	6	6	**C_1-C_4**

3.2.3 Results and discussion

3.2.3.1 Properties of standard (reference) sample

Under standard condition nanoparticles with regular polyhedral morphologies were obtained as shown in **Figure 3.2.1 a**. The size histogram can be fitted well with a normal Gaussian distribution. It gives a mean size of 13.00 nm with a standard deviation of 1.1 nm and hence a

polydispersity of ~ 8.5% (**Figure 3.2.1 b**). The reference nanoparticles are monodisperse with a narrow size distribution. Particle aggregation is effectively hindered by the surfactant, and well dispersed colloidal solutions in hexane or toluene are obtained. The ligand shell around the nanoparticles consists predominantly of oleate as determined from the FTIR spectra of the nanoparticles (as discussed in detail in section 1 of Chapter 3). In the high resolution TEM (HRTEM) images of the nanoparticles, shown in the inset of **Figure 3.2.1 a**, demonstrates that the crystalline structure is extended up to the edge of the nanoparticles, thereby minimizing the thickness of the disordered shell[16-17] at the particle surface. In the next step we investigate the influences of the amount of A) solvent, B) precursor, and C) surfactants on the size evolution (dispersity) of the nanoparticles.

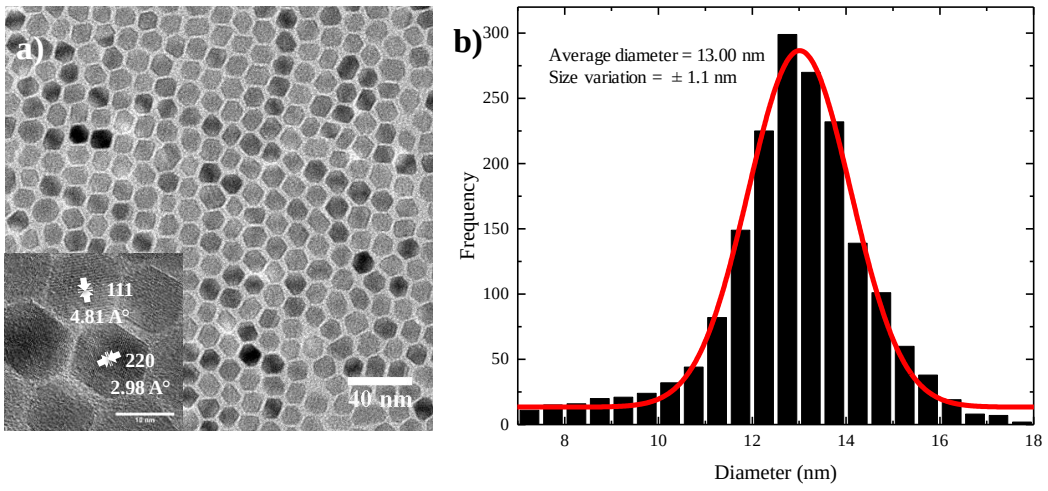

Figure 3.2.1 (a) TEM images of nanoparticles prepared under standard condition. The inset shows a typical HRTEM image where crystalline planes are indicated. (b) Size distribution obtained for more than 2000 particles.

3.2.3.2 The role of solvent amount

Different reactions were performed where only the amount of solvent (A) was systematically varied, 12 ml (A_1), 16 ml (A_2), 20 ml (standard sample), 24 ml (A_3) to 28 ml (A_4). TEM images of the resulting nanoparticles are shown in **Figure 3.2.2 a-d**. XRD diffractograms of all samples are shown in **Figure A3.2.1 a**. The crystal structure of all samples are comparable with standard sample and are indexed in the fcc inverse cubic spinel structure of magnetite.[18-21]

The crystallite size of the nanoparticles were calculated from the XRD diffractograms using Scherrer's formula.[22-23] TGA traces of all nanoparticles (A_1-A_4) show (**Figure A3.2.1 b**) that the grafting densities for all samples were almost ~ 3 molecules/nm^2 compared to the standard reference.

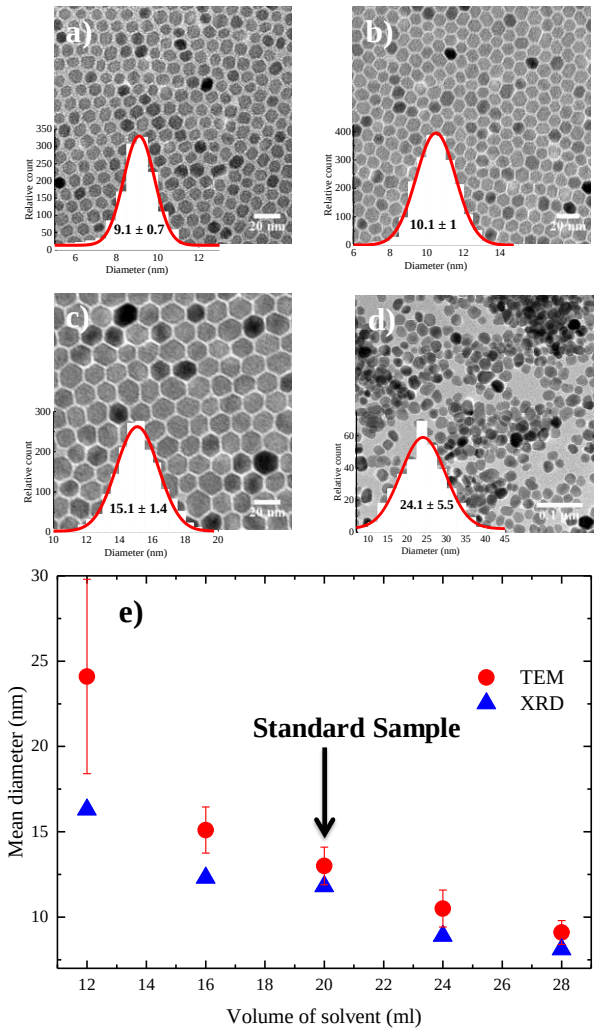

Figure 3.2.2 TEM images and particle size distribution of samples (a) A_1, (b) A_2, (c) A_3 and (d) A_4. (e) Evolution of nanoparticle size as a function of solvent volume. Nanoparticle diameters were determined from both TEM and XRD analysis.

The nanoparticles A_1-A_3 are truly monodisperse with polydispersities well below 10%. With increasing amount of solvent (from 12 ml to 28 mL), *i.e.* decreasing concentration, the average size of the nanoparticle drops from 24.1 ± 5.7 nm to 9.1 ± 0.71 nm (as depicted in

Figure 3.2.2 e). The observed drop in the size with increasing the solvent volume can be explained by the decrease in the concentration of monomer in the reaction medium. At low solvent volume, the concentration of monomer in solution is high. The concentration of the available monomers at the interface of the nuclei (the crystal growth front) is close to that of the bulk solution. Hence the diffusion distance for monomers is shorter, which leads to a higher mass transfer and therefore higher growth rate.[6] As a result, larger nanoparticles are formed during the same growth period compared to the standard condition. We note that for low solvent volumes (high concentrations) nanoparticle growth is reaction controlled as the growth rate is mainly governed by reactions on the surface of the nanoparticles. As the amount of solvent increases (low concentration), the concentration of precursor, and therefore monomer, is lowered which increases diffusion constant and reduces the growth rate due to less mass transfer in the reaction medium. Nanoparticle growth is therefore diffusion limited. Therefore, smaller nanoparticles are formed during the same growth time compared to the reference condition.

3.2.3.3 The role of precursor amount

The amount of $Fe(acac)_3$ (B) was systematically varied from 0.6 to 6 mmol (B_1-B_6). TEM images of the resulting nanoparticles with corresponding size distribution are shown in **Figure 3.2.3 a-f**. The nanoparticle size evolution is given in **Figure 3.2.3 g**. Two different size regimes were observed. In the first regime, the size of the nanoparticles increases from 6 ± 0.9 nm to 13.00 ± 1.1 nm by increasing the amount of precursor from 0.6 to 2 mmol. The increase in size can be understood based on the increased concentration of the monomer in the fixed reaction volume, as discussed for the solvent case. To show that the governing mechanism is the same we have plotted size evolution for both series A and B as a function of precursor concentration in **Figure 3.2.4 a**. The trend observed for the case of solvent variation describes well the first regime in **Figure 3.2.3 g**. The trend of increasing size is hold up to a precursor concentration of 2 mmol, beyond which the nanoparticle size continuously drops. We note that as the concentration of precursor increases in a fixed reaction volume two parameters are changed simultaneously: the precursor concentration and the ratio between surfactants and $Fe(acac)_3$. The drop in size can be attributed to the decreasing amount of surfactants available for the stabilization of the monomers. Therefore the saturation concentration of monomer increases and more nuclei are

formed. As a result, less monomer is available for the growth and hence smaller nanoparticles are formed.[9-10, 24] To substantiate the role of the surfactant to precursor ratio, we systematically varied the amount of surfactant in the next step.

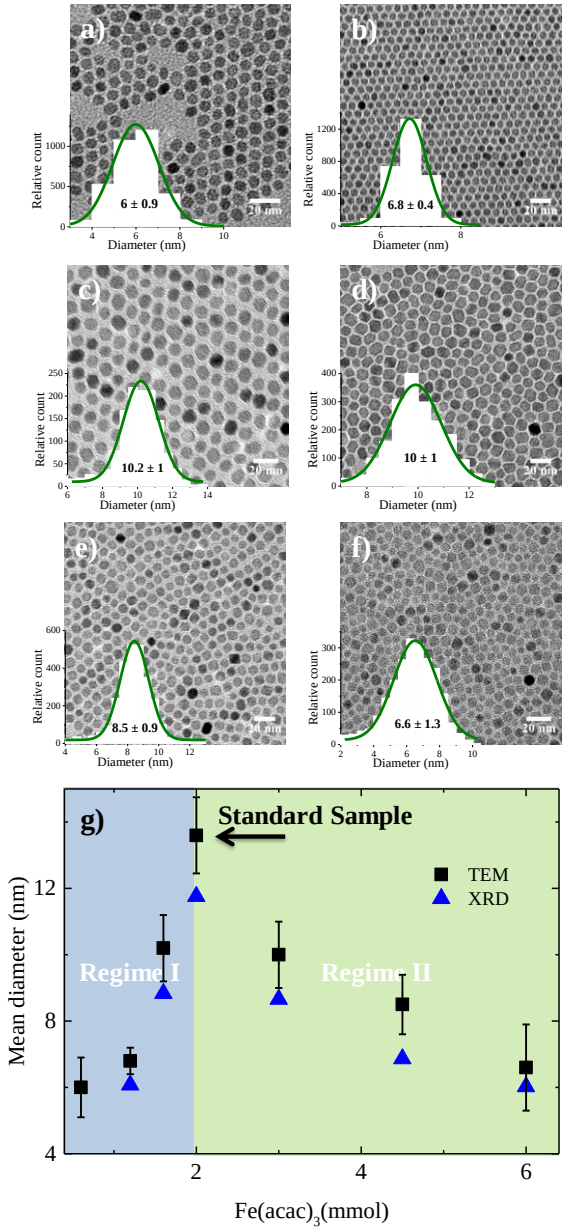

Figure 3.2.3 TEM images of samples (a) B_1, (b) B_2, (c) B_3, (d) B_4, (e) B_5 and (f) B_6. Particle size distributions obtained by fitting TEM histograms are also shown. (g) Evolution of the nanoparticle size (TEM and XRD) as a function of precursor amount.

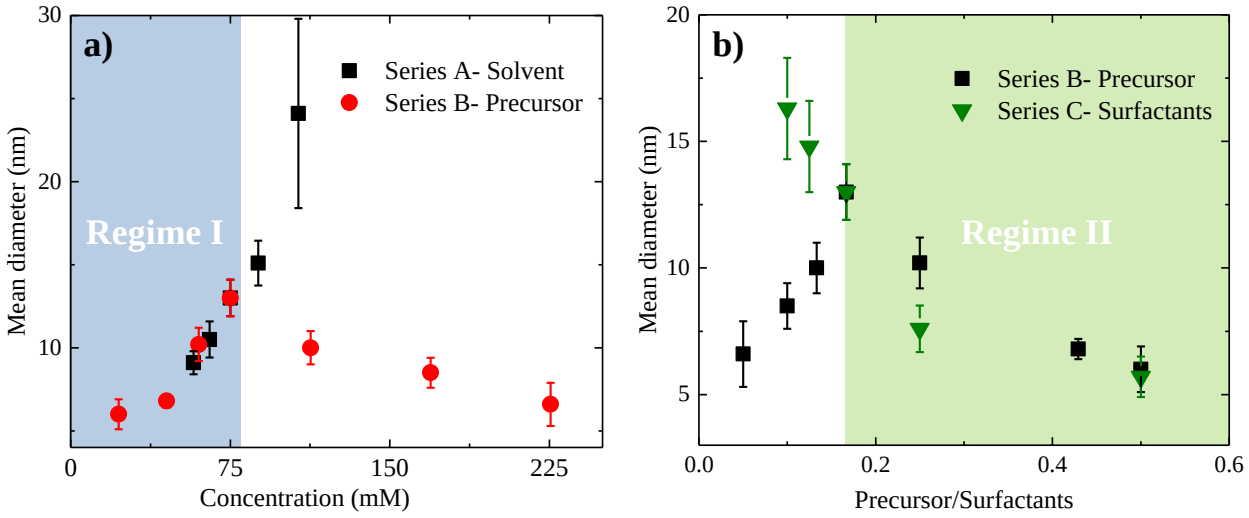

Figure 3.2.4 The evolution of mean diameter as function of (a) precursor concentration and (b) precursor to surfactants ratio.

3.2.3.4 The role of surfactant amount

Several studies have investigated the effect of surfactant concentration. By increasing the ratio, both trends of either increasing[5, 7, 9-10, 25-27] or decreasing the size[7-8, 28-29] has been observed. To elucidate on the role of precursor/surfactant ratio, different synthesis were performed wherein only the amount of surfactant (OAC + OAM = C, OAC/OAM= 1) was systematically varied from 2 mmol to 10 mmol (C_1-C_4). TEM images of the resulting nanoparticles are shown in **Figure 3.2.5 a-d**. The mean nanoparticle size (**Figure 3.5.4 e**) continuously increases from 5.8 ± 0.8 nm to around 16.3 ± 2 nm as the precursor/surfactant ratio decreases. As the amount of surfactant increases, more oleate molecules react with the precursor and more stable monomers with reduced reactivity are formed.[7, 9-10, 24-25, 30] According to LaMer model[12] for nucleation and growth, reduced active monomer concentration reduces the nucleation rate and hinders formation of a large number of nuclei hence favors the growth of larger nanoparticles. We have also plotted size evolution for both series B and C as a function of precursor/surfactant ratio in **Figure 3.2.4 b**. The trend observed for the case for surfactant variation describes well the second regime in **Figure 3.2.3 g**. We note that an excess of surfactants prevents nanoparticle growth by blocking growth sites and stabilizing the growth species[7, 24] and manifested a dramatic drop in the mass reaction yield of nanoparticles.

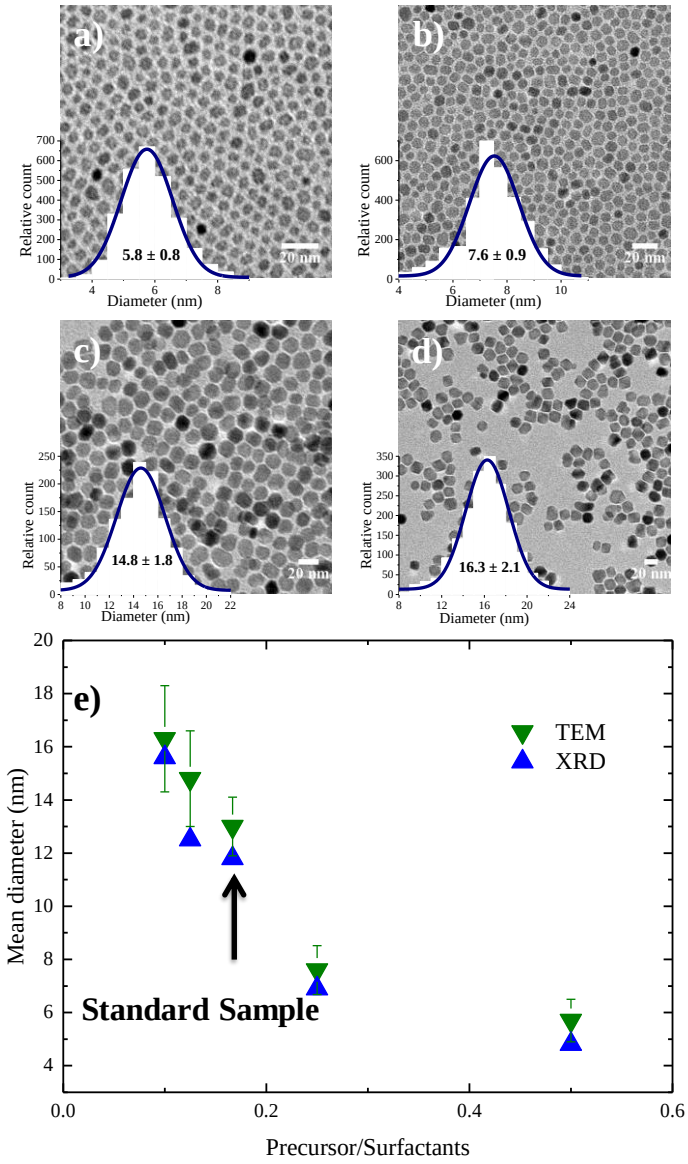

Figure 3.2.5 TEM images of samples (a) C_1, (b) C_2, (c) C_3 and (d) C_4. Particle size distributions obtained by fitting TEM histograms are also shown. (e) Size (based on TEM and XRD) evolution of the nanoparticles as function of precursor/surfactants ratio. The dashed line is guide to the eye.

3.2.3.5 Magnetic properties

Magnetic properties of the particles depend on the size.[8, 31] Representative magnetization hysteresis loops of samples A_1-A_4 as a function of applied field measured at 300 and 2 K are given in **Figure 3.2.6 a, b**, respectively. At 300 K, no hysteresis loops were observed for samples A_1-A_4, confirming that the nanoparticles are superparamagnetic. However, sample A_4 (24.1±

5.7nm) showed a hysteresis loop with a small coercivity, H_C (~10 Oe), and remnant magnetization, indicating that the critical nanoparticle size is reached. [26, 32-33] Hysteresis loops at 2 K confirm that all the samples are ferri-ferromagnetic at 2 K. As the size of the nanoparticles increases M_s approaches the values reported for the bulk phase magnetite (84 emu/g) and the theoretically predicted value (98 emu/g) at low temperature.[16, 18, 34-37] The blocking temperature T_B was determined with zero-field (ZFC) and field cooling (FC) in an applied magnetic field of 100 Oe between 5 K - 320 K (**Figure 3.2.6 a**). With increasing temperature, the thermal energy increases, and the ZFC curve starts to plunge as T_B is reached. The values of T_B are given in **Figure 3.2.6 b** as a function of size. With increasing size the volume of the nanoparticle increases, and T_B moves to higher temperatures.[4, 35, 38] The increase in T_B with size is caused by the increased magnetocrystalline energy (**Figure 3.2.6 b**). Consequently, higher thermal energies are required to unblock the magnetic moment of larger nanoparticles. The anisotropy constant K increases because of the increased surface to volume ratio as nanoparticle size decreases.[4, 10, 37-39]

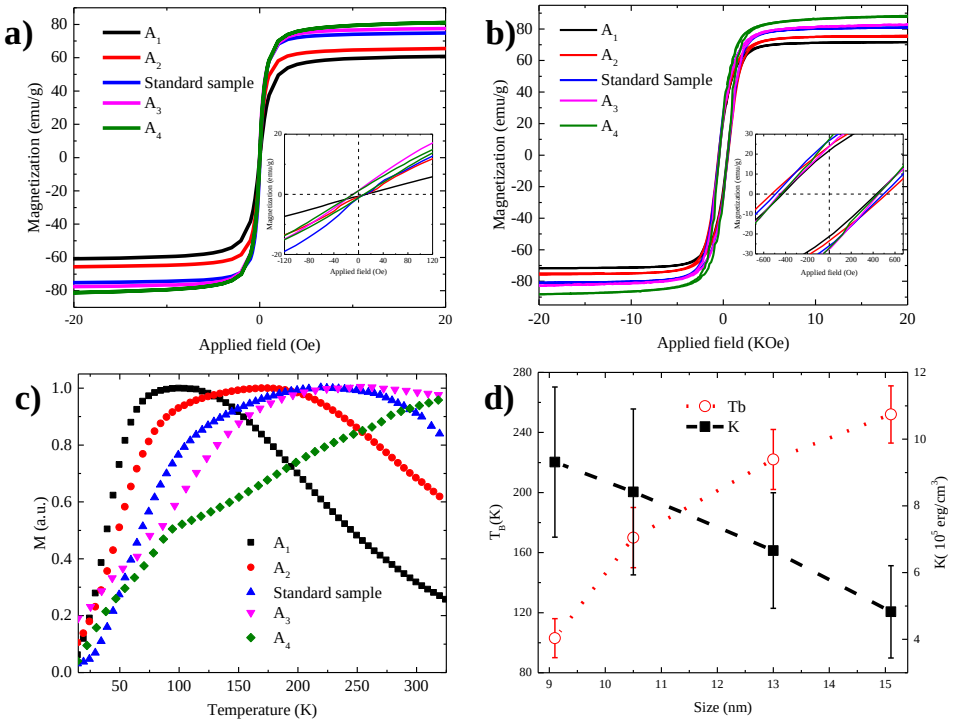

Figure 3.2.6 Hysteresis loops of all samples at (a) 300 K and (b) 2 K. (c) Temperature dependence of magnetization measured after zero-field cooling (ZFC) at 100 Oe. The magnetization data are normalized with respect to the value at the maximum of the ZFC magnetization $M(T_B)$ for each sample. (d) Values of T_B (blocking temperature) and K (anisotropy constant) as a function of size.

3.2.4 Conclusion

In summary, changing the concentration via (1) the amount of solvent or (2) the amount of precursor can control the size of iron oxide nanoparticle. Two competing mechanisms were identified that influence nucleation and growth of the nanoparticles: (i) concentration dependent monomer diffusion and (ii) monomer stabilization by excessive amount of surfactant. The former controls the size when the amount of solvent (to some extent, precursor concentration) is changed. At a fixed solvent amount, lowering the precursor amount, changes precursor/surfactant ratio which can lead to monomer stabilization, less nucleation and hence growth of larger nanoparticles. The resulting nanoparticles show superparamagnetic behavior at room temperature and ferro-ferrimagnetic behavior at low temperature with a high M_S close to the theoretical value for magnetite.

3.2.5 References

1. Assa, F.; Jafarizadeh-Malmiri, H.; Ajamein, H.; Anarjan, N.; Vaghari, H.; Sayyar, Z.; Berenjian, A., A biotechnological perspective on the application of iron oxide nanoparticles. *Nano Res.* **2016,** *9*, 2203-2225.
2. Dinali, R.; Ebrahiminezhad, A.; Manley-Harris, M.; Ghasemi, Y.; Berenjian, A., Iron oxide nanoparticles in modern microbiology and biotechnology. *Crit. Rev. Microbiol.* **2017,** *43*, 493-507.
3. Reddy, L. H.; Arias, J. L.; Nicolas, J.; Couvreur, P., Magnetic nanoparticles: design and characterization, toxicity and biocompatibility, pharmaceutical and biomedical applications. *Chem. Rev.* **2012,** *112*, 5818-5878.
4. Huang, J.-H.; Parab, H. J.; Liu, R.-S.; Lai, T.-C.; Hsiao, M.; Chen, C.-H.; Sheu, H.-S.; Chen, J.-M.; Tsai, D.-P.; Hwu, Y.-K., Investigation of the growth mechanism of iron oxide nanoparticles via a seed-mediated method and its cytotoxicity studies. *Journal of Physical Chemistry C* **2008,** *112*, 15684-15690.
5. Hufschmid, R.; Arami, H.; Ferguson, R. M.; Gonzales, M.; Teeman, E.; Brush, L. N.; Browning, N. D.; Krishnan, K. M., Synthesis of phase-pure and monodisperse iron oxide nanoparticles by thermal decomposition. *Nanoscale* **2015,** *7*, 11142-11154.
6. Zeng, H.; Rice, P. M.; Wang, S. X.; Sun, S., Shape-controlled synthesis and shape-induced texture of MnFe2O4 nanoparticles. *J. Am. Chem. Soc.* **2004,** *126*, 11458-11459.
7. Baaziz, W.; Pichon, B. P.; Fleutot, S.; Liu, Y.; Lefevre, C.; Greneche, J.-M.; Toumi, M.; Mhiri, T.; Begin-Colin, S., Magnetic iron oxide nanoparticles: reproducible tuning of the size and nanosized-dependent composition, defects, and spin canting. *J. Physc. Chem. C* **2014,** *118*, 3795-3810.
8. Guardia, P.; Pérez, N.; Labarta, A.; Batlle, X., Controlled synthesis of iron oxide nanoparticles over a wide size range. *Langmuir* **2009,** *26*, 5843-5847.

9. Meledandri, C. J.; Stolarczyk, J. K.; Ghosh, S.; Brougham, D. F., Nonaqueous magnetic nanoparticle suspensions with controlled particle size and nuclear magnetic resonance properties. *Langmuir* **2008,** *24*, 14159-14165.
10. Demortiere, A.; Panissod, P.; Pichon, B.; Pourroy, G.; Guillon, D.; Donnio, B.; Begin-Colin, S., Size-dependent properties of magnetic iron oxide nanocrystals. *Nanoscale* **2011,** *3*, 225-232.
11. Effenberger, F. B.; Couto, R. A.; Kiyohara, P. K.; Machado, G.; Masunaga, S. H.; Jardim, R. F.; Rossi, L. M., Economically attractive route for the preparation of high quality magnetic nanoparticles by the thermal decomposition of iron (III) acetylacetonate. *Nanotechnology* **2017,** *28*, 115603-11570.
12. LaMer, V. K.; Dinegar, R. H., Theory, production and mechanism of formation of monodispersed hydrosols. *J. Am. Chem. Soc.* **1950,** *72*, 4847-4854.
13. Cabrera, L. I.; Somoza, Á.; Marco, J. F.; Serna, C. J.; Morales, M. P., Synthesis and surface modification of uniform MFe2O4 (M= Fe, Mn, and Co) nanoparticles with tunable sizes and functionalities. *J. Nanopart. Res.* **2012,** *14*, 1-14.
14. Miguel-Sancho, N.; Bomati-Miguel, O.; Roca, A. G.; Martinez, G.; Arruebo, M.; Santamaria, J., Synthesis of magnetic nanocrystals by thermal decomposition in glycol media: effect of process variables and mechanistic study. *Ind. Eng. Chem. Res.* **2012,** *51*, 8348-8357.
15. Li, Y.; Liu, J.; Wang, Y.; Wang, Z. L., Preparation of monodispersed Fe− Mo nanoparticles as the catalyst for CVD synthesis of carbon nanotubes. *Chem. Mater.* **2001,** *13*, 1008-1014.
16. Mohapatra, J.; Mitra, A.; Bahadur, D.; Aslam, M., Surface controlled synthesis of MFe 2 O 4 (M= Mn, Fe, Co, Ni and Zn) nanoparticles and their magnetic characteristics. *CrystEngComm* **2013,** *15*, 524-532.
17. Unni, M.; Uhl, A. M.; Savliwala, S.; Savitzky, B. H.; Dhavalikar, R.; Garraud, N.; Arnold, D. P.; Kourkoutis, L. F.; Andrew, J. S.; Rinaldi, C., Thermal decomposition synthesis of iron oxide nanoparticles with diminished magnetic dead layer by controlled addition of oxygen. *ACS Nano* **2017,** *11*, 2284-2303.
18. Sun, S.; Zeng, H.; Robinson, D. B.; Raoux, S.; Rice, P. M.; Wang, S. X.; Li, G., Monodisperse MFe2O4 (M= Fe, Co, Mn) nanoparticles. *J. Am. Chem. Soc.* **2004,** *126*, 273-279.
19. Belaïd, S.; Laurent, S.; Vermeersch, M.; Vander Elst, L.; Perez-Morga, D.; Muller, R. N., A new approach to follow the formation of iron oxide nanoparticles synthesized by thermal decomposition. *Nanotechnology* **2013,** *24*, 055705-055712.
20. Teng, X.; Yang, H., Effects of surfactants and synthetic conditions on the sizes and self-assembly of monodisperse iron oxide nanoparticles. *J. Mater. Chem.* **2004,** *14*, 774-779.
21. Cornell, R. M.; Schwertmann, U., *The iron oxides: structure, properties, reactions, occurrences and uses*. John Wiley & Sons: 2003.
22. Eom, Y.; Abbas, M.; Noh, H.; Kim, C., Morphology-controlled synthesis of highly crystalline Fe 3 O 4 and CoFe 2 O 4 nanoparticles using a facile thermal decomposition method. *RSC Adv.* **2016,** *6*, 15861-15867.
23. Arrhenius, G., X-ray diffraction procedures for polycrystalline and amorphous materials. *J. Chem. Educ* **1955,** *32*, 228-229.
24. Yin, M.; Willis, A.; Redl, F.; Turro, N. J.; O'Brien, S. P., Influence of Capping Groups on the Synthesis of γ-Fe 2 O 3 Nanocrystals. *J. Mater. Res.* **2004,** *19*, 1208-1215.
25. William, W. Y.; Falkner, J. C.; Yavuz, C. T.; Colvin, V. L., Synthesis of monodisperse iron oxide nanocrystals by thermal decomposition of iron carboxylate salts. *Chem. Commun.* **2004**, 2306-2307.
26. Zhu, Y.; Jiang, F.; Chen, K.; Kang, F.; Tang, Z., Size-controlled synthesis of monodisperse superparamagnetic iron oxide nanoparticles. *J. Alloys Compd.* **2011,** *509*, 8549-8553.
27. Chen, Z., Size and shape controllable synthesis of monodisperse iron oxide nanoparticles by thermal decomposition of iron oleate complex. *Synthesis and Reactivity in Inorganic, Metal-Organic, and Nano-Metal Chemistry* **2012,** *42*, 1040-1046.

28. Moya, C.; Batlle, X.; Labarta, A., The effect of oleic acid on the synthesis of Fe 3− x O 4 nanoparticles over a wide size range. *Phys. Chem. Chem. Phys.* **2015,** *17*, 27373-27379.
29. Vargas, J.; Zysler, R., Tailoring the size in colloidal iron oxide magnetic nanoparticles. *Nanotechnology* **2005,** *16*, 1474-1479.
30. Yu, W. W.; Peng, X., Formation of high-quality CdS and other II–VI semiconductor nanocrystals in noncoordinating solvents: tunable reactivity of monomers. *Angew. Chem. Int. Ed.* **2002,** *41*, 2368-2371.
31. Kolhatkar, A. G.; Jamison, A. C.; Litvinov, D.; Willson, R. C.; Lee, T. R., Tuning the magnetic properties of nanoparticles. *Int. J. Mol. Sci.* **2013,** *14*, 15977-16009.
32. Wu, L.; Mendoza-Garcia, A.; Li, Q.; Sun, S., Organic phase syntheses of magnetic nanoparticles and their applications. *Chem. Rev.* **2016,** *116*, 10473-10512.
33. Leslie-Pelecky, D. L.; Rieke, R. D., Magnetic properties of nanostructured materials. *Chem. Mater.* **1996,** *8*, 1770-1783.
34. O'grady, K.; Bradbury, A., Particle size analysis in ferrofluids. *J. Magn. Magn. Mater.* **1983,** *39*, 91-94.
35. Roca, A.; Morales, M.; O'Grady, K.; Serna, C., Structural and magnetic properties of uniform magnetite nanoparticles prepared by high temperature decomposition of organic precursors. *Nanotechnology* **2006,** *17*, 2783-2788.
36. Jiles, D., *Introduction to magnetism and magnetic materials*. CRC press: 2015.
37. Caruntu, D.; Caruntu, G.; O'Connor, C. J., Magnetic properties of variable-sized Fe3O4 nanoparticles synthesized from non-aqueous homogeneous solutions of polyols. *J. Phys. D: Appl. Phys.* **2007,** *40*, 5801-5809.
38. Park, J.; An, K.; Hwang, Y.; Park, J.-G.; Noh, H.-J.; Kim, J.-Y.; Park, J.-H.; Hwang, N.-M.; Hyeon, T., Ultra-large-scale syntheses of monodisperse nanocrystals. *Nat. Mater.* **2004,** *3*, 891-895.
39. Mørup, S.; Tronc, E., Superparamagnetic relaxation of weakly interacting particles. *Phys. Rev. Lett.* **1994,** *72*, 3278-3281.

Chapter 3

Section 3

Impact of Binding Energy of Surfactant on Polydispersity of Iron-Oxide Nanoparticles[1]

3.3.1 Introduction

As synthesized nanoparticles, typically show a wide distribution in size. Usually, size selective precipitation[1-3] is performed to narrow the size distribution and lower poly dispersity index (PDI) of the nanoparticles. It is therefore highly desirable to find a recipe that eliminates any post purification steps. It has been shown that surfactants play a key role in the final size distribution of the nanoparticles. [4-8] The surfactant molecules bind to the growth species and therefore control the growth rate of the nucleated nanoparticles.

In a thermal decomposition synthesis of iron-oxide nanoparticles, usually oleic acid (OAC),[9-10] olelyamine (OAM) [11-14] or the combination of both OAC/OAM with, mainly, 1/1 molar ratio[15-19] have been used as surfactant.[15, 20-22 23-25] Presence of OAM, in a mixture of OAC/OAM deprotonates OAC molecules more efficiently via the following acid-base reactions (**Equations 3.3.1** and **3.3.2**), hence improving the adsorption of OAC, the primary surfactant, to the surface of the nanoparticles.

[1] **The results of this chapter are fully or in part published in *Langmuir* with DOI: *10.1021/acs.langmuir.8b01337* by H. Sharifi et al.**

$$RCOOH + RCNH_2 \leftrightarrows RCOO^- + RCNH_3^+ \quad (3.3.1)$$

$$RCOOH \leftrightarrows RCOO^- + H^+ \quad \text{and} \quad RCNH_2 + H^+ \leftrightarrows RCNH_3^+ \quad (3.3.2)$$

The free protons (H^+), is neutralized in the reaction medium by OAM through formation of $RCNH_3^+$ or by desorbing of a bounded oleic acid group ($RCOO^-$) from the nanoparticle surface.[24-25] Therefore, next to the type and concentration of the surfactant in the reaction, the molar ratio between them plays a key role in the reaction, and critically influence the nanoparticles' shape, size and size distribution. Since the surfactant molecules bind to the growth species and control the growth rate, it is therefore highly desirable to find an optimum surfactant concentration, and ratio between OAC and OAM that yields truly monodisperse nanoparticles. Numerous studies have investigated the role of surfactants concentration.[4, 7, 17, 26-28] However, only a handful of reports investigated the effect of the surfactants molar ratio.[24, 29-31] A combined experimental/theoretical study on the role of molar ratio between OAC and OAM on the size, and PDI of the nanoparticle is still missing, and the optimum OAC/OAM ratio is still unknown.

3.3.1.1 Motivation

The motivation of this chapter is to study the role of surfactant and the interplay between the molar ratio between OAC and OAM on the size, and PDI of the nanoparticle.

3.3.1.2 Aim of this section

In this chapter, we present a detailed experiment wherein the ratio of OAC to OAM is systematically varied in three different ways, all ranging from OAC-rich to OAM-rich reaction. We reemphasis that only the surfactant amounts are changed. All other synthesis parameters are held constant. We performed molecular dynamic (MD) simulations to further elucidate the role of surfactant and its binding energy on PDI of the nanoparticles. We aim to find an optimum OAC/OAM ratio that gives the lowest PDI, and use the optimum ratio to synthesize nanoparticles with one-nanometer control over the size with very narrow size distribution, preferably without any post synthesize purification such as size selective precipitation just by changing the reaction heating rate.

3.3.2 Experiment and simulation

3.3.2.1 Synthesis method

The detail of synthesis method is reported in previous sections in detail (Section 1 and 2 of Chapter 3).[7, 32-33] 2 mmol of iron acetylacetonate, 10 mmol of 1,2 Hexadecandiol as reducing agent, and 20 mL of benzyl ether as solvent were charged in a three-necked flask. OAC and OAM were added by (Series A) fixing the total initial moles of the both surfactants (mol_{OAC}+ mol_{OAM} = 12 mmol) and changing the ratio between them, or by (Series B) fixing the mole of OAM at 6 mmol and changing the amount of OAC from 2 mmol to 22 mmol, or finally (Series C) by keeping the amount of OAC fixed at 6 mmol, and varying the amount of OAM from 0.86 mmol to 18 mmol. Total of 22 different syntheses were performed, each at least twice, to ensure reproducibility of the results. A summary of the reaction series is given in **Table 3.3.1**.

Table 3.3.1 Summary of experimental conditions. With the variable parameters as:
A = 0 (A_1), 3 (A_2), 4.5 (A_3), 6 (A_4), 7.5 (A_5), 8.25 (A_6), 9 (A_7), 9.75 (A_8), 10.5 (A_9), 12 (A_{10}) mmol
B = 2 (B_1), 6 (B_2), 10 (B_3), 14 (B_4), 18 (B_5), 22 (B_6) mmol
C = 0.86 (C_1), 1.38 (C_2), 2 (C_3), 2.5 (C_4), 6 (C_5), 10 (C_6), 14 (C_7), 18 (C_8) mmol

	Seri A	**Seri B**	**Seri C**
$Fe(acac)_3$ (mmol)	2	2	2
Benzyl Ether (ml)	20	20	20
OAC (mmol)	**A**	**B**	6
OAM (mmol)	12-**A**	6	**C**

All reaction mixtures were stirred, purged with nitrogen and heated to 110 °C, and kept at the same temperature under vacuum for 60 min to remove water traces and dissolve the reactants. The temperature is then raised to 180 °C under N_2 blanketing, with a heating rate of about 6-7 K/min. the reactions were kept at 180 °C for 120 min for complete decomposition of the precursor. Afterward the solution is heated to 300 °C with a constant growth heating rate (H.R.). The reaction is cooled to room temperature after being for 60 minutes at the reflux temperature. The nanoparticles were precipitated by the addition of ethanol. No further post synthesis processes such as size selective precipitation is performed. The particles were characterized by TEM, HR-TEM, XRD, FTIR, TGA and VSM (Cryogenic Ltd). The conditions of the characterization techniques are given in previous section (Section 1 of Chapter 3).

3.3.2.2 Simulation details

Theory and simulation method: the simulation was done by Richard Anthony Harris. In the following a brief description regarding simulation details is given. The adsorption locator module of the Materials

Studio 6.0 software package is used to simulate the initial adsorptions. The details of the simulation is given in previous report by Harris.[24] Different ratios of the number of OAC/OAM- molecules are used and the molecules are simultaneously adsorbed onto the nanoparticle surface. These ratios are produced by first keeping the sum of OAC and OAM constant (for an array of different surfactant concentrations), as the number of OAC and OAM is varied. Possible adsorption configurations is identified by carrying out Monte Carlo searches of the configurational space of the substrate-adsorbate system as the temperature is slowly decreased according to a simulated annealing schedule. For the initial adsorption, a universal force-field is used and the charges are assigned using the charge equilibration method. As a check, the same experiments are repeated using the charge consistent valence force-field with charges assigned by the force-field. The same results are generated. The summation method for the electrostatics and the Van der Waals interactions are both atom based and the quality of the calculation is set to ultra-fine. The experiment is repeated 15 times for each OAC/OAM ratio.

Geometry Optimization: molecular mechanics are used to do geometry optimization for each of the resulting OAC, OAM nanoparticle systems. The 'Discover' module of MS6.0 is employed for this task. The cvff force-field is used with charges assigned by the force-field. Settings are applied to both Van der Waals and Coulomb forces with an 'atom based'-summation method. A smart minimization algorithm is employed which uses combinations of the steepest descent, conjugate gradient and newton methods. The Fletcher-Reeves algorithm is used for the conjugate gradient method and for the newton method the Broyden-Fletcher-Goldfarb-Shanno (BFGS) algorithm is used.

Molecular Dynamics simulations: the resulting geometries from the molecular mechanics geometry optimization calculations are used as input to the molecular dynamics simulations to arrive at the final, energy-optimized systems. A constant temperature, constant volume ensemble (NVT) at room temperature is used with a time step of 1.0 femtoseconds and a dynamic time of 20.0 picoseconds. An Anderson-thermostat is used with a collision ratio of 1.0 and the number of simulation steps are selected as 20 000.

Binding Energy: the total energy of the system ($E_{totalsystem}$) is the sum of the total energy of each separate system plus, *i.e.* the interaction energy between the surfactants (E_s) (OAC and OAM), between the nanoparticles (E_{np}), and the binding energy of the surfactants to the nanoparticle and (E_b). The binding energy is calculated according to:

$$E_b = (E_{totalsystem}) - E_{np} - E_s \qquad (3.3.3)$$

After the optimum configuration of the nanoparticle-ligand systems are determined, the nanoparticle is removed from the system. A single point energy calculation is carried out, from which the total energy of the surfactant is determined. To calculate the total energy of the nanoparticle, the surfactants are removed and a single point energy calculation is carried out to obtain the total energy of the nanoparticle.

3.3.3 Results and discussions

We start with series A, OAC+OAM is fixed at 12 mmol. The OAC concentration is changed from 0 (A_1), 3 (A_2), 4.5 (A_3), 6 (A_4), 7.5 (A_5), 8.25 (A_6), 9 (A_7), 9.75 (A_8), 10.5 (A_9), and 12 (A_{10}) mmol. The representative TEM images of the series A with different OAC amount (different OAC/OAM ratio), and the respective size distribution for nanoparticles are given in **Figure 3.3.1**. The nanoparticles size evolution of the series A as a function of increasing the amount of OAC is given in **Figure 3.3.4 a**. As the amount of OAC increases in the reaction from 0 mmol, the nanoparticle size steadily increases from 6.6 nm (PDI = 14.5 %). Simultaneously, PDI increases steadily. At OAC concentration of 9 mmol, the size suddenly dropped to 9.8 nm with significant fall in PDI = 7.1 %. Upon further increasing of OAC concentration, the size shows a sharp rise, as well as a sharp rise in the PDI. The crystalline size of nanoparticles determined from XRD (**Figure 3.3.4 a**, red circles) using Scherrer's formula[32, 34] (details in Section 1 of Chapter 3), follows the trend observed for TEM size.

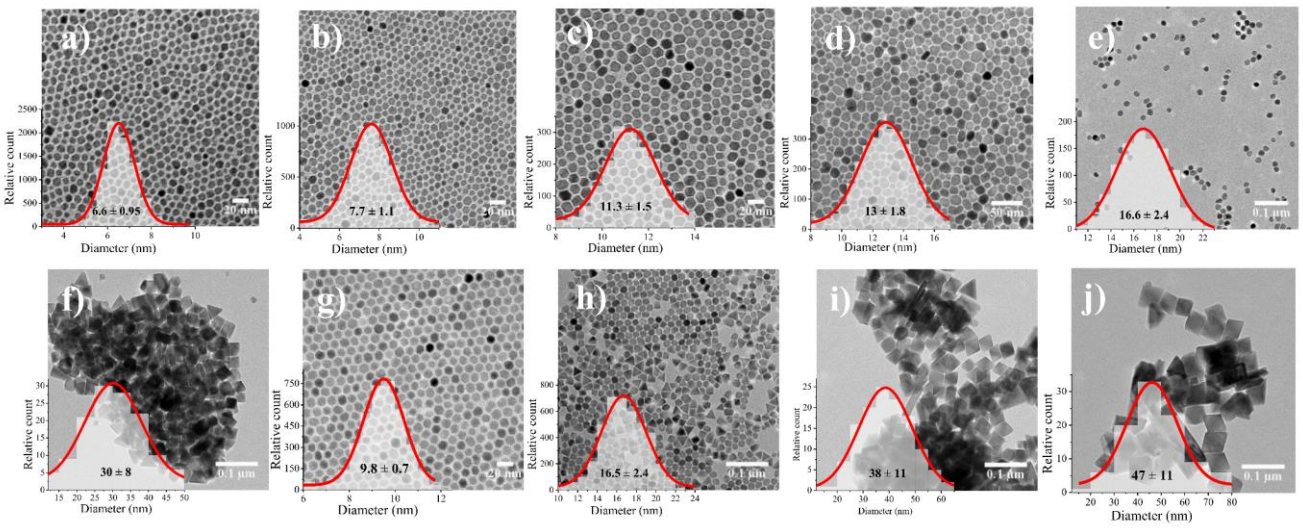

Figure 3.3.1 TEM images of samples (a) A_1, (b) A_2, (c) A_3, (d) A_4, (e) A_5, (f) A_6, (g) A_7, (h) A_8, (i) A_9 and (j) A_{10}. Particle size distributions obtained by fitting TEM histograms are also shown.

Next, the concentration of OAM is fixed at 6 mmol, and OAC concentration is freely changed from 2 (B_1), 6 (B_2), 10 (B_3), 14 (B_4), 18 (B_5) to 22 (B_6) mmol. Details of TEM size analysis are given in **Figure 3.3.2**. The size evolution of the series B as a function of increasing OAC is given in **Figure 3.3.4 b**. As the amount of OAC increases in the reaction the nanoparticle showed a steady increase in both size and PDI until OAC concentration is 18 mmol at which the size suddenly dropped to 11.8 nm with very low PDI of 6 %. Upon increasing of OAC concentration to 22 mmol, the size shows again a sharp rise, with a dramatic increase in PDI.

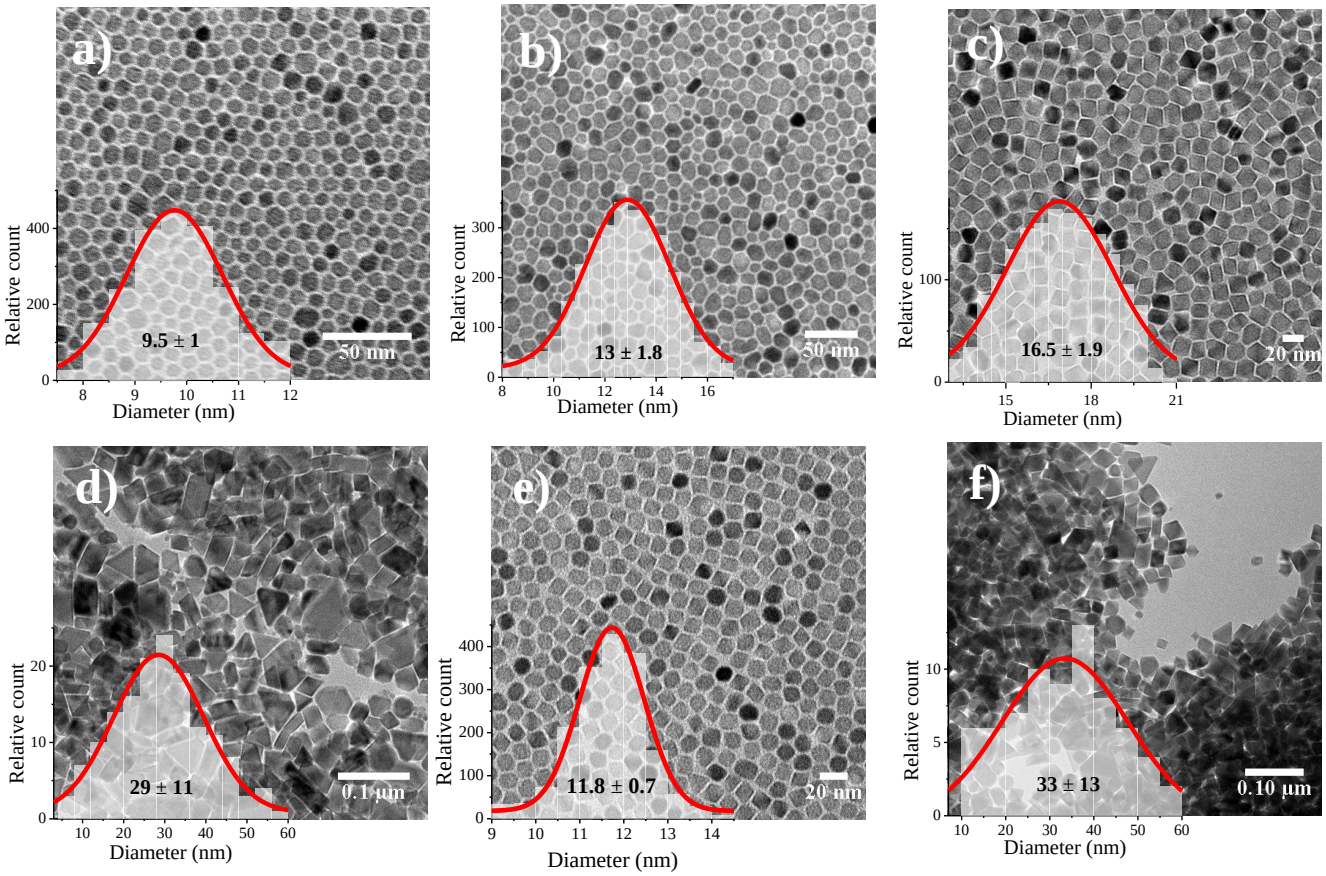

Figure 3.3.2 TEM images of samples (a) B_1, (b) B_2, (c) B_3, (d) B_4, (e) B_5, and (f) B_6. Particle size distributions obtained by fitting TEM histograms are also shown. The image of (b) is also given in before.

For the third experiment, series C, OAC concentration is fixed and OAM concentration is changed from 0.86 (C_1), 1.38 (C_2), 2 (C_3), 2.5 (C_4), 6 (C_5), 10 (C_6), 14 (C_7), to 18 (C_8) mmol. Details of the TEM size analysis are given in **Figure 3.3.3**. The size evolution is given in **Figure 3.3.4 c**. At low OAM concentration, the nanoparticle size is large with large variation in size (high PDI). At 2 mmol OAM, the size drops to 9.5 nm with the lowest PDI (7.6 %). A slight increase in OAC to 2.5 mmol, leads to an increase in the size and its dispersity. By further increasing the OAM concentration, the

average diameter monotonically decreased, and PDI despite a slight decrease, remains always well above 10%.

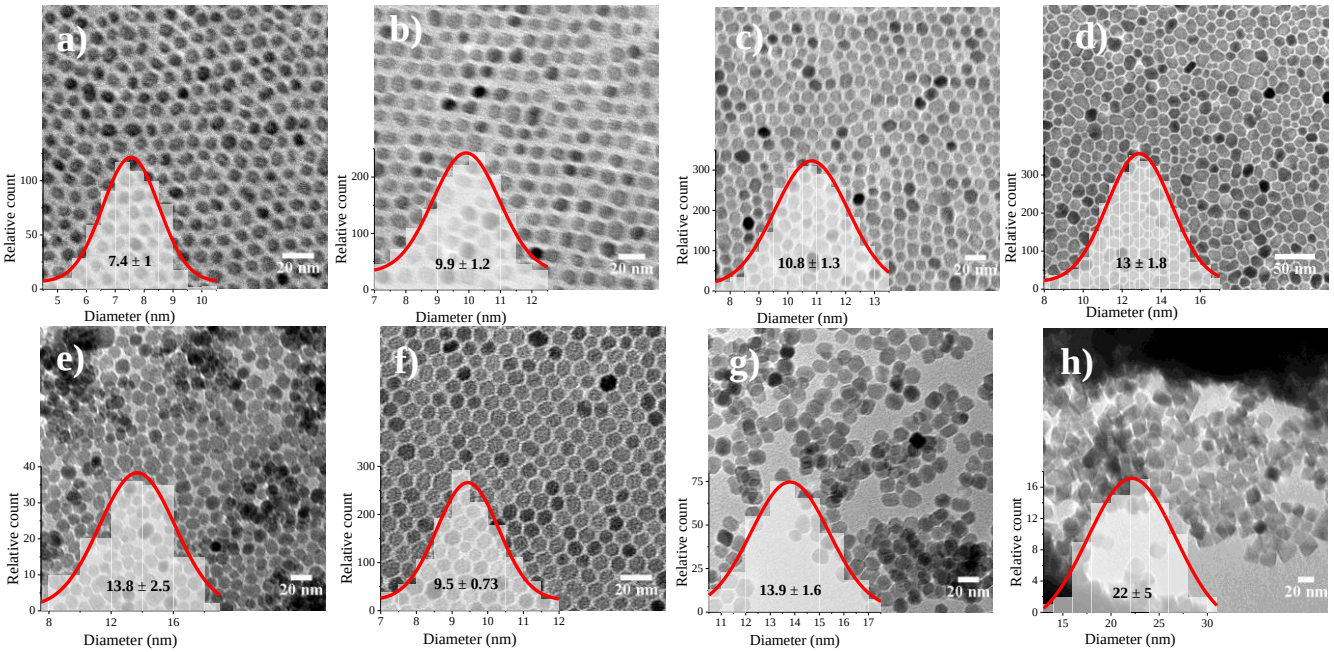

Figure 3.3.3 TEM images of samples (a) C_1, (b) C_2, (c) C_3, (d) C_4, (e) C_5, (f) C_6, (g) C_7 and (f) C_8. Particle size distributions obtained by fitting TEM histograms are also shown. The image of (d) and (f) are also given in before.

The size evolution and PDI is plotted as a function of OAC/OAM in **Figure 3.3.5 a** and **b**, respectively. Strikingly, all different series follow the same general trend in size for OAC/OAM ratios below 3/1 where upon increasing the OAC/OAM ratio, the nanoparticle size increases. PDI follows the same increasing trend as the OAC/OAM ratio increases. At an exact OAC/OAM ratio of 3/1 the trend is interrupted, all synthesis series yield smaller nanoparticles which are of nearly the same size (9-12 nm) with strikingly low PDIs well below < 8 %. We note that nanoparticles obtained with the OAC/OAM ratio of 3 are readily monodisperse after the synthesis and further post synthesis purification such as size selective precipitation is not needed. Further increase of OAC/OAM ratio beyond 3, yields colossal increase in the size with large PDI and shape irregularity of the nanoparticles. We conclude therefore that the OAC/OAM of 3 is the optimum ratio in the synthesis of truly monodisperse iron oxide nanoparticles with regular shape.

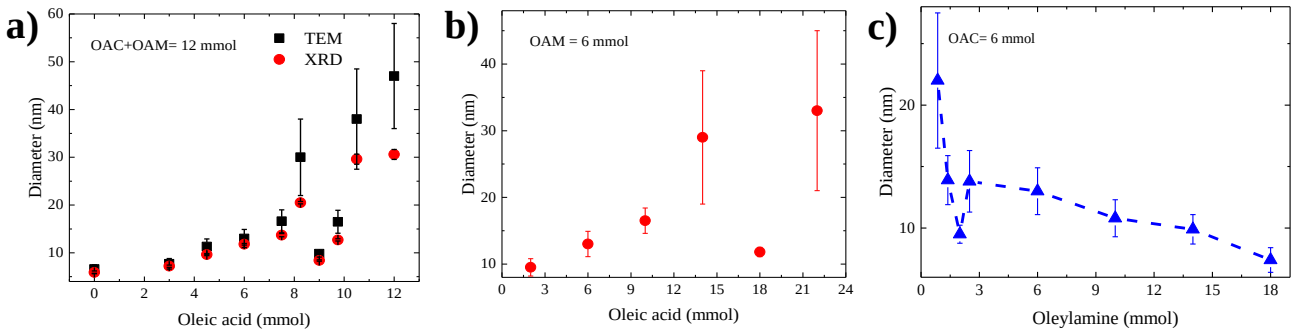

Figure 3.3.4 The average diameter of the nanoparticles for Series A (OAC+OAM= 12mmol= constant) (a), Series B (OAM= 6mmol= constant) (b) and Series C (OAC= 6mmol= constant) (c).

The trend of increase in size observed in **Figure 3.3.5 a** for OAC/OAM ratio smaller than 3 can be explained by the acid-base complex formation. As the OAC/OAM ratio increases the amount of $RCOO^-$ increases, which leads to formation of more stable intermediate metal complexes (growth species). As a result, activity of the growth species is lowered. According to the LaMer's theory[35] of nucleation and growth, less nuclei with larger sizes are formed and therefore nanoparticles of bigger size are yielded.[12-13, 17, 26, 36]

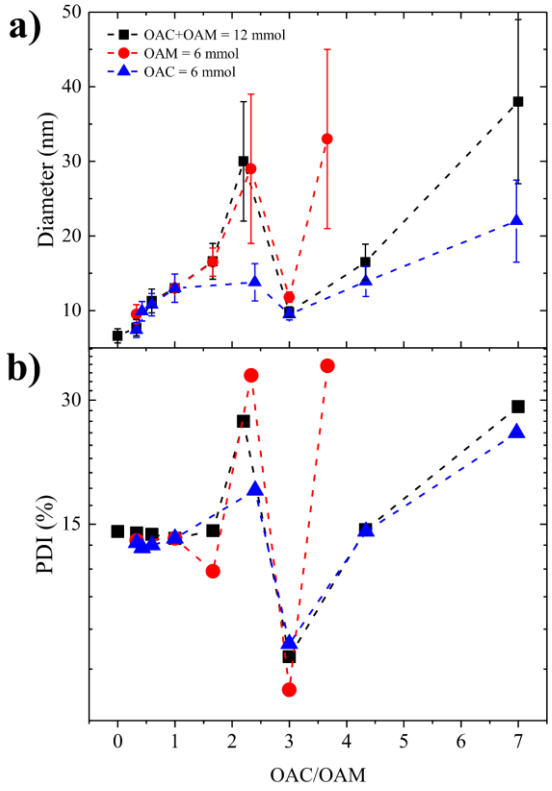

Figure 3.3.5 General graph for size evolution (a) and PDI (b) of the nanoparticles as a function of ratio (OAC/OAM) for all three series (A, B and C).

The drop in size and formation of truly monodisperse nanoparticles for all reaction series occurring at the specific OAC/OAM ratio of 3/1 is rather unexpected. To understand the exact mechanism, we perform molecular dynamic (MD) simulations.[24] The binding energy (kcal/mol) of the oleate to the nanoparticles is calculated for two different situations; I) the amine groups of the OAM do not absorb the deprotonated H^+ atoms and remain as NH_2, whereas in situation II) the amine groups of the OAM can absorb deprotonated H^+ atoms and form NH_3^+.

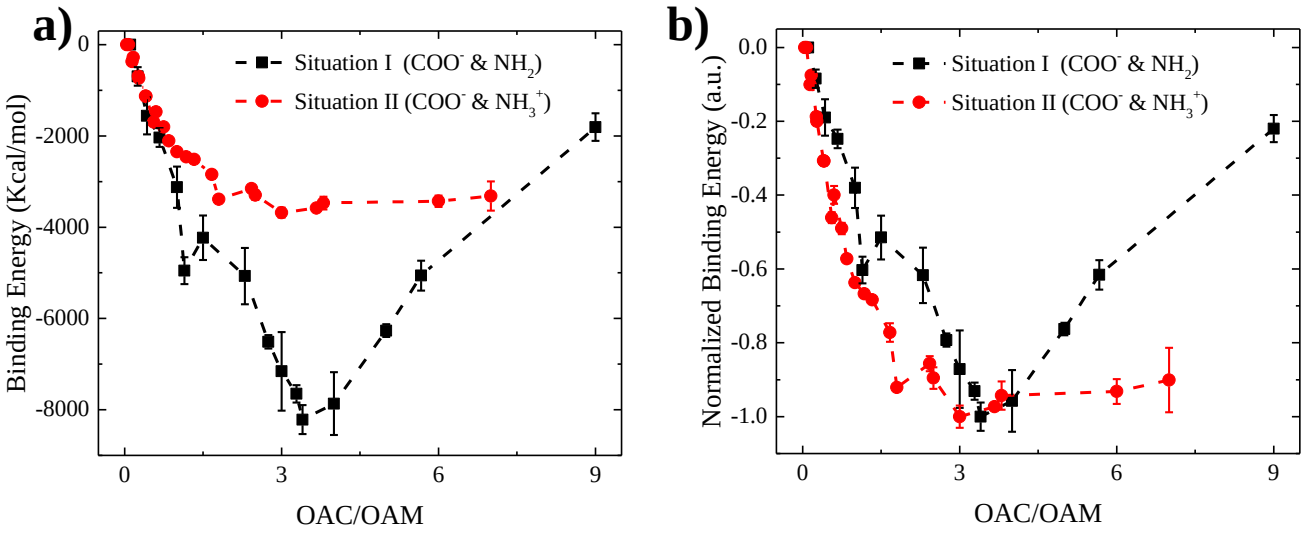

Figure 3.3.6 Binding energies (a) and normalized binding energy (b) of surfactants as a function of OAC/OAM ratio to the NP for different situation of I and II).

The calculated binding energies for both situations are shown in **Figure 3.3.6 a**. The binding energy extremum lies at OAC/OAM ratio between 3 and 4, as shown in the **Figure 3.3.6 b** for the normalized binding energies. The maximum values of binding energies reach -8000 and -4000 kcal/mol for situation I and II), respectively. The oleate binding in situation I) however is stronger than situation II). In reality, the number of surfactant molecules is large. The number of absorbed deprotonated H^+ atoms are significantly lower and therefore the number of predominant NH_2 functional groups remain unchanged. Hence, situation I) where the amine group does not absorb the deprotonated H^+ is the most likely mechanism.[24] Due to the strong binding energy, the rate of desorption of oleate from the surface of the nanoparticle (via free protons) reduces, thereby lowering the growth kinetic of the nanoparticle (more controlled synthesis).[24] Therefore, smaller nanoparticles with much narrower size distribution and shape regularity are formed **(Figure 3.3.7 a-c)**. Due to the stability of the oleate-nanoparticle bond at the specific ratio of 3/1, higher oleate (surfactant) coverage is also expected. Experimentally, OAC/OAM ratio of 3/1 produced the lowest PDI (< 8 %) **(Figure 3.3.5 b)**, in agreement with the MD simulation.

Several studies have investigated the effect of surfactant concentration.[4-6, 9, 17, 26, 28, 37-39] We showed in previous section that the ratio of precursor to surfactant is a critical parameter that controls the size when surfactant amount is changing. For a fixed precursor amount, increasing the amount of surfactant increases the nanoparticle size because more oleate molecules react with the precursor leading to formation of more stabilized monomers.[4-6, 17, 40-41] According to the nucleation and growth model of LaMer,[35] reduced concentration of active monomer lowers the nucleation and inhibits formation of a large number of nuclei hence favoring the growth of larger nanoparticles. We have plotted in **Figure 3.3.7 d**, size evolution of the nanoparticles as a function of precursor/surfactant ratio for both OAC/OAM ratios of 1 and 3. The trend observed for the case of OAC/OAM=1 shows a steep slope, whereas for the case of OAC/OAM=3, the slope is substantially reduced and the particle size is almost constant for the range investigated. The results of MD simulations rationalizes the insensitivity of the size to precursor/surfactant. At OAC/OAM=3, binding energy of the oleate to the growth species is maximized, which leads to the formation of highly stable growth species with reduced growth rate, which is manifested in the insensitivity of the final size to precursor/surfactant ratio.

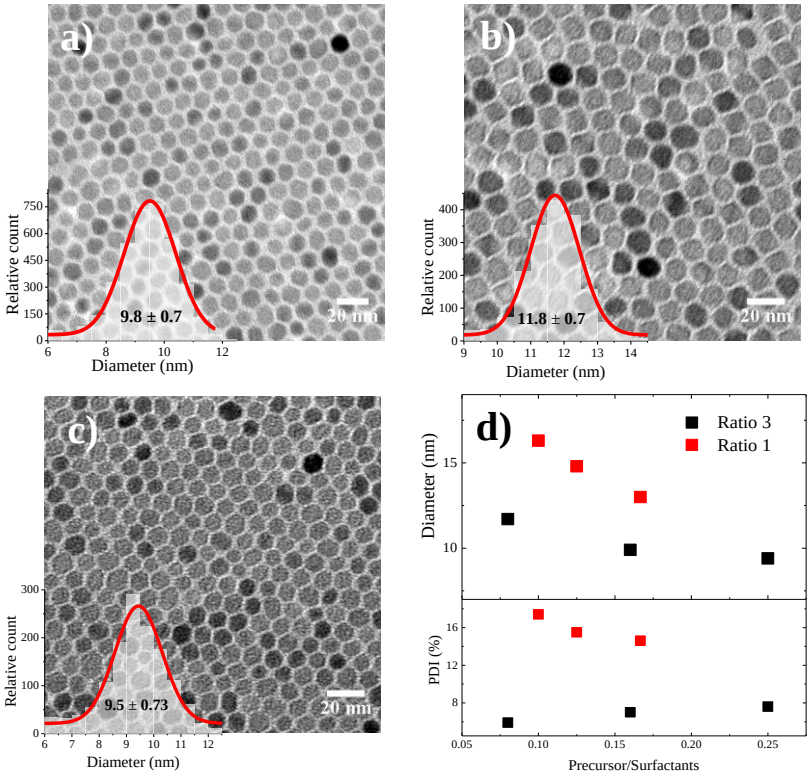

Figure 3.3.7 TEM images of samples with ratio 3 for three different synthesis series of (a) series A, sample A_7 OAC/OAM = 9/3 (b) Series B, sample B_5 OAC/OAM = 18/6 and (c) series C, sample C_3 OAC/OAM= 6/2. (d) The evolution of average diameter and PDI as a function of precursor/surfactants ratio in both OAC/OAM ratios of 1 and 3.

We also measure the values of surfactants grafting density of series A using TGA (**Figure 3.3.8 a**). Interestingly, the surfactant grafting density shows a maximum value of 4.7 molecules/nm^2 for the specific ratio of 3/1 (OAC/OAM), whereas for other un-optimized OAC/OAM ratios remains almost constant at ~3 molecules/nm^2 with further reduction via increasing the amount of OAC **(Figure 3.3.8 b)**. At OAC/OAM ratios above 3/1, the amount of OAC present in the reaction becomes more important. Excessive OAC concentrations, leads to an increased concentration of free protons in the reaction medium. Due to a limited number of amine groups the free protons are not completely neutralized. As a result the electrostatic pressure and chemical potential between the medium and the surface of the nanoparticle increases leading to desorption of the bonded oleate from the surface (lower grafting density in higher ratios).[24-25] The nanoparticle surface becomes unprotected and therefore anisotropic colossal growth occurs, yielding faceted large nanoparticles as shown in TEM images for higher OAC concentration. The trend observed for colossal growth in the reactions of different A, B and C series is in agreement with the above justification, since the amount of OAC for series B > series A > series C. Therefore, uncontrolled growth in series B is more pronounced.

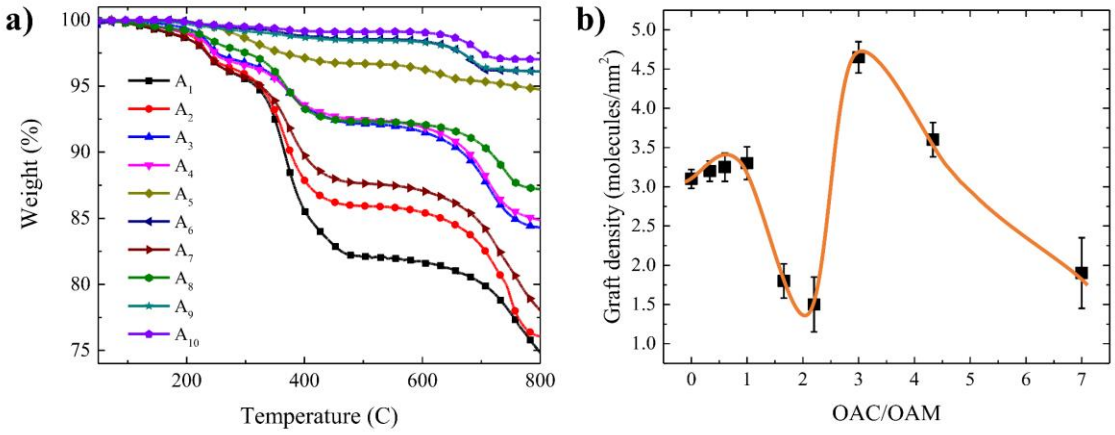

Figure 3.3.8 (a) TGA of Series A nanoparticles, (b) the values of graft densities as a function of ratio. The red line is a guide to the eye.

It has been shown in the Section 1 of Chapter 3, that the nanoparticle size of the syntheses with equimolar 1/1 OAC/OAM ratio can be controlled by changing the reaction heating rate.[32, 42] The effect of heating rate on the size and dispersity of the nanoparticle has been studied in depth previously. To perform size tuning we changed the heating rate for both equimolar 1/1 and the optimized 3/1 OAC/OAM ratios. Four heating rates for each molar ratios are tested. For the equimolar OAC/OAM = 1/1 we performed post synthesis size selective precipitation. To demonstrate the power of the new synthesis recipe of OAC/OAM = 3/1 in production of monodisperse particles, we do not perform post

synthesis size selection procedures. Exemplary TEM images of the samples for both ratio of 1 and 3 are shown in **Figures 3.3.9 (a)-(h)**. The size of the nanoparticles obtained from both reactions show the same reducing trend as the heating rate increased **(Figure 3.3.10 a)**. It has been shown that in the nucleation and growth of iron oxide nanoparticles, the relative time scales associated with the heating and precursors to monomer conversion rates determines the nanoparticle final size.[32, 35, 42] The synthesis with OAC/OAM= 3 ratio yields the same trend in size evolution with heating rate but with PDI below < 8 %, as shown in **Figure 3.3.10 b**. Due to the low PDI, the synthesis with OAC/OAM = 3 ratio allows for precise control of the nanoparticle size at the nanometer level.

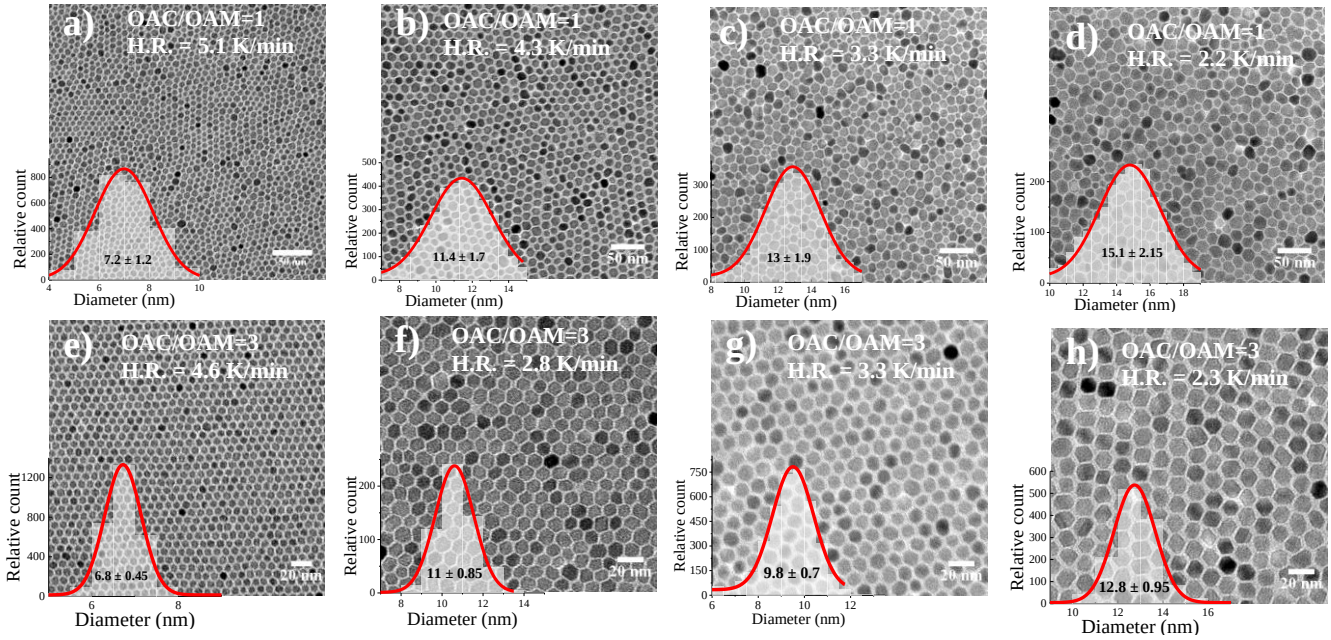

Figure 3.3.9 TEM images of samples at ratio surfactant ratio of 1 (a)-(d) and ratio 3 (b)-(h) with their corresponding size distribution histogram obtained at different heating rates.

In the next step, we investigate whether the new OAC/OAM ratio affects the crystallinity and the magnetic properties of the resulting nanoparticles. The XRD diffractograms, shown in **Figure 3.3.11 a**, indicate that both nanoparticles have a fcc inverse spinel structure with high crystallinity.[9, 32-33] The mean values of inter-planer distances and the lattice parameters amounts to 8.39 Å for both ratio 3 and 1, which matches well with the reported value for magnetite.[4, 33, 43-44] The crystalline size of the NPs is shown in **Figure 3.3.4 b**.[34] The consistent agreement obtained with the statistical analysis of the TEM images, demonstrated that each individual particle is a single crystal.[33] HRTEM image and SAED pattern for the nanoparticle obtained with OAC/OAM=3/1 (sample A_7), given in **Figure 3.3.11 c**, indicated that the crystalline structure is extended up to the edge of the nanoparticle.[45] The OAC/OAM = 3/1 ratio has therefore no influence on the crystalline structure of the nanoparticles.

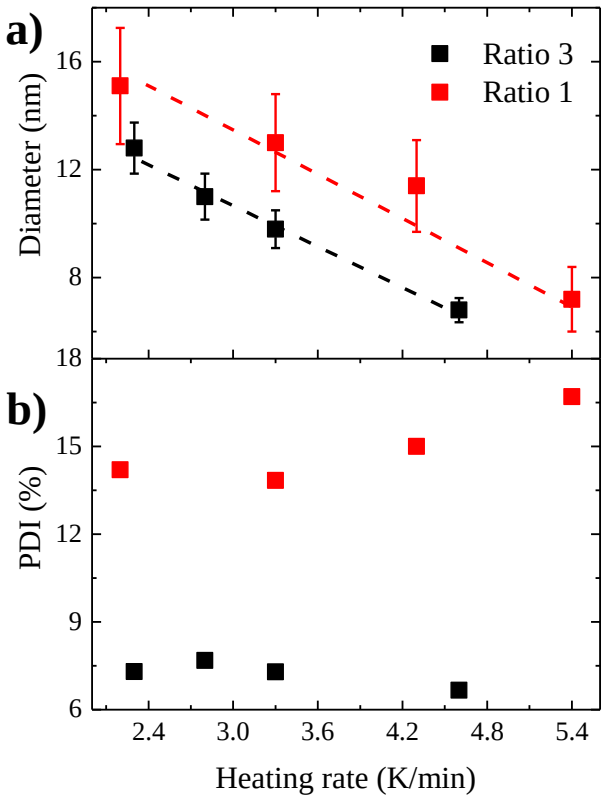

Figure 3.3.10 The average diameter of nanoparticle (e) and PDI (f) as a function of heating rate for the ones with ratio 1 (OAC/OAM of 6 mmol/6mmol) (red dots) and black dots with ratio 3 (OAC/OAM of 9 mmol/3 mmol).

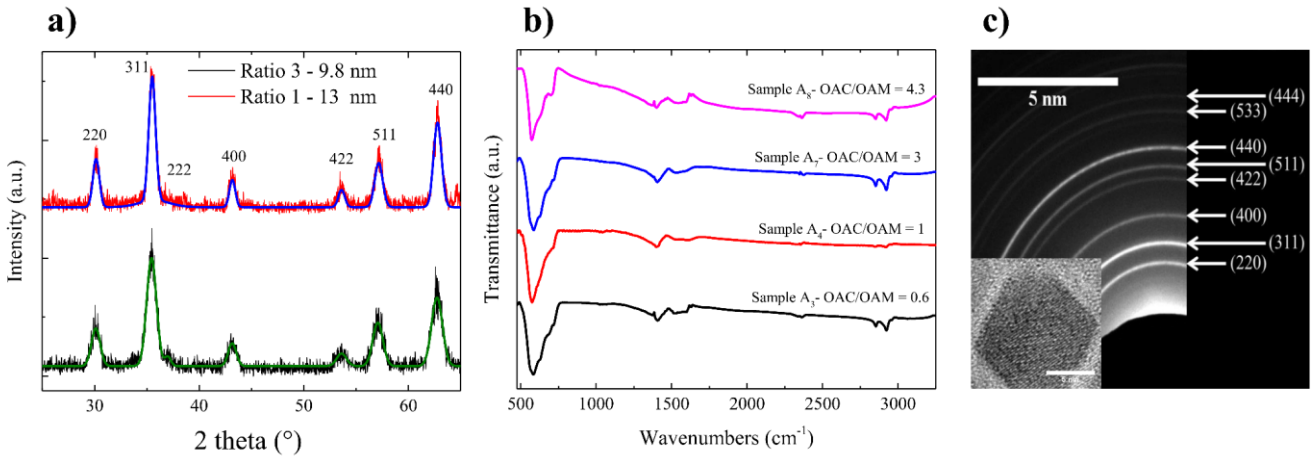

Figure 3.3.11 (a) XRD diffractograms of ratio 1 (red) and its corresponding modelling (blue) and of ratio 3 (black) and its corresponding modelling (green). (b) FTIR spectrum of samples with different ratio of OAC/OAM. (c) HRTEM images of sample with ratio 3 and (h) SAED pattern of the same sample.

FTIR spectra of the nanoparticles obtained at different OAC/OAM ratios, given in **Figure 3.3.11 b**, showed similar feature for all synthesis. The sharp peak at 570-590 cm^{-1} attributed to the Fe-O stretch of iron oxide nanoparticle. The bands at 2920 and 2850 cm^{-1} are assigned to asymmetric and symmetric stretch of methyl group (CH_2), respectively. The broadband between 1370 and 1650 cm^{-1} is characteristic of asymmetric and symmetric stretch of COO-. For high ratio of OAC/OAM (OAC rich) no peak of pure OAC (like 1710 cm^{-1}) is observed, showing that the OAC molecules are chemically adsorbed to the surface of nanoparticle via carboxylate group. We note that for low ratio of OAC/OAM (OAM rich), no peaks of amine-containing group (NH_2) are detected.

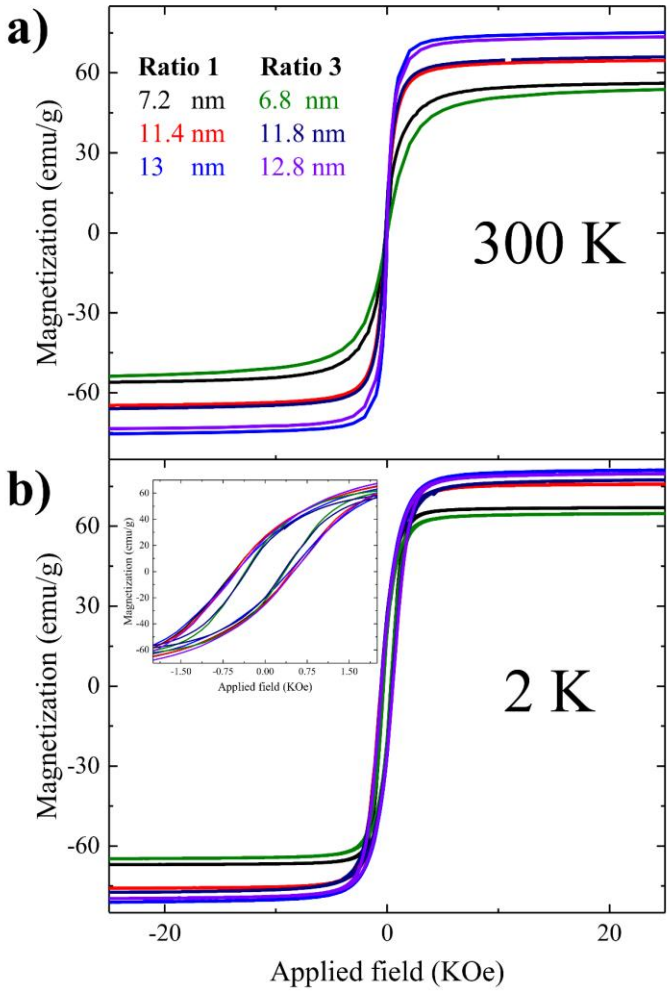

Figure 3.3.12 Hysteresis loops of samples with ratio 3 and 1 at (a) 300 K and (b) 2 K. The details are given in **Table 3.3.2**.

Subsequently magnetic hysteresis loops of both nanoparticle batches are measured using VSM. Nanoparticles obtained from OAC/OAM = 3 ratio with different sizes, are compared to the

nanoparticles obtained from the conventional OAC/OAM = 1 synthesis. To reach a fair comparison, we selected particles of nearly the same size from both syntheses.

The hysteresis loops recorded at 300 K and 2 K are shown in **Figure 3.3.12 a** and **b**, respectively. At 300 K all nanoparticles are superparamagnetic **(Figure 3.3.12 a)**. At 2 K all nanoparticles show ferri/ferromagnetic behavior **(Figure 3.3.12 b)** with saturation magnetization (M_s), remanent magnetization (M_r), and coercive field (H_C) values that are nearly the same for all nanoparticles and similar to reported values for magnetic iron oxide nanoparticles (See also **Table 3.3.2**).[28, 45-47] Slight differences in M_s, M_r and H_c values are due to nanoparticle size variation. By comparing the magnetic responses, we conclude that the excess of OAC in the synthesis with OAC/OAM = 3, has no measurable influence on the macroscopic magnetic properties of the nanoparticles.

Table 3.3.2 Summary of the magnetic properties of iron oxide NPs with surfactants ratio of 1 and 3 at 300 K and 2 K.

OAC (mmol)/OAM (mmol)	Heating rate (K/min)	Size (TEM)	M_S (300 K) (emu/g)	M_S (2 K) (emu/g)	H_C (2 K) (Oe)
6 / 6	5.1	7.2 ± 1.2 nm	55.6	67	350
6 / 6	4.3	11.4 ± 1.7 nm	64.7	75.6	525
6 / 6	3.3	13 ± 1.9 nm	75.2	81.2	496
9 / 3	4.6	6.8 ± 0.45 nm	53.9	64.5	330
9 / 3	3.3	9.8 ± 0.7 nm	62.2	73.6	475
18 / 6	3.3	11.8 ± 0.7 nm	66.1	77.5	520
9 / 3	2.3	12.8 ± 0.95 nm	73.4	79.8	505

3.3.4 Conclusion

The surfactant ratio plays a critical role on the final size of the iron oxide nanoparticles and its respective dispersity obtained through thermal decomposition. An optimized OAC/OAM ratio of 3/1 yields nanoparticles with lowest monodispersity without a need for any post synthesis size selective precipitation. Molecular dynamic simulations reveal that the binding energy of oleic acid to the nanoparticle is maximized at an acid/amin ratio of 3/1, leading to a better control of the nucleation and growth of the nanoparticles. The nanoparticles synthesized using the new synthesis recipe show similar structural and super-paramagnetic properties comparable to those obtained from the conventional 1/1

ratio of OAC/OAM. Variation of the reaction heating rate allows for precise control of the nanoparticle size with one nanometer precision.

3.3.5 References

1. Li, D.; Yun, H.; Diroll, B. T.; Doan-Nguyen, V. V.; Kikkawa, J. M.; Murray, C. B., Synthesis and Size-Selective Precipitation of Monodisperse Nonstoichiometric M x Fe3–x O4 (M= Mn, Co) Nanocrystals and Their DC and AC Magnetic Properties. *Chem. Mater.* **2016,** *28*, 480-489.
2. Weidman, M. C.; Beck, M. E.; Hoffman, R. S.; Prins, F.; Tisdale, W. A., Monodisperse, air-stable PbS nanocrystals via precursor stoichiometry control. *ACS nano* **2014,** *8*, 6363-6371.
3. Cademartiri, L.; Bertolotti, J.; Sapienza, R.; Wiersma, D. S.; Von Freymann, G.; Ozin, G. A., Multigram scale, solventless, and diffusion-controlled route to highly monodisperse PbS nanocrystals. *J. Phys. Chem. B* **2006,** *110*, 671-673.
4. Baaziz, W.; Pichon, B. P.; Fleutot, S.; Liu, Y.; Lefevre, C.; Greneche, J.-M.; Toumi, M.; Mhiri, T.; Begin-Colin, S., Magnetic iron oxide nanoparticles: reproducible tuning of the size and nanosized-dependent composition, defects, and spin canting. *J. Phys. Chem. C* **2014,** *118*, 3795-3810.
5. Demortiere, A.; Panissod, P.; Pichon, B.; Pourroy, G.; Guillon, D.; Donnio, B.; Begin-Colin, S., Size-dependent properties of magnetic iron oxide nanocrystals. *Nanoscale* **2011,** *3*, 225-232.
6. William, W. Y.; Falkner, J. C.; Yavuz, C. T.; Colvin, V. L., Synthesis of monodisperse iron oxide nanocrystals by thermal decomposition of iron carboxylate salts. *Chem. Commun.* **2004**, 2306-2307.
7. Dehsari, H. S.; Ribeiro, A. H.; Ersöz, B.; Tremel, W.; Jakob, G.; Asadi, K., Effect of precursor concentration on size evolution of iron oxide nanoparticles. *CrystEngComm* **2017,** *19*, 6694-6702.
8. Guardia, P.; Batlle-Brugal, B.; Roca, A.; Iglesias, O.; Morales, M.; Serna, C.; Labarta, A.; Batlle, X., Surfactant effects in magnetite nanoparticles of controlled size. *J. Magn. Magn. Mater.* **2007,** *316*, e756-e759.
9. Moya, C.; Batlle, X.; Labarta, A., The effect of oleic acid on the synthesis of Fe 3− x O 4 nanoparticles over a wide size range. *Phys. Chem. Chem. Phys.* **2015,** *17*, 27373-27379.
10. Kim, D.; Lee, N.; Park, M.; Kim, B. H.; An, K.; Hyeon, T., Synthesis of uniform ferrimagnetic magnetite nanocubes. *J. Am. Chem. Soc.* **2008,** *131*, 454-455.
11. Pérez-Mirabet, L.; Solano, E.; Martínez-Julián, F.; Guzmán, R.; Arbiol, J.; Puig, T.; Obradors, X.; Pomar, A.; Yáñez, R.; Ros, J., One-pot synthesis of stable colloidal solutions of MFe 2 O 4 nanoparticles using oleylamine as solvent and stabilizer. *Mater. Res. Bull.* **2013,** *48*, 966-972.
12. Mourdikoudis, S.; Liz-Marzán, L. M., Oleylamine in nanoparticle synthesis. *Chem. Mater.* **2013,** *25*, 1465-1476.
13. Xu, Z.; Shen, C.; Hou, Y.; Gao, H.; Sun, S., Oleylamine as both reducing agent and stabilizer in a facile synthesis of magnetite nanoparticles. *Chem. Mater.* **2009,** *21*, 1778-1780.
14. Zeng, Y.; Hao, R.; Xing, B.; Hou, Y.; Xu, Z., One-pot synthesis of Fe 3 O 4 nanoprisms with controlled electrochemical properties. *Chem. Commun.* **2010,** *46*, 3920-3922.
15. Sun, S.; Zeng, H., Size-controlled synthesis of magnetite nanoparticles. *J. Am. Chem. Soc.* **2002,** *124*, 8204-8205.
16. Lu, L. T.; Dung, N. T.; Tung, L. D.; Thanh, C. T.; Quy, O. K.; Chuc, N. V.; Maenosono, S.; Thanh, N. T., Synthesis of magnetic cobalt ferrite nanoparticles with controlled morphology, monodispersity and composition: the influence of solvent, surfactant, reductant and synthetic conditions. *Nanoscale* **2015,** *7*, 19596-19610.
17. Meledandri, C. J.; Stolarczyk, J. K.; Ghosh, S.; Brougham, D. F., Nonaqueous magnetic nanoparticle suspensions with controlled particle size and nuclear magnetic resonance properties. *Langmuir* **2008,** *24*, 14159-14165.
18. Roca, A. G.; Marco, J. F.; Morales, M. d. P.; Serna, C. J., Effect of nature and particle size on properties of uniform magnetite and maghemite nanoparticles. *J. Phys. Chem. C* **2007,** *111*, 18577-18584.
19. Zhang, L.; He, R.; Gu, H.-C., Oleic acid coating on the monodisperse magnetite nanoparticles. *Appl. Surf. Sci.* **2006,** *253*, 2611-2617.

20. Hou, Y.; Xu, Z.; Sun, S., Controlled synthesis and chemical conversions of FeO nanoparticles. *Angew. Chem. Int. Ed.* **2007,** *46*, 6329-6332.
21. Yang, H.; Ogawa, T.; Hasegawa, D.; Takahashi, M., Synthesis and magnetic properties of monodisperse magnetite nanocubes. *J. Appl. Phys.* **2008,** *103*, 07D526.
22. Castellanos-Rubio, I.; Insausti, M.; Garaio, E.; de Muro, I. G.; Plazaola, F.; Rojo, T.; Lezama, L., Fe 3 O 4 nanoparticles prepared by the seeded-growth route for hyperthermia: electron magnetic resonance as a key tool to evaluate size distribution in magnetic nanoparticles. *Nanoscale* **2014,** *6*, 7542-7552.
23. Li, Y.; Liu, J.; Wang, Y.; Wang, Z. L., Preparation of monodispersed Fe− Mo nanoparticles as the catalyst for CVD synthesis of carbon nanotubes. *Chem. Mater.* **2001,** *13*, 1008-1014.
24. Harris, R. A.; Shumbula, P. M.; van der Walt, H. t., Analysis of the interaction of surfactants oleic acid and oleylamine with iron oxide nanoparticles through molecular mechanics modeling. *Langmuir* **2015,** *31*, 3934-3943.
25. Klokkenburg, M.; Hilhorst, J.; Erne, B., Surface analysis of magnetite nanoparticles in cyclohexane solutions of oleic acid and oleylamine. *Vib. Spectrosc* **2007,** *43*, 243-248.
26. Hufschmid, R.; Arami, H.; Ferguson, R. M.; Gonzales, M.; Teeman, E.; Brush, L. N.; Browning, N. D.; Krishnan, K. M., Synthesis of phase-pure and monodisperse iron oxide nanoparticles by thermal decomposition. *Nanoscale* **2015,** *7*, 11142-11154.
27. Cabrera, L. I.; Somoza, Á.; Marco, J. F.; Serna, C. J.; Morales, M. P., Synthesis and surface modification of uniform MFe 2 O 4 (M= Fe, Mn, and Co) nanoparticles with tunable sizes and functionalities. *J. Nanopart. Res.* **2012,** *14*, 873.
28. Guardia, P.; Pérez, N.; Labarta, A.; Batlle, X., Controlled synthesis of iron oxide nanoparticles over a wide size range. *Langmuir* **2009,** *26*, 5843-5847.
29. Crouse, C. A.; Barron, A. R., Reagent control over the size, uniformity, and composition of Co–Fe–O nanoparticles. *J. Mater. Chem.* **2008,** *18*, 4146-4153.
30. Gao, G.; Liu, X.; Shi, R.; Zhou, K.; Shi, Y.; Ma, R.; Takayama-Muromachi, E.; Qiu, G., Shape-controlled synthesis and magnetic properties of monodisperse Fe3O4 nanocubes. *Crystal Growth & Design* **2010,** *10*, 2888-2894.
31. Dinh, C.-T.; Nguyen, T.-D.; Kleitz, F.; Do, T.-O., Shape-controlled synthesis of highly crystalline titania nanocrystals. *ACS nano* **2009,** *3*, 3737-3743.
32. Sharifi Dehsari, H.; Heidari, M.; Halda Ribeiro, A.; Tremel, W.; Jakob, G.; Donadio, D.; Potestio, R.; Asadi, K., Combined Experimental and Theoretical Investigation of Heating Rate on Growth of Iron Oxide Nanoparticles. *Chem. Mater.* **2017,** *29*, 9648-9656.
33. Sun, S.; Zeng, H.; Robinson, D. B.; Raoux, S.; Rice, P. M.; Wang, S. X.; Li, G., Monodisperse MFe2O4 (M= Fe, Co, Mn) nanoparticles. *J. Am. Chem. Soc.* **2004,** *126*, 273-279.
34. Eom, Y.; Abbas, M.; Noh, H.; Kim, C., Morphology-controlled synthesis of highly crystalline Fe 3 O 4 and CoFe 2 O 4 nanoparticles using a facile thermal decomposition method. *RSC Adv.* **2016,** *6*, 15861-15867.
35. LaMer, V. K.; Dinegar, R. H., Theory, production and mechanism of formation of monodispersed hydrosols. *J. Am. Chem. Soc.* **1950,** *72*, 4847-4854.
36. Miguel-Sancho, N.; Bomati-Miguel, O.; Roca, A. G.; Martinez, G.; Arruebo, M.; Santamaria, J., Synthesis of magnetic nanocrystals by thermal decomposition in glycol media: effect of process variables and mechanistic study. *Ind. Eng. Chem. Res.* **2012,** *51*, 8348-8357.
37. Zhu, Y.; Jiang, F.; Chen, K.; Kang, F.; Tang, Z., Size-controlled synthesis of monodisperse superparamagnetic iron oxide nanoparticles. *J. Alloys Compd.* **2011,** *509*, 8549-8553.
38. Chen, Z., Size and shape controllable synthesis of monodisperse iron oxide nanoparticles by thermal decomposition of iron oleate complex. *Synth. React. Inorg., Met.-Org., Nano-Met. Chem.* **2012,** *42*, 1040-1046.
39. Vargas, J.; Zysler, R., Tailoring the size in colloidal iron oxide magnetic nanoparticles. *Nanotechnology* **2005,** *16*, 1474-1479.
40. Yu, W. W.; Peng, X., Formation of high-quality CdS and other II–VI semiconductor nanocrystals in noncoordinating solvents: tunable reactivity of monomers. *Angew. Chem. Int. Ed.* **2002,** *41*, 2368-2371.
41. Yin, M.; Willis, A.; Redl, F.; Turro, N. J.; O'Brien, S. P., Influence of Capping Groups on the Synthesis of γ-Fe 2 O 3 Nanocrystals. *J. Mater. Res.* **2004,** *19*, 1208-1215.

42. Guardia, P.; Perez-Juste, J.; Labarta, A.; Batlle, X.; Liz-Marzán, L. M., Heating rate influence on the synthesis of iron oxide nanoparticles: the case of decanoic acid. *Chem. Commun.* **2010,** *46*, 6108-6110.
43. Belaïd, S.; Laurent, S.; Vermeersch, M.; Vander Elst, L.; Perez-Morga, D.; Muller, R. N., A new approach to follow the formation of iron oxide nanoparticles synthesized by thermal decomposition. *Nanotechnology* **2013,** *24*, 055705.
44. Klug, H. P.; Alexander, L. E., X-ray diffraction procedures: for polycrystalline and amorphous materials. *X-Ray Diffraction Procedures: For Polycrystalline and Amorphous Materials, 2nd Edition, by Harold P. Klug, Leroy E. Alexander, pp. 992. ISBN 0-471-49369-4. Wiley-VCH, May 1974.* **1974**, 992.
45. Unni, M.; Uhl, A. M.; Savliwala, S.; Savitzky, B. H.; Dhavalikar, R.; Garraud, N.; Arnold, D. P.; Kourkoutis, L. F.; Andrew, J. S.; Rinaldi, C., Thermal decomposition synthesis of iron oxide nanoparticles with diminished magnetic dead layer by controlled addition of oxygen. *ACS nano* **2017,** *11*, 2284-2303.
46. Guardia, P.; Labarta, A.; Batlle, X., Tuning the size, the shape, and the magnetic properties of iron oxide nanoparticles. *J. Phys. Chem. C* **2010,** *115*, 390-396.
47. Hou, Y.; Yu, J.; Gao, S., Solvothermal reduction synthesis and characterization of superparamagnetic magnetite nanoparticles. *J. Mater. Chem.* **2003,** *13*, 1983-1987.

Chapter 4

Composition and Size Dependent Properties of $Co_xFe_{3-x}O_4$ Nanoparticles[1]

4.1 Introduction

Iron-oxide nanoparticles (NPs) are usually composed of both Fe_3O_4 and Fe_2O_3 phases, which become superparamagnetic or a weak ferro/ferrimagnetic as the NP size reduces below a critical value.[1] The critical size depends on the composition of the NPs. For iron-oxide NPs, the superparamagnetic behavior is typically observed below 25 nm (for spherical NPs).[2-3] Due to low magnetocrytalline anisotropy of the iron-oxide nanoparticle, achieving ferromagnetic nano-magnets with a size (diameter) below 50 nm and with stable magnetization at room-temperature is challenging. Engineering of the magnetocrystalline anisotropy is required to achieve such nano-sized magnets in order to be used in multiferroic nanocomposites.

Metal-oxide nanoparticles (NPs) with a large magnetocrystalline anisotropy like cobalt-ferrite ($Co_xFe_{3-x}O_4$) [6, 13-14, 17-18] nanoparticles are particularly attractive candidates because of high

[1] **The results of this chapter are fully or in part published in *J. Phys. Chem. C* with DOI: *10.1021/acs.jpcc.8b09276* by H. Sharifi et al.**

coercivity, Curie temperature, remanent magnetization, good physical and chemical stability, excellent corrosion resistance and ease of synthesis.[4-8] The magnetic properties of the cobalt-ferrite NPs can be finely tuned by changing the cobalt content or the size of the NPs.[5-6, 9-15]Moreover, synthesis of cobalt-ferrite NPs are more cost-effective in comparison with other ferrimagnet NPs such as FePt, SmCo and NdFeB. Cobalt-ferrites are also relevant in other field of applications such as in biomedicine, magnetic hyperthermia, spintronic, magnetic resonance imaging (MRI), catalyst, and sensors.[4-5, 16-25] For the aforementioned applications, a detailed systematic study of the magnetic properties of the $Co_xFe_{3-x}O_4$ NPs as a function of cobalt stoichiometry, *x*, and the size of the NPs, is required to achieve nano-magnets with stable remanent magnetization at room-temperature, high coercivity and large magnetocrytalline anisotropy.

Among the various techniques for preparation of $Co_xFe_{3-x}O_4$ NPs,[26-30] thermal decomposition of metal complexes is a promising methods to finely control the size and composition.[5, 7, 12, 31] The magnetic properties, and in particular magnetocrytalline anisotropy, of the NPs strongly depends on the cobalt stoichiometry, *x*, which can be affected among many factors by the ratio/amount/type of precursors, growth temperature, and growth time.[4-6, 26, 32-33] Moreover, the magnetic properties of the NPs strongly depends on their size, [5, 9, 22, 34-36] which could be tuned by varying the thermal decomposition reaction parameters such as reagent concentration, boiling point of the solvent, and reaction heating rate. [5, 36-41] Therefore, for realization of cobalt-ferrite nano-magnet with stable room-temperature magnetization, a thorough study of the magnetic properties as a function of both cobalt stoichiometry and NP size is required.

4.1.1 Motivation

We would like to systematically explore the parameter space of the thermal decomposition reaction for the synthesis of $Co_xFe_{3-x}O_4$ NPs to find the value of *x* that gives the optimal magnetic properties at room temperature and room temperature, and tuned the size of the magnetic NPs at this optimal composition.

4.1.2 Aim of this chapter

The aim is to present a detailed study on the evolution of the coercive field, H_C, remanent magnetization, M_r, saturation magnetization, M_S, blocking temperature, T_B, and magnetic anisotropy energy as a function cobalt stoichiometry and size over a wide range of temperatures ranging from 2 K to 400 K. At a fixed NP size, the value of x in the $Co_xFe_{3-x}O_4$ NPs nanocrystals is systematically changed by changing the feed ratio of cobalt and iron precursors to find the optimal stoichiometric value that provides the best compromise between H_C, M_S, room temperature stability of M_r and the highest T_B.[42-43] We Subsequently experimentally determine the lowest size limit, for the nanoparticle with stable room temperature remanence and coercivity by size tuning at the optimum x value. To tune the size, the following parameters are changed: (1) the amount of solvent, (2) precursors concentration, (3) heating rate and (4) molar ratio of surfactant to total metal (Co + Fe) precursors.

4.2 Experiment

4.2.1 Materials

Cobalt (II) acetylacetonate (99 %) was purchased from Sigma Aldrich and was used as received. The rest of the materials are the same as the ones for synthesize of iron oxide nanoparticles as described in Chapter 3.

4.2.2 Synthesis of cobalt ferrite NPs

$Co_xFe_{3-x}O_4$ NPs were synthesized by thermal decomposition following the previously described procedure in Chapter 3.[12, 37, 39, 44] The only difference is using the combination of both cobalt and iron precursors. Syntheses conditions for all the NPs, their respective size and compositions are summarized in **Table 4.1** and **4.2**. In total, 43 different syntheses were performed, each at least twice, to ensure reproducibility and good statistics of the results. All the NPs showed colloidal stability, due to surfactant coating.

Table 4.1 Synthesis conditions for all the synthesized NPs with different cobalt stoichiometry. The values of initial precursors (both iron and cobalt), solvent, surfactants, heating rate, and average diameter of the NPs and final compositions of $Co_xFe_{3-x}O_4$ are reported.

Name	$Co(acac)_2$ (mmol)	$Fe(acac)_3$ (mmol)	OAC (mmol)	OAM (mmol)	BE (ml)	H. R. (K/min)	Diameter (nm)	σ (nm)	Final Composition
A_0	0	2	6	6	20	3.3	10.8	1.0	$Co_{0.00}Fe_{3.00}O_4$
A_1	0	2	6	6	20	2.8	12.1	1.0	$Co_{0.00}Fe_{3.00}O_4$
A_2	0.1	2	6	6	20	3.3	11.1	1.15	$Co_{0.10}Fe_{2.90}O_4$
A_3	0.1	2	6	6	20	2.8	12.3	1.25	$Co_{0.10}Fe_{2.90}O_4$
A_4	0.2	2	6	6	20	3.3	11.5	1.35	$Co_{0.17}Fe_{2.83}O_4$
A_5	0.2	2	6	6	20	2.8	12.5	1.4	$Co_{0.18}Fe_{2.82}O_4$
A_6	0.3	2	6	6	20	3.3	11.9	1.5	$Co_{0.28}Fe_{2.72}O_4$
A_7	0.3	2	6	6	20	2.8	12.7	1.6	$Co_{0.26}Fe_{2.74}O_4$
A_8	0.6	2	6	6	20	3.3	12.5	1.6	$Co_{0.45}Fe_{2.55}O_4$
A_9	0.8	2	6	6	20	3.3	12.7	1.7	$Co_{0.58}Fe_{2.42}O_4$
A_{10}	1	2	6	6	20	3.3	13.2	1.7	$Co_{0.72}Fe_{2.28}O_4$
A_{11}	1.2	2	6	6	20	3.3	13.7	1.85	$Co_{0.83}Fe_{2.17}O_4$
A_{12}	1.4	2	6	6	20	3.3	14.1	2.4	$Co_{0.95}Fe_{2.07}O_4$
A_{13}	1.6	2	6	6	20	3.3	14.0	2.2	$Co_{1.17}Fe_{1.83}O_4$
A_{14}	1.8	2	6	6	20	3.3	13.5	2.6	$Co_{1.25}Fe_{1.75}O_4$
A_{15}	2	2	6	6	20	3.3	14.1	4	$Co_{1.30}Fe_{1.70}O_4$
A_{16}	2.4	2	6	6	20	3.3	13.9	3.7	$Co_{1.52}Fe_{1.48}O_4$

Table 4.2 Synthesis conditions for all the synthesized NPs with different size. The values of initial precursors (both iron and cobalt), solvent, surfactants, heating rate, average diameter of the NPs and final compositions of $Co_xFe_{3-x}O_4$ are reported.

Method	Sample	$Co(acac)_2$ (mmol)	$Fe(acac)_3$ (mmol)	OAC (mmol)	OAM (mmol)	BE (ml)	H. R. (K/min)	Diameter (nm)	σ (nm)	Final Composition
Heating rate	A_{17}	1	2	6	6	20	1.0	22.5	3.7	$Co_{0.71}Fe_{2.29}O_4$
	A_{18}	1	2	6	6	20	1.25	18.2	3.5	$Co_{0.70}Fe_{2.30}O_4$
	A_{19}	1	2	6	6	20	1.5	17.5	3.2	$Co_{0.70}Fe_{2.30}O_4$
	A_{20}	1	2	6	6	20	2.5	15.5	2.4	$Co_{0.72}Fe_{2.28}O_4$
	A_{10}	1	2	6	6	20	3.3	13.2	1.7	$Co_{0.72}Fe_{2.28}O_4$

	A_{21}	1	2	6	6	20	6.4	11.5	1.2	$Co_{0.73}Fe_{2.28}O_4$
	A_{22}	1	2	6	6	20	8.4	10	1.1	$Co_{0.69}Fe_{2.31}O_4$
	A_{23}	1	2	6	6	20	11	8.7	0.95	$Co_{0.70}Fe_{2.30}O_4$
	A_{24}	1	2	6	6	20	20	6.8	0.8	$Co_{0.71}Fe_{2.29}O_4$
Solvent amount	A_{25}	1	2	6	6	13	3.3	18.1	3.2	$Co_{0.69}Fe_{2.31}O_4$
	A_{26}	1	2	6	6	14.5	3.3	17.6	3.0	$Co_{0.71}Fe_{2.29}O_4$
	A_{27}	1	2	6	6	16	3.3	16.5	2.8	$Co_{0.72}Fe_{2.28}O_4$
	A_{28}	1	2	6	6	17.5	3.3	15.5	2.5	$Co_{0.69}Fe_{2.31}O_4$
	A_{10}	1	2	6	6	20	3.3	13.2	1.7	$Co_{0.72}Fe_{2.28}O_4$
	A_{29}	1	2	6	6	24	3.3	10.1	1.25	$Co_{0.70}Fe_{2.30}O_4$
	A_{30}	1	2	6	6	28	3.3	9.5	1	$Co_{0.71}Fe_{2.29}O_4$
	A_{31}	1	2	6	6	32	3.3	7.2	0.95	$Co_{0.71}Fe_{2.29}O_4$
Precursors amount	A_{32}	0.33	0.67	6	6	20	3.3	7.1	0.85	$Co_{0.69}Fe_{2.31}O_4$
	A_{33}	0.5	1	6	6	20	3.3	9.4	1	$Co_{0.69}Fe_{2.31}O_4$
	A_{34}	0.67	1.33	6	6	20	3.3	11.9	1.4	$Co_{0.73}Fe_{2.27}O_4$
	A_{10}	1	2	6	6	20	3.3	13.2	1.7	$Co_{0.72}Fe_{2.28}O_4$
	A_{35}	1.34	2.66	6	6	20	3.3	9.9	1.3	$Co_{0.72}Fe_{2.28}O_4$
	A_{36}	2	4	6	6	20	3.3	8.4	1.2	$Co_{0.68}Fe_{2.32}O_4$
	A_{37}	2.7	5.3	6	6	20	3.3	7.9	1.75	$Co_{0.71}Fe_{2.29}O_4$
Surfactants amount	A_{38}	1	2	2	2	20	3.3	9	0.95	$Co_{0.75}Fe_{2.25}O_4$
	A_{39}	1	2	4	4	20	3.3	10.2	1	$Co_{0.7}Fe_{2.3}O_4$
	A_{10}	1	2	6	6	20	3.3	13.2	1.7	$Co_{0.72}Fe_{2.28}O_4$
	A_{40}	1	2	8	8	20	3.3	16.5	3.5	$Co_{0.69}Fe_{2.31}O_4$
	A_{41}	1	2	10	10	20	3.3	17.4	2.8	$Co_{0.73}Fe_{2.27}O_4$
	A_{42}	1	2	12	12	20	3.3	17.6	3	$Co_{0.68}Fe_{2.32}O_4$

4.2.3 Characterizations

To quantify the cobalt and iron stoichiometry, Inductively Coupled Plasma Optical Emission Spectroscopy (ICP-OES) analysis was performed using ACTIVA M. Samples of MNPs were digested in concentrated aqua regia (3:1 ratio of hydrochloric acid to nitric acid) for

1 hours. The resulting solutions were diluted to 50 ppm. The metal calibration standards (0.1−100 ppm) were prepared by diluting aliquots from inorganic ventures stock solutions of 1000 ppm metal content (iron, cobalt). Since the composition of the cobalt ferrite NPs is defined as $Co_xFe_{3-x}O_4$, it is possible to calculate the cobalt stoichiometry(x) according to the following expression:[5]

$$x = \frac{3[\frac{Co}{Fe}]_{ICP}}{1+[\frac{Co}{Fe}]_{ICP}} \qquad (4.1)$$

Interaction effects in magnetic NPs are usually examined via ΔM technique,[45-47] which is based on the comparison of the isothermal remanent magnetization (IRM) and the DC demagnetizing remanence (DCD) curves and it is explained well in the literature. [45-47] The IRM curve, $m_r(H) = M_r(H)/M_r(H_{max})$, which is obtained by measuring the remanence from the initially demagnetized state and taking the sample through progressively increasing loops and the DCD curve, $m_d(H) = M_d(H)/M_d(H_{max})$, which is obtained by measuring the remanence with progressively increasing demagnetization in a previously saturated sample. In non-interacting systems $m_r(H)$ and $m_d(H)$ are expected to be related within the Stoner–Wohlfarth model through:[48-49]

$$m_d(H) = 1 - 2m_r(H) \qquad (4.2)$$

Wohlfarth[49] predicted that the two remanence curves should be identical for non-interacting sample and hence $\Delta M = 0$. If $\Delta M \neq 0$ there is magnetic interactions which can be either demagnetizing or magnetizing interactions.[45-47]

For the DCD measurements we used the following sequence of applied fields: $-H_{sat}$, (ΔH, 0), (2ΔH, 0), ... In this method a negative saturation field $-H_{sat}$ is applied only at the beginning of the experiment and each data point is obtained at $H = 0$ after applying a field of $H = n\Delta H$. H_{sat} and ΔH depend on the corecieve field of the sample. The IRM curve is acquired by starting from a demagnetized state and measuring the magnetization at zero field following the sequence: (ΔH, 0), (2ΔH, 0), ... There are many different ways to demagnetize a sample like heating the sample above the Curie temperature, T_C, and then cooling in zero field. However, due

to the high T_C of cobalt ferrite MNPs (> 600 °C), we used other method to demagnetize the samples in which the sample is saturated in one direction and a sequence of decreasing fields is applied in both senses, until zero field is reached.

The elemental distribution within the NPs was determined by energy-filtered TEM (EFTEM), carried out on a FEI Tecnai F20 200 kV TEM. On the same instrument, operated in high angle annular dark field scanning TEM (HAADF-STEM) mode, elemental quantification of the samples was then performed via energy dispersive X-ray spectroscopy (EDS) analysis. The details for the other characterization techniques were given in previous Chapter.

4.3 Results and discussion

4.3.1 Tuning Co stoichiometry at a fixed size

Initial series of syntheses were performed in which the amount of cobalt precursor (here $Co(acac)_2$) added to the reaction flask was systematically varied from 0 to 2.4 mmol (A_0-A_{16}), while the amounts of all other chemicals were kept fixed (see **Table 4.1**). The representative TEM images of the resulting NPs and the corresponding size distribution histograms are shown in **Figure 4.1 a-i**. The cobalt stoichiometry, *x*, in the $Co_xFe_{3-x}O_4$ NPs is given in **Figure 4.1 j**. Upon increasing the $Co(acac)_2/Fe(acac)_2$, *i.e.* the Co/Fe feed ratio, from 0 to 1.2, the Co stoichiometry, *x*, changes from 0 to 1.5. The rate of change in *x* with Co/Fe feed ratio is linear. [5-6] The Co/Fe ratio found in the NPs is always lower than the initial Co/Fe feed ratio. These findings are in agreement with previous literatures.[5-6]The evolution in the NPs size as a function of Co stoichiometry, *x*, in the NPs is shown in **Figure 4.1 k**. In general by increasing the *x* from 0.0 to ~ 1.0, the NP size slightly increased from 10.8 to 13.5 nm. For $x > 1.0$ the size remained constant. Considering the observed polydispersity and also shape irregularities, one can disregard the variation in the diameter of the NPs for $x > 0.4$, hence an average diameter of ~ 13 ± 1.7 nm could be assumed. The magnetic properties strongly depend on the size. Therefore, for a fair comparison between magnetic properties of the NPs with different *x*, similar NP sizes are required. To increase the average size of the NPs with $x < 0.4$ (A_0, A_2, A_4, A_6- detail in **Table**

4.1) to same size regime of ~ 13 nm, we lowered the growth heating rate from 3.3 K/min to 2.8 K/min. The size of the resulting NPs, as depicted in **Figure 4.1 k**, increased to the range of ~ 13 nm. We discussed in Section 1 of Chapter 3 that growth heating rate is an efficient way to tune the NP size and has no influence on the stoichiometry.

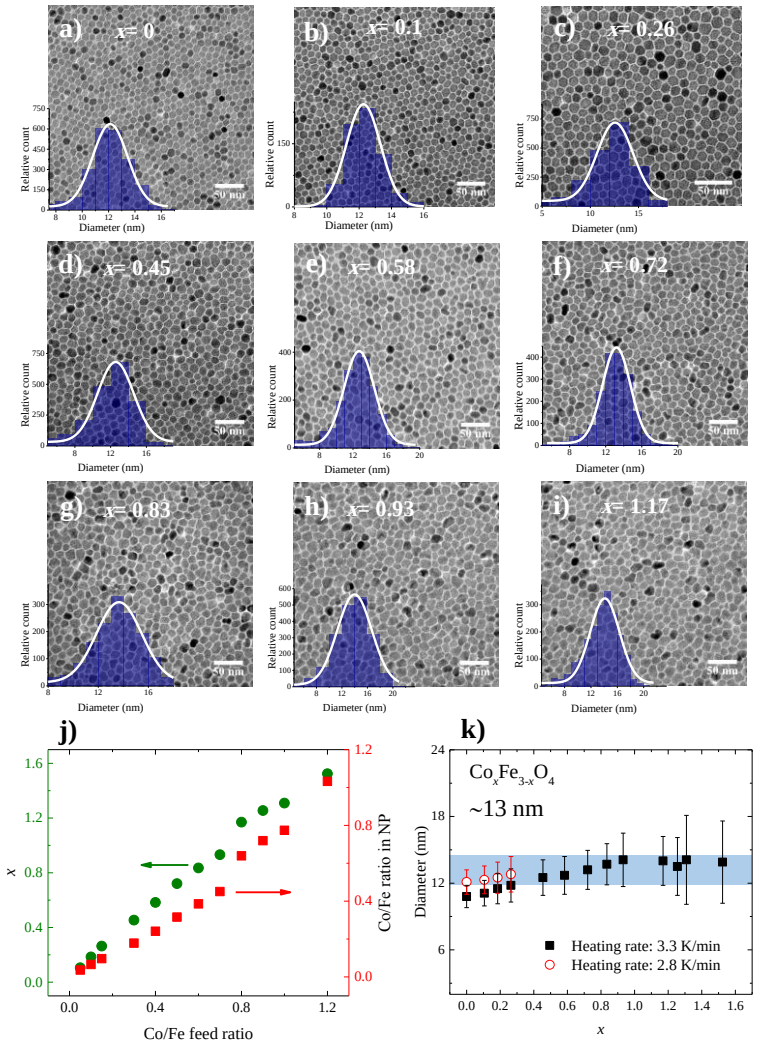

Figure 4.1 TEM images of the NPs obtained with different $Co(acac)_2/Fe(acac)_2$ feed ratio as (a) A_1, (b) A_3, (c) A_7, (d) A_8, (e) A_9, (f) A_{10}, (g) A_{11}, (h) A_{12} and (i) A_{13} (see **Table 4.1** for details of the reaction conditions). The inset shows the corresponding size distribution histogram. j) The cobalt stoichiometry (left) and Co/Fe ratio (right) in the NPs measured with ICP as a function of the ratio of cobalt precursor and iron precursor in the reaction. k) The average diameter of NPs as a function of cobalt content. Black squares are for the samples when the heating rate is 3.3 K/min and red dots are for the state that heating rate is 2.8 K/min. Note that all the other synthesis parameter remains unchanged.

A representative HR-TEM image of the NPs is given in **Figure 4.2 a** for the NPs batch A_{10} with average diameter of almost 13.2 nm and cobalt content of x= 0.72. Observation of the lattice fringes indicated formation of well-crystallized NPs. The measured distances of 2.91 Å and 2.51 Å can be attributed, respectively, to the d_{hkl} of 220 and 311 planes of the spinel structure of $CoFe_2O_4$, respectively, in agreement with the literature reports.[12, 26, 50] The crystalline structure of the NPs with different cobalt content and the same average size, were further characterized by powder X-ray diffraction (XRD). The recorded XRD patterns of the NPs are shown in **Figure 4.2 b**. For the NPs with x < 1, the XRD patterns matched the bulk pattern for the stoichiometric $CoFe_2O_4$ spinel ferrite crystal structure (JSPDC card number 22−1086). It can be therefore concluded that the NPs do not contain impurities ascribable to FeO, CoO, or Co_3O_4. However, for the NPs with x > 1, a secondary wustite phase of FeO or CoO appeared.[5]

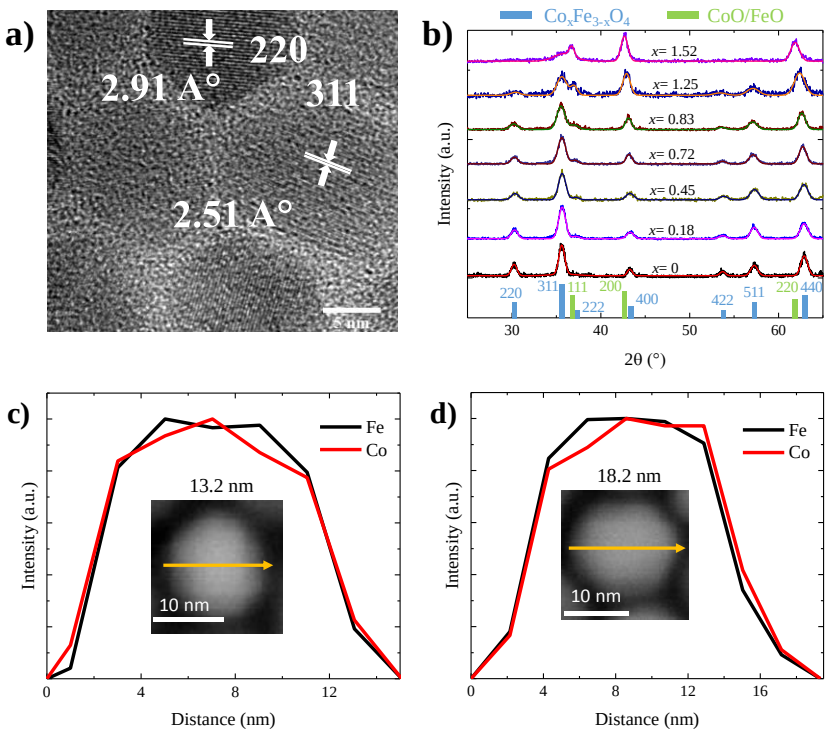

Figure 4.2 (a) HR-TEM images of sample A_{10} (13.2 nm and x= 0.72). (b) XRD patterns of samples with almost fixed size (~ 13 nm) and different cobalt stoichiometry (x). HAADF-STEM images of a single NPs from each sample and profile of the normalized Fe and Co Ka peaks along the diagonal lines drawn for each sample of (c) 13.2 nm (A_{10}) and (d) 18.2 nm (A_{18}).

To rule out formation of Co- (or Fe-) rich phases within the NPs, we performed EFTEM to probe the distribution of Co and Fe within the NPs. A representative EFTEM image for the nanoparticle A_{10}, with size 13.2 ± 1.7 nm and x = 0.72 is given in **Figure 4.2 c**. The elemental map indicated a homogeneous distribution of Fe and Co within the NPs, without any evidence of a core-shell structure or enrichment of Co (or Fe) on surface (or in bulk). The EFTEM image of larger NPs with diameter of 18.2 nm, and x=0.70 (details to be discussed later), **Figure 4.2 d,** indicates a homogenous distribution of Co and Fe. Therefore, EFTEM confirms that our synthesis yields NPs with good crystallinity, and elemental homogeneity.

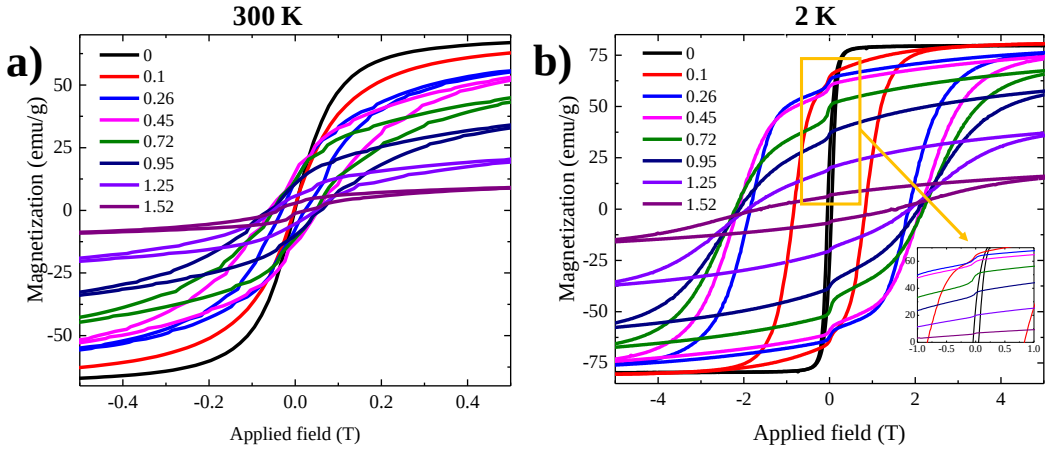

Figure 4.3 *M-H* hysteresis loops at (a) 300 K and (b) 2 K of samples with different cobalt stoichiometry, *x*, and fixed size of almost 13 nm.

To characterize the magnetic properties of the nanoparticles, we performed magnetization measurements and recorded magnetization, *M*, as a function of magnetic field, *H*. The *M-H* loops shown in **Figure 4.3 a** and **b** were recorded at 300 K (room temperature) and at 2 K, respectively for the NPs with *x* varying from 0 to 1.52. The characteristic feature for room-temperature ferro- or ferrimagnetic NPs is the observation of a hysteretic *M-H* curve and finite coercive field, H_C (or coercivity). The cobalt ferrite NPs exhibited H_C at room-temperature and a hysteresis behavior for $x > 0.1$. The coercivity however is accompanied with compromised saturated magnetization, M_S. The cobalt ferrit NPs showed lower M_S values. The *M-H* curves obtained at 2 K, showed a clear shift in the H_C towards higher fields, which is due to the higher magnetic ordering at low temperature.[51]

Similar to previous studies, the *M-H* curves of the cobalt ferrit NPs showed "bi-magnetic" behavior at 2 K; a sudden reduction of *M* as the field approached from a large value to zero.[5, 26] Different mechanisms have been proposed for the observation of bi-magnetic behavior, such as presence of two different NP size distribution with the sample,[52] formation of a core-shell structure[5, 26, 53] and strong dipolar interaction between the NPs.[5, 54] In the present cases, it was evident from the TEM analysis that samples had narrow size distributions. Furthermore, the EFTEM measurements ruled out formation of a core-shell structure. Therefore, we conclude that the bi-magnetic behavior is due to the presence of strong inter-particle interactions. The isothermal remanent magnetization (IRM) and dc demagnetization (DCD) measurements were performed in order to clarify the magnetic coupling interactions between cobalt ferrite NPs.[46, 55-56] For non-interacting NPs, ΔM should be zero at any value of applied field while deviations of ΔM curves from zero in magnetic materials are ascribed due to magnetic coupling interactions between NPs. [46, 56] The calculated ΔM curves (**Figure 4.4**) revealed a negative peak with a magnitude of -0.5 for the oleate-coated $Co_{0.7}Fe_{2.3}O_4$ NPs. This negative value is indicative of magnetic dipole coupling interactions. Similar results were reported for ferromagnetic cobalt ferrite[46] and FePt nanoparticles.[56] So, the observed bi-magnetic behavior can be ascribed by the existence of strong coupling interaction between NPs.

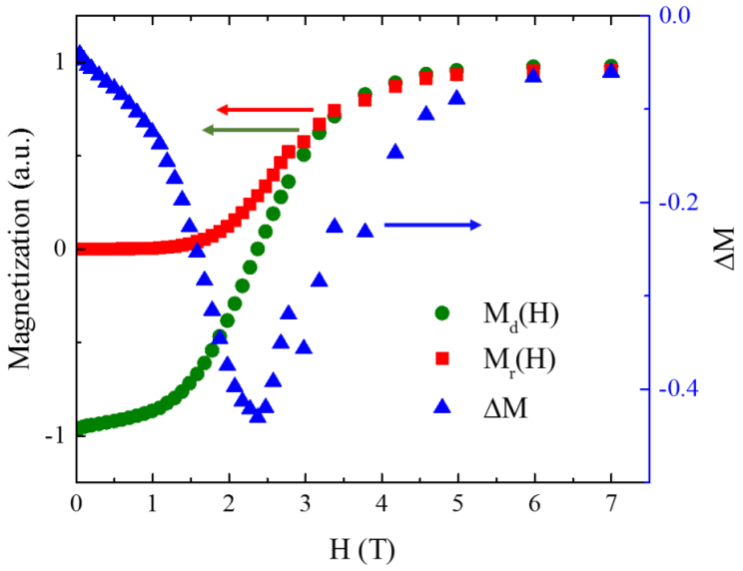

Figure 4.4. m_r *(H)*, m_d *(H)* and ΔM curves for a $Co_{0.7}Fe_{2.3}O_4$ sample with 13.2 nm diameter, at 2 K.

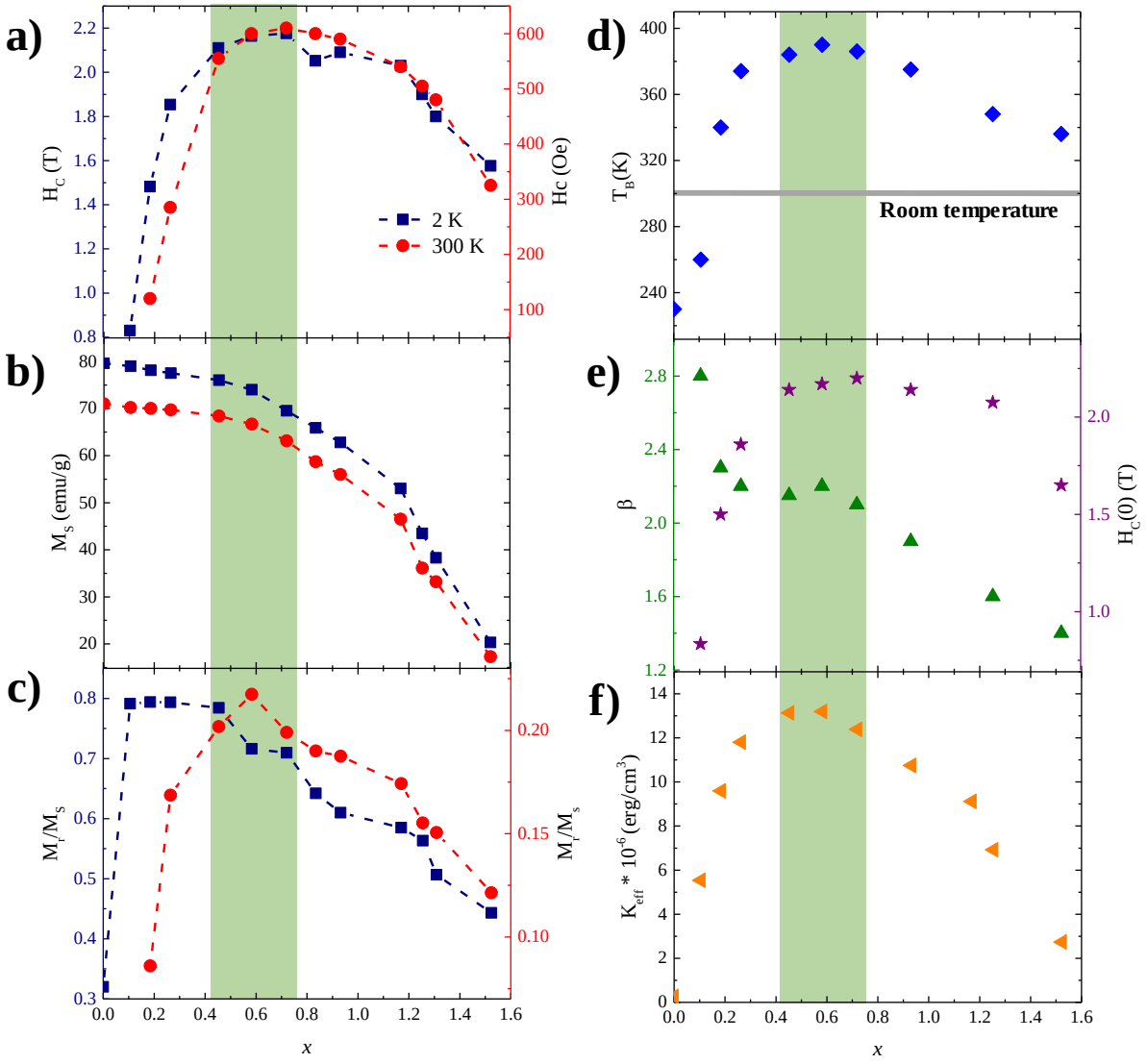

Figure 4.5 Variation of (a) coercive field (H_C), (b) saturation magnetization (M_S), (c) M_r/M_s and (d) T_B of samples with different cobalt content and fixed size (~ 13 nm) at both 300 K and 2 K. (e) Effective magnetic anisotropy, K_{eff}, of cobalt ferrite NPs with different cobalt stoichiometry in a fixed size of ~ 13 nm. (f) the value of β and $H_C(0)$ as a function of average diameter of NPs. The data were obtained from *M-H* loops at different temperature, with the assumption of only coherent rotation switching mode and neglecting any temperature dependent term.

From the *M-H* curves at 300 and 2 K, we extracted H_C, M_S, remanent magnetization, M_r, and calculated squareness, M_r/M_S. The values for H_C, M_S, and M_r/M_S as a function of cobalt stoichiometry, x, in the range $0 \leq x \leq 1.5$ are shown in **Figure 4.5 a-c**. For the $Co_xFe_{3-x}O_4$ NPs with an average diameter of 13 nm, H_C increased from 120 to 610 Oe at 300 K when x increased

from 0.1 to 0.7 (**Figure 4.5 a**). Further increase of *x* from 0.8 to 1.5, H_C lead to a continuous drop in H_C to 325 Oe for *x*=1.5. The observed maxima in H_C at $x \sim 0.7$ is consistent with literature reports.[5-6] H_C showed a similar trend at 2 K, and showed a peaked again at $x \sim 0.7$. Due to increased magnetic ordering,[51] the low temperature value of H_C at $x \sim 0.7$ reached 21.7 kOe, which to best of our knowledge is amongst the highest reported values for cobalt ferrite NPs. Larger H_C of the $Co_xFe_{3-x}O_4$ NPs compared with the Fe_3O_4 NPs, indicates Co_2^+ substitution of Fe^{2+} in the magnetite structure improving the magnetocrystalline anisotropy energy and coercivity. Interestingly, the NPs with $0.5 < x < 0.7$ show the highest H_C and effective magnetic anisotropy compared to the $CoFe_2O_4$ NPs, and therefore are magnetically harder.

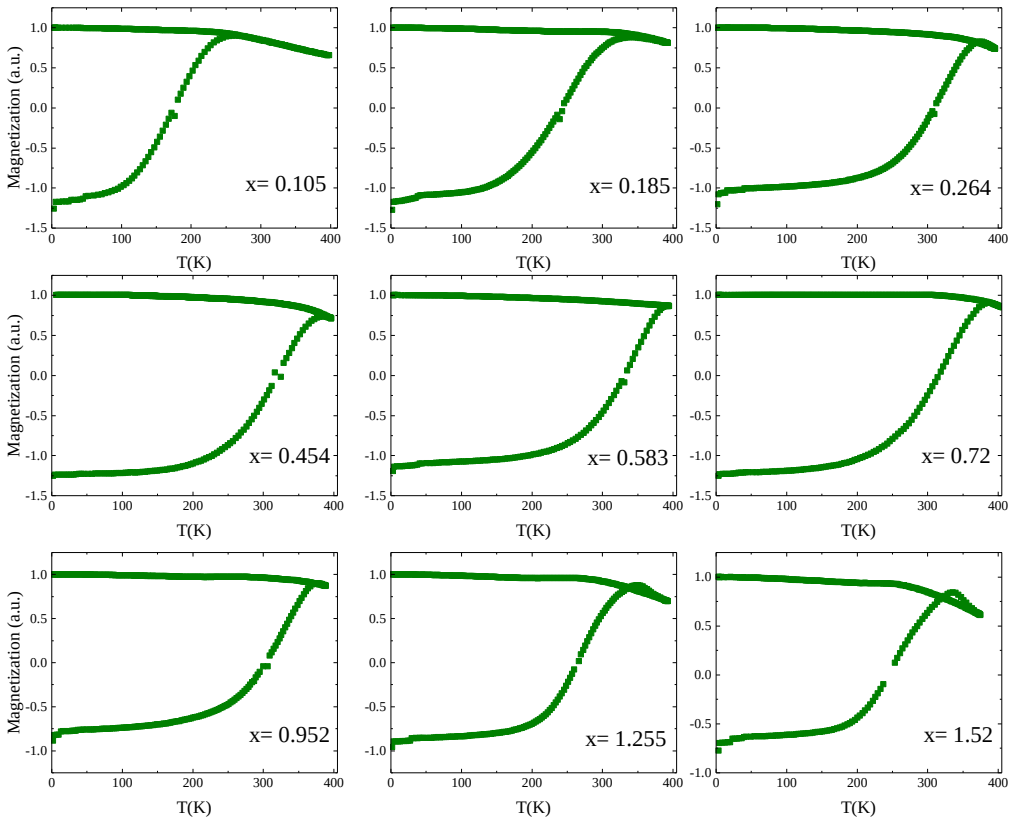

Figure 4.6 ZFC and FC measurement of the samples with different cobalt content, *x*, and fixed size of ~ 13 nm.

The M_S of $Co_xFe_{3-x}O_4$ NPs, shows the same decreasing trend, both at 300 and 2 K, as a function of *x*, as shown in **Figure 4.5 b**. This trend is rationalized because Co has a lower magnetic moment than the Fe (in Bohr magneton), hence resulting lower M_s. The Co^{2+} ions with

equal probability occupy both octahedral and tetrahedral sites in the inverse spinel structure of Fe_3O_4. The mixed occupancy breaks the antiferromagnetic ordering among the Fe^{3+} ions.[5-6] In contrast to M_S, the squareness, M_r/M_S shows a non-monotonic variation with x. At room-temperature, 300 K, the highest squareness of 0.22 is observed for $0.5 < x < 0.7$. At 2 K, the maximum squarennes is 0.8 and is observed for the range $0.1 < x < 0.5$. Blocking temperature, T_B, defined as the temperature below which the magnetic moments are blocked, was determined from the magnetization measured as a function of temperature after zero field (ZFC) and field cooling (FC). ZFC-FC plots for all the $Co_xFe_{3-x}O_4$ NPs are given in (**Figure 4.6**).

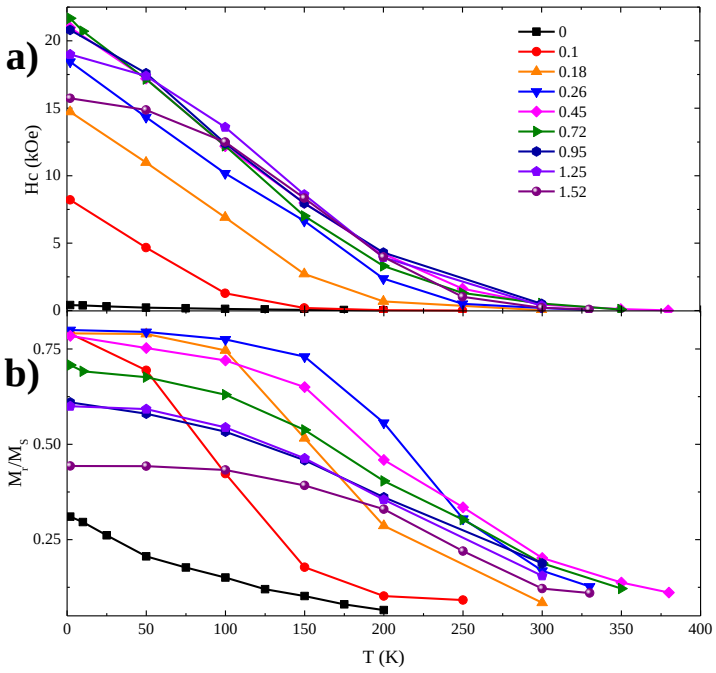

Figure 4.7 Evolution of (a) H_C and (b) M_r/M_S as a function of temperature for the series of cobalt ferrite NPs with different cobalt content and at almost fixed size of ~ 13 nm.

The extracted T_B values are given in **Figure 4.5 d**. All the samples (except x = 0.0 and 0.1) showed T_B that was above room temperature. Interestingly, T_B exhibited a maximum for the $Co_xFe_{3-x}O_4$ NPs with x between 0.4 and 0.7. Above T_B, the nanoparticles show superparamagnetic behavior and no coercivity. Below T_B, the coercivity, H_C, and squareness, M_r/M_S, are temperature dependent.

We note, to the best of our knowledge, the temperature dependence of H_C and squareness have been overlooked in the literature (see **Table 4.3**). We therefore measured the *M-H* curves at various temperatures, in the range of 2-400 K (data is not given here), from which we extracted the values of H_C and M_r/M_S at different temperatures for the $Co_xFe_{3-x}O_4$ NPs at every x composition. The temperature evolution of H_C and M_r/M_S in different cobalt content are shown in **Figure 4.7 a** and **b**, respectively. Besides strong dependence on the cobalt content, x, the H_C and M_r/M_S showed strong dependence on temperature; decaying with increasing temperature, vanishing at $T = T_B$.

Temperature dependence of H_C is well describe with Stohner-Wohlfarth (SW) model:[48-49]

$$H_C = H_C(0)[1 - (T/T_B)]^{\beta} \qquad (4.3)$$

where $H_C(0)$ is the coercive field at 0 K and β is the decay factor.[57-58 58-59]. By fitting **Equation 4.3** to the experimentally obtained H_C-T plot of **Figure 4.7 a,** the values of $H_C(0)$ and β were obtained. The β values, given in **Figure 4.4 e**, showed a monotonic drop from 2.8 to 1.4 upon increasing the cobalt content in the $Co_xFe_{3-x}O_4$ NPs. The $H_C(0)$ values as a function of composition are given in **Figure 4.4 e**. The SW model provides an estimate for the effective magnetic anisotropy (K_{eff}):[33, 48-50, 57-60]

$$K_{eff} = H_C(0)M_S/\ 0.64 \qquad (4.4)$$

by assuming that K_{eff} is temperature-independent.[33, 50, 60], [22, 61-65] The $H_C(0)$ is determined from **Equation 4.3**. The calculated K_{eff}, **Figure 4.4 f**, exhibited again a non-monotonic dependence on x with the maximum occurring for $0.5 < x < 0.7$. The maximum K_{eff} value amounted to 13.2×10^6 erg/cm^3 for $0.6 < x < 0.7$, which is close to the value for the stoichiometric bulk $CoFe_2O_4$ (19×10^6 erg/cm^3). [22, 66] For the compositional range of $0.5 < x < 0.7$ the cobalt-ferrite NPs show the highest values for H_C, squareness, T_B and K_{eff}, indicating stability of the remanent magnetization at room-temperature and suitability of the NPs for nano-magnet applications. The best compositional region for the $Co_xFe_{3-x}O_4$ NPs at which the NPs are stable at room-temperature are highlighted on **Figure 4.4**. Therefore, $Co_xFe_{3-x}O_4$ NPs with $0.5 < x < 0.7$ are suited the envisioned applications as nano-magnets in for instance non-volatile memories.

4.3.2 Size tuning at the optimum Co stoichiometry

The magnetic properties, next to the stoichiometry, strongly depend on the size of the NPs. Therefore we set out to tune the size of the NPs. At the optimized cobalt stoichiometry of $x \sim 0.7$, we tune the size of the NPs by changing different reaction parameters *i.e.* (i) growth heating rate, (ii) concentration of the surfactants, (iii) concentration of the precursor and investigate the effect of each reaction parameter on average diameter, polydispersity, stoichiometry, crystalline structure, and magnetic properties.

(i) Growth heating rate

Changing the growth heating rate (from 180 °C to 300 °C) is an easy way to tune the size of the NPs.[37-38, 67] Here we changed the heating rate from 1 to 20 K/min (detail is **Table 4.2**) while the other reaction parameters were unchanged. The TEM images of the resulting NPs, with their corresponding size distribution diagram is shown in **Figure 4.8 a-h**.

To determine the effect of the heating rate on the cobalt stoichiometry, *x*, we first measured the cobalt content, using ICP, for different average diameters. The cobalt stoichiometry remained almost constant ($x \sim 0.7$) for all the NPs obtained using different growth heating rates (as depicted in **Figure 4.8 i**). Changing growth heating rate, therefore does not affect the stoichiometry. The evolution of the average diameter of the NPs as a function of heating rate is shown in **Figure 4.8 i**. As the heating rate increased from 1.0 K min^{-1} to 20 K min^{-1} the final average diameter of NPs droped from ~ 22.5 nm to ~ 6.8 nm.

We have shown in previous chapter (Chapter 3 and Section 1) the underlying mechanism responsible for size tuning of iron-oxide nanoparticles by changing growth heating rate. [37] The size reduction trend is due to the dominant effect of growth heating rate on nucleation. Briefly, the higher the heating rate results in the higher production of monomer which based on the LaMer theory,[68] leads to formation of higher number of smaller nuclei after nucleation. The higher number of nuclei contributes to formation of smaller nanoparticles.[37-38] At low heating rates, polydispersity was higher. Higher polydispersity is due to the less defined threshold between nucleation and growth under low heating rates, which results in the formation and growth of nuclei during a longer time.

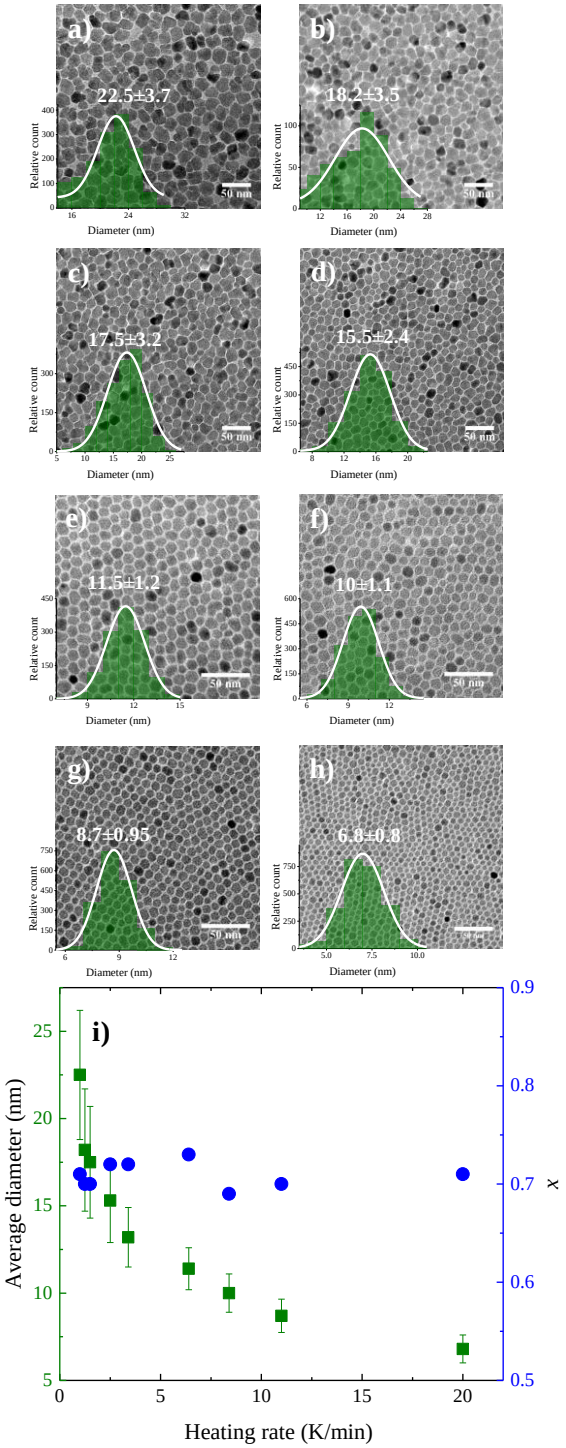

Figure 4.8 TEM images of the NPs with fixed cobalt stoichiometry (x ~ 0.7) and different heating rate (a) 1 (A_{17}), (b) 1.25 (A_{18}), (c) 1.5 (A_{19}), (d) 2.5 (A_{20}), (e) 3.4 (A_{10}), (f) 6.4 (A_{21}), (g) 8.4 (A_{22}), (h) 11 (A_{23}) and (i) 20 (A_{24}) K/min with their corresponding size distribution histogram (see **Table 4.2** for details of the reaction conditions). (j) The summary of average diameter and the cobalt stoichiometry of the NPs as a function of heating rate.

(ii) Surfactants concentration

To clarify the role of the surfactants concentration, different syntheses were performed wherein only the total amount of surfactants OAC+OAM was systematically varied from 4 mmol to 24 mmol while keeping the ratio of OAC/OAM=1. All other reaction parameters were unchanged (**Table 4.2**).

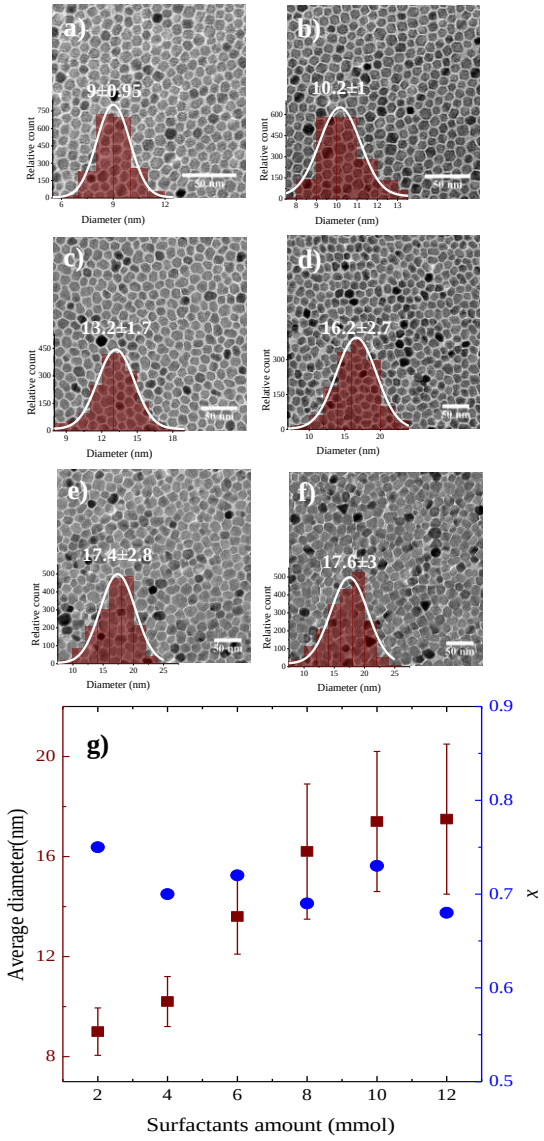

Figure 4.9 TEM images of samples with different total amount of surfactants (OAC+OAM, OAC/OAM=1), (a) 4 (A_{38}), (b) 8 (A_{39}), (c) 12 (A_{10}), (d) 16 (A_{40}), (e) 20 (A_{41}) and (f) 24 (A_{42}) mmol (see **Table 4.2** for details of the reaction conditions). (g) The average diameter and the cobalt stoichiometry of NPs as a function of total surfactants amount.

The TEM images of the resulting NPs with their corresponding size distribution histograms are shown in **Figure 4.9 a-f**. Altering the surfactant concentration did not show any influence on the cobalt stoichiometry, *x*, as all the NPs showed $x \sim 0.7$ hence remained unchanged for all the NPs (as shown in **Figure 4.9 g**). The size evolution of the NPs, **Figure 4.9 g**, shows that the mean nanoparticle diameter continuously increased from 9 nm to around 17.6 nm as the amount of surfactants increased from 4 mmol to 24 mmol.

Oleate surfactant in the synthesis acts as the surfactant to stabilize the monomer also as the growth rate controller of different crystallographic plans of the crystal structure.[4, 6, 44] The growth rate of each crystal plan depends on the coverage of surfactant on the respective plan. Oleate molecules attach preferentially to the lowest energy [100] crystal plane and inhibit the growth of the NPs in the respective direction by forming a dense layer. The hindered growth of the [100] and faster growth of [111] or [110] planes yields truncated and cubic NPs.[7, 33, 41, 69-71] At low surfactant concentration the surfactant layer is not dense enough to reduce the growth of the [100] plane, thus more spherical shape are formed, and the shape anisotropy is not pronounced.[7, 35] At high surfactant concentration, the shape of the NPs change from semi-spherical to more truncated NPs. We note the surfactant also play a role as a monomer stabilizer and control the size. The observed trend of increasing the size of the NPs by increasing surfactants amount can be rationalized by the formation of more stable monomer upon adding more surfactants amount. As the amount of surfactants increases, more oleate molecules ($RCOO^-$) react with the precursor and bind to monomer, which leads to the formation of more stable monomers with, reduced reactivity. According to LaMer's model,[68] a reduced active monomer concentration reduces the nucleation leading to the formation of less nuclei. As a result of the reduction in nucleation, nanoparticles with bigger size forms. [34, 36, 39, 72-76]

(iii) Precursor concentration

Changing the concentration of precursor in the reaction medium was obtained in two different ways: (1) by changing the amount of solvent or (2) by varying the amount of precursors.

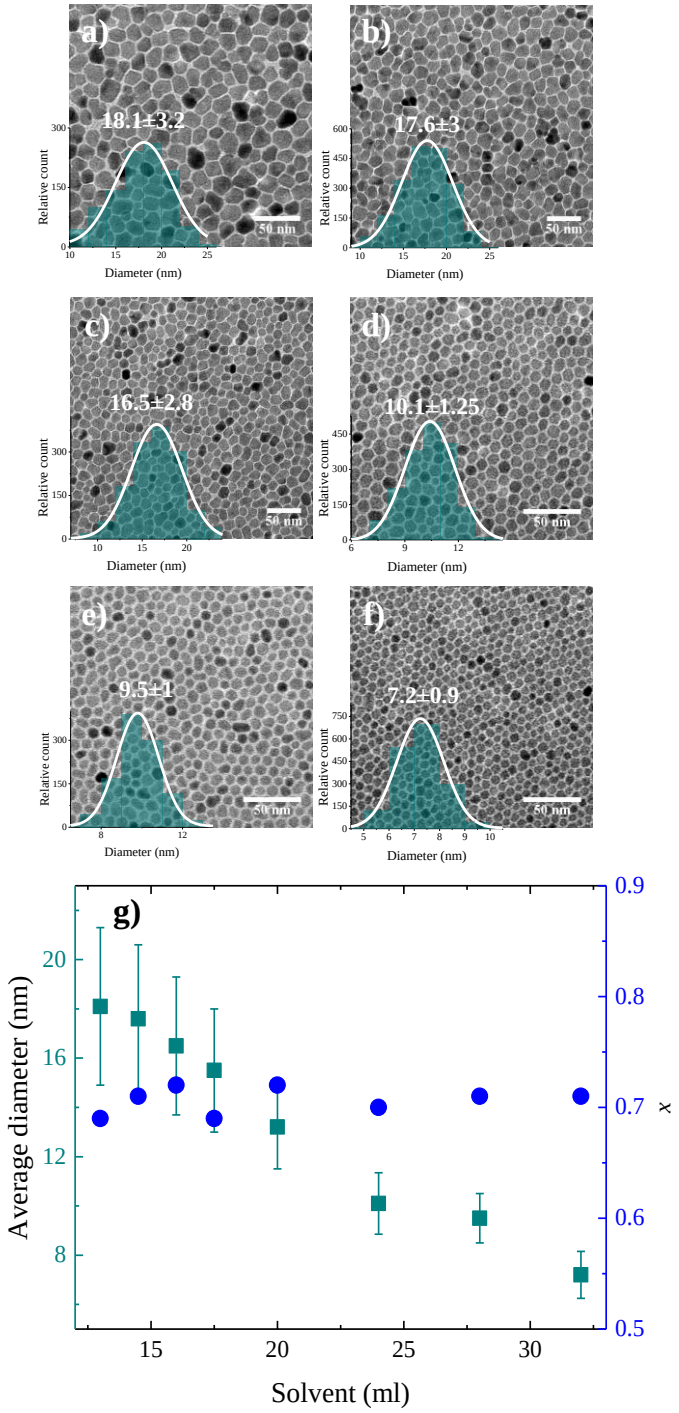

Figure 4.10 TEM images of the NPs prepared with different amount of solvent (a) 13 (A_{25}), (b) 14.5 (A_{26}), (c) 16 (A_{27}), (d) 20 (A_{10}) (e) 24 (A_{29}), (f) 28 (A_{30}) and (g) 32 (A_{31}) ml with their corresponding size distribution histogram (see **Table 4.2** for details of the reaction conditions). (h) The average diameter and the cobalt stoichiometry of the NPs as a function of solvent amount.

(1) The amount of solvent in the reaction medium was varied from 13 ml to 32 ml, while keeping the other reaction parameters unchanged (detail in **Table 4.2**). TEM images of NPs with their corresponding size distribution histograms are shown in **Figure 4.10 a-g**. The average diameter of the $Co_xFe_{3-x}O_4$ NPs as a function of solvent volume is shown in **Figure 4.10 g**. By increasing the amount of solvent from 13 ml to 32 ml, the average diameter of the nanoparticle dropped monotonously from 18.1 nm to 7.2 nm. For all the $Co_xFe_{3-x}O_4$ NPs, ICP measurements showed that changing the amount of solvent does not influence the stoichiometry value of x in $Co_xFe_{3-x}O_4$ and it remains unchanged (x~ 0.69-0.72) for all sizes (as depicted in **Figure 4.10 g**).

Similar size drop with the amount of solvent has been shown in previous chapter for the growth of iron oxide NPs.[39] The solvent in the reaction medium has only a dilution effect on the growth species. At high solvent amount, (hence low precursor concentration), diffusion distance for the growth species from the bulk solution to the surface of the growing NPs becomes large. The diffusion therefore becomes the limiting step in the growth process, lowering the growth rate and yielding smaller NPs. At low amount of solvent, the concentration of the growth species in the bulk solution is high such that the concentration of growth species at the interface of nuclei and in the bulk solution are nearly equal. Under these conditions, the diffusion distance is shorter, leading to higher mass transfer and growth rates and therefore larger NPs. [39, 72, 77-79]

(2) Amount of precursor ($Fe(acac)_3$ + $Co(acac)_2$) in the standard synthesis was changed from 1 to 8 mmol, while the ratio of $Co(acac)_2/Fe(acac)_3$= 0.5 was fixed. All other synthesis parameters were unchanged (detail in **Table 4.2**). [39, 72, 78] **Figure 4.11 a-f** shows TEM images of samples with different precursor concentration with their corresponding size distribution histogram.

The size evolution of the NPs is given in **Figure 4.11 g**. Similar to iron oxide NPs (Section 2 of Chapter 3) two different size regimes were observed (marked with yellow and green). In the yellow regime, the concentration of the precursor is low. The size of the nanoparticles increased from 7.1 ± 0.85 nm to 13.2 ± 1.7 nm by increasing the total amount of the precursors from 1 to 3 mmol. The change in precursor concentration in the yellow region has only dilution effect, similar to the case of solvent. The trend of increasing in size was held up to

a precursor's concentration of 3 mmol, beyond which the nanoparticle size continuously dropped (the green regime).

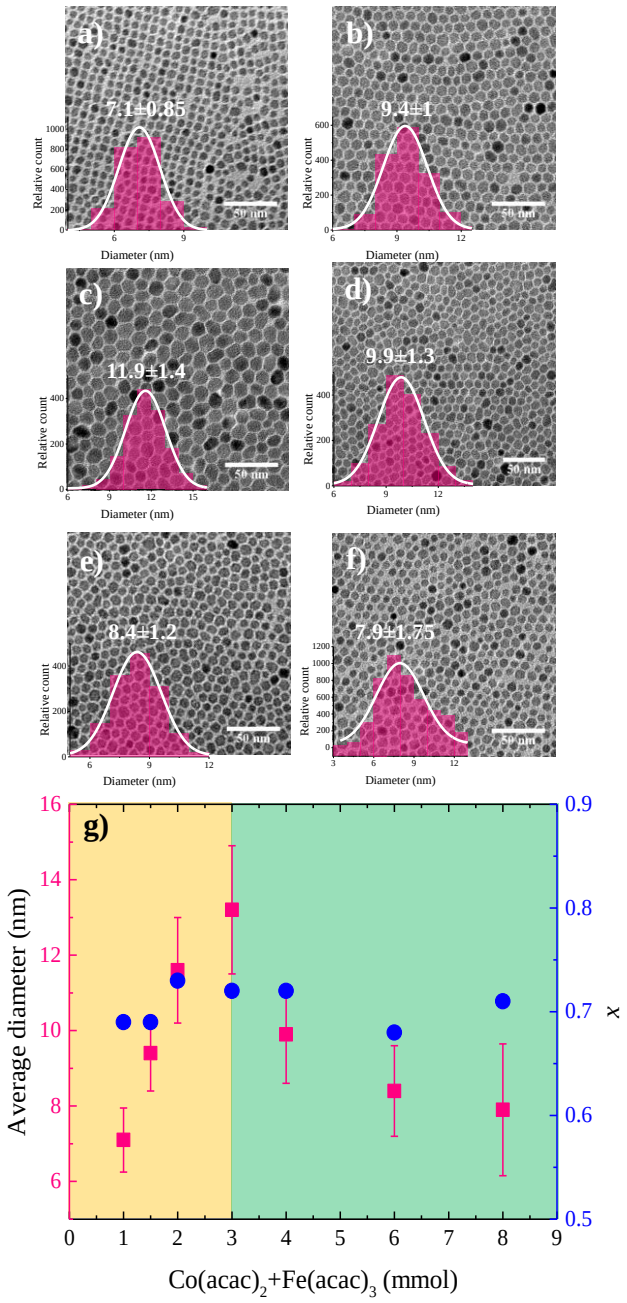

Figure 4.11 TEM images of the NPs with different total precursors amount ($Co(acac)_2/Fe(acac)_3$ = 0.5) of (a) 1 (A_{32}), (b) 1.5 (A_{33}), (c) 2 (A_{34}), (d) 3 (A_{10}), (e) 4 (A_{35}), (f) 6 (A_{36}) and (g) 8 (A_{37}) mmol with their corresponding size distribution histogram (see **Table 4.2** for details of the reaction conditions). (h) The average diameter and the cobalt stoichiometry of NPs as a function of total precursor's amount.

The drop in the green regime is attributed to the reduction of the amount of surfactants available for the stabilization of the monomers (as explained in details in Chapter 3). The saturation concentration of the active monomers increases and more nuclei are formed, which based on LaMer' theory, leads to formation of the NPs with smaller size. The results are in agreement for our previous result of Fe_3O_4.[39]

Finally, we performed ICP to determine the cobalt content. The value of *x* remains almost unchanged by changing the size of NPs via varying the amount of precursors (**Figure 4.11 g**). The ICP measurements of the size tuned NPs showed that the cobalt stoichiometry in the $Co_xFe_{3-x}O_4$ NPs is insensitive to the variation of the aforementioned reaction parameters, and is only sensitive to the $Co(acac)_2/Fe(acac)_3$ feed ratio. We note that we have not investigated the influence of the reaction time and growth temperature on the final stoichiometry of the NPs. However, Sun *et al*[6] have demonstrated increase in the *x* value for prolonged reaction times.

Moreover, we performed XRD measurements on the size tuned NPs obtained from the different syntheses batches. For the size tuned NPs, the XRD patterns, **Figure 4.12**, matched well with the bulk pattern of the stoichiometric $CoFe_2O_4$ spinel ferrite crystal structure (JSPDC card number 22−1086) without any traces of impurities like FeO, CoO, or Co_3O_4. The series of diffractograms (**Figure 4.12**) reveals the expected gradual narrowing of the peaks associated with the increase of average diameter. The values of lattice parameter for NPs with size 18.2 nm (A_{18}), 15.5 nm (A_{20}), 13.2 nm (A_{10}), 11.5 nm (A_{21}) and 8.7 nm (A_{23}) are 8.437, 8,423, 8.407, 8.357 and 8.346 A° respectively, which is increasing via increasing the size of NPs. The observed enhancement of lattice parameter via increasing the size of ferrite NPs are in agreement with previous reports and similar to iron oxide.[22, 36-37] These values are slightly higher than the one of bulk $CoFe_2O_4$ (8.391 A, JCPDS file 22-1086) which can be assigned either to a lower concentration in cobalt or to a different cationic distribution.[26]

Furthermore, EFTEM on the NPs with the size of 13.2 and 18.2 nm, as shown in **Figure 4.2 d**, showed a homogenous distribution of Co and Fe within the NPs. No evidence for the core-shell and Co or Fe enriched structures (on the surface or bulk) were observed (in agreement with the XRD findings).

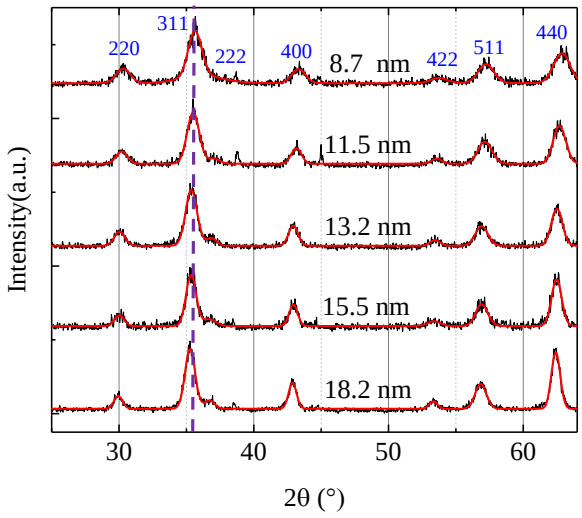

Figure 4.12 XRD diffractograms of cobalt ferrite NPs with different sizes and same cobalt content of *x*~0.7.

The *M-H* hysteresis curves of the $Co_{0.7}Fe_{2.3}O_4$ NPs with different sizes (ranging from 6.8-22.5 nm) were recorded at 300 K and 2 K, as shown in **Figure 4.13**. At 2 K, all loops exhibited nonzero M_r and H_C. At 300 K, the NPs smaller than 10 nm showed superparamagnetic and those larger than 10 nm showed ferri/ferromagnetic behavior.[3-5] We note that at 2 K, most of the NPs showed the bi-magnetic behavior, which we discussed in detail earlier.

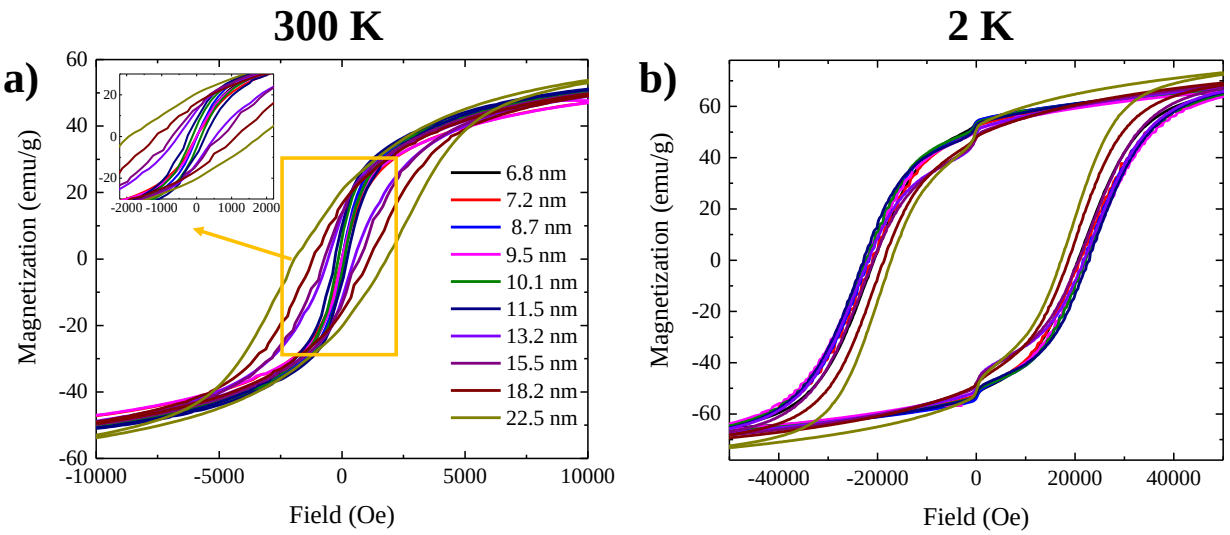

Figure 4.13 *M-H* hysteresis loops at (a) 300 K and (b) 2 K of samples with different size and fixed cobalt stoichiometry of *x*~ 0.7.

The evolution of H_C, M_S and M_r/M_S as a function of the NP size is shown in **Figure 4.14 a-c**. A non-monotonous dependence of H_C with average diameter was observed, **Figure 4.14 a**, in accordance with previous reports.[4-5, 22, 80] At 300 K, the NPs with an average diameter below 10 nm, are superparamagnetic and show hysteresis-free *M-H* curves. For the NPs larger than 10 nm, H_C showed a linear growth with the NPs' size, and reached 1884 Oe for the NPs with average diameter of 22.5 nm. At 2 K however, H_C initially increased until it reaches the maximum value of 22.8 kOe for an average diameter of 11.5 nm. To the best of our knowledge, H_C is the highest reported values for cobalt ferrite NPs in this range of size. [5-6, 12, 22, 26] For the NPs with average diameter beyond 11.5 nm, H_C dropped. The observation of the maxima in H_C at 2 K can be ascribed to transition from a magnetic single domain NP to a multi-domain one,[3, 36, 80-84] or to the combination of a crossover on magnetic rotation (changing from uniform coherent rotation of all atomic spins to an incoherent curling mode).[22, 50, 85] It has been also shown that at higher temperature this non-monotonic behavior shifts to larger NP size.[22, 85] However, we did not observe this behavior in the range of the NPs sizes investigated here. M_S showed the same increasing trend with increasing the NPs size at both 300 K and 2 K (**Figure 4.14 b**). The M_S values are in accordance with the previously reported values.[5, 22, 26, 33, 36-37, 79, 86-87] To the best of our knowledge, H_C is the highest reported values for cobalt-ferrite NPs in this range of particle size. To substantiate our claim, we have provided in **Table 4.3** a comparison of the reported H_C and M_S, T_B and M_r/M_S both at room-temperature and at low-temperature between literature and the present work.

The squareness, M_r/M_S, showed different behavior at 2 K and 300 K (**Figure 4.14 c**). At 2 K, squareness, remained unchanged at 0.75 for the NP size below 12 nm, and only slightly changed to 0.70 at NP sizes larger than 12 nm. The squareness values of M_r/M_S at 2 K are in good agreement with the theoretically expected ones for randomly oriented cobalt-ferrite nano grains.[5, 22] At 300 K however, the squareness was zero for the NP sizes below 10 nm, and then gradually increased to 0.25 for the NP sizes above 15 nm. On the other hand, the values of M_r/M_S at room T, due to thermal effects, is lower and the variation in M_r/M_S values are more pronounce via changing the size of NPs.[5, 22, 88]

Variation in the NP size, substantially changes T_B. We therefore performed ZFC and FC measurements (inset of **Figure 4.14 d**). The $Co_{0.7}Fe_{2.3}O_4$ NPs smaller than 10 nm showed T_B below the room temperature (300 K).[3] NPs larger than 10 nm showed T_B > 300 K and therefore blocked magnetization at room temperature. We have therefore identified the lowest size limit of 10 nm for the cobalt ferrit NPs with the optimized cobalt stoichiometry (x ~ 0.7) at which the nanoparticles showed remanence and coercivity at room temperature.

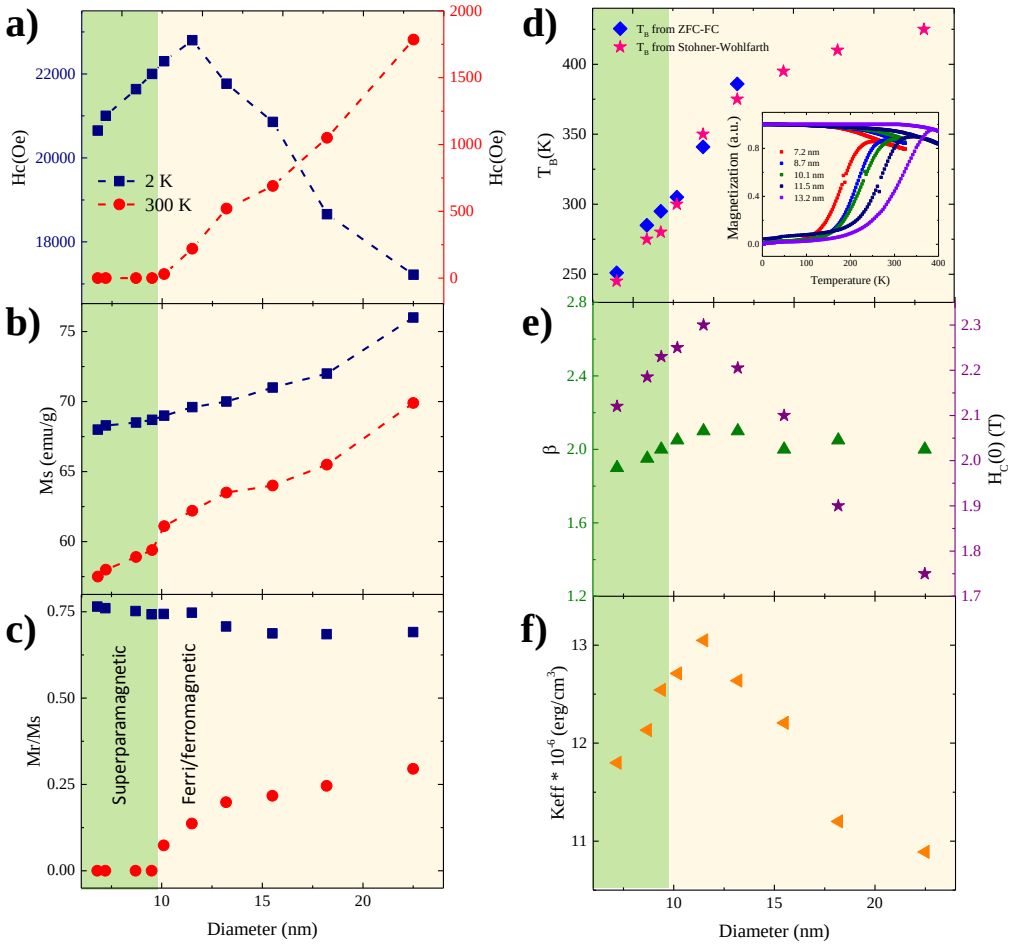

Figure 4.14 Evolution of (a) H_C, (b) M_S and (c) M_r/M_S as a function of average diameter of NPs in a fixed cobalt content of ~ 0.7. (d) Size dependence of the blocking temperature, T_B , which obtained via ZFC-FC measurement (balk dots) or by fitting H_C versus T curves to the Stohner-Wohlfarth equation, $H_C = H_C(0)[1-(T/T_B)]^{\beta}$ (redo dots). (e) Effective magnetic anisotropy, K_{eff}, of cobalt ferrite with different sizes in a fixed cobalt content of 0.7 and (f) the value of β and $H_C(0)$ as a function of average diameter of NPs. The inset of (d) shows ZFC and FC curves of samples with different size and fixed cobalt content of x~ 0.7. Superparamagnetic and ferri/ferromagnetic regions are marked with green and yellow, respectively.

For the NPs larger than 14 nm, T_B can not be measured due to limitation of our VSM setup. We therefore estimated T_B using the SW model (**Equation 4.3**).[22, 57-58] To estimate the value of T_B, *M-H* loops at different temperature were measured to extract H_C as a function of temperature (**Figure 4.15 a**). Subsequently, the value of T_B was calculated using **Equation 4.3**. The calculated T_B for the small NPs matched well the experimentally extracted ones from ZFC magnetization curves, supporting the validity of this approach. The calculated T_B increased with increasing NPs size.[89] The values of β (**Figure 4.14 e**) are also in the range of $1.9 < \beta < 2.1$ which matches well for the previous reported values for metal ferrite NPs.[22]

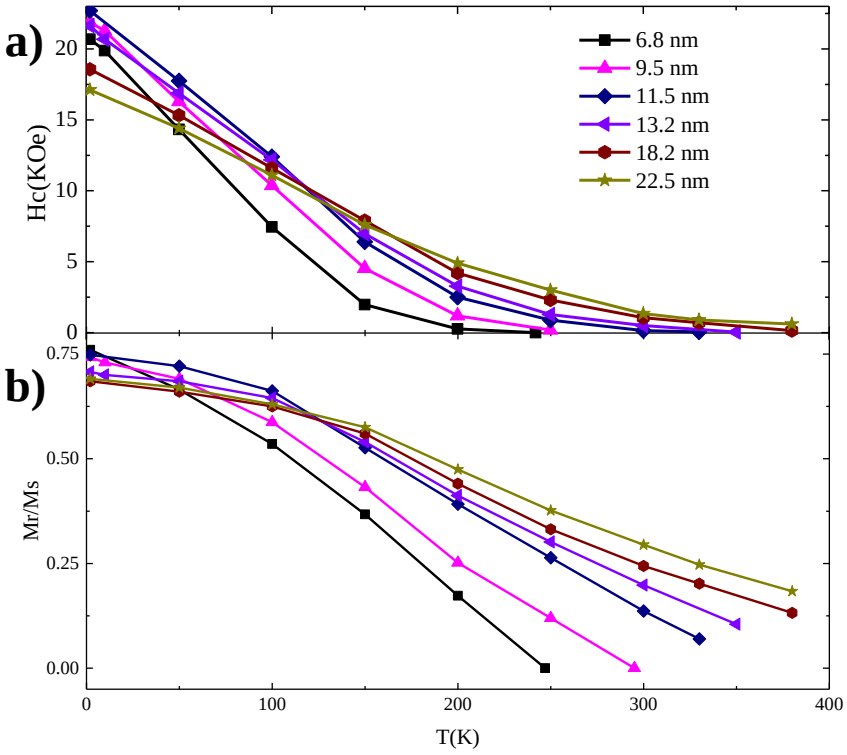

Figure 4.15 Evolution of (a) H_C and (b) M_r/M_S as a function of temperature for different size of NPs in a fixed cobalt content of x~ 0.7.

The calculated K_{eff} [22, 61-62] as a function of particle size, **Figure 4.14 f**, showed a linear increase as the particle size increased from 7.8 nm to 11.4 nm, where K_{eff} showed a maximum value of 13.1×10^6 erg/cm^3 (comparable with K_{eff} value for the stoichiometric bulk $CoFe_2O_4$ (19×10^6 erg/cm^3).[22, 66]

In addition, temperature dependence of H_C and M_r/M_S changs with the size of the NPs, as shown in **Figure 4.15 a** and **b**. H_C always showed reduction with increasing temperature (**Figure 4.15 a**) with different curvatures for different sizes,[22, 85] linear for the small and convex for the large NPs.[22] The squareness, M_r/M_S, **Figure 4.15 b**, decays linearly with temperature for the small NPs while for the large NPs, initially shows a plateau at low temperatures followed by a smooth drop upon increasing temperature.[22]

4.4 Conclusion

The magnetic properties of $Co_xFe_{3-x}O_4$ NPs are thoroughly investigated as function of varying cobalt stoichiometry and size. The NPs have been synthesized by thermal decomposition of cobalt and iron precursors. By changing the cobalt to iron precursor feed ratio, the cobalt stoichiometry is varied from 0 to 1.5, at a fixed NP size (~ 13 nm). We have experimentally shown that the variation of the reaction heating rate, and the amount of solvent, precursor, does not affect the stoichiometry and only modifies the nanoparticle size. We have determined the best range for cobalt stoichiometry where the NPs show stable remanent magnetization at room-temperature. The optimum x value is in the range of 0.5-0.7 at which the NPs have exhibited the highest H_C, M_r/M_S, T_B and K_{eff}, suited for room-temperature applications of the cobalt-ferrite NPs as nano-magnets. Within the framework of LaMer's theory of nucleation and growth, we have explained how variation in the reaction heating rate and solvent/precursor/surfactant concentration enable fine-tuning of the NP size. We have experimentally showed that the NPs with a size smaller than 11.5 nm, are composed of single magnetic domains, whereas larger nanoparticles are composed of magnetic multi domains. Furthermore, we unambiguously show that the commonly observed bi-magnetic behavior of cobalt-ferrite NPs is due the inter-particle magnetic interactions. Finally, at an optimum cobalt stoichiometry (x ~ 0.7), we have achieved room-temperature stability of remanent magnetization for NPs with diameter as small as 10 nm, which is highly promising for instance for multiferroic polymer nanocomposites and magnetic non-volatile memory applications.

Table 4.3 Comparison of the values for H_C, M_S, M_r/M_S and T_B reported in literatures[a] and in this work for cobalt ferrite NPs.

Ref.	***x*** $Co_xFe_{3-x}O_4$	**Size** (nm)	$\mathbf{M_S}$ (emu/g)	$\mathbf{M_r/M_S}$	$\mathbf{H_C}$ (Oe)	$\mathbf{M_S}$ (emu/g)	$\mathbf{M_r/M_S}$	$\mathbf{H_C}$ (Oe)	$\mathbf{T_B}$ (K)
			Room temperature			**Low temperature** [b]			
[4]	0.6	20 ± 1	55	-	810	-	-	-	-
		15 ± 0.6	47	-	170	-	-	-	-
		10	40	-	15	-	-	-	-
[5]	0.1	20 ± 2	75	-	100	87	-	9000	-
	0.3	20 ± 1.8	65	-	700	85	-	9500	-
	0.4	20 ± 2	68	-	750	75	-	11000	-
	0.5	20 ± 1.5	60	0.46	1100	70	0.82	13500	-
	0.6	20 ± 2	50	-	1000	71	-	12000	-
	0.7	20 ± 2.3	45	-	450	60	-	7500	-
	0.85	20 ± 2.2	60	-	300	80	-	8000	-
	1	15 ± 2	47	-	670	57	-	9300	-
		19 ± 2	48	-	300	64	-	8000	-
		20 ± 2.5	40	-	500	55	-	7500	-
		27 ± 3	62	0.32	400	74	0.71	7000	-
[22]	1	4 ± 1	48	SPM[c]	no	59.4	0.5	11000	85
		7 ± 1	65	SPM	no	77.4	0.78	13500	220
		11 ± 1	64	SPM	no	80	0.77	14700	300
		20 ± 2	80	0.48	950	85.5	0.82	16700	420
		30 ± 4	85	0.5	1550	89.1	0.79	12100	487
		40 ± 7	82	0.56	2900	88.7	0.77	10000	545
		60 ± 4	82	0.48	2100	84.7	0.75	8000	619
[9]	0.06	6.3 ± 1.13	74.7	SPM	no	83.3	0.45	2000	70
	0.12	5.9 ± 0.76	79.8	SPM	no	93.7	0.64	5000	118
	0.19	6 ± 0.9	65.6	SPM	no	71.6	0.70	10000	145
	0.37	6 ± 0.72	69.2	SPM	no	83.4	0.83	15000	178
	0.42	6.4 ± 0.64	75.2	SPM	no	80.9	0.83	17000	220
	0.55	6.4 ± 0.64	80.5	SPM	no	85.4	0.84	20000	230
[6]	0.2	35 ± 4	-	-	300	-	-	-	-
	0.4	35 ± 4	-	-	1050	-	-	-	-
	0.6	35 ± 4	-	-	1250	-	-	-	-
	1	35 ± 4	-	-	1100	-	-	-	-
	1.2	35 ± 4	-	-	1000	-	-	-	-
	0.6	35 ± 4	81.8	0.66	1690	-	-	-	-
	0.9	35 ± 4	90.3	0.6	1180	-	-	-	-
[26]	1	8 ± 1.6	-	SPM	0	38	-	19000	212
		15.7 ± 2.6	-	-	-	68	-	20600	340

Ref.	*x* $Co_xFe_{3-x}O_4$	Size (nm)	M_S (emu/g)	M_r/M_S	H_C (Oe)	M_S (emu/g)	M_r/M_S	H_C (Oe)	T_B (K)
			Room temperature			**Low temperature** [b]			
[33]	1	5	-	-	-	77	0.51	11000	150
		8	-	-	-	79	0.54	14000	245
		10	-	-	-	80	0.65	17000	280
		12	-	-	-	81	0.72	18000	340
		13	-	-	-	80	0.72	14000	410
		8	-	-	-	80	0.62	9000	270
		9	-	-	-	80	0.68	10000	330
		10	-	-	-	79	0.76	11000	360
		11	-	-	-	80	0.75	7500	400
[79]	1	11.9 ± 2	50	0.08	180	54	0.4	17250	-
[90]	1	16	-	-	400	-	-	20000	-
[91]	1	9.5	68	SPM	no	82	-	12500	-
[92]	1	8.1 ± 4.9	67	-	7	79	-	17200	270
		8.8 ± 5.3	60	SPM	no	70	-	15100	222
		12.2 ± 7.4	30	-	60	35	-	9100	>300
[93]	0.9	5 ± 0.8	24	SPM	no	30		4875	42
	0.54	8.8 ± 1.3	43	SPM	no	54	-	20064	182
	0.77	11 ± 1.6	51	SPM	no	61	-	11500	259
	0.68	13.3 ± 1.3	76	SPM	no	86	-	20064	306
	0.67	14.3 ± 2.6	57	-	-	66	-	20064	345
	0.61	16.8 ± 1.7	47	-	-	55	-	17500	>400
	0.66	18.6 ± 2.1	47	-	-	57	-	18750	>400
	0.7	25 ± 4.1	48	-	-	53	-	12875	>400
[94]	1	17.5	56	-	800	-	-	-	
		21	65	-	1080	-	-	-	263
		24	68	0.43	1250	40.8	0.85	11000	267
		26	70	-	1150	-	-	-	
		32	72	-	1100	-	-	-	270
		38	75	-	650	-	-	-	-
		42	76	-	300	-	-	-	-
		48	79	-	330	-	-	-	-
This work	0.1	12.3 ± 1.2	70.2	SPM	no	79	0.7911	8302.5	260
	0.185	12.5 ± 1.4	70	0.086	120	78.1	0.7938	14820	340
	0.26	12.7 ± 1.6	69.7	0.168	285	77.5	0.7935	18537	374
	0.45	12.5 ± 1.6	68.4	0.201	555	76	0.7852	21100	384
	0.58	12.7 ± 1.7	66.7	0.217	600	74	0.7162	21640	392
	0.72	13.2 ± 1.7	63.15	0.2	610	69.5	0.7093	21765	386
	0.83	13.7 ± 1.8	58.7	0.19	600	65.9	0.6418	20518	-
	0.93	14.1 ± 2.4	56	0.187	590	62.8	0.6098	20905	375

Ref.	x $Co_xFe_{3-x}O_4$	Size (nm)	M_S (emu/g)	M_r/M_S	H_C (Oe)	M_S (emu/g)	M_r/M_S	H_C (Oe)	T_B (K)
			Room temperature			Low temperature [b]			
	1.17	14 ± 2.2	46.5	0.174	540	53	0.5849	20300	-
	1.25	13.5 ± 2.6	36.1	0.155	505	43.5	0.5632	19000	348
	1.32	14.1 ± 4	33.2	0.150	480	38.3	0.5065	18000	-
	1.52	13.9 ± 3.7	17.3	0.121	325	20.3	0.4433	15762	336
	~ 0.7	6.8 ± 0.8	57.5	SPM	0	68	0.7647	20650	-
		7.2 ± 0.95	58	SPM	0	68.3	0.7598	21000	251
		8.7 ± 0.95	58.9	SPM	0	68.5	0.7518	21635	285
		9.5 ± 1	59.4	SPM	0	68.7	0.7423	22000	295
		10.1 ± 1.2	61.1	0.0736	30	69	0.7434	22300	305
		11.5 ± 1.4	62.2	0.1366	150	69.6	0.7471	22800	341
		13.2 ± 1.7	63.5	0.1984	520	70	0.7071	21765	386
		15.5 ± 2.5	64	0.2171	650	71	0.6873	20855	395[d]
		18.2 ± 4	65.5	0.2458	1050	72	0.6847	18660	410[d]
		22.5 ± 4	69.9	0.2949	1785	76	0.6907	17220	425[d]

[a] The literature values are extracted by digitizing the reported *M-H* loops. [b] The low temperature measurements are performed at 5 K in references [5], [22], [26], [33], [79], [92] and [93], at 10 K in reference [90] and [91] at 15 K in reference [9], at 77 K in reference [94] and finally at 2 K in present work. [c] SPM stands for superparamagnetic behavior. [d] Calculated from Stohner-Wohlfarth.

4.5 References

1. Sharifi Dehsari, H.; Ksenofontov, V.; Möller, A.; Jakob, G.; Asadi, K., Determining Magnetite/Maghemite Composition and Core-Shell Nanostructure from Magnetization Curve for Iron Oxide Nanoparticles. *The Journal of Physical Chemistry C* **2018**.
2. Frenkel, J.; Doefman, J., Spontaneous and induced magnetisation in ferromagnetic bodies. *Nature* **1930,** *126*, 274.
3. Kolhatkar, A. G.; Jamison, A. C.; Litvinov, D.; Willson, R. C.; Lee, T. R., Tuning the magnetic properties of nanoparticles. *Int. J. Mol. Sci.* **2013,** *14*, 15977-16009.
4. Wu, L.; Jubert, P.-O.; Berman, D.; Imaino, W.; Nelson, A.; Zhu, H.; Zhang, S.; Sun, S., Monolayer Assembly of Ferrimagnetic Co x Fe3–x O4 Nanocubes for Magnetic Recording. *Nano Lett.* **2014,** *14*, 3395-3399.
5. Sathya, A.; Guardia, P.; Brescia, R.; Silvestri, N.; Pugliese, G.; Nitti, S.; Manna, L.; Pellegrino, T., Co x Fe3–x O4 Nanocubes for Theranostic Applications: Effect of Cobalt Content and Particle Size. *Chem. Mater.* **2016,** *28*, 1769-1780.
6. Yu, Y.; Mendoza-Garcia, A.; Ning, B.; Sun, S., Cobalt-substituted magnetite nanoparticles and their assembly into ferrimagnetic nanoparticle arrays. *Adv. Mater.* **2013,** *25*, 3090-3094.

7. Lu, L. T.; Dung, N. T.; Tung, L. D.; Thanh, C. T.; Quy, O. K.; Chuc, N. V.; Maenosono, S.; Thanh, N. T., Synthesis of magnetic cobalt ferrite nanoparticles with controlled morphology, monodispersity and composition: the influence of solvent, surfactant, reductant and synthetic conditions. *Nanoscale* **2015,** *7*, 19596-19610.
8. López-Ortega, A.; Lottini, E.; Bertoni, G.; de Julián Fernández, C.; Sangregorio, C., Topotaxial phase transformation in cobalt doped iron oxide core/shell hard magnetic nanoparticles. *Chem. Mater.* **2017,** *29*, 1279-1289.
9. Li, D.; Yun, H.; Diroll, B. T.; Doan-Nguyen, V. V.; Kikkawa, J. M.; Murray, C. B., Synthesis and Size-Selective Precipitation of Monodisperse Nonstoichiometric M x Fe3–x O4 (M= Mn, Co) Nanocrystals and Their DC and AC Magnetic Properties. *Chem. Mater.* **2016,** *28*, 480-489.
10. Mameli, V.; Musinu, A.; Ardu, A.; Ennas, G.; Peddis, D.; Niznansky, D.; Sangregorio, C.; Innocenti, C.; Thanh, N. T.; Cannas, C., Studying the effect of Zn-substitution on the magnetic and hyperthermic properties of cobalt ferrite nanoparticles. *Nanoscale* **2016,** *8*, 10124-10137.
11. Schultz-Sikma, E. A.; Joshi, H. M.; Ma, Q.; MacRenaris, K. W.; Eckermann, A. L.; Dravid, V. P.; Meade, T. J., Probing the chemical stability of mixed ferrites: implications for magnetic resonance contrast agent design. *Chem. Mater.* **2011,** *23*, 2657-2664.
12. Park, J.; An, K.; Hwang, Y.; Park, J.-G.; Noh, H.-J.; Kim, J.-Y.; Park, J.-H.; Hwang, N.-M.; Hyeon, T., Ultra-large-scale syntheses of monodisperse nanocrystals. *Nat. Mater.* **2004,** *3*, 891-895.
13. Bodnarchuk, M. I.; Kovalenko, M. V.; Groiss, H.; Resel, R.; Reissner, M.; Hesser, G.; Lechner, R. T.; Steiner, W.; Schäffler, F.; Heiss, W., Exchange-Coupled Bimagnetic Wüstite/Metal Ferrite Core/Shell Nanocrystals: Size, Shape, and Compositional Control. *Small* **2009,** *5*, 2247-2252.
14. Lima Jr, E.; Winkler, E. L.; Tobia, D.; Troiani, H. E.; Zysler, R. D.; Agostinelli, E.; Fiorani, D., Bimagnetic CoO Core/CoFe2O4 shell nanoparticles: synthesis and magnetic properties. *Chem. Mater.* **2012,** *24*, 512-516.
15. Noh, S.-h.; Na, W.; Jang, J.-t.; Lee, J.-H.; Lee, E. J.; Moon, S. H.; Lim, Y.; Shin, J.-S.; Cheon, J., Nanoscale magnetism control via surface and exchange anisotropy for optimized ferrimagnetic hysteresis. *Nano Lett.* **2012,** *12*, 3716-3721.
16. Frey, N. A.; Peng, S.; Cheng, K.; Sun, S., Magnetic nanoparticles: synthesis, functionalization, and applications in bioimaging and magnetic energy storage. *Chem. Soc. Rev.* **2009,** *38*, 2532-2542.
17. De, M.; Ghosh, P. S.; Rotello, V. M., Applications of nanoparticles in biology. *Adv. Mater.* **2008,** *20*, 4225-4241.
18. Kim, J.; Piao, Y.; Hyeon, T., Multifunctional nanostructured materials for multimodal imaging, and simultaneous imaging and therapy. *Chem. Soc. Rev.* **2009,** *38*, 372-390.
19. Reiss, G.; Hütten, A., Magnetic nanoparticles: applications beyond data storage. *Nat. Mater.* **2005,** *4*, 725-726.
20. Hyeon, T., Chemical synthesis of magnetic nanoparticles. *Chem. Commun.* **2003**, 927-934.
21. Li, S.; Ding, W.; Meitzner, G. D.; Iglesia, E., Spectroscopic and transient kinetic studies of site requirements in iron-catalyzed Fischer− Tropsch synthesis. *J. Phys. Chem. B* **2002,** *106*, 85-91.
22. López-Ortega, A.; Lottini, E.; Fernandez, C. d. J.; Sangregorio, C., Exploring the magnetic properties of cobalt-ferrite nanoparticles for the development of a rare-earth-free permanent magnet. *Chem. Mater.* **2015,** *27*, 4048-4056.
23. Lee, J.-H.; Huh, Y.-M.; Jun, Y.-w.; Seo, J.-w.; Jang, J.-t.; Song, H.-T.; Kim, S.; Cho, E.-J.; Yoon, H.-G.; Suh, J.-S., Artificially engineered magnetic nanoparticles for ultra-sensitive molecular imaging. *Nat. Med.* **2007,** *13*, 95.
24. Carey, M.; Maat, S.; Rice, P.; Farrow, R.; Marks, R.; Kellock, A.; Nguyen, P.; Gurney, B., Spin valves using insulating cobalt ferrite exchange-spring pinning layers. *Appl. Phys. Lett.* **2002,** *81*, 1044-1046.

25. Rajput, J. K.; Kaur, G., Synthesis and applications of CoFe 2 O 4 nanoparticles for multicomponent reactions. *Catal. Sci. Technol.* **2014,** *4*, 142-151.
26. Baaziz, W.; Pichon, B. P.; Liu, Y.; Grenèche, J.-M.; Ulhaq-Bouillet, C.; Terrier, E.; Bergeard, N.; Halté, V. r.; Boeglin, C.; Choueikani, F., Tuning of Synthesis Conditions by Thermal Decomposition toward Core–Shell Co x Fe1–x O@ Co y Fe3–y O4 and CoFe2O4 Nanoparticles with Spherical and Cubic Shapes. *Chem. Mater.* **2014,** *26*, 5063-5073.
27. Wang, S.-B.; Min, Y.-L.; Yu, S.-H., Synthesis and magnetic properties of uniform hematite nanocubes. *J. Physc. Chem. C* **2007,** *111*, 3551-3554.
28. Chen, Y.-X.; Chen, S.-P.; Zhou, Z.-Y.; Tian, N.; Jiang, Y.-X.; Sun, S.-G.; Ding, Y.; Wang, Z. L., Tuning the shape and catalytic activity of Fe nanocrystals from rhombic dodecahedra and tetragonal bipyramids to cubes by electrochemistry. *J. Am. Chem. Soc.* **2009,** *131*, 10860-10862.
29. Mazarío, E.; Herrasti, P.; Morales, M.; Menéndez, N., Synthesis and characterization of CoFe2O4 ferrite nanoparticles obtained by an electrochemical method. *Nanotechnology* **2012,** *23*, 355708.
30. Xiong, Y.; Ye, J.; Gu, X.; Chen, Q.-w., Synthesis and assembly of magnetite nanocubes into flux-closure rings. *J. Physc. Chem. C* **2007,** *111*, 6998-7003.
31. Pichon, B. P.; Gerber, O.; Lefevre, C.; Florea, I.; Fleutot, S.; Baaziz, W.; Pauly, M.; Ohlmann, M.; Ulhaq, C.; Ersen, O., Microstructural and Magnetic Investigations of Wüstite-Spinel Core-Shell Cubic-Shaped Nanoparticles. *Chem. Mater.* **2011,** *23*, 2886-2900.
32. Nidhin, M.; Nazeer, S. S.; Jayasree, R. S.; Kiran, M. S.; Nair, B. U.; Sreeram, K. J., Flower shaped assembly of cobalt ferrite nanoparticles: application as T 2 contrast agent in MRI. *RSC Adv.* **2013,** *3*, 6906-6912.
33. Song, Q.; Zhang, Z. J., Shape control and associated magnetic properties of spinel cobalt ferrite nanocrystals. *J. Am. Chem. Soc.* **2004,** *126*, 6164-6168.
34. Demortiere, A.; Panissod, P.; Pichon, B.; Pourroy, G.; Guillon, D.; Donnio, B.; Begin-Colin, S., Size-dependent properties of magnetic iron oxide nanocrystals. *Nanoscale* **2011,** *3*, 225-232.
35. Zhou, Z.; Zhu, X.; Wu, D.; Chen, Q.; Huang, D.; Sun, C.; Xin, J.; Ni, K.; Gao, J., Anisotropic shaped iron oxide nanostructures: controlled synthesis and proton relaxation shortening effects. *Chem. Mater.* **2015,** *27*, 3505-3515.
36. Baaziz, W.; Pichon, B. P.; Fleutot, S.; Liu, Y.; Lefevre, C.; Greneche, J.-M.; Toumi, M.; Mhiri, T.; Begin-Colin, S., Magnetic iron oxide nanoparticles: reproducible tuning of the size and nanosized-dependent composition, defects, and spin canting. *J. Physc. Chem. C* **2014,** *118*, 3795-3810.
37. Sharifi Dehsari, H.; Heidari, M.; Halda Ribeiro, A.; Tremel, W.; Jakob, G.; Donadio, D.; Potestio, R.; Asadi, K., Combined Experimental and Theoretical Investigation of Heating Rate on Growth of Iron Oxide Nanoparticles. *Chem. Mater.* **2017,** *29*, 9648-9656.
38. Guardia, P.; Perez-Juste, J.; Labarta, A.; Batlle, X.; Liz-Marzán, L. M., Heating rate influence on the synthesis of iron oxide nanoparticles: the case of decanoic acid. *Chem. Commun.* **2010,** *46*, 6108-6110.
39. Dehsari, H. S.; Ribeiro, A. H.; Ersöz, B.; Tremel, W.; Jakob, G.; Asadi, K., Effect of precursor concentration on size evolution of iron oxide nanoparticles. *CrystEngComm* **2017,** *19*, 6694-6702.
40. Kovalenko, M. V.; Bodnarchuk, M. I.; Lechner, R. T.; Hesser, G.; Schäffler, F.; Heiss, W., Fatty acid salts as stabilizers in size-and shape-controlled nanocrystal synthesis: the case of inverse spinel iron oxide. *J. Am. Chem. Soc.* **2007,** *129*, 6352-6353.
41. Kim, D.; Lee, N.; Park, M.; Kim, B. H.; An, K.; Hyeon, T., Synthesis of uniform ferrimagnetic magnetite nanocubes. *J. Am. Chem. Soc.* **2008,** *131*, 454-455.
42. Weller, D.; Moser, A., Thermal effect limits in ultrahigh-density magnetic recording. *IEEE Trans. Magn.* **1999,** *35*, 4423-4439.
43. Weller, D.; Doerner, M. F., Extremely high-density longitudinal magnetic recording media. *Annu. Rev. Mater. Sci.* **2000,** *30*, 611-644.

44. Sharifi Dehsari, H.; Harris, R. A.; Ribeiro, A. H.; Tremel, W.; Asadi, K., Optimizing the Binding Energy of the Surfactant to Iron Oxide Yields Truly Monodisperse Nanoparticles. *Langmuir* **2018,** *34*, 6582-6590.
45. Franco, V.; Batlle, X.; Labarta, A.; O'grady, K., The nature of magnetic interactions in CoFe-Ag (Cu) granular thin films. *J. Phys. D: Appl. Phys.* **2000,** *33*, 609.
46. Dai, Q.; Berman, D.; Virwani, K.; Frommer, J.; Jubert, P.-O.; Lam, M.; Topuria, T.; Imaino, W.; Nelson, A., Self-assembled ferrimagnet− polymer composites for magnetic recording media. *Nano letters* **2010,** *10*, 3216-3221.
47. Kelly, P.; O'Grady, K.; Mayo, P.; Chantrell, R., Switching mechanisms in cobalt-phosphorus thin films. *IEEE Trans. Magn.* **1989,** *25*, 3881-3883.
48. Wohlfarth, E., A mechanism of magnetic hysteresis in heterogeneous alloys. *Phil. Trans. R. Soc. Lond. A* **1948,** *240*, 599-642.
49. Wohlfarth, E., Relations between different modes of acquisition of the remanent magnetization of ferromagnetic particles. *J. Appl. Phys.* **1958,** *29*, 595-596.
50. Salazar-Alvarez, G.; Qin, J.; Sepelak, V.; Bergmann, I.; Vasilakaki, M.; Trohidou, K.; Ardisson, J.; Macedo, W.; Mikhaylova, M.; Muhammed, M., Cubic versus spherical magnetic nanoparticles: the role of surface anisotropy. *J. Am. Chem. Soc.* **2008,** *130*, 13234-13239.
51. Moumen, N.; Pileni, M., New syntheses of cobalt ferrite particles in the range 2− 5 nm: comparison of the magnetic properties of the nanosized particles in dispersed fluid or in powder form. *Chem. Mater.* **1996,** *8*, 1128-1134.
52. Sun, S.; Zeng, H., Size-controlled synthesis of magnetite nanoparticles. *J. Am. Chem. Soc.* **2002,** *124*, 8204-8205.
53. López-Ortega, A.; Estrader, M.; Salazar-Alvarez, G.; Estradé, S.; Golosovsky, I. V.; Dumas, R. K.; Keavney, D. J.; Vasilakaki, M.; Trohidou, K. N.; Sort, J., Strongly exchange coupled inverse ferrimagnetic soft/hard, Mn x Fe 3− x O 4/Fe x Mn 3− x O 4, core/shell heterostructured nanoparticles. *Nanoscale* **2012,** *4*, 5138-5147.
54. Ammar, S.; Helfen, A.; Jouini, N.; Fievet, F.; Rosenman, I.; Villain, F.; Molinie, P.; Danot, M., Magnetic properties of ultrafine cobalt ferrite particles synthesized by hydrolysis in a polyol mediumBasis of a presentation given at Materials Discussion No. 3, 26–29 September, 2000, University of Cambridge, UK. *J. Mater. Chem.* **2001,** *11*, 186-192.
55. Wang, S.; Khapikov, A.; Brown, S.; Harrell, J., Thermal effects on delta-M measurements in magnetic thin films. *IEEE Trans. Magn.* **2001,** *37*, 1518-1520.
56. Zeng, H.; Li, J.; Wang, Z. L.; Liu, J. P.; Sun, S., Interparticle interactions in annealed FePt nanoparticle assemblies. *IEEE Trans. Magn.* **2002,** *38*, 2598-2600.
57. Kneller, E.; Luborsky, F., Particle size dependence of coercivity and remanence of single-domain particles. *J. Appl. Phys.* **1963,** *34*, 656-658.
58. Garcıa-Otero, J.; Garcıa-Bastida, A.; Rivas, J., Influence of temperature on the coercive field of non-interacting fine magnetic particles. *J. Magn. Magn. Mater.* **1998,** *189*, 377-383.
59. Dormann, J.; D'Orazio, F.; Lucari, F.; Tronc, E.; Prené, P.; Jolivet, J.; Fiorani, D.; Cherkaoui, R.; Nogues, M., Thermal variation of the relaxation time of the magnetic moment of γ-Fe 2 O 3 nanoparticles with interparticle interactions of various strengths. *Phys. Rev. B* **1996,** *53*, 14291.
60. Cullity, B. D.; Graham, C. D., *Introduction to magnetic materials*. John Wiley & Sons: 2011.
61. Garcıa-Otero, J.; Porto, M.; Rivas, J.; Bunde, A., Monte Carlo simulation of hysteresis loops of single-domain particles with cubic anisotropy and their temperature dependence. *J. Magn. Magn. Mater.* **1999,** *203*, 268-270.
62. Usov, N.; Peschany, S., Theoretical hysteresis loops for single-domain particles with cubic anisotropy. *J. Magn. Magn. Mater.* **1997,** *174*, 247-260.

63. Praveena, K.; Sadhana, K., Ferromagnetic Properties of Zn substituted Spinel Ferrites for High Frequency Applications. *Int. J. Sci. Res. Pub.* **2015,** *5*, 1-21.
64. Fonseca, F.; Ferlauto, A.; Alvarez, F.; Goya, G.; Jardim, R., Morphological and magnetic properties of carbon–nickel nanocomposite thin films. *J. Appl. Phys.* **2005,** *97*, 044313-044319.
65. Guardia, P.; Batlle-Brugal, B.; Roca, A.; Iglesias, O.; Morales, M.; Serna, C.; Labarta, A.; Batlle, X., Surfactant Effects in Monodisperse Magnetite Nanoparticles of Controlled Size. *J. Magn. Magn. Mater* **2007,** *316*, e756-e759.
66. Shenker, H., Magnetic anisotropy of cobalt ferrite (Co 1.01 Fe 2.00 O 3.62) and nickel cobalt ferrite (Ni 0.72 Fe 0.20 Co 0.08 Fe 2 O 4). *Phys. Rev.* **1957,** *107*, 1246-1249.
67. Guardia, P.; Riedinger, A.; Nitti, S.; Pugliese, G.; Marras, S.; Genovese, A.; Materia, M. E.; Lefevre, C.; Manna, L.; Pellegrino, T., One pot synthesis of monodisperse water soluble iron oxide nanocrystals with high values of the specific absorption rate. *J. Mat. Chem. C* **2014,** *2*, 4426-4434.
68. LaMer, V. K.; Dinegar, R. H., Theory, production and mechanism of formation of monodispersed hydrosols. *J. Am. Chem. Soc.* **1950,** *72*, 4847-4854.
69. Davies, M. J.; Parker, S. C.; Watson, G. W., Atomistic simulation of the surface structure of spinel. *J. Mater. Chem.* **1994,** *4*, 813-816.
70. Gao, G.; Liu, X.; Shi, R.; Zhou, K.; Shi, Y.; Ma, R.; Takayama-Muromachi, E.; Qiu, G., Shape-controlled synthesis and magnetic properties of monodisperse Fe3O4 nanocubes. *Crystal Growth & Design* **2010,** *10*, 2888-2894.
71. Ung, D.; Tung, L. D.; Caruntu, G.; Delaportas, D.; Alexandrou, I.; Prior, I. A.; Thanh, N. T., Variant shape growth of nanoparticles of metallic Fe–Pt, Fe–Pd and Fe–Pt–Pd alloys. *CrystEngComm* **2009,** *11*, 1309-1316.
72. Hufschmid, R.; Arami, H.; Ferguson, R. M.; Gonzales, M.; Teeman, E.; Brush, L. N.; Browning, N. D.; Krishnan, K. M., Synthesis of phase-pure and monodisperse iron oxide nanoparticles by thermal decomposition. *Nanoscale* **2015,** *7*, 11142-11154.
73. William, W. Y.; Falkner, J. C.; Yavuz, C. T.; Colvin, V. L., Synthesis of monodisperse iron oxide nanocrystals by thermal decomposition of iron carboxylate salts. *Chem. Commun.* **2004**, 2306-2307.
74. Guardia, P.; Pérez, N.; Labarta, A.; Batlle, X., Controlled synthesis of iron oxide nanoparticles over a wide size range. *Langmuir* **2009,** *26*, 5843-5847.
75. Moya, C.; Batlle, X.; Labarta, A., The effect of oleic acid on the synthesis of Fe 3− x O 4 nanoparticles over a wide size range. *Phys. Chem. Chem. Phys.* **2015,** *17*, 27373-27379.
76. Vargas, J. M.; Zysler, R. D., Tailoring the size in colloidal iron oxide magnetic nanoparticles. *Nanotechnology* **2005,** *16*, 1474-1476.
77. Zeng, H.; Rice, P. M.; Wang, S. X.; Sun, S., Shape-controlled synthesis and shape-induced texture of MnFe2O4 nanoparticles. *J. Am. Chem. Soc.* **2004,** *126*, 11458-11459.
78. Huang, J.-H.; Parab, H. J.; Liu, R.-S.; Lai, T.-C.; Hsiao, M.; Chen, C.-H.; Sheu, H.-S.; Chen, J.-M.; Tsai, D.-P.; Hwu, Y.-K., Investigation of the growth mechanism of iron oxide nanoparticles via a seed-mediated method and its cytotoxicity studies. *J. Physc. Chem. C* **2008,** *112*, 15684-15690.
79. Cabrera, L. I.; Somoza, Á.; Marco, J. F.; Serna, C. J.; Morales, M. P., Synthesis and surface modification of uniform MFe2O4 (M= Fe, Mn, and Co) nanoparticles with tunable sizes and functionalities. *J. Nanopart. Res.* **2012,** *14*, 873-886.
80. Chinnasamy, C.; Jeyadevan, B.; Shinoda, K.; Tohji, K.; Djayaprawira, D.; Takahashi, M.; Joseyphus, R. J.; Narayanasamy, A., Unusually high coercivity and critical single-domain size of nearly monodispersed CoFe 2 O 4 nanoparticles. *Appl. Phys. Lett.* **2003,** *83*, 2862-2864.
81. Leslie-Pelecky, D. L.; Rieke, R. D., Magnetic properties of nanostructured materials. *Chem. Mater.* **1996,** *8*, 1770-1783.
82. Jian, G.; Fu, Q.; Zhou, D., Particles size effects of single domain CoFe 2 O 4 on suspensions stability. *J. Magn. Magn. Mater.* **2012,** *324*, 671-676.

83. Wang, J.; Zhao, F.; Wu, W.; Cao, S.-H.; Zhao, G.-m., Magnetic properties in silica-coated CoFe 2 O 4 nanoparticles: Quantitative test for a theory of single-domain particles with cubic anisotropy. *Phys. Lett. A* **2012,** *376*, 547-549.
84. Chinnasamy, C.; Jeyadevan, B.; Perales-Perez, O.; Shinoda, K.; Tohji, K.; Kasuya, A., Growth dominant co-precipitation process to achieve high coercivity at room temperature in CoFe/sub 2/O/sub 4/nanoparticles. *IEEE Trans. Magn.* **2002,** *38*, 2640-2642.
85. Maaz, K.; Mumtaz, A.; Hasanain, S.; Bertino, M., Temperature dependent coercivity and magnetization of nickel ferrite nanoparticles. *J. Magn. Magn. Mater.* **2010,** *322*, 2199-2202.
86. Smit, J.; Wijn, H. P. J., *Ferrites: physical properties of ferrimagnetic oxides in relation to their technical applications*. Eindhoven : N.V. Philips Gloeilampenfabrieken, 1959: 1959.
87. Morales, M. d. P.; Veintemillas-Verdaguer, S.; Montero, M.; Serna, C.; Roig, A.; Casas, L.; Martinez, B.; Sandiumenge, F., Surface and internal spin canting in γ-Fe2O3 nanoparticles. *Chem. Mater.* **1999,** *11*, 3058-3064.
88. Chikazumi, S.; Graham, C. D., *Physics of Ferromagnetism 2e*. Oxford University Press on Demand: 2009; Vol. 94.
89. Knobel, M.; Nunes, W.; Socolovsky, L.; De Biasi, E.; Vargas, J.; Denardin, J., Superparamagnetism and other magnetic features in granular materials: a review on ideal and real systems. *Journal of nanoscience and nanotechnology* **2008,** *8*, 2836-2857.
90. Sun, S.; Zeng, H.; Robinson, D. B.; Raoux, S.; Rice, P. M.; Wang, S. X.; Li, G., Monodisperse mfe2o4 (m= fe, co, mn) nanoparticles. *J. Am. Chem. Soc.* **2004,** *126*, 273-279.
91. Pérez-Mirabet, L.; Solano, E.; Martínez-Julián, F.; Guzmán, R.; Arbiol, J.; Puig, T.; Obradors, X.; Pomar, A.; Yáñez, R.; Ros, J., One-pot synthesis of stable colloidal solutions of MFe2O4 nanoparticles using oleylamine as solvent and stabilizer. *Mater. Res. Bull.* **2013,** *48*, 966-972.
92. Moya, C.; del Puerto Morales, M.; Batlle, X.; Labarta, A., Tuning the magnetic properties of Co-ferrite nanoparticles through the 1, 2-hexadecanediol concentration in the reaction mixture. *Phys. Chem. Chem. Phys.* **2015,** *17*, 13143-13149.
93. Torres, T.; Lima Jr, E.; Mayoral, A.; Ibarra, A.; Marquina, C.; Ibarra, M. R.; Goya, G. F., Validity of the Néel-Arrhenius model for highly anisotropic CoxFe3− xO4 nanoparticles. *J. Appl. Phys.* **2015,** *118*, 183902.
94. Maaz, K.; Mumtaz, A.; Hasanain, S.; Ceylan, A., Synthesis and magnetic properties of cobalt ferrite (CoFe2O4) nanoparticles prepared by wet chemical route. *J. Magn. Magn. Mater.* **2007,** *308*, 289-295.

Chapter 5

Surface Modification of the Magnetic Nanoparticles with PMMA Shell[1]

5.1 Introduction

The polymer multiferroic nanocomposites based on P(VDF-TrFE)/magnetic nanoparticles (MNPs) are advantageous for many applications due to their flexibility, simple fabrication, ease of processing and shaping for large area applications. However, agglomeration and eventually phase separation of the MNPs within the P(VDF-TrFE) matrix is the long standing issue. It has been well recognized that the aggregation and inhomogeneity of MNPs are the main reasons resulting in deterioration of electrical properties in polymer multiferroic nanocomposites.[1-2] The agglomeration will not only increase loss (leakage) but also give rise to low breakdown strength and consequently low functional device yield, particularly when thin films of multiferroic nanocomposites or high loadings of MNPs are used.

[1] **The results of this chapter are fully or in part are ready for submitting to *Adv. Func. Mater.* by H. Sharifi et al.**

Absence of inter-particle repulsive interactions is detrimental for obtaining a uniform dispersion because the nanoparticles favor clustering and agglomeration due to attractive inter-particle van der Waals interactions. For the case of MNPs, in particular the nano-magnets, agglomeration can be further amplified by attractive magnetic thereby impairing particle dispersion uniformity inside the matrix.

Furthermore, magnetic information storage application requires dense but well-separated (individual) nano-magnets in a two- or three dimensional arrays.[3-8] Hence, the ability to form a film with tunable packing density of nano-magnets is important. The only solution processed thin-film of nano-magnets has been reported by Dai *et al.*, where the nanoparticle are modified via grafting-to approach.[3] However, their report does not provide large-scale surface area formation of nano-magnet thin-films with controllable particle packing density (inter-particle distances). To the best of our knowledge there are not enough reports regarding solution-processed thin-films of MNPs with controllable packing density.[3]

One way to effectively overcome the aggregation of MNPs and also to make them solution processable is to functionalize the surface of them with polymer chains, which are compatible with the matrix.[9-13] Several techniques have been used for modifying the surface of the MNPs with a polymer chains.[14-17] There are two main strategies; grafting to and grafting from the MNPs.[14-15] The grafting to strategy involves the attachment of pre-synthesized polymers with a suitable end-group to the surface of MNPs, suffers from several limitations, such as steric repulsions between the polymer chains and inefficient reaction between the end-groups and the surface of the MNPs especially for high molecular weight polymers (leading to low grafting density).[14, 18-22] In grafting from strategy, growth of the polymer chains are directly initiated from the surface of MNPs resulting in high grafting density.[14-15]

Among the various grafting from approaches, surface initiated living radical polymerization (SI-LRP) is one of the most promising ones.[14, 16-17, 23] Among the different available SI-LRP techniques, atom transfer radical polymerization (ATRP) has been most extensively used to produce polymer brushes.[23-38] Compared to other LRP techniques, ATRP is chemically versatile and robust which allows precise controlling of the molecular weight and polydispersity of grafted polymer.

The first crucial step in SI-ATRP, is to functionalize the MNPs' surface with surface initiator from which the polymer brushes grow on the surface. Therefore, effective coverage of the MNP by polymer brushes is obtained by controlling the number of initiators on the surface. One of the most promising surface initiator for grafting of a wide range of polymer brushes with SI-ATRP is 2-(4-chlorosulfonylphenyl)ethyltrichlorosilane (CTCS) (**Figure 5.1)**.[30, 32, 34, 39] The second crucial step in SI-ATRP is to tune the reaction conditions such that the grafted polymer shell grows on every individual MNP, not on a bundle of particles. Various reports have employed SI-ATRP on superparamagnetic iron-oxide nanoparticles for biomedical applications. Only a limited number of reports have investigated SI-ATRP for realization of well-separated ferri/ferromagnetic MNPs.[40] The reported SI-ATRPs on MNPs have shown a wide variability in reaction conditions and the final morphology of the grafted-MNPs, *viz.* aggregated versus well-separated MNPs.[26, 28-30, 32, 34] To the best of our knowledge, a complete systematic study on the effect of different reaction parameters of SI-ATRP (temperature, concentration of initiator, superparamagnetic or ferri/ferromagnetic MNPs *etc*) on kinetic of grafting polymerization, molecular weight and PDI of grafted polymer is still lacking.

5.1.1 Motivation

To functionalize the surface of the MNPs with a polymer shell that: i) allow for solution processing of the polymer-grafted MNPs using spin-coating, ii) avoid aggregation in solution and iii) is compatible with P(VDF-TrFE) matrix which will later be used for the fabrication of the multiferroic polymer nanocomposite. The growth of the polymer chains should be achieved in a very controlled fashion. Moreover, in order to control the electrical and magnetic interaction between materials and also to tune packing density of MNPs in nanocomposite thin films, MNPs with controllable shell thickness that are homogenously dispersed inside nanocomposite are required.

5.1.2 Aim of this section

This chapter presents a systematic study from the initial state of synthesis of MNPs to the end of preparation of solution processable magnetic thin film. First, truly monodisperse and well-shaped MNPs of both superparamagnetic (Fe_3O_4) and ferro/ferrimagnetic ($CoFe_2O_4$) MNPs at

room temperature with thermal decomposition technique are synthesized. Then the surface initiator (CTCS) is anchored to the surface of MNPs (**Figure 5.1**) and the effect of different reaction parameters such as the concentration of surface initiator and the time of reaction on grafting density and grafting yield of surface initiator are investigated to obtain the optimum reaction condition.

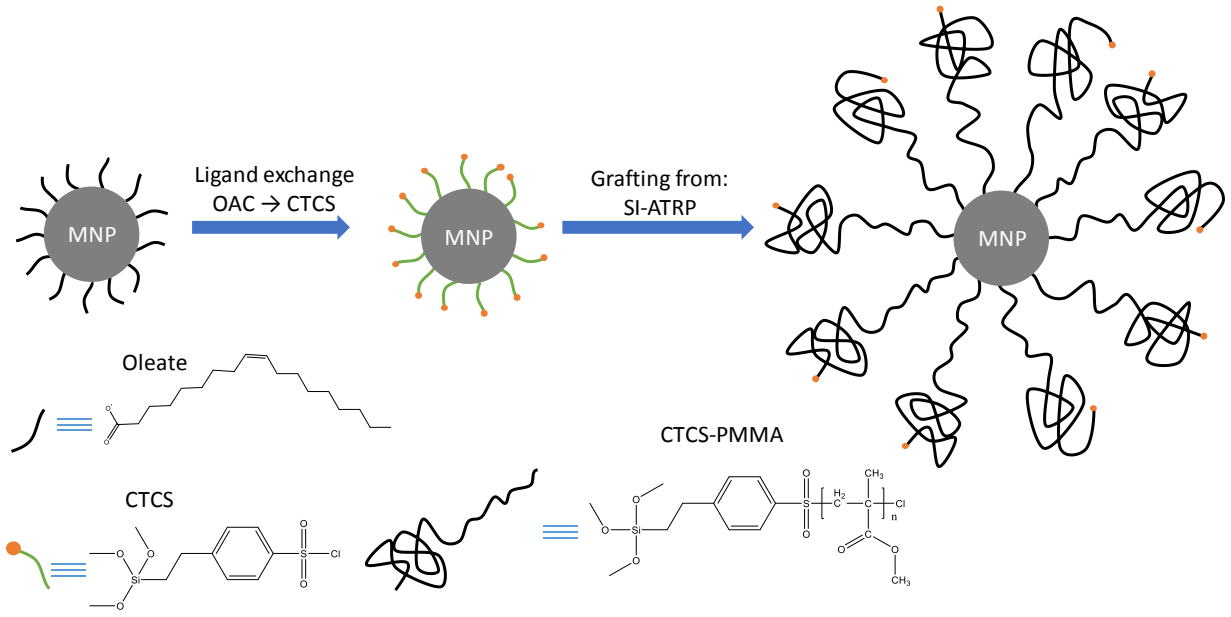

Figure 5.1 Schematic representation for the synthesis of polymer-coated MNPs by SI-ATRP.

Afterward poly methyl methacrylate (PMMA) brushes are grown from the surface of both iron oxide (superparamagnetic) and cobalt ferrite (ferri/ferromagnetic) MNPs with SI-ATRP technique (**Figure 5.1)**. We suggest a new method of SI-ATRP in which the polymerization is performed in the bath sonication in order to keep MNPs separated during reaction. The effect of different reaction parameters such as temperature and the concentration of free initiator on the kinetic of the polymerization, molecular weight of the grafted polymer, poly dispersity index (PDI) *etc*. are investigated. We change the molecular weight of polymer (at a constant PDI, and grafting density) to allow for tuning the shell thickness of PMMA brushes. Then we systematically investigate the effect of polymer shell thickness on magnetic properties and particularly inter-particle magnetic dipole-dipole interaction. Finally, superparamagnetic and ferri/ferromagnetic thin films of MNPs with different film processing techniques (dip coating

and spin coating) are fabricated. The individual nanoparticles can be realized with a packing density that is controlled by the molecular weight of the grafted PMMA-brushes.

5.2 Experiment

5.2.1 Materials

4,4′-dinonyl-2,2′-bipyridine (dNbipy, 97 %), copper(I) bromide (Cu(I)Br, 99.9 %), p-toluenesulfonylchloride (TsCl, 99 %), methyl methacrylate (MMA, 99%), hydrochloric acid (HCl), nitric acid, extra dry toluene (99.99 %), hexane, ethanol, tetrahydrofuran and acetone were all purchased from Sigma Aldrich. 2-(4-chlorosulfonylphenyl)ethyltrichlorosilane (CTCS, 50% solution in CH_2Cl_2) was purchased from ABCR. Methyl methacrylate (MMA) was purified prior to use by washing 2 times with 5 % NaOH solution to remove inhibitor, followed by washing 2 times with deionized water and then drying over anhydrous $MgSO_4$. Afterward MMA was distilled over CaH_2, then degassed by argon bubbling and stored under agron atmosphere in the fridge (-20 °C). Copper bromide was purified with glacial acetic acid (5 times washing), washed with pure ethanol (3 times washing), then washed with extra dry diethyl ether (5 times washing) and stored under argon.[41] All the other chemicals were used as received.

5.2.2 Synthesis of MNPs

Iron oxide (Fe_3O_4) and cobalt ferrite MNPs were synthesized as described in detail in Chapters 3 and 4.[42-44]

5.2.3 Fixation of ATRP-initiator on the surface of MNPs

Fixation of surface initiator was performed by exchanging oleate with CTCS (ligand exchange). In general, MNPs were dried at 60 °C under vacuum overnight. Then 100 mg of MNPs, were loaded in a two necked pre degassed flask (degassed three times and refill with argon) followed by adding 30 ml extra dry toluene under argon blanketing. The mixture was kept at 25 °C during the ligand exchange, under bath sonication (equipped with temperature controller) in order to obtain and keep a homogenous MNP dispersion. After 20 min, CTCS was added drop-wise while sonicating. The reaction was stopped after a certain time. Different

parameters such as CTCS concentration and reaction time were investigated. The modified MNPs were washed 4 times with fresh THF and 2 times toluene by consecutive separation and re-dispersion. Finally, the MNPs were dispersed in toluene and stored under argon.

5.2.4 SI-ATRP of PMMA brushes on the surface of MNPs

The initiator-fixated MNPs suspensions were re-dispersed in dry toluene (8.3 wt %) in a pyrex glass tube. Subsequently, MMA (32 g- 0.3 mol), TsCl (I_1= 19 mg (99.7 µmol), I_2= 11.4 mg (59.8 µmol) or I_3= 44 mg (231 µmol)) and dNbipy (485 mg) were quickly added. TsCl and dNbipy were used as free initiator and ligand for complexation with copper, respectively. After adding Cu(I)Br (85.2 mg) to the mixture, the glass tube was immediately degassed four times by freeze−pump−thaw cycles and sealed off under vacuum. The polymerization was carried out in a temperature controlled bath sonication (3510 Branson). Two different reaction temperatures of 65 °C (T_1) and 50 °C (T_2) were investigated. The reactions were performed on different time scales, after which the solution temperature was quenched to room temperature. To gain the polymer-grafted MNPs, the reaction mixture was diluted with acetone and centrifuged (25000 rpm, 3h). The centrifugation and re-dispersion cycle was performed five times to collect PMMA-grafted MNPs without any trace of free, unbounded PMMA chains. To determine the molecular weight of grated polymer, grafted PMMA was cleaved from the MNPs by removing of particles with 37 % aqueous HCl. 2 mL of HCl solution was added to 20 mg of MNPs dispersed in 2 mL of toluene. Then, two phases were vigorously stirred for 2 h. The organic part of solution was washed with aqueous $NaHCO_3$ solution and water, precipitated via methanol, filtered, and then subjected to GPC to determine the molecular weight and its distribution.

5.2.5 Thin film formation of MNPs

Thin films of MNPs-PMMA were prepared on thermally oxidized Si-wafers by spin coating and dip coating. Spin-coated thin-films were prepared from toluene solution (10 mg/mL) by spinning at 300 rpm for 10 s and subsequently 1000 rpm for 60 s. Dip-coated films were prepared by pouring a drop of the 1 mg/ml suspension of the PMMA-grafted MNPs in toluene on the surface of DI water in a Becher (diameter: 5 cm). Thermally oxidized Si-substrate or the copper grid for TEM measurement, were positioned in water parallel to water surface. The film

formed on the water surface, was carefully transferred onto the substrate by vertically lifting the Si-wafer or the TEM-grid with constant speed of 0.5 cm min^{-1}.[23]

5.2.6 Characterizations

Gel Permeation Chromatography (GPC) measurements were carried out on Agilent Technologies 1260 Infinity system equipped with a RI and an UV detectors. THF was used as solvent with a flow rate of 1 mg/ml and with PMMA as standard reference. Hydrodynamic radii of PMMA-grafted MNPs brushes in toluene solution (concentration of almost 1 mg/ml) were determined by dynamic light scattering (DLS) analysis using a Malvern Nano-S90. Hydrodynamic radii are reported as averaged number values.

5.3 Results and discussion

5.3.1 Magnetic nanoparticles

Representative TEM images of iron-oxide and cobalt-ferrite MNPs are shown in **Figure 5.2 a** and **b**, respectively. Fitting a Gaussian a distribution function to the size distribution histograms gives an average particle diameter of 12 ± 1 nm for iron-oxide and 12.6 ± 1.6 nm for cobalt-ferrite MNPs. The polydispersity index of MNP size is low and is nearly 15%. We note both MNPs do not show any aggregation and are well dispersed in hexane or toluene, indicating effective surface coverage by OAC surfactant molecules. However, for the cobalt-ferrite MNPs, OAC alone cannot stabilize dispersion of the particles beyond few weeks, because irreversible magnetically induced aggregation, and eventual precipitation from solution occurs.

The cobalt stoichiometry in the cobalt-ferrite nanoparticles ($Co_xFe_{3-x}O_4$) is determined by ICP-AES analysis. The value of x amounts to 0.7. We note the choice of cobalt stoichiometry of x = 0.7 is intentional because of the optimal room-temperature magnetic properties of the nanoparticles, *viz.* with the highest coercive field and remanent magnetization (detail in Chapter 4).[45-46] **Figure 5.2 c** shows magnetization of the MNPs as a function of external magnetic field at room temperature (300 K). The iron-oxide MNPs show superparamagnetic behavior, whereas the cobalt-ferrite nanoparticles show hysteresis and remanent magnetization at 300 K. Therefore

cobalt-ferrite nanoparticles are regarded as nano-magnets at 300 K. The values of M_r/M_S (squarness) and coercive field, H_C for the cobalt-ferrite nanoparticles amount to 0.19 and 465 Oe at 300 K, respectively. The values of saturation magnetizations, M_S, at magnetic field of 5 Tesla amount to 62 and 63.5 emu/g for iron-oxide and cobalt-ferrite nanoparticles, respectively, in accordance with literature.[45, 47-49] Both types of MNPs show feri/ferromagnetic behavior at 4 K (**Figure 5.2 d**). The values *of* M_S, M_r/M_S and H_C are amounted to 72 emu/g, 475 Oe and 0.32 for iron oxide MNPs and 71 emu/g, 22400 Oe and 0.74 for cobalt ferrite MNPs.

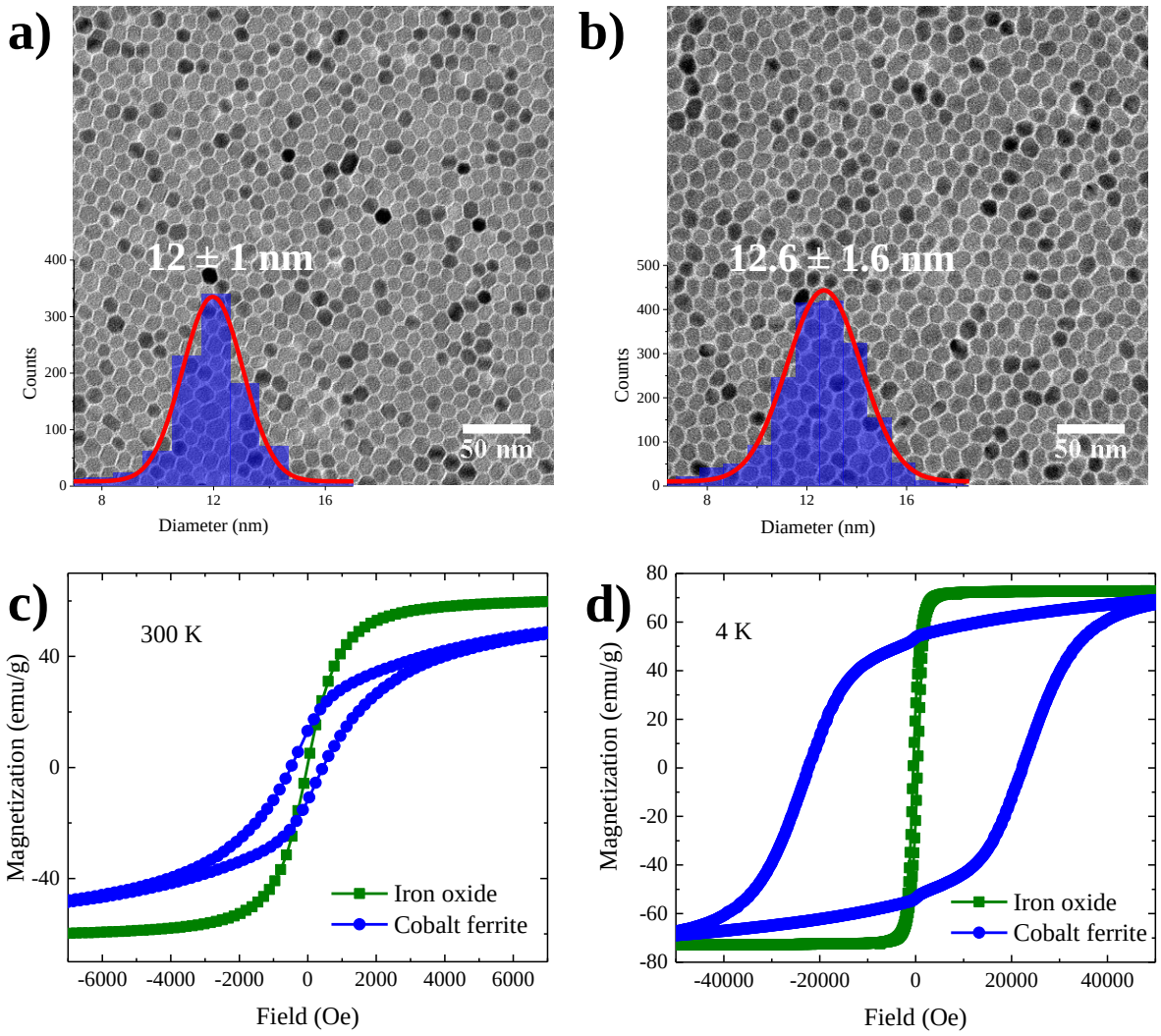

Figure 5.2 TEM images of iron oxide (a) and cobalt ferrite (b) MNPs. The insets show a typical Size distribution histograms obtained for more than 2000 particles. (c) Magnetization as a function of applied magnetic field at 300 K (c) and 4 K (b) for both iron oxide (green) and cobalt iron oxide (blue) nanoparticles.

5.3.2 Fixation of the surface initiator on MNPs

The surface initiator, CTCS, was anchored to the MNPs by reaction of the organosilane with the hydroxyl group which covers the surface of MNPs, as depicted in **Figure 5.1** and **Figure 5.3**.

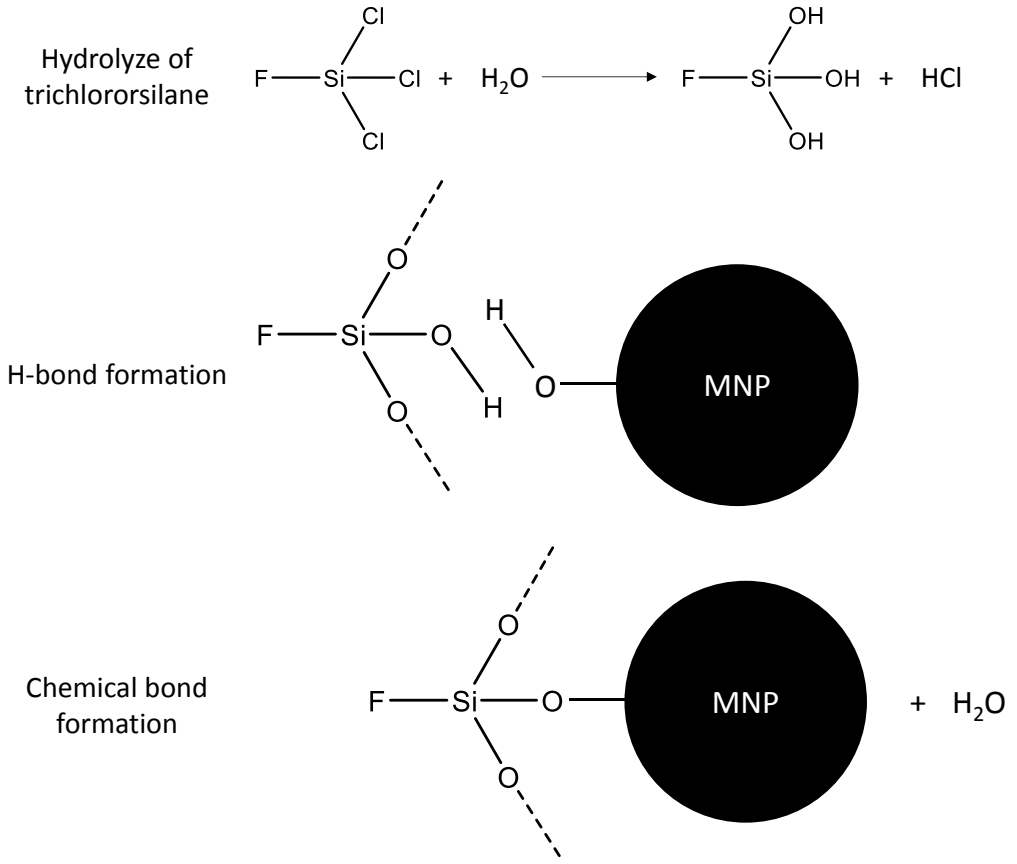

Figure 5.3 Schematic of the condensation reaction between silane molecules and an oxide surface. The Si–Cl bonds hydrolyze readily with water to form silanol Si–OH groups, which can then condense with each other to form polymeric structures with hydroxyl groups on the material surface. F: organo-functional group

After exchanging ligands with CTCS, the particles are less protected against aggregation, since the long chain surfactants of (oleate) on the surface of MNPs are replaced by short CTCS chains. The exchange of oleic acid with CTCS is confirmed using FT-IR spectroscopy (**Figure 5.4 a**). The IR spectrum of initiator coated MNPs shows a large band observed at 1000-1150 cm^{-1} that is attributed to Si-O-Si and Fe-O-Si vibrations.[29-30, 34] It also shows a new absorption peak at 1380-1390 cm^{-1}, which can be assigned to the S=O stretching of CTCS.[30]

TGA studies are carried out for the MNPs before and after anchoring CTCS in order to determine grafting density and grafting yield. **Figure 5.4 b** shows the TGA curves before and after grafting surface initiator to the surface of iron oxide MNPs. Iron oxide MNPs show a weight loss of almost 18 % due to removal of physically and chemically adsorbed surfactants. However, the thermogram of iron oxide MNP-CTCS sample shows a broad degradation regime between 100 and 700 °C. The DTG pattern (the curve is not plotted here) indicates that the organic parts are released in different steps. The initial weight loss at 50-100 °C is due to the removal of absorbed water. Then the CTCS grafted on MNP start to decompose from T> 200 °C.

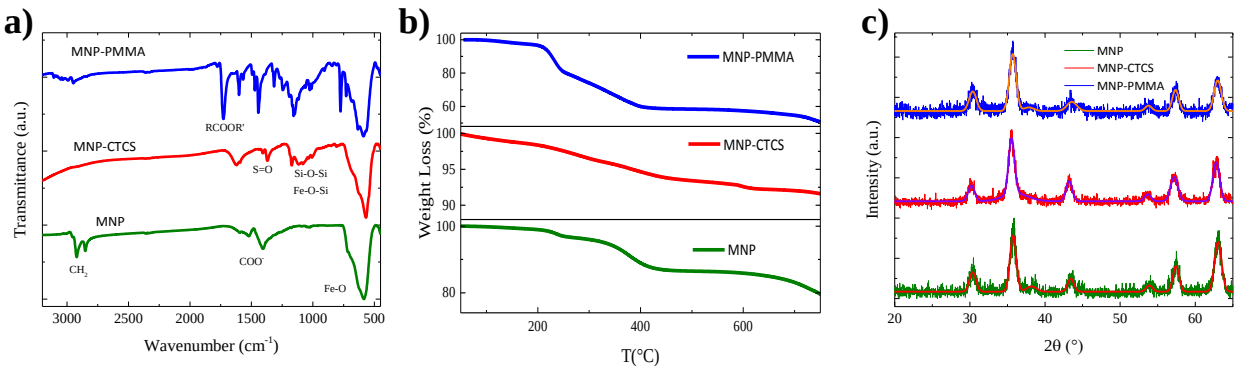

Figure 5.4 (a) FTIR, (b) TGA and (d) XRD of MNPs (Fe_3O_4) before and after surface modifications. The condition of reaction is 3 mmol CTCS/gMNP for 3 hours at 25 °C. The molecular weight of grafted polymer is 50 kg/mol.

CTCS concentration in the reaction is varied from 0.75 to 1, 1.5, 2, 3, 4, 5, 10 to 20 mmol per gram of iron-oxide MNPs (mmol/gr-nanoparticle) in the reaction medium. Initially, the reaction time was fixed to three hours. The values of grafting densities and grafting yields as a function of CTCS concentration are shown in **Figure 5.5 a**. The grafting density sharply increases from 0.9 molecules/nm^2 to 2.2 molecules/nm^2 by increasing CTCS concentration from 0.75 to 3 mmol CTCS/gr-nanoparticle, beyond which, the grafting density gently increases to 2.7 molecules/nm^2 when CTCS concentration increases to 20 mmol/g-nanoparticle. Further increase in CTCS concentration does not have pronounce effect on grafting density and it may even cause silane condensation self-polymerization (as shown in **Figure A5.1**),[50-51] with formation of HCl, which adversely affects the properties of MNPs.[50]

To evaluate the influence of the reaction time on the grafting density, we choose four different CTCS concentrations, namely 1, 2, 3 and 5 mmol/gr-nanoparticle, and varied the

reaction time from 1 to 2, 3, 4 and 5 h. **Figure 5.5 b** shows the values of grafting density as a function of reaction time. For all the concentrations, the grafting density shows an initial sharp increase until reaction time of 3 h, after which the grafting density saturates. Moreover, reactions with lower CTCS concentration, show higher sensitivity of the grafting density with time. The observed trend is due the high reactivity of trichlorosilane coupling agents, which quickly react at the initial stage of the reaction with the OH groups at the surface of the nanoparticles. Based on **Figure 5.5**, we have chosen CTCS concentration of 3 mmol/gr-nanoparticle and reaction time of 3 h as an optimum condition for fixation of CTCS surface initiator.

Figure 5.4 c illustrates XRD patterns after grafting CTCS on iron oxide MNPs. Diffraction pattern of the MNPs remained unchanged, which proves that the ligand exchange with CTCS does not affect the crystalline structure of the MNPs. We noted that cobalt ferrite MNPs show the same characteristics as iron oxide MNPs in FTIR, XRD and TGA.

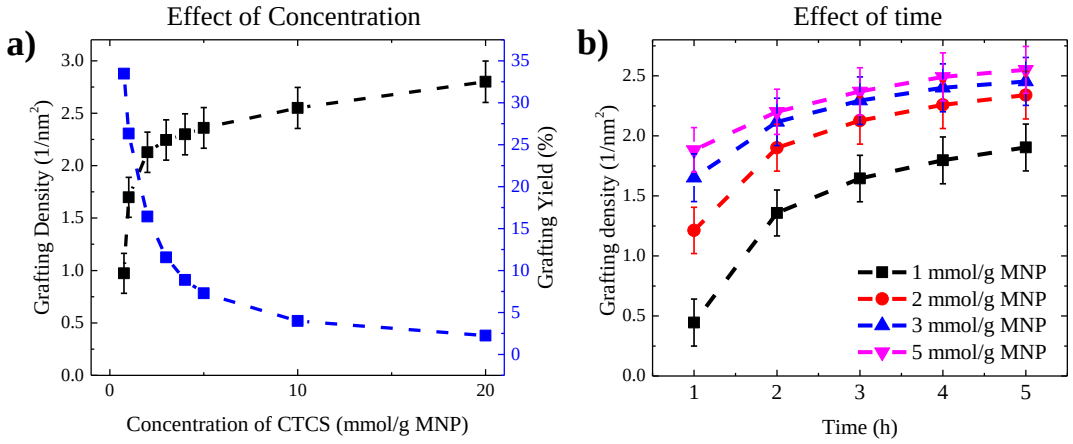

Figure 5.5 (a) The amount of grafting density and grafting yield as a function of ligand concentration in the reaction medium after 3 h of reaction. (b) The amount of grafting density as a function of reaction time for four different ligand concentrations.

5.3.3 SI-ATRP of MMA

The initiator coated Fe_3O_4 and $Co_{0.7}Fe_{2.3}O_4$ MNPs are subsequently subjected to the ultrasound-mediated ATRP of MMA (**Figure 5.2**). To obtain a satisfactory result, we paid particular attention to the following points: first, the polymerization solution is constantly sonicated inside an ultrasonic bath with a controlled temperature to avoid aggregation of the MNPs during the polymerization. Second, the initiator coated MNPs should not be dried before

starting the polymerization. Third, we perform the polymerization in the presence of sacrificial (free) initiator of TsCl to control the process so called persistent radical effect, as described in Chapter 2.[23, 25-26, 52] Another role of the free initiator is to prevent inter-particle coupling and particle aggregation during polymerization. Since the free polymer, which produced by free initiator keep the particles separated while it is difficult for the MNPs to diffuse through the entangled network of polymer chains.

A systematic study is carried out with MMA as a monomer to investigate the effect of different reaction parameters on the polymerization reaction of both Fe_3O_4 (12 nm) and $Co_{0.7}Fe_{2.3}O_4$ (12.6 nm) MNPs. We have investigated the effect of reaction temperature and concentrations of free initiator on kinetic of reaction, molecular weight and poly dispersity index (PDI). To investigate the effect of the reaction temperature, polymerization is performed at two temperatures *i.e.* 50 °C and 65 °C while keeping the other polymerization parameters unchanged. The Ln($[M]_0$/Ln[M]) (where $[M]_0$ and [M] are initial concentration of monomer and concentration of monomer in defined time) is monitored in time.

Figure 5.6 a shows Ln($[M]_0$/Ln[M]) versus time for two different reaction temperatures. As illustrated in **Figure 5.6 a**, the rate of change in monomer concentration remains constant and it is linear as a function of time during the polymerization. As we explained in detail in Chapter 2, this is due to the negligible contribution of non-reversible termination, so that the concentration of the active propagating species is constant. Hence, the polymerization follows a first order kinetic. The linear relationship between monomer concentration and time at both temperatures reveals that the concentration of the propagating radical species remains constant throughout the polymerization time. The slope of the curve exhibites the rate of the polymerization reaction. As we expect, the slope is higher for higher temperature, since the monomer consumption rate is faster at higher temperatures. The rate of ATRP is given by:

$$R = kpKeq[I]\frac{[CuBr]}{[CuBr2]}[M] \qquad (5.1)$$

where k_p is the rate constant for propagating, K_{eq} is the ratio between the rate constant of activation and deactivation, [I] is the concentration of initiator, [$CuBr$] and [$CuBr_2$] are the concentrations of catalyst and deactivator, respectively and [M] is the monomer concentration.

Since all reaction parameters are kept constant, the ratio of the ATRP reaction rates at different temperatures can be written as $R_{65\,°C}/R_{50\,°C} = kp_{65\,°C}/kp_{50\,°C}$. From the slopes of the **Figure 5.6 a**, we obtain $kp_{65\,°C}/kp_{50\,°C}$ = 1.48. Therefore, the rate of reaction is almost 1.5 times faster when the temperature is 65 °C compare to 50 °C. We note for ATRP of stand-alone PMMA, k_p values of 915 and 632 L mol^{-1} s^{-1} have been reported for ATRP polymerization at, 65 °C and 50 °C respectively,[27, 53-55] which would give a relative rate of propagating of $k_{p\ 65\,°C}/k_{p\ 50\,°C}$ = 1.44. This ratio is interestingly similar to the ratio which we obtained in our SI-ATRP system.

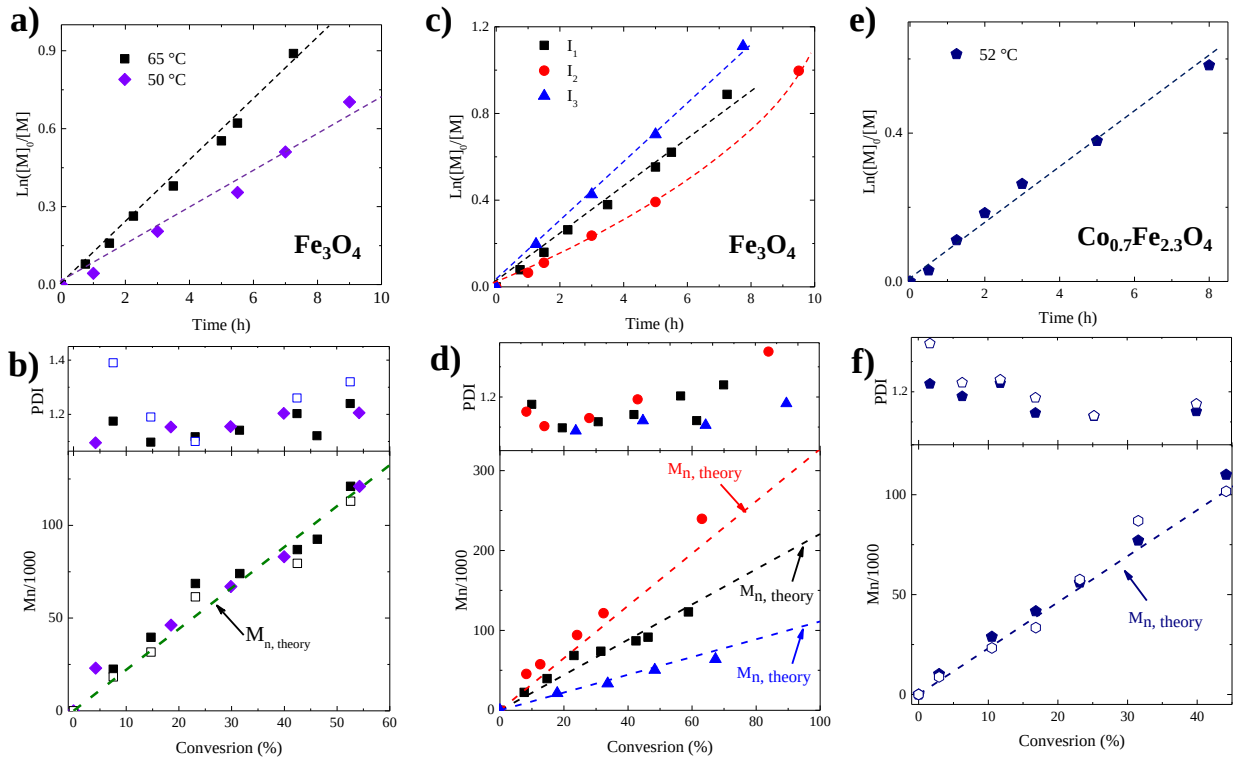

Figure 5.6 (a) Plot of ln([*M*]$_0$/[*M*]) versus time for MMA polymerization at different reaction temperature of 50 and 65 °C for iron-oxide nanoparticles with [MMA]$_0$: [p-TsCl]$_0$: [Cu(I)Cl]$_0$: [dNbipy]$_0$ 3000:1:6:12, and (b) the evolution of M_n and PDI (top) and M_n (bottom) of free PMMA (filled symbols) and grafted-PMMA (hollow symbols) as a function of monomer conversion. (c) Ln([*M*]$_0$/[*M*]) versus time for MMA polymerization from the surface of iron-oxide nanoparticles at 65 °C with different free initiator concentrations of [MMA]$_0$: [p-TsCl]$_0$: [Cu(I)Cl]$_0$: [dNbipy]$_0$ of 3000:0.60 6:12 (red) 3000:1:6:12 (black) , and 3000:2.3:6:12 (blue). (d) Evolution of PDI (top) and M_n (bottom) of the free PMAA as a function of monomer conversion for different initiator concentration of part c). (e) Plot of ln([*M*]$_0$/[*M*]) versus time for MMA polymerization from the surface of cobalt-ferrite nanoparticle at 50 °C with [MMA]$_0$: [p-TsCl]$_0$: [Cu(I)Cl]$_0$: [dNbipy]$_0$) of 3000:1:6:12, and (f) the evolution of PDI (top) and M_n (bottom) of the grafted PMMA on cobalt-ferrite nanoparticles as a function of monomer conversion. The dotted lines in panels b), d) and f) show theoretically calculated M_n.

The top panel of **Figure 5.6 b** shows the evolution of PDI (defined as the ratio of molecular weight to number-average molecular weight *i.e.* M_w/M_n) of the grafted-PMMA as function of monomer conversion at 50 and 65 °C. We calculated monomer conversion by dividing the mass of synthesized polymer (sum of free and grafted polymer) to the initial mass of monomer. The PDI at both polymerization temperatures is below 1.2, indicating that the polymerization proceeded in a living fashion.[53] For both temperatures, M_n grows linearly as a function of conversion and is temperature independent. We compared the molecular weight of the grafted-PMMA, after cleavage from the nanoparticle surface, with that of a free polymer. As it is illustrated in **Figure 5.6 b**, M_n values of the grafted-PMMA (hollow symbols) and that of a free polymer (filled symbols) are nearly identical and both increase via increasing the monomer conversion. [23, 25-26, 34] This maybe indicative of similar kinetic of growth for free polymer and grafted polymer.

As we discussed in detail in Chapter 2, following the conditions for a living polymerization, where all propagating chains grow at the same rate and for the same length of time, the molecular weight of polymerization can be calculated by:

$$M_{n,theory} = \frac{M_{MMA} \times p \times [MMA]_0}{[TsCl]_0 + [CTCS\ on\ surface]_0} \qquad (5.2)$$

where M_{MMA} is the molecular weight of MMA (100.1 g/mol), p is the conversion, and $[MMA]_0$ and $[TsCl]_0$ are the initial feed concentrations of MMA and free initiator, respectively. $[CTCS\ on\ surface]_0$is the number of CTCS sites available on the nanoparticle's surface, which is determined from grafting density obtained by TGA. The grafting density of the CTCS on the surface of iron oxide is amounted to 2.2 molecules/nm^2. The density of iron oxide MNPs is 5.18 g/cm^3. Therefore, the $[CTCS\ on\ surface]_0$ calculates to 35.3 µmol. Since all the other parameters are set experimentally, $M_{n,theory}$ is easily calculated, and is plotted in **Figure 5.6 b**, as dotted line. The experimental M_n values agree well with $M_{n,theory}$ which further proves that the reaction is following the first order kinetic.

Next we investigate the effect of free initiator concentration on the reaction kinetic. The monomer conversion as a function of time at a fixed temperature of 65 °C for three different free

initiator concentrations is shown in **Figure 5.6 c** for SI-ATRP on iron-oxide nanoparticles' surface. For all cases, the monomer consumption follows the first order kinetic with linear time dependence of monomer consumption. However, we note that, when the concentration of the free initiator is low (I_2) the curve starts to show nonlinear behavior in longer reaction time. As we explained earlier, an upward curvature in the kinetic plot indicates an increase in the concentration of propagating species, which occurs for the case of slow initiation. In lower concentration of free initiator (I_2), the rate of initiation and as a result deactivation is lower in comparison to the rate of propagation in ATRP.[36] Therefore, we observe the deviation in the kinetic of reaction. The deviation gets more pronounced in longer time due to the increased viscosity of the system that leads to reduced termination, enhanced polymerization rate, gel effect or slow initiation.[23]

Increasing the initiator concentration, as shown in **Figure 5.6 c**, enhances the polymerization rate in agreement with the polymerization rate **Equation 5.1**. The enhancement in polymerization rate is due to the growing number of propagating chains by increasing the concentration of free initiator. As a result, lower M_n at higher free initiator concentration is expected due to the higher number of propagating chains (assuming that all the chains grow with the same rate), which is in agreement with the measured molecular weight, as shown in **Figure 5.6 d**. The values of PDI as a function of conversion are shown in top panel of **Figure 5.6 d**. Interestingly, the value of PDI, remains insensitive to initiator concentration. The slight deviation between $M_{n,theory}$ and experimentally obtained M_n for low concentration of initiator (I_2) can be rationalized due to the slight deviation of reaction kinetic from first order. We also compared the experimentally obtained M_n with $M_{n,Theory}$ using **Equation 5.2**. The experimental M_n values agree well with $M_{n,theory}$ which further proves that the reaction is following the first order kinetic.

We also perform ultrasound-mediated SI-ATRP from the surface of CTCS-coated $Co_{0.7}Fe_{2.3}O_4$ MNPs with the average diameter of 12.6 nm. The reaction was conducted at 52 °C with $[MMA]_0$: $[p\text{-}TsCl]_0$: $[Cu(I)Cl]_0$: $[dNbipy]_0$ 3000:1:6:12 for different time in order to obtain different molecular weights. The polymerization follows a first order kinetic (**Figure 5.6 e**). The M_n values, **Figure 5.6 f**, of the graft- and free PMMA are identical, and both increase linearly. While M_n increases proportionally as a function of the monomer conversion, the PDI

remains around 1.2, proving that polymerization proceeds in a living fashion. We also compare the experimentally obtained M_n and $M_{n,theory}$. The grafting density of the CTCS on the surface of cobalt ferrite MNPs is amounted to 2.1 molecules/nm^2. The density of cobalt ferrite MNPs is 5.25g/cm^3. Therefore the $[CTCS\ on\ surface]_0$ amounts to 31.6 µmol. The experimentally obtained M_n values agree well with $M_{n,theory}$ which further proves that the reaction is following the first order kinetic.

A comparison of FTIR spectra of MNPs before and after polymerization is shown in **Figure 5.4 a**. The spectrum of polymerized MNP clearly shows a sharp absorption peak at 1730 cm^{-1} which is characteristic peak of the ester group of PMMA and confirms the success of the polymerization.[30, 34] XRD of MNPs after polymerization is also shown in **Figure 5.4 c**. All the diffraction peaks remains unaffected, which shows that the SI-ATRP with PMMA did not affect the crystalline structure of the magnetic core of MNPs.

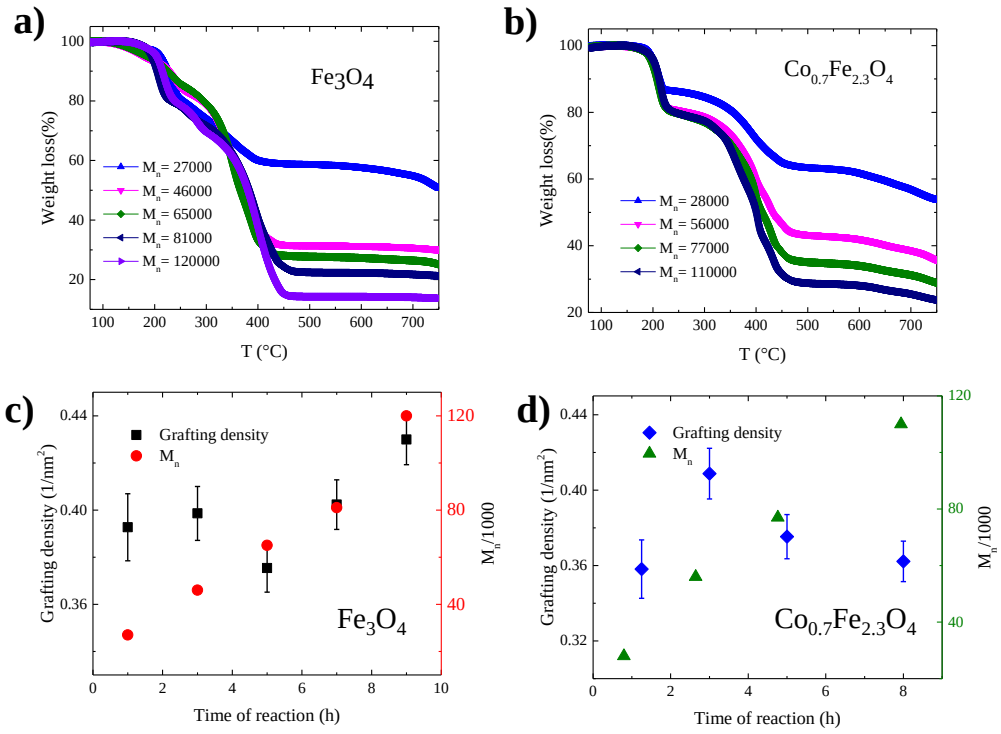

Figure 5.7 TGA of samples with different molecular weight of polymer shell for both (a) Fe_3O_4 and (b) $Co_{0.7}Fe_{2.3}O_4$. The grafting densities and their corresponding M_n (g/mol) as a function of reaction time for both (c) iron oxide and (d) cobalt ferrite MNPs.

TGA tests were also performed for both polymer coated iron oxide and cobalt ferrite MNPs to determine the grafting density of PMMA on the surface of MNPs (**Figure 5.7 a** and **b**). For the MNPs-PMMA, the decomposition of polymer starts when the temperature is ~ 200 °C and it fully decomposes when the temperature is above ~ 400 °C. This decomposition trend is similar to the pure PMMA chains.[23, 32, 34] Moreover, by increasing the molecular weight of polymer, the amount of weight loss increases. The value of grafting density as a function of reaction time amounts to the average value of 0.4 and 0.36 molecules/nm^2 for polymer coated iron oxide and cobalt ferrite MNPs, respectively, as it is shown in **Figure 5.7 c** and **d**. The grafting density remains nearly unchanged and independent of polymerization time and the molecular weight, which indicates the growth of initially grafted chains by increasing reaction time.[23, 25-26, 34, 56]

5.3.4 Morphology of the MNPs-PMMA

The MNP-PMMA, were easily dispersed in toluene (or common solvents of PMMA) after polymerization. We measured the hydrodynamic radius, D_h, of the nanoparticles using DLS. We note that, the D_h values for all MNPs (both iron-oxide and cobalt-ferrite) remains unchanged in time demonstrating high colloidal stability of the MNPs-PMMA. Both MNPs remains dispersable in organic solvent over a long time and do not separate even in the presence of strong magnet. The pictures of cobalt-ferrite MNPs in toluene before and after SI-ATRP when exposed to an external magnet are shown in **Figure 5.8**.

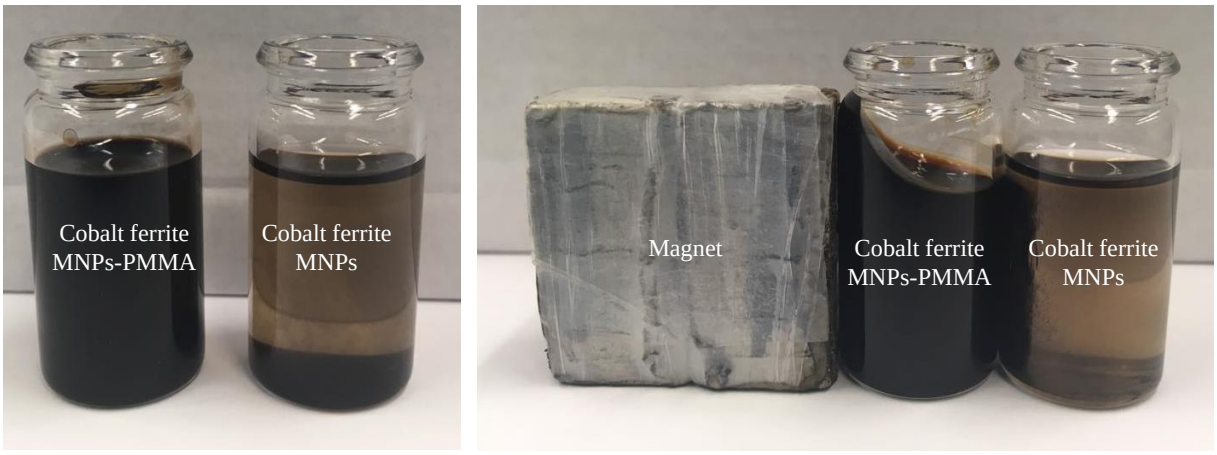

Figure 5.8 Colloidal stability of ferrimagnet cobalt ferrite MNPs after polymerization in toluene.

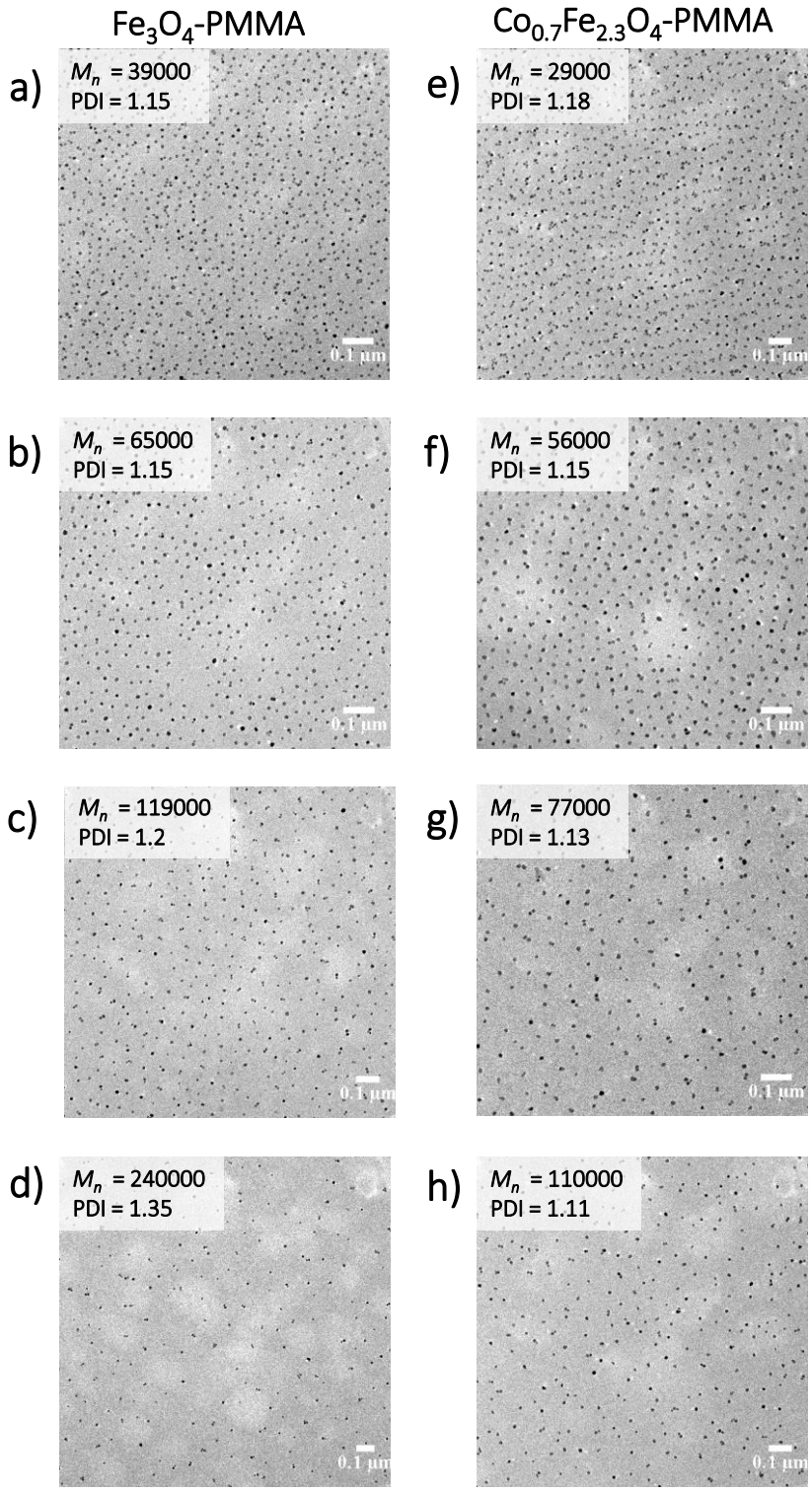

Figure 5.9 TEM images of thin films of Iron oxide (a-d) and cobalt ferrite (e-h) end-grafted with PMMA brushes with different number-average molecular weight.

Representative TEM images of PMMA-grafted iron-oxide and cobalt-ferrite MNPs, are shown in **Figures 5.9 a-d** and **5.9 e-h**, respectively. Unfortunately, direct observation of the polymer shell is not possible due to the low contrast of PMMA under TEM. The nanoparticles are however easily identified. We do not observe any aggregation of particle. PMMA-grafting has yield particles that are individually separated. Center-to-center distance was calculated by analyzing All TEM images. **Figure 5.10 a** and **c** shows that the TEM center-to-center distance for both iron-oxide and cobalt-ferrite MNPs increases by increasing the degree of polymerization (N) of the grafted-PMMA. Note that we assume the similar molecular weight for both free and grafted-PMMA.

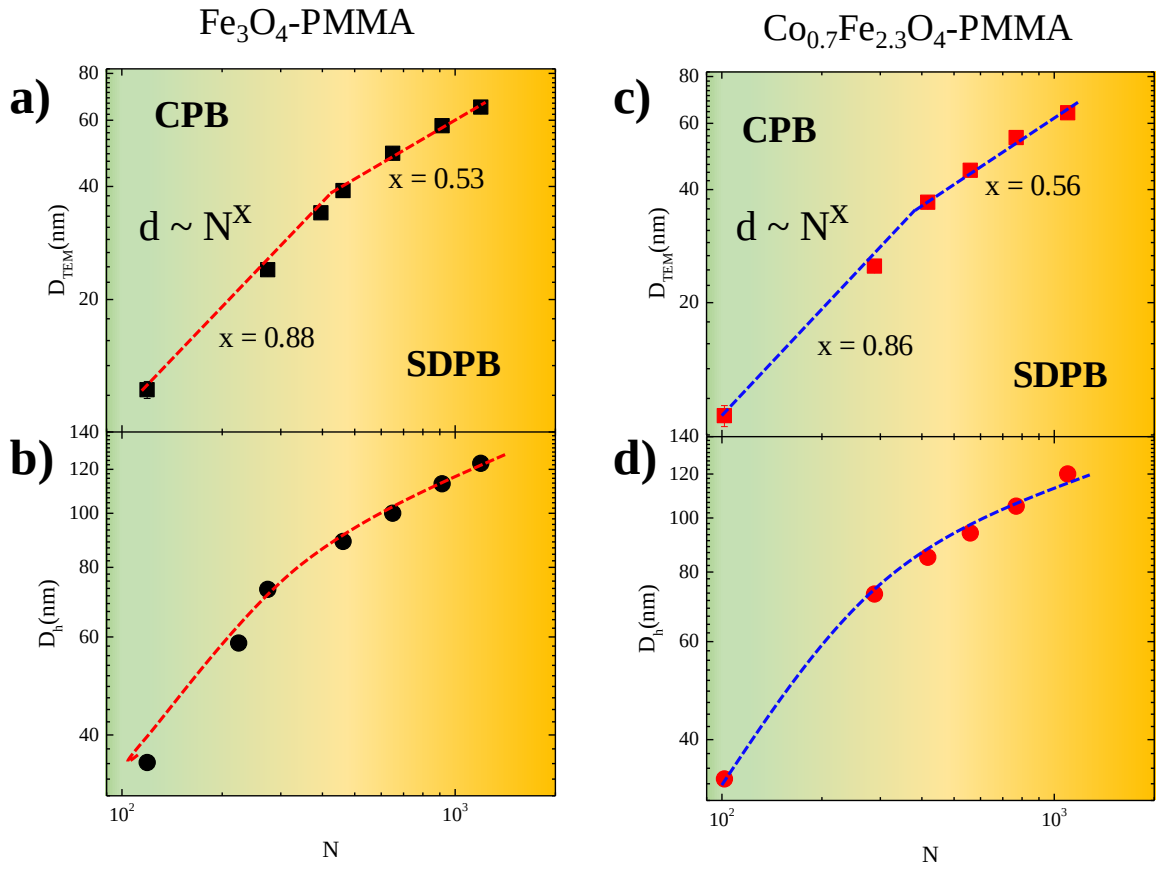

Figure 5.10 Center-to-center distance between MNPs after polymerization as a function of degree of polymerization (N) of the grafted PMMA for both ferrite (a) and cobalt ferrite (c) and hydrodynamic diameter (D_h) of Fe_3O_4-PMMA MNPs (b) and $Co_{0.7}Fe_{2.3}O_4$-PMMA (d) as a function of degree of polymerization (N). The D_h values were determined by dynamic light scattering in dilute toluene suspension at 30 °C.

Moreover, the hydrodynamic diameter of the MNPs-PMMA is estimated by DLS. Measurements were performed for the MNPs with different molecular weight of the grafted-PMMA in dilute toluene. The D_h, for both types of MNPs are given in **Figure 5.10 b** and **d** as a function of the degree of polymerization, N, of the grafted-PMMA. Generally, D_h rises with increasing M_n. However, two regimes can be identified; at low N values, D_h increases with a steeper slope (TEM analysis also yielded the same trend, **Figure 5.10 a** and **c**). Similar trend has been also reported for grafted-silicon nanoparticles.[25, 33, 57-58] At low M_n, regime I, due to the high grafting density of PMMA and segmental repulsion between the chains, the PMMA chains are fully extended, the state that is known as 'concentrated particle brush' (CPB). At high M_n ,regime II, segmental repulsion between PMMA chains is reduced, and the chains transform to a more relaxed coil conformations, the state is known as 'semi-dilute particle brush' (SDPB). Both CPB and SDPB are shown schematically in **Figure 5.11**.[33, 57-59] Therefore, as we expect, the distance between MNPs increases faster by increasing N in when the chains are in CPB regime than SDPB regime. Moreover, it has been shown theoretically that when the distance between particles are assumed to be in the CPB regime (with $d \sim N^x$ and $0.6<x<1$) whereas for the SDPB regime ($x \sim 0.6$) is expected.[58, 60] We have observed the similar values of x as depicted in **Figure 5.10**. It is known that, the SDPB regime has better mechanical properties due to effective entanglement of the particles brush.[23, 60]

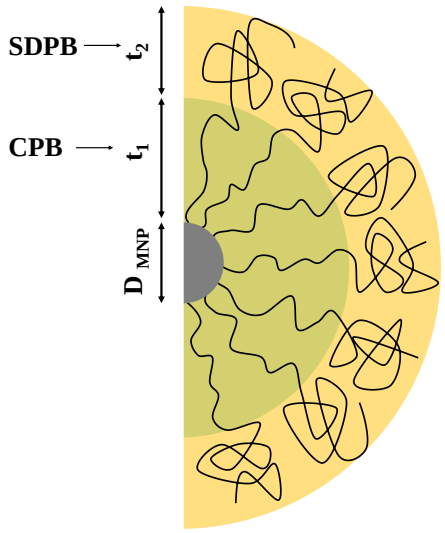

Figure 5.11 Illustration of a particle brush system with stretched (CPB) and relaxed/coiled chain conformation (SDPB).

5.3.5 Magnetic properties of MNPs-PMMA

The *M-H* curves of the Fe_3O_4-PMMA MNPs at 300 K and 4 K are shown in **Figure 5.12 a** and **c**, respectively. Fe_3O_4-PMMA MNPs show superparamagnetic behavior at 300 K and ferri/ferromagnetic behavior at 4 K.

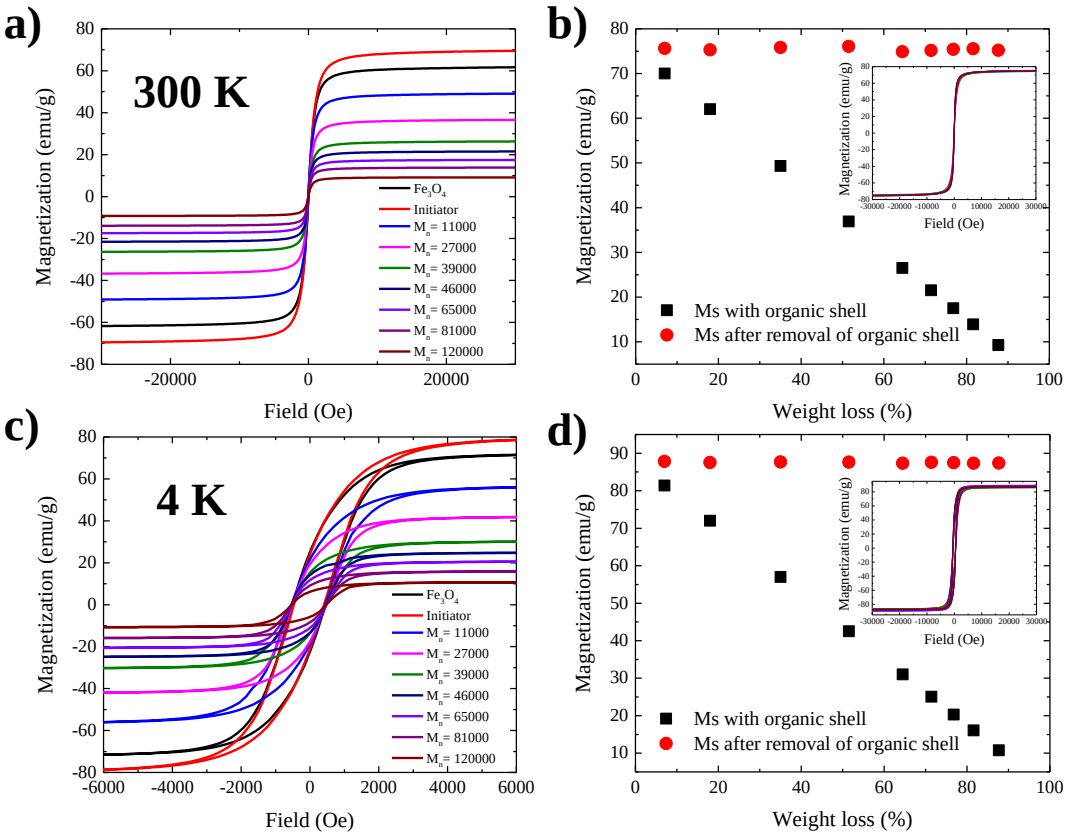

Figure 5.12 Field dependence of magnetization curves for polymer coated iron oxide nanoparticles with different molecular weight at two different temperatures of (a) 300 K and (c) 4 K. The amount of saturation magnetization as a function of organic shell percentage (obtained from TGA) at both temperature of (b) 300 K and (d) 4 K. The insets show the *M-H* curves after removing the organic shell.

Moreover, it is shown in **Figure 5.12 b** and **d** that by increasing the molecular weight of grafted polymer the value of saturation magnetization of MNPs-PMMA reduces (black square) at both temperatures. However, when the amount of magnetizations are corrected by removal of the mass of organic part (obtained from TGA measurement (**Figure 5.7 a** and **c**)), no significant difference on saturation magnetizations are observed among the MNPs with different grafted PMMA molecular weights at both temperatures (**Figure 5.12 b** and **d**). The value of saturation

magnetization (after removal of organic part) amount to 76 emu/g and 88 emu/g at 300 K and 4 K, respectively. These values are in agreement with the values obtained for bare iron oxide MNPs (oleate coated MNPs) given in **Chapter 3** with similar average diameter. Therefore, polymerization has no effect on the saturation magnetization of the iron oxide MNPs.

$Co_{0.7}Fe_{2.3}O_4$-PMMA shows ferri/ferromagnetic behavior at both 300 K and 4 K (**Figure 5.13 a** and **c**). Similar to Fe_3O_4-PMMA, the same trend of decreasing saturation magnetization by increasing the molecular weight of polymer is observed. We correct the value of saturation magnetization to the amount of core magnetic part (obtained from TGA results, **Figure 5.7 b** and **d**), as depict in **Figure 5.13 c** and **d** at 300 K and 4 K respectively. Regardless of the molecular weight of PMMA, they show the saturation magnetization of 79 emu/g and 89 emu/g at 300 K and at 4 K, respectively, which is close to the bulk value of pure cobalt ferrite.[45, 49]

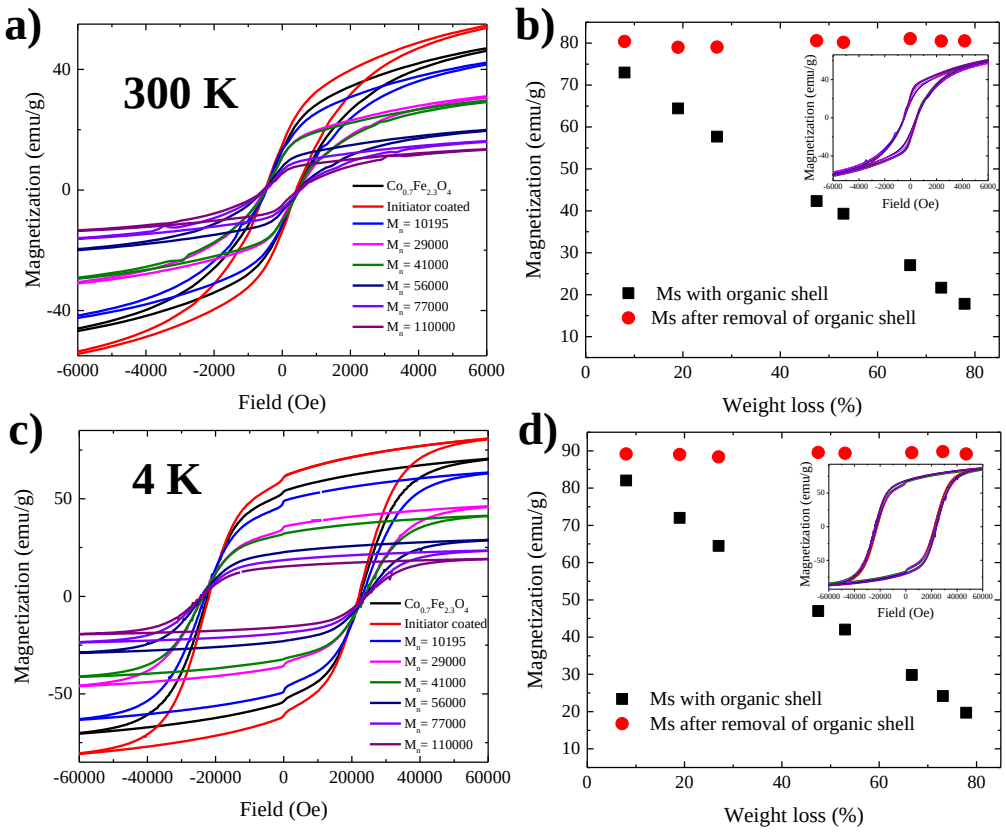

Figure 5.13 Field dependence of magnetization curves for polymer coated cobalt ferrite nanoparticles with different molecular weight at two different temperatures of (a) 300 K and (c) 4 K. The amount of saturation magnetization as a function of organic shell percentage (obtained from TGA) at both temperature of (b) 300 K and (d) 4 K. The insets show the *M-H* curves after removing the organic shell.

Figure 5.14 a and **b** show the variation of squarness (M_r/M_S) and coercivity (H_C) for Fe_3O_4-PMMA as a function of the molecular weight of grafted organic shell at 4 K (Fe_3O_4-PMMA MNPs show no remanent and coercivity at 300 K) . **Figure 5.14 c-f** shows the same characteristics at 300 K and 4 K for $Co_{0.7}Fe_{2.3}O_4$-PMMA. Regardless of the MNP's type and the measurement temperature, squareness and corecivity increase sharply with increasing the molecular weight of grafted PMMA and then slightly rises (with slower steep) at high molecular weight (M_n> 60 kg/mol).

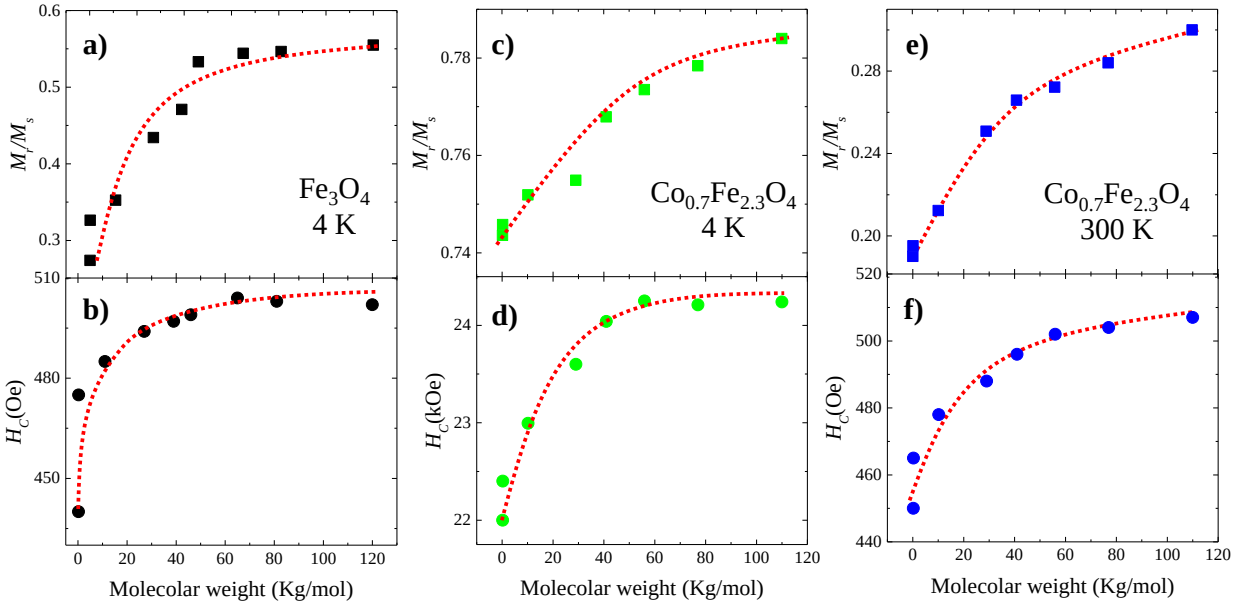

Figure 5.14 M_r/M_S and H_C of MNPs-PMMA for (a) and (b) Fe_3O_4 and (c)-(f) $Co_{0.7}Fe_{2.3}O_4$ at 4 K in panels (a) and (d) and 300 K in panels (e) and (f).

Next, ZFC and FC measurements were performed to determine the blocking temperature, T_B, of MNPs-PMMA in different molecular weight of grafted PMMA. The curves are illustrated in **Figure A5.2** and **Figure A5.3** for Fe_3O_4-PMMA and $Co_{0.7}Fe_{2.3}O_4$-PMMA, respectively. In **Figure 5.15 a** and **b** we summarize the variation of T_B as a function of the M_n of grafted PMMA for Fe_3O_4-PMMA and $Co_{0.7}Fe_{2.3}O_4$-PMMA, respectively. For both types, T_B decreases sharply as the molecular weight increases till almost M_n= 60 kg/mol. Then after this abrupt decrease, further increasing of the molecular weight slightly reduces the value of T_B. Such similarities in the

variation pattern of T_B, H_C and M_r/M_S with the polymer molecular weight suggest that they have the same origin, which is the magnetic interaction between MNPs.

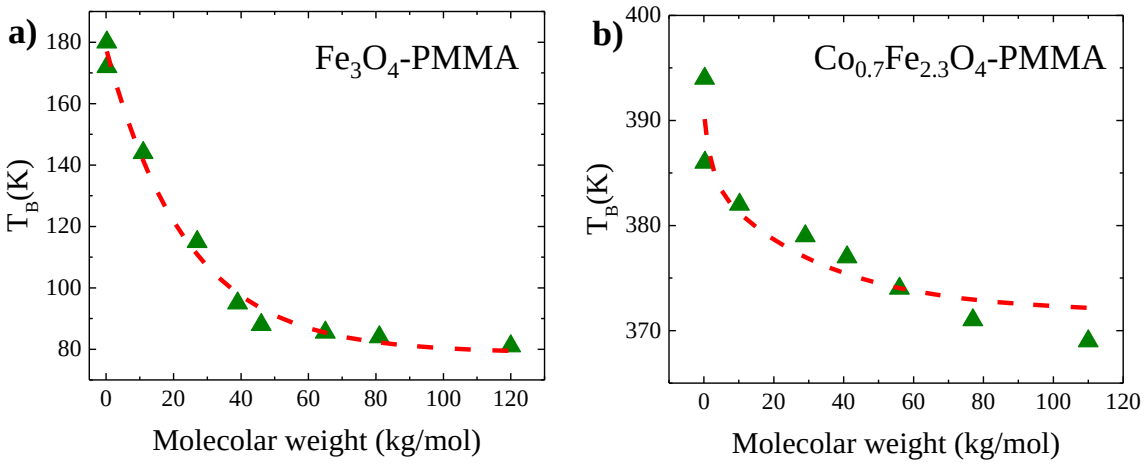

Figure 5.15 The values of blocking temperatures (T_B) as a function of the molecular weight of grafted organic shell for (a) Fe_3O_4 and (b) $Co_{0.7}Fe_{2.3}O_4$.

This behavior can be explained by the Dormann–Bessais–Fiorani (DBF) model which introduces an extra energy factor (E_d) in the expression of the anisotropy energy barrier (E_A) of a magnetic system with inter-particle interactions. In general, for interacting MNPs, extra energy factor introduces in the expression of the anisotropy energy barrier (E_A):

$$E_A = KVSin^2\theta + E_d + E_{ex} \qquad (5.3)$$

where K represents the anisotropy constant, V is the volume of the magnetic particle, θ stands for the angle between the easy axis of the magnetic particle and the magnetization direction in an applied magnetic field. E_d and E_{ex} are energy factors describing the inter-particle interactions and exchange interaction energy, respectively.[61-64] However, when the nanocrystals' surface is functionalized with long chain organic polymers the exchange couplings are minimized and, thus, the energy factor E_d from the equation of the anisotropy energy barrier (E_A) is dominated by the magnetic dipole-dipole interactions. For a magnetic system of single-domain particles, the energy corresponding to the magnetic dipole–dipole interactions can be expressed as:

$$E_d = -\frac{\mu_0 m_0^2}{4\pi d^3} \qquad (5.4)$$

where μ_0 represents the permeability constant of the vacuum and m_0 stands for the magnetic moment of the particle.[61, 65] Based on the equation above, increasing the distance between MNPs (d) results in the reduction of the strength of the magnetic dipolar interaction. Therefore, decrease of the anisotropy energy barrier (E_A).[61]

As we illustrated in **Figure 5.10**, by increasing the molecular weight of grafted polymer, the inter-particle distance between MNPs increases. Therefore, by increasing magnetic inter-particle distance, E_d and subsequently E_A decreases resulting in decrease of the T_B and the increase of H_C and M_r/M_S. Decrease of M_r/M_S indicates positive effect of magnetic dipole-dipole interactions on demagnetization process. We note that, above a certain molecular weight of almost (~ 60 kg/mol) and consequently certain inter-particle distance, the change in T_B, H_C and M_r/M_S become negligible. Since above a certain inter-particle distance, the magnetic inter-particle dipole-dipole interactions become extremely weak so that the further increase of it has no significant influence on the aforementioned values.[66-70]

In addition, as we discussed in Chapter 4, the *M-H* curves of the cobalt ferrit MNPs show bi-magnetic behavior at low temperature; a sudden reduction of *M* as the field approached from a large value to zero.[45, 49] The observed bi-magnetic behavior was ascribed by the existence of strong coupling interaction between MNPs. However, as it is shown in **Figure 5.13 c**, by increasing the molecular weight of grafted PMMA, the bi-magnetic behaviors are disappeared. This is another indication of the reduction of the magnetic dipole interaction between cobalt ferrite MNPs by increasing the molecular weight of grafted PMMA.

The isothermal remanent magnetization (IRM) and dc demagnetization (DCD) measurements were performed in order to clarify the magnetic coupling interactions between polymer coated iron oxide and cobalt ferrite MNPs (details of the measurement were given in Chapter 4).[3, 71-72] As we explained in Chapter 4, for non-interacting MNPs, magnetization and demagnetization process are equivalent. Therefore ΔM ($\Delta M = m_d(H) - [1 - 2m_r(H)]$) should be zero at any value of applied field while deviations of ΔM curves from zero in magnetic materials are ascribed due to magnetic coupling interactions between the MNPs. [3, 72-73] $\Delta M < 0$ suggests that interactions are demagnetizing (since the measured $m_d\ (H)$ is smaller than the expected value ($1\text{-}2m_r\ (H)$)) indicating that the sample demagnetizes faster than when particles

are non-interacting. While when $\Delta M > 0$ suggests that interactions are magnetizing. The calculated ΔM curves for both polymer coated Fe_3O_4 (at 4 K) and $Co_{0.7}Fe_{2.3}O_4$ in different molecular weights of grafted polymer are shown in **Figure 5.16 a** and **b**, respectively. **Figure 5.16** revealed a negative peak with a magnitude of almost -0.5 for them. This negative value is indicative of demagnetizing magnetic dipolar interactions. However, by increasing the molecular weight of the grafted polymer and subsequently increasing in inter-particle distance, the absolute value of ΔM reduces for both types of MNPs and remains unchanged when the molecular weight exceeds almost 60 kg/mol. This indicated effective weakening of magnetic dipolar interaction by increasing the inter-particle distance. The results of ΔM measurements are in accordance with the variation of T_B, M_r/M_S and H_C by increasing the molecular weight of grafted polymer.

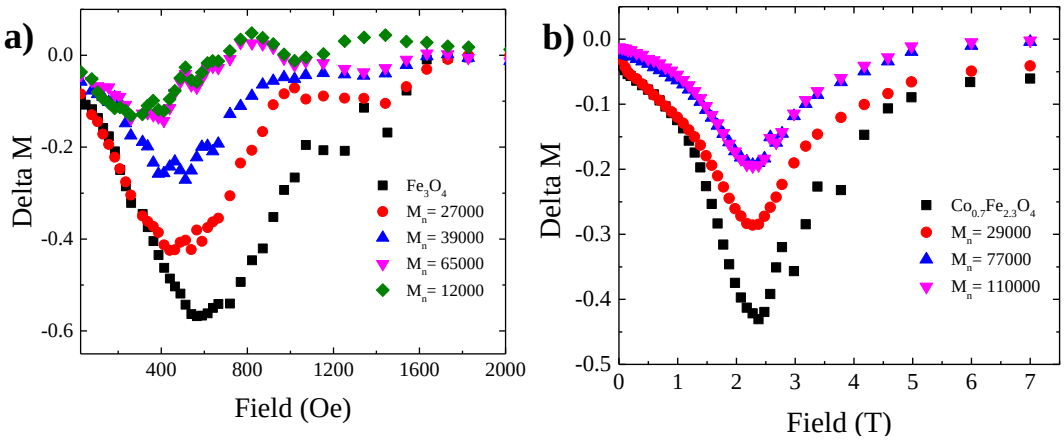

Figure 5.16 ΔM value as a function applied field for different molecular weight of grafted polymer for (a) Fe_3O_4 (4 K) and (b) $Co_{0.7}Fe_{2.3}O_4$.

5.3.6 Solution processing of magnetic thin films

After polymerization due to the presence of PMMA shell, thin film assemblies of the MNPs can be prepared by different film processing techniques. **Figure 5.17 a-c** shows SEM images of the thin films with different grafted PMMA molecular weight obtained by spin coating. Uniformly distributed self-organized MNPs films are obtained. The MNPs are single by single separated from each other without any obvious aggregation (in agreement with TEM results). The cross sectional images of spin coated thin films for different molecular weight are

shown in the inset of **Figure 5.17 a-c** revealing no aggregation and well distribution of nanoparticles.

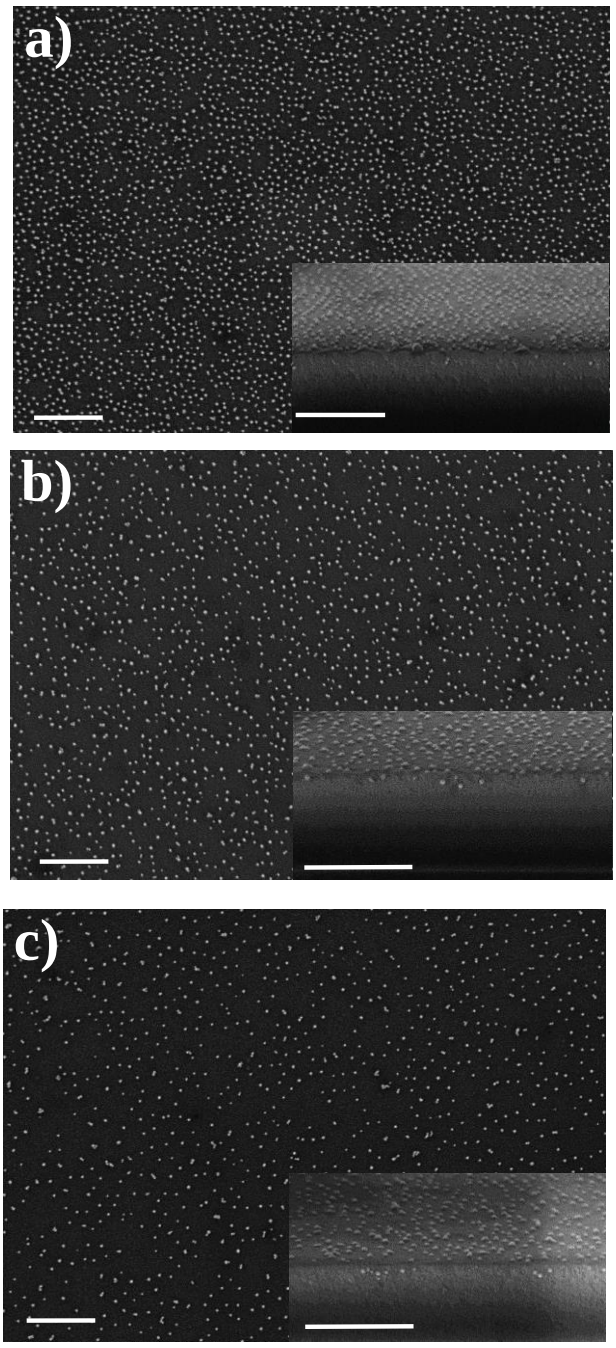

Figure 5.17 Top view SEM images of Fe_3O_4-PMMA thin films obtained by spin coating with different molecular weight of (a) 46 K, (b) 65 K and (c) 120 K. The cross-section images are shown in the inset. The scale bar is 300 nm.

Due to the absence of aggregation, the MNPs can be addressed individually. The packing density of the MNPs can be tuned by changing the molecular weight of the grafted polymer shell. The densities of the particles are estimated from the images as a function of molecular weight, as depicted in **Figure 5.18 a**. The packing density is decreasing by increasing the molecular weight of grafted polymer. This high packing density enables the fabrication of high recording density magnetic tape memories. Room-temperature *M-H* curves of thin film prepared by spin coating from Fe_3O_4-PMMA and $Co_{0.7}Fe_{2.3}O_4$-PMMA are shown in **Figure 5.18 b**. Therefore, solution processable thin films of both superparamagnetic (Fe_3O_4-PMMA) and ferri/ferromagnetic ($Co_{0.7}Fe_{2.3}O_4$-PMMA) behavior are obtained at room temperature. In addition, after polymerization due to presence of PMMA shell on the surface of MNPs, they become compatible with ferroelectric polymer matrix. Therefore, they homogeneously disperse inside ferroelectric polymer matrix and do not aggregate. The details will be given in **Chapter 7**.

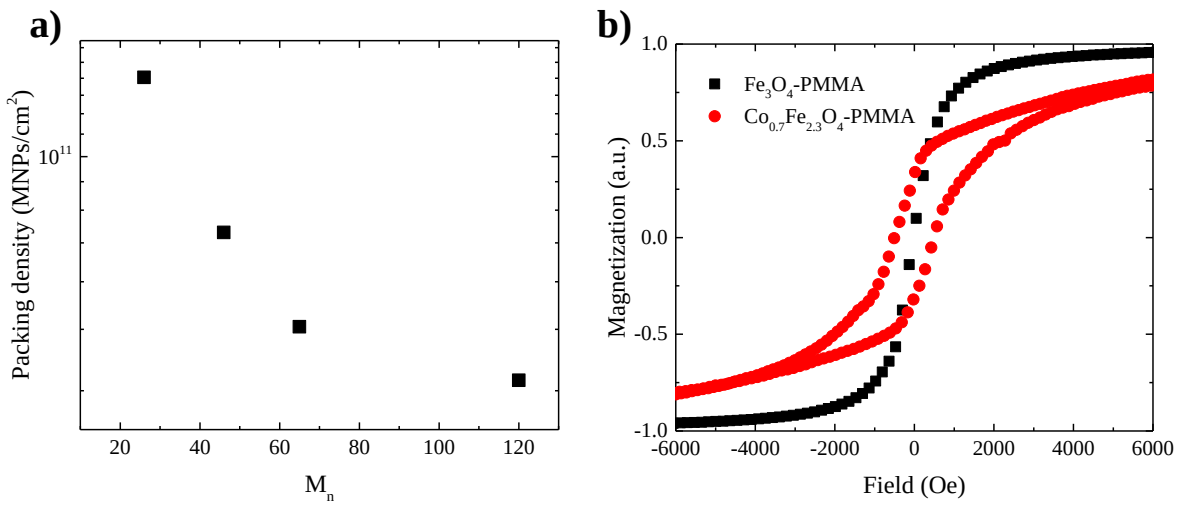

Figure 5.18 (a) Packing density of the spin coated thin films as a function of M_n. (b) Normalized *M-H* magnetization curve of spin coated superparamagnetic and ferri/ferromagnetic thin film at room temperature.

5.4 Conclusion

Monodisperse superparamagnetic (Fe_3O_4) and ferri/ferromagnetic ($Co_{0.7}Fe_{2.3}O_4$) MNPs were synthesized using thermal decomposition method. The surface of the MNPs was functionalized with CTCS as surface initiator for SI-ATRP. The grafting densities for CTCS can

be tuned ranging from 1 to 3 molecules/nm^2. SI-ATRP of MMA was performed in bath sonication and preceded in a living fashion. This process provided perfectly dispersed MNPs particles grafted with well-defined and dense PMMA shell with variable thickness. The effect of different polymerization reaction conditions on kinetic, molecular weight and PDI of grafted polymer were investigated. Grafting the MNPs with PMMA shell, improved the colloidal stability of the MNPs by reducing the inter-particle magnetic interactions. Due to presence of PMMA shell, MNPs can be easily dispersed in common organic solvents. Therefore, we prepared spin-coated thin-films of the MNPs with high degree of packing order and wide controllability of the inter-particle distances.

In addition, we showed that surface modification does not have pronounced effect on crystal structure of MNPs. On the other hand, growing polymer shell from the surface of MNPs affects the magnetic properties of MNPs. Since, growing polymer form the surface of MNPs, change inter-particle distance. This leads to the change in magnetic dipole-dipole interaction and subsequently magnetic anisotropy energy.

5.5 References

1. Xie, L.; Huang, X.; Huang, Y.; Yang, K.; Jiang, P., Core@ double-shell structured BaTiO3–polymer nanocomposites with high dielectric constant and low dielectric loss for energy storage application. *J. Phys. Chem. C* **2013,** *117*, 22525-22537.
2. Zhu, M.; Huang, X.; Yang, K.; Zhai, X.; Zhang, J.; He, J.; Jiang, P., Energy storage in ferroelectric polymer nanocomposites filled with core–shell structured polymer@ BaTiO3 nanoparticles: understanding the role of polymer shells in the interfacial regions. *ACS Appl. Mater. Interfaces* **2014,** *6*, 19644-19654.
3. Dai, Q.; Berman, D.; Virwani, K.; Frommer, J.; Jubert, P.-O.; Lam, M.; Topuria, T.; Imaino, W.; Nelson, A., Self-assembled ferrimagnet− polymer composites for magnetic recording media. *Nano Lett.* **2010,** *10*, 3216-3221.
4. Wu, L.; Jubert, P.-O.; Berman, D.; Imaino, W.; Nelson, A.; Zhu, H.; Zhang, S.; Sun, S., Monolayer Assembly of Ferrimagnetic Co x Fe3–x O4 Nanocubes for Magnetic Recording. *Nano Lett.* **2014,** *14*, 3395-3399.
5. Sun, S.; Anders, S.; Thomson, T.; Baglin, J.; Toney, M. F.; Hamann, H. F.; Murray, C.; Terris, B. D., Controlled synthesis and assembly of FePt nanoparticles. *J. Phys. Chem. B* **2003,** *107*, 5419-5425.
6. Argumedo, A. J.; Berman, D.; Biskeborn, R. G.; Cherubini, G.; Cideciyan, R. D.; Eleftheriou, E.; Häberle, W.; Hellman, D. J.; Hutchins, R.; Imaino, W., Scaling tape-recording areal densities to 100 Gb/in 2. *IBM Journal of Research and Development* **2008,** *52*, 513-527.
7. Holzner, F.; Paul, P.; Drechsler, U.; Despont, M.; Knoll, A.; Duerig, U., High density multi-level recording for archival data preservation. *Appl. Phys. Lett.* **2011,** *99*, 023110.

8. Dai, Q.; Frommer, J.; Berman, D.; Virwani, K.; Davis, B.; Cheng, J. Y.; Nelson, A., High-throughput directed self-assembly of core–shell ferrimagnetic nanoparticle arrays. *Langmuir* **2013,** *29*, 7472-7477.
9. Corbierre, M. K.; Cameron, N. S.; Sutton, M.; Mochrie, S. G.; Lurio, L. B.; Rühm, A.; Lennox, R. B., Polymer-stabilized gold nanoparticles and their incorporation into polymer matrices. *J. Am. Chem. Soc.* **2001,** *123*, 10411-10412.
10. Huang, X.; Jiang, P., Core–shell structured high-k polymer nanocomposites for energy storage and dielectric applications. *Adv. Mater.* **2015,** *27*, 546-554.
11. Li, K.; Liu, B., Polymer-encapsulated organic nanoparticles for fluorescence and photoacoustic imaging. *Chem. Soc. Rev.* **2014,** *43*, 6570-6597.
12. Jouault, N.; Lee, D.; Zhao, D.; Kumar, S. K., Block-Copolymer-Mediated Nanoparticle Dispersion and Assembly in Polymer Nanocomposites. *Adv. Mater.* **2014,** *26*, 4031-4036.
13. Xu, C.; Ohno, K.; Ladmiral, V.; Composto, R. J., Dispersion of polymer-grafted magnetic nanoparticles in homopolymers and block copolymers. *Polymer* **2008,** *49*, 3568-3577.
14. Barbey, R.; Lavanant, L.; Paripovic, D.; Schüwer, N.; Sugnaux, C.; Tugulu, S.; Klok, H.-A., Polymer brushes via surface-initiated controlled radical polymerization: synthesis, characterization, properties, and applications. *Chem. Rev.* **2009,** *109*, 5437-5527.
15. Kango, S.; Kalia, S.; Celli, A.; Njuguna, J.; Habibi, Y.; Kumar, R., Surface modification of inorganic nanoparticles for development of organic–inorganic nanocomposites—A review. *Prog. Polym. Sci.* **2013,** *38*, 1232-1261.
16. Hui, C. M.; Pietrasik, J.; Schmitt, M.; Mahoney, C.; Choi, J.; Bockstaller, M. R.; Matyjaszewski, K., Surface-initiated polymerization as an enabling tool for multifunctional (nano-) engineered hybrid materials. *Chem. Mater.* **2013,** *26*, 745-762.
17. Tsujii, Y.; Ohno, K.; Yamamoto, S.; Goto, A.; Fukuda, T., Structure and properties of high-density polymer brushes prepared by surface-initiated living radical polymerization. In *Surface-initiated polymerization I*, Springer: 2006; pp 1-45.
18. Rühe, J.; Knoll, W., Functional polymer brushes. *Journal of Macromolecular Science, Part C: Polymer Reviews* **2002,** *42*, 91-138.
19. Mansky, P.; Liu, Y.; Huang, E.; Russell, T.; Hawker, C., Controlling polymer-surface interactions with random copolymer brushes. *Science* **1997,** *275*, 1458-1460.
20. Brandani, P.; Stroeve, P., Adsorption and desorption of PEO− PPO− PEO triblock copolymers on a self-assembled hydrophobic surface. *Macromolecules* **2003,** *36*, 9492-9501.
21. Huang, N.-P.; Michel, R.; Voros, J.; Textor, M.; Hofer, R.; Rossi, A.; Elbert, D. L.; Hubbell, J. A.; Spencer, N. D., Poly (L-lysine)-g-poly (ethylene glycol) layers on metal oxide surfaces: surface-analytical characterization and resistance to serum and fibrinogen adsorption. *Langmuir* **2001,** *17*, 489-498.
22. Tran, Y.; Auroy, P., Synthesis of poly (styrene sulfonate) brushes. *J. Am. Chem. Soc.* **2001,** *123*, 3644-3654.
23. Ohno, K.; Morinaga, T.; Koh, K.; Tsujii, Y.; Fukuda, T., Synthesis of monodisperse silica particles coated with well-defined, high-density polymer brushes by surface-initiated atom transfer radical polymerization. *Macromolecules* **2005,** *38*, 2137-2142.
24. Pyun, J.; Jia, S.; Kowalewski, T.; Patterson, G. D.; Matyjaszewski, K., Synthesis and characterization of organic/inorganic hybrid nanoparticles: kinetics of surface-initiated atom transfer radical polymerization and morphology of hybrid nanoparticle ultrathin films. *Macromolecules* **2003,** *36*, 5094-5104.
25. Ohno, K.; Akashi, T.; Huang, Y.; Tsujii, Y., Surface-initiated living radical polymerization from narrowly size-distributed silica nanoparticles of diameters less than 100 nm. *Macromolecules* **2010,** *43*, 8805-8812.

26. Ohno, K.; Mori, C.; Akashi, T.; Yoshida, S.; Tago, Y.; Tsujii, Y.; Tabata, Y., Fabrication of contrast agents for magnetic resonance imaging from polymer-brush-afforded iron oxide magnetic nanoparticles prepared by surface-initiated living radical polymerization. *Biomacromolecules* **2013,** *14*, 3453-3462.
27. Kang, C.; Crockett, R.; Spencer, N. D., The influence of surface grafting on the growth rate of polymer chains. *Polym. Chem.* **2016,** *7*, 302-309.
28. Sun, Y.; Ding, X.; Zheng, Z.; Cheng, X.; Hu, X.; Peng, Y., Surface initiated ATRP in the synthesis of iron oxide/polystyrene core/shell nanoparticles. *Eur. Polym. J.* **2007,** *43*, 762-772.
29. Babu, K.; Dhamodharan, R., Synthesis of polymer grafted magnetite nanoparticle with the highest grafting density via controlled radical polymerization. *Nanoscale Res. Lett.* **2009,** *4*, 1090.
30. Galeotti, F.; Bertini, F.; Scavia, G.; Bolognesi, A., A controlled approach to iron oxide nanoparticles functionalization for magnetic polymer brushes. *J. Colloid Interface Sci.* **2011,** *360*, 540-547.
31. Louis Chakkalakal, G.; Alexandre, M.; Abetz, C.; Boschetti-de-Fierro, A.; Abetz, V., Surface-Initiated Controlled Radical Polymerization from Silica Nanoparticles with High Initiator Density. *Macromol. Chem. Phys.* **2012,** *213*, 513-528.
32. Garcia, I.; Zafeiropoulos, N.; Janke, A.; Tercjak, A.; Eceiza, A.; Stamm, M.; Mondragon, I., Functionalization of iron oxide magnetic nanoparticles with poly (methyl methacrylate) brushes via grafting-from atom transfer radical polymerization. *J. Polym. Sci., Part A: Polym. Chem.* **2007,** *45*, 925-932.
33. Choi, J.; Hui, C. M.; Pietrasik, J.; Dong, H.; Matyjaszewski, K.; Bockstaller, M. R., Toughening fragile matter: mechanical properties of particle solids assembled from polymer-grafted hybrid particles synthesized by ATRP. *Soft Matter* **2012,** *8*, 4072-4082.
34. Marutani, E.; Yamamoto, S.; Ninjbadgar, T.; Tsujii, Y.; Fukuda, T.; Takano, M., Surface-initiated atom transfer radical polymerization of methyl methacrylate on magnetite nanoparticles. *Polymer* **2004,** *45*, 2231-2235.
35. Xue, Y.-H.; Zhu, Y.-L.; Quan, W.; Qu, F.-H.; Han, C.; Fan, J.-T.; Liu, H., Polymer-grafted nanoparticles prepared by surface-initiated polymerization: the characterization of polymer chain conformation, grafting density and polydispersity correlated to the grafting surface curvature. *Phys. Chem. Chem. Phys.* **2013,** *15*, 15356-15364.
36. Matyjaszewski, K.; Xia, J., Atom transfer radical polymerization. *Chem. Rev.* **2001,** *101*, 2921-2990.
37. Yan, J.; Pan, X.; Schmitt, M.; Wang, Z.; Bockstaller, M. R.; Matyjaszewski, K., Enhancing initiation efficiency in metal-free surface-initiated atom transfer radical polymerization (SI-ATRP). *ACS Macro Lett.* **2016,** *5*, 661-665.
38. Yan, J.; Kristufek, T.; Schmitt, M.; Wang, Z.; Xie, G.; Dang, A.; Hui, C. M.; Pietrasik, J.; Bockstaller, M. R.; Matyjaszewski, K., Matrix-free particle brush system with bimodal molecular weight distribution prepared by SI-ATRP. *Macromolecules* **2015,** *48*, 8208-8218.
39. Garcia, I.; Tercjak, A.; Zafeiropoulos, N.; Stamm, M.; Mondragon, I., Generation of core/shell iron oxide magnetic nanoparticles with polystyrene brushes by atom transfer radical polymerization. *J. Polym. Sci., Part A: Polym. Chem.* **2007,** *45*, 4744-4750.
40. Ourry, L.; Mammeri, F.; Toulemon, D.; Gaudisson, T.; Delamar, M.; Ammar, S., A tandem polyol process and ATRP used to design new processable hybrid exchange-biased Co x Fe 3− x O 4@ CoO@ PMMA nanoparticles. *RSC adv.* **2016,** *6*, 49973-49979.
41. Keller, R.; Wrcoff, H.; Marchi, L. E., Copper (I) chloride. *Inorg. Synth.* **1946,** *2*, 1-4.
42. Dehsari, H. S.; Ribeiro, A. H.; Ersöz, B.; Tremel, W.; Jakob, G.; Asadi, K., Effect of precursor concentration on size evolution of iron oxide nanoparticles. *CrystEngComm* **2017,** *19*, 6694-6702.

43. Sharifi Dehsari, H.; Heidari, M.; Halda Ribeiro, A.; Tremel, W.; Jakob, G.; Donadio, D.; Potestio, R.; Asadi, K., Combined Experimental and Theoretical Investigation of Heating Rate on Growth of Iron Oxide Nanoparticles. *Chem. Mater.* **2017,** *29*, 9648-9656.
44. Sharifi Dehsari, H.; Harris, R. A.; Ribeiro, A. H.; Tremel, W.; Asadi, K., Optimizing the Binding Energy of the Surfactant to Iron Oxide Yields Truly Monodisperse Nanoparticles. *Langmuir* **2018,** *34*, 6582-6590.
45. Sathya, A.; Guardia, P.; Brescia, R.; Silvestri, N.; Pugliese, G.; Nitti, S.; Manna, L.; Pellegrino, T., Co x Fe3–x O4 nanocubes for theranostic applications: effect of cobalt content and particle size. *Chem. Mater.* **2016,** *28*, 1769-1780.
46. Yu, Y.; Mendoza-Garcia, A.; Ning, B.; Sun, S., Cobalt-substituted magnetite nanoparticles and their assembly into ferrimagnetic nanoparticle arrays. *Advanced Materials* **2013,** *25*, 3090-3094.
47. Park, J.; An, K.; Hwang, Y.; Park, J.-G.; Noh, H.-J.; Kim, J.-Y.; Park, J.-H.; Hwang, N.-M.; Hyeon, T., Ultra-large-scale syntheses of monodisperse nanocrystals. *Nature materials* **2004,** *3*, 891.
48. Baaziz, W.; Pichon, B. P.; Fleutot, S.; Liu, Y.; Lefevre, C.; Greneche, J.-M.; Toumi, M.; Mhiri, T.; Begin-Colin, S., Magnetic iron oxide nanoparticles: reproducible tuning of the size and nanosized-dependent composition, defects, and spin canting. *J. Phys. Chem. C* **2014,** *118*, 3795-3810.
49. Baaziz, W.; Pichon, B. P.; Liu, Y.; Grenèche, J.-M.; Ulhaq-Bouillet, C.; Terrier, E.; Bergeard, N.; Halté, V. r.; Boeglin, C.; Choueikani, F., Tuning of Synthesis Conditions by Thermal Decomposition toward Core–Shell Co x Fe1–x O@ Co y Fe3–y O4 and CoFe2O4 Nanoparticles with Spherical and Cubic Shapes. *Chem. Mater.* **2014,** *26*, 5063-5073.
50. Kansara, A. M.; Aswal, V. K.; Singh, P. S., Preparation and characterization of new poly (dimethylsiloxane) membrane series via a 'cross-linking'reaction using monomolecular trichloro (alkyl) silane of different alkyl chain and type. *RSC adv.* **2015,** *5*, 51608-51620.
51. Brinker, C. J., Hydrolysis and condensation of silicates: effects on structure. *J. Non-Cryst. Solids* **1988,** *100*, 31-50.
52. Fischer, H., The persistent radical effect: a principle for selective radical reactions and living radical polymerizations. *Chem. Rev.* **2001,** *101*, 3581-3610.
53. Patten, T. E.; Matyjaszewski, K., Atom transfer radical polymerization and the synthesis of polymeric materials. *Adv. Mater.* **1998,** *10*, 901-915.
54. Beuermann, S.; Buback, M., Rate coefficients of free-radical polymerization deduced from pulsed laser experiments. *Prog. Polym. Sci.* **2002,** *27*, 191-254.
55. Beuermann, S.; Buback, M.; Davis, T. P.; Gilbert, R. G.; Hutchinson, R. A.; Olaj, O. F.; Russell, G. T.; Schweer, J.; van Herk, A. M., Critically evaluated rate coefficients for free-radical polymerization, 2.. Propagation rate coefficients for methyl methacrylate. *Macromol. Chem. Phys.* **1997,** *198*, 1545-1560.
56. Huang, Y.; Ishige, R.; Tsujii, Y.; Ohno, K., Synthesis of Iron Oxide Rods Coated with Polymer Brushes and Control of Their Assembly in Thin Films. *Langmuir* **2015,** *31*, 1172-1179.
57. Pietrasik, J.; Hui, C. M.; Chaladaj, W.; Dong, H.; Choi, J.; Jurczak, J.; Bockstaller, M. R.; Matyjaszewski, K., Silica-Polymethacrylate Hybrid Particles Synthesized Using High-Pressure Atom Transfer Radical Polymerization. *Macromol. Rapid Commun.* **2011,** *32*, 295-301.
58. Ohno, K.; Morinaga, T.; Takeno, S.; Tsujii, Y.; Fukuda, T., Suspensions of silica particles grafted with concentrated polymer brush: a new family of colloidal crystals. *Macromolecules* **2006,** *39*, 1245-1249.
59. Ohno, K.; Koh, K.; Tsujii, Y.; Fukuda, T., Fabrication of Ordered Arrays of Gold Nanoparticles Coated with High-Density Polymer Brushes. *Angew. Chem. Int. Ed.* **2003,** *42*, 2751-2754.
60. Ohno, K.; Morinaga, T.; Takeno, S.; Tsujii, Y.; Fukuda, T., Suspensions of silica particles grafted with concentrated polymer brush: Effects of graft chain length on brush layer thickness and colloidal crystallization. *Macromolecules* **2007,** *40*, 9143-9150.

61. Caruntu, D.; Caruntu, G.; O'Connor, C. J., Magnetic properties of variable-sized Fe3O4 nanoparticles synthesized from non-aqueous homogeneous solutions of polyols. *J. Phys. D: Appl. Phys.* **2007,** *40*, 5801.
62. Aslibeiki, B.; Kameli, P.; Salamati, H., The effect of dipole-dipole interactions on coercivity, anisotropy constant, and blocking temperature of MnFe2O4 nanoparticles. *J. Appl. Phys.* **2016,** *119*, 063901.
63. Frankamp, B. L.; Boal, A. K.; Tuominen, M. T.; Rotello, V. M., Direct control of the magnetic interaction between iron oxide nanoparticles through dendrimer-mediated self-assembly. *J. Am. Chem. Soc.* **2005,** *127*, 9731-9735.
64. Dormann, J.; Fiorani, D.; Tronc, E., On the models for interparticle interactions in nanoparticle assemblies: comparison with experimental results. *J. Magn. Magn. Mater.* **1999,** *202*, 251-267.
65. Chen, J.; Sorensen, C.; Klabunde, K.; Hadjipanayis, G.; Devlin, E.; Kostikas, A., Size-dependent magnetic properties of MnFe 2 O 4 fine particles synthesized by coprecipitation. *Phys. Rev. B* **1996,** *54*, 9288.
66. Fleutot, S.; Nealon, G. L.; Pauly, M.; Pichon, B. P.; Leuvrey, C.; Drillon, M.; Gallani, J.-L.; Guillon, D.; Donnio, B.; Begin-Colin, S., Spacing-dependent dipolar interactions in dendronized magnetic iron oxide nanoparticle 2D arrays and powders. *Nanoscale* **2013,** *5*, 1507-1516.
67. Nadeem, K.; Krenn, H.; Traußnig, T.; Würschum, R.; Szabó, D.; Letofsky-Papst, I., Effect of dipolar and exchange interactions on magnetic blocking of maghemite nanoparticles. *J. Magn. Magn. Mater.* **2011,** *323*, 1998-2004.
68. Coşkun, M.; Korkmaz, M., The effect of SiO 2 shell thickness on the magnetic properties of ZnFe 2 O 4 nanoparticles. *J. Nanopart. Res.* **2014,** *16*, 2316.
69. Dávila-Ibáñez, A. B.; Buurma, N. J.; Salgueiriño, V., Assessment of DNA complexation onto polyelectrolyte-coated magnetic silica nanoparticles. *Nanoscale* **2013,** *5*, 4797-4807.
70. Kostopoulou, A.; Brintakis, K.; Vasilakaki, M.; Trohidou, K.; Douvalis, A.; Lascialfari, A.; Manna, L.; Lappas, A., Assembly-mediated interplay of dipolar interactions and surface spin disorder in colloidal maghemite nanoclusters. *Nanoscale* **2014,** *6*, 3764-3776.
71. Wang, S.; Khapikov, A.; Brown, S.; Harrell, J., Thermal effects on delta-M measurements in magnetic thin films. *IEEE transactions on magnetics* **2001,** *37*, 1518-1520.
72. Zeng, H.; Li, J.; Wang, Z. L.; Liu, J. P.; Sun, S., Interparticle interactions in annealed FePt nanoparticle assemblies. *IEEE transactions on magnetics* **2002,** *38*, 2598-2600.
73. Franco, V.; Batlle, X.; Labarta, A.; O'grady, K., The nature of magnetic interactions in CoFe-Ag (Cu) granular thin films. *J. Phys. D: Appl. Phys.* **2000,** *33*, 609.

Chapter 6

Processing of Ferroelectric Polymers for Microelectronics[1]

6.1 Introduction

Non-volatile memories based on solution-cast thin films of ferroelectric polymers have emerged as a promising low-cost information storage technology for large-area microelectronic applications.[1-2] The random copolymer poly(vinylidene-fluoride-co-triflouroethylene) (P(VDF-TrFE)) is the most attractive material due to its high remanent polarization[3-5] and therefore frequently used in memory elements, such as capacitors,[6-7] ferroelectric field-effect transistors[8-9] and diodes.[10-13] To write/erase data, the ferroelectric polarization is switched by an external electric field that is larger than the coercive field, E_c, which for P(VDF-TrFE) amounts to ~50 MV/m.[4-5] In principle, this high coercive field of P(VDF-TrFE) requires a high voltages for polarization switching. To keep the operation voltage below 10 V, polymer films with a thickness below 200 nm are required. Moreover, recently research interests were shifted towards

[1] **The results of this chapter are fully or in part published in *J. Mat. Chem. C* with DOI: *10.1039/C7TC01495C* by H. Sharifi et al.**

polymer based ME thins films due to their distinctive advantages However, thin layer-devices are more susceptible to film imperfections, such as a rough microstructure, which prohibitively suppress the yield of functional devices.

Limited device yield, and concomitant large scatter in coercive voltage, hinders upscaling of integrated arrays of P(VDF-TrFE) memory elements. Generally, P(VDF-TrFE) is cast from dimethylformamide (DMF) or ketones, which are often hygroscopic. For the homopolymer poly(vinylidene fluoride) (PVDF), it has been shown that condensation of ambient water into the DMF solution causes vapor-induced phase separation (VIPS), because water is a non-solvent for PVDF.[14-15] When, a PVDF film is cast from, a high boiling point solvent (DMF) that evaporates slowly. Water vapor from humidified air is fully miscible with DMF and penetrates the wet film by diffusion. The evaporation of DMF is slower than the intake of water. Since water is a non-solvent for PVDF, phase separation occurs (see **Figure 6.1**). The resulting microstructure compromises PVDF film integrity and smoothness. Smooth PVDF films have so far only been obtained under inert atmosphere,[15-18] or at elevated substrate temperature,[15, 19] conditions that are not beneficial for cost-effective production *viz.* processing under ambient conditions (20 °C, 50% relative humidity (RH)). VIPS is also expected to occur for P(VDF-TrFE) since its properties are similar to PVDF. Although avoiding processing-related film defects is still a major challenge for sub-200 nm thin-films, consistent studies considering the full spectrum of material properties, processing conditions, microstructure formation and thin film device performance are unfortunately still lacking.

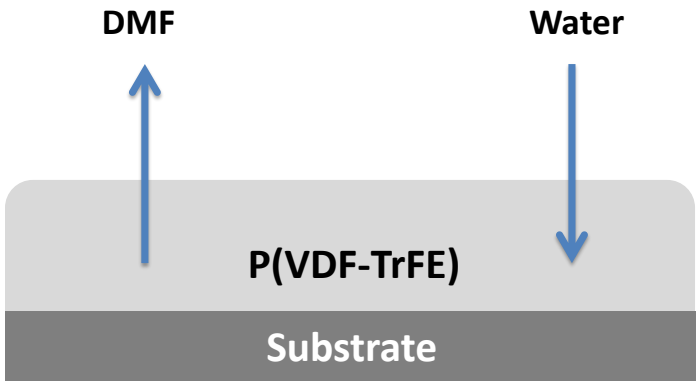

Figure 6.1 Vapor induced phase separation (VIPS) of P(VDF-TrFE) films.

6.1.1 Motivation

To understand the underlying film forming mechanisms of solution processed P(VDF-TrFE), and to obtain ultra-smooth thin films with superior performance in electronic devices such as capacitors.

6.1.2 Aim of this chapter

This section aims to provide insight in the dynamics of the early stages of VIPS, and how these relate to dry film integrity and device performance. This section covers all aspects of device preparation, starting with modeling and simulation of VIPS to pre-estimate solution behavior, proceeds with detailed microstructural analysis of cast P(VDF-TrFE) films and finally discusses device fabrication and electrical characterization. As such, a direct link is established between material properties, processing conditions and device performance. The main goal is to achieve ultra-smooth pin-hole free thin films of P(VDF-TrFE) by modifying processing condition. The approach is general and applicable not only to the field of thin-film electronics, but hopefully to any technology relying on polymer/solvent/non-solvent processing, perhaps most prominently the manufacture of microporous membranes.

6.2 Experiment

6.2.1 Materials, methods and devices

Materials

Ferroelectric copolymer P(VDF-TrFE) (65% - 35% molar) with molecular weight, M_n= 140000 (PDI=2.5) was purchased from Solvay. Poly(3,4-ethylenedioxythiophene)-poly(styrenesulfonate) (PEDOT:PSS) was purchased from Clevios. N,N-dimethylformamide (DMF), anhydrous DMF (a-DMF) (≥ 99.9%), cyclohexanone and cyclopentanone were purchased from Sigma Aldrich. All the chemicals were used as-received without further purification.

Film preparation

P(VDF-TrFE) was dissolved in different solvents (DMF, a-DMF, cyclohexanone and cyclopentanone) at a concentration of 100 mg/ml. Glass substrates were cleaned by scrubbing in soap-water and subsequently sonicated for 10 minutes in deionized water, acetone and propanol, respectively. After drying at 120 °C for 10 minutes, the substrates were treated for 5 minutes with UV-O_3. P(VDF-TrFE) films were coated under humidity-controlled conditions from solution using a wire-bar coating (K202 control coater, RK Print- see **Figure A6.1a**). Substrate temperature was varied between 20 °C and 80 °C. The relative humidity was adjusted between 10% and 80%. Film thicknesses were measured using a Dektak profilometer. The polymer films for morphological analysis were cast using the same initial solution volume of 100 µL and the same wire bar diameter. Since the initial concentration is constant, each coated film hence contained the same amount of polymer material.[15] Polymer films prepared for devices were all tuned to have the same apparent mean thickness. This was accomplished by adjusting the concentration of the casting solution.

Sample preparation for specific AFM analysis

To probe the morphology at the polymer/substrate interface, a sacrificial layer of PEDOT:PSS (~ 80 nm) was spin coated and dried in vacuum 100 °C for 10 minutes prior to P(VDF-TrFE) spin coating. After spin coating of the P(VDF-TrFE) layer, the substrates were submerged in deionized water to dissolve the PEDOT:PSS. The P(VDF-TrFE) films were picked up-side-down using a piece of mica. Both polymer/air and polymer/substrate interfaces were probed using atomic force microscopy (AFM) (Nanoscope Dimension 3100 Bruker). The topography and roughness were characterized before and after annealing at 140 °C for an area of 30 µm × 30 µm.

Thin-film devices

Ferroelectric capacitors were fabricated by thermal evaporation of Au (70 nm) on the substrates using Cr (2 nm) adhesion interlayer. Contact lines were defined using shadow masks. P(VDF-TrFE) thin films were deposited under ambient conditions (20 °C and 50% RH). The

nominal layer thickness was tuned to be 150 ± 20 nm for all the solvents via changing the concentration of polymer solution. After annealing at 140°C for 2h in vacuum, a 70 nm Au top electrode was evaporated through a shadow mask. The schematic of the device is given in **Figure A6.1b**. Electric displacement versus electric field, *D-E* loops were measured under ambient conditions using a Sawyer-Tower circuit. Details about Sawyer-Tower measurement is given in the following

Sawyer-Tower measurements were performed using a Tektronix AFG3022B function generator, a LeCroy waverunner LT372 oscilloscope and a Krohn- Hite 7602M wide-band amplifier. A schematic of the setup is presented in **Figure A6.1c**. The function generator (FG) provides a triangular waveform, which defines the frequency (typically 100 Hz or 1 kHz). The bias is then amplified and applied to the ferroelectric capacitor. The capacitor is in series with a reference capacitor. The bias applied to the circuit is measured as a function of time (triangular waveform on the left) by the first channel of the oscilloscope (*Ch 1*). The voltage drop over the reference capacitor is measured as a function of time by the second channel of the oscilloscope (*Ch 2*). If the reference capacitance is known, the amount of charges on the reference capacitor can be calculated. This amount is equivalent to that of the ferroelectric capacitor, because both elements are in series. Therefore, the displacement can be determined by dividing the charge by the capacitor's area. The electric field is the applied voltage divided by the thickness of the ferroelectric film. Ferroelectric hysteresis curves can be shown, by plotting the displacement as a function of the applied electric. Note that the capacitance of the reference capacitor should be orders of magnitude higher than the capacitance of the ferroelectric capacitor. Then, the voltage measured for *Ch 2* is approximately equivalent to the voltage over the ferroelectric capacitor, because the voltage drop over the reference capacitor is very small and can be disregarded.[20-21]

6.2.2 Input parameters for modeling

Input parameters Flory-Huggins model

The simulation (modeling) here has done by Dr. Jasper J Michels. In the following I will give a brief overview. The Flory-Huggins free energy density for our ternary blend is given by:[22]

$$\frac{f}{kT} = \frac{\phi_P}{N_P}\ln\phi_P + \frac{\phi_W}{N_W}\ln\phi_P + \frac{\phi_S}{N_S}\ln\phi_P + \chi_{PW}\phi_P\phi_W + \chi_{PS}\phi_P\phi_S + \chi_{WS}\phi_W\phi_S \qquad (6.1)$$

We obtain the effective molecular sizes N_i in terms of numbers of lattice sites by normalizing the molar volumes of all components by that of the smallest species in the mixture (here water, so: N_W = 1). The polymer is obviously much larger and taken to have an effective degree of polymerization of N_P = 1000. The average molecular weight of the experimentally used P(VDF-TrFE) (see Experimental section) even suggests N_P ~7000. We nevertheless take the lower value as it renders more numerical stability while calculating the binodal concentrations, with only minor changes to the phase diagram and demixing dynamics. We take N_S = 5 for cyclohexanone and cyclopentanone and N_S = 4 for DMF, with the remark that the exact molecular size of the solvent does not noticeably affect the phase behavior. The binary interaction parameters used in our study are: χ_{PW} = 2.8, χ_{PS} = 0.1 and χ_{WS} = 0.89, 1.67 and 2.3 for DMF, cyclohexanone and cyclopentanone respectively. The value for χ_{PW} is consistent with the literature value for PVDF:water,[23] assuming a comparable interaction for P(VDF-TrFE). The value for χ_{PS} assumes the solvent to be moderate to good in all cases, in line with experimental observations. The values for χ_{WS} for the interaction between water and the various solvents are to some extent a trade-off between approaching physical reality as closely as possible and obtaining numerical stability. The value for $\chi_{water\text{-}DMF}$ assures full miscibility between water and solvent. The values for $\chi_{water\text{-}cyclohexanone}$ and $\chi_{water\text{-}cyclopentanone}$ give water saturation concentrations of ~14% and ~4%, respectively, and somewhat overestimate the water compatibility of both solvents at 20 ^{o}C. The former is in fair agreement with tabulated data.[24] The latter is overestimated in comparison to tabulated data,[25] but that does not affect our reasoning. In contrast, it even sketches a "worser case" scenario.

Vapor pressures water and solvents.

The vapor pressures relevant to this work have been retrieved from readily accessible tabulated values: $p^{\circ}_{W}(20\,℃) = 2333$ Pa (subscript "*W*" for water), $p^{\circ}_{\text{cyclohexanone}}(20\,℃) = 667$ Pa, and $p^{\circ}_{\text{cyclopentanone}}(20\,℃) = 1467$ Pa. The polymer (indicated by subscript "*P*") is non-volatile: $p^{\circ}_{P} = 0$ Pa. The applied partial pressures are assumed constant and taken to be

$p_i^{\infty} = 0$ Pa for i = *S*, *P* (subscripts "*S*" and "*P*" for solvent and polymer) and $p_W^{\infty} = \frac{\mathrm{RH}}{100} \cdot p_W^{\circ}(20\ ℃)$ for water, with RH the relative humidity given as a percentage of $p_{\mathrm{H_2O}}^{\circ}$.

Mass transfer coefficient

The mass transfer coefficient k is (for all modeled blends) assigned a value of 0.01 $D_S^0 M_S / \rho_S \kappa RT$, with D_S^0, M_S and ρ_S the self-diffusivity, molar weight and mass density of the solvent, κ an effective gradient energy coefficient (see below), R the ideal gas constant and T the absolute temperature (here assumed to be 293 K). The choice for the value of *k*, which in reality is hard to establish, represents a situation wherein, roughly stated, the typical timescale for evaporation somewhat exceeds that of solvent diffusion. Changing the magnitude of *k* does affect demixing dynamics, but the general trends in the humidity-dependence of the characteristic time and length scales associated to vapor-induced demixing predicted by our ternary phase field model remains.

6.3 Results and discussion

6.3.1 Model predictions

In order to pre-estimate whether the water-affinity of the solvent could cause VIPS to occur during solution casting under ambient conditions, we calculated for three different solvent polarities the isothermal phase diagrams of the ternary blend of P(VDF-TrFE) polymer ("*P*")/water (= "non-solvent") ("*W*")/solvent ("*S*"), as well as the composition trajectories drawn through the phase diagram upon simultaneous solvent evaporation and water vapor dissolution. As mentioned above, three solvents were considered: DMF, cyclohexanone, and cyclopentanone, all known to be good solvents for P(VDF-TrFE). Especially cyclohexanone is often used for the fabrication of P(VDF-TrFE)-based capacitors and memory diodes.[11, 20] DMF is fully miscible with water,[26] whereas cyclohexanone and cyclopentanone exhibit partial miscibility: 86g and 9g water per liter at 20 °C, respectively.[24-25] The phase diagrams were calculated using Flory-Huggins theory[22, 27] based on input parameters, *i.e.* binary interaction parameters χ_{ij} and relative

molecular size *N*, either derived directly from literature, or matched so as to represent the above given water-solvent miscibilities. The calculated diagrams which is plotted in **Figures 6.2**, are consistent with previously reported (experimental) ones for polymer/non-solvent/solvent blends.[14, 23, 28]

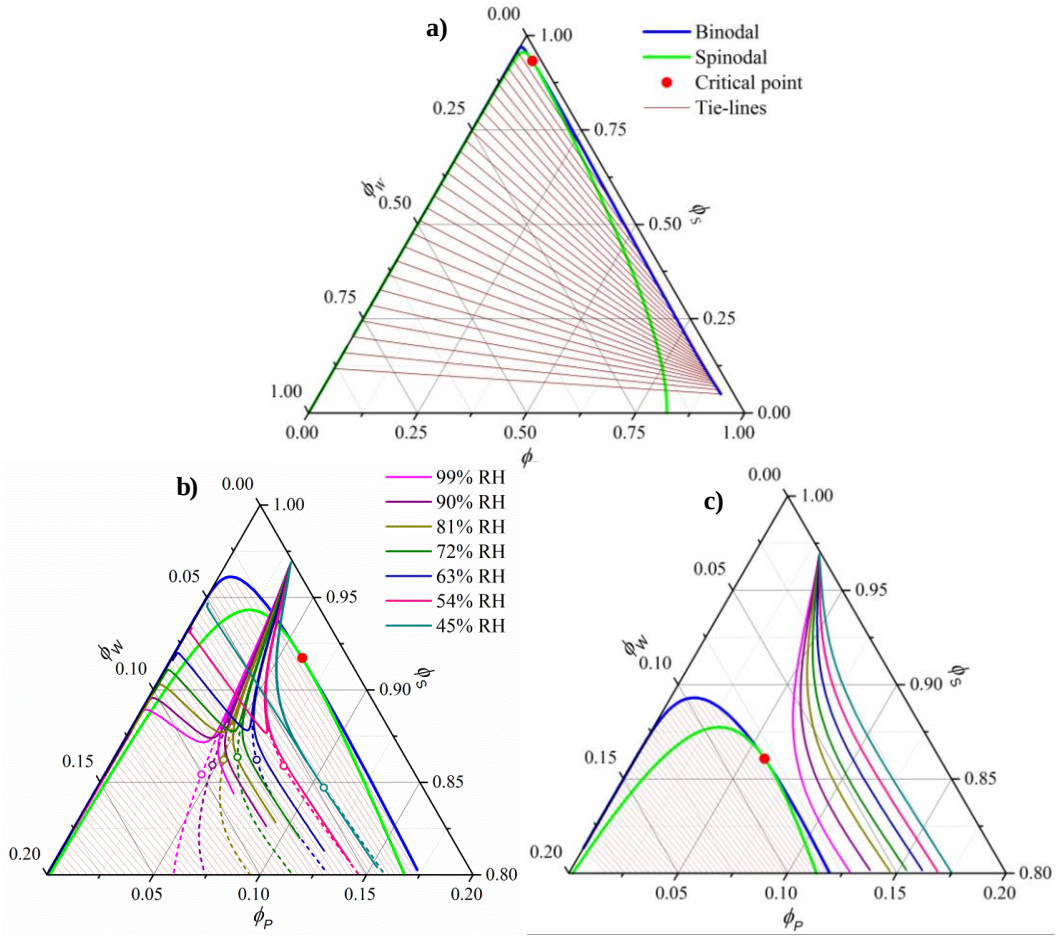

Figure 6.2 (color online) Calculated ternary phase diagrams for polymer (P)/water (W)/solvent (S) blends with S representing a) DMF, b) cyclohexanone, and c) cyclopentanone. For b) and c) only the high-solvent region is shown. The curved colored lines in a) and b) indicate the numerically simulated composition trajectories associated with exposing an initially dry 3 vol% polymer solution to an atmosphere carrying a relative humidity in the range 45 - 99%. In b) demixing occurs, where the open symbols indicate the mean composition (dashed) at which the mixtures phase separate. The dash-dotted black line represents critical mean compositions, for which a bicontinuous structure is expected upon demixing.

The phase diagram for DMF (**Figure 6.2 a**) is shown completely, whereas of the ones for cyclohexanone and cyclopentanone (**Figure 6.2 b** and **c**), which are of comparable nature to the

one for DMF, only the top part is shown for clarity's sake. The phase diagrams are characteristic for a polymer/non-solvent/solvent ternary, evidenced by i) a large miscibility gap, ii) a pronounced asymmetry, and iii) steeply tilted tie-lines. The first feature is mainly due to the high value of the polymer-nonsolvent interaction parameter (χ_{PW} = 2.8). The asymmetry is a result of the difference in molecular size between a polymer and a water molecule and the tilt in the tie lines shows that if VIPS occurs, the solvent strongly prefers the polymer-poor phase. **Figure 6.2 c** shows that a lower solvent polarity reduces the miscibility gap somewhat.

The colored curves in **Figures 6.2 b** and **c** represent calculated (mean) composition trajectories resulting from simultaneous solvent evaporation and water ingress from/into the drying polymer solution, at various RH levels (see legend). These curves were calculated assuming the volume flux σ_i of a blend component i across the liquid-vapor interface to be governed by the difference between its partial pressure just above the film and the applied partial pressure p_i^{∞} away from the vapor-liquid interface. Just above the drying film, a liquid-vapor equilibrium is assumed, so that the fluxes of water and solvent are given by:

$$\begin{pmatrix}\sigma_P\\ \sigma_W\end{pmatrix} = k\begin{pmatrix} -1 & \frac{\langle\phi_P\rangle}{1-\langle\phi_W\rangle} & \frac{\langle\phi_P\rangle}{1-\langle\phi_S\rangle}\\ \frac{\langle\phi_W\rangle}{1-\langle\phi_P\rangle} & -1 & \frac{\langle\phi_W\rangle}{1-\langle\phi_S\rangle}\end{pmatrix}\begin{pmatrix} p_P^{\circ}\exp\left(\frac{\langle\mu_P\rangle}{RT}\right) - p_P^{\infty}\\ p_W^{\circ}\exp\left(\frac{\langle\mu_W\rangle}{RT}\right) - p_W^{\infty}\\ p_S^{\circ}\exp\left(\frac{\langle\mu_S\rangle}{RT}\right) - p_S^{\infty}\end{pmatrix} \qquad (6.2)$$

with $\langle\phi_i\rangle$ the mean volume fraction, $\langle\mu_i\rangle$ the mean chemical potential, p_i° the vapor pressure of the pure substance (tabulated for all solvents and water), and k a mass transfer coefficient expressed in units of $Pa^{-1}s^{-1}$ and for simplicity taken equal for water and solvent. The coefficient matrix on the RHS of **Equation 6.2** enforces incompressibility. By defining $p_W^{\infty} > 0$ and $p_S^{\infty} = 0$ and by combining **Equations 6.2** with the generalized 2D-diffusion model we published earlier,[27, 29-30] we not only track composition as a function of time, but also model the actual dynamics of structure formation due to VIPS.

The calculations (**Figure 6.2 b** and **c**) assume an initially dry solution with a polymer concentration of 3 vol%. In the case of cyclohexanone the mean composition (dashed lines) readily enters the spinodal region, whereas for the more hydrophobic cyclopentanone, the

trajectories remain within the single phase region. The calculations hence predict that for cyclohexanone spinodal VIPS occurs, but probably not for cyclopentanone even for high relative humidity. For DMF the results were similar to cyclohexanone and are hence not explicitly shown.

6.3.2 Microscopic analysis

As a next step we performed microscopic (AFM) analysis on dry P(VDF-TrFE) thin films cast from the above mentioned solvents under controlled humidity and substrate temperature conditions. Below only representative data are reported to substantiate the discussion. The appendix contains a full account of all casting experiments and AFM analyses (**Figure A6.2-Figure A6.6**).

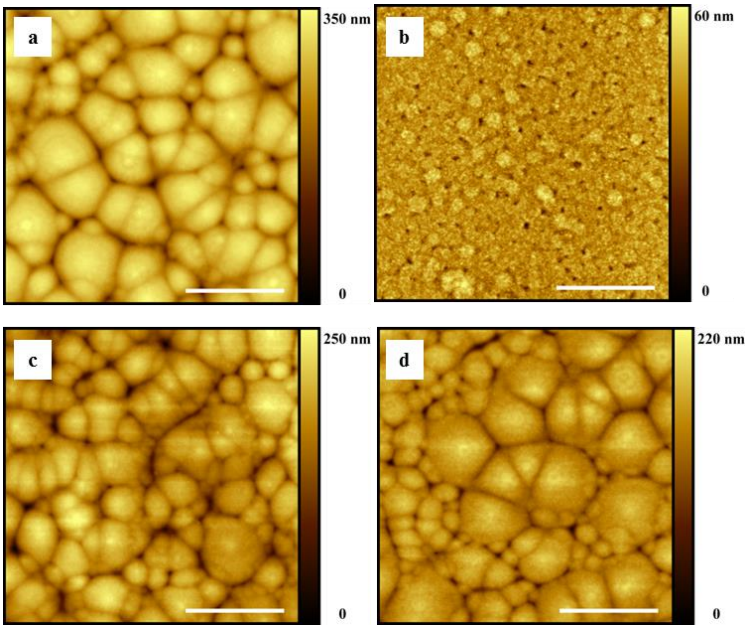

Figure 6.3 Tapping mode AFM height images of P(VDF-TrFE) thin films coated at (a) DMF, 20°C and 50% relative humidity, (b) 65°C and 50% relative humidity, (c) DMF, 20°C and 10% relative humidity, and (d) a-DMF, 20°C and 50% relative humidity. The scale bar is 10 μm.

Figure 6.3 shows AFM topology images of films cast from wet (*i.e.* equilibrated) and anhydrous DMF under various conditions (see caption). **Figures 6.3 a**, **c** and **d** show that at a substrate temperature of 20 ^{o}C the polymer layers consist of impinged micron-sized drop-like

domains having considerable topological gradients, irrespective of the RH. For these films a root mean square (rms) roughness of ~50 nm was obtained. In contrast, at a substrate temperature of 65 ^{o}C the films show much smaller features and are significantly smoother (**Figure 6.3 b**), the rms roughness decreasing to ~5 nm.

Just as observed previously for PVDF in DMF,[15] and in line with the modeling results, the morphologies in **Figures 6.3 a, c** and **d** form due to water-vapor induced phase separation, initially giving polymer-rich droplets suspended in a DMF-swollen medium. During evaporation ripening and coalescence of the P(VDF-TrFE)-rich droplets takes place until solvent is depleted and the film solidifies. The grain structure in the dry film suggests that at some point coarsening halts and the droplets impinge onto each other. The fact that DMF and anhydrous DMF give similar structure sizes indicates that water ingress is fast compared to solvent evaporation. VIPS seems virtually absent at 65 ^{o}C, even at 50 % RH, which suggests i) a decreased water miscibility at elevated temperature and/or ii) suppression of VIPS domain growth due to fast solidification upon enhanced solvent evaporation. We note that a similar decrease in roughness with substrate temperature has also been observed for DMF-cast films of PVDF.[15]

Figure 6.4 shows AFM topology images of P(VDF-TrFE) films cast from cyclohexanone (**Figure 6.4 a** and **b**) and cyclopentanone (**Figure 6.4 c** and **d**) 20 ^{o}C, with RH values varied between 10%, 50% and 80%. In excellent agreement with the model, microstructure formation due to VIPS is observed for cyclohexanone and not for cyclopentanone, even at 80% RH. It is however fair to note that the significantly higher vapor pressure of cyclopentanone further suppresses possible VIPS due to fast solidification of the film. The effect of solidification, which for P(VDF-TrFE) probably partly relies on crosslink formation via nano-crystallization, is not taken into account by our model.

We note that the used cyclohexanone was not anhydrous. Hence, demixing might have been induced by water already present in solution prior to casting.[15] Just as for DMF, the cyclohexanone solutions produce smooth and uniform films at elevated substrate temperature (**Figure A6.5**). In the case of cyclopentanone, the surface roughness and morphology does not change substantially upon increasing the substrate temperature (**Figure A6.6**). Evidently, for ambient processing of P(VDF-TrFE), VIPS can only be avoided if a hydrophobic solvent with a water-miscibility well below 10 wt% is used.

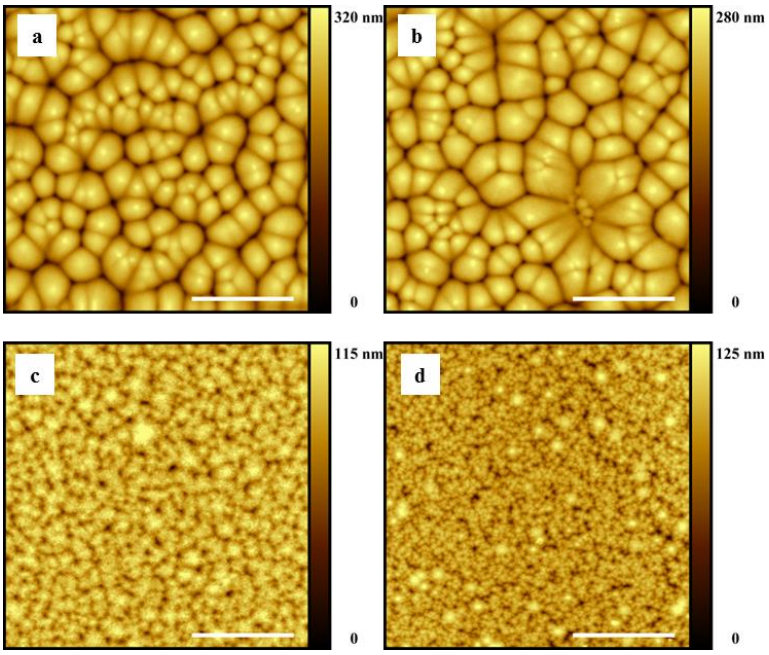

Figure 6.4 AFM height images of P(VDF-TrFE) thin films coated from cyclohexanone (a,b) and cyclopentanonbe (c,d). Conditions: (a,c) 20°C, 50% RH, (b) 20°C, 10% RH, (d) 20°C, 80% RH. The scale bar is 10 μm.

In order to discriminate the VIPS-related dry film features from possible spherulitic crystallization, we also scanned the topology at the polymer-substrate interface. To this end, dry films were floated of the substrate and placed upside down under the AFM tip (see Experimental section for details). The recorded images are given in **Figure 6.5** for cyclohexanone (**Figure 6.5 a)** and cyclopentanone (**Figure 6.5 b**). Since in both cases the topological and microstructural features are the same as those at the polymer-vapor interface heterogeneously nucleated spherulitic crystal growth can be ruled out, as that would not lead to topological gradients at the polymer-substrate interface.

Film thickness and rms roughness, acquired at 50% RH for all three solvents are plotted in **Figure 6.6 a** and **b** as a function of substrate temperature (also for 10% RH in **Figure 6.6 c** and **d**). **Figure 6.6 a** shows that for the films processed from DMF and cyclohexanone under ambient conditions the apparent mean thickness is strongly overestimated due to the large topological features resulting from VIPS (**Figure 6.7a**). By increasing substrate temperature the structure densifies and the apparent mean thickness saturates at a value of 300 nm. Expectedly, the rms roughness follows the same trend (**Figure 6.6 b**). For cyclopentanone however, due to

the absence of VIPS, a dense smooth film of 300 nm with ~10 nm rms roughness is already obtained at room temperature, irrespective of relative humidity (**Figure 6.7 b**).

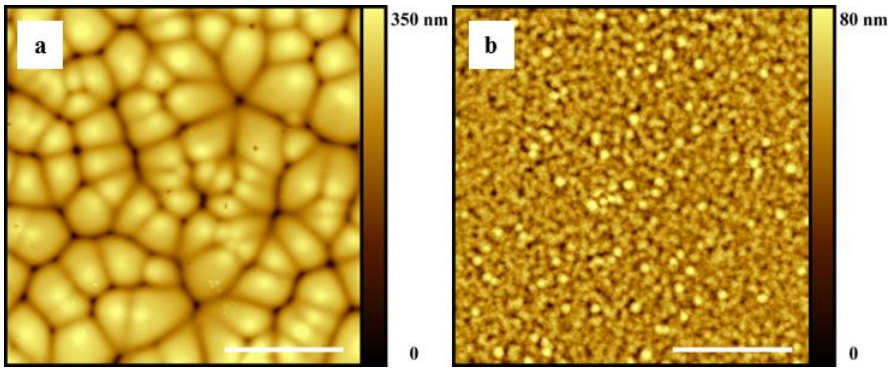

Figure 6.5 AFM topography images of the polymer/substrate interface of P(VDF-TrFE) layers cast from (a) cyclohexanone and (b) cyclopentanone. The substrate temperature and relative humidity were fixed at 20°C and 50% in both cases. The scale bar is 10 μm.

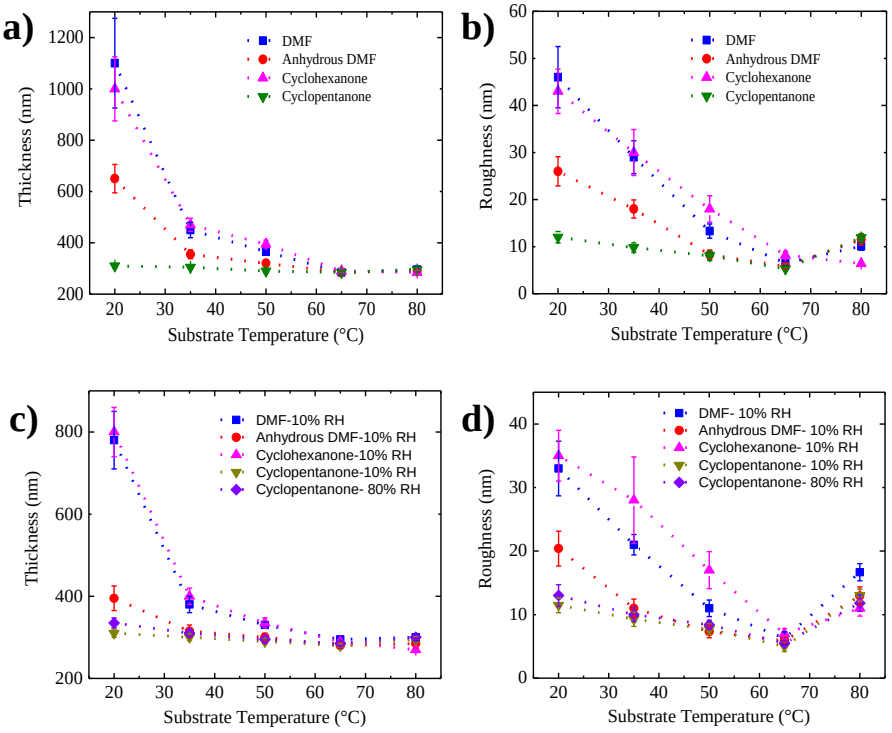

Figure 6.6 (color online) (a) Layer thickness and (b) rms roughness plotted as a function of substrate temperature measured for films prepared at a fixed relative humidity of 50%. (c) Layer thickness and (d) rms roughness plotted as a function of substrate temperature measured for films prepared films at a fixed relative humidity of 10% (80% only for cyclopentanone).

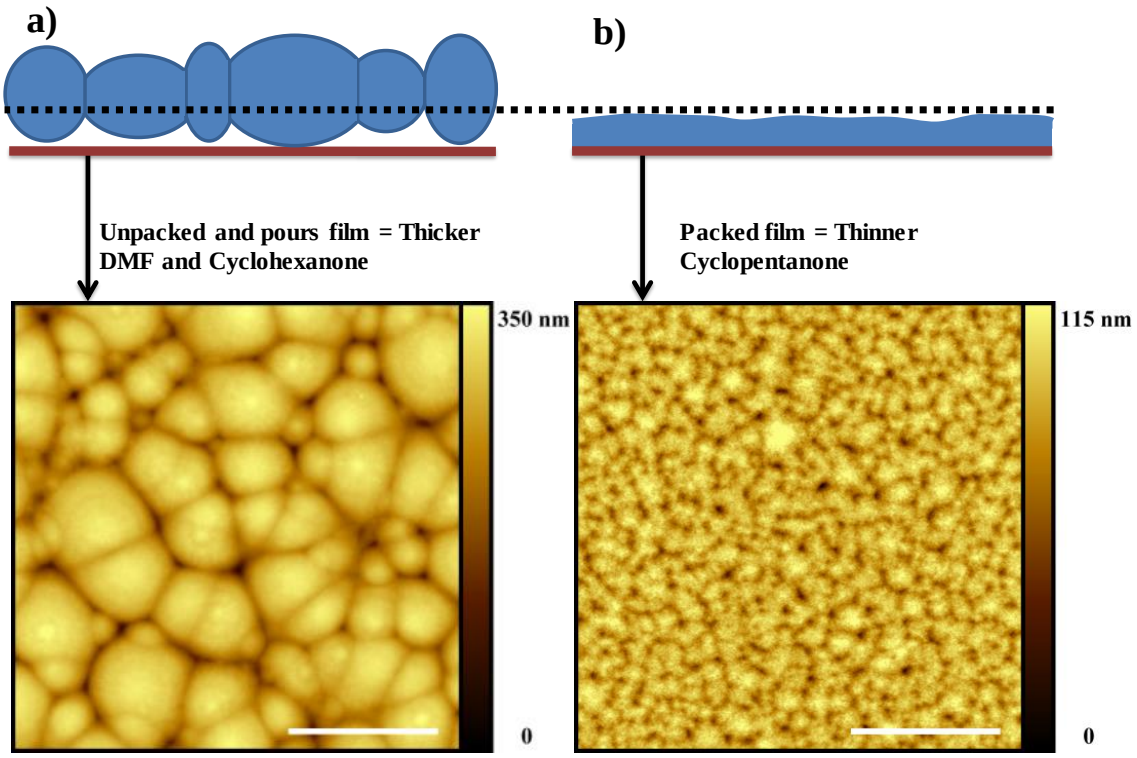

Figure 6.7 Schematic cross-sectional images explaining why the mean thickness of VIPS-influenced films is overestimated due to the high roughness. Films cast under under ambient conditions (20°C and 50% RH) from (a) cyclohexanone and (b) cyclopentanone. The scale bar is 10 µm.

In what follows we give our view on the origin of the impinged dry-film domain structure resulting from VIPS (*e.g.* **Figure 6.4 a** and **b**). The morphology suggests that at some point during drying coarsening ceases, whereby the polymer-rich droplets mutually impinge and deform from their circular or spherical shape. We speculate that elastic stresses occurring in the final stages of drying underlie this phenomenon. In general, free energy reduction by elastic deformation competes with domain coarsening driven by liquid-liquid interface minimization. The question is whether the dry film structure develops under influence of purely elastic or viscoelastic stress. In case of the former, domain deformation is caused by elastic asymmetry, such as a difference in shear modulus between the phases.[31-33] Reduction of the total free energy is accomplished by anisotropic deformation of the softer phase into an extended network-like structure embedding domains of the harder phase.[31]

In contrast, *visco*elastic structure development is driven by a dynamic asymmetry between the phases in a fluid mixture.[34] In this case structure development is governed by the partitioning of the total stress between the phases, as governed by the force balance condition. In contrast to elastic demixing, morphologies develop in which the temporarily harder, *i.e.* more viscoelastic, phase forms the network surrounding domains of the "softer"/more fluid phase. We argue that the impinged dry film morphologies form under the influence of elastic rather than viscoelastic stress. We hypothesize that the elastic anisotropy, and the concomitant stagnation of coarsening, is introduced by late-stage development of P(VDF-TrFE) crystallites, giving rise to a gel-like state in polymer-rich regions.

6.3.3 Device characteristics

To probe the effect of solvent hygroscopicity on device performance we carried out a systematic study involving more than 100 ferroelectric capacitors fabricated per each solvent under ambient condition (20°C and 50% RH). The device architecture is depicted in the inset of **Figure 6.9 b**. The (apparent) mean film thickness was fixed at $\langle d \rangle$ = 150 ± 20 nm by adjusting the polymer concentration in solution. We noted that the morphology is not affected by varying the thickness. Enhanced crystallinity by subsequent annealing of the P(VDF-TrFE) films at 140 ^{o}C (see Experimental Section), only marginally increased the film roughness (**Figure 6.8 a** and **b**). The annealed samples show needle-like domains (**Figure 6.8 c**) which are typical structure for crystallized P(VDF-TrFE).

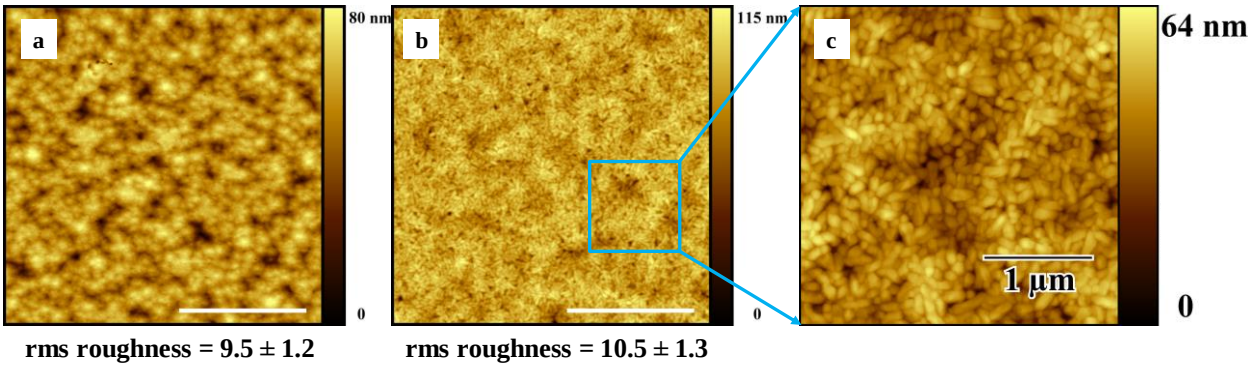

Figure 6.8 AFM height images of P(VDF-TrFE) thin films coated from solution in cyclopentanone at 50% relative humidity and substrates temperature of 20°C (a) before and (b) after annealing. The scale bar is 4 µm.(c) a zoom in image of (b).

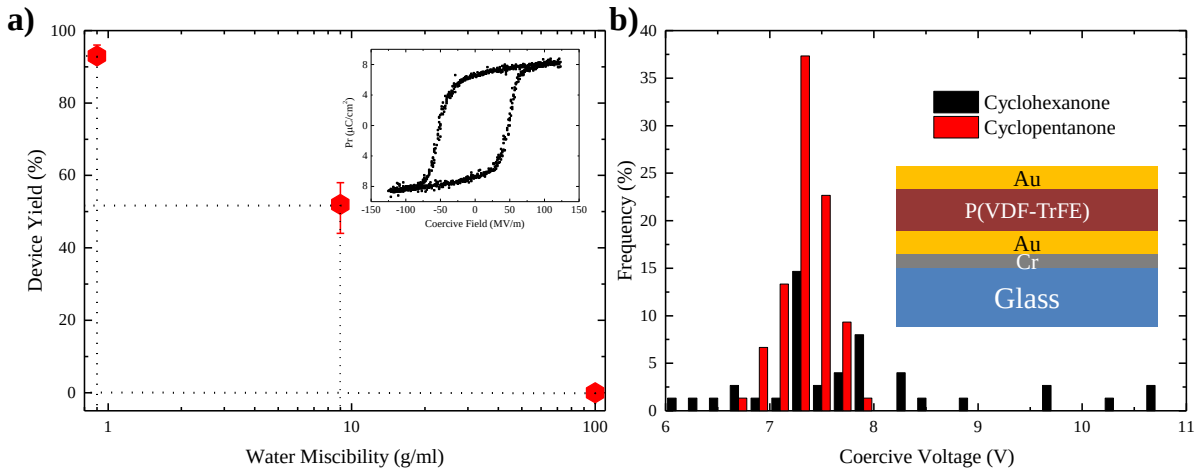

Figure 6.9 (a) Device yield as a function of water miscibility of solvents. (b) Histogram of coercive voltage for cyclohexanone and cyclopentanone. The insets show a ferroelectric displacement loop for P(VDF-TrFE) capacitor and capacitor layout. The capacitors were measured with a continuous triangular bias at a frequency of 100 Hz and using a reference capacitor of 220 nF.

A typical hysteresis loop of P(VDF-TrFE) is presented in the inset of **Figure 6.9 a**. The ferroelectric remanent polarization of all the capacitors was about the same and amounted to 6-7 μC/cm^2, in agreement with literature data.[3-5] The graph in **Figure 6.9 a** shows that the yield of functioning thin-film capacitors drops substantially with increasing water miscibility of the solvent: whereas no functional capacitor was obtained using DMF, cyclohexanone gave a yield of ~50%. However, processing devices using cyclopentanone gave an impressive yield of >93%, the few non-working devices probably resulting from particle-induced short-circuits, rather than morphological flaws. Ferroelectric thin-film quality is also reflected by scatter in the coercive voltage, *i.e.* the voltage at which the polarization switches sign. **Figure 6.9 b** shows the histogram of the coercive voltages measured for capacitors fabricated from cyclohexanone and cyclopentanone. Whereas the coercive voltage of cyclohexanone-processed devices shows significant scatter, a narrow distribution of 7.3 ± 0.5V is obtained in case of cyclopentanone, reflecting the low surface roughness and excellent film uniformity.

6.4 Conclusions

The role of ambient humidity, temperature and solvent hygroscopicity on the microstructure of P(VDF-TrFE) thin-films applied in flexible memory devices has been

investigated. Computational predictions using a combination of phase diagram calculations and structure evolution modeling provides detailed insight in the mechanism of water vapor-induced phase separation (VIPS) during solution casting of the polymer under ambient conditions. Simultaneous solvent evaporation and water ingress destabilizes the blend in case the solvent is fully or partially miscible with water. We demonstrate that VIPS can occur even in solvents with a water-miscibility as low as 10%. The model predicts the formation of polymer-rich droplets suspended in a solvent-rich medium, which is consistent with AFM analysis on solid P(VDF-TrFE) films cast from DMF and cyclohexanone, which indeed comprise clear drop-like features. In contrast, the more hydrophobic cyclopentanone gave smooth, near featureless layers, also in agreement with model predictions. Film quality is directly reflected by thin-film capacitor yield, which for DMF and cyclohexanone remains well below 50% with considerable scattering in coercive voltages, but increases to >93% and narrowly distributed coercive voltage when cyclopentanone is used.

6.5 References

1. Naber, R. C.; Asadi, K.; Blom, P. W.; de Leeuw, D. M.; de Boer, B., Organic nonvolatile memory devices based on ferroelectricity. *Adv. Mater.* **2010,** *22*, 933-945.
2. Heremans, P.; Gelinck, G. H.; Muller, R.; Baeg, K.-J.; Kim, D.-Y.; Noh, Y.-Y., Polymer and organic nonvolatile memory devices. *Chem. Mater.* **2010,** *23*, 341-358.
3. Lovinger, A. J., Ferroelectric polymers. *Science* **1983,** *220*, 1115-1121.
4. Furukawa, T., Structure and functional properties of ferroelectric polymers. *Adv. Colloid Interface Sci.* **1997,** *71*, 183-208.
5. Mao, D.; Quevedo-Lopez, M.; Stiegler, H.; Gnade, B. E.; Alshareef, H. N., Optimization of poly (vinylidene fluoride-trifluoroethylene) films as non-volatile memory for flexible electronics. *Org. Electron.* **2010,** *11*, 925-932.
6. Naber, R.; Blom, P.; Marsman, A.; De Leeuw, D., Low voltage switching of a spin cast ferroelectric polymer. *Appl. Phys. Lett.* **2004,** *85*, 2032-2034.
7. Furukawa, T.; Nakajima, T.; Takahashi, Y., Factors governing ferroelectric switching characteristics of thin VDF/TrFE copolymer films. *IEEE Trans. Dielectr. Electr. Insul.* **2006,** *13*, 1120-1131.
8. Naber, R. C.; Tanase, C.; Blom, P. W.; Gelinck, G. H.; Marsman, A. W.; Touwslager, F. J.; Setayesh, S.; De Leeuw, D. M., High-performance solution-processed polymer ferroelectric field-effect transistors. *Nat. Mater.* **2005,** *4*, 243-248.
9. Khan, M. A.; Bhansali, U. S.; Alshareef, H. N., High-Performance Non-Volatile Organic Ferroelectric Memory on Banknotes. *Adv. Mater.* **2012,** *24*, 2165-2170.

10. Asadi, K.; De Leeuw, D. M.; De Boer, B.; Blom, P. W., Organic non-volatile memories from ferroelectric phase-separated blends. *Nat. Mater.* **2008,** *7*, 547-550.
11. Li, M.; Stingelin, N.; Michels, J. J.; Spijkman, M. J.; Asadi, K.; Beerends, R.; Biscarini, F.; Blom, P. W.; de Leeuw, D. M., Processing and Low Voltage Switching of Organic Ferroelectric Phase-Separated Bistable Diodes. *Adv. Funct. Mater.* **2012,** *22*, 2750-2757.
12. Van Breemen, A.; Kam, B.; Cobb, B.; Rodriguez, F. G.; Van Heck, G.; Myny, K.; Marrani, A.; Vinciguerra, V.; Gelinck, G., Ferroelectric transistor memory arrays on flexible foils. *Org. Electron.* **2013,** *14*, 1966-1971.
13. van Breemen, A. J.; van der Steen, J.-L.; van Heck, G.; Wang, R.; Khikhlovskyi, V.; Kemerink, M.; Gelinck, G. H., Crossbar arrays of nonvolatile, rewritable polymer ferroelectric diode memories on plastic substrates. *Appl. Phys. Express* **2014,** *7*, 031602.
14. Matsuyama, H.; Teramoto, M.; Nakatani, R.; Maki, T., Membrane formation via phase separation induced by penetration of nonsolvent from vapor phase. II. Membrane morphology. *J. Appl. Polym. Sci.* **1999,** *74*, 171-178.
15. Li, M.; Katsouras, I.; Piliego, C.; Glasser, G.; Lieberwirth, I.; Blom, P. W.; de Leeuw, D. M., Controlling the microstructure of poly (vinylidene-fluoride)(PVDF) thin films for microelectronics. *Journal of Materials Chemistry C* **2013,** *1*, 7695-7702.
16. Benz, M.; Euler, W. B.; Gregory, O. J., The role of solution phase water on the deposition of thin films of poly (vinylidene fluoride). *Macromolecules* **2002,** *35*, 2682-2688.
17. Kang, S. J.; Park, Y. J.; Hwang, J.; Jeong, H. J.; Lee, J. S.; Kim, K. J.; Kim, H. C.; Huh, J.; Park, C., Localized Pressure-Induced Ferroelectric Pattern Arrays of Semicrystalline Poly (vinylidene fluoride) by Microimprinting. *Adv. Mater.* **2007,** *19*, 581-586.
18. Kang, S. J.; Park, Y. J.; Sung, J.; Jo, P. S.; Park, C.; Kim, K. J.; Cho, B. O., Spin cast ferroelectric beta poly (vinylidene fluoride) thin films via rapid thermal annealing. *Appl. Phys. Lett.* **2008,** *92*, 012921.
19. Ramasundaram, S.; Yoon, S.; Kim, K. J.; Lee, J. S.; Park, C., Crystalline structure and ferroelectric response of poly (vinylidene fluoride)/organically modified silicate thin films prepared by heat controlled spin coating. *Macromol. Chem. Phys.* **2009,** *210*, 951-960.
20. Lenz, T.; Sharifi Dehsari, H.; Asadi, K.; Blom, P. W.; Groen, W. A.; de Leeuw, D. M., Thin film thermistor with positive temperature coefficient of resistance based on phase separated blends of ferroelectric and semiconducting polymers. *Appl. Phys. Lett.* **2016,** *109*, 133302.
21. Lenz, T. Device physics and nanostructuring of organic ferroelectric memory diodes. Johannes Gutenberg-Universität Mainz, 2017.
22. Flory, P. J., *Principles of polymer chemistry*. Cornell University Press: 1953.
23. Ghodsi, A.; Fashandi, H.; Zarrebini, M.; Abolhasani, M. M.; Gorji, M., Highly effective CO 2 capture using super-fine PVDF hollow fiber membranes with sub-layer large cavities. *RSC Adv.* **2015,** *5*, 92234-92253.
24. Information., N. C. f. B., PubChem Compound Database. PubChem Compound Database

2017.
25. Information., N. C. f. B., PubChem Compound Data. PubChem Compound Database.: 2017.
26. Information, N. C. f. B., PubChem Compound Database. PubChem Compound Database.: 2017.
27. Schaefer, C.; Michels, J. J.; van der Schoot, P., Structuring of thin-film polymer mixtures upon solvent evaporation. *Macromolecules* **2016,** *49*, 6858-6870.
28. Matsuyama, H.; Teramoto, M.; Nakatani, R.; Maki, T., Membrane formation via phase separation induced by penetration of nonsolvent from vapor phase. I. Phase diagram and mass transfer process. *J. Appl. Polym. Sci.* **1999,** *74*, 159-170.
29. Michels, J. J.; Moons, E., Simulation of surface-directed phase separation in a solution-processed polymer/PCBM blend. *Macromolecules* **2013,** *46*, 8693-8701.

30. Schaefer, C.; van der Schoot, P.; Michels, J., Structuring of polymer solutions upon solvent evaporation. *Physical Review E* **2015,** *91*, 022602.
31. Onuki, A.; Nishimori, H., Anomalously slow domain growth due to a modulus inhomogeneity in phase-separating alloys. *Phys. Rev. B* **1991,** *43*, 13649.
32. Sagui, C.; Somoza, A.; Desai, R. C., Spinodal decomposition in an order-disorder phase transition with elastic fields. *Phys. Rev. E* **1994,** *50*, 4865.
33. Orlikowski, D.; Sagui, C.; Somoza, A.; Roland, C., Large-scale simulations of phase separation of elastically coherent binary alloy systems. *Phys. Rev. B* **1999,** *59*, 8646.

34. Tanaka, H., Viscoelastic phase separation. *J. Phys.: Condens. Matter* **2000,** *12*, R207.

Chapter 7

Section 1

Thin-Film Polymer Nanocomposites for Multi-Ferroic Applications Based on MNPs/(PVDF-TrFE) [1]

7.1.1 Introduction

Ferroelectric polymers, such as polyvinylidene fluoride (PVDF) and in particular its random copolymer poly(vinylidene-fluoride-co-triflouroethylene) (P(VDF-TrFE)) have been recently investigated for their potential applications in flexible non-volatile memories, energy storage, and multiferroic composites.[1-20] P(VDF-TrFE) has a relatively low remanent polarization, P_r and a high coercive field, E_C, which depending on the VDF to TrFE composition, amounts to 5-8 μC/cm^2 and 45-65 MV/m, respectively.[21-22] The high coercive field of P(VDF-TrFE) mandates realization of thin films that should be operable at voltages suited for microelectronic applications.[23-24] Since inorganic ferroelectrics, such as $BaTiO_3$, generally

[1] **The results of this chapter are fully or in part published in *ACS Appl. Nano Mat.* with DOI: *10.1021/acsanm.8b01443* by H. Sharifi et al.**

exhibit higher P_r and a lower E_C, mixing PVDF or P(VDF-TrFE) with inorganic ferroelectric nanoparticles has been pursued to create a composite with higher P_r and lower E_C, and higher dielectric permittivity, ε.[21, 25-30] Moreover, recently P(VDF-TrFE) nanocomposites have been suggested (depending on the filler properties) for polymer multiferroic and energy storage applications, and therefore are of high technological interests.[31-42] Intuitively, addition of non-ferroelectric fillers should reduce P_r, because the volume of the P(VDF-TrFE) phase in nanocomposite is lowered. Hence, upon addition of fillers, reduction of P_r is expected. Interestingly, as the filler loading increases both increasing[34-39] or decreasing trends in P_r,[31, 33] E_C and ε have been reported.

In **Figure 7.1.1**, we have plotted the reported trends of P_r and E_C after addition of different types of NPs. For comparison, the values for each data series are normalized to the P_r and E_C values at 0 wt% loading of the same series. Interestingly, P_r as high as 18.1 μC/cm^2 has been reported which is nearly two times the maximum theoretically achievable P_r of P(VDF-TrFE).[34-35, 43-44] A summary of the film thickness of the filler size, filler type, P_r and E_C values of the nanocomposite films at 0 wt% loading is given in **Table 7.1.1**. The overall reported results so far are however inconclusive. The proposals on the origin of the increased P_r are diverse and vary depending on the type of the nanoparticle used. Subash *et al.* [37] have argued that addition of zinc oxide nanoparticles generally leads to the formation of more ferroelectric β-phase crystals in P(VDF-TrFE). Park *et al.* [38] have argued that metallic (Ag) nanoparticles enhance the dipolar alignment due to the field concentrations in the matrix. For the same Ag nanoparticles in P(VDF-TrFE) system, Tsutsumi *et al.* [39] have attributed the increased remnant polarization to a high dielectric constant of the nanoparticle and higher local electric field on the crystalline phase, whereas Zou *et al.* [36] have suggested that the Ag nanoparticles reduce depolarization. Li *et al.*[32] have suggested existence of a large Maxwell–Wagner–Sillars (MWS) interfacial polarization at low frequencies for TiO_2 nano fillers. For ferrite magnetic nanoparticle fillers, Martins *et al.*[35] have suggested that, the ferrite nanoparticles simultaneously act as heterogeneous nucleation centers for ferroelectric domains and provide additional free charges required for stabilizing the polarization. On the other hand, the large interfacial area promotes the exchange coupling effect through a dipolar interface layer. However, the have investigated the thick films of with inhomogeneous MNPs and presence of huge aggregation in matrix.

It is evident from the literature overview, **Figure 7.1.1**, that a systematic and self-consistent study on P(VDF-TrFE)/MNPs nanocomposite thin film is still missing. Despite the interesting results reported so far, there is still much need of a reliable data sets and studies that investigate the effect of the magnetic fillers on the microstructure of the nanocomposite, the remanent polarization and its switching time. Data presented in **Figure 7.1.1**, and **Table 7.1.1**, spans over eight orders of magnitude, but were extracted from ten different reports. A systematic study on the influence of magnetic nanoparticle loading on polarization switching dynamics of P(VDF-TrFE) in the nanocomposite is also lacking in the literature.[39, 45] Moreover, microstructural studies of the nanocomposite and the effect of the filler loading on the dynamic of the ferroic properties have not been extensively reported yet. Understanding and engineering of the microstructure is of crucial importance for the application of the P(VDF-TrFE)/MNPs nanocomposites in multiferroic applications.

7.1.1.1 Motivation

A solid understanding of the microstructure evolution upon adding MNPs to P(VDF-TrFE) and its relation to the ferroelectric performance,(*i.e.* P_r, E_c, ε, switching time) and magnetic properties of the nanocomposite thin film, would help to design polymer based multiferroic nanocomposites with optimized performance.

7.1.1.2 Aim of this section

This section reports in-depth investigations on the influence of the MNPs fillers on the microstructure, ferroelectric and magnetic properties of the nanocomposite thin films using P(VDF-TrFE) as a polymer matrix. For the first time, to the best of knowledge, the filler loading is varied over an unprecedented range of nearly six orders of magnitude. As filler, we have used freshly synthesized truly monodisperse magnetic iron oxide (superparamagnetic) and cobalt ferrite (ferromagnetic) MNPs.[46-48] The loading is changed from 10^{-4} wt% to 30 wt%. Smooth and pinhole free nanocomposite thin- and thick films have been produced by suppression of vapor induced phase separation (VIPS).[49] We have realized thin-films of P(VDF-TrFE)/MNPs nanocomposites suited for low-voltage operations. Besides investigating the effect of nanoparticle loading on the evolution of microstructure, crystallinity, P_r and E_c, we have studied

the evolution of the dielectric properties, kinetics of the ferroelectric polarization reversal and magnetic properties upon filler loading over the whole composition range.

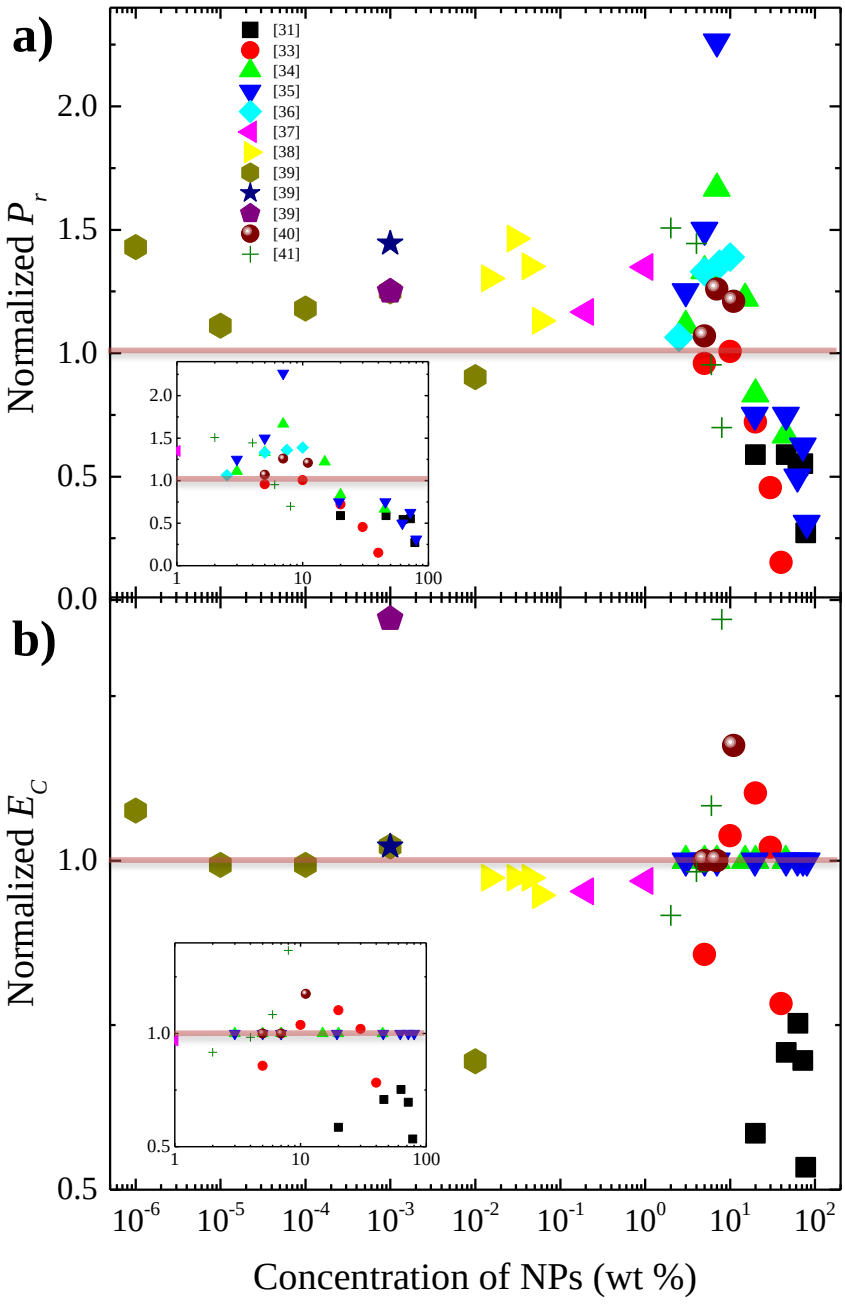

Figure 7.1.1 Overview of the reported normalized (a) P_r and (b) E_c of P(VDF-TrFE) composites with non-ferroelectric fillers. All the points were normalized to their respective value of 0 wt % given in **Table 7.1.1**. The insets show the zoom in of each graphs in the range of 1-100 wt %.

Table 7.1.1 Overview of the non-ferroelectric fillers, size, and film thickness on the ferroelectric properties of the P(VDF-TrFE) composite.

Ref.	P(VDF-TrFE) composition	Nanoparticle	Nanoparticle size (nm)	Composite thickness (μm)	P_r (μm/cm^2) at 0 wt%	E_C (MV/m) at 0 wt%
[31]	70/30	$CoFe_2O_4$	80-100	80	10.7	58.6
[32]*	78.8/5.4/15.8	TiO_2	50-70	25-50	6.3	-
[33]	75/25	$Ni_{0.5}Zn_{0.5}Fe_2O_4$	10-20	50-60	8.25	40
[34]	75/25	$Ni_{0.5}Zn_{0.5}Fe_2O_4$	10-30	25, 50 and 75	9	50
[35]	-	$CoFe_2O_4$	35-50	50	9.5	65
[36]	70/30	Ag	-	-	5.6	-
[37]	70/30	ZnO	40-100	1	3.43	64
[38]	75/25	Ag	-	15	8.29	38
[39]	75/25	Au,Ag,SiO_2	10-60	0.28	7.2	60.4
[40]	-	$CoFe_2O_4$	35-50	50	6.5	40
[41]	70/30	MgO	< 50	20	6.3	60

* P(VDF-TrFE-CtFE) was used as matrix

7.1.2 Experiment

Details of the synthesis of monodisperse magnetic nanoparticles (iron oxide and cobalt ferrite) have been reported in Chapters 3 and 4.[46, 48, 50-52] P(VDF-TrFE) (65 %-35 %) was purchased from Solvey. The detail of solution preparation, thin film processing and device preparation are given in Chapter 6.[49, 53-54] Briefly, stock solution of P(VDF-TrFE) (3.5 wt %) and nanoparticles (1 wt%) in Tetrahydrofuran (or cyclopentanone) were first prepared. Subsequently, P(VDF-TrFE) solution mixtures with 0, 10^{-4}, 10^{-3}, 10^{-2}, 10^{-1}, 0.5, 1, 4, 6, 10, 15, 20 and 30 wt % iron oxide MNPs and with 0, 3, 6, 12, 20, 30 and 40 wt% cobalt ferrite MNPs were prepared. The mixture was sonicated under bath sonication (3510 Branson) for 8 hours at room temperature to obtain a good disperssion. To prepare capacitors, glass slides were first throughly cleaned in aceton, propanol and DI-water. As bottom electrode, 50 nm Au/1 nm Cr

electrode were evaporated. Films of P(VDF-TrFE) nanocomposites were formed by spin coating or bar coating under low humidity of <10 % to supress VIPS (as discussed in detail in previous Chapter 6).[49] Instead of THF we can use cyclopentanone as a hydrophobic solvent. Then we can avoid VIPS without any requirement for low humidity film processing condition. We tuned the solution concentration or spin coating condition to arrive at comparable layer thicknesses for all nanocomposites, which was in the range of 350 to 450 nm for thin-films and 1900 to 2100 nm for thick-films (measured using Dektak profilometer). Root mean square (rms) roughness of pristine P(VDF-TrFE) film was well below 10 nm, indicating effective suppresion of VIPS. The rms roughness of the nanocomposite thin-films slightly increased to nearly 22 nm for 20 wt% loading, **Figure 7.1.2**. Considering that the diameter of the nanoparticles are in the range of 11-14 nm, the increase in roughness is fully justified, as shall be seen later. After film formations, the substrates were annealed at 140 °C for 2 h in vacuum (10^{-1} mbar) to increase the crytallinity of P(VDF-TrFE). The capacitors were finished by evaporation of a 50 nm Au top electrode. The capacitor areas amounted to 0.0016-0.04 cm^2. To arrive at a reliable statistics, more than 50 capacitors for each loading ratio were tested.

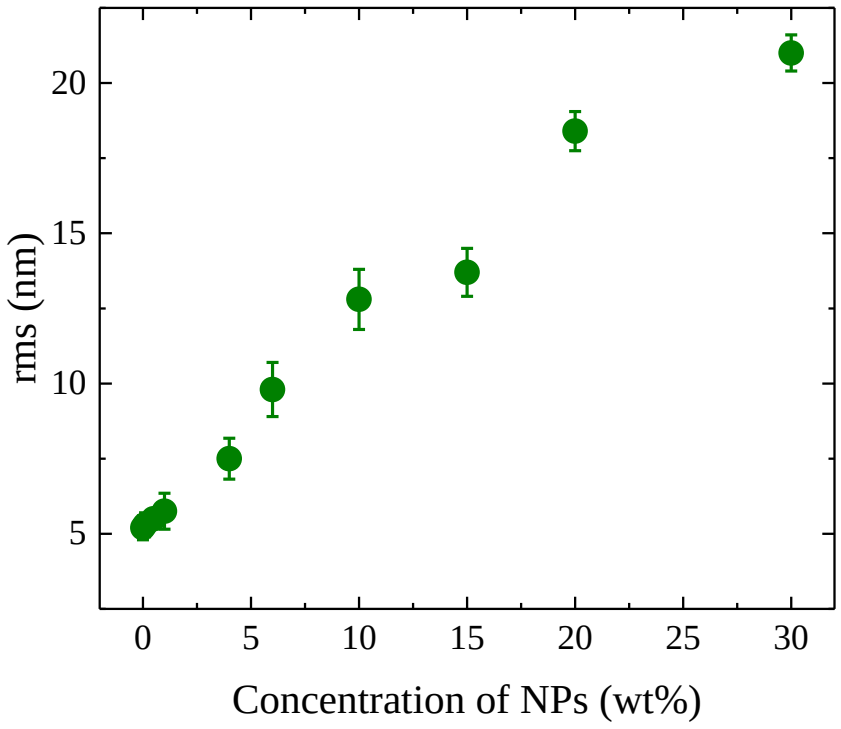

Figure 7.1.2 Roughness of thin-film nanocomposites as a function of nanoparticle loading (Iron oxide MNPs).

The ferroelectric properties were determined using a Sawyer-Tower circuit for low loadings (below 4 wt%) and Positive-Up-Negative-Down (PUND) pulse sequence for higer loadings (due to the persence of huge leakage current).[55] Details of the measurements are given elsewhere.[56] Briefly, first we apply a negative pulse to fully polarize the capacitor to $-P_r$. Then, we short the capacitor to ensure that any extra charges at the electrodes are removed; only the compensating, equal to the remanent, polarization remains. We then apply a positive square pulse. The pulse is long enough to reach complete polarization reversal. We measure the voltage drop over the reference capacitor and calculate the polarization as a function of time. Afterwards, the same positive square pulse is applied to measure the nonswitching contribution. Subtracting the two transients then yields the net polarization as a function of time.[56] Details of the Differential scanning calorimetry (DSC) was conducted under N_2 atmosphere, on as-cast films, at a scan rate of 10 °C/min, using a Mettler Toledo calorimeter. The degree of crystallinity of the P(VDF-TrFE) nanocomposites was calculated according to the weight fraction of polymer using the calculated value of enthalpy corresponding to a theoretical 100% crystalline P(VDF-TrFE) (70/30) copolymer as 91.45 J/g.[57] The schematic of the whole experimental part is shown in **Figure 7.1.3**.

PUND measurements: it stands for positive-up, negative-down pulse. PUND allows separating the switchable from the non-switchable part of the polarization. The pulse (positive or negative) is a pair of pulses. The first pulse is the "switching" pulse which integrates both switching and non-switching charge. The second pulse only integrates non-switching charge (see **Figure A7.1.1**). By subtracting both, then, the true remanent polarization can be revealed. The electrical measurement methods have been discussed in detail in recent reviews.[56, 58-60]

Dielectric spectroscopy: dielectric properties were characterized using a Novocontrol spectrometer with a frequency sweep from 0.1 Hz to 10 MHz. Dielectric spectroscopy measures the dielectric permittivity as a function of frequency. The material permittivity is a complex number, which consists of a real part ε' and an imaginary part ε''. ε' is a measure of the energy stored whereas ε'' is a measure of energy loss. Another useful quantity is the loss factor

$$Tan\,(\delta) = \frac{\varepsilon''}{\varepsilon'} \qquad (7.1.1)$$

The term Tanδ is called loss tangent and loss angle δ is correlated with impedance phase angle θ, for a lossless capacitor, voltage drop always lags current by 90°, so the impedance phase angle is -90° and Tanδ is 0. But because of material absorption, the impedance phase angle of the real capacitor is

$$\theta = -(90 - \delta) \qquad (7.1.2)$$

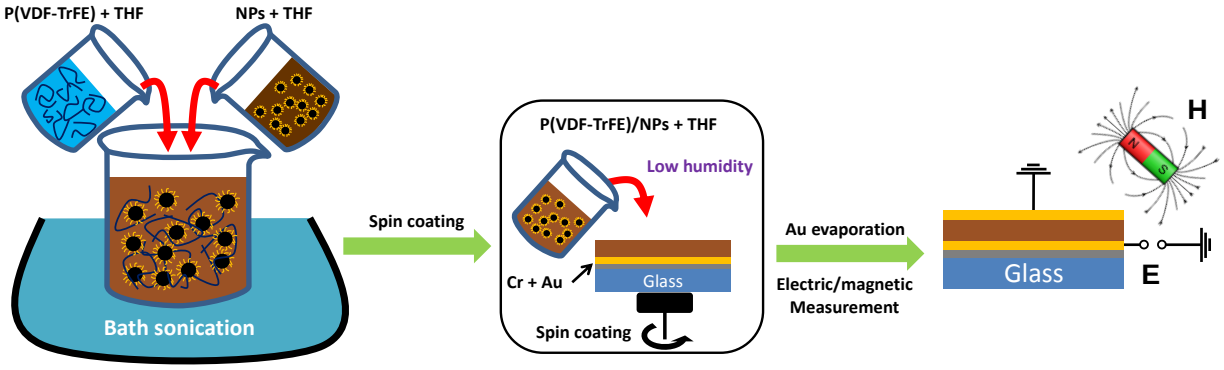

Figure 7.1.3 The schematic of experimental process. Note that cyclopentanone can be also used as solvent without any requirements for low humidity processing. Moreover, the film processing can be also done by bar coating technique.

7.1.3 Results and discussion

A typical TEM image of the nanoparticles for iron oxide and cobalt ferrite nanoparticles are shown in **Figure 7.1.4 a** and **b** respectively. Nanoparticles have regular polyhedral (pseudo spherical) shapes. The nanoparticles show a Gaussian size distribution, inset of **Figure 7.1.4 a** and **b**, with mean size of 11.5 ± 1 nm and 16.2 ± 2.7 nm. Polydispersity index is therefore 9.1 % and 16.6 % for iron and cobalt ferrite NPs, respectively.[50] The iron oxide NPs are super-paramagnetic and cobalt ferrite NPs are ferri/ferromagnetic at room temperature with saturation magnetization at 50000 Oe that amounts to 62 emu/g and 64 emu/g, respectively, as shown in **Figure 7.1.4 c**. The value of H_C and M_r/M_S for cobalt ferrite MNPs at room temperature are 0.22 and 720 Oe respectively.

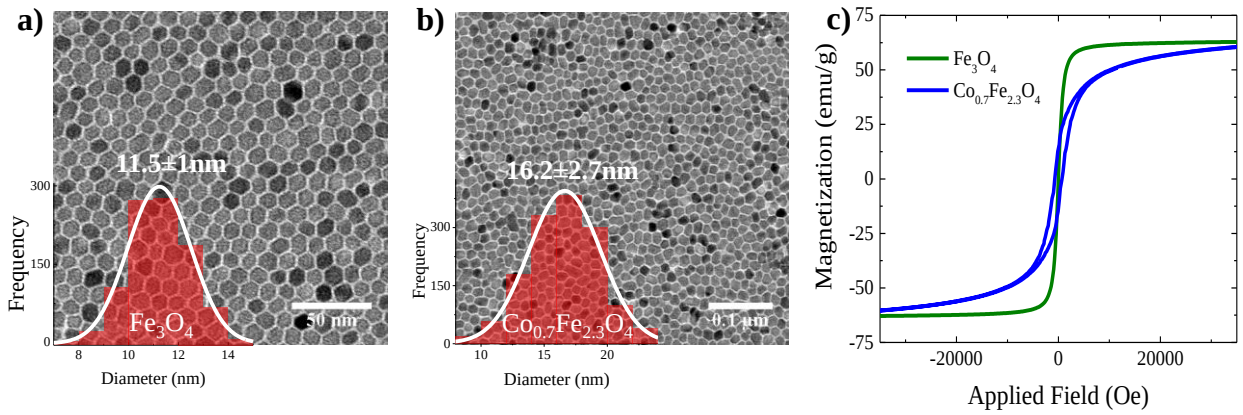

Figure 7.1.4 TEM images of (a) iron oxide and (b) cobalt ferrite NPs with their corresponding size distribution histogram. (c) Magnetization as a function of applied magnetic field for both types of MNPs at room temperature.

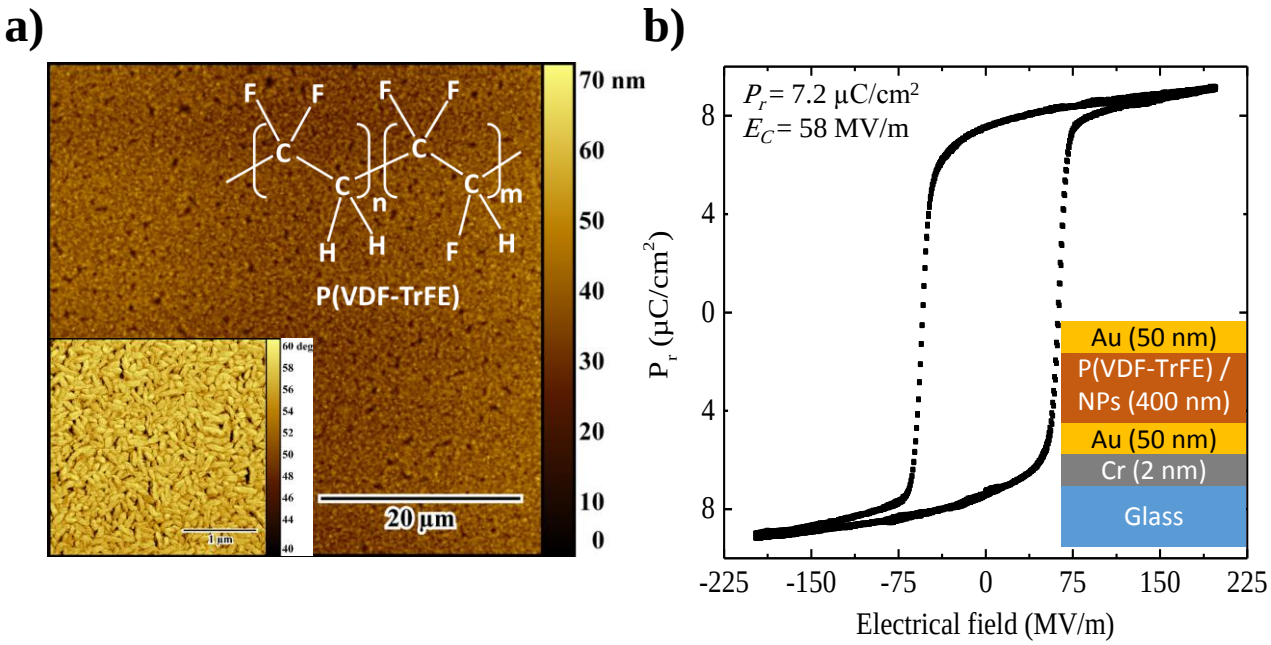

Figure 7.1.5 a) AFM height and phase (inset) image of P(VDF-TrFE) film processed under low humidity conditions (chemical structure of P(VDF-TrFE) is given in the inset). b) A typical ferroelectric hysteresis loop of pristine P(VDF-TrFE) capacitor. The inset shows the capacitor layout.

Room-temperature film processing of P(VDF-TrFE) under humid condition (humidity> 20 %) results in a rough and pours structure due to VIPS. While using hydrophilic solvent (like THF), by coating P(VDF-TrFE) films at humidity levels well below 10 %, VIPS between polymer and water is effectively suppressed and a smooth thin-film is obtained (the details were

described in Chapter 6).[49, 61-62] We obtained a same morphology by using cyclopentanone as a solvent. Since cyclopentanone is a hydrophobic solvent, VIPS is avoided without any requirement for low humidity film processing condition. A typical AFM image of the pristine P(VDF-TrFE) film is given in **Figure 7.1.5 a**. The root mean square roughness is below 7 nm.

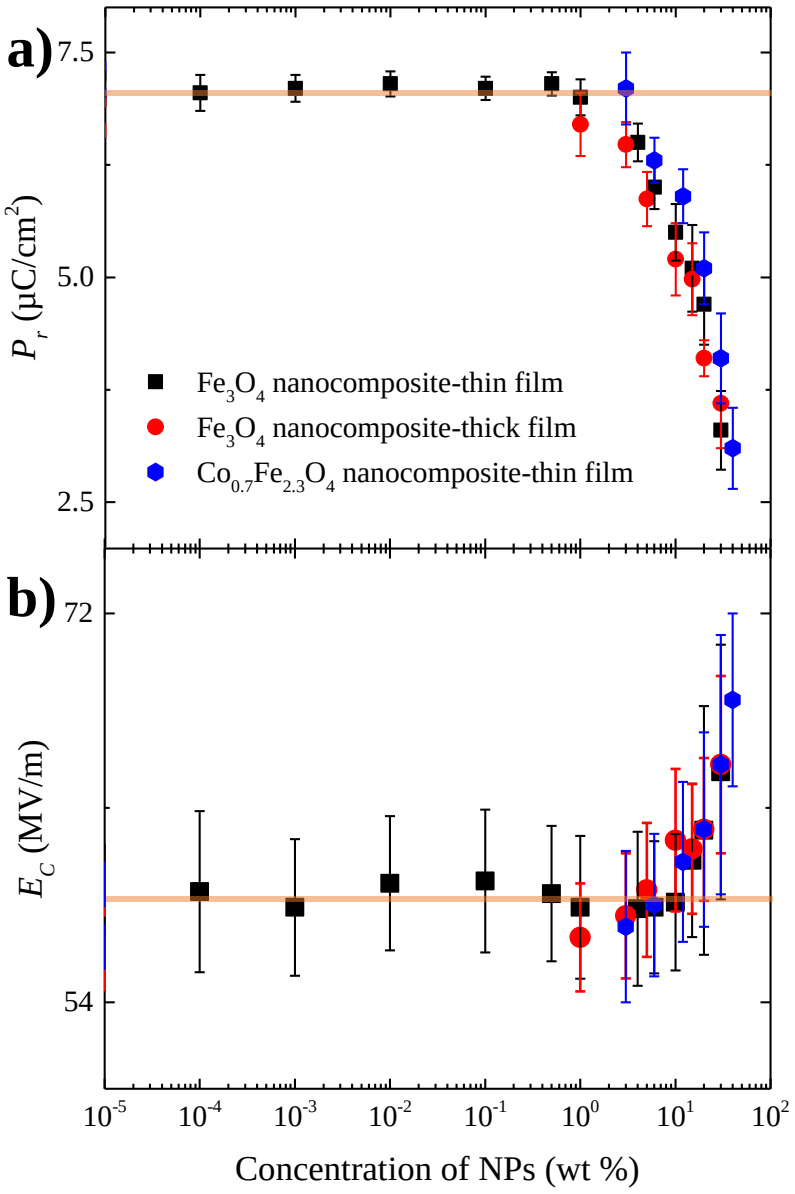

Figure 7.1.6 The amount of (a) P_r and (b) E_c of P(VDF-TrFE)/MNPs nsanocomposite thin film as a function of nanoparticles (both iron oxide and cobalt ferrite) concentration for both thin and thick films. The solid-orange line show the value of P_r and E_c for the pristine P(VDF-TrFE).

The film thickness amounts to 350 to 450 nm, and therefore the films are suitable for low-voltage operation. The ferroelectric hysteresis loop of the pristine P(VDF-TrFE) capacitor is shown in **Figure 7.1.5 b**. The remanent polarization and the coercive field amount to 7.2 μC/cm^2 and 58 MV/m, respectively, in agreement with literature data.[4, 49] The capacitors operate at voltages lower than 25 V.

Next, we test the effect of iron oxide (and cobalt ferrite) nanoparticle fillers on the ferroelectric properties of the P(VDF-TrFE) nanocomposite. To have a fair comparison, the mean film thickness for the nanocomposites films are kept the same amount in the range of 350-450 nm for thin-film, and 1900-2100 nm for thick-films for different loading ratios. Summary of the ferroelectric measurements (P_r, E_C) of the nanocomposite films are given in **Figure 7.1.6**. The evolution of P_r for both thin and thick film nanocomposites and also for both types of nanoparticles follows the same trend and begins to drop when the concentration of MNPs is ≥4 wt% (**Figure 7.1.6 a**). We do not observe any enhancement of P_r over the wide range of filler loading for both types of nanoparticles and different thicknesses. At the same time, E_c of the nanocomposite did not show any significant change and only increased slightly at high loading ratios (**Figure 7.1.6 b**).

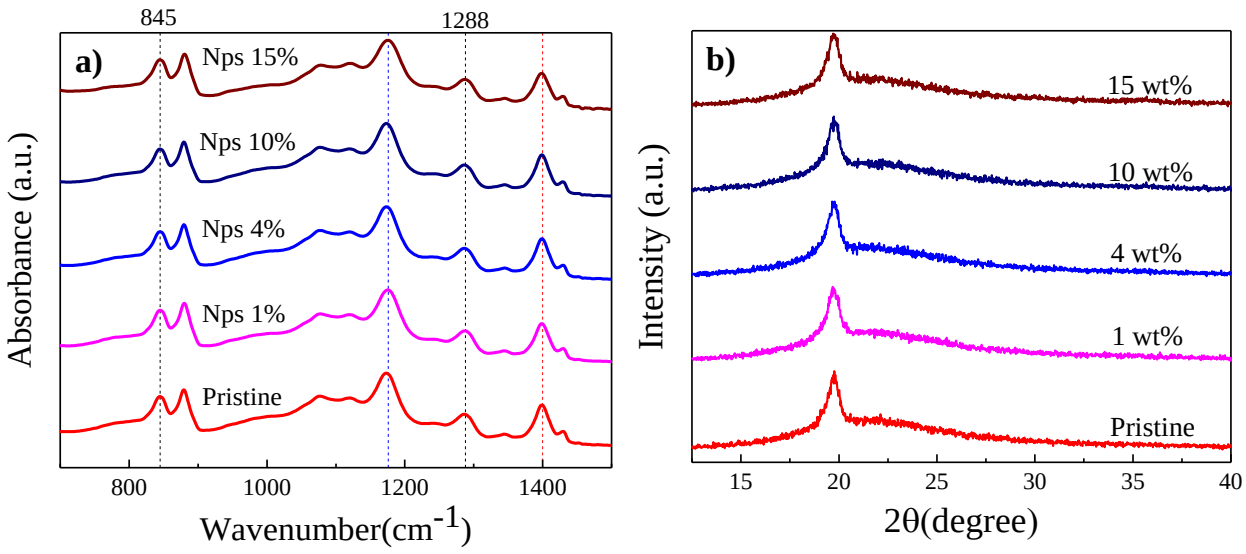

Figure 7.1.7 (a) FTIR spectra and (b) XRD diffractograms of thin P(VDF-TrFE)/nanoparticle nancomposite (Fe_3O_4) for different nanoparticle loadings.

We perform FTIR and XRD on the nanocomposites with different loadings. FTIR measurements, **Figure 7.1.7 a**, show characteristic peaks of the β-phase P(VDF-TrFE) for nanocomposites.[54, 63-64] Appearance of new crystalline phases does not observed.[65] The XRD patterns, **Figure 7.1.7 b**, show the characteristic 2θ=19.7° peak (with FWHM=0.84) of the crystalline β-phase of P(VDF-TrFE). The diffraction peak corresponds to the overlapping (110) and (200) reflections.[39, 66-67] For all nanocomposites films with different loadings, P(VDF-TrFE) crystallizes into its ferroelectric β-phase and the lattice spacing remains unchanged. Hence, addition of MNPs in the film does not hinder formation of ferroelectric β-phase.[53-54, 64]

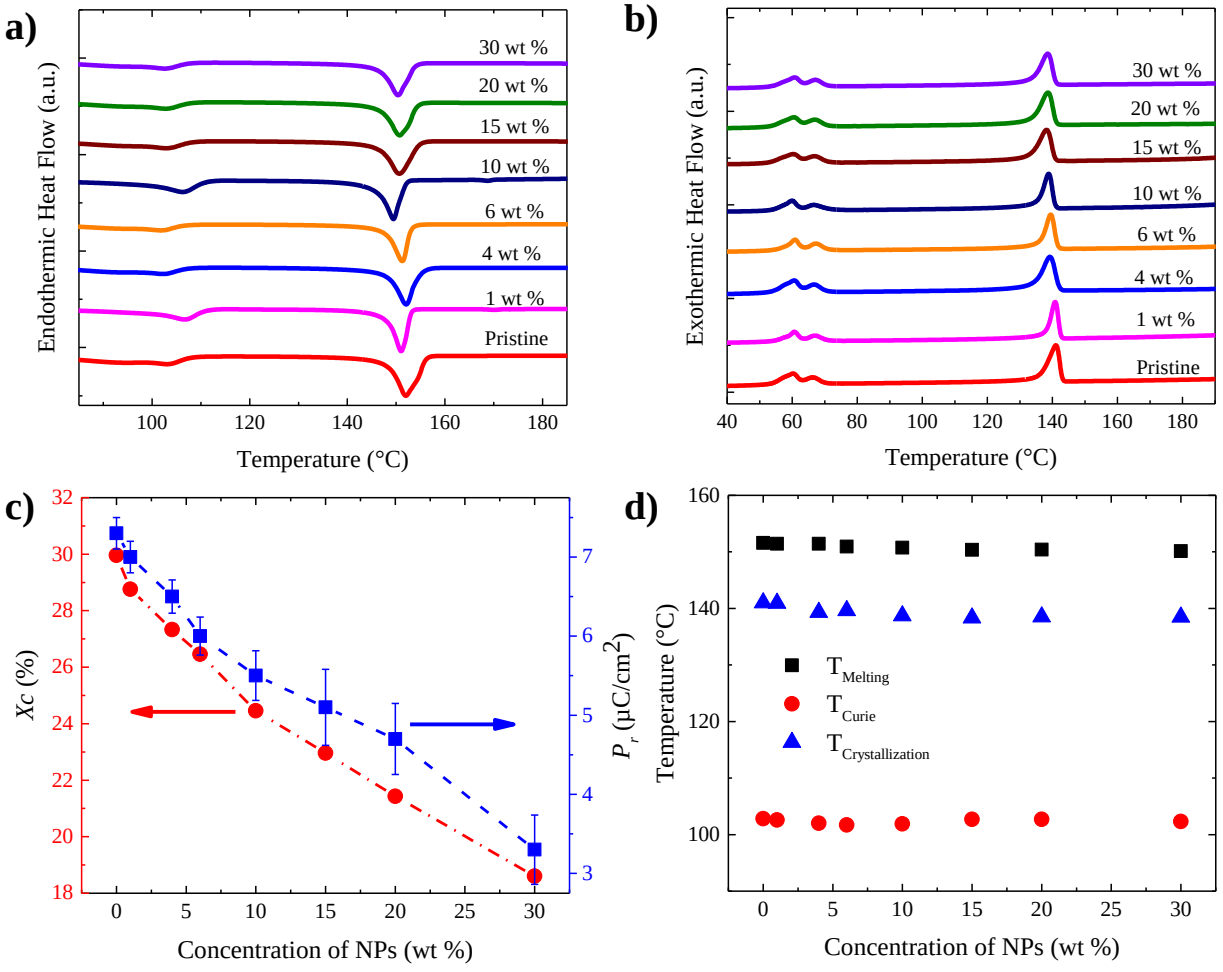

Figure 7.1.8 DSC thermogram ((a) heating and (b) cooling) for Fe_3O_4 nanocomposites. The values of (c) X_c and (d) $T_{Melting}$, T_{curie}, $T_{Crystalization}$ as a function of the concentration of nanoparticle loading.

To investigate the crystallinity, DSC analysis is performed on pristine P(VDF-TrFE) and nanocomposites with different nanoparticle loading. Endo- and exotherms are shown in **Figure 7.1.8 a** and **8 b**, respectively. We calculate the melting enthalpy of the P(VDF-TrFE) nanocomposites from the melting peak of the first heating endotherms. The degree of crystallinity was obtained by dividing the calculated enthalpy of the nanocomposite by that of the pristine P(VDF-TrFE) film *viz.* 91.45 J/g.[57] The calculated crystallinity, X_c, as shown in **Figure 7.1.8 c** steadily decreases with increasing the concentration of nanoparticles in the nanocomposite. For comparison, measured P_r values are also plotted on the same graph. Reduction of crystallinity can therefore consistently describe depression of P_r.[39, 68-71] For the composite we defined polarization as $P_r = \sum \mu / V$, as the superposition of the dipole moment μ of the constituent phases per total volume of the nanocomposite. Iron-oxide nanoparticles are not ferroelectric and therefore have no contribution in the measured polarization. Hence polarization of the nanocomposite is solely due to the ferroelectric P(VDF-TrFE) matrix.

Furthermore, we extract melting ($T_{Melting}$), Curie (T_{Curie}) and crystallization temperatures ($T_{Crystalization}$), **Figure 7.1.8 d**, remain constant for all nanocomposites. Hence, P(VDF-TrFE)/ nanoparticle nanocomposite is a non-interacting system which undergoes a phase separation process upon film forming. To study the phase separation and film microstructure, we perform SEM. The micrographs are shown in **Figure 7.1.9** for nanocomposite thin films with different filler loading. The pristine P(VDF-TrFE) film, **Figure 7.1.9 a**, showed typical needle like domains of β-phase crystals. The featureless areas between the crystallite form the non-ferroelectric amorphous regions. For the nanocomposite with only 1 wt% filler loading, **Figure 7.1.9 b**, the nanoparticles are accommodated in P(VDF-TrFE) amorphous phase. Accommodation of the filler in the amorphous phase continues as the loading increases, to 4, 6 and 10 wt %, **Figure 7.1.9 c-e**. The crystalline domain of P(VDF-TrFE) pushes the nanoparticles into amorphous phase and phase separation and agglomeration of nanoparticles occur. Cross-sectional SEM image of the 10 wt % nanocomposite, **Figure 7.1.9 i**, confirms exclusion of the fillers from the P(VDF-TrFE) crystallites and also agglomeration of MNPs throughout the film. We note that, for polymers such as P(VDF-TrFE) that are made of both amorphous and crystalline phases, mechanical breaking leads to stretched amorphous phase, leaving holes in the cross sectional area, which then appear as pores in the SEM image. When the amount of

nanoparticles is low, there is no obvious aggregation while, in higher loading (≥ 4 wt %) the nanoparticles starts to aggregate, which is particularly visible for loading of 15 wt %, **Figure 7.1.9 f**. Upon further increase of loading to 20 and 30 wt %, a bilayer structure is formed wherein a thin ad-layer of nanoparticle is formed on top of the nanocomposite thin film. We note the same microstructure as shown in **Figure 7.1.9** was observed while using cobalt ferrite nanoparticles.

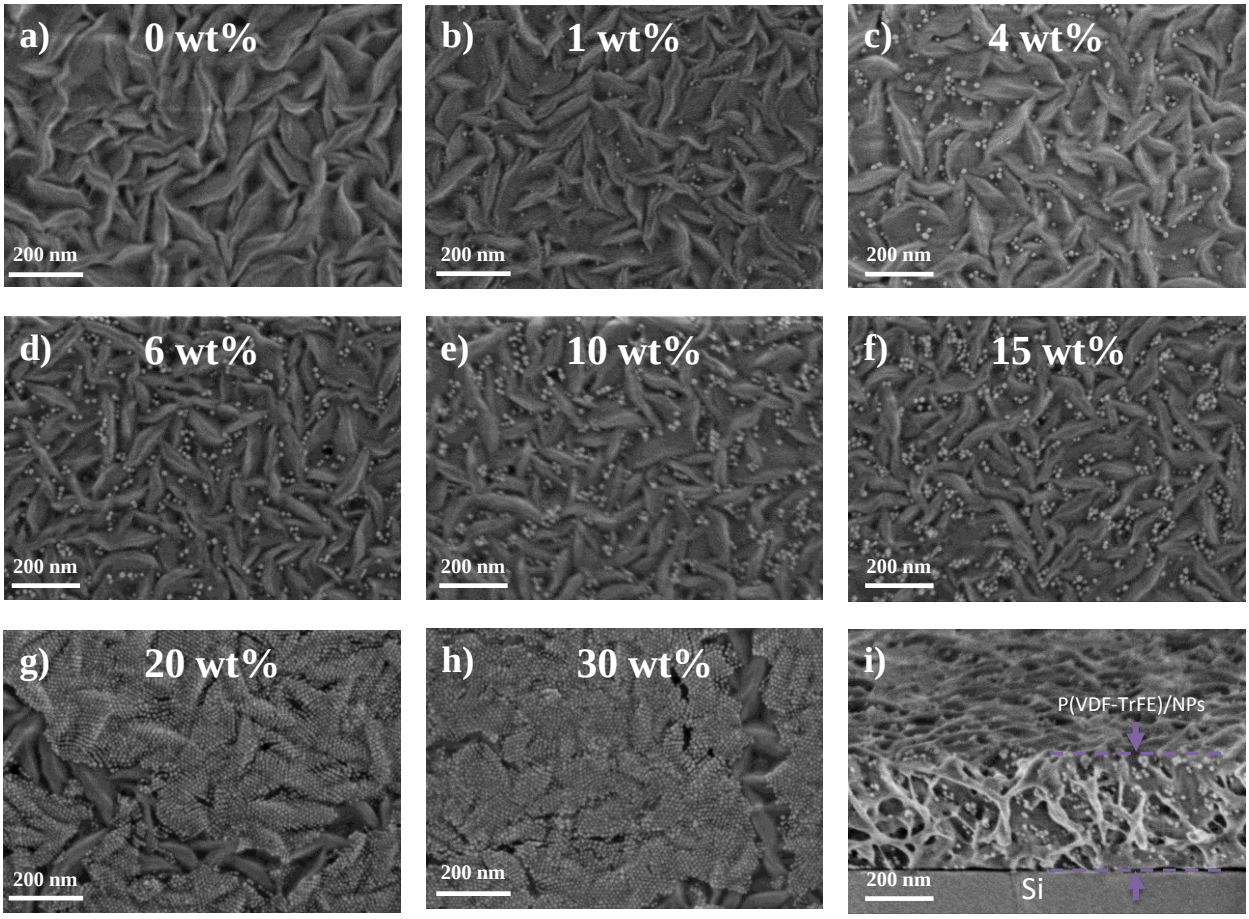

Figure 7.1.9 (a)-(h) SEM images of thin films samples with different loading of nanoparticles. (i) Cross section SEM image of nanocomposite with 10 wt % loading of nanoparticles.

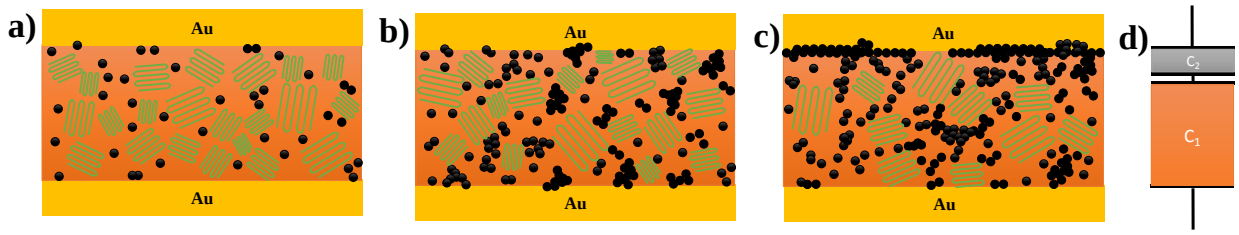

Figure 7.1.10 Cross sectional schematic of device structure under (a) low, (b) medium and (c) high loading of ferrite nanoparticles. (d) Schematic of extra series capacitors due to the formation of ad-layer in high loading of nanoparticles.

Oleate grafting helps colloidal stability of the nanoparticles. Pristine nanoparticles in THF are stable over weeks. The solutions of nanoparticles in P(VDF-TrFE) showed long-term stability. Hence presence of oleate cannot explain formation of the nanoparticle aggregates. The oleate is not miscible with P(VDF-TrFE). Hence oleate-coated nanoparticles are immiscible with P(VDF-TrFE).[72] The DSC measurement clearly shows that P(VDF-TrFE) and the nanoparticles are not interacting. Hence, upon film formation from solution, the oleate-coated nanoparticles and P(VDF-TrFE) separate, meaning that regions of nanoparticle-rich polymer-poor and polymer-rich nanoparticle-poor are formed. Beside the separation of the nanocomposite constituent into distinct regions, P(VDF-TrFE) also crystalize. The crystalline phase contains pure P(VDF-TrFE) and does not accept any impurities. Therefore, during the crystallization the crystalline regions repel the nanoparticles into the amorphous phase. At dilute nanoparticle concentrations, the amorphous regions of P(VDF-TrFE) can accommodate the nanoparticles, and therefore crystallinity of P(VDF-TrFE) is not altered. Simultaneously, within the amorphous region of P(VDF-TrFE) phase separation between P(VDF-TrFE) and the nanoparticles takes place. At low nanoparticle loading, phase separation is not pronounced. As the loading larger goes beyond 4 wt %, the phase separation within the amorphous regions becomes pronounced leading to the formation of nanoparticle agglomeration. At high loadings, P(VDF-TrFE) amorphous region, phase separation leads to a vertically phase separated nanocomposite and therefore formation of a nanoparticle ad-layer. The schematic of composite's microstructure structure at different loading (low, medium and high) is depicted in **Figure 7.1.10 a-c**. We note that formation of a non-ferroelectric ad-layer at high loading ratios leads to formation of an extra series capacitor in the device stack, **Figure 7.1.10 d**, which has been shown that ad-layer

facilitate further suppression of P_r due to depolarization. Details of the mechanism has been discussed elsewhere.[73-74]

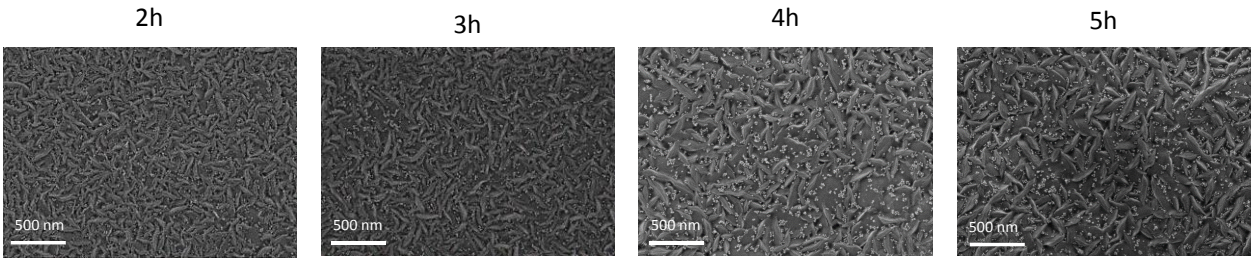

Figure 7.1.11 The top vie SEM images of 10 wt% P(VDF-TrFE)/MNPs nanocomposite thin films in different annealing temperature at 140 °C.

To investigate the possibility of thermally induced phase separation (TIPS) on the microstructure formation, we studied microstructure evolution as a function of annealing time. For a composite with 10 wt% filler loading, we changed the annealing time at 140 °C from 2 to 5 hours. Representative SEM topographical images are shown in **Figure 7.1.11**. The SEM images revealed that the surface topography did not change substantially upon prolonged annealing time, and statistically, similar topographies were obtained. Hence, the influence of TIPS on microstructure formation for thin-films annealed at 140°C is minimal.

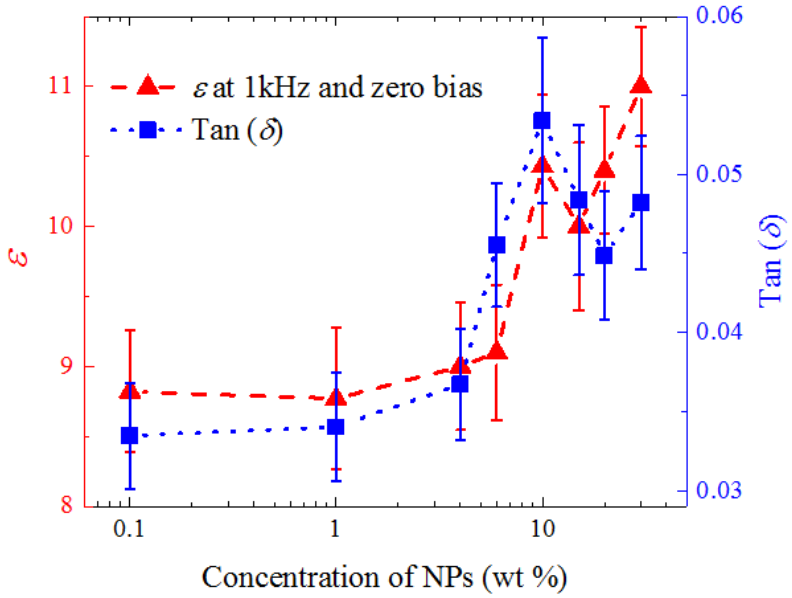

Figure 7.1.12 Dielectric constant and Tan (δ) of nanocomposites measured at 1 kHz and zero bias as a function of different ferrite nanoparticle loading (iron oxide).

To investigate the effect of nanoparticles content on the dielectric constant of the nanocomposite, we measure the dielectric permittivity, ε. The dielectric constant for pristine P(VDF-TrFE) is amounted to ~ 9 and did not change significantly in the presence of MNPs up to 4 wt % (**Figure 7.1.12**). Further loading slightly increases the dielectric constant of the nanocomposite from 9 for the 6 wt % loading, and eventually to 11 for the 30 wt % nanocomposite. We note that the observed increase in dielectric constant can be due to roughness, variation in the device area, or even leakage current (loss).

The measured loss (Tan (δ)) for the nanocomposites thin films followed the same trend as the dielectric constant for loadings below 10 wt %. It significantly increases from 0.022 for 0 wt% to 0.056 for 10 wt% and eventually to 0.05 for 30 wt% nanocomposite. The significant increase in loss is due to aggregation of the NPs and phase separation between them and P(VDF-TrFE) phase. To prevent phase separation and subsequently reduction of loss we propose surface modification of the nanoparticles in such a way to increase the interaction with P(VDF-TrFE) polymer chains towards better dispersion. At 10 wt %, the loss shows a peak, and then slightly reduces for 20 wt%. However, further increasing the concentration of MNPs to 30 wt% causes higher loss. Interestingly, the peak position coincides with the loading ratio at which an ad-layer of MNPs forms. We note that dielectric measurements follow the same trend as cobalt ferrite nanocomposite thin films.

We note that for higher loading of MNPs ($\geq$ 4 wt%), when the MNPs start to aggregate in the nanocomposite films, the electrical leakage in capacitor devices is too high resulting in low electrical break down strength. Hence, we observed really low functional device yield of almost 10-20% for high loadings. Moreover, due to randomly distribution of agglomerated MNPs inside polymer matrix, we observe variation in the device performance and ferroelectric properties. These effects get more pronounce for higher loading concentrations and also lower thickness of the films. This observation is in accordance with dielectric spectroscopy measurements that we observed higher loss in higher loadings. Moreover, aggregation of the MNPs inside ferroelectric polymer matrix reduces the interface between magnetic and ferroelectric phase which adversely affect the multiferroic properties.

To investigate the effect of the filler addition on the switching mechanism of P(VDF-TrFE), we perform polarization switching time study and polarization transient measurements.[75] Details of the measurement protocol are described elsewhere.[56] **Figure 7.1.13 a** shows polarization transients for pristine P(VDF-TrFE) and three representative nanocomposite thin films with different loadings at a fixed field of 110 MV/m. For all cases, the polarization evolution can be well described by the KAI model used for the study of ferroelectric switching, using a compressed exponential function:

$$\frac{\Delta P(t)}{2P_r} = 1 - exp\left(-\left(\frac{t}{t_0}\right)^n\right) \qquad (7.1.3)$$

where t_0 is a characteristic switching time, and n is the Avrami index. Since the switching time strongly depends on the applied field, we perform polarization transient at different fields for all the nanocomposites, and then extract t_0. A summary of the Avrami indexes for different nanocomposites is given in **Figure 7.1.13 b**. For the pristine P(VDF-TrFE), n is 1.7 at low field of 75 MV/m, and decreases to 1.0 as the field is increased to 160 MV/m. The Avrami index is very sensitive to the presence of nanofillers in the nanocomposites. For the nanocomposite with loading of 0.1, 1 and 4 wt %, at nearly the same low field (75 MV/m), n is lowered to 1.65, 1.5 and 1.3 respectively, whereas at high field regime, n is 1. For the filler loading of above 4 wt %, n is close to 1 for the field range investigated here.

It has been shown that for the pristine P(VDF-TrFE) the Avrami index is close to 2, indicating a two dimensional nucleation and growth of domains.[56] Decreasing n is indicative of an increased number of nucleation sites, where the reversed polarization state sets in upon field application. Numerical simulation has shown that for the case of n= 1 irregular highly entangled domains are formed which indicates growth of one-dimensional wires. We therefore conclude that polarization reversal is nucleated along the P(VDF-TrFE) backbone at the vicinity of the nanoparticle which in time grows to the crystalline part.

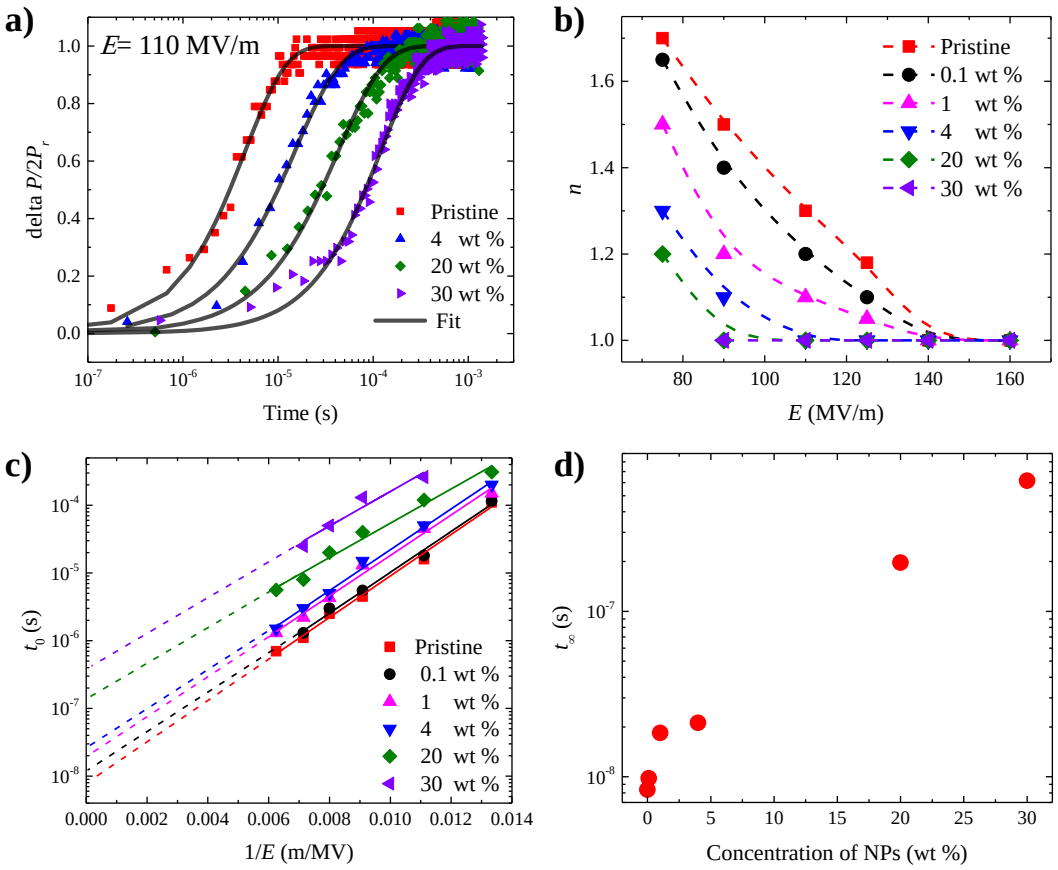

Figure 7.1.13 (a) Polarization reversal of plot and the respective fits using **Equation 7.1.3**. (b) The values of Avrami index (*n*) as a function of electrical field in different loadings. (c) The characteristic switching time t_0 as a function of reciprocal applied electric field. The lines show the fit obtained by Merz law. d) Evolution of t_∞ as a function of nanoparticle loading.

Dependence of the switching time on the applied field is plotted in **Figure 7.1.13 c**. Field dependence of the switching time in pristine P(VDF-TrFE) follows the empirical Merz law: [56, 75,76]

$$t_0 = t_\infty exp\left(\frac{E_{act}}{E}\right) \qquad (7.1.4)$$

where t_∞ is the switching time at infinite applied electric field, E, and E_{act} is the activation field. Fitting **Equation 7.1.4** to the experimental data we have obtained t_∞ and E_{act} for all nanocomposites. The activation field and t_∞ for P(VDF-TrFE) pristine film amounted to 800 MV/m and 8 ns, respectively in perfect agreement with previous reported values.[45, 56, 77-79] The activation field for polarization reversal in nucleation-limited regime amounts to 1 GV/m.[45, 80-81]

Observation of high E_{act} for the nanocomposites indicates that the polarization reversal is nucleation limited. We note that, switching dynamics in P(VDF-TrFE) thin-films can be affected by many parameter such as sample processing conditions, thickness, electrodes, electric fields, temperature, pre-polarization conditions, to name a few. For instance, use of electrodes, such as Ag, Al and Cu, which are prone to formation of an oxide layer, may lead to an over-estimation of switching time, and activation energies, because of voltage drop over a metal-oxide layer that inevitably forms. Hence, slight differences in the reported numbers can be extrinsic. Filler loading mainly influences $t_{\infty,}$ whereas E_{act} remaines almost unchanged around 750 ± 50 MV/m in the nucleation-limited regime. The t_{∞} stays unchanged for nanoparticle loading below 0.1 wt% but increases exponentially to 600 ns for nanoparticle loading of 30 wt%, as shown in **Figure 7.1.13 d**. We therefore conclude that addition of the nanoparticles into the ferroelectric matrix lowers the polarization dynamic substantially, such that at loading of 30 wt%, the polarization switching dynamic is nearly 100 times slower than in pristine P(VDF-TrFE).

In the final step, we investigate the magnetic properties of the nanocomposite films for both superparamagnetic and ferromagnetic nanoparticles. Magnetization response as a function of applied magnetic field is shown in **Figure 7.1.14 a** and **b** for iron oxide and cobalt ferrite nanoparticles in different MNPs loadings, respectively. Depending on the types of MNPs, we obtain both superparamagnetic and ferromagnetic behavior. Magnetization shows linear dependence with the amount of MNPs for both types of nanoparticles as shown in the inset of **Figure 7.1.14**. Normalization of M_S of the nanocomposites corrected for the mass of MNPs content leads to values of 61 ± 3 emu/g and 63 emu/g ± 2.5 for iron oxide and cobalt ferrite respectively, which is the M_S value measured for MNPs powder (**Figure 7.1.3**). Hence, presence of the ferroelectric matrix does not alter the saturation magnetization of the nanoparticles.

On the other hand, for the nanocomposite of cobalt ferrite MNPs/P(VDF-TrFE), the values of H_C and M_r/M_S as depicted in (**Figure 7.1.14 c**). These values differ by changing the concentration of cobalt ferrite MNPs inside nanocomposite. Such observations can be rationalized by changing the particle-particle distances. It is know that, changing the distance between MNPs may alter the magnetic dipole-dipole interaction between them. By any change in ferromagnetic nanoparticles compaction, the magnetic properties (such as H_C and M_r/M_S) of system are affected, because it changes the magnetic interactions strength between the

ferromagnetic MNPs (dipole-dipole interaction). The M_r/M_S shows an increase from 0.22 for 100 wt% cobalt ferrite MNPs to 0.33 for nanocomposite with 6 wt%. We note that, by reducing the concentration of MNPs in nanocomposite, the particle-particle distance increases. Therefore, decrease of M_r/M_S indicates positive effect of magnetic dipole-dipole interactions on demagnetization process.

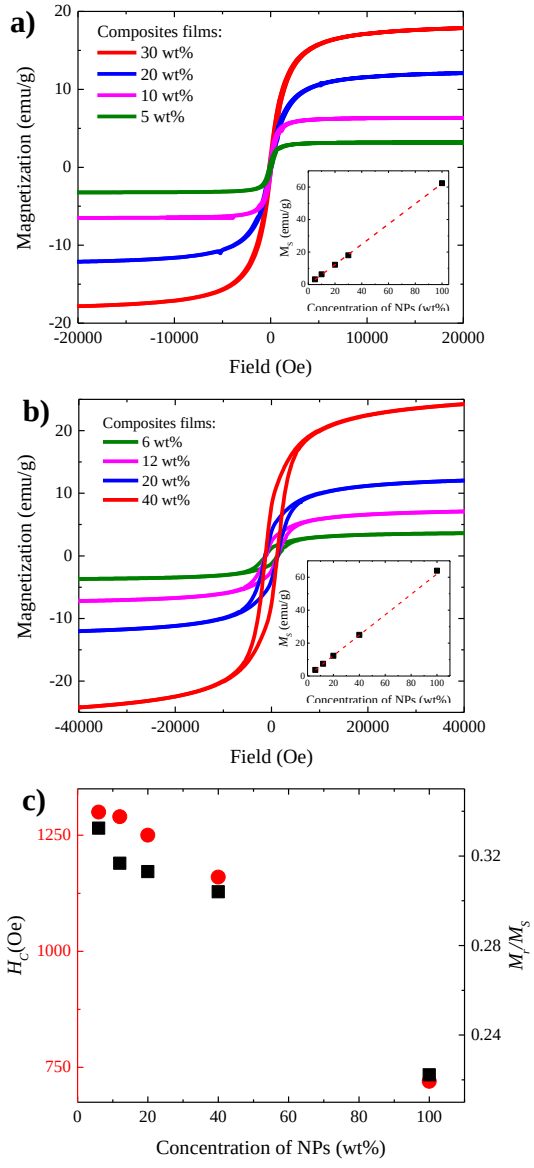

Figure 7.1.14 The magnetization response of the nanocomposites films with different loading ratios at room temperature for (a) iron oxide and (b) cobalt ferrite. Inset shows the linear evolution of saturation magnetization as a function of loading. (c) The values of H_C and M_r/M_S as a function of loading concentration, extracted from *M-H* curves of cobalt ferrite nanocomposite films.

Moreover, by decreasing the concentration of cobalt ferrite MNPs, the value of H_C increases from 720 Oe for 100 wt% cobalt ferrite NPs to 1300 Oe for nanocomposite with 6 wt% loading. The change in coercive field by changing the concentration of MNPs is also due to changing the distance between NPs and subsequently changing the dipole-dipole interaction between ferromagnetic NPs. The simple expression of the magnetic interactions effect on coercivity was presented by Neel as:[82-83]

$$H_C = H_C(0)(1 - p) \qquad (7.1.5)$$

where p is the density ratio of a sample with respect to individual particle, which is known as packing fraction. Based on this model, by increasing the loading concentration, the packing factor in a constant volume increases which results to the reduction of H_C. We also observe the same trend in our experimental results (**Figure 7.1.14 c**).

7.1.4 Conclusion

We have demonstrated solution-processed thin-film nanocomposite by loading superparamagnetic and ferri/ferromagnetic ferrite nanoparticle in P(VDF-TrFE). The ferroic properties of the thin-film were investigated over an unprecedented loading of nearly six orders of magnitude ranging from 10^{-4} wt % to 30 wt %. We have shown that the ferroic properties of the thin-film is similar to that of the bulk thick-films. We have identified a critical loading of 4 wt % below which the ferroic properties of the nanocompositie, *e.g.* P_r and E_C, ε, and the switching time, within the error margins, stay at the value of pristine P(VDF-TrFE). For nanoparticle loading above of 4 wt % up to 30 wt%, P_r significantly drops, E_C and ε slightly increase, while the switching time shows a significant increase. The increase in the switching time was attributed to the shift of the polarization switching dynamic from a two- to a one-dimensional process. We showed that for higher loading of MNPs ($\geq$ 4 wt%), when the MNPs start to aggregate in the nanocomposite films, the electrical leakage in capacitor devices increases which results to low electrical break down strength, lower functional device yield and variation in the performance of devices.

P(VDF-TrFE) and the oleate-coated nanoparticle are non-interacting (both chemically and physically). This means that even that the solution of P(VDF-TrFE)/nanoparticle is colloidally stable over time, up on solution casting and solvent evaporation, the nanocomposite phase separates. We have shown that the phase separation process induces agglomeration of the nanoparticle in the amorphous regions of the P(VDF-TrFE) matrix. At high nanoparticle loading, the phase separation is stratified leading to a bilayer film. We have unambiguously shown that addition of the non-ferroelectric nanoparticles does not enhance formation of the ferroelectric β-phase or other crystalline phases in P(VDF-TrFE). We showed that, depending on the concentration of MNPs inside nanocomposite films, the magnetic properties vary. We attributed that to the change in particle-particle distance and as a result variation in magnetic dipole-dipole interaction.

The insight gained here, particularly on formation of the microstructure, is very useful in the design of nanocomposites with optimized electric performance, particularly for PVDF-based nanocomposites in thin film multi-ferroics. To prevent phase separation and subsequently suppression of aforementioned problems we propose surface modification of the nanoparticles in such a way to increase the interaction with P(VDF-TrFE) polymer chains towards better dispersion. The results of the nanocomposites based on modified MNPs/P(VDF-TrFE) are given in the next section of this chapter.

7.1.5 References

1. Naber, R. C.; Asadi, K.; Blom, P. W.; de Leeuw, D. M.; de Boer, B., Organic nonvolatile memory devices based on ferroelectricity. *Advanced materials* **2010,** *22*, 933-945.
2. Heremans, P.; Gelinck, G. H.; Muller, R.; Baeg, K.-J.; Kim, D.-Y.; Noh, Y.-Y., Polymer and organic nonvolatile memory devices. *Chemistry of Materials* **2010,** *23*, 341-358.
3. Furukawa, T., Structure and functional properties of ferroelectric polymers. *Advances in Colloid and Interface Science* **1997,** *71*, 183-208.
4. Lovinger, A. J., Ferroelectric polymers. *Science* **1983,** *220*, 1115-1121.
5. Bauer, S., Poled polymers for sensors and photonic applications. *Journal of Applied Physics* **1996,** *80*, 5531-5558.
6. Mao, D.; Quevedo-Lopez, M.; Stiegler, H.; Gnade, B. E.; Alshareef, H. N., Optimization of poly (vinylidene fluoride-trifluoroethylene) films as non-volatile memory for flexible electronics. *Organic Electronics* **2010,** *11*, 925-932.

7. Martins, P.; Larrea, A.; Gonçalves, R.; Botelho, G.; Ramana, E.; Mendiratta, S.; Sebastian, V.; Lanceros-Mendez, S., Novel anisotropic magnetoelectric effect on δ-FeO (OH)/P (VDF-TrFE) multiferroic composites. *ACS applied materials & interfaces* **2015,** *7*, 11224-11229.
8. Martins, P.; Kolen'ko, Y. V.; Rivas, J.; Lanceros-Mendez, S., Tailored magnetic and magnetoelectric responses of polymer-based composites. *ACS applied materials & interfaces* **2015,** *7*, 15017-15022.
9. Ma, J.; Hu, J.; Li, Z.; Nan, C. W., Recent progress in multiferroic magnetoelectric composites: from bulk to thin films. *Advanced Materials* **2011,** *23*, 1062-1087.
10. Wang, Q.; Zhu, L., Polymer nanocomposites for electrical energy storage. *Journal of Polymer Science Part B: Polymer Physics* **2011,** *49*, 1421-1429.
11. Zhu, L.; Wang, Q., Novel ferroelectric polymers for high energy density and low loss dielectrics. *Macromolecules* **2012,** *45*, 2937-2954.
12. Martins, P.; Lanceros-Méndez, S., Polymer-based magnetoelectric materials. *Advanced Functional Materials* **2013,** *23*, 3371-3385.
13. Furukawa, T.; Nakajima, T.; Takahashi, Y., Factors governing ferroelectric switching characteristics of thin VDF/TrFE copolymer films. *IEEE Transactions on Dielectrics and Electrical Insulation* **2006,** *13*, 1120-1131.
14. Asadi, K.; De Leeuw, D. M.; De Boer, B.; Blom, P. W., Organic non-volatile memories from ferroelectric phase-separated blends. *Nature materials* **2008,** *7*, 547-550.
15. Khan, M. A.; Bhansali, U. S.; Alshareef, H. N., High-Performance Non-Volatile Organic Ferroelectric Memory on Banknotes. *Advanced Materials* **2012,** *24*, 2165-2170.
16. Van Breemen, A.; Kam, B.; Cobb, B.; Rodriguez, F. G.; Van Heck, G.; Myny, K.; Marrani, A.; Vinciguerra, V.; Gelinck, G., Ferroelectric transistor memory arrays on flexible foils. *Organic Electronics* **2013,** *14*, 1966-1971.
17. Lenz, T.; Sharifi Dehsari, H.; Asadi, K.; Blom, P. W.; Groen, W. A.; de Leeuw, D. M., Thin film thermistor with positive temperature coefficient of resistance based on phase separated blends of ferroelectric and semiconducting polymers. *Applied Physics Letters* **2016,** *109*, 133302-133305.
18. Ghittorelli, M.; Lenz, T.; Dehsari, H. S.; Zhao, D.; Asadi, K.; Blom, P. W.; Kovács-Vajna, Z. M.; de Leeuw, D. M.; Torricelli, F., Quantum tunnelling and charge accumulation in organic ferroelectric memory diodes. *Nature communication* **2017,** *8*, 15841-15848.
19. Xia, W.; Peter, C.; Weng, J.; Zhang, J.; Kliem, H.; Jiang, Y.; Zhu, G., Epitaxy of Ferroelectric P (VDF-TrFE) Films via Removable PTFE Templates and Its Application in Semiconducting/Ferroelectric Blend Resistive Memory. *ACS applied materials & interfaces* **2017,** *9*, 12130-12137.
20. Sun, C.; Guo, Y.; Fang, B.; Yang, J.; Qin, B.; Duan, H.; Chen, Y.; Li, H.; Liu, H., Enhanced photovoltaic performance of perovskite solar cells using polymer P (VDF-TrFE) as a processed additive. *The Journal of Physical Chemistry C* **2016,** *120*, 12980-12988.
21. Chan, H. L.; Ng, P.; Choy, C., Effect of poling procedure on the properties of lead zirconate titanate/vinylidene fluoride-trifluoroethylene composites. *Applied physics letters* **1999,** *74*, 3029-3031.
22. Banno, H., Recent developments of piezoelectric ceramic products and composites of synthetic rubber and piezoelectric ceramic particles. *Ferroelectrics* **1983,** *50*, 3-12.
23. Naber, R.; Blom, P.; Marsman, A.; De Leeuw, D., Low voltage switching of a spin cast ferroelectric polymer. *Applied Physics Letters* **2004,** *85*, 2032-2034.
24. Li, M.; Stingelin, N.; Michels, J. J.; Spijkman, M. J.; Asadi, K.; Beerends, R.; Biscarini, F.; Blom, P. W.; de Leeuw, D. M., Processing and Low Voltage Switching of Organic Ferroelectric Phase-Separated Bistable Diodes. *Advanced Functional Materials* **2012,** *22*, 2750-2757.
25. Mahdi, R.; Gan, W.; Halim, N.; Velayutham, T.; Majid, W. A., Ferroelectric and pyroelectric properties of novel lead-free polyvinylidenefluoride-trifluoroethylene–Bi0. 5Na0. 5TiO3 nanocomposite thin films for sensing applications. *Ceramics International* **2015,** *41*, 13836-13843.

26. Shafee, E. E.; Behery, S., Preparation, characterization and properties of novel 0–3 ferroelectric composites of Ba0. 95Ca0. 05Ti0. 8Zr0. 2O3–poly (vinylidene fluoride-trifluoroethylene). *Materials Chemistry and Physics* **2012,** *132*, 740-746.
27. Dietze, M.; Es-Souni, M., Structural and functional properties of screen-printed PZT–PVDF-TrFE composites. *Sensors and Actuators A: Physical* **2008,** *143*, 329-334.
28. Valiyaneerilakkal, U.; Varghese, S., Poly (vinylidene fluoride-trifluoroethylene)/barium titanate nanocomposite for ferroelectric nonvolatile memory devices. *Aip Advances* **2013,** *3*, 042131-042135.
29. Wang, X.; Lam, K.; Tang, X.; Chan, H., Dielectric characteristics and polarization response of lead-free ferroelectric (Bi0. 5Na0. 5) 0.94 Ba0. 06TiO3–P (VDF-TrFE) 0–3 composites. *Solid state communications* **2004,** *130*, 695-699.
30. Song, Y.; Shen, Y.; Liu, H.; Lin, Y.; Li, M.; Nan, C.-W., Enhanced dielectric and ferroelectric properties induced by dopamine-modified BaTiO 3 nanofibers in flexible poly (vinylidene fluoride-trifluoroethylene) nanocomposites. *Journal of Materials Chemistry* **2012,** *22*, 8063-8068.
31. Zhang, J.; Dai, J.; So, L.; Sun, C.; Lo, C.; Or, S.; Chan, H. L., The effect of magnetic nanoparticles on the morphology, ferroelectric, and magnetoelectric behaviors of CFO/P (VDF-TrFE) 0–3 nanocomposites. *Journal of Applied Physics* **2009,** *105*, 054102-054107.
32. Li, J.; Seok, S. I.; Chu, B.; Dogan, F.; Zhang, Q.; Wang, Q., Nanocomposites of ferroelectric polymers with TiO2 nanoparticles exhibiting significantly enhanced electrical energy density. *Advanced Materials* **2009,** *21*, 217-221.
33. Guo, Y.; Liu, Y.; Wang, J.; Withers, R. L.; Chen, H.; Jin, L.; Smith, P., Giant magnetodielectric effect in 0− 3 Ni0. 5Zn0. 5Fe2O4-Poly (vinylidene-fluoride) nanocomposite films. *Journal of Physical Chemistry C* **2010,** *114*, 13861-13866.
34. Martins, P.; Moya, X.; Phillips, L.; Kar-Narayan, S.; Mathur, N.; Lanceros-Mendez, S., Linear anhysteretic direct magnetoelectric effect in Ni0. 5Zn0. 5Fe2O4/poly (vinylidene fluoride-trifluoroethylene) 0-3 nanocomposites. *Journal of Physics D: Applied Physics* **2011,** *44*, 482001-482004.
35. Martins, P.; Lasheras, A.; Gutiérrez, J.; Barandiaran, J. M.; Orue, I.; Lanceros-Mendez, S., Optimizing piezoelectric and magnetoelectric responses on CoFe2O4/P (VDF-TrFE) nanocomposites. *Journal of Physics D: Applied Physics* **2011,** *44*, 495303-49509.
36. Zou, Y.; Han, L.; Yuan, G.; Liu, B.; Zhao, X.; Tian, B.; Wang, J.; Sun, S.; Sun, J.; Meng, X., Enhanced ferroelectric and dielectric properties of the P (VDF-TrFE)/Ag nanoparticles composite thin films. *Journal of Materials Science: Materials in Electronics* **2014,** *25*, 3461-3465.
37. Valiyaneerilakkal, U.; Singh, K.; Varghese, S., Device level optimization of poly (vinylidene fluoride-trifluoroethylene)–zinc oxide polymer nanocomposite thin films for ferroelectric applications. *Journal of Applied Physics* **2015,** *118*, 204102-204109.
38. Paik, H.; Choi, Y.-Y.; Hong, S.; No, K., Effect of Ag nanoparticle concentration on the electrical and ferroelectric properties of Ag/P (VDF-TrFE) composite films. *Scientific reports* **2015,** *5*, 13209-13215.
39. Tsutsumi, N.; Kosugi, R.; Kinashi, K.; Sakai, W., Nature of the enhancement in ferroelectric properties by gold nanoparticles in vinylidene fluoride and trifluoroethylene copolymer. *ACS applied materials & interfaces* **2016,** *8*, 16816-16822.
40. Svirskas, Š.; Belovickis, J.; Šemeliovas, D.; Martins, P.; Lanceros-Méndez, S.; Banys, J., Temperature and frequency dependence of the dielectric and piezoelectric response of P (VDF–TrFE)/CoFe2O4 magnetoelectric composites. *Lithuanian Journal of Physics* **2017,** *57*, 103-111.
41. Singh, D.; Choudhary, A.; Garg, A., Flexible and robust piezoelectric polymer nanocomposites based energy harvesters. *ACS applied materials & interfaces* **2018,** *10*, 2793-2800.
42. Ahlawat, A.; Satapathy, S.; Shirolkar, M. M.; Li, J.; Khan, A. A.; Deshmukh, P.; Wang, H.; Choudhary, R.; Karnal, A., Tunable Magnetoelectric Nonvolatile Memory Devices Based on SmFeO3/P (VDF-TrFE) Nanocomposite Films. *ACS Applied Nano Materials* **2018,** *1*, 3196-3203.

43. Martins, P.; Gonçalves, R.; Lanceros-Mendez, S.; Lasheras, A.; Gutiérrez, J.; Barandiarán, J., Effect of filler dispersion and dispersion method on the piezoelectric and magnetoelectric response of CoFe2O4/P (VDF-TrFE) nanocomposites. *Applied Surface Science* **2014,** *313*, 215-219.
44. Li, Q.; Wang, Q., Ferroelectric Polymers and Their Energy-Related Applications. *Macromolecular Chemistry and Physics* **2016,** *217*, 1228-1244.
45. Kusuma, D. Y.; Nguyen, C. A.; Lee, P. S., Enhanced ferroelectric switching characteristics of P (VDF-TrFE) for organic memory devices. *Journal of Physical Chemistry B* **2010,** *114*, 13289-13293.
46. Dehsari, H. S.; Ribeiro, A. H.; Ersöz, B.; Tremel, W.; Jakob, G.; Asadi, K., Effect of precursor concentration on size evolution of iron oxide nanoparticles. *CrystEngComm* **2017,** *19*, 6694-6702.
47. Wu, L.; Mendoza-Garcia, A.; Li, Q.; Sun, S., Organic phase syntheses of magnetic nanoparticles and their applications. *Chemical reviews* **2016,** *116*, 10473-10512.
48. Sharifi Dehsari, H.; Asadi, K., The Impact of Stoichiometry and Size on Magnetic Properties of Cobalt-Ferrite Nanoparticles. *The Journal of Physical Chemistry C* **2018**.
49. Dehsari, H. S.; Michels, J. J.; Asadi, K., Processing of ferroelectric polymers for microelectronics: from morphological analysis to functional devices. *Journal of Materials Chemistry C* **2017,** *5*, 10490-10497.
50. Sharifi Dehsari, H.; Heidari, M.; Halda Ribeiro, A.; Tremel, W.; Jakob, G.; Donadio, D.; Potestio, R.; Asadi, K., Combined Experimental and Theoretical Investigation of Heating Rate on Growth of Iron Oxide Nanoparticles. *Chemistry of Materials* **2017,** *29*, 9648-9656.
51. Sharifi Dehsari, H.; Harris, R. A.; Ribeiro, A. H.; Tremel, W.; Asadi, K., Optimizing the Binding Energy of the Surfactant to Iron-Oxide Yields Truly Monodisperse Nanoparticles. *Langmuir* **2018,** *34*, 6582-6590.
52. Guardia, P.; Labarta, A.; Batlle, X., Tuning the size, the shape, and the magnetic properties of iron oxide nanoparticles. *Journal of Physical Chemistry C* **2010,** *115*, 390-396.
53. Ribeiro, C.; Costa, C. M.; Correia, D. M.; Nunes-Pereira, J.; Oliveira, J.; Martins, P.; Gonçalves, R.; Cardoso, V. F.; Lanceros-Méndez, S., Electroactive poly (vinylidene fluoride)-based structures for advanced applications. *Nature protocols* **2018,** *13*, 681-694.
54. Cardoso, V.; Costa, C. M.; Minas, G.; Lanceros-Mendez, S., Improving the optical and electroactive response of poly (vinylidene fluoride–trifluoroethylene) spin-coated films for sensor and actuator applications. *Smart Materials and Structures* **2012,** *21*, 085020-085027.
55. Asadi, K.; van der Veen, M. A., Ferroelectricity in Metal–Organic Frameworks: Characterization and Mechanisms. *European Journal of Inorganic Chemistry* **2016,** *2016*, 4332-4344.
56. Zhao, D.; Katsouras, I.; Asadi, K.; Blom, P. W.; de Leeuw, D. M., Switching dynamics in ferroelectric P (VDF-TrFE) thin films. *Physical Review B* **2015,** *92*, 214115-214122.
57. Clements, J.; Davies, G.; Ward, I., A broad-line nuclear magnetic resonance study of a vinylidene fluoride/trifluoroethylene copolymer. *Polymer* **1992,** *33*, 1623-1629.
58. Jin, L.; Li, F.; Zhang, S., Decoding the fingerprint of ferroelectric loops: comprehension of the material properties and structures. *Journal of the American Ceramic Society* **2014,** *97*, 1-27.
59. Schenk, T.; Yurchuk, E.; Mueller, S.; Schroeder, U.; Starschich, S.; Böttger, U.; Mikolajick, T., About the deformation of ferroelectric hystereses. *Applied physics reviews* **2014,** *1*, 041103.
60. Nagar, S.; Rao, K. V.; Belova, L. M.; Catalan, G.; Hong, J.; Scott, J.; Tyagi, A.; Jayakumar, O.; Shukla, R.; Sheng, Y., Room Temperature Ferromagnetism and Lack of Ferroelectricity in Thin Films of 'Biferroic'YbCrO 3. *MRS Online Proceedings Library Archive* **2009,** *1161*.
61. Li, M.; Katsouras, I.; Piliego, C.; Glasser, G.; Lieberwirth, I.; Blom, P. W.; de Leeuw, D. M., Controlling the microstructure of poly (vinylidene-fluoride)(PVDF) thin films for microelectronics. *Journal of Materials Chemistry C* **2013,** *1*, 7695-7702.
62. Kumar, M.; Sharifi Dehsari, H.; Anwar, S.; Asadi, K., Air-stable memory array of bistable rectifying diodes based on ferroelectric-semiconductor polymer blends. *Applied Physics Letters* **2018,** *112*, 123302-123305.

63. Xia, W.; Gu, Y.; You, C.; Cao, C.; Xu, Z.; Zhang, Z., A crystal phase transition and its effect on the dielectric properties of a hydrogenated P (VDF-co-TrFE) with low TrFE molar content. *RSC Advances* **2015,** *5*, 107557-107565.
64. Martins, P.; Lopes, A.; Lanceros-Mendez, S., Electroactive phases of poly (vinylidene fluoride): determination, processing and applications. *Progress in polymer science* **2014,** *39*, 683-706.
65. Li, Z.; Wang, J.; Wang, X.; Yang, Q.; Zhang, Z., Ferro-and piezo-electric properties of a poly (vinyl fluoride) film with high ferro-to para-electric phase transition temperature. *RSC Advances* **2015,** *5*, 80950-80955.
66. Chen, X.-Z.; Li, X.; Qian, X.-S.; Wu, S.; Lu, S.-G.; Gu, H.-M.; Lin, M.; Shen, Q.-D.; Zhang, Q., A polymer blend approach to tailor the ferroelectric responses in P (VDF–TrFE) based copolymers. *Polymer* **2013,** *54*, 2373-2381.
67. Ma, W.; Zhang, J.; Wang, X.; Wang, S., Effect of PMMA on crystallization behavior and hydrophilicity of poly (vinylidene fluoride)/poly (methyl methacrylate) blend prepared in semi-dilute solutions. *Applied Surface Science* **2007,** *253*, 8377-8388.
68. Rouxel, D.; Vincent, B.; Badie, L.; Dos Santos, F. D.; Lamouroux, E.; Fort, Y., Influence of cluster size and surface functionalization of ZnO nanoparticles on the morphology, thermomechanical and piezoelectric properties of P (VDF-TrFE) nanocomposite films. *Applied surface science* **2013,** *279*, 204-211.
69. Martins, P.; Costa, C. M.; Lanceros-Mendez, S., Nucleation of electroactive β-phase poly (vinilidene fluoride) with CoFe2O4 and NiFe2O4 nanofillers: a new method for the preparation of multiferroic nanocomposites. *Applied Physics A* **2011,** *103*, 233-237.
70. Lonjon, A.; Demont, P.; Dantras, E.; Lacabanne, C., Mechanical improvement of P (VDF-TrFE)/nickel nanowires conductive nanocomposites: Influence of particles aspect ratio. *Journal of non-crystalline solids* **2012,** *358*, 236-240.
71. Lonjon, A.; Laffont, L.; Demont, P.; Dantras, E.; Lacabanne, C., Structural and electrical properties of gold nanowires/P (VDF-TrFE) nanocomposites. *Journal of Physics D: Applied Physics* **2010,** *43*, 345401-345407.
72. Yao, Y.; Metwalli, E.; Su, B.; Körstgens, V.; Moseguí González, D.; Miasnikova, A.; Laschewsky, A.; Opel, M.; Santoro, G.; Roth, S. V., Arrangement of Maghemite Nanoparticles via Wet Chemical Self-Assembly in PS-b-PNIPAM Diblock Copolymer Films. *ACS Appl. Mater. Interfaces* **2015,** *7*, 13080-13091.
73. Katsouras, I.; Zhao, D.; Spijkman, M.-J.; Li, M.; Blom, P. W.; De Leeuw, D. M.; Asadi, K., Controlling the on/off current ratio of ferroelectric field-effect transistors. *Scientific reports* **2015,** *5*, 12094-12101.
74. Black, C.; Farrell, C.; Licata, T. J., Suppression of ferroelectric polarization by an adjustable depolarization field. *Applied physics letters* **1997,** *71*, 2041-2043.
75. Hu, W. J.; Juo, D.-M.; You, L.; Wang, J.; Chen, Y.-C.; Chu, Y.-H.; Wu, T., Universal ferroelectric switching dynamics of vinylidene fluoride-trifluoroethylene copolymer films. *Scientific reports* **2014,** *4*, 4772-4779.
76. Merz, W. J., Domain Formation and Domain Wall Motions in Ferroelectric BaTi O 3 Single Crystals. *Physical Review* **1954,** *95*, 690-704.
77. Furukawa, T.; Kanai, S.; Okada, A.; Takahashi, Y.; Yamamoto, R., Ferroelectric switching dynamics in VDF-TrFE copolymer thin films spin coated on Si substrate. *Journal of Applied Physics* **2009,** *105*, 061636-061642.
78. Kim, E.; Kim, K.; Yoon, S., Investigation of the ferroelectric switching behavior of P (VDF-TrFE)-PMMA blended films for synaptic device applications. *Journal of Physics D: Applied Physics* **2016,** *49*, 075105-075112.

79. Mai, M.; Ke, S.; Lin, P.; Zeng, X., Intrinsic and extrinsic effects on the ferroelectric switching of thin poly (vinylidene fluoride/trifluoroethylene) copolymer films. *APL Materials* **2016,** *4*, 046107-046114.
80. Gaynutdinov, R.; Lysova, O.; Yudin, S.; Tolstikhina, A.; Kholkin, A.; Fridkin, V.; Ducharme, S., Polarization switching kinetics of ferroelectric nanomesas of vinylidene fluoride-trifluoroethylene copolymer. *Applied Physics Letters* **2009,** *95*, 023303-023305.
81. Kim, Y.; Kim, W.; Choi, H.; Hong, S.; Ko, H.; Lee, H.; No, K., Nanoscale domain growth dynamics of ferroelectric poly (vinylidene fluoride-co-trifluoroethylene) thin films. *Applied Physics Letters* **2010,** *96*, 012908-012910.
82. Aslibeiki, B.; Kameli, P.; Salamati, H., The effect of dipole-dipole interactions on coercivity, anisotropy constant, and blocking temperature of MnFe2O4 nanoparticles. *Journal of Applied Physics* **2016,** *119*, 063901.
83. Wohlfarth, E., The effect of particle interaction on the coercive force of ferromagnetic micropowders. *Proc. R. Soc. Lond. A* **1955,** *232*, 208-227.

Chapter 7

Section 2

Thin-Film Polymer Nanocomposites for Multi-Ferroic Applications Based on MNPs-PMMA/(PVDF-TrFE)[1]

7.2.1 Introduction

The polymer multiferroic nanocomposites are advantageous for many applications due to their flexibility, simple fabrication, ease of processing and shaping for large area applications. As shown in the previous section, agglomeration and eventually phase separation of the magnetic nanoparticle within the P(VDF-TrFE) matrix is the long standing issue. It has been well recognized that the aggregation and inhomogeneity of MNPs are the main reasons resulting in deterioration of electrical properties in polymer nanocomposites thin films.[1-3] The agglomeration of MNPs not only increases loss (leakage) but also gives rise to low breakdown strength, lowers functional device yield and reduced the reproducibility of nanocomposite performance. Moreover, in nanocomposite systems the magnetoelectric effect arises from a mechanical coupling between a magnetic and a ferroelectric phase. In order to enhance this coupling the

[1] **The results of this chapter are under preparation for submission.**

interfacial area between the two phases should be maximized. This can be accomplished with homogenously distributed nanoparticles inside ferroelectric matrix, which have a large surface to volume ratio. Therefore, agglomeration of the MNPs inside the polymer matrix should be avoided, particularly at high nanoparticle loadings and nanocomposite thin films. In Chapter 5, polymer grafted MNPs with different polymer shell thickness were synthesized, in order to improve the compatibility of the MNPs with P(VDF-TrFE) matrix. As a polymer shell we used PMMA. We chose PMMA, since it is miscible with VDF polymers (as a ferroelectric phase in the nanocomposite) and thermodynamically stable at all compositions due to the dipole/dipole interaction between the $>CF_2$ groups of P(VDF-TrFE) and the >C=O groups of PMMA and to the hydrogen bonding between the double bonded oxygen of the carbonyl group and the acidic hydrogen of the $–CH_2$-CF_2- group.[4]

7.2.1.1 Motivation

Developing new type of multiferroic polymer nanocomposite thin films based on P(VDF-TrFE)/MNPs-PMMA such that the nanocomposite has a homogeneous dispersion and therefore better performance.

7.2.1.2 Aim of this section

The aim of this section is to avoid the aggregation of MNPs inside P(VDF-TrFE) by using PMMA coated MNPs. Since PMMA is one of the few exception polymers that is fully miscible with PVDF.[4-5] In this section, we systematically investigate the evolution of the microstructure of P(VDF-TrFE) nanocomposite thin films after addition of PMMA-coated MNPs (both superparamagnetic and ferromagnetic) in different loading concentrations. Moreover, we systematically study the ferroelectric, polarization switching, dielectric, magnetic properties of the nanocomposite thin films.

7.2.2 Experiment

Materials

Ferroelectric copolymer P(VDF-TrFE) (75% - 25% molar) with molecular weight, M_W= 400000 was purchased from Solvay. The iron oxide and cobalt ferrite MNPs were synthesized and subsequently functionalized as described in details in previous chapters.

Device fabrications

Stock solutions of P(VDF-TrFE) (10 and 20 wt %) and MNPs-PMMA (4 wt%) in THF (or cyclopentanone) were first prepared. Then, by mixing the stock solutions in proper ratios, nanocomposite of P(VDF-TrFE)/MNPs-PMMA with different loading concentrations were obtained. The mixture was sonicated under bath sonication (3510 Branson) for 30 minutes at room temperature to obtain a good disperssion. To prepare capacitors, glass slides (or silicone wafers) were first throughly cleaned in aceton, propanol and DI-water. As bottom electrode, 1 nm/50 nm of Cr/Au were evaporated. Films of P(VDF-TrFE) nanocomposites were formed by either spin coating or bar coating. The smooth nanocomposite thin films were prepared by avoiding VIPS under film formation. This was done either by processing under modified coating condition while using THF as a hydrophilic solvent, *i.e.* low humidity of <10 % and high substrate temperature of 50°C, or under normal coating condition by using hydrophobic solvent (cyclopentanone) to supress VIPS (see Chapter 6).[6] We tuned the solution concentration or coating condition to arrive at comparable layer thicknesses for all nanocomposite thin films, which were in the range of 300 to 400 nm (measured using Dektak profilometer). The surface roughness (root mean square) of nanocomposites thin films for all the loading concentrations remained below 7 nm even in high loadings. This low value of rms roughness for all concentrations is idicative of fine distribution of MNPs-PMMA inside polymer matrix and absence of agglomoration as well as suppresion of VIPS during film formation. As we showed in previous section, we observed increasing in roughnes via increasing the loading concentration of MNPs inside polymer matrix. After film formations, the substrates were annealed at 140 °C for 2 h in a vacuum (10^{-1} mbar) to increase the crytallinity of P(VDF-TrFE). The capacitors were finished by evaporation of a 50 nm Au top electrode. The capacitor area changed over a wide range from 0.16 mm^2 to 4 mm^2. To arrive at a reliable statistics, more than 50 capacitors for each loading ratio were tested.

Electric displacement versus electric field, *D-E* loops was measured under ambient conditions using a Sawyer-Tower circuit. VSM measurements were perfomed on nanocomposite films. The other characterizations techniques were explanied in detail in previous section.

7.2.3 Results and discussion

The average diameter of iron oxide and cobalt ferrite MNPs are 12 ± 1 and 12.6 ± 1.6 nm, respectively. The cobalt stoichiometry is $x = 0.7$ ($Co_{0.7}Fe_{2.3}O_4$), since it gives the optimum magnetic properties (see **Chapter 4**).[7-9] The molecular weight (M_n) of the grafted PMMA shell from the surface of Fe_3O and $Co_{0.7}Fe_{2.3}O_4$ are 50 and 41 kg/mol, respectively. The TEM images before and after polymerization for both types of MNPs are shown in **Figure 7.2.1**. The weight loss of the organic part for polymer coated iron oxide and cobalt ferrite MNPs (measured by TGA) are ~ 70 and ~ 50 % respectively. The details of synthesis, modifications and characterizations of MNPs are given in **Chapter 3-5**.

The MNP-PMMA/(PVDF-TrFE) solution, were easily dispersed in toluene (or common solvents of PMMA and P(VDF-TrFE)). In contrary to oleate coated MNPs, MNPs-PMMA (iron oxide and cobalt ferrite) remains dispersable in nanocomposite solution over a long time and do not separate even in the presence of strong magnet.

The SEM images of the nanocomposite thin films for iron oxide-PMMA MNPs inside P(VDF-TrFE) after annealing at 140 °C for two hours are given in **Figure 7.2.2 a-f**. The MNPs are single by single separated from each other inside the polymer matrix without any aggregation. We note that, MNPs-PMMA reside in the amorphous phase of the P(VDF-TrFE). Cross-sectional SEM images of the 12 and 36 wt % nanocomposite thin films, **Figure 7.2.2 g-h**, confirms exclusion of the fillers from the P(VDF-TrFE) crystallites and also no agglomeration of MNPs-PMMA throughout the film. We note that, for polymers such as P(VDF-TrFE) that are made of both amorphous and crystalline phases, mechanical breaking leads to stretched amorphous phase, leaving holes in the cross sectional area, which then appear as pores in the SEM image. Overall, the SEM images prove that the NPs are homogenously distributed inside P(VDF-TrFE) and no aggregation was observed even for high loading. The similar

microstructure was also observed for the nanocomposites using PMMA-coated cobalt-ferrite nanoparticles.

We note that by changing the molecular weight of grafted polymer we can tune the inter-particle distance between the MNPs and hence control the packing density of MNPs inside nanocomposite thin films. Therefore, by using MNPs-PMMA with lower molecular weight of PMMA, we can increase the percentage (as well as packing density) of MNPs inside nanocomposite thin. However, the molecular weight of polymer chains should be high enough to avoid magnetically induced aggregation of the MNPs.

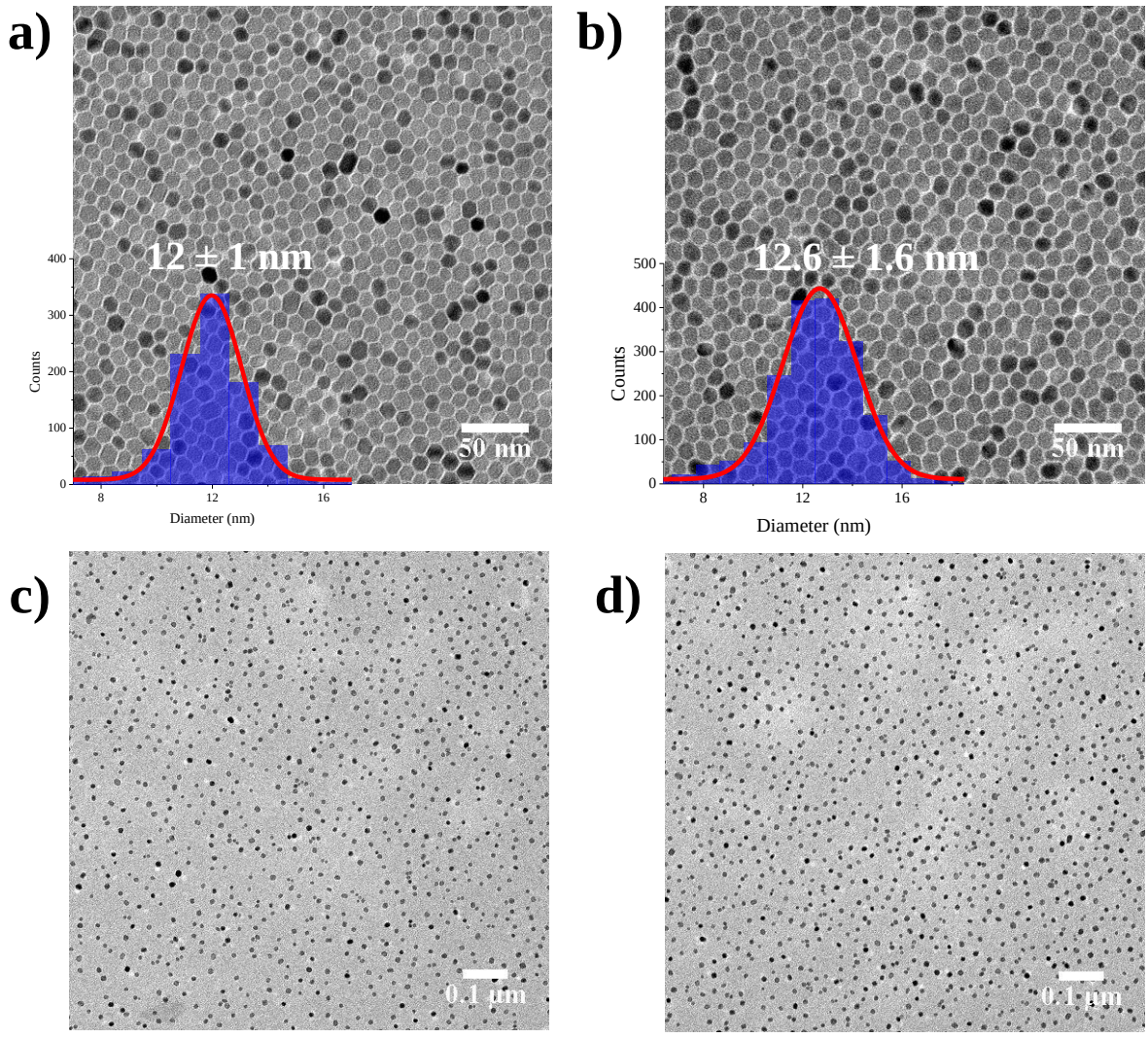

Figure 7.2.1 TEM images of oleate coated iron oxide (a) and cobalt ferrite MNPs (b). TEM images of polymer coated (PMMA) iron oxide (c) and cobalt ferrite (b) MNPs with M_n of 50 and 41 kg/mol respectively.

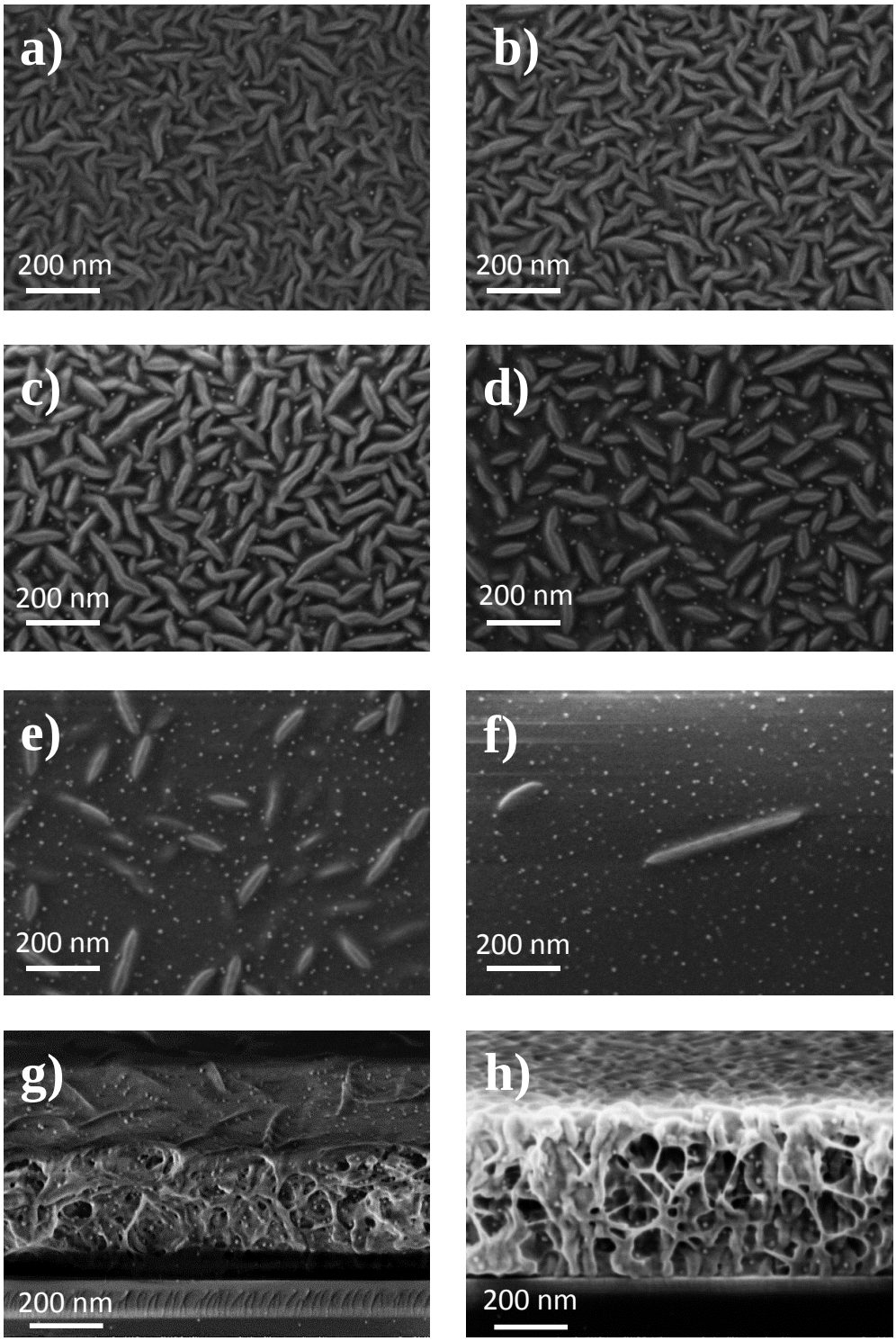

Figure 7.2.2 SEM images of the nanocomposite thin film of Fe_3O_4-PMMA/P(VDF-TrFE) with different concentraton of (a) 3 wt%, (b) 6 wt%, (c) 12 wt%, (d) 24 wt%, (e) 36 wt% and (f) 48 wt%. Cress-sectional SEM images of nanocomposite tin films with (g) 12 wt% and (h) 36 wt% loading concentration.

Moreover, the SEM images show that by increasing the loadings of MNPs-PMMA inside P(VDF-TrFE) matrix, the density of needle shape crystalline domains of P(VDF-TrFE) is suppressed. The closely packed crystallites are loosened with the addition of MNPs-PMMA. We speculate that at high MNPs-PMMA loadings, the crystallites disappear and the nanocomposite becomes more amorphous. Therefore, addition of the MNPs with an amorphous PMMA shell into the P(VDF-TrFE) expands the amorphous region between the crystalline domains. The similar morphology evolution has been observed in the literature by addition of PMMA chains to P(VDF-TrFE).[10] We also note that, by using MNPs-PMMA with lower M_n of grated PMMA, the rate of disappearing ferroelectric crystal phase gets slower. Moreover, we can tune the packing density of MNP inside nanocomposite by controlling the molecular weight and subsequently the inter-particle distance between MNPs. In order to have the maximum percentages of both phases (magnetic and ferroelectric crystals) and subsequently more interface between two phases, it is better to reduce the molecular weight of grafted PMMA. However, the size of polymer chains should be high enough to avoid aggregation of the MNPs.

To substantiate the claim, DSC analysis is performed on the pristine P(VDF-TrFE) and the nanocomposites films with different loadings. Endo- and exothermic heat flows of nanocoposites films with different loading are shown in **Figure 7.2.3 a** and **b**. We calculate the melting enthalpy of the P(VDF-TrFE) nanocomposites from the melting peak of the first heating endotherms. The degree of crystallinity is obtained by dividing the calculated enthalpy of the nanocomposite by that of the pristine P(VDF-TrFE) film *viz.* 91.45 J/g.[11] The calculated crystallinity, X_c, as shown in **Figure 7.2.3 c** steadily decreases with increasing the concentration of MNPs-PMMA in the nanocomposite film. The rate of the reduction depends on the molecular weight of the grafted chains, MNPs-PMMA. In addition, we observe similar trend of the reduction in crystallinity of the nanocomposite by addition of oleate coated MNPs to P(VDF-TrFE). Furthermore, we extract melting ($T_{Melting}$), Curie (T_{Curie}) and crystallization temperatures ($T_{Crystalization}$), **Figure 7.2.3 d**. The melting point, crystallization temperature and Curie temperature, of P(VDF-TrFE) nanocomposite monotonically decrease with addition of MNPs-PMMA. This observation confirms that P(VDF-TrFE) and MNPs-PMMA are miscible and interacting with each other over the entire composition range both in the melt and when quenched into a vitreous solid solution. We showed in previous section that, oleate and P(VDF-

TrFE) are non-interacting system and they are not miscible. Therefore addition of oleate coated MNPs into P(VDF-TrFE) did not change $T_{Melting}$, T_{Curie}, and $T_{Crystalization}$.

In addition, for nanocomposite film comprising 48 wt % MNPs-PMMA or more, PVDF does not recrystallize and the films remain amorphous. Hence, we expect to observe no ferroelectric properties when the concentration of MNP-PMMA exceed above 48 wt%. However, the concentration limit above which we lose ferroelectric properties depends on the molecular weight of grafted polymer shell. We note that the concentration limit increases to higher loadings of MNP-PMMA while using grafted polymer shell with lower molecular weight.

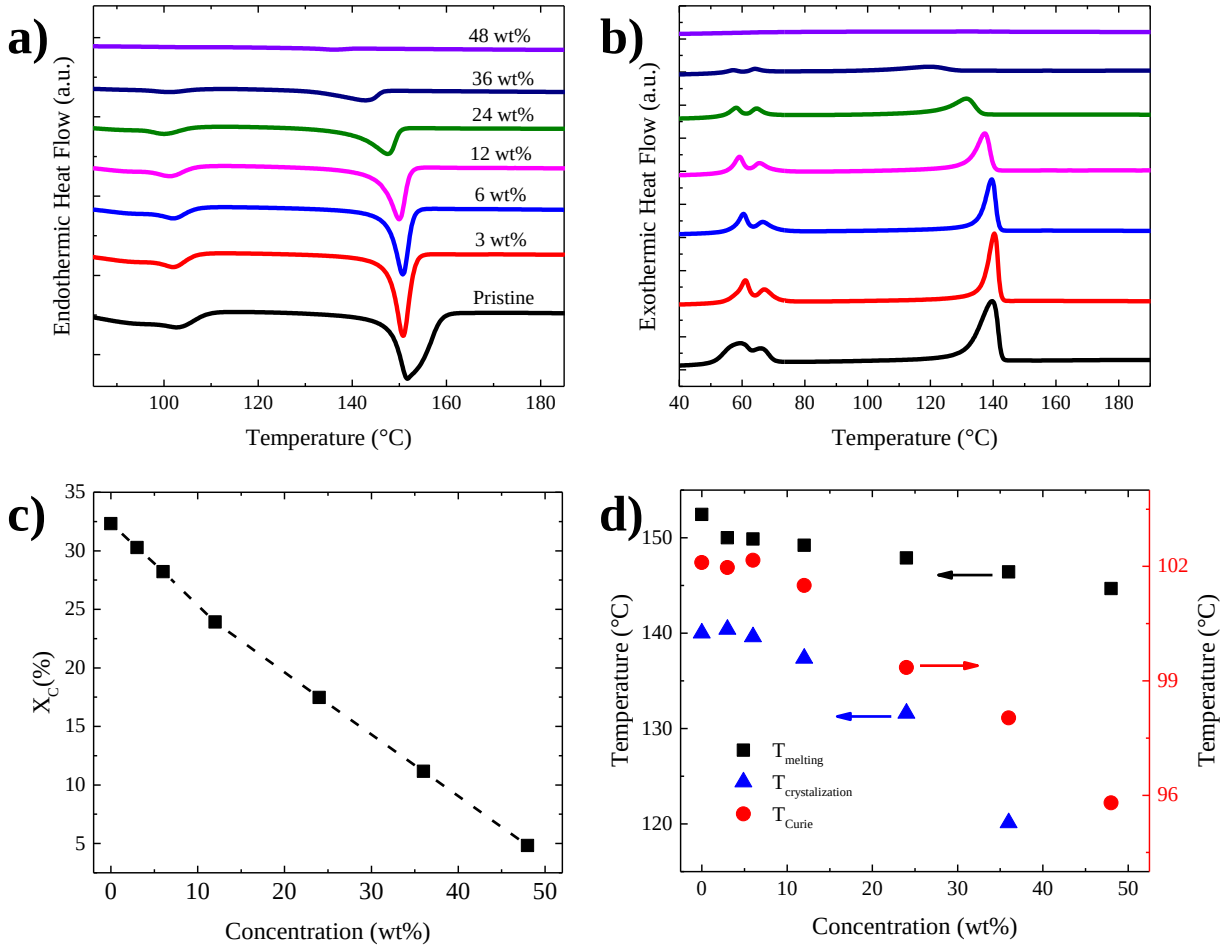

Figure 7.2.3 DSC thermogram of (a) heating and (b) cooling for Fe_3O_4-PMMA/P(VDF-TrFE) nanocomposite films. The values of (c) *Xc* and (d) $T_{Melting}$, T_{Curie}, $T_{Crystalization}$ as a function of the concentration of nanoparticle loading inside polymer matrix. Similar results have been observed for the nanocomposite films with $Co_{0.7}Fe_{2.3}O_4$-PMMA.

We measured the surface rms roughness of the nanocomposite thin films. We note that despite changing the loading of the MNPs-PMMA inside nanocomposite thin films, the film

surface shows almost no change in root mean square (rms) roughness and it remains at approximately 7 ± 3 nm for all the loadings. This is indicative of well distribution of MNPs throughout the film as well as suppression of VIPS during film formation. This observation is in contrast to oleate coated MNPs in which we observe increasing in rms roughness by increasing loading concentration. The increase in the rms roughness by addition of oleate coated MNPs is attributed to agglomeration of MNPs on the surface of nanocomposite film.

Figure 7.2.4 shows FTIR results for nanocomposite films with different ratio of MNPs-PMMA inside polymer matrix of P(VDF-TrFE) thermally annealed at 140 °C for 2 h. P(VDF-TrFE) film without MNPs-PMMA exhibits the characteristic IR bands at 840 cm^{-1} and 1280 cm^{-1}, showing that the film mostly consists of ferroelectric β crystal phases. However, by increasing the concentration of MNPs-PMMA in the nanocomposite film, the characteristic β absorptions decreases and disappears for loadings of >48% of MNPs-PMMA. The results are in agreement with SEM and DSC.

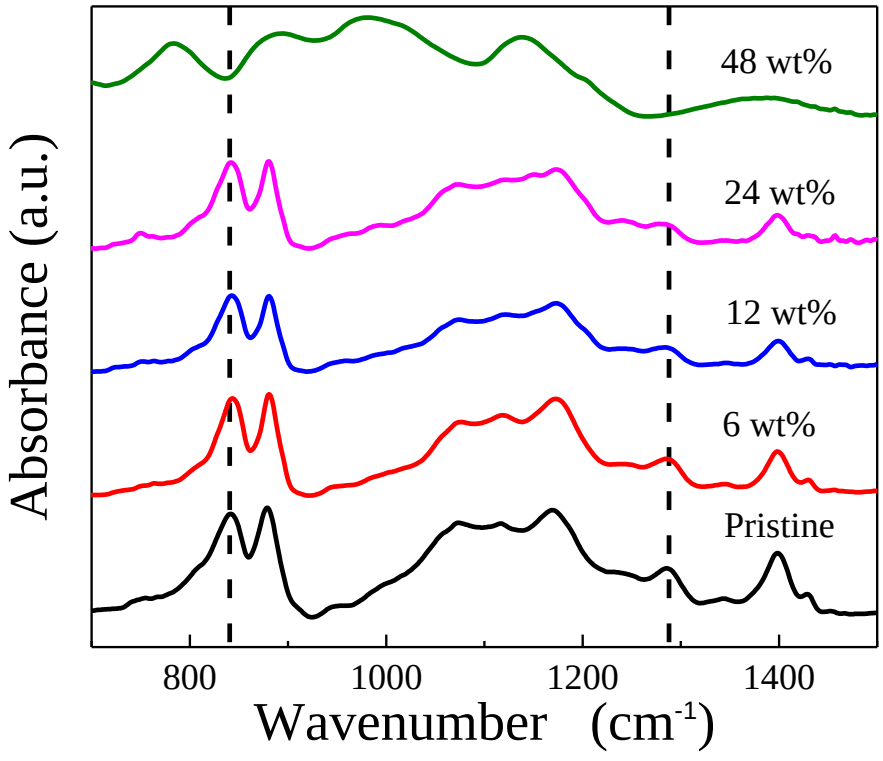

Figure 7.2.4 FTIR spectra of nanocomposite films with different concentrations of Fe_3O_4-PMMA MNPs inside polymer matrix of P(VDF-TrFE). Similar FTIR results have observed for the nanocomposite with $Co_{0.7}Fe_{2.3}O_4$-PMMA.

The *D-E* loops of the nanocomposite thin films of both PMMA-coated iron oxide and cobalt-ferrite MNPs/P(VDF-TrFE) with different loadings are depicted in **Figure 7.2.5**. The rest of the *D-E* loops for nanocomposite thin films of Fe_3O_4-PMMA and $Co_{0.7}Fe_{2.3}O_4$-PMMA/P(VDF-TrFE) are given in **Figure A7.2.1** and **Figure A7.2.2**, respectively. For comparison, *D-E* loops of oleate-coated MNPs with 4 and 8 wt% are also given (**Figure 7.2.5 a** and **b**). As we discussed in previous section, the nanocomposites films with the oleate-coated MNPs suffer from huge leakage, low breakdown strength, low functional device yield and high variation in device performance. The leakage current is due to the phase separation and aggregation of MNPs inside polymer matrix. We note that, these aforementioned problems get worse in higher loadings and thinner films of the nanocomposite.

On the other hand, the *D-E* loop of the nanocomposites with MNPs-PMMA, show no leakage current in the hysteresis loops (**Figure 7.2.5 c-f**), for both iron and cobalt ferrite. Since PMMA and P(VDF-TrFE) are miscible with each other, surface modification of the MNPs with a PMMA shell, improves the compatibility between MNPs and polymer matrix and subsequently avoids aggregation of the MNPs. Therefore, due to suppression of the aggregation and single by single separation of MNPs inside polymer matrix, no leakage current is present in the hysteresis loops (**Figure 7.2.5 c-f**). Moreover, we note that, when we use MNPs-PMMA inside P(VDF-TrFE) the yield of functional devices remains > 90% for all loading concentrations. However, by using oleate coated MNPs, due to the aggregation of the MNPs, the functional device yield significantly decreases by increasing the loading concentration (to about 10-20% for high loadings) as well as the break down filed of the devices is low.

The remanent polarization and the coercive field of pristine P(VDF-TrFE) amount to 6.2 $\mu C/cm^2$ and 52 MV/m, respectively. The summary of the extracted values of P_r and E_C of nanocomposite thin films with different loading concentrations of Fe_3O_4-PMMA and $Co_{0.7}Fe_{2.3}O_4$-PMMA inside polymer matrix are shown in **Figure 7.2.6a** and **b**, respectively. The value of P_r reduces by increasing the loading while the value of E_C increases. For the composite we defined polarization as $P_r = \sum \mu / V$, as the superposition of the dipole moment μ of the constituent phases per total volume of the nanocomposite. Therefore, the decrease in P_r in the polarization hysteresis loops by addition of MNPs-PMMA originates from the decrease of the density of ferroelectric β crystals inside nanocomposite film. The evolution of ferroelectric

properties (P_r and E_C) regardless of the type of MNPs (superparamagnetic and ferri/ferromagnetic) follows the same trend.

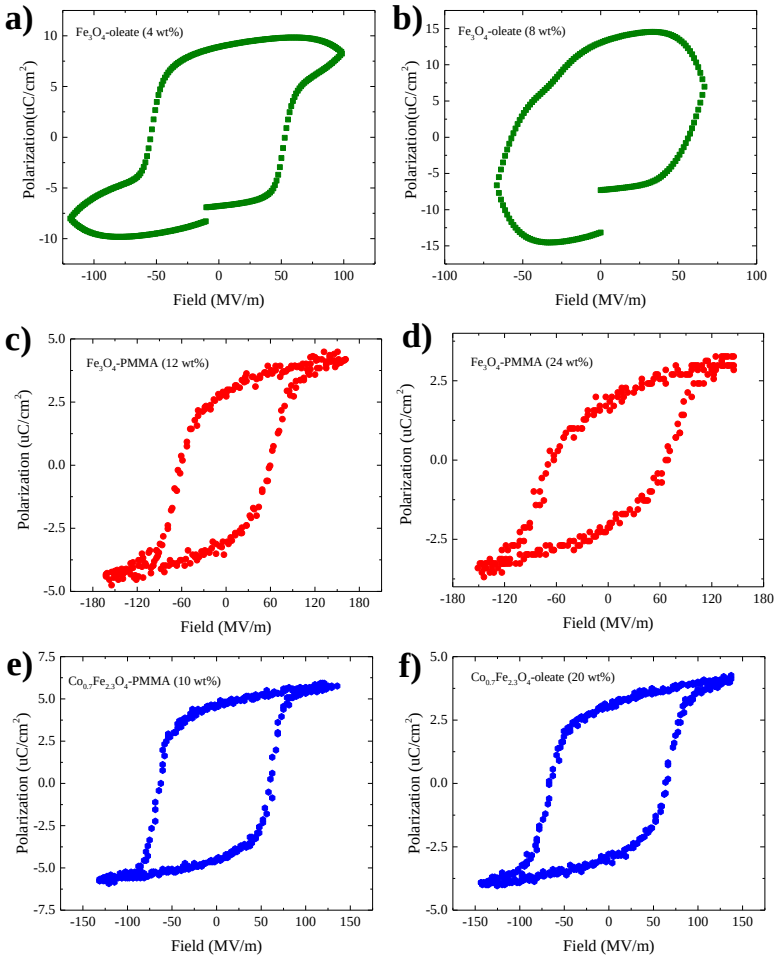

Figure 7.2.5 *D-E* loops of nanocomposite thin films of oleate coated iron oxide MNPs with (a) 4 wt% and (b) 8 wt%, Fe_3O_4-PMMA MNPs with (c) 12 wt% and (d) 24 wt% and (c) $Co_{0.7}Fe_{2.3}O_4$-PMMA MNPs with (e) 10 wt% and (f) 20 wt%.

To study the effect of the addition of MNPs-PMMA on the switching mechanism of P(VDF-TrFE), we perform polarization switching time study and performed polarization transient measurements.[12] Details of the measurement protocol are described in previous section.[13] **Figure 7.2.7a** shows polarization transients for pristine P(VDF-TrFE) and three representative nanocomposites thin films with different loading concentrations at a fixed field of 125 MV/m. For all cases, the polarization evolution can be well described by the KAI model used for the study of ferroelectric switching behavior (**Equations 7.1.1**). We also perform the

measurements of the polarization switching for the ferroelectric nanocomposite thin films with the logarithmic plots of the polarization *P* against the elapsed time *t* at different electrical field as a function of MNPs-PMMA compositions from 0 wt% to 36 wt%.

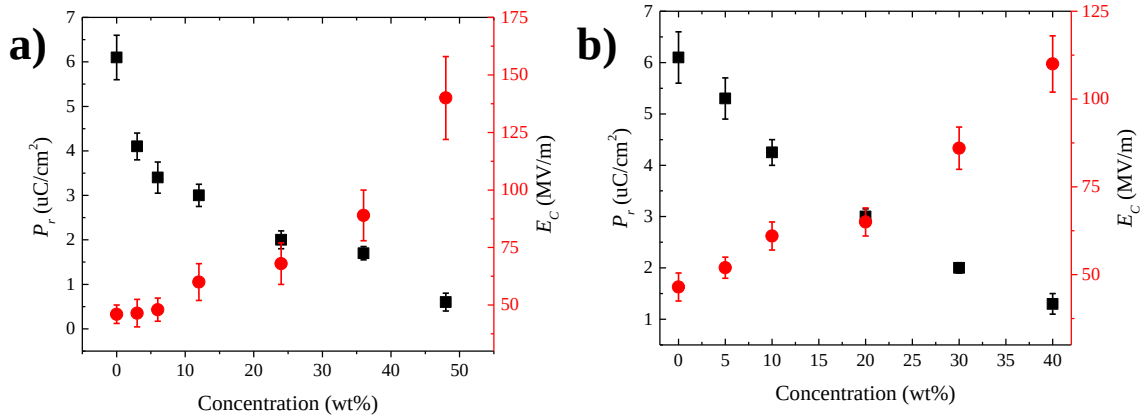

Figure 7.2.6 P_r and E_C of nanocomposite thin films from both (a) Fe_3O_4-PMMA/P(VDF-TrFE) and (b) $Co_{0.7}Fe_{2.3}O_4$-PMMA/P(VDF-TrFE).

The avrami index, *n*, for pristine P(VDF-TrFE) is very sensitive to the electrical field and amounts to *n* ~1.2 when the electrical field is125 MV/m.[14] For the nanocomposites with MNPs-PMMA, *n* is amounted to 1.2 for loading below 3 wt%. At loading >3 wt%, *n* remains unchangend (amount to 1) and becomes independent to the electrical field. As we mentioned in previous section, higher value of *n* for the pristine P(VDF-TrFE), indicates two dimensional nucleation and growth of domains.[15] Decreasing *n* is indicative of an increased number of nucleation sites, where the reversed polarization state sets in upon field application. Numerical simulation has shown that for the case of *n*= 1 irregular highly entangled domains are formed which indicates growth of one-dimensional wires. We therefore conclude that polarization reversal is nucleated along the P(VDF-TrFE) backbone at the vicinity of the MNPs-PMMA which in time grows to the crystalline part.

The dependence of the switching time on the applied electrical field is plotted in **Figure 7.2.7 b**. The field dependence of the switching time follows the empirical Merz law (**Equation 7.1.2**). From the fitting of the Merz law, we determine the values of t_∞ and E_{act}, as shown in **Figure 7.2.7 c**. The t_∞ of the nanocomposite thin film steadily increases from 8 ns to 400 ns as the loading increases from 0 wt% to 36 wt%. We therefore conclude that, the addition of the MNPs-PMMA results in the retardation of the switching speed. The similar increasing in

switching time by addition of PMMA chains into P(VDF-TrFE) has been shown in the literature.[10] On the other hand, E_{act} slightly reduces from 800 MV/m to 600 MV/m from 0 wt% to 36 wt%. Therefore, the activation field for polarization reversal remained in the nucleation-limited regime (~1 GV/m).

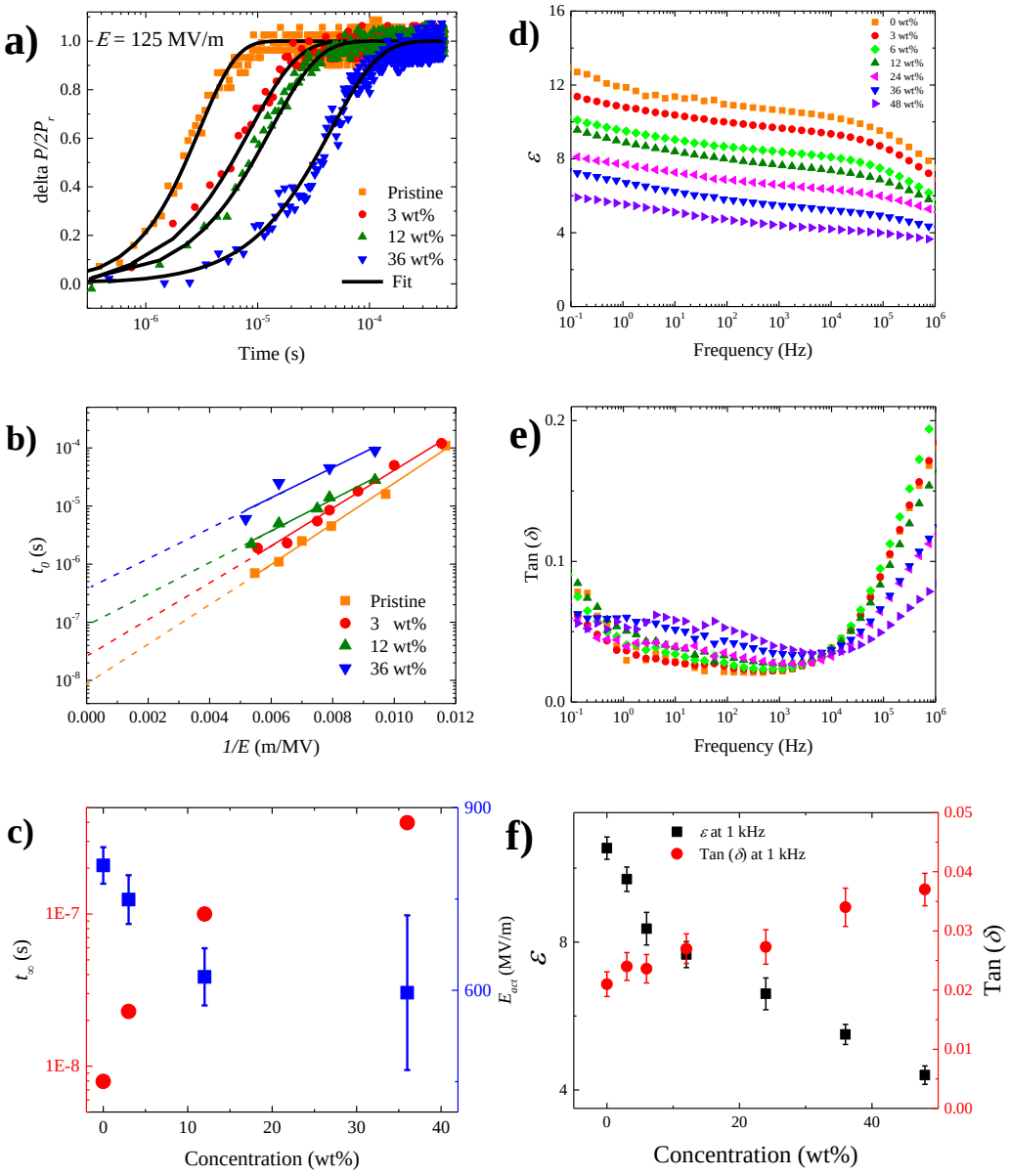

Figure 7.2.7 (a) Polarization reversal plot and the respective fits using KAI model. (b) The characteristic switching time t_0 as a function of reciprocal applied electric field. The lines show the fit obtained by Merz law. (c) Evolution of t_∞ and E_{act} as a function of nanoparticle loading. (d) Dielectric constant and (e) Tan(δ) of nanocomposite thin films as a function of frequency. (f) The summary of dielectric constant and Tan(δ) in different Fe_3O_4-PMMA concentration at 1kHz.

To investigate the effect of the addition of MNPs-PMMA on the dielectric constant and loss of the P(VDF-TrFE) nanocomposite thin films. We measure the dielectric permittivity, ε, and Tan(δ) at different frequencies. The dielectric constant for pristine P(VDF-TrFE) at 1 kHz amounts to ~10 and steadily decreases upon addition of MNPs-PMMA to 4.3 at 48% loading of Fe_3O_4-PMMA, as depicted in **Figure 7.2.7 e** and **g**. We note that addition of $Co_{0.7}Fe_{2.3}O_4$-PMMA has the same effect on the dielectric properties.

Based on the Maxwell-Garnett model, addition of the low dielectric constant material to high dielectric constant matrix reduced the effective dielectric constant of the whole blend. Here, the reduction in dielectric constant of the nanocomposite thin film, can be rationalized by addition of low dielectric constant material (PMMA) to high dielectric constant P(VDF-TrFE). The measured loss (Tan(δ)) of the nanocomposite thin films as a function of MNPs-PMMA loading is given in **Figure 7.2.7 f** and **g**. The value Tan(δ) slightly increases from 0.021 at 0% to 0.037 at 48% loading but still remain extremely low, at a comparable value with pristine P(VDF-TrFE). We note for the MNPs-PMMA, the loss is much lower in comparison with the oleate-coated MNPs especially at high loadings. These results are in accordance with the *D-E* loops, in which we observe huge leakage for MNPs-oleate but no leakage for MNPs-PMMA.

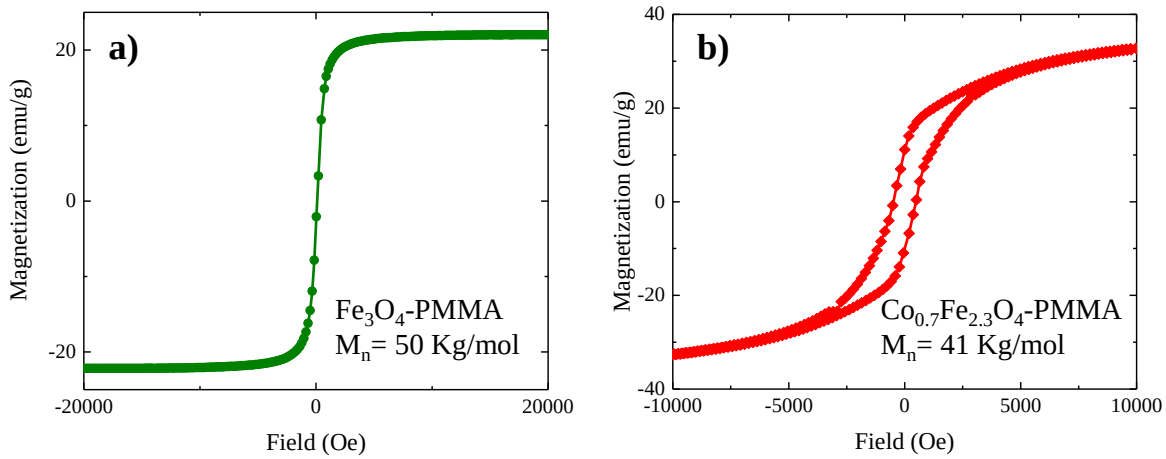

Figure 7.2.8 *M-H* curves of (a) Fe_3O_4-PMMA and (b) $Co_{0.7}Fe_{2.3}O_4$-PMMA MNPs.

Room temperature *M-H* curve of the PMMA-coated iron oxide and cobalt ferrite NPs are given in **Figure 7.2.8 a** and **b** respectively. The PMMA-Fe_3O_4 MNPs show superparamagnetic behavior at room temperature with saturation magnetization (M_S) of 22.5 emu/g. $Co_{0.7}Fe_{2.3}O_4$-

PMMA MNPs shows ferri/ferromagnetic behavior at room temperature with M_S of 38.3 emu/g, remanent magnetization (M_r) of 10.5 mu/g and corecieve field (H_C) of 496 Oe.

Moreover, normalization of the M_S of the nanocomposite corrected to the mass of the magnetic core of MNPs (after removal of the organic part, obtained by TGA results) results in the values of 72 ± 3 emu/g and 77 ± 4 emu/g for polymer coated iron and cobalt ferrite MNPs, respectively. These values for M_S are in agreement with the previous reported values and reported values in previous chapters.[16-19]

Room-temperature *M-H* curves of the nanocomposites of PMMA-coated iron oxide and cobalt-ferrite MNPs inside P(VDF-TrFE) matrix for different loadings as a function of applied magnetic field are given in **Figure 7.2.9 a** and **b**, respectively. The nanocomposite films show superparamagnetic or ferri/ferromagnetic behavior at room-temperature depending on the type of MNPs. Saturation magnetization (M_S) shows linear dependence with the concentration of MNP-PMMA inside nanocomposite films for both cases, as shown in the insets of the **Figure 7.2.9 a** and **b**.

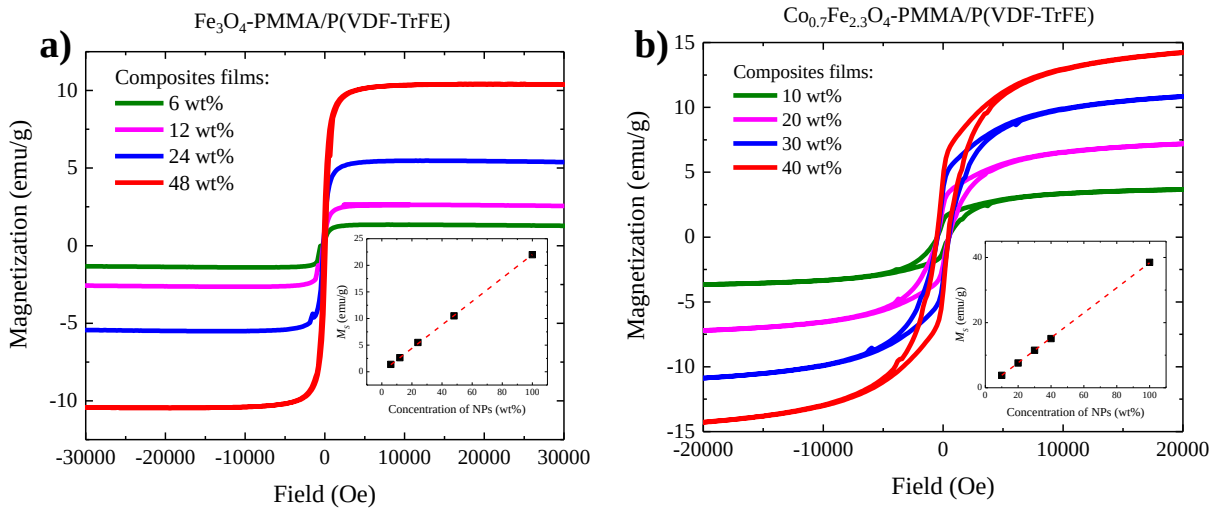

Figure 7.2.9 Field dependence of magnetization curves for nanocomposite film of polymer coated iron oxide (a) and cobalt ferrite (b) nanoparticles with different concentration at room temperature of 300 K. The amounts of saturation magnetization as a function of loading concentration for both types of MNPs are given in the inset of images.

We note that, the values of H_C at room temperature for the nanocomposite film in different loadings of $Co_{0.7}Fe_{2.3}O_4$-PMMA, remains unchanged (amounts to 485-505 Oe). The evolution in coercive field is different than addition of oleate coated MNPs (details in previous

section) into P(VDF-TrFE) matrix. There we observed increasing in coercive field by reducing the concentration of MNPs inside polymer matrix. We attributed that to the change in inter-particle distance by varying loading concentration which leads to the change in magnetic dipole-dipole interaction and subsequently the values of H_C and M_r/M_S. For the case of MNPs-PMMA, due to the presence of PMMA chains, the MNPs are already separated from each other. Therefore, further diluting the MNPs inside P(VDF-TrFE) matrix do not significantly change the magnetic dipole-dipole interaction. Hence, the coercive field remains unaffected.

7.2.4 Conclusion

We have successfully demonstrated solution-processed nanocomposite thin-film by loading modified ferrite MNPs (both superparamagnetic and ferromagnetic) in P(VDF-TrFE) matrix. By using MNPs-PMMA we effectively prevents agglomeration of the MNPs, since PMMA chains are miscible with P(VDF-TrFE) matrix even at high MNP loadings. Therefore, due to suppression of the MNPs aggregation inside polymer matrix, we removed leakage current, increase electrical breakdown strength, improve reproducibility of device performance and increase functional device yield. We showed that the dielectric loss at all loadings remained low at the value comparable to that of pristine P(VDF-TrFE) matrix. However, by using oleate coated MNPs, the functional device yield was significantly low especially for higher loadings and thinner nanocomposites films due to significant leakage current in capacitor devices. We observe that, by increasing the concentration of MNPs-PMMA, the crystallinity of nanocomposite decreases and leads to decreased P_r. In addition, we have shown that polarization reversal dynamics is highly sensitive to the nanoparticle concentration and the switching time increases upon loading of MNPs-PMMA.

The new developed multiferroic nanocomposite thin film shows both ferroelectric and magnetic properties (ferromagnetic and superparamagnetic) simultaneously without any particle aggregation and electrical loss in the system. The MNPs-PMMA and P(VDF-TrFE) are compatible and they are interacting system (both chemically and physically). Surface modification of nanoparticles is an efficient way to avoid aggregation inside polymer matrix and subsequently improve interfacial area between magnetic and ferroelectric phases (which may leads to increase of ME coupling). However, in order to increase the contribution of both phases

(magnetic and ferroelectric crystals) and subsequently more interface between them, it is better to reduce the molecular weight of grafted PMMA. On the other hand, the molecular weight of polymer chains should be high enough to avoid aggregation of the MNPs. The insight gained here, is very useful in the design of nanocomposites with optimized electric performance, particularly for PVDF-based nanocomposites in multiferroic and energy storage applications.

7.2.5 References

1. Xie, L.; Huang, X.; Huang, Y.; Yang, K.; Jiang, P., Core@ double-shell structured BaTiO3–polymer nanocomposites with high dielectric constant and low dielectric loss for energy storage application. *J. Phys. Chem. C* **2013,** *117*, 22525-22537.
2. Zhu, M.; Huang, X.; Yang, K.; Zhai, X.; Zhang, J.; He, J.; Jiang, P., Energy storage in ferroelectric polymer nanocomposites filled with core–shell structured polymer@ BaTiO3 nanoparticles: understanding the role of polymer shells in the interfacial regions. *ACS Appl. Mater. Interfaces* **2014,** *6*, 19644-19654.
3. Dehsari, H. S.; Kumar, M.; Saad, A.; Amiri, M. H.; Yan, C.; Anwar, S.; Glasser, G.; Asadi, K., Thin-Film Polymer Nanocomposites for Multiferroic Applications. *ACS Applied Nano Materials* **2018,** *1*, 6247-6257.
4. Li, M.; Stingelin, N.; Michels, J. J.; Spijkman, M.-J.; Asadi, K.; Feldman, K.; Blom, P. W.; de Leeuw, D. M., Ferroelectric phase diagram of PVDF: PMMA. *Macromolecules* **2012,** *45*, 7477-7485.
5. Kang, S. J.; Park, Y. J.; Bae, I.; Kim, K. J.; Kim, H. C.; Bauer, S.; Thomas, E. L.; Park, C., Printable ferroelectric PVDF/PMMA blend films with ultralow roughness for low voltage non-volatile polymer memory. *Adv. Funct. Mater.* **2009,** *19*, 2812-2818.
6. Dehsari, H. S.; Michels, J. J.; Asadi, K., Processing of ferroelectric polymers for microelectronics: from morphological analysis to functional devices. *Journal of Materials Chemistry C* **2017,** *5*, 10490-10497.
7. Sharifi Dehsari, H.; Asadi, K., The Impact of Stoichiometry and Size on Magnetic Properties of Cobalt-Ferrite Nanoparticles. *J. Phys. Chem. C* **2018**.
8. Dehsari, H. S.; Harris, R. A.; Ribeiro, A. H.; Tremel, W.; Asadi, K., Optimizing the Binding Energy of the Surfactant to Iron Oxide Yields Truly Monodisperse Nanoparticles.
9. Sharifi Dehsari, H.; Ksenofontov, V.; Möller, A.; Jakob, G.; Asadi, K., Determining Magnetite/Maghemite Composition and Core-Shell Nanostructure from Magnetization Curve for Iron Oxide Nanoparticles. *J. Phys. Chem. C* **2018**.
10. Bae, I.; Kang, S. J.; Park, Y. J.; Furukawa, T.; Park, C., Organic ferroelectric field-effect transistor with P (VDF-TrFE)/PMMA blend thin films for non-volatile memory applications. *Current Applied Physics* **2010,** *10*, e54-e57.
11. Clements, J.; Davies, G.; Ward, I., A broad-line nuclear magnetic resonance study of a vinylidene fluoride/trifluoroethylene copolymer. *Polymer* **1992,** *33*, 1623-1629.
12. Hu, W. J.; Juo, D.-M.; You, L.; Wang, J.; Chen, Y.-C.; Chu, Y.-H.; Wu, T., Universal Ferroelectric Switching Dynamics of Vinylidene fluoride-trifluoroethylene Copolymer Films. *Sci. Rep.* **2014,** *4*, 4772-4779.
13. Zhao, D.; Katsouras, I.; Asadi, K.; Blom, P. W.; de Leeuw, D. M., Switching Dynamics in Ferroelectric P(VDF-TrFE) Thin Films. *Phys. Rev. B* **2015,** *92*, 214115-214122.

14. Sharifi Dehsari, H.; Kumar, M.; Saad, A.; Hassanpour Amiri, M.; Yan, C.; Anwar, S.; Glasser, G.; Asadi, K., Thin-Film Polymer Nanocomposites for Multi-Ferroic Applications. *ACS Applied Nano Materials* **2018**.
15. Zhao, D.; Katsouras, I.; Asadi, K.; Blom, P. W.; de Leeuw, D. M., Switching dynamics in ferroelectric P (VDF-TrFE) thin films. *Physical Review B* **2015,** *92*, 214115-214122.
16. Dehsari, H. S.; Ribeiro, A. H.; Ersöz, B.; Tremel, W.; Jakob, G.; Asadi, K., Effect of precursor concentration on size evolution of iron oxide nanoparticles. *CrystEngComm* **2017,** *19*, 6694-6702.
17. Sharifi Dehsari, H.; Heidari, M.; Halda Ribeiro, A.; Tremel, W.; Jakob, G.; Donadio, D.; Potestio, R.; Asadi, K., Combined Experimental and Theoretical Investigation of Heating Rate on Growth of Iron Oxide Nanoparticles. *Chem. Mater.* **2017,** *29*, 9648-9656.
18. Park, J.; An, K.; Hwang, Y.; Park, J.-G.; Noh, H.-J.; Kim, J.-Y.; Park, J.-H.; Hwang, N.-M.; Hyeon, T., Ultra-large-scale syntheses of monodisperse nanocrystals. *Nat. Mater.* **2004,** *3*, 891.
19. Roca, A.; Morales, M.; O'Grady, K.; Serna, C., Structural and magnetic properties of uniform magnetite nanoparticles prepared by high temperature decomposition of organic precursors. *Nanotechnology* **2006,** *17*, 2783.

Chapter 8

Conclusion and Outlook

8.1 Summary

In developing multi-phase material systems, many variables like nanocomposite processing technique, synthesis and optimization of the constituent phases as well as their implementation into polymer matrix come into play. Only by addressing each step systematically, a new material with novel properties can be developed. In this thesis, a new type of room-temperature ferroelectric magnetic nanocomposite thin films based on (cobalt-) ferrite magnetic nanoparticles and ferroelectric polymer (P(VDF-TrFE)) was developed.

This work began with synthesize of truly monodisperse superparamagnetic (Fe_3O_4) and ferromagnetic ($Co_xFe_{3-x}O_4$) magnetic nanoparticles (MNPs) with different size and stoichiometry. We systematically investigated different reaction parameters to achieve nanoparticles with well-controlled size and with low polydispersity index (PDI), below 10%. Within the framework of LaMer's theory of nucleation and growth, we have explained how variation in the reaction heating rate and solvent/precursor/surfactant concentration enable fine-tuning of the MNP size. We accompanied the experimental findings with the numerical simulation to explain the observed trends. We controlled the size of synthesized iron oxide MNPs in the range of 5-25 nm with a narrow size distribution. In addition, we have fully characterized the magnetic properties of the MNPs in a long size span. We showed that, due to

low magnetocrytalline anisotropy of the iron-oxide MNPs, synthesized nanoparticles showed superparamagnetic behavior when the average diameter is below 20 nm.

Furthermore, we thoroughly investigated the magnetic properties of $Co_xFe_{3-x}O_4$ MNPs as function of different cobalt stoichiometry (x) as well as size. We showed that, the optimum x value was obtained in the range of 0.5-0.7 at which the MNPs exhibited the highest H_C, M_r/M_S, T_B and K_{eff}, suited for room-temperature applications of the cobalt-ferrite MNPs as ferromagnetic nanomaterial. Moreover, we experimentally demonstrated that the commonly observed bi-magnetic behavior of magnetization in cobalt-ferrite MNPs is due to inter-particle dipolar interactions. Then, at the optimum cobalt stoichiometry, we tuned the size of the cobalt-ferrite MNPs through a systematic change of the reaction parameters in thermal decomposition. We experimentally demonstrated that 10 nm is the smallest particle diameter at which cobalt-ferrite MNPs show remanent magnetization stable at room-temperature.

Next we presented a systematic study on surface functionalization of the MNPs with a poly methyl methacrylate (PMMA) polymer chains that: i) allows for solution processing of the polymer-grafted MNPs using solution processing techniques, ii) improves the colloidal stability of MNPs and iii) is compatible with P(VDF-TrFE) matrix which later was used for the fabrication of the multiferroic polymer nanocomposite thin films.

We used grafting from polymerization method based on SI-ATRP to grow PMMA shell on the surface of MNPs. Our new method of SI-ATRP in bath sonication for the polymerization of PMMA yielded perfectly dispersed MNPs particles grafted with well-defined and dense PMMA shell with controllable shell thickness. The effect of different polymerization reaction conditions (such as temperature and concentration of reagents) on kinetic, molecular weight and PDI of grafted polymer were investigated. Grafting the MNPs with PMMA shell, improved the colloidal stability of the MNPs by reducing the inter-particle magnetic interactions. We prepared spin-coated thin films of the MNPs with high degree of packing order and wide controllability of the inter-particle distances. Growing PMMA shell influenced the magnetic properties of the MNPs (H_C, T_B, M_r/M_S) through modifying the inter-particle, which led to the change in magnetic dipole-dipole interaction and subsequently anisotropy energy. We observed that by increasing the inter-particle distance the H_C and M_r/M_S increased while T_B decreased.

Our prime candidate as ferroelectric polymer in ME nanocomposite thin films is the ferroelectric polymer, P(VDF-TrFE). However, solution processing of P(VDF-TrFE) under normal condition resulted in rough and porous thin films which typically gives a low yield of working devices (ferroelectric capacitors, ferroelectric memory diodes and *etc.*). A major challenge is ambient water vapor condensing into the drying solution, causing non-solvent vapor-induced phase separation (VIPS). Therefore, by integrating solution-stage modeling, microscopic analysis and ferroelectric thin film capacitor characterization, we introduced ways to improve the thin film quality. We showed that the hydrophilicity of solvent is a deciding factor in obtaining properly functioning capacitive memory elements based on P(VDF-TrFE) thin films. We obtained smooth thin films of P(VDF-TrFE) under optimized processing condition (at an inert atmosphere or at an elevated substrate temperature) or by using sufficiently low solvent hygroscopicity. By improving the thin film quality we increased the functional device yield and narrow down the coercive voltage distribution.

In the next step, once the MNPs and thin film solution processing have been modified, thin-films of solution processed P(VDF-TrFE) nanocomposites with both unmodified and modified MNPs were prepared. We observed that the crystallinity of nanocomposite films decreases and leads to reduction of P_r by increasing the concentration of MNPs. We observed that, the $T_{Melting}$, T_{Curie}, and $T_{Crystalization}$, of P(VDF-TrFE) nanocomposite monotonically decreased with addition of MNPs-PMMA. This observation confirmed that P(VDF-TrFE) and MNPs-PMMA were miscible and interacting with each other over the entire composition range both in the melt and when quenched into a vitreous solid solution. Oleate and P(VDF-TrFE) are non-interacting system and addition of oleate-coated MNPs into P(VDF-TrFE) did not change $T_{Melting}$, T_{Curie}, and $T_{Crystalization}$. We have unambiguously shown that addition of the non-ferroelectric nanoparticles did not enhance formation of the ferroelectric β-phase or other crystalline phases in P(VDF-TrFE). In addition, we have shown that polarization reversal dynamics is highly sensitive to the nanoparticle concentration and the switching time increased upon loading of the MNPs. We have attributed the increase in the switching time to the shift of the polarization switching dynamic from a two- to a one-dimensional process. The nanocomposite films showed either superparamagnetic or ferromagnetic properties depending on the type of MNPs. Moreover, we noted that, the magnetic properties (H_C, T_B, M_r/M_S) depended on the concentration of MNPs

inside nanocomposite films. We attributed this observation to the change in particle-particle distance inside polymer matrix by changing the concentration of MNPs and as a result variation in magnetic dipole-dipole interaction.

We observed that, the solution of oleate coated MNPs/P(VDF-TrFE) is colloidally stable for some time. Up on solution casting and solvent evaporation, the MNPs inside nanocomposite thin films phase separated. We showed that the phase separation process led to the agglomeration of the nanoparticle in the amorphous regions of the P(VDF-TrFE) matrix. At high nanoparticle loading, the phase separation yielded a stratified bilayer film. The agglomerations of MNPs not only increased leakage but also gave rise to low breakdown strength, lowered functional device yield and reduced the reproducibility. We effectively prevented agglomeration of the MNPs inside polymer matrix by using modified MNPs-PMMA even at high loadings. Therefore, due to suppression of the MNPs aggregation inside polymer matrix, we removed leakage current, increased electrical breakdown strength, improved reproducibility of the devices and increased functional device yield. We showed that the dielectric loss at all loadings remained low at the value comparable to that of pristine P(VDF-TrFE) matrix. The newly developed multiferroic nanocomposite thin film showed both ferroelectric and magnetic properties (ferromagnetic and superparamagnetic) simultaneously without any particle aggregation and electrical loss in the system.

8.2 Outlook

Results of this dissertation open up the door for several interesting investigations in future. This dissertation has developed a new type of polymer-based ME nanocomposite thin films consisting ferroelectric polymer and inorganic MNPs. The next step is to determine the coupling between the MNPs and the ferroelectric polymer matrix. Then it is necessary to investigate the effect of PMMA shell thickness on the coupling strength and determine the optimum shell thickness while keeping the homogenously distributed MNPs. The insight gained here, particularly on formation of the microstructure, is very useful in the design of the nanocomposites with optimized electric performance, especially for preparing high dielectric constant PVDF-based nanocomposites for energy storage application. Moreover, using other ferroelectric polymers combined with MNPs deserve attention due to novel properties they bring

to ME nanocomposites. For instance, nylon and poly lactic acid (PLA) are important ferroelectric materials which can offer new approaches for different type of application in energy storage and biomedical, respectively. Moreover, the vision gained here regarding synthesis and surface modification of inorganic nanoparticles and processing of the nanocomposite is useful for preparing different types of nanocomposites for other application such as in electronics, biology, energy storage and data storage.

Appendix

A3.1 Chapter 3 and Section 1

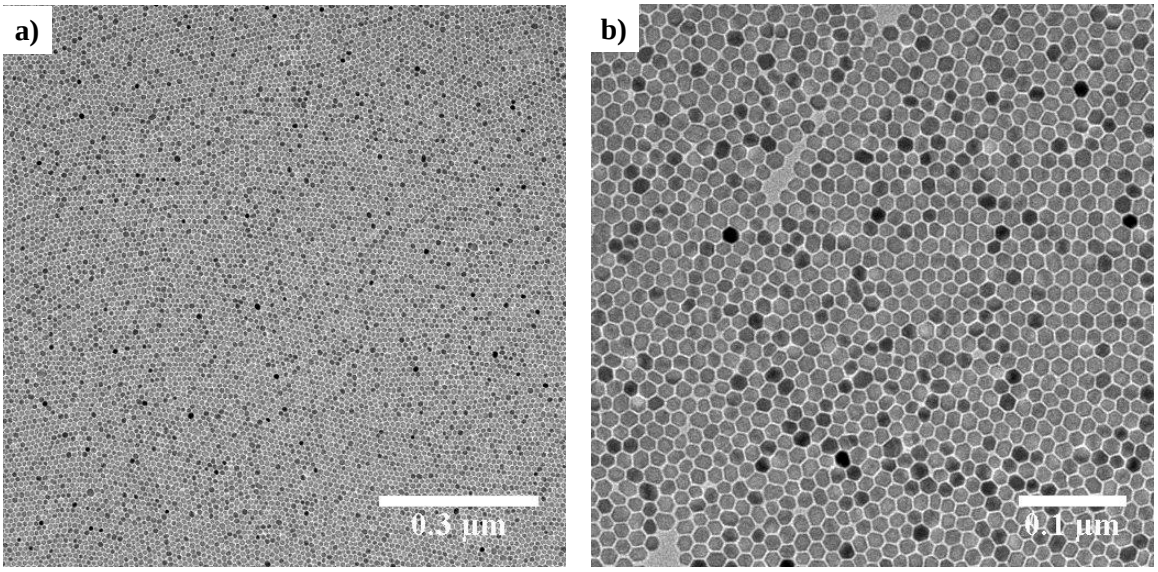

Figure A3.1.1 Large scale TEM images of samples (a) A_3 and (b) A_5.

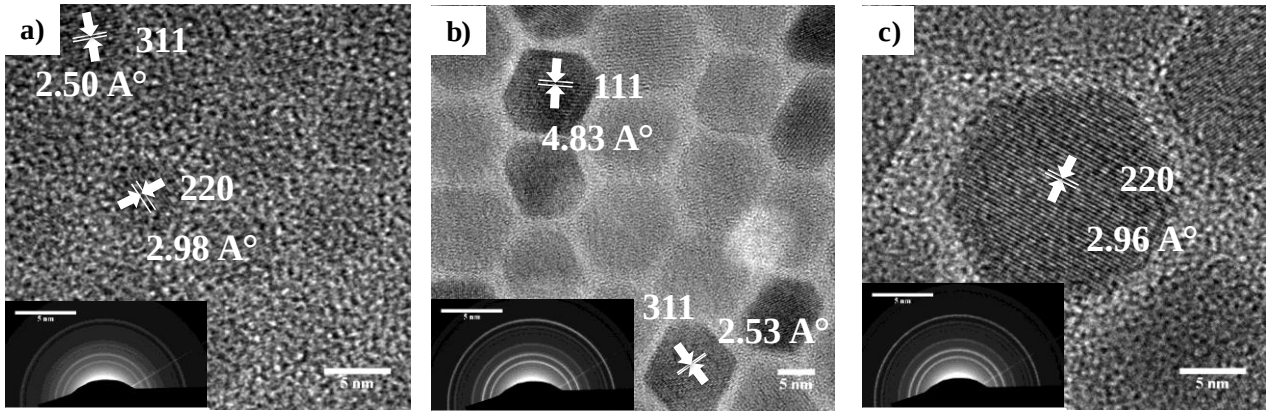

Figure A3.1.2 HRTEM images of samples (a) A_1, (b) A_3 and (c) A_6. Selected area electron diffraction (SAED) patterns are also shown in the inset of the respective images.

A3.2 Chapter 3 and Section 2

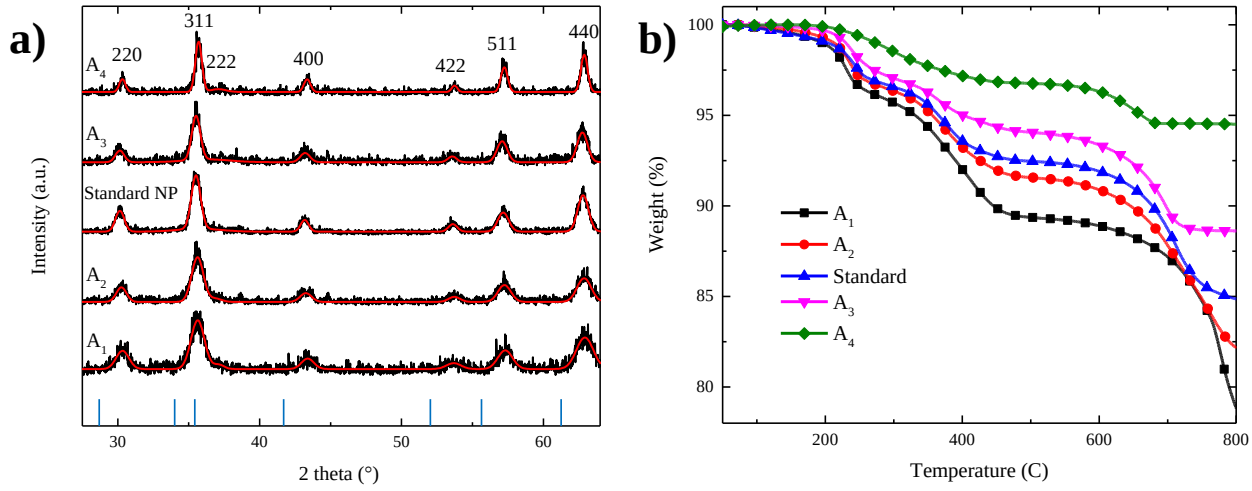

Figure A3.2.1 (a) XRD patterns of five batches of Nanoparticles (black data) and their corresponding modelisations (red data). Positions of the Bragg reflections are represented by vertical blue bars. (b) TGA graphs of the samples A_1-A_4 from 30-800 °C under N_2.

A5. Chapter 5

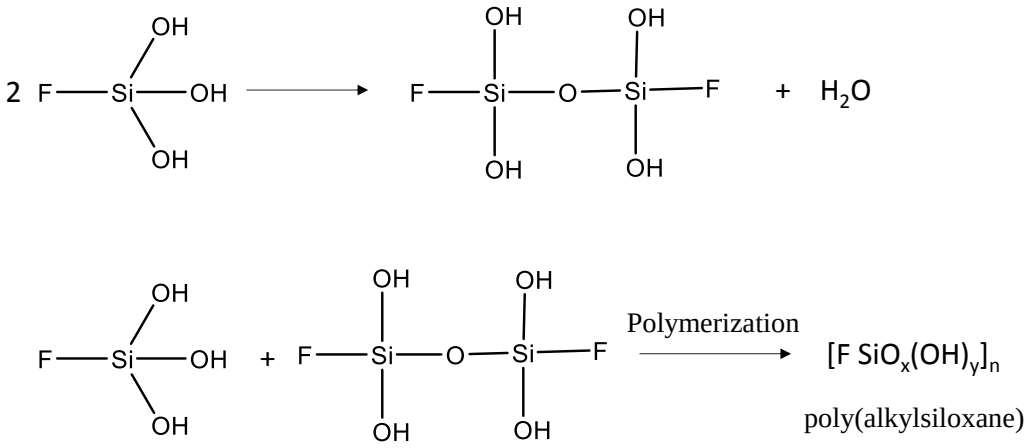

Figure A5.1 Formation of poly(alkylsiloxane) upon condensation and polymerization.

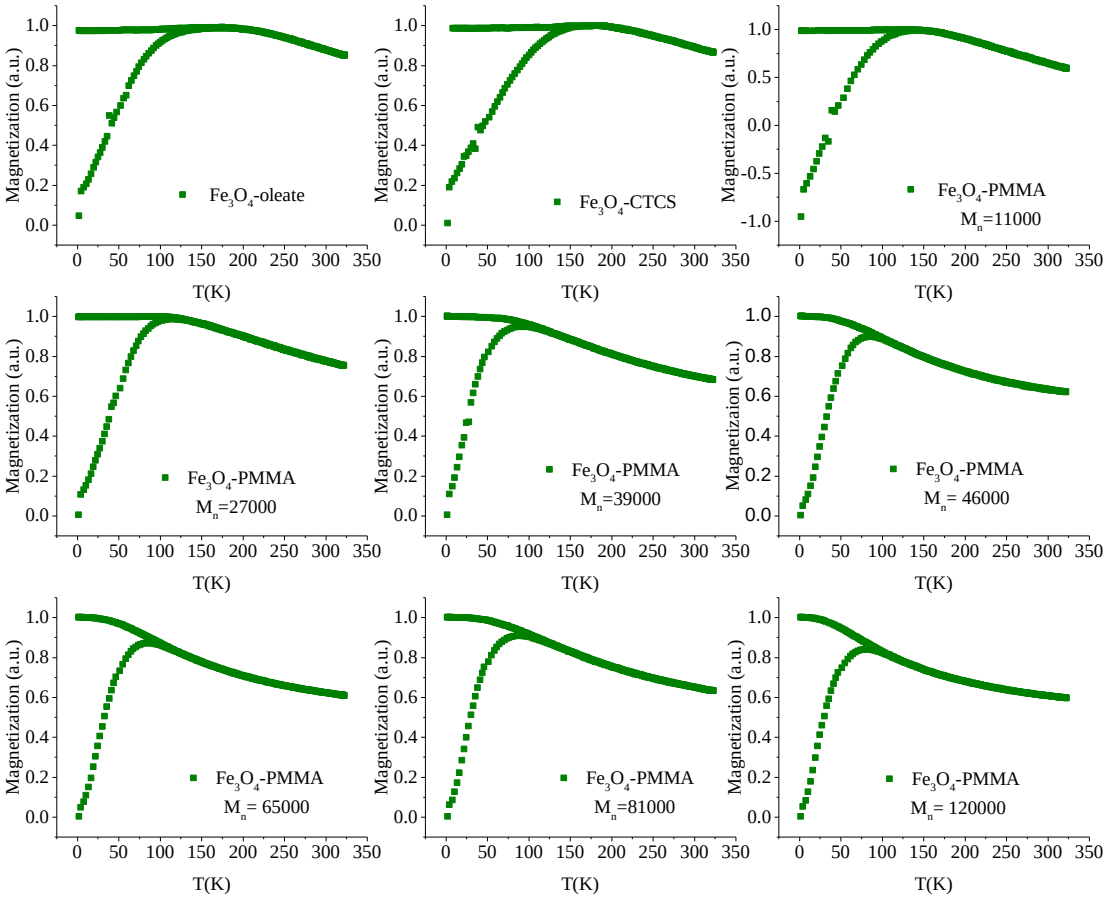

Figure A5.2 ZFC and FC curves of Fe_3O_4-PMMA with different molecular weight of grafted organic material.

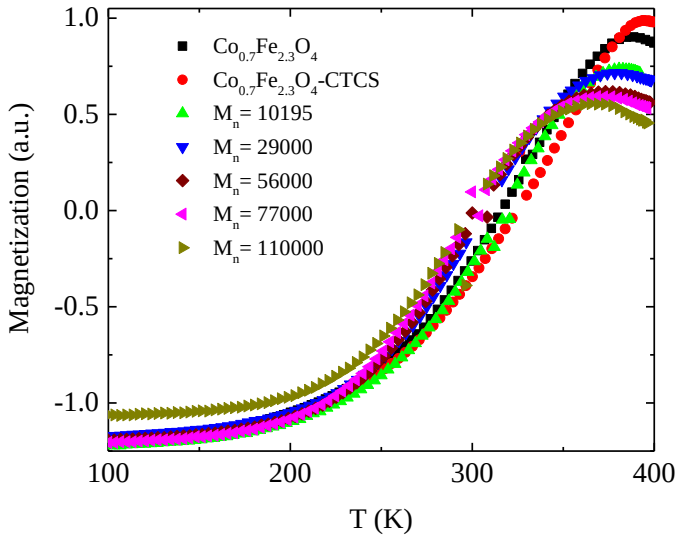

Figure A5.3 ZFC and FC curves of $Co_{0.7}Fe_{2.3}O_4$-PMMA with different molecular weight of grafted organic material.

A6.1 Chapter 6 and Section 1

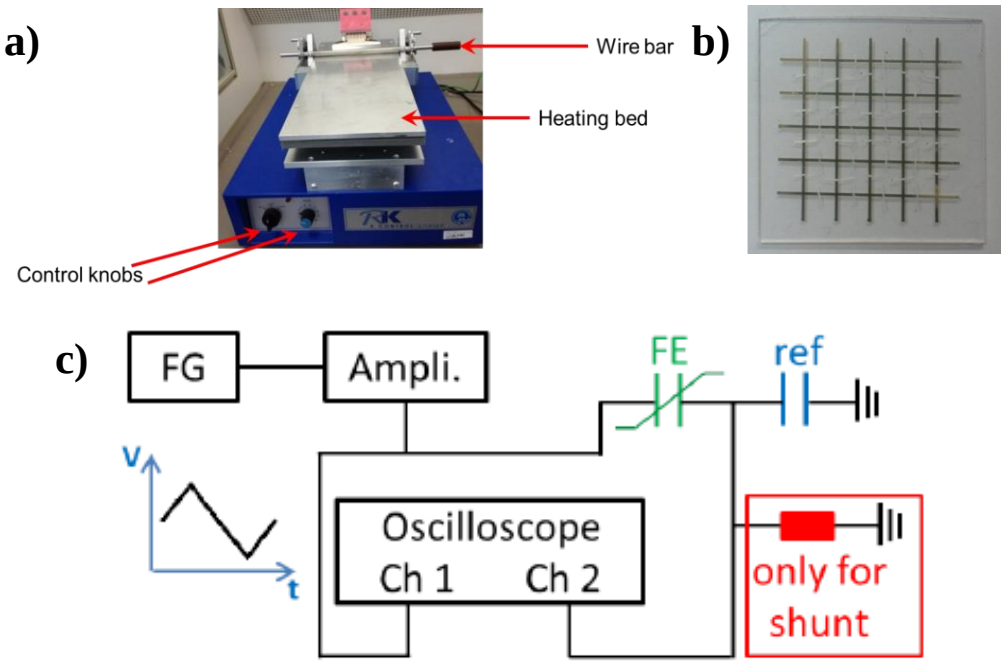

Figure A6.1 (a) K102 K Control Coater from RK PrintCoat. (b) Architecture of capacitor device on a glass substrate. (c) Schematic of the Sawyer-Tower measurement setup. A triangular waveform provided by a function generator (FG) is amplified (Ampli.) and applied to the ferroelectric capacitor that shall be investigated. The ferroelectric capacitor is in series with a reference capacitor, the capacitance of which is high and known. The

connected oscilloscope measures two voltage transients. Channel 1 (*Ch 1*) measures the voltage applied over the entire circuit, while Channel 2 (*Ch 2*) measures the voltage drop over the reference capacitor. Since the capacitance is known, the charge can be determined, which has to be equivalent to the charge on the ferroelectric capacitor, because both are in series. Based on that, the ferroelectric displacement can be determined. The Sawyer-Tower measurement setup can be transformed into a shunt measurement setup by simply replacing the reference capacitor by a reference resistor. The image and explanation has been adapted from Ref. 21 of Chapter 6.

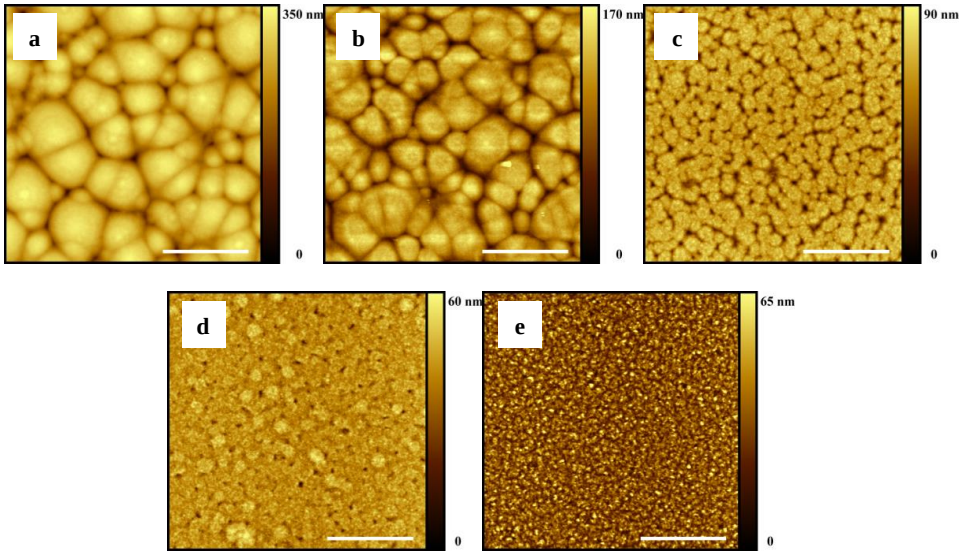

Figure A6.2 AFM height images of P(VDF-TrFE) thin films coated from solution in DMF at 50% relative humidity and substrates temperature of (a) 20°C, (b) 35°C, (c) 50°C, (d) 65°C and (d) 80°C. The scale bar is 10 µm.

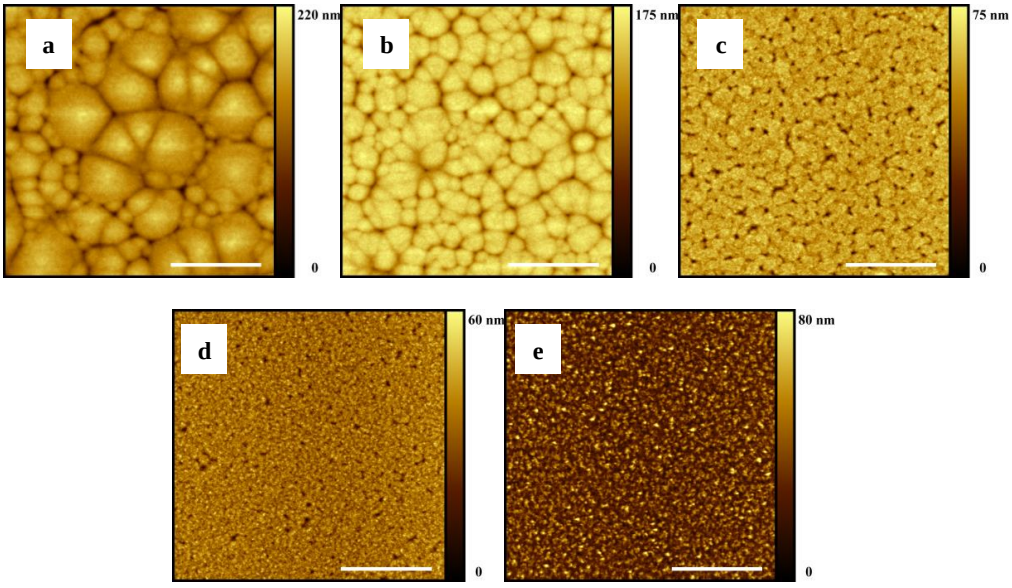

Figure A6.3 AFM height images of P(VDF-TrFE) thin films coated from solution in a-DMF at 50% relative humidity and substrates temperature of (a) 20°C, (b) 35°C, (c) 50°C, (d) 65°C and (d) 80°C. The scale bar is 10 µm.

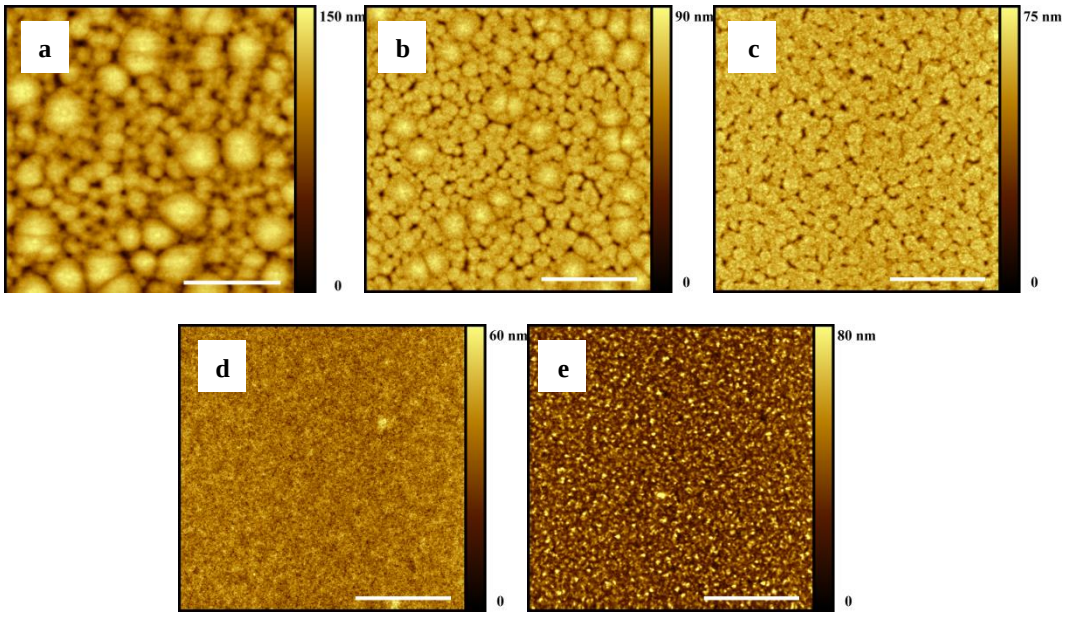

Figure A6.4 AFM height images of P(VDF-TrFE) thin films coated from solution in a-DMF at 10% relative humidity and substrates temperature of (a) 20°C, (b) 35°C, (c) 50°C, (d) 65°C and (d) 80°C. The scale bar is 10 µm.

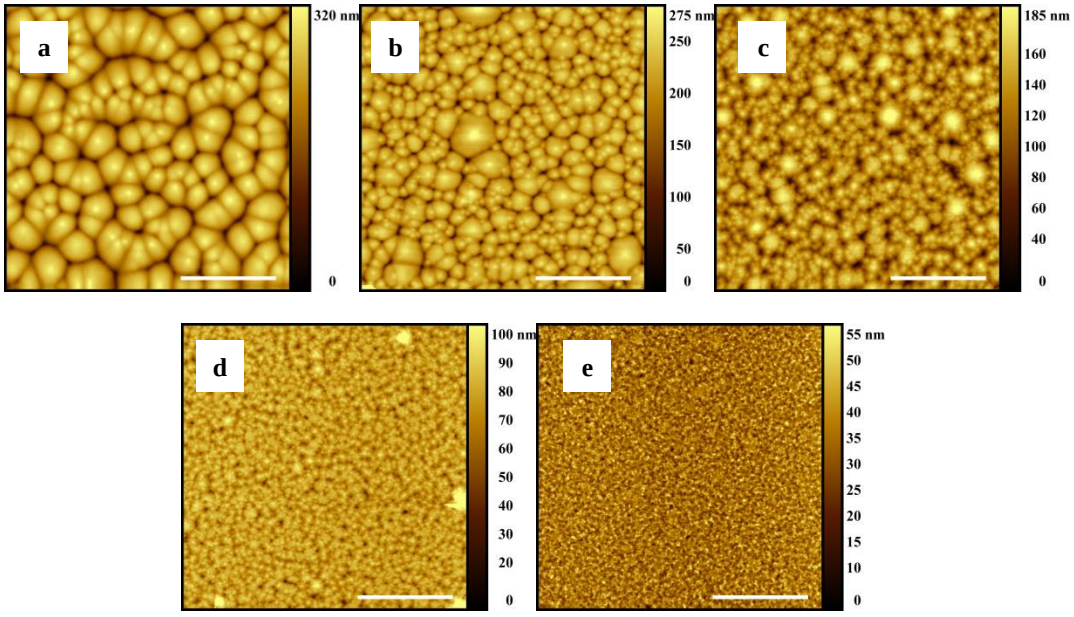

Figure A6.5 AFM height images of P(VDF-TrFE) thin films coated from solution in cyclohexanone at 50% relative humidity and substrates temperature of (a) 20°C, (b) 35°C, (c) 50°C, (d) 65°C and (d) 80°C. The scale bar is 10 µm.

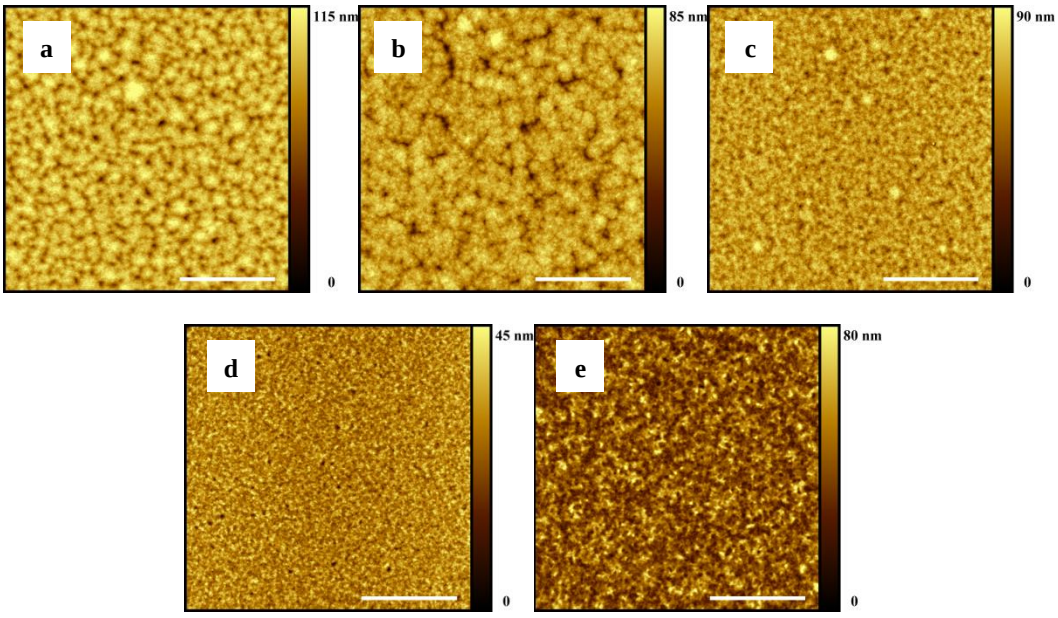

Figure A6.6 AFM height images of P(VDF-TrFE) thin films coated from solution in cyclopentanone at 50% relative humidity and substrates temperature of (a) 20°C, (b) 35°C, (c) 50°C, (d) 65°C and (d) 80°C. The scale bar is 10 μm.

A7.1 Chapter 7 and Section 1

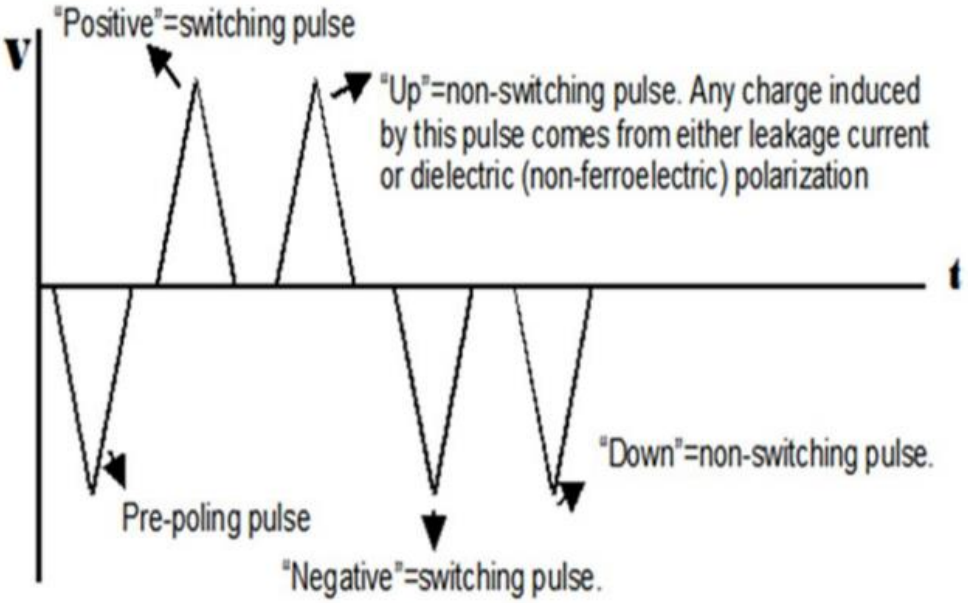

Figure A7.1.1 Schematic of a PUND measurement. The image has adapted from Ref. 60 (section 1 of Chapter 7).

A7.2 Chapter 7 and Section 2

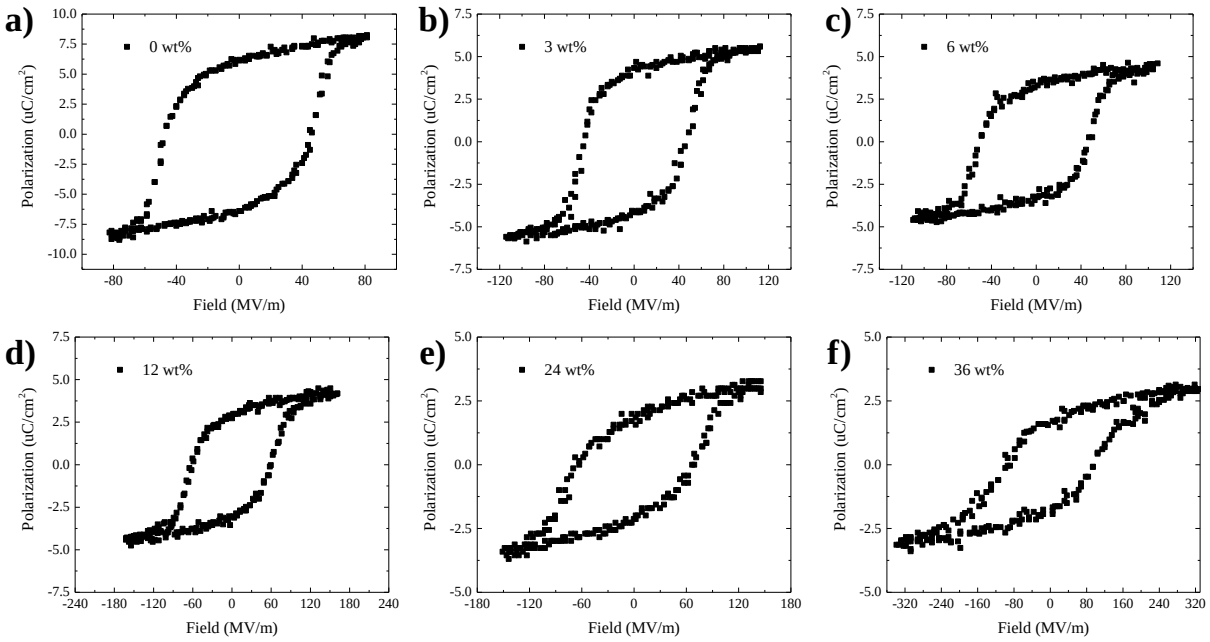

Figure S7.2.1 *D-E* loops of nanocomposite thin films for different concentrations of Fe_3O_4-PMMA.

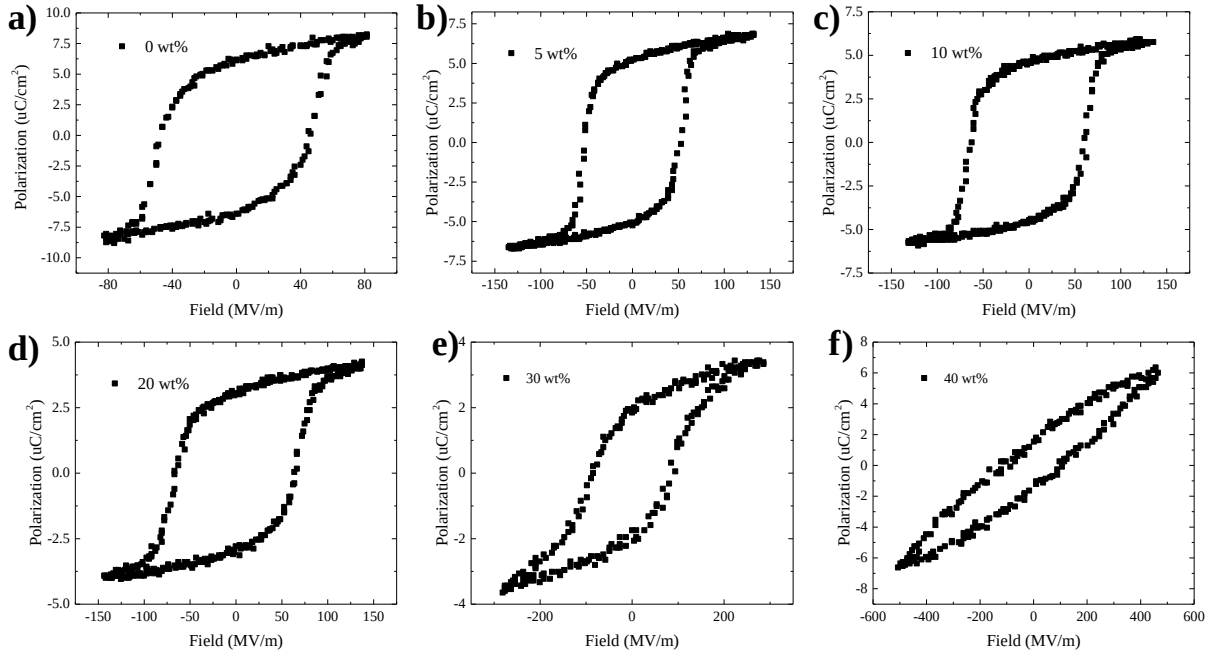

Figure S7.2.2 *D-E* loops of nanocomposite thin films for different concentrations of $Co_{0.7}Fe2_{.3}O_4$-PMMA.

Publications:

Accepted:

1. The Impact of Stoichiometry and Size on Magnetic Properties of Cobalt-Ferrite Nanoparticles

H. Sharifi, K. Asadi, *J. Phys. Chem. C*, 2018, 29106.

2. Determining Magnetite/Maghemite Composition and Core-Shell Nanostructure from Magnetization Curve for Iron Oxide Nanoparticles

H. Sharifi, V. Ksenofontov, A. Möller, G. Jakob, K. Asadi, *J. Phys. Chem. C*, 2018, 28292.

3. Thin-Film Polymer Nanocomposites for Multiferroic Applications

H. Sharifi, M. Kumar, A. Saad, M. H. Amiri, C. Yan, S. Anwar, G. Glasser, K. Asadi, *ACS Appl. Nano Mater.*, 2018, 6247.

4. Optimizing the Binding Energy of the Surfactant to Iron-Oxide Yields Truly Monodisperse Nanoparticles

H. Sharifi, R. A. Harris, A. H. Rebeiro, W. Tremel, K. Asadi, *Langmuir, 2018*, 6582.

5. Interfacial conduction in organic ferroelectric memory diodes

H. Sharifi, M. Kumar, M. Ghittorelli, T. Lenz, D. M. De Leeuw, F. Torricelli, K. Asadi. *Appl. Phys. Lett., 2018*, 093302.

6. Ammonia-Sensing Using a Composite of Graphene Oxide and Conducting Polymer

A. Hasani, **H. Sharifi**, M. A. Lafmejani, A. Salehi, F. A. Taromi, K. Asadi, S. Y. Kim, *physica status solidi (RRL)–Rapid Research Letters*, 2018, 1870317.

7. Air-stable Memory Array of Switchable Rectifying Diodes Based on Phase-Separated Ferroelectric Blends

M. Kumar, **H. Sharifi**, S. Anwar, K. Asadi, Appl. Phys. Lett., 2018, 123302.

8. Elastic wave propagation in smooth and wrinkled stratified polymer films

M. Hesami, A. Gueddida, N. Gomopoulos, **H. Sharifi**, K. Asadi, S. Rudykh, H. J. Butt, B. Djafari-Rouhani, G. Fytas, *Nanotechnology*, 2018, 045709.

9. Solution-processed transparent ferroelectric nylon thin-films

S. Anwar, D. Pinkal, W. Zajaczkowski, P. Tiedemann, **H. Sharifi**, M. Kumar, T. Lenz, U. Kemmer-Jonas, W. Pisula, M. Wagner, R. Graf, H. Frey, K. Asadi, *Sci. Adv., Under Review*, 2018.

10. Combined Experimental and Theoretical Investigation of Heating Rate on Growth of Iron Oxide Nanoparticles

H. Sharifi, M. Heidari, A. H. Ribeiro, Wo. Tremel, G. Jakob, D. Donadio, R. Potestio, K. Asadi.,

Chem.Mater., 2017, 9648.

11. Effect of Precursor Concentration on Size Evolution of Iron Oxide Nanoparticles

H. Sharifi, A. H. Ribeiro, B. Ersöz, W. Tremel, G. Jakob, K. Asadi, *CrystEngComm*, 2017, 19, 6694.

12. Processing of Ferroelectric Polymers for Microelectronics: From Morphological Analysis to Functional Devices

H. Sharifi, J. J. Michels, K. Asadi, *J. Mat. Chem. C*, 2017, 5, 10490.

13. Quantum Tunneling and Charge Accumulation in Organic Ferroelectric Memory Diodes

M. Ghittorelli, T. Lenz, **H. Sharifi**, D. Zhao, K. Asadi, P. W. M. Blom, Z. M. Kovács-Vajna, D. M. de Leeuw, F. Torricelli, *Nat. Commun.*, 2017, 15741.

14. Thin Film Thermistor with Positive Temperature Coefficient of Resistance Based on Phase Separated Blends of Ferroelectric and Semiconducting Polymers

T. Lenz, **H. Sharifi**, K. Asadi, P. W.M. Blom, W. A. Groen, D. M. De Leeuw, *Appl. Phys. Lett.*, 2016, 133302.

To be submitted:

15. Large-Area Solution Processable Thin-Films of Nano-Magnets with Controllable Packing Density

H. Sharifi, W. Tremel, J. Yan, K. Matyjaszweski, K. Asadi, *Adv. Func. Mater.*, 2018.

16. Novel Thin-Film Polymer Nanocomposites of P(VDF-TrFE) and PMMA coated magnetic nanoparticles for multiferroic application

H. Sharifi, M. H. Amiri, K. Asadi, *Under preparation*, 2019.

17. Self-Assembled Magnetic Nanoparticles-Polymer Shell Nanocomposites for Magnetic Recording Media

H. Sharifi, K. Asadi, *Under preparation*, 2019.

18. Thin-Film Polymer Nanocomposites for Multi-Ferroic Applications Based on Magnetic Nanoparticles-Polymer Shell and P(VDF-TrFE)

H. Sharifi, M. Hassanpour, K. Asadi, *Under preparation*, 2019.

19. Ferroelectric and Dielectric Properties of Poly(vinylidene fluoride) Nanocomposite Thin Films Filled with Iron Oxide Nanoparticles

H. Sharifi, C. Yan, S. Anwar, M. Kumar, K. Asadi, *Under preparation*, 2019.

20. Water-Dispersible Magnetic Nanoparticles with high stability and selective Surface Functionalities

A. Amiri, **H. Sharifi**, K. Asadi, *Under preparation*, 2018.

Conferences:

1. Vapour-Induced Demixing in Solution-Processed Ferroelectric Films for Organic Memory Applications

J. Michels, **H. Sharifi**, K. Asadi, **(Oral)**, *Am. Phys. Soc. March meeting,* 2018, Los Angeles, California.

2. Toward Solution Processed Magnetic Nanoparticles for non-Volatile Memory Applications

H. Sharifi, A. H. Ribeiro, K. Asadi, **(Oral)**, *SPIE Organic Photonics+Electronics,* 2017, San Diego, United States.

3. Ambient Processing of P(VDF-TrFE) Ferroelectric Thin-Films for Application in non-Volatile Memory Devices

H. Sharifi, A. Saad, J. J. Michels, K. Asadi, **(Oral)**. *16th International Symposium on Electrets (ISE16),* 2017, Leuven, Belgium.

4. Theoretical Understanding of Film Formation in Solution-processed Ferroelectric Polymers

H. Sharifi, D. M. de Leeuw, P. W. M. Blom, J. J. Michels, K. Asadi, **(Oral)**, *ISAF/ECAPD/PFM Conference, 2016,* Darmstadt, Germany.

5. Solution Processed Magnetic Nanoparticles Synthesized Using Surface Initiated Atom Transfer Radical Polymerization of Methyl Methacrylate for non-Volatile Memory Applications

H. Sharifi, A. H. Ribeiro, K. Asadi. **(Poster)**, *14th European Conference on Molecular Electronics,* 2017, Dresden, Germany.

6. Ambient Processing of P(VDF-TrFE) Ferroelectric Thin-Films for Application in non-Volatile Memory Devices

H. Sharifi, J. J. Michels and K. Asadi. **(Best Poster Prize)**, *13th International Conference on Organic Electronics(ICOE),* 2017, St. Petersburg, Russia.